

Shiny helmets: investigation of tinning, manufacture and corrosion of Greek helmets (7th-5th c. BC).

Panagiota Manti

Department of Archaeology and Conservation

School of History, Archaeology and Religious Studies

Thesis submitted in fulfilment of the requirements for the

Degree of Doctor of Philosophy

Cardiff University

2011



Manti, Panagiota (2012). Shiny helmets: investigation of tinning, manufacture and corrosion of Greek helmets (7th-5th c. BC). PhD thesis, Cardiff University.

Supervisors: Prof. D. Watkinson, Prof. Ian Freestone

Examination date: 19th March 2012.

Examiners: Prof. Mark Pollard, RLAHA, University of Oxford.

Dr John Merkel, Institute of Archaeology, UCL.

Some figures have been removed for copyright reasons.

Copyright is owned by the author unless otherwise stated.



DECLARATION

This work has not previously been accepted in substance for any degree and is not concurrently submitted in candidature for any degree.

Signed (candidate) Date

STATEMENT 1

This thesis is being submitted in partial fulfilment of the requirements for the degree of(insert MCh, MD, MPhil, PhD etc, as appropriate)

Signed (candidate) Date

STATEMENT 2

This thesis is the result of my own independent work/investigation, except where otherwise stated. Other sources are acknowledged by explicit references.

Signed (candidate) Date

STATEMENT 3

I hereby give consent for my thesis, if accepted, to be available for photocopying and for inter-library loan, and for the title and summary to be made available to outside organisations.

Signed (candidate) Date

STATEMENT 4: PREVIOUSLY APPROVED BAR ON ACCESS

I hereby give consent for my thesis, if accepted, to be available for photocopying and for inter-library loans **after expiry of a bar on access previously approved by the Graduate Development Committee.**

Signed (candidate) Date

Cardiff University Electronic Theses and Dissertations Publication Form

This form is to be completed by those choosing to make the full text of their work electronically available.

Details of the Work

I hereby deposit the following item in the digital repository (ORCA) maintained by Cardiff University, and/or in any other repository authorized for use by Cardiff University:

Author Name: Panagiota Manti

Title: Shiny helmets: investigation of tinning, manufacture and corrosion of Greek helmets (7th-5th c. BC).

Supervisor/School: David Watkinson, Department of Archaeology & Conservation, SHARE

Research grant (if any):

Qualification/Degree obtained: PhD Conservation

This item is a product of my own research endeavours and is covered by the agreement below in which the item is referred to as “the Work”.

Non-exclusive Rights

Rights granted to the digital repository through this agreement are entirely non-exclusive. I am free to publish the Work in its present version or future versions elsewhere.

I agree that Cardiff University may electronically store, copy or translate the Work to any approved medium or format for the purpose of future preservation and accessibility. Cardiff University is not under any obligation to reproduce or display the Work in the same formats or resolutions in which it was originally deposited.

Cardiff University Digital Repository

I understand that work deposited in the digital repository will be accessible to a wide variety of people and institutions, including automated agents and search engines via the World Wide Web.

I understand that once the Work is deposited, the item and its metadata may be incorporated into public access catalogues or services, national databases of electronic theses and dissertations such as the British Library’s EThOS or any service provided by the National Library of Wales.

I understand that the Work may be made available via the National Library of Wales Online Electronic Theses Service under the declared terms and conditions of use (link or append). I agree that as part of this service the National Library of Wales may electronically store, copy or convert the Work to any approved medium or format for the purpose of future preservation and accessibility. The National Library of Wales is not under any obligation to reproduce or display the Work in the same formats or resolutions in which it was originally deposited.

The Student's attention is particularly drawn to the following clauses.

I agree as follows:

1. That I am the author or have the authority of the author/s to make this agreement and do hereby give Cardiff University the right to make available the Work in the way described above.
2. That the electronic copy of the Work deposited in the digital repository and covered by this agreement, is the final corrected version of the Work, subject to point 4 below.
3. That I have exercised reasonable care to ensure that the Work is original and, to the best of my knowledge, does not breach any laws including those relating to defamation, libel, copyright, data protection or any other intellectual property rights.
4. That I have, in instances where the intellectual property of other authors or copyright holders is included in the Work, gained explicit permission where appropriate for the inclusion of that material in the Work, and in the electronic form of the Work as accessed through an open access digital repository, or that I have identified and removed that material for which adequate permission has not been obtained.
5. That Cardiff University does not hold any obligation to take legal action on behalf of the Depositor, or other rights holders, in the event of a breach of intellectual property rights, or any other right, in the material deposited.
6. That I will indemnify and keep indemnified Cardiff University and the National Library of Wales from and against any loss, liability, claim or damage, including without limitation any related legal fees and court costs (on a full indemnity basis), related to any breach by myself of any term of this agreement.

Signature P. Manti

Date

SUMMARY

This thesis examines surface finishes and tinning on Archaic period (7th-5th c. BC) Greek helmets. Experiments are designed to review and further understanding of what comprises evidence of tinning on low-tin archaeological bronzes and to investigate the efficacy of common and non-destructive methods for its detection. Methods examined include SEM, XRD and neutron diffraction. Problems related to composition analysis are identified and the thesis offers new data on the corrosion profiles of low tin bronzes, which adds to current understanding. A ternary diagram to aid interpretation of compositional data is proposed. This thesis also provides new data on the manufacturing and development of the Corinthian and Illyrian type helmets.

ACKNOWLEDGMENTS

I would like to express my gratitude to my supervisors David Watkinson and Prof Ian Freestone for their support and advice. Dr Winfried Kockelmann and Dr Manolis Pantos are thanked for their encouragement, advice and training on synchrotron based X-ray and neutron diffraction methods. This study would have not been possible without their contribution and friendship.

This work depended on accessing museum collections and excavated helmets from sites in Greece and museums in the UK. I thank all those who facilitated this process or permitted sampling of helmets: Dr Susan Walker, Prof Michael Vickers, Mr Mark Norman, Mr Daniel Bone at the Ashmolean Oxford University Museum; Dr Lucilla Burn, Ms Julie Dawson at the Fitzwilliam Cambridge University Museum; Professor John Prag, Ms Irit Narkiss and Mr Malcolm J. Chapman at the Manchester University Museum; Dr Richard Brewer, Ms Mary Davies and Mrs Penny Hill at the National Museum Wales, Cardiff; Mrs Birgitte Speake, Mrs Gali Beiner, Mr Jeremy Coote, Mrs Julia Nicholson, Mrs Zena McGreevy at the Pitt Rivers Museum, Oxford.

Also, Dr Polixeni Adam-Veleni, Ms Niki Kapizioni, Mrs Despoina Ignatiadou, Dr Dimitrios Grammenos, Ms Styliana Galiniki, Mrs S. Athanasiadou, Mrs A. Papadimitropoulou the Archaeological Museum of Thessaloniki; Dr Lilian Achilara, Dr Aikaterini Despoini (Excavator of the Sindos Cemetery), Dr Vasiliki Misailidou-Despotidou (Excavator of the Nea Philadelphia Cemetery) and Dr Konstantinos Sismanidis (Excavator of the Agia Paraskevi Cemetery), for permission to study and publish material from their excavations, from the 16th Ephorate of Prehistoric and Classical Antiquities of Greece (ΙΣΤ' ΕΡΚΑ), Thessaloniki; Dr Maria Akamati, Dr Pavlos Chrisostomou (Excavator of the Archontiko Cemetery) and Dr Anastasia Georgiadou from the 17th Ephorate of Prehistoric and Classical Antiquities of Greece (ΙΖ' ΕΡΚΑ), Pella; Dr Georgia Hatz-Spiliopoulou, Mr Christos Liagouras, Miss Olga Petropoulou, Mr Christos Anagnostakos from the 7th Ephorate of Prehistoric and Classical Antiquities of Greece (Ζ' ΕΡΚΑ), Olympia Museum; Dr Reinhard

Senff, Miss Susanne Bocher, for permitting and facilitating access to material for study and sampling from the German Archaeological Institute at Athens (DAI) and Mrs Heide Frielinghaus (from the Institute for Classical Archaeology, University of Regensburg, Germany), for useful communications over selected helmets. Finally, the Greek Ministry of Culture, Directorate of Conservation for permitting sampling of helmets in Greece according to ΥΠΠΟ/ ΓΔΑΠΚ/ΑΡΧ/Α2/ Φ30/22268/778/ 5-3-2004.

In relation to access to analysis I would like to thank Dr Anastasia Tourta, Mrs Dimitra Lazidou, Mrs Dimitra Drosaki, Mrs Fenia Mpeltzi from the Byzantine Culture Museum, Thessaloniki, Greece for facilitating the X-Radiography of selected helmets from the Archaeological Museum of Thessaloniki. Mr Michael Lambert and Mr Tom Cotterell at the Geology Department of the National Museum Wales Cardiff for access and discussions on XRD. Mr Phil Parkes from SHARE, for support with the SEM. Mrs Nicole Stahl and Dr Melanie Rimmer are thanked for translation of German text Born, 2007 and Dr Dani Hoffman for translation of Kunze, 1958; 1961; 1967; 1994 and Pflug, 1988a, b, c, d, and for proof reading parts of this thesis. Effie Verveniotou is thanked for assistance with the database of the helmets.

Aspects of this work were supported financially from the School of History and Archaeology, Cardiff University, (Postgraduate Fees Studentship, Jan 2005-2008), the Postgraduate Quality Committee Fund at HISAR for assistance with travelling money for participation at selected workshops, conferences and study of museum material in Greece and the UK. Also, COST for the participation at European activities and the STFC (previously CCLRC) Daresbury Laboratory and ISIS Facility at Rutherford Appleton Laboratory for beam-time allocation (Daresbury, 10-16 October 2005), ROTAX (RB610547 October 2006), GEM (RB720553 October 2008).

Last but not least, I would like to warmly thank those who believed in this work, and my family and friends for offering their love and support through these years.

TABLE OF CONTENTS

SUMMARY.....	I
ACKNOWLEDGMENTS	II
TABLE OF CONTENTS.....	IV
LIST OF TABLES.....	IX
LIST OF FIGURES.....	XII
CHAPTER 1. INTRODUCTION	1
CHAPTER 2. BACKGROUND AND RATIONALE.....	4
2.1. Surface finishes and polychromy of Greek helmets.....	4
2.1.1. The helmet in the Greek Archaic society	4
2.1.2. Polychromy in art and metallurgy	5
2.1.3. Artistic representations of helmets.....	6
2.1.4. Archaeometric evidence of helmet polychromy	7
2.2. Tinning, patination & corrosion of low-tin bronzes	8
2.2.1. The concept of patina and intentional patination	8
2.2.2. Silver, black and coloured corrosion patinas.....	9
2.2.3. Manufacture methods for silvery appearance and the Cu-Sn phase diagram	11
2.2.4. Tin coating methods and growth of Cu-Sn intermetallics.....	14
2.2.5. Identification of corroded tin coatings and the presence of cassiterite patinas	17
2.3. Research objectives and limitations.....	20
CHAPTER 3. METHODOLOGY AND EXPERIMENTAL	22
3.1. Overview	22
3.2. Objects investigated and selection of samples.....	24
3.3. X-radiography	27
3.4. Documentation and mounting of samples.....	28
3.5. Polarised microscopy	29
3.6. Scanning electron microscope based methods	30
3.6.1. Energy dispersive X-ray analysis.....	30

3.6.1.1. System evaluation for composition analyses of low-tin bronzes.....	31
3.6.1.2. System verification for analysis of oxygen and corrosion products.....	33
3.6.2. SEM-EDX elemental mapping.....	35
3.6.3. Backscattered electron imaging.....	35
3.7. Tinning procedure for model samples.....	35
3.8. Diffraction methods used in this study.....	38
3.8.1. Background and evaluation of methods.....	38
3.8.1.1. Basic principles.....	38
3.8.1.2. Comparison of diffraction methods and instrumentation.....	40
3.8.1.3. Information in the diffraction pattern relevant to this study	43
3.8.2. Experimental set-up and instrumentation	47
3.8.2.1. Time-of-flight neutron diffraction (ToF-ND).....	48
3.8.2.2. CuK α and synchrotron radiation X-ray diffraction	50
3.8.2.3. Data analysis	54
3.9. Summary	55
CHAPTER 4. DEVELOPMENT AND DETECTION OF CU-SN INTERMETALLICS	56
4.1. Introduction.....	56
4.2. Morphological and EDX analyses of tinned tokens	57
4.2.1. As-tinned wipe-tinned copper tokens	58
4.2.2. Annealed wipe-tinned copper tokens.....	60
4.2.3. Annealed wipe-tinned bronze tokens.....	66
4.3. Diffraction analyses of tinned tokens	68
4.3.1. X-ray diffraction.....	71
4.3.1.1. Wipe-tinned copper tokens	71
4.3.1.2. Wipe-tinned bronze tokens	81
4.3.2. Time of flight neutron diffraction	84
4.4. Investigation of Roman bronzes	91
4.4.1. X-ray diffraction on the surface of samples	93
4.4.2. Surface and cross-sectional examination.....	95
4.4.3. SEM-EDX composition analysis	99
4.5. General discussion and conclusions.....	104
4.5.1. IMC growth and changes by heat.....	104
4.5.1.1. Phases formed during tinning and the nature of η -Cu ₆ Sn ₅	104
4.5.1.2. Transformations by heat: post-tinning	106
4.5.2. The crystalline nature of IMCs and diffraction methods.....	108
4.6. Summary	109
CHAPTER 5. MANUFACTURE AND TYPOLOGY OF HELMETS	111

5.1. Introduction.....	111
5.2. Published helmet typologies and date sequences	112
5.2.1. Distribution and dating of Greek Helmets.....	112
5.2.2. Helmet typology and technological evolution.....	115
5.2.2.1. The Illyrian type.....	117
5.2.2.2. The Corinthian type	120
5.3. Stylistic categorisation of investigated helmets.....	123
5.4. Macroscopic evidence of shaping and decoration	128
5.4.1. Evidence of casting: Corinthian type helmets	128
5.4.2. Evidence of hammering: Illyrian type helmets	131
5.5. Thickness and position of samples on helmets	135
5.6. Metallographic investigation of manufacture	138
5.6.1. Polarised microscopy and SEM-EDX mapping	138
5.6.2. Time-of-flight neutron diffraction and texture analysis	140
5.6.3. Microscopy of etched cross-sections	142
5.6.4. Bronze grain size of etched cross-sections	145
5.6.5. Discussion of metallographic results	147
5.7. SEM-EDX analysis of copper alloy composition	151
5.8. General discussion and conclusions.....	154
5.8.1. Technical evolution of the Illyrian & Corinthian types.....	154
5.8.2. Artistic evidence of helmet manufacture techniques	159
5.8.3. A note on helmet workshops	162
5.9. Summary	164
CHAPTER 6. SURFACE FINISHES, TINNING AND CORROSION OF HELMETS.....	165
6.1. Introduction.....	165
6.2. General assessment of helmet appearance	168
6.3. Investigation of polishing marks and tinning.....	175
6.3.1. Plan-view SEM-BSE examination of un-mounted samples.....	175
6.3.1.1. Evidence of polishing marks.....	175
6.3.1.2. Evidence of tinning.....	179
6.3.2. Cross-sectional examination of the patina deposit interface	180
6.3.2.1. Morphology of the marker of original surface (MOS).....	180
6.3.2.2. Unusual features at the patina deposit interface: searching for η -Cu ₆ Sn ₅	182
6.3.2.3. Characteristically straight fine patinas: searching for ε -Cu ₃ Sn	186
6.4. Investigation of corrosion patina profiles	191
6.4.1. Microscopic characterisation of corrosion profiles.....	191
6.4.1.1. Criteria of characterisation.....	191

6.4.1.2. Corrosion Profile 1: one corrosion layer	194
6.4.1.3. Corrosion Profile 2: absence of a distinct red/yellow inner zone	194
6.4.1.4. Corrosion Profile 3: with red/orange-yellow inner zone	202
6.4.2. SEM-EDX composition analyses	206
6.4.2.1. Relationships between Cu, Sn, O, TSE and fCu in corrosion profiles	212
6.4.2.2. Cu, Sn, O and TSE variation in and between corrosion profiles	218
6.4.2.3. Relationships between corrosion profiles and corrosion deposit	222
6.4.2.4. The fCu	223
6.5. General discussion and conclusions	226
6.5.1. Corrosion profiles and the burial environment	226
6.5.1.1. Fine black patinas associated with azurite deposits	229
6.5.1.2. Fine red/brown patinas associated with malachite deposits	233
6.5.1.3. Uneven or coarse patinas that grow outwards	237
6.5.2. Identification of tinning based on EDX data: a comparison of data from helmet patinas and Roman tinned bronzes	238
6.5.3. A note on metallurgy and its impact on corrosion	241
6.5.4. Surface finishes on helmets	244
6.6. Summary	244
CHAPTER 7. SUMMARY AND FUTURE WORK	245
7.1. Research outcomes and contribution	245
7.2. Future work	251
REFERENCES	252
APPENDIX 1. DETAILS OF INVESTIGATED HELMETS	273
A.1.1. Illyrian	273
Illyrian Early Phase (I)	273
Illyrian Middle Phase (II)	273
Illyrian Late Phase (III)	275
Group IIIA1 (with rivets at the rim)	275
Group IIIA2 (with punched decorative rivets at the rim)	279
Group IIIA3 (with smooth rim, no rivets)	281
Group IIIB1	283
A.1.2. Corinthian	284
Corinthian Early Phase (I)	284
With crest-track and embryonic noseguard	288
Corinthian Middle Phase (II)	289
Myros Group	295
Corinthian with Crest-track	298

Corinthian Late Phase (III)	299
A.1.3. Attic	301
A.1.4. Chalkidian	302
A.1.5. Etruscan	303
APPENDIX 2. A NOTE ON RESULTS OF MODEL TANNING	305
The presence of Kirkendall voids in annealed tokens	305
The presence of an unusual phase in annealed wipe-tinned copper tokens	306

LIST OF TABLES

Table 3.1: Workflow of scientific investigations and outline of methods used.....	23
Table 3.2 (below): List of helmets investigated. EDX and MET denote the investigation of cross-sections for corrosion and metallurgy. GEM and ROTAX indicate time-of-flight neutron diffraction and XRAY X-radiography.	25
Table 3.3 (below): List of investigated Roman objects.....	27
Table 3.4: Normalised wt% SEM-EDX analyses on reference bronze C71-34 standard by BNF Metals for evaluation of system performance on low-tin bronze. Negative measurement values and original totals are reported for completeness.	33
Table 3.5: Summary of performance statistics of EDX analysis on standard bronze C71-34 by BFN Metals.	33
Table 3.6: Summary of performance statistics of EDX analysis on wollastonite standard undertaken to evaluate system performance for the measurement of oxygen in crystalline materials.	34
Table 3.7: Normalised wt% SEM-EDX analyses of wollastonite for evaluation of system performance for the detection of oxygen. The last column includes original total values.....	34
Table 3.8: List of experimental tinned samples produced by wiping or dipping tin on copper and bronze substrates. Annealing temperature/time is shown per sample. Bronze substrates were annealed at 550°C for 6 hours prior to tinning.	38
Table 3.9: Calculated X-ray beam penetration range (μm) of different X-ray wavelengths in Cu-Sn phases as a function of incident angle θ (5, 90°).	51
Table 4.1: Approximate thickness of metallic coating and of layers of Cu-Sn intermetallics observed in polished cross-sections of annealed wipe-tinned copper tokens as identified using SEM-BSE and EDX.	60
Table 4.2: Approximate thickness of metallic coating and layers of Cu-Sn intermetallic compounds on annealed wipe-tinned bronze tokens.....	67
Table 4.3: Summary of selected crystallographic data reported for the η -Cu ₆ Sn ₅ and ε -Cu ₃ Sn phases. η' notes the room temperature structure.	69
Table 4.4: Normalised intensity % of diffraction lines at selected d-spacing (\AA) characteristic of Sn, η -Cu ₆ Sn ₅ , ε -Cu ₃ Sn and δ -Cu ₄₁ Sn ₁₁ present in the experimental data and reference diffraction patterns. η and ε notes peak positions where overlap of the two phases occurs. The intensity of diffraction lines at selected d-spacings from IMCs is recorded based on Larsson's η -Cu ₆ Sn ₅ and Burkhardt's ε -Cu ₃ Sn reference patterns. The ratio of the intensity of 2.79/2.92 \AA is presented as indication of texture in Sn.	74
Table 4.5: Semi-quantitative wt% phase composition analyses of tokens analysed at ROTAX-bank 3 and quantitative wt% phase composition analysis of tokens analysed at GEM. The remaining wt% composition is copper and trace amounts of oxides. The incident neutron beam size was c. 15x25mm and the thickness of the copper tokens 3.25mm. α -bronze observed on S19 is of c. 13wt% Sn.	90
Table 4.6: List of Roman objects investigated.....	91

Table 4.7: Results of EDX wt% analyses from η -Cu ₆ Sn ₅ scallop and areas of interest in the corrosion profiles of cross-sectioned samples from the Brecon Gaer harness fitting and the Ceredigion and Manorbier skilllets. Values below the detection limit of each element are removed from the table. ...	100
Table 4.8: wt% and at% EDX composition analyses of surface features in cross-sections of Roman samples normalised excluding elements other than Cu, Sn, O and normalised excluding elements other than Cu and Sn. The nominal composition of selected Sn oxides and IMCs is presented for comparison. Interpretation of data is included in parenthesis.....	101
Table 5.1: Details and typological sequence of helmets included in this thesis. * notes helmets within a subgroup that are almost identical.	125
Table 5.2: Details of x-radiographed helmets.	128
Table 5.3: Details of the position and thickness of samples removed from 36 helmets for metallurgical investigation and examination of surface finishes. Average section thickness ($\pm 10\mu\text{m}$).....	136
Table 5.4: Summary of microscopical observations in cross-sectioned samples presented by helmet type. Notice that the Myros helmets exhibit slip lines only in a few grains.	144
Table 5.5: Averaged normalised wt% SEM-EDX analysis of core metal composition. The table includes spread of values (STDEV) between analyses taken at different areas within each sample. Only concentrations above sigma % for each element are shown (green). The maximum values for each column are in bold. Measured Zn, Sb, Au, Bi, Ag, S and P were below the detection limit.	153
Table 5.6: Standard deviation of Sn wt% concentration in helmets AP5, OL4, OL57, PE1 and PE2, and their corresponding samples.....	154
Table 5.7: Collection of published composition (wt%) analyses of Greek bronze helmets using flameless atomic absorption spectroscopy (Craddock 1971, 1977) and electron probe microanalyses (Northover, 1991; Blyth, 1993).....	163
Table 6.1: List of helmet cross-sectioned samples analysed showing sample position, thickness, chronology and bulk Sn wt% concentration with corresponding deviation (SD). The surface of these samples was investigated in plan view before mounting and polishing to examine surface finishes and tinning.....	167
Table 6.2: Groups of helmets based on the relative abundance of azurite and/or malachite established by macroscopic observation. Note that the red patinas are encountered with malachite deposits and black or grey patinas are predominantly found in the presence of azurite.....	170
Table 6.3: Results of SEM-BSE investigation of polishing marks on the surface of helmet samples.	179
Table 6.4: Quality of the marker of original surface (MOS) on helmets. SMOS denotes a sharply defined marker of the original surface and BMOS a broadly defined MOS.	181
Table 6.5: Summary of microstructural details in corrosion profiles.....	193
Table 6.6: (next page) Normalised wt% SEM-EDX analysis of areas of interest in the outer helmet side of cross-sectioned samples. The table includes spread of values (STDEV) between analyses taken at different areas within each analysed area of interest. The table includes the total of elements other than O, Cu and Sn, which are noted as Total Soil Elements (TSE). Concentrations of individual soil elements that are below the detection method are excluded from the table.....	208
Table 6.7: SEM-EDX weight and atomic % composition analyses of areas of data presented in Table 6.6 normalised as Cu+Sn+O=100%. The last column includes the copper dissolution factor or tin enrichment factor $f_{\text{Cu}} = 1 - [(Cu_{\text{patina}}/Sn_{\text{patina}})/(Cu_{\text{bronze}}/Sn_{\text{bronze}})]$ using bronze composition data in Table 5.5.	211
Table 6.8: Pivot table showing relative abundance of elements and Sn/Cu at% ratio groups of analyses from areas of interest at the outer helmet side in cross-sectioned samples. Based on averaged data normalised as Cu+Sn+O+TSE=100%.....	215

Table 6.9: Pivot table showing analysis from the outer and inner corrosion zones in corrosion profiles grouped by Sn/Cu ratio. Highlighted are $f_{Cu} < 0.94$, $TSE < 6at\%$, $Si < 3at\%$ and $Cr > 0.1 at\%$. The majority of analysis from samples with Corrosion Profile 2.1 have high Sn/Cu, f_{Cu} , Cr and Si content.	221
Table 6.10: Summary of observations with regards to predominant deposit, physical nature of corrosion profiles and chemical composition in the outer corrosion zone.....	222
Table 6.11: Pivot table showing analysis results from the outer corrosion zone (outer helmet side only) with corresponding chemical and physical corrosion profile (CP1 to CP3.2) and appearance group assigned based on macroscopic observation of the predominance of malachite or azurite.	223
Table 6.12: Summary of physical and key chemical characteristics of investigated samples and helmets. Highlighted are $f_{Cu} > 0.94$, $TSE > 6at\%$, $Si > 3at\%$ and $Cr > 0.1 at\%$	225

LIST OF FIGURES

Figure 2.1: Type I corrosion or ‘even’ corrosion on archaeological bronzes that preserves the marker of original surface. Diagram redrawn based on Piccardo <i>et al.</i> 2007 fig. 14.1 and Robbiola <i>et al.</i> 1998a.....	10
Figure 2.2 (below): Above: Composition and commonly reported crystal structure of Cu-Sn phases. Adopted from Saunders and Miodownik (1990), with calculated wt% values. Below: Phase Diagram of the Cu-Sn binary system at full equilibrium (Gale and Totemeier, 2004).	13
Figure 2.3: Typical profile and intermetallics formed during tinning and species diffusion during annealing. A, B and C indicate moving directions of interfaces during solid-state diffusion at thermal aging (from Peng <i>et al.</i> , 2007). Cu atoms diffuse from the substrate to be consumed at the Cu ₃ Sn Cu ₆ Sn ₅ interface and Sn atoms can reach the Cu Cu ₃ Sn interface leading to growth of Cu ₃ Sn. The dotted line shows the original Cu Cu ₆ Sn ₅ interface before annealing. In cases where Cu is present at the tin coating (or solder), this is mainly consumed at the Cu ₆ Sn ₅ Sn interface.....	17
Figure 3.1: Common experimental diffractometer geometries in angle dispersive systems. Left: Bragg-Brentano parafocusing diffractometer commonly used with a flat sample, a divergent beam and in reflection mode; Right: Debye Scherrer diffractometer commonly used with thin or capillary samples, with a parallel beam and in transmission mode. Figures from Anne, 2007. For applications and limitations of the different geometries (see Louer, 2002).	41
Figure 3.2: Diffraction patterns obtained using ToF-ND (ROTAX diffractometer, ISIS) showing shifting of the major copper peaks (left) due to increasing amount of Sn in the bronze alloy and detail of the shape and position of the {111} αCu reflection (right). The bronzes are fully homogenised. The δ-phase has a distinct diffraction pattern and appeared at 16wt% Sn content. (From Siano <i>et al.</i> , 2003).	44
Figure 3.3: (a) Schematic representation of points in the χ (tilt axis from 0° centre to 90° perimeter) and φ (rotation axis) space measured to produce a pole figure for a single reflection (top view). (b) Schematic of random orientation distribution of crystallites in side view and (c) viewed from top (Wessels <i>et al.</i> , 2002). (d) Stereographic projection of pole sphere, with (e) poles marked on the equatorial plane and, (f) 2-D projection of a reflection (Kockelmann <i>et al.</i> , 2004b).....	46
Figure 3.4: Experimental pole figures of binary (Sn 4wt%) bronze for {111}, {200} and {220} planes in multiple of random distribution (mrd). Upper row: c.8% thickness reduction by hammering. Lower row: 46% thickness reduction by hammering (from Siano <i>et al.</i> , 2006).....	46
Figure 3.5: The ROTAX diffractometer at the ISIS neutron spallation source (Kockelmann <i>et al.</i> , 2004b).....	49
Figure 3.6: X-ray absorption edges for Cu and Sn (top) with detail (bottom), which includes calculated experimental mac for X-ray wavelengths (Å) used at ESRF, SRS and CuKα sources. This demonstrates that calculated mac values seen in Table 3.9 for SRS 10.1 beamline are due to the X-ray absorption edge of Cu(K line) at 1.3808Å(NIST, 2010), Conversion of energy to wavelength is based on E=hc/λ, E(keV) =12.3983/Å (Energy=Planck’s constant x velocity of light / wavelength) and NASA’s energy conversion tool (NASA, 2010).....	52

Figure 3.7: Example of sample position in reflection geometry used in SRS beamline 10.1. Data were collected between Z-15 and 20 mm and by rotating the sample between 74-85° in the φ -axis from the large annotated yellow area. (Photo by E. Pantos) 53

Figure 4.1: Laboratory tinned copper tokens showing a range of coating thickness produced by the wiping (left, S1, S3) and the dipping methods (right, S2, S4). 58

Figure 4.2: Morphology of the surface of wipe-tinned copper sample (S1). (a) Tinned surface exhibiting striations due to uneven application/wiping of tin. (b) BSE image of the same surface showing a granular surface (darker areas) under tin patches (brighter areas). (c) Plan-view BSE image of η -Cu₆Sn₅ scallops separated by intergranular channels; tin was dissolved using 5% HCl, some remnant tin is visible as particles on the top of η -Cu₆Sn₅ (the scale is 1 μ m). (d) Cross-sectional BSE showing a thin (4 μ m) scallopy η -Cu₆Sn₅ layer formed between the Cu substrate/Sn coating interface (scale is 10 μ m). 59

Figure 4.3: X-ray diffraction pattern from surface corrosion product developed during annealing of S15 tinned copper token at 450°C for 1 hour. 61

Figure 4.4: X-ray diffraction pattern from surface corrosion product developed during annealing of S19 tinned copper token at 550°C for 1 hour. 61

Figure 4.5: Optical micrographs of the surface of annealed wipe-tinned copper tokens (left) and cross-sectional SEM-BSE images of corresponding samples (right). Scale in BSE images is 10 μ m, apart from images S11 and S15 where it is 20 μ m. 65

Figure 4.6: SEM-BSE image of surface on S19 in plan-view showing dendritic nature of δ -Cu₄₁Sn₁₁ below a layer of metallic tin. 66

Figure 4.7: Cross-sectional SEM-BSE images of annealed wipe-tinned bronze tokens. 68

Figure 4.8: Selected reference diffraction patterns of the η -Cu₆Sn₅ and ϵ -Cu₃Sn phases. Jones's ϵ -Cu₃Sn (PDF01-1240) and Westgren's η -Cu₆Sn₅ pattern (PDF2-0713) are commonly cited in archaeological science work (e.g. Meeks, 1986, Oddy and Bimson, 1985, Qinglin and Scott, 2003) .. 70

Figure 4.9: Normalised XRD patterns of as-tinned and annealed copper tinned tokens shown with BSE images of corresponding cross-sectioned samples. 72

Figure 4.10: X-ray diffractograms of S1, S3 (as tinned), with stick patterns of reference structures scaled to provide a rough guide of amounts present. Normalised 100% intensity (x-axis is d-spacing in Å). η -Cu₆Sn₅, Sn and Cu are the dominant components and a very small amount of ϵ -Cu₃Sn is present. 76

Figure 4.11: X-ray diffractograms of S5 and S9 in d-spacing Å, with assigned reference phases scaled to provide a rough guide of amounts present. Normalised 100% intensity. Sn is the main component with some η -Cu₆Sn₅. 77

Figure 4.12: X-ray diffractograms of S7 and S11 tinned tokens in d-spacing Å. Reference structures are scaled to give an indication of relative amounts of each phase. Normalised intensity 100%. The diffraction patterns fit Larsson's η -Cu₆Sn₅ and Burkhardt's ϵ -Cu₃Sn. S7 has more η -Cu₆Sn₅ than S11 observed by the intensity of the line at 2.96 Å. Texture of η -Cu₆Sn₅ is evident by changes in the 2.42/2.96Å between the samples. 78

Figure 4.13: X-ray diffractograms of S13 and S15 tinned tokens in d-spacing Å. Reference structures are scaled to give an indication of relative amounts of each phase. Normalised intensity 100%. Sn is less in S15 than in S13. The unusually intense diffraction line at 1.38Å may be due to extreme crystallite preferred orientation in ϵ -Cu₃Sn. 79

Figure 4.14: X-ray diffractograms of S17 and S19 tinned tokens in d-spacing Å. Reference structures are scaled to give an indication of relative amounts of each phase. Normalised intensity 100%. S17 shows diffraction lines from δ -Cu₄₁Sn₁₁, Sn, η -Cu₆Sn₅ and ϵ -Cu₃Sn. δ -Cu₄₁Sn₁₁ is the main phase in

S19, which includes some α -bronze, a small amount of SnO_2 and perhaps a tiny concentration of $\epsilon\text{-Cu}_3\text{Sn}$	80
Figure 4.15: XRD diffractogram of the c. 10wt% bronze substrate used in the tinning experiment. As-cast and after annealing for 6 hours at 500°C prior to tinning. A shift in the d-spacing from the Cu values (e.g. at from 2.09 to 2.12Å) is due to the Sn content in the phase. Some other diffraction lines are from SnO_2 , Cu_2O and CuO which were removed from the surface before tinning.....	82
Figure 4.16: XRD pattern of B6 showing diffraction lines from Sn, $\eta\text{-Cu}_6\text{Sn}_5$ the substrate, and $\epsilon\text{-Cu}_3\text{Sn}$	82
Figure 4.17: XRD pattern of B7 showing diffraction lines from $\epsilon\text{-Cu}_3\text{Sn}$, Sn, $\eta\text{-Cu}_6\text{Sn}_5$ and small amounts of oxides. Both IMCs are textured as seen by the intensity of diffraction lines at 1.38 and 2.78Å.	83
Figure 4.18: XRD pattern of B8 showing Bragg reflections from $\epsilon\text{-Cu}_3\text{Sn}$, Sn and $\eta\text{-Cu}_6\text{Sn}_5$ and oxides including Cu_2O and SnO . $\delta\text{-Cu}_{41}\text{Sn}_{11}$ is absent.	83
Figure 4.19: XRD pattern of B9 showing of $\delta\text{-Cu}_{41}\text{Sn}_{11}$, $\epsilon\text{-Cu}_3\text{Sn}$ and increased concentration of oxides. Some Sn is present, but α and $\eta\text{-Cu}_6\text{Sn}_5$ cannot be confirmed.	84
Figure 4.20: Neutron diffraction patterns of S15 collected by GEM detector banks 4 (top) and 5 (bottom), which are positioned at different fixed 2θ angles. The 2.39Å is present in diffraction data from bank 5 but is absent in bank 4, indicating crystallite preferred orientation. The line represents reference data for $\epsilon\text{-Cu}_3\text{Sn}$	85
Figure 4.21: Diffraction patterns of S1, S4 and S5 of data collected at ROTAX bank 3.	87
Figure 4.22: Diffraction patterns of S2, S5, S9 of data collected from GEM bank 5.	87
Figure 4.23: Diffraction patterns of S7 and S11 of data collected at GEM-bank 5.....	88
Figure 4.24: Diffraction patterns of S15 and S19 of data collected from GEM-bank 5.	88
Figure 4.25: Diffraction patterns of S12, S13, S14 and S15 of data collected from ROTAX-bank 3 ...	89
Figure 4.26: Diffraction patterns of S17, S18, S19 and S20 of data collected from ROTAX-bank 3 ...	89
Figure 4.27: Roman objects investigated. (a) fragment from Manorbier skillet (MB); (b) Ceredigion skillet (CER); (c) Brecon Gear harness fitting (BG); (d) Boverton collar (BOV).	92
Figure 4.28: Micrographs of cross-sectioned samples showing evidence of manufacture. MB1 (skillet): annealed and work hardened microstructure. CER1 (skillet): corroded cast dendritic microstructure. BG1 (harness): corroded microstructure with lead inclusions and areas of unusually shaped α -bronze. BOV (collar): wrought microstructure. Samples are polished but not etched.	93
Figure 4.29: XRD pattern of fragment BG1 from the Brecon Gaer harness fitting. The pattern is dominated by $\eta\text{-Cu}_6\text{Sn}_5$ (PDF 65-2303). Alternative reference diffraction patterns are provided for comparison.	94
Figure 4.30: XRD pattern of fragment MB3 from the Manorbier skillet. Burkhardt's $\epsilon\text{-Cu}_3\text{Sn}$ dominates the pattern.....	94
Figure 4.31: SEM-BSE images of samples from Ceredigion skillet. CER1: plan-view BSE image showing Cu_6Sn_5 scallops. CER2: BSE image showing scallops on the surface of the polished section. Unetched samples.	96
Figure 4.32: EDX maps of $\text{PbM}\beta$, $\text{OK}\alpha$, $\text{SnL}\alpha$ and $\text{CuK}\alpha$ X-ray lines of CER2 polished section seen above. The key indicates the counts of $\text{PbM}\beta$. Unetched polished sample naturally corroded.....	96
Figure 4.33: Cross-sectional SEM-BSE images and EDX map of sample from the Brecon Gear harness fitting. (a) BSE image showing general condition and Cu_6Sn_5 scallops on the surface below corrosion deposits. (b) BSE in high magnification showing detail of scallop layer. EDX maps showing	

elemental distribution of PbM β , OK α , SnL α and CuK α . The key indicates the counts of CuK α . Unetched polished section.....97

Figure 4.34: Plan and cross-sectional SEM-BSE and BFPM images of samples from Manorbier skillet and Boverton collar. (a) plan-view BSE image of the surface of showing polishing marks preserved on a very fine non-metallic corroded surface. (b) BFPM image of MB3 cross-section showing the full corrosion profile and a darker black/grey colour at the upper part of the corrosion profile. (c) BSE of MB3 cross-section showing thin patchy tin-rich outermost corrosion surface. (d) BSE of BOV cross-section showing tin-rich layer with voids at its interface with its underlying corrosion.....98

Figure 4.35: Cu-Sn-O ternary diagram of at% EDX composition analyses results from different areas in the analysed Roman samples. Each point in the graph represents individual spot analysis.....103

Figure 5.1: Map of part of Greece showing places mentioned in this text.114

Figure 5.2: Variants of the *Kegelhelm* (Geometric Helmet) (Pflug, 1988a).....116

Figure 5.3: Illyrian type helmets: summary of typological and chronological development. Based on information in Pflug 1988e, Snodgrass 1967, Kunze 1967, Moustaka 2000, figures from Moustaka, 2000.119

Figure 5.4: Chalkidian type helmet variants. This type starts appearing in the mid 6th c. BC. Although Kunze (Kunze, 1994) places its origins at Chalkis, Euboia (and named it accordingly), its distribution focuses on *Magna Grecia*, hence arguing for a southern Italian origin. Figure from (Pflug, 1988d)..120

Figure 5.5: Stylistic development of Corinthian Helmets. Images from Pflug, 1988d, drawings Kunze, 1961122

Figure 5.6: Investigated Corinthian type helmets presented according to their stylistic grouping.126

Figure 5.7: Investigated Illyrian type helmets presented according to their stylistic grouping.....127

Figure 5.8: Examples of cast features on helmets. (a) Cast noseguard and decoration (OL_B10518). (b) Cast and punched decoration on noseguard (OL68). (c) Casting shrinkage and crude filing marks at the back of noseguard (OL68). (d) Dendritic microstructure on the crown of OL80 (Myros group) emphasised by corrosion.129

Figure 5.9: X-Radiographs of selected Corinthian type helmets.....130

Figure 5.10: Examples of hammering work on helmets. (a) Hammering tool marks at the inner side of cheekpiece of Illyrian type helmet PE2. The tool used was approximately 3mm wide and was applied on the surface in a relatively regular manner. The ridge found at the edge is hammered out from the inner side of the helmet. (b) Hammering marks formed during working of the edge (AP5). (c) Tool marks at the outer side of high ridge on the crown of helmet (PE2). (d) Cheekpiece in the shape of the head of a ram shaped by the *repoussé* technique (OL79). (e) Inner side of *repoussé* decoration on cheekpiece (OL78).....132

Figure 5.11: X-radiographs of the crown of selected Illyrian type helmets.....134

Figure 5.12: X-radiograph of Illyrian Type helmet S1 showing casting porosity134

Figure 5.13: Graph showing sample position of individual samples and their average thickness (μm). Details of plotted data are found in Table 5.3. The plot shows that sample thickness does not strictly depend on their position on a helmet.137

Figure 5.14: Graph showing sample thickness as a function of helmet type and chronological phase. Left: Corinthian helmets showing trend to move from thicker to thinner helmets, with the exception of a Myros Group outlier in the Middle Phase II. Right: Illyrian type helmets follow a similar broad trend, but interpretation is hindered by the small number of samples from Phase I and II.137

Figure 5.15: BFPM images of etched cross-sections showing types of inclusions present in the bronze. (a) Large roundish and elongated inclusions in OL78.1. (b) Fine elongated inclusions in OL71.1.....139

- Figure 5.16: Bright field polarised (BFPM) images showing examples of fibering or banding in the core of cross-sectioned samples due to extensive directional working. (a) OL11.1 showing cuprite bands parallel to the surface of the helmet. (b) PR1.1 with exposed banding after metallographic etching.139
- Figure 5.17: Cross-sectioned sample PE1.1 showing uneven compositional distribution due to extensive hammering. (a) BFPM image of polished section. (b) BFPM image after etching revealing a worked and annealed microstructure but not fibering. (c) SEM-EDX map for CuL α . (d) SEM-EDX map for SnL α showing directional bands depleted of tin.....140
- Figure 5.18: Pole figures of PE1.1, PE2.1 and OL79.1 in multiples of random distribution (mrd) showing grain orientation distribution typical of a compressed hammered texture. Data collected at GEM (Figures and analyses by W. Kockelmann).141
- Figure 5.19: Neutron diffraction pattern for NMW2 and NMW6. NMW6 reflections are shifted to higher d-spacing due to its higher tin content, and both are shifted when compared to copper (dashed line). Characteristic peak broadening for NMW2 shows that the alloy was left in the as-cast state and NMW6 in the annealed state. Data collected at ROTAX diffractometer bank (Analysis by W. Kockelmann).141
- Figure 5.20: (below) Microscopy images of polished cross-sections shown in increasing grain size; taken at the same magnification (x500).....142
- Figure 5.21: Graph showing the approximate size of homogenised bronze grains (μm) in the samples as a function of their thickness (μm).146
- Figure 5.22: Graph showing the approximate bronze grain size (μm) in samples as a function of helmet type and chronological phase.....146
- Figure 5.23: Part of the Cu-Sn phase diagram showing phases formed under different working conditions including full thermodynamic equilibrium, annealing and usual casting conditions where full equilibrium is not achieved (image from Scott, 1991: 123). The α solid solution is present in annealed low-tin bronzes (up to c. 14wt%) at room temperature.155
- Figure 5.24: Sn wt% concentration of samples plotted against chronological phase of helmet type. Left: Corinthian type helmets exhibiting a slight trend for increasing tin content at the Late Phase III. Right: Illyrian type helmets showing clustering of Sn composition based on provenience (green, Aghia Paraskevi) or stylistic subgroup (red).158
- Figure 5.25: Cast Bronze statuette of helmet maker, late 8th-early 7th c. BC, Metropolitan Museum (from Mattusch, 1988:34).....159
- Figure 5.26: Evidence of helmet manufacture from Greek vase paintings. (a) Man hammering metal. From red-figure kylix, c. 500 BC. Staatliche Museen Berlin, No 1980.7. (b) Nude helmet-smith works on helmet with rasp. Notice the tools hanging on the wall. Red-figure kylix, 480 BC. Ashmolean Museum, Oxford, No 518. (c) Nude helmet-smith hammering helmet. Red-figure pyxis of Thaliarhos 520-500 BC. Petit Palais, Paris, No 382. (d) Hephaestus hammering Achilles helmet in the presence of Thetis who holds decorated shield. Red-figure kylix, 490-480 BC. Staatliche Museen Berlin, No 2294. (e) Hephaestus polishes Achilles shield in the presence of Thetis. Notice the helmet and tools at the background. Red-figure amphora, 490-480 BC. Museum of Fine Arts, Boston, No 13.188. (f) Young man working on a greave using saw. Red-figure kylix, 515-510 BC. Museo Archeologico Nazionale, Florence, No PD117. Images from Chatzidimitriou, 2005.160
- Figure 6.1: Diffraction patterns of corrosion deposits from helmets OL74, OL79 and PE1 confirming the presence of azurite. SR-XRD, SRS 10.1, $\lambda=0.92\text{\AA}$, corrosion flakes analysed in reflection geometry. SRS 14.1, $\lambda=1.488\text{\AA}$, corrosion powder samples analysed in transmission geometry.168
- Figure 6.2: Selected diffraction patterns of powder corrosion samples from helmets PE1, PE2, PE3, PR1 and PR4 confirming the presence of malachite. SRS beamline 14.1, $\lambda=1.488\text{\AA}$, in transmission geometry.169

Figure 6.3: (next page) Details of the surface corrosion and colour of helmets investigated. Note that samples from OL46 and OL13 are covered by blue deposits and the pictures shown here may not be representative of the selected samples..... 170

Figure 6.4 (next page): Plan-view BSE images showing characteristic conditions of MOS and types of corrosion deposits. OL79.1: MOS in superb condition with minor cracking. OL74.1: fine MOS with minor pitting covered by spiky corrosion deposit. OL73.1: pitted MOS covered by spiky corrosion and soil deposits. OL49.1: fine MOS with extensive pitting disfiguring evidence of polishing; covered by flat compact deposit. OL71.1: flat corrosion deposit covering surface, which is damaged in uncovered areas. OL9.2: flat layer of fibrous corrosion situated between a flat compact corrosion layer and porous MOS that resembles the fibrous nature of the deposit. OL69.1: general view of layered corrosion deposits on damaged MOS; detail of ‘sea-urchin’ corrosion deposit on the same sample. Scale is 200µm at x100, 50µm at x500 and 20µm at x1000 magnification. 175

Figure 6.5: Images showing the condition and polishing marks on helmet OL74. (a) Optical image showing detached corrosion deposit from the surface; the flake is composed of azurite as confirmed by diffraction. (b) BSE image of the MOS of the patina that preserves polishing marks. (c) Detail of the underside of the azurite deposit flake, which shows imprints of polishing marks. (d) BSE in high magnification showing detail of fine groove (less than 1µm width) created by polishing. Scale is 50µm at x500, 20µm at x1000 and 5µm at x5000 magnification..... 177

Figure 6.6: SEM-BSE images of the surface of helmet samples showing polishing marks preserved on the marker of original surface at the patina / corrosion deposit interface. PR4.1: scratches on the surface due to post excavation cleaning. Scale is 200µm at x100, 50µm at x500 and 20µm at x1000 magnification..... 178

Figure 6.7: SEM-BSE images of the surface of OL13.1 and PE1.1 showing localised uneven composition in their patinas; patches of higher average atomic number are observed. 180

Figure 6.8: BSE and BFPM images showing characteristic qualities of the marker of original surface at the patina | corrosion deposit interface. OL74.1: sharp MOS (SMOS) with no corrosion deposit. OL63.1: heavily cracked and banded patina (SMOS-aged) covered with brown/red spiky corrosion deposit. AP4.2: broadly defined MOS (BMOS) under malachite deposits. OL70.1: broadly defined MOS (BMOS) under spiky azurite deposits. Scale is 40µm in BSE images apart from AP4.2 where is 50µm. 182

Figure 6.9: BSE images showing in the corrosion deposits unusual compound with higher average atomic number relatively to its underlying corrosion that marks the limit of the original bronze surface. Scale is 100µm at x200, 20µm at x1000 and 7µm at x3000. 183

Figure 6.10: BFPM and BSE showing spiky azurite deposit with cuprite base. OL74.1 inner helmet side..... 184

Figure 6.11: BFPM, BSE images and EDX maps of $OK\alpha$, $SnL\alpha$ and $CuK\alpha$, showing spiky azurite crystal formation onto cuprite layer. The key notes X-ray counts for $SnL\alpha$. Sample OL50.1. 184

Figure 6.12: BFPM, BSE images and EDX maps of $OK\alpha$, $SnL\alpha$ and $CuK\alpha$, showing ‘sea-urchin’ shaped spiky malachite crystals elongating from spiky cuprite layer. The key notes X-ray counts for $CuK\alpha$. Sample OL78.1 inner helmet side. 185

Figure 6.13: BFPM and BSE images and EDX maps of $OK\alpha$, $SnL\alpha$ and $CuK\alpha$ showing ‘sea-urchin’ shaped spiky malachite crystal directly formed onto green patina. The key notes X-ray counts for $CuK\alpha$. Sample OL44.1. 186

Figure 6.14: BFPM and BSE images showing a sharp black corrosion patina with a distinct outermost layer in OL79.1 cross-section. SEM-EDX map of $OK\alpha$, $SnL\alpha$ and $CuK\alpha$ shows spatial distribution of elements in patina. The key notes X-ray counts of $CuK\alpha$ 189

Figure 6.15: BFPM and BSE images showing the nature of the grey/silver patina in PE1.1 in cross-section. SEM-EDX map of $OK\alpha$, $SnL\alpha$ and $CuK\alpha$ shows spatial distribution of elements in patina.

The patina appears orange/yellow in BFPM but it is richer in Sn than in Cu. The key notes X-ray counts of SnL α	190
Figure 6.16: BSE detail of the c. 2 μ m thick tin-rich layer in PE1.1 showing small voids at its interface with the underlying corroded bronze. Scale is 2 μ m.	190
Figure 6.17: SR-X ray diffraction patterns of surface of fragments from helmets OL79, PE1 and OL74 that exhibit a fine smooth black, grey and green/dark grey patinas respectively. The patinas of OL79 and PE1 are composed predominantly of azurite and, OL74 both of malachite and azurite. Silica is present in OL74 and OL79 and a small amount in addition to cuprite is in PE1. SRS, beamline 10.1, $\lambda=0.92\text{\AA}$, analysed in reflection geometry.	191
Figure 6.18: BFPM and BSE images of cross-sectioned samples that exhibit relatively uniform single layer patina characteristic of <i>Corrosion Profile 1</i> group.	194
Figure 6.19: BSE images in high magnification showing extremely fine fibre-like corrosion feature at the inner corrosion zone near the bronze/corrosion interface.	196
Figure 6.20: Analysis images of OL73.1 showing uniform outer layer with increased Sn concentration relatively to the inner corrosion zone. Characteristic filaments rich in Cu and O are present at the inner corrosion zone and appear yellow / orange in BFPM. Top left: BFPM image showing watercolour patina with orange/red filaments. Top right: BSE showing the overall nature of the patina. Bottom: SEM-EDX maps at x500 magnification of OK α , SnL α and CuK α . The key notes X-ray counts for SnL α	196
Figure 6.21: SEM-EDX map of OK α , SnL α and CuK α showing Sn-enrichment of the outer corrosion zone relatively to the inner, which has more Cu. OL5.1, x1000 magnification. The key notes CuK α X-ray counts.	197
Figure 6.22: (next pages) BFPM and BSE images of cross-sectioned samples in Corrosion Profile 2 which exhibit two corrosion zones and the inner zone is free of cuprite or orange/yellow compounds.	197
Figure 6.23: BFPM images showing cuprite and/or orange yellow compounds forming an inner corrosion zone. OL69.1: detail showing fine straight filaments pseudomorphs of slip lines. OL53.1: partially etched sample showing slip lines in the strained work-hardened α -bronze grains continuing into the cuprite zone. OL21.1 and OL41.1: detail showing cuprite slip line pseudomorphs changing into orange/yellow colour as they elongate into the green/blue outer corrosion zone where they are no longer visible in BFPM images.	202
Figure 6.24: (next pages) BFPM and BSE images of cross-sectioned samples in <i>Corrosion Profile 3</i> which exhibit two corrosion zones and the inner zone is composed of cuprite or orange/yellow compounds.	203
Figure 6.25: Scatter plots of all analyses data (Table 6.6) in atomic % showing relationships between Cu, Sn, O and total soil elements (TSE) in the corrosion profiles. Plots include analyses from areas of interest within the corrosion profile of both inner and outer helmet sides.	213
Figure 6.26: Scatter plot of Sn/Cu and TSE/O at% ratios of analyses from the outer and inner corrosion zones in corrosion profiles. It shows trend for TSE to increase with increasing Sn. The f_{Cu} increases with increasing Sn in the corrosion profile, but some samples show a high f_{Cu} at low Sn/Cu. Marked is analysis from samples with uncommonly high amount of total soil elements.	214
Figure 6.27: Scatter plots showing relationship of soil elements with Cu.	217
Figure 6.28: Scatter plot showing relationship of Si, Al and Cr to Sn at% in the bulk analysis results.	218
Figure 6.29: Cu-Sn-O at% ternary plot of all EDX data. It shows that the outer part of the patina can reach stability (plot area near SnO $_2$.2H $_2$ O) or mineralization (plot area near copper carbonates).	219

- Figure 6.30: Detail of Cu-Sn-O at% ternary plots showing analysis data from the inner and outer corrosion zones of samples with different physical microstructures. (a) Corrosion profiles CP1 and CP2.1. (b) Corrosion profiles CP2.2 and CP3.1. (c) Corrosion profile CP3.2.220
- Figure 6.31: Scatter plot of Sn at% in the bronze alloy substrate and Sn at% in the outer corrosion layer in cross sections. The corresponding f_{Cu} is included for reference. Calculations based bronze composition data in Table 5.5, corrosion profile s in Table 6.6 and $f_{Cu} = 1 - [(Cu_{patina}/Sn_{patina}) / (Cu_{bronze}/Sn_{bronze})]$224
- Figure 6.32: Equilibrium potential – pH diagrams for the Cu-CO₂-H₂O ternary system at 25°C. (a) 10⁻³ molal CO₂ total dissolved (44ppm). (b) 10⁻² molal CO₂ total dissolved (440 ppm). (c) 10⁻¹ molal CO₂ total dissolved (4400 ppm). (d) 1 molal CO₂ total dissolved (44,000 ppm) (Pourbaix, 1977).227
- Figure 6.33: Schematic of Type I corrosion structure according to Robbiola’s corrosion model, which results in even or noble patinas that grow inwards and preserve the marker of the original surface. The outer part of the patina has a high Sn/Cu ratio, which is lower at the inner corrosion zone (Robbiola *et al.*, 1998a). Diagram redrawn from Piccardo *et al.*, (2007).228
- Figure 6.34: Schematic of Type II corrosion structure according to Robbiola’s corrosion model, which results in ‘vile’ or coarse patinas that grow outwards and do not preserve the marker of the original surface. Characteristic to this corrosion type is the presence of an inner cuprite or cuprite-rich corrosion zone (Robbiola *et al.*, 1998a). Diagram redrawn from Piccardo *et al.*, (2007).229
- Figure 6.35: Schematic of corrosion profile CP2.1 which preserves a fine corrosion surface and the marker of the original surface. The surface is free of corrosion deposits or associated to the predominance of azurite deposits. The structure fits criteria of Robbiola’s Type I corrosion structure. The outer part of the patina is rich in soil elements and has a higher Sn/Cu relatively to the inner corrosion zone.230
- Figure 6.36: Schematic of corrosion profile CP3.2, which preserves a fine corrosion surface and the marker of the original surface.234
- Figure 6.37: Equilibrium potential – pH diagrams for the Cu-CO₂-H₂O ternary system at 25°C. (a) 10⁻³ molal CO₂ total dissolved (44ppm). (b) 1 molal CO₂ total dissolved (44,000 ppm). (Adopted from Pourbaix, 1977).235
- Figure 6.38: Schematic of corrosion profiles CP2.2 and CP3.1 which do not preserve a fine corrosion surface and the marker of the original surface is only broadly defined. The surface is covered extensively mainly by malachite and/or azurite corrosion deposits.237
- Figure 6.39: Cu-Sn-O at% ternary plot of EDX analyses data collected from corrosion profiles in helmet samples. The yellow data points are collected from η -Cu₆Sn₅ scallops and areas suspected to be ϵ -Cu₃Sn in sections of tinned Roman bronzes (section 4.4.3, Figure 4.35). The blue and green dotted lines denote trends for hypothetical changes in composition for the mineralization of η -Cu₆Sn₅ into SnO₂.2H₂O (Lower line blue) and ϵ -Cu₃Sn to SnO₂.2H₂O respectively.240
- Figure 6.40: Cu-Sn-O ternary plot for EDX at% analyses with annotated characteristic compositional regions for the discrimination between intermetallics and high-Sn corrosion on low-tin archaeological bronzes. The graph notes compositional regions as indicated from analyses from η -Cu₆Sn₅ scallops (red line), ϵ -Cu₃Sn (green line), high-Sn fine ‘noble’ patinas, uneven patinas, and red-orange-yellow areas at the inner corrosion zone in corrosion profiles.241
- Figure 6.41: Scatter plot showing relationship of the thickness of the cross section (includes patina) and the thickness of the patina (μ m).243
- Figure 6.42: Scatter plot showing relationship of the thickness of the patina in cross sections (μ m) and the grain size (μ m) of the underlying bronze.243

CHAPTER 1. INTRODUCTION

This thesis begins to explore surface finishes and the original appearance of bronze helmets during the Archaic period (roughly 670-470 BC) in Greece. It is part of a broader ongoing project, which investigates technology and production workshops of Archaic Greek helmets. The overall aim is to explore the original appearance of Greek helmets which requires investigation of a wide range of analytical and corrosion questions. Results produced important contributions to understanding the corrosion of archaeological low-tin bronze and the effectiveness of analytical methodologies for determining this.

Understanding the original appearance of helmets is vital for comprehending the aesthetics of the time and for interpreting practical and contextual aspects of their use. Additionally, the choice of a particular surface treatment, such as tinning, silvering or painting would affect the visibility of a warrior on the battlefield and mark his status or his affiliation to a particular unit (Van Wees, 2004). A polished tinned helmet would have mirror-like properties and reflect light to a great distance. Tinning would also create a hard surface due to the development of hard intermetallic compounds that affect the mechanical properties of the surface and confer a degree of corrosion durability on the bronze.

Research on the aesthetics of Greek armour is generally approached from a stylistic and art historical perspective. Literary and artistic evidence on the nature of decoration occurring on Greek helmets (Born, 1990, 1993; Snodgrass, 1967, 1998) support the working hypothesis of this thesis that plating or decorative patination could be practiced on ancient Greek helmets (Chapter 2). This hypothesis is strengthened by the only occurrence known to the author of a 5th c. BC Greek helmet (British Museum GR 1856.12-26.616) reported to be tin plated and claimed to be the earliest tin plated museum object from the Mediterranean (Meeks, 1986; Meeks, 1993b). There is no published systematic analytical investigation of Greek helmets. This research examines tinning and patination of Archaic Greek helmets using scientific analysis of samples from helmets from excavations in Greece and from museums in the UK,

utilising non-destructive methods where possible. Effective identification of plating and patination on corroded bronzes relies on understanding (a) what comprises evidence of tinning on corroded bronzes, (b) the metallurgy and corrosion of the bronze and tinning, and (c) selection of appropriate analytical methodology and instrumentation.

Scientific evaluation of the original visual appearance of Greek helmets focuses on the grey, silver and black surfaces that can present evidence of tinning or patination (Chapter 2). Interpretation of material evidence is challenging in the case of low-tin bronzes such as helmets, because silver/grey, tin-rich surfaces can also result from corrosion (Robbiola *et al.*, 1998a). The tin content of corrosion may be similar to the ϵ -Cu₃Sn (37.7 - 39.4wt% Sn) intermetallic phase, which can be developed during tinning. Data interpretation from investigations that utilise only surface composition analyses can thus be problematic for the characterisation of tinning on archaeological low-tin bronzes making careful selection of analytical methodology important. A literature review (Chapter 2) identifies diffraction analysis, which can be used for the identification of crystalline phases such as intermetallics, as being undervalued for investigating surface finishes and tinning, as is the potential non-destructive character of these diffraction methods (Chapter 3). For these reasons, before analysing the helmets investigated, the evidence of tinning and the methodologies for its effective identification are reviewed (Chapter 4). Analyses combine diffraction and compositional data with microstructural evidence derived from modern experimental tinned tokens and Roman objects. Microstructures developed on the experimental tinned tokens are cross-characterised using bench X-ray diffraction and scanning electron microscopy prior to neutron diffraction undertaken at ISIS Neutron Spallation Source (Beamtime RB720553). A detailed look at interactions at the Cu-Sn system provides new information on the non-destructive microscopic characterisation of tinning evidence on archaeological bronzes and the results are critically evaluated in relation to the limitations of the methods used.

Inevitably, manufacturing techniques and the typology of helmets are studied because metallurgy and bronze composition affect corrosion mechanisms and the original appearance of helmets (Chapter 5). Because helmet typology is linked to manufacturing methods and chronology, the helmets investigated had to be placed within the broader established typological sequence prior to analyses. Using published typologies, an overview of the production of Archaic Greek helmets from the end of the 8th to the mid 5th c. BC is provided, which places the helmets examined in archaeological context and chronology. Two main types are selected for study: the Corinthian and Illyrian type. Problems related to the dating of the helmets are noted and a brief discussion on helmet distribution, regionalism, or

individualism of styles is included. This is followed by analysis of compositional and manufacturing data. These include visual observations supported by x-radiography and metallography. Bulk composition analysis using scanning electron microscopy-energy dispersive X-ray (SEM-EDX) spectroscopy of polished sections facilitates discussion on alloying, which is linked to corrosion paths in the following chapter. Neutron texture analysis at ISIS was used directly on selected helmets without removal of samples and provides powerful non-destructive information on their metallurgy (RB610547). Results on alloying and manufacturing are discussed in relation to the technology employed over time. Since this is the largest group of helmets chemically analysed in a single study to date, the potential of grouping helmets based on element composition is discussed.

Surface finishes and corrosion of the helmet samples is examined to search for evidence of tinning and to develop understanding of surface corrosion that produces finishes deceptively similar to tinning or intentional patination (Chapter 6). Examination includes observations of the surface based on SEM-backscattered electron (BSE) imaging. Marks preserved on the corrosion marker layer of the original surface are sought to provide evidence of polishing or tinning. Polarised microscopy and BSE imaging of cross-sections of the same samples give information on the stratigraphy of microstructures present and EDX analyses of their composition. Interpretation of analysis data focuses on corrosion phenomena that result in tin-rich fine patinas, the presence of particular soil elements such as chromium, and their role in the coloration of patinas. A discussion on the formation of grey/silver and black patinas examines relationships between physical morphology and compositional gradients within patinas and attempts to link patina types to burial environments. This adds new data to enhance current understanding of corrosion mechanisms of low-tin archaeological bronzes.

In summary, this work was designed to develop scientific evidence of surface finishes of Greek helmets during the Archaic period, to review what comprises evidence of tinning using new data and to develop a methodology for its efficient detection. 154 helmets were macroscopically examined, 107 were sampled and 58 of these are included in this thesis as examples of technical varieties. 38 of these were further analysed for surface finishes and tinning. Chapter 2 provides the background and rationale for this work and sets out the aims and limitations of this study and the wider framework of the research. Chapter 3 describes experimental set-ups and methods used. This is followed by underpinning experimental tinning to evaluate the development and detection of Cu-Sn intermetallics (Ch. 4), investigation of the metallurgy and composition of selected helmets (Ch. 5), and examination of silver/grey, black or other colour fine surfaces observed on helmets (Ch. 6).

CHAPTER 2. BACKGROUND AND RATIONALE

2.1. SURFACE FINISHES AND POLYCHROMY OF GREEK HELMETS

2.1.1. THE HELMET IN THE GREEK ARCHAIC SOCIETY

The period starting from the middle of the 8th c. BC is characterised by great development and innovation in Greece. There is a dynamic change in the internal political organisation, which coincides with the introduction of the alphabet, a major revival in representational art, and a transformation of arms and warfare (Snodgrass, 1967: 48). Greek colonisation and the growth in trade brought the Greeks into increased contact and conflict with the rest of the Mediterranean, which resulted in the introduction of obligatory military service that would determine Greek warfare for several centuries (Sage, 1996: xvi). The rise of the fully-armed Greek infantryman, the hoplite, which is associated with the introduction of the phalanx formation, was a significant innovation that became the core of Greek armies, and was to receive a great deal of kudos and reputation (Snodgrass, 1967: 49). The hoplite was normally equipped with a copper alloy corselet, greaves, helmet and a great round shield or *hoplon* alongside offensive weapons (Snodgrass, 1967: 57).

Among a hoplite's weapons, the helmet is seen as an item of great significance to the degree that it has become a symbol of Greek warfare. By the mid 8th c. BC, representations occur in plastic art and pottery painting and actual copper alloy helmets are known archaeologically (Snodgrass, 1967: 41). The frequency with which helmets appear in ancient Greek art reveals that helmet production remained a significant part of ancient Greek metalworking for many centuries (Born, 1990). One of the earliest artistic examples of helmets are small bronze male figurines decorating tripod cauldrons, such as those found at the sanctuary at Olympia (Kaltsas, 2004: 47,49). They are nude, but wear a helmet demonstrating their capacity as

warriors (Snodgrass, 1964; 1967: 51). Although by the 6th c. BC such figurines also depict other parts of armour, the social significance of the helmet is apparent from early times. During later periods, Aristotle informs us that possession of armament was a precondition to civic rights (Aristotle, Politics IV10.7-10, in Jarva, 1995: 11) and that part of the equipment was supplied at the soldier's expense (Aristotle XLII:4, in Snodgrass, 1967: 59), its cost limiting the numbers of hoplites. This practice is thought to be a method for limiting participation in the hoplite armies to the aristocracy (Sage, 1996: xvii). Evidently, '*to the hoplite, his equipment become a source of pride not only as a status-symbol to show that he belonged to the class which could afford it, but as the principle medium through which he served his city*' (Snodgrass, 1967: 58).

2.1.2. POLYCHROMY IN ART AND METALLURGY

In the field of art history and theory, this pattern of change and innovation during the Archaic period is defined by the '*search of constant norms in art and laws governing beauty*' and the alleged love of the Greeks for '*the living reality and sensory perception*' (Tatarkiewicz, 2006: 13). The latter is evidenced in the gradually more lively representations of the human body and the use of colour to enhance sculptures. Artificial surface finishes in sculpture and in the decorative arts were not only used to imitate other expensive materials. Polychromy was an important aspect of overall aesthetics and for this reason it imparts '*the vital element in the visual coherence and signification of objects*' (Hughes, 1993). Metals and alloys were selected based on their working properties, but also their natural colour (*ibid.*). This is not unique to Greece: in ancient India, metals were usually highly polished because their colour was significant. In contrast, in China bronzes were usually lacquered, and thus the colour of the alloy was less important (Craddock, 2009:152). Archaeometric evidence has demonstrated that since the Bronze Age, Greek craftsmen were aware of the optical properties of different alloys (Hughes, 1993; see also examples in Charbonneau, 1962: 36; for classical bronze Varoufakis, 1980; Craddock, 1988; Haynes, 1992: 85; Tylecote, 1992: 27; Craddock and Giunlia-Mair, 1993). For example, different alloys were employed on the same object to produce a polychrome effect. The most important innovation was Corinthian bronze, a golden colour alloy designed to create a particular colour in finished products (Charbonneau, 1962:36), no doubt with primarily aesthetic ends in mind (Haynes, 1992:85; Hughes, 1993; Craddock, 1988).

2.1.3. ARTISTIC REPRESENTATIONS OF HELMETS

Helmets being objects of significance and status, had an important aesthetic, as well as practical role (Blyth, 1988). Artistic representations on pottery add greatly to our understanding of the original appearance of helmets: warriors are shown with helmets bearing engraved, painted or plated designs (Born, 1990; Craddock and Giumlia-Mair, 1993; Snodgrass, 1998). The accuracy of artistic representations of Greek armour on painted pottery is much debated (see discussion in Snodgrass, 1998). Evidence of the appearance of helmets based on artistic sources may include problematic aspects, such as the accurate dating of pottery, anachronistic relationships between the artistic context and manufacturing date, and issues related to ‘artistic licence’ and inspiration. However, it is generally accepted that pottery provides datable information and it has been extensively used for the construction of chronological typologies of helmets (Kunze, 1958, 1961, 1967; Pflug, 1988c, 1988b, 1988a). Archaeological finds have been compared to (and dated based on) artistic representations (Snodgrass, 1982; Jarva, 1995: 15; Snodgrass, 1998). On this basis, it is reasonable to assume that the tradition of polychromy was embraced in the making of armaments, as demonstrated by numerous artistic representations. Polychromy could be achieved by painting, patination or decoration using different coloured metal alloys or plating methods such as gilding and tinning.

Homer’s famous description of the making of Achilles’ shield by Hephaestus (Iliad, 18.468-613) is the earliest literary evidence supporting polychrome decoration on metals (see Hughes and Rowe, 1982; Penhallurick, 1986: 79; Born, 1993; Hughes, 1993). The description of the vineyard depicted on the shield is an excellent example of the use of different colour metals and/or patination: grapes were made of gold with clusters that hung dark purple (or black), vine poles were of silver, enamel was used for the enclosing ditch and tin for the fence (Iliad.561-571). This may be interpreted as evidence for the attachment of different metals, or of tinning, gilding, artificial patination or painting of the bronze shield. In general, the use of gold for decorative purposes is mentioned in the Iliad mainly in relation to shields, and on one occasion for the crest of Achilles’ helmet (Iliad 18.612). There are numerous references to the use of tin for decorating shields and making greaves in the Iliad¹. Helmets in the Iliad are copper-based and appear flashing and shiny, such as that of Hector (6.465-474) (Borchhardt,

¹ For examples see Iliad 11.25; 11.34; 18.474, 565, 574, 613; 20.271; 21.592; 23.503, 561.

1972)². Since ‘*there has been some agreement by authorities that the Iliad may have reached its final Homeric form as early as the mid-eighth century*’ (Snodgrass, 1998: 12-13), it is likely that the descriptions of helmets in the Iliad were inspired by the technology extant at the time of writing (*ibid.*). The archaeological record supports this, with material evidence of bronze helmets in Greece starting from the Late Geometric period (9th-8th c. BC). Decorated helmets occur on painted pottery from the 7th c. BC (Born, 1990), after the first appearances of painted emblems on bronze shields depicted on pottery; the employment of painted emblems on shields is attributed to the growing regionalism in Greece (Snodgrass, 1967:67). In agreement with pictorial sources, material evidence shows that helmets start being decorated by engraving, chasing and rising from the mid 7th c. BC, with the major example being the Myros group of Corinthian type helmets.

2.1.4. ARCHAEOLOGICAL EVIDENCE OF HELMET POLYCHROMY

While a number of scientific analyses on helmet manufacture show that helmets of this period are made from low-tin bronze (c. 7-12wt% Sn) (Hoffmann, 1972; Craddock, 1976; Swaddling, 1987; Blyth, 1988; 1991; Hockey *et al.*, 1992; Blyth, 1993; McNamara, 2000), archaeometric evidence on decoration and the original appearance of helmets is scarce. Scientific examination of a 6th c. BC Illyrian type helmet from Olympia³, now in the British Museum (GR 1914.4-8.1), revealed the use of silver rivets (with 2 wt% Cu) on the low-tin bronze helmet (Hockey *et al.*, 1992). The bronze would have a light golden tint if polished, creating a polychromatic effect with the silver decoration. Further analysis of this helmet supports the use of tin solder for the application of a very thin silver foil onto the bronze, whilst silver foil *repoussé* decoration was attached to the cheekpieces using a calcite based adhesive. This is perhaps the earliest known example for the use of these plating methods (Hockey *et al.*, 1992; La Niece, 1993). In general, little is known on the adhesives used for applying silver or gold foil decoration on bronzes. A single study demonstrated the use of gold leaf decoration applied with a birch pitch organic adhesive on a polished bronze helmet for burial purposes, a practice which appears to be common in the mid to late Archaic period

² Borchhardt provides a detailed study for the ancient terms for ‘helmet’ and the adjectives that characterise it in the Homeric text. For example, *κόρυς*, *κυνέη* and *τροφάλεια* are all used for ‘helmet’, the words *πήληξ*, *στεφάνη*, *μάς*, *κύμβαχος*, *λόφος*, *πίλος*, *φάλος* and others refer to helmet parts, whilst common words to characterise the material and appearance of a helmet are, amongst others, *χαλκήρης*, *χαλκείος*, *εύχαλκος*, *πάγχαλκος*, *λαμπρός*, *φωτεινός*. For a full list of words and their occurrences in the Iliad see Borchhardt 1972, Beilage C.

³ An identical example is on display in the Olympia Museum.

in northern Greece for material from Archontiko and Aghia Paraskevi (Manti and Watkinson, 2008). This is a particularly significant finding because in this case, a warrior's status would be denoted by gilded decoration during burial practices. A bronze helmet found in northern Italy (circa 500 BC) is reported painted with white, grey and red colours; unfortunately, no analysis data are reported (Born, 1990:189). The only reported tinned helmet known to the author is a 5th c. BC Greek helmet in the British Museum (GR 1856.12-26.616), claimed to be the earliest tin plated museum object from the Mediterranean (Meeks, 1986; Meeks, 1993b). A systematic scientific investigation of surface finishes on Archaic period helmets is absent and this research aims to fill this gap.

2.2. TINNING, PATINATION & CORROSION OF LOW-TIN BRONZES

2.2.1. THE CONCEPT OF PATINA AND INTENTIONAL PATINATION

The study of the surface of archaeological bronzes is vital for understanding how objects looked in antiquity, understanding technological choices for plating and metallic coatings and for identifying potential forgeries in museum collections (Craddock and Giumlia-Mair, 1993; Craddock, 2009:349). Excavated bronze helmets have acquired a 'patina' of corrosion that developed during burial; questions relating to this are whether it can be linked to original plating, intentional patination or if it is just a result of corrosion.

In conservation literature, the term 'patina' is not strictly defined but is broadly associated with the presence of a layer that marks the original surface (Bertholon, 2001). The concept of 'patina' goes back to the aesthetical perceptions of art historians since the Renaissance period, when it was believed that classical bronzes were originally deliberately patinated black because in later periods organic coatings were applied on bronzes to darken their appearance (Craddock, 2009: 353). Coloured bronzes can be achieved by artificial patination, which is in fact a deliberately induced corrosion process that results in desirable corrosion compounds chemically similar to those developed during burial (see examples in Hughes, 1993). As seen above, colouration could theoretically have been practiced in Greek antiquity, predominantly during the classical period (Hughes and Rowe, 1982; Born, 1990, 1991; 1993; Hughes, 1993). The main argument against artificial patination and painting of bronzes in antiquity is that ancient Greek literature sources refer to the regular cleaning and protection of bronzes using oils (Hughes, 1993; Charbonneaux, 1962:39; Craddock and Giumlia-Mair, 1993). In the case

of armour, shields displayed in the Painted Stoa in Athens were cleaned and covered in pitch to preserve them (Pausanias 1.15.4 in Whitley, 2006). This would prevent corrosion (Craddock, 2009: 355) and unless specifically applied to protect artificially induced corrosion or patination, it would have most likely removed it.

In practical terms, artificial patination is extremely difficult to discriminate from natural corrosion using scientific methods alone (see discussion in Craddock, 2009: 352-353). So far, in the literature, a 'finishing patina' is most often inferred from a combination of evidence deriving from ancient illustrations and literature, rather than its survival on metalwork itself. It would perhaps be possible to discriminate between an artificial and a natural patina in cases where (a) during artificial patination an unusual corrosion product was formed which remained unchanged during burial, for example a uniform Cu-S based layer on bronze excavated from burials with no sulphur concentrations; or (b) where there is clear evidence of polishing of a compact corrosion layer that would normally be expected to grow during burial in a non compact crystalline form.

2.2.2. SILVER, BLACK AND COLOURED CORROSION PATINAS

Examination of corrosion mechanisms of bronzes during their burial is fundamental in understanding what comprises evidence of intentional patination, plating, or other surface treatments. Recent work showed that corrosion could result in the development of blue, green, brown and light or dark grey patinas that can preserve polishing marks (Robbiola *et al.*, 1998a; Piccardo *et al.*, 2007; Robbiola *et al.*, 2008). These surfaces, named Type I or 'even' corrosion by Robbiola and co-workers, are passive corrosion layers which are rich in tin and consist of hydrated tin compounds, cupric compounds (Cu_{II}) and a small amount of extraneous elements (Piccardo *et al.*, 2007). Such tin-rich corrosion layers form via complex internal oxidation phenomena that involve migration processes through the corrosion layers characterised by the outward migration of copper cations (Cu^+ , Cu^{++}) from the bronze and the inward migration of ions of soil elements (Figure 2.1) (*ibid.* 242). The degree of tin-enrichment is related to the original tin concentration of the bulk alloy, whereas the colour is reported as a factor of the total amount of soil elements incorporated in the patina (mainly Si, P, Fe and Cl) (Robbiola *et al.*, 1998a). Bright grey patinas appear to incorporate the least amount of soil elements compared to blue that have the largest amounts and which are followed by green patinas; dark green and dark grey show irregular soil element concentrations (*ibid.*).

Tin-rich Type I corrosion can develop *in situ* preserving evidence of what once was the original surface of the object, in contrast to Type II corrosion mechanisms that lead to loss and disruption of the surface (see Robbiola *et al.*, 1998a). Because of the association of the word patina with what marks the original surface, this thesis uses the word patina to refer to natural or artificial corrosion surfaces that preserve the marker of the original bronze surface onto which copper compounds are deposited due to interaction with soil elements in the burial (Figure 2.1).

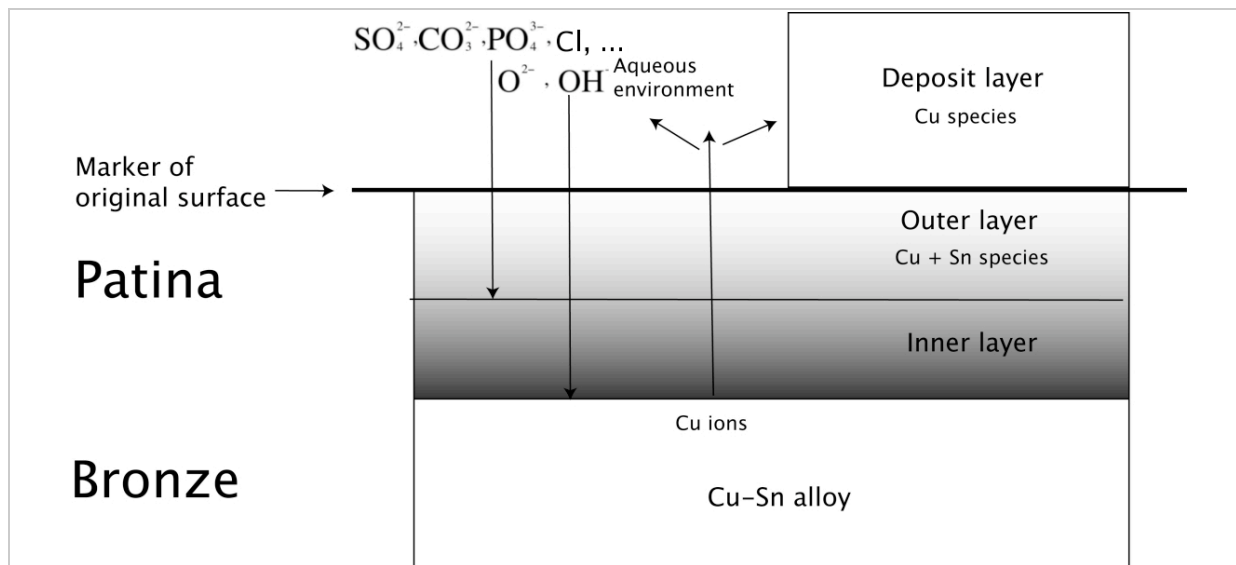


Figure 2.1: Type I corrosion or ‘even’ corrosion on archaeological bronzes that preserves the marker of original surface. Diagram redrawn based on Piccardo *et al.* 2007 fig. 14.1 and Robbiola *et al.* 1998a.

Tin-rich surfaces are predominantly reported on high-tin archaeological bronzes (Weisser, 1975; Oddy and Meeks, 1982; Meeks, 1986; Turgoose, 1989; Meeks, 1993a; Scott, 2002: 340), but it is now clear that they also occur on low-tin bronzes (Robbiola *et al.*, 1998a; Piccardo *et al.*, 2007; Robbiola *et al.*, 2008). However, findings on low-tin bronzes were based on the surface examination of 16 small bronze objects, only 3 of which were further investigated in cross-section (Robbiola *et al.*, 1998a). More data deriving from low-tin archaeological bronzes is necessary to further understanding of corrosion mechanisms that result in the formation of such fine grey/silver, black or blue patinas.

The actual role of soil elements and their threshold concentrations in the development of coloured smooth patinas is not clear, especially with regards to the silver/grey and black patinas. For instance, it was suggested that the presence of 2wt% chromium found in the patina of a c. 12w% Sn (with c. 2wt% Pb) Chinese bronze spearhead was responsible for its smooth black patina and corrosion resistant properties (Han Rubin *et al.*, 1983). X-ray Diffraction confirmed the presence of CrO_2 and SnO on this object. This was attributed to

intentional patination, although other small finds with similar patina found in the same burial context did not contain such a significant amount of chromium (0.2wt%) (Han Rubin *et al.*, 1983). For this reason, Meeks (1993b) disputed the hypothesis of intentional patination of these Chinese bronzes and attributed the presence of the black surface to corrosion phenomena. Detailed composition and diffraction analysis of patinas found on helmets provide the means to offer further understanding of the role of soil elements in the colouration of fine patinas.

2.2.3. MANUFACTURE METHODS FOR SILVERY APPEARANCE AND THE CU-SN PHASE DIAGRAM

That bright grey/silver or black patinas on low-tin bronzes can be a result of corrosion causes interpretation problems, because silvery or bright to dark grey surfaces on archaeological bronzes can look deceptively similar to corroded tin coating (Meeks 1986) or silvering (La Niece, 1993), as well as the intentional or accidental product of various manufacturing methods (Hughes, 1993). Manufacturing methods can result in the formation of Cu-Sn phases that, when found un-corroded, appear metallic grey/silver. Alloy composition, heating temperatures, cooling rates and manufacturing processes such as casting or hammering control the types of Cu-Sn phases present in the object.

During cooling of a Cu-Sn binary alloy, based on solubility limits of Cu in Sn, surplus atoms of Sn can separate out as distinct phases (hitherto referred to as intermetallic compounds IMCs) that tend to have uniform physical and chemical properties, fixed stoichiometric compositions and atomically ordered crystal structures (Ashby and Jones, 2006: 18). At full thermodynamic equilibrium conditions the $\alpha+\epsilon$ intermetallic is stable at room temperatures (Figure 2.2) (Saunders and Miodownik, 1990). Cast archaeological bronzes do not reach full equilibrium conditions, as this requires a prolonged annealing time (c. 1000 hours), therefore precipitation of the ϵ -phase in a saturated α bronze solid solution is inhibited (Cuthbertson, 1960) and the $\alpha+\delta$ eutectoid is present at room temperature instead (Bailey, 1984:2; Scott, 2002:401; Meeks, 1986). A single-phase homogenous α bronze can be present over a range of Sn concentrations typically up to about 14 wt% Sn depending on the degree of alloy homogenisation during hammering and annealing. With increasing Sn content in equilibrium conditions, above c. 30 wt% δ is stable in room temperature and the $\delta + \epsilon$ eutectoid appears after annealing (Scott, 1991:18-25), $\epsilon + \eta'$ is present in alloys with 40-60 wt % Sn and $\eta' + \text{Sn}$ when Sn is more than 61 wt%. β , γ and ζ phases are formed on quenching from high temperatures; interestingly a metastable ζ phase has been observed at lower temperatures

(200-300°C) in alloys with 19.53 wt% and 31.15 wt% Sn mixed with a supersaturated α (Saunders and Miodownik, 1990; Gale and Totemeier, 2004). All phases with increased tin content (e.g. δ , ϵ , η' and η) are silvery in colour (Figure 2.2).

That high-tin phases exhibit a silver colour was utilised in antiquity to produce silver-colour bronzes; for example the use of high-tin bronzes such as speculum would result in a silver-coloured object with mirror-like appearance when polished (Meeks, 1993b). Published composition analyses of helmets shows that helmets are of low-tin bronze ranging 7-12wt% with traces of other elements (Table 5.7) (Craddock, 1977, x9 helmets; Swaddling, 1987, x1 helmet; Northover, 1991, x2 fragments; McNamara, 2000, x4 helmets).

Casting of low-tin bronzes can lead to increased tin concentrations towards the surface due to inverse tin segregation or 'tin sweat'. This is a natural phenomenon which occurs during casting of low-tin bronzes typically 8-15wt% tin (Meeks, 1993b), with increased occurrence at 10-14 wt% tin (Oddy and Bimson, 1985). Segregation takes place in the molten state and results in the formation of silver colour $\alpha+\delta$ eutectoid structure on the surface upon cooling, the rate of which is critical (Oddy and Meeks, 1982; Oddy and Bimson, 1985; Tylecote, 1985; Meeks, 1986). Tylecote (1985) demonstrated that the formation of a mixture of δ and ϵ -Cu₃Sn phases is also possible. Inverse tin segregation could be a deliberate technological choice employed for tin-bronzes (Oddy and Bimson, 1985) as it is reported for Early Bronze Age cast arsenical-copper Scottish axes which show inverse arsenic segregation (Tylecote, 1985).

In another case, the unusual presence of $\alpha+\delta$ found on the polished surface of a heavily worked 12wt% Sn Early Bronze Age axe (c. 2000 BC) was attributed to the intentional use of a cassiterite reduction method, whereby a slurry of cassiterite was applied onto the bronze and heated in reducing charcoal fire to produce $\alpha+\delta$. This method is thought to be the earliest method of deliberate 'tinning' and is reported on prehistoric British axes (Kinnes *et al.*, 1979; Oddy, 1980; Kinnes and Needham, 1981; Oddy and Bimson, 1985; Meeks, 1986; Meeks, 1993b). It is likely that this method was not used in Archaic Greece. If the use of cassiterite instead of metallic tin was necessary in EBA due to rarity of metallic tin, this should not be the case in Archaic Greece, because metal smelting technologies were more advanced. This method was experimentally proven to form $\alpha+\delta$ on the surface, but $\alpha+\delta$ can equally be the result of the transformation of Cu-Sn intermetallics due to exposure to heat (Meeks, 1986). The systematic investigation of EBA axes is important to re-examine the evidence for cassiterite reduction as a possible tinning method employed in antiquity.

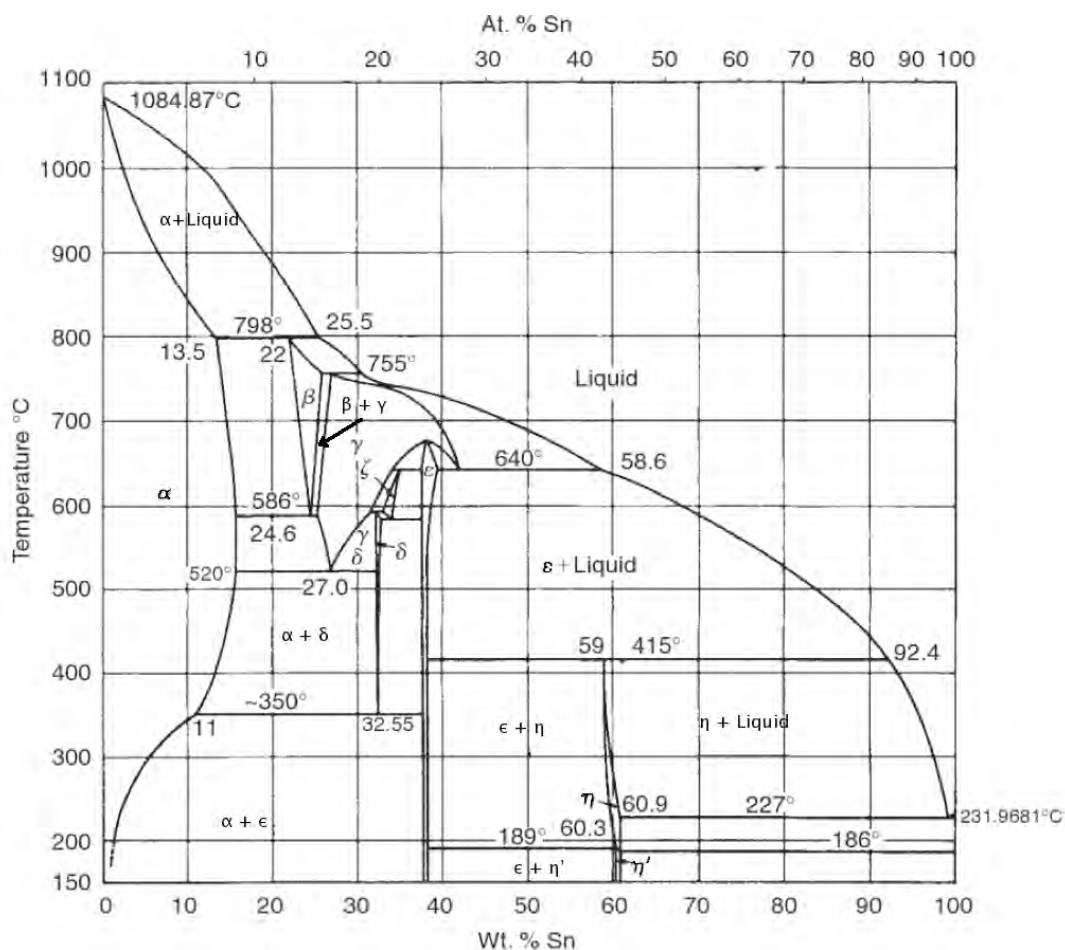
Chemical tinning by boiling an object for several days in a solution of potassium bitartrate

containing granules of metallic tin may have been used since the 5th c. AD, but there is little evidence to support use of this process before the 18th c. AD (Kinnes *et al.*, 1979; Oddy, 1980). Mercury amalgam tinning is mainly practiced in China and has not been identified as a practice in the Mediterranean (Anheuser, 2000). Hence, it is not discussed in this thesis.

Although an important overview of methods used to produce silver-coloured surfaces has been produced (Meeks, 1986; Meeks, 1993b), a systematic investigation of the type and distribution of tinned objects in antiquity is absent. Scientific investigations focus on individual pieces or small groups of museum objects with an emphasis on low and high-tin Roman and Chinese mirrors (Meeks, 1993b, 1993a), black or silver coloured surfaces on high-tin Chinese bronzes (Shoukang and Tangkun, 1993; Chase, 1994), Bronze Age axes (Kinnes *et al.*, 1979; Oddy, 1980; Kinnes and Needham, 1981; Tylecote, 1985) and small objects such as brooches and amulets which are reported to be dipped-tinned (Oddy and Bimson, 1985). With the exception of a wrought Bronze Age vessel from the North Caucasus (0.7 wt% As bronze) (Ryndina, 2009) and a wrought low-tin Greek bronze shield (Born, 2007) (no diffraction data are provided in either case), research seems to focus on cast tinned objects. Whether this is a coincidence or whether preservation of tin coatings is somehow related to object manufacture is unknown. More work is required to examine this.

Figure 2.2 (below): Above: Composition and commonly reported crystal structure of Cu-Sn phases. Adopted from Saunders and Miodownik (1990), with calculated wt% values. Below: Phase Diagram of the Cu-Sn binary system at full equilibrium (Gale and Totemeier, 2004).

Phase	Phase Composition limits		Formula	Structure type	Structure (prototype)	Pearson Symbol	Space Group	
	Left boundary	Right boundary						
α	at%	0	9.1	Cu	fcc	Cu	<i>cF</i> 4	<i>Fm</i> 3 <i>m</i>
	wt%	0	15.75					
β	at%	13.1	16.5	Cu ₃ Sn	bcc	W	<i>cI</i> 2	<i>Im</i> 3 <i>m</i>
	wt%	21.97	26.96					
γ	at%	15.5	27.5	Cu ₃₁ Sn ₈	By ordering of β	BiF ₃	<i>cF</i> 16	<i>Fm</i> 3 <i>m</i>
	wt%	25.52	41.47					
δ	at%	20	21	Also Cu ₂₃ Sn ₂		Cu ₄₁ Sn ₁₁	<i>cF</i> 416	<i>F43m</i>
	wt%	31.83	33.18					
ζ	at%	20.3	22.5		hexagonal	Cu ₁₀ Sn ₃	<i>hP</i> 26	<i>P63</i>
	wt%	32.24	35.16					
ϵ	at%	24.5	25.9	Cu ₃ Sn	Uncertain, large superstructure cph unit cell	Cu ₃ Sn	<i>oC</i> 80	<i>Cm</i> <i>cm</i>
	wt%	37.74	39.5					
η	at%	43.5	44.5	Cu ₆ Sn ₅	Change at 186-189°C	NiAs	<i>hP</i> 4	<i>P</i> 63/ <i>mmc</i>
	wt%	58.98	59.96					
η'	at%	45	-	Cu ₆ Sn ₅			(a)	
	wt%	60.45	-					
β Sn		100	100			β Sn	<i>tI</i> 4	<i>I41/amd</i>
α Sn		100	100			Diamond	<i>cF</i> 8	<i>Fd</i> 3 <i>m</i>



2.2.4. TIN COATING METHODS AND GROWTH OF CU-SN INTERMETALLICS

The processes of tin coating changed little until modern times (Davies, 1882; Fuller, 1894: 20-21; Politis, 2005; Panagiotis, 2007). Tinning of low-tin bronzes to prevent corrosion of cooking vessels is documented in the literature since Roman times (Pliny, Natural History, cited in Oddy, 1980). Even if tin objects are documented from the 5th mil. BC (Muhly, 1985; Craddock, 1999; Weeks, 1999), the earliest evidence of tin coating are Bronze Age ceramic vessels (Gillis, 2001) and 5th c. BC Greek and Etruscan bronzes (Meeks, 1993a), closely followed by copper alloy objects from Britain (Oddy, 1980; Meeks, 1986).

The two traditional tinning methods flux the warmed bronze with rosin (colophony) or other organic flux⁴ followed either by wiping tin on the surface over an open fire at a temperature

⁴ For the use of colophony as an organic flux of tin-solders see (Theophilus, III-89, p.182)

above the melting point of Sn, or by immersion in a Sn bath (Oddy, 1980). This could be followed by scouring with fine white sand or sawdust and by polishing with linen or cotton rags (Fuller, 1894: 20-21). The wiping method requires experience to achieve a fine, smooth, continuous tin coating and is the commonly reported method in technical literature of the recent past (*ibid*). It is unlikely that immersion tinning was employed in antiquity because of the un-economic amount of tin required and contamination of the tin bath with copper (Meeks, 1993b).

Tinning at elevated temperatures results in the formation of Cu_3Sn (*epsilon*, ϵ) and Cu_6Sn_5 (*eta*, η) intermetallic compounds at the bronze/tin interface, typically with the $\text{Cu} | \text{Cu}_3\text{Sn} | \text{Cu}_6\text{Sn}_5 | \text{Sn}$ profile (ITRI, 1983: 58) (Figure 2.3). Both intermetallics (IMCs) have a tight Sn concentration range but compositional variations between the interfaces of the IMCs are reported (Lee and Duh, 1999; Chao *et al.*, 2009) (Figure 2.2). The presence of either phase is considered evidence of tinning on low-tin archaeological bronzes (Meeks, 1986). In uncorroded samples, the characteristic Sn concentration of these intermetallics aids identification of these phases via EDXA. There are two problems emerging from literature regarding the accurate detection and interpretation of these metallic phases: changes due to diffusion phenomena and inconsistencies in their crystalline structural form.

During cooling of a melted tin coating in thermodynamic equilibrium conditions, the high temperature η - Cu_6Sn_5 transforms into η' - Cu_6Sn_5 which is the stable structural form at room temperature (Figure 2.2). This structural change takes place between 186-189°C (Saunders and Miodownik, 1990) or around 170°C (Tu, 1973). Laurila has disputed that this occurs in common experimental set ups (in their case soldering) due to kinetic constraints and showed that the high temperature η - Cu_6Sn_5 can remain at room temperature as a metastable phase (Laurila *et al.*, 2005)⁵. Reviewing recent literature on tin solders used in electronics (COST, 2006; Ipsier, 2007; Watson *et al.*, 2007; Zivkovic, 2007; COST, 2008; Hayes *et al.*, 2009; Lai *et al.*, 2009) and the limited available diffraction data from archaeological bronzes shows that there is inconsistency on the reported crystalline structures of both Cu_6Sn_5 and Cu_3Sn . This inconsistency can complicate accurate detection of these phases using diffraction analysis, which would provide useful insights on the technology employed for tinning. The high temperature ordered monoclinic form of η - Cu_6Sn_5 is most often cited in the electronics

⁵ Laurila, Vuorinen and Kivilahti, 2005 were able to detect the transformation of η to η' to start after 6 min at 175°C using differential scanning calorimetry (DSC).

literature whereas, the high temperature hexagonal η -Cu_{6.26}Sn₅ (PDF 47-1575) is reported at modern tinned bronze (Qinglin and Scott 2003) and electroplated copper samples (Kim *et al.*, 2008), but a high temperature hexagonal η -Cu₆Sn₅ (PDF2-0713) is reported on archaeological objects (Oddy and Bimson, 1985; Meeks, 1986; Qinglin and Scott, 2003). It is therefore likely that the room temperature η' -Cu₆Sn₅ does not commonly occur unless samples are cooled after tinning very slowly. A similar variety of crystalline structures reported for Cu₃Sn is available in crystallographic databases (Table 4.3) but this phase is commonly reported as of orthorhombic lattice symmetry ϵ -Cu_{3.02}Sn_{0.98} (PDF 65-5721) in electronics' literature (Chen and Lai, 2009) or as ϵ -Cu₃Sn (PDF 01-1240) on archaeological objects (Oddy and Bimson, 1985; Meeks, 1986; Qinglin and Scott, 2003). Due to these uncertainties, both Cu₃Sn and Cu₆Sn₅ are notated in this text as found in papers cited or using their generic forms (ϵ -Cu₃Sn and η -Cu₆Sn₅) until their nature is verified on analysed samples by diffraction analysis.

Application of heat on a tinned object, for example during cooking, changes the nature of the Cu | IMCs | Sn profile as a function of time ultimately resulting to the loss of surface tin and gradual change of IMC profile due to diffusion (see Meeks, 1986). Diffusion phenomena result in IMC changes and growth and take place both at temperatures above the melting point of tin (232°C) at the liquid-Sn/solid-substrate interface and at temperatures below that at the solid state (Laurila *et al.*, 2005). Experiments with nanometer thick metallic films (350nm Sn on 600nm Cu) showed that during annealing for one year at room temperature, and as low as -2°C, Cu atoms diffuse interstitially into Sn forming η' -Cu₆Sn₅; η' -Cu₆Sn₅ continues to grow in thickness until all Sn is consumed (Tu, 1973). The linear growth rate of η' -Cu₆Sn₅ in room temperature was calculated to be in the range of 3.5 and 6 nm/day, for thinner and thicker nano-coatings respectively (Tu, 2007: 80). ϵ -Cu₃Sn was not observed at annealing at room temperature.

ϵ -Cu₃Sn is formed by solid-state diffusion at temperatures above 60°C and grows at the expense (or at least partly) of η' -Cu₆Sn₅. Both phases continue to grow in a parabolic rate depending on Sn availability that controls the reaction (Laurila *et al.*, 2009). Aspects of solid-state diffusion phenomena are still uncertain; for example, diffusion coefficients of Cu and Sn in IMCs at different temperatures that control reactions at the Cu | Sn interface are inconsistent⁶. There seems to be agreement that during solid state diffusion Cu atoms diffuse

⁶ See discussion on inconsistency of reported diffusivities in Laurila *et al.*, 2005 and examples of inconsistently reported diffusivities in Tu, 1973; Chao *et al.*, 2009; Seo *et al.*, 2009.

from the substrate and are mainly consumed at the $\text{Cu}_3\text{Sn} | \text{Cu}_6\text{Sn}_5$ interface whereas Sn atoms can reach the $\text{Cu} | \text{Cu}_3\text{Sn}$ interface where they are consumed to form more Cu_3Sn (Peng *et al.*, 2007), (Figure 2.3). These phenomena are important when investigating archaeological objects, as it seems that elevated temperatures from prolonged exposure to direct sunlight could result in IMC changes and further growth of Cu_3Sn or the continued growth of Cu_6Sn_5 . The effects of room temperature diffusion phenomena at the $\text{Cu}|\text{IMCs}|\text{Sn}$ system in archaeological times scales are unknown.

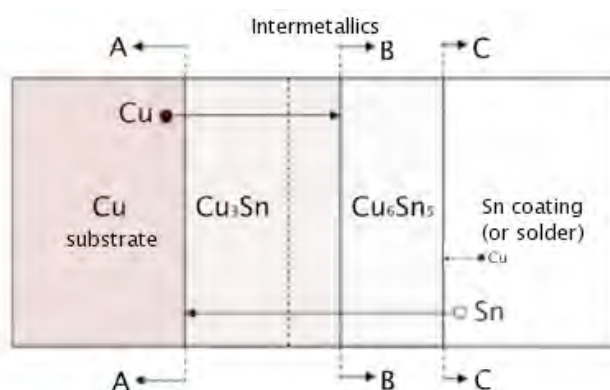


Figure 2.3: Typical profile and intermetallics formed during tinning and species diffusion during annealing. A, B and C indicate moving directions of interfaces during solid-state diffusion at thermal aging (from Peng *et al.*, 2007). Cu atoms diffuse from the substrate to be consumed at the $\text{Cu}_3\text{Sn}|\text{Cu}_6\text{Sn}_5$ interface and Sn atoms can reach the $\text{Cu}|\text{Cu}_3\text{Sn}$ interface leading to growth of Cu_3Sn . The dotted line shows the original $\text{Cu}|\text{Cu}_6\text{Sn}_5$ interface before annealing. In cases where Cu is present at the tin coating (or solder), this is mainly consumed at the $\text{Cu}_6\text{Sn}_5|\text{Sn}$ interface.

2.2.5. IDENTIFICATION OF CORRODED TIN COATINGS AND THE PRESENCE OF CASSITERITE PATINAS

Identification of $\epsilon\text{-Cu}_3\text{Sn}$ (37.74-39.5 wt% Sn) and $\eta\text{-Cu}_6\text{Sn}_5$ (61.31 wt% Sn) in corroded archaeological samples is challenging when using only composition analysis, because similar Sn composition ranges are found as surface corrosion on low-tin bronzes, which can vary in colour but can be bright or dark grey (Organ, 1962, 1963; Tylecote, 1979; Oddy, 1980; Oddy and Meeks, 1982; Scott, 1985; Tylecote, 1985; Robbiola and Hurtel, 1997; Dorigo *et al.*, 1998; Robbiola *et al.*, 1998a; Piccardo *et al.*, 2007). It is also unclear how these phases corrode in the burial environment, because a systematic investigation of the corrosion behaviour of the $\text{Cu} | \text{IMCs} | \text{Sn}$ system is absent. Sn is theoretically anodic to copper and to low-tin bronze due to electrode potential differences at the $\text{Cu}|\text{Sn}$ bimetallic couple; Sn therefore is expected to preferentially corrode in this system (Hedges, 1960; Wranglén, 1972: 184; Mattsson, 1996: 107). Meeks (1993b) points out that metallic tin coating has not been found on the surface of buried objects, which is supported by diffraction analyses of several

archaeological tinned brooches (Oddy and Bimson, 1985). This could support the hypothesis that tin corrodes preferentially during burial. These findings were challenged by a recent study where a nearly pure tin layer (c.1 μ m thick) was found on a leaded archaeological bronze (Šmit *et al.*, 2008) but oxygen content was not reported to fully assess the state of this layer.

The Cu-Sn intermetallic compounds are reported as cathodic to both copper and tin (Hedges, 1960; Turgoose, 1985). IMCs are generally expected to be preserved and are found between an underlying corroded bronze substrate and an oxidised tin layer; the latter may be completely lost due to dissolution in the burial environment, depending mainly on the potential/pH of the soil (Turgoose, 1985). Corrosion resistance of IMCs is deciphered by comparison to other high-tin phases such as δ -Cu₄₁Sn₁₁ rather than experimentally which is often preserved in the α + δ eutectoid of cast archaeological bronzes (Chase, 1977; Tylecote, 1985; Meeks, 1993b; Chase, 1994). However, corrosion that follows the δ dendritic pattern can occur via copper depletion from the dendrite cores that are richer in copper, suggesting that preferential corrosion in this system is possible (Scott, 1991: 107, fig.161; 2002: 340). It is unknown if ϵ -Cu₃Sn and η -Cu₆Sn₅ can be depleted of copper due to corrosion in particular environments. The limited number of corrosion studies focusing on η -Cu₆Sn₅ alone show that in near neutral aqueous (synthetic saliva) environments at 37°C, there is no indication of anodic tin dissolution (Fairhurst *et al.*, 1978), which in another experiment was attributed to the strong tendency of the phase to form protective films (Clarke and Britton, 1963).

Preservation of tin coatings on archaeological bronzes is generally attributed to the formation of thermodynamically stable tin oxides such as cassiterite which delay the corrosion rates of the underlying layer(s) (Britton, 1952: 13; Turgoose, 1985). Cassiterite (SnO₂) is reported on uniform lustrous black polished surfaces formed due to corrosion and found on high tin Chinese and Roman mirrors (Chase, 1977; Meeks, 1993b, 1993a; Shoukang and Tangkun, 1993) or other high tin bronzes (Oddy and Meeks, 1982; Meeks, 1993a), and Bronze Age axes ‘tinned’ by the cassiterite reduction method (Kinnes *et al.*, 1979; Oddy, 1980; Kinnes and Needham, 1981; Tylecote, 1985). Studies of black and silver surfaces on high-tin bronzes show that copper dissolution from α in the α + δ eutectoid (Chase, 1977) leaves a large volume behind permitting the *in situ* formation of poorly crystalline cassiterite which retains the originally smooth polished surface (SnO₂ PDF 41-1445 identified by SR-XRD) (Taube *et al.*, 1996; Taube *et al.*, 2008). Cassiterite patinas can contain small amounts of Cu, Fe, Pb and Si

besides Sn and it is likely that they are of $\text{Sn}_{1-x}(\text{CuFePbSi})_x\text{O}_2$ structure, as some atoms from soil elements probably replace Sn atoms in the SnO_2 lattice (Chase, 1994; Wang *et al.*, 1995).

Detection of cassiterite on low-tin bronzes is infrequent. A thin flaking white/grey cassiterite layer was reported on a heavily wrought 10wt% Sn bronze shield (Colacicchi-Alessandri and Ferretti, 2002). Robbiola (and Hurtel 1997; *et al.*, 1998a) have suggested that the presence of insoluble hydrated stannic oxides ($\text{SnO}_2 \cdot x\text{H}_2\text{O}$), which could be mixed with Cu-containing compounds are responsible for the corrosion resistance of archaeological bronzes. Such mixture of Sn_{IV} oxides / hydroxides and copper corrosion is generally reported as the result of Type I corrosion but their precise nature is unclear (Piccardo *et al.*, 2007). Piccardo *et al.*, (2007) attempted to identify these corrosion compounds and tin oxides and hydroxides on archaeological bronzes using Raman spectroscopy but experienced difficulties in detecting hydrated stannic oxides. This was due to low intensity of characteristic Sn_{IV} peaks which was attributed to be a function of the degree of crystallinity of the compound and due to peak overlap with Cu_I oxide peaks (*ibid.*). This study concludes that a very small crystal size and/or the presence of amorphous dehydrated stannic oxide could be present on the archaeological samples examined.

Analysis of a corroded Sn-solder where in fact IMCs could be present reports the complete conversion of tin to tin oxides (Piccardo *et al.*, 2007). The analysis area (K4) contained traces of lead and Sn_{IV} oxides and hydroxides without copper; the 2-7at% Cu reported at areas close to the bronze substrate was assigned to the migration of Cu ions and the substitution of Sn ions in the SnO_2 crystal lattice rather than the potential presence of a corroding IMC. More work is required to understand the corrosion behaviour of the Cu/IMCs/Sn system in order to interpret analyses and link them to surface finishes and appearance of helmets in antiquity.

A small number of case studies successfully employed X-ray diffraction to detect Cu-Sn phases produced by tinning on archaeological bronzes (Oddy, 1980; Oddy and Bimson, 1985; Meeks, 1986; Qinglin and Scott, 2003). Time-of-flight neutron diffraction has been successfully employed as a non-destructive analytical method to characterise archaeological bronzes (Kockelmann *et al.*, 2000; Siano *et al.*, 2002; Kockelmann *et al.*, 2004a) and other materials in heritage science research (Adriaens and Demortier, 2004; Adriaens *et al.*, 2005), but its potential for analyses of tinned objects has not yet been explored. This non-destructive method would permit analysis of precious objects where sampling is prohibited, and would in principle increase the potential to detect patchy evidence of tinning hidden under corrosion of archaeological bronzes due to its ability to analyse larger volume areas on an object.

2.3. RESEARCH OBJECTIVES AND LIMITATIONS

Since Greek helmets could have polychrome decoration by means of plating, painting or patination, as supported by artistic evidence and the currently limited archaeometric research, a systematic scientific investigation of surface finishes could provide evidence for their original visual appearance. A literature review showed that grey, silver, black or other colour patinas found on archaeological low-tin bronzes can be the result of corrosion, intentional corrosion (patination) or surface plating (e.g. tinning). Corrosion obscures Cu-Sn intermetallic phases (IMCs) developed during tinning and it is unclear how they change during burial. Tin concentration of IMCs can lie within the range of corrosion found in patinas of low-tin archaeological bronzes making SEM-EDX composition analysis challenging for their identification. It seems that, based on the frequency of its use, the usefulness of diffraction analysis is undervalued when investigating surface finishes and tinning. More scientific data and an evaluation of diffraction methods is required to further understand tinning microstructures and the development of smooth black / grey patinas on archaeological bronzes.

This research offers scientific evidence on the surface finishes of helmets in the Archaic period based on analyses of actual helmets. Effective identification of plating and patination on corroded bronzes relies on understanding (a) what comprises evidence of tinning on corroded bronzes, (b) the metallurgy and corrosion of the bronze and tinning, and (c) selection of appropriate analytical methodology and instrumentation. Since each subject potentially merits a more profound investigation than is possible here, research focuses on information relevant to the primary aim of this study: the characterisation of surface finishes on the selected helmets. A major part of the methodology attempts to develop understanding of what constitutes evidence of tinning and how this can be effectively detected and distinguished from silver/black corrosion surfaces. This approach is taken for three main reasons:

(a) While Meeks' systematic work (1986) reports extensive microstructural evidence that could be employed to identify tinning methods, this now needs to be viewed in the light of current knowledge of Cu-Sn interactions to better understand what constitutes evidence of tinning. Questions asked include which intermetallic compound is the predominant phase developed during tinning of copper and low-tin bronzes and if it can be used as a 'marker' phase that evidences tinning.

(b) According to Meeks (1986, 133), *'[t]he continuing interest and the need for research into the nature of tin-rich surfaces on bronze antiquities is underlined by the uncertainties that*

occur in their classification by curatorial, conservation and scientific staff at museums. The problems are particularly associated with interpretation of the mechanisms by which the complex surface microstructures are formed. These problems are still valid. Currently, identification of tinning is based mainly on investigations of cross-sectional samples. Analysis relies on scanning electron microscopy with backscattered electron imaging and elemental mapping with no (or rarely available) supporting diffraction analysis of phases. Sampling of tinned objects is often prohibited by museum policy due to object shape/condition, or it may not be representative due to sparse remains of tinning. The necessity for non-destructive analytical methods for the investigation of tinned objects is obvious. For this reason, the methodology employed seeks to evaluate the potential of microscopic methods and state of the art technologies such as neutron diffraction for the characterisation of tinning evidence on archaeological low-tin bronzes.

(c) Robbiola's milestone work (Robbiola *et al.*, 1998a) for understanding corrosion mechanisms of low-tin archaeological bronzes has been based on a limited number of cross-sectioned samples. It is envisaged that this unique set of helmet samples will add data to the current knowledge bank, with focus on grey and black colour surfaces, and how these may differ to tinning remains.

CHAPTER 3. METHODOLOGY AND EXPERIMENTAL

3.1. OVERVIEW

The nature of this project required the use of a variety of analytical methods; access to a large number of helmets; knowledge of traditional tinning methods for laboratory replication; access to X-ray and neutron diffraction sources to characterise experimental tinned samples; and access to a small number of archaeological objects that are likely to be tinned used as a pilot work to understand evidence of tinning on corroded samples. Challenges related to sampling archaeological material and details of access protocol are discussed elsewhere (Manti and Watkinson, 2007; Henderson and Manti, 2008). This chapter presents background principles and discusses advantages and limitations of methods used, to support their role and service to this study. Diffraction methods are described in detail because this study assesses their effectiveness for detecting Cu-Sn intermetallics. Analysis procedures, materials used, and instrumental details are reported below, including calibration and quality assurance checks for SEM-EDX analysis.

Prior to scientific investigation of surface finishes of Archaic period Greek helmets (end 8th – mid 5th c. BC, an experimental protocol was designed to (a) review what comprises evidence of tinning based on new data and develop a methodology for its efficient detection using SEM-BSE and diffraction methods; and (b) identify composition and metallurgy of helmets because they affect surface appearance and corrosion. Mechanical properties, corrosion resistance and the diffusion coefficient of metals are directly related to their alloy composition and microstructure (Petzow, 1999). Findings from these two research phases input knowledge for interpretation of surfaces observed on helmets. The workflow and an outline of the methodology employed and method used is presented in Table 3.1.

Analytical Investigation		
Experimental tinning	Typology and metallurgy of helmets	Surface finishes on helmets
Aims		
<ul style="list-style-type: none"> • Characterisation of Cu-Sn phases on modern and selected archaeological samples, to understand what comprises evidence of tinning • Evaluation of effectiveness of diffraction methods to detect Cu-Sn intermetallics on archaeological bronzes 	<ul style="list-style-type: none"> • Identification of alloy composition and metallurgy because they affect surface appearance and corrosion 	<ul style="list-style-type: none"> • Investigation of the surface to evaluate evidence of tinning, patination or polishing • Examination of fine grey/silver, black or other colour patinas to explore mechanisms of formation
Workflow and methods in sequence of use		
<ul style="list-style-type: none"> • Observation and interview of tinsmith • Laboratory tinning • Macroscopic optical observation of model tinned tokens • SEM-BSE imaging of surface • SEM-BSE imaging of tinned profiles in cross-sectioned samples • CuKα XRD of surface of tinned tokens • ToF-ND of tinned tokens • Evaluation of available crystallographic data and model selection • Qualitative analysis of XRD and ND data • Rietveld quantitative analysis of ND data from tinned tokens • Identification of problems and effectiveness of SEM-BSE and diffraction methods • Testing of methodology on small number of Roman bronzes 	<ul style="list-style-type: none"> • Characterisation of typology and chronology to place helmets in archaeological context • Macroscopic examination of technical features • X-radiography of a small number of helmets • ToF-ND texture analyses of selected helmets and helmet samples to understand metallurgy • SEM-EDX composition analyses of core metal • Metallography of etched cross-sectioned samples 	<ul style="list-style-type: none"> • Macroscopic observation of surface of helmets • SEM-BSE imaging of the surface of samples • CuKα and SR-XRD of the surface of selected samples • Polarised microscopy of mounted cross-sectioned samples before etching for metallography • SEM-BSE imaging of corrosion profiles in cross-sections • SEM-EDX composition analysis and mapping of corrosion layers in cross-section

Table 3.1: Workflow of scientific investigations and outline of methods used.

The physical nature of surface finishes and tinning on helmets, a small number of other archaeological objects and experimental tinned copper and bronze tokens were investigated using scanning electron microscopy (SEM) with backscattered electron imaging (BSE) employed in plan-view and in cross section. Cross-sectional investigation of the surface of the samples was undertaken using SEM-BSE imaging, energy dispersive X-ray spectroscopy composition analyses (EDX), SEM-EDX mapping and polarised microscopy. These methods were also used to investigate the manufacture of objects. Metallurgical evaluation was supported by macroscopic observations, x-radiography and neutron diffraction texture analysis (Manti and Watkinson, 2007). CuK α X-ray diffraction (XRD), synchrotron radiation X-ray diffraction (SR-XRD) and time-of-flight neutron diffraction (ToF-ND) were used selectively to characterise qualitatively crystalline corrosion and quantitatively intermetallic compounds on experimental tinned tokens and archaeological samples.

A small number of selected Roman bronze items exhibiting silver/grey surface are included as a pilot study to further understanding of physical evidence of tinning on archaeological bronzes. Experimental tinning was designed to produce examples of Cu-Sn intermetallic compounds (IMCs), which develop during tinning in order to provide insights into their formation, physical nature and structure. Model tinned samples were cross-evaluated with SEM-BSE and XRD prior to investigating the potential of ToF-ND for the non-destructive detection of tinning phases on low-tin bronzes.

3.2. OBJECTS INVESTIGATED AND SELECTION OF SAMPLES

The selection of archaeological material for study was influenced primarily by access opportunities to archaeological material and an academic interest for the archaeology of northern Greece. The study includes helmets from excavations at the sanctuary at Olympia by the German Archaeological Institute, Archaic period cemeteries at Sindos, Aghia Paraskevi and Nea Philadelphia that are held in the Archaeological Museum of Thessaloniki and helmets from the Archontiko cemetery at Pella. Other helmets are part of museum collections belonging to the Ashmolean, the Pitt Rivers, the Fitzwilliam and the National Museum of Wales. In total, 154 helmets were closely examined and documented, 107 of which were sampled within a broader project on the characterisation of helmet manufacture and production workshops. Small fragments were removed from unobtrusive areas on helmets or at fractured areas using metal clippers. 58 of these are included in this thesis as examples of

technical varieties. 36 out of the 58 helmets exhibited a surface undisturbed from mechanical or chemical cleaning to permit investigation of their fine grey, black or other corrosion surface. Small fragments removed from these 36 helmets were investigated for surface finishes and tinning.

The selected helmets are of the two major Greek types, Corinthian and Illyrian; one Attic, two Chalkidian, and one Etruscan style helmet are included for comparison (Table 3.2). Note that sample naming (e.g. OL56.1) refers to the place of excavation (e.g. OL=Olympia or PE=Pella), the number of helmet (e.g. 56) and the sample number (e.g. .1). Because information on dating and context was unavailable for most of the investigated pieces, the helmets were placed in a typological/chronological frame to support discussion of manufacture prior to analyses. This was based on stylistic similarities and, where known, the archaeological context of each helmet. Technical description of the helmets and the typological/ chronological framework followed here is mainly that described by Pflug (1988a; 1988b; 1988c; 1988d; 1988e) and it is discussed in Chapter 4, with stylistic description of each helmet in Appendix 1.

A small number of Roman (1st – 2nd AD) archaeological bronzes from the National Museum of Wales with visual evidence of a silver/grey surface were selected for analysis (Table 3.3) to examine the presence and nature of Cu-Sn intermetallic phases on corroded bronzes. Selection was based on availability of samples, appearance, and contextual information on the objects' use in antiquity, which increased the likelihood that the grey/silver surface on the objects was due to tinning. Examination and analysis of these samples are in Chapter 3.

Table 3.2 (below): List of helmets investigated. EDX and MET denote the investigation of cross-sections for corrosion and metallurgy. GEM and ROTAX indicate time-of-flight neutron diffraction and XRAY X-radiography.

Helmet Type	Museum Acc. No.	Archaeological Context	Code	Analysis
Archaeological Museum, Olympia, German Archaeological Institute				
Chalkidian	B7080	Not available	OL66	EDX, MET
	B5239	Not available	OL79	EDX, MET, GEM
Corinthian	B10518	Not available	OL_B10518	DISCUSSION
	ab34	Not available	OL17	EDX, MET
	ab64	Not available	OL21	EDX, MET
	B9805	Not available	OL27	EDX, MET
	B2608	Not available	OL29	EDX, MET
	B2648	Not available	OL31	EDX, MET
	B10534	Not available	OL41	EDX, MET
	B7073	Not available	OL44	EDX, MET
	B1501	Not available	OL46	EDX, MET
	B4411	Stadium, North Wall, Well 13 (in groundwater), 27/11/1959	OL49	EDX, MET
	B4698	Not available	OL50	EDX, MET
	B6550	Not available	OL53	EDX, MET
	B10526	Not available	OL57	EDX, MET
	B10528	Not available	OL58	EDX, MET
	B5177	Not available	OL63	EDX, MET
	B6131	Not available	OL65	DISCUSSION
	B4150	Not available	OL68	DISCUSSION
	B10527	Not available	OL69	EDX, MET
	B4799	Not available	OL70	EDX, MET
	B5070	Stadium, North Wall, Well 21, 17/10/1960	OL71	EDX, MET
	B5167	Stadium, North Wall, Well 21, 17/10/1960	OL73	EDX, MET
	B5176	Stadium, North Wall, Well 14, 2/12/1959	OL74	EDX, MET
	B5178	Stadium, North Wall, Well 23, 11/2/1960	OL75	EDX, MET
B6960	Not available	OL80	DISCUSSION	
Illyrian	B7170	Not available	OL11	EDX, MET
	BE58	Not available	OL13	EDX, MET
	B3348	Not available	OL4	EDX, MET
	B4821	Not available	OL5	EDX, MET
	B4667	Not available	OL78	EDX, MET
	B5115	Not available	OL9	EDX, MET
Archaeological Museum, Pella, Archontiko cemetery				
Attic	A2002G189	Field Taousanidi, pit grave 189, 14/6/2002	PE4	EDX, MET
Illyrian	A2001G10	Field Taousanidi, pit grave 10, orygmata 3, 24/6/2001	PE1	EDX, MET, GEM
	A2002G194	Field Taousanidi, pit grave 194, 10/7/2002	PE2	EDX, MET, GEM
	A2001G9	Field Taousanidi, pit grave 9, orygmata 2, 24/6/2001	PE3	EDX, MET

Helmet Type	Museum	Acc. No.	Archaeological Context	Code	Analysis
Archaeological Museum, Thessaloniki					
Sindos cemetery					
Illyrian	M08563	T111		S9	XRAY
	M08561	T E1		S1	XRAY
Aghia Paraskevi cemetery					
Illyrian	M09119	T14		AP1	XRAY
	M016405	T322, 8/3/1990		AP4	EDX, MET, XRAY
	M016423	T325, 8/3/1990		AP5	EDX, MET
	M016603	T349, 8/10/1990		AP6	XRAY
Nea Philadelphia cemetery					
Illyrian	M023115	Not available		NF5	XRAY
Fitzwilliam Museum, Cambridge, Unknown excavation					
Illyrian	GR.B.5	Unknown		FZ2	DISCUSSION
National Museum Wales, Cardiff, Unknown excavation					
Corinthian	47.409_7.24	De Walden Collection		NMW1	XRAY
	47.409_cat36	De Walden Collection		NMW11	XRAY
	47.409_7.26	De Walden Collection		NMW2	XRAY, ROTAX
	47.409_7.33	De Walden Collection		NMW3	XRAY
	47.409_7.36	De Walden Collection		NMW4	XRAY
	47.409_7.39	De Walden Collection		NMW5	XRAY
	47.409_7.40	De Walden Collection		NMW6	XRAY, ROTAX
	47.409_7.41	De Walden Collection		NMW7	XRAY
	47.409_7.42	De Walden Collection		NMW8	XRAY
		NMW_877	De Walden Collection		NMW9
Illyrian	47.409_cat27	De Walden Collection		NMW10	XRAY
Pitt Rivers Museum, Oxford, Unknown excavation					
Corinthian	1884.32.16	Unknown		PR1	EDX, MET
Etruscan	1884.32.15	Unknown		PR4	EDX, MET

Table 3.3 (below): List of investigated Roman objects

Object type	Excavation	Code	Samples
National Museum Wales, Cardiff - Roman period (1-2nd c. AD) objects			
Harness fitting	Brecon Gaer Roman fort	BG	BG1 to BG2
Skillet	Manorbier	MB	MB1 to MB3
Decorated collar	Boverton, Vale of Glamorgan	BOV	BOV
Ceredigion museum, Aberystwyth - Roman period (1-2nd c. AD) objects			
Skillet	Unknown	CER	CER1 to CER2

3.3. X-RADIOGRAPHY

X-radiography is commonly employed to reveal evidence of manufacture of archaeological bronzes, such as casting porosity or uneven thickness due to hammering that can be in distinct patterns (Lang, 1997: 41; Craddock, 2009: 157). The 11 investigated helmets belonging to the National Museum of Wales had X-radiographs taken by museum staff prior to this study. The archaeological museums at Olympia, Thessaloniki and Pella do not have x-radiography facilities. Transportation of a portable X-ray machine to the premises of these museums was not possible due to lack of funds. Only 6 helmets from the Archaeological Museum of

Thessaloniki were additionally X-rayed at the premises of the nearby Museum of Byzantine Culture in Thessaloniki (Table 3.2).

3.4. DOCUMENTATION AND MOUNTING OF SAMPLES

All samples were documented using microscopy prior to investigation with the SEM, before mounting in plan view and after mounting and polishing in cross-section. The samples were examined and documented using a Nikon SMZ1000™ stereomicroscope fitted with a Nikon CoolPix 4500™ camera and EclipseNet™ software. This contributed to surface evaluation and selection of previously untreated samples for study.

Cross-sectioned samples were prepared by mounting in Struers Epofix™ epoxy resin, followed by grinding and polishing. A small number of samples were embedded in Technovit 5071™ methyl-methacrylate based resin, which is reversible in acetone and would facilitate potential future plan-view surface investigations. Grinding and polishing of mounted samples took place using a Struers Labopol-5™ machine with progressively finer grit of silicon carbide papers (180, 320, 1600, 1200, 2500, 4000) and Metadi™ diamond polishing pastes (3-1/4 µm) using aqueous media for model tinned samples. Non-aqueous media and white spirit were used for polishing archaeological samples to prevent dissolution of water-soluble species such as chloride from the corrosion layers. Polished blocks were kept in desiccated storage.

Samples were carbon coated for both plan-view and cross-sectional SEM observation using the Emitech K450™ Carbon Coater with carbon fibre strands. To facilitate SEM investigation of the surface of selected model tinned tokens, excess tin was dissolved from the surface using 5% HCl in water (of a 32% conc. HCl stock solution), followed by cleaning with water and drying with acetone. This revealed the three-dimensional nature of the underlying intermetallic compounds (Gagliano and Fine, 2001; Prakash and Sritharan, 2001; Kang *et al.*, 2002; Suh *et al.*, 2008).

Following EDX composition analyses and BSE imaging, the carbon coating was carefully removed using industrial methylated spirit, to prepare helmet samples for etching and metallographic examination. Etching of polished helmet sections took place using 5% alcoholic ferric chloride.

3.5. POLARISED MICROSCOPY

Investigation and documentation of corrosion profiles and metallographic structures of cross-sectioned samples was undertaken using bright (BF) and dark field (DF) reflected light set-ups at the Nikon Eclipse ME600D™ metallurgical microscope fitted with the SPOT RT™ colour digital camera. Polarised microscopy is a commonly employed method for microstructural observations (McCrone *et al.*, 1978: 64;86; Bailey, 1982; Scott, 1991; Vander Voort, 2004a; Vander Voort, 2004b).

Metallic tin is optically anisotropic and gives rise to colour effects under polarised light (Scott, 1991: 49). Tin appears light silvery in colour, η -Cu₆Sn₅ is slightly grey/blue, ϵ -Cu₃Sn is darker blue and δ -Cu₄₁Sn₁₁ is light mid-grey/blue which could aid their identification on experimental tinned samples (Meeks, 1986; Scott, 2002: 403). Corrosion compounds such as cuprite (Cu₂O) show distinct colour in plane polarised light, assisting their characterisation (Scott, 2002; De Ryck *et al.*, 2003). Recently it was shown that the colour of red-orange-yellow layered surface corrosion structures on low-tin bronzes depends on the relative proportion of copper oxides and tin oxides and hydroxides in each phase aiding their characterisation (Piccardo *et al.*, 2007).

Metallographic examination provides information on the manufacturing history of an object via observations of features such as the crystal size and shape of single or multiphase metals, the presence of micro-segregation, inhomogeneities, porosity, void formation or structural imperfections such as twinning originating from crystal growth processes (Vander Voort, 2004c: 23-24). Grain boundaries are typically revealed with selective chemical dissolution (etching) of micro-constituents from a flat-polished cross-sectioned sample (Bailey, 1984: 3; Petzow and Elssner, 1985: 59;56; Ricksecker and Bower, 1985). Microstructural features such as grain boundaries and twins on cross-sectioned samples were revealed here by etching with alcoholic ferric chloride solution [5g FeCl₃, 15ml HCl (32% conc. stock solution), 60ml ethanol (96% conc.)] applied with a cotton swab for a few seconds. Grain size measurements took place in order to provide an indication of grain growth during annealing contributing to discussions on the nature of core microstructures. This was based on common techniques counting the number of grain boundaries in a known surface area manually (Higginson and Sellars, 2003) from calibrated images using ImageJ™ software (Rasband, 2008).

3.6. SCANNING ELECTRON MICROSCOPE BASED METHODS

The versatile nature of the Scanning Electron Microscope (SEM) makes it the most commonly used instrument in solid materials research because it combines high-resolution large-depth-of-field micrographs with microanalyses (Meeks, 1987; Meeks, 1988; Scott, 1988). It is commonly used for investigating tinning phases (Meeks, 1986; Meeks, 1993b, 1993a; Anheuser, 1996; Tu, 1996; Lee and Duh, 1999; Anheuser, 2000; Gagliano and Fine, 2001; Yu *et al.*, 2005; for example Suh *et al.*, 2008) and for the characterisation of corroded bronzes (Oddy and Meeks, 1982; Scott, 1985; Robbiola *et al.*, 1993; Robbiola and Hurtel, 1997; Dorigo *et al.*, 1998; Robbiola *et al.*, 1998a). In this work, the CamScan 2040 Scanning Electron Microscope was used that is coupled with the Oxford Link Pentafet 5518 Dispersive X-ray spectrometer, situated at the Department of Archaeology and Conservation, Cardiff University. SEM-BSE imaging and SEM-EDX analysis were employed for plan-view and cross-sectional investigations of model tinned and archaeological samples.

In an SEM, electrons generated by an electron gun (emission current) are accelerated to a given energy (beam current keV) and are focused onto the specimen with electron lenses (Goodhew *et al.*, 2001; Goldstein, 2003). The electron beam moves to a series of fixed locations along lines on the specimen where it interacts with the specimen producing a variety of signals including backscattered (BSE), secondary electrons (SEI) and X-rays which can be collected simultaneously by different detectors (Goldstein, 2003: 12-16). BSE images are generated by elastic scattering occurring when beam electrons are deflected into a new path without any energy loss and SEI and X-ray analysis signals by inelastic scattering which occurs due to energy loss because of the gradual transfer of e^- to the specimen's atoms (Goldstein, 2003: 63; Daintith Daintith, 2009). These processes occur simultaneously and result in a three-dimensional interaction volume on the sample; its shape and dimensions depend on the beam energy and the elemental composition of the sample area. For copper at 20keV beam current, this can be a pear shaped $1-2\mu\text{m}^3$ volume area; for alloys it depends on the density of the matrix (g/cm^3) and the mass absorption coefficient ($\mu_m = \mu/\rho$) of the elements present (Goldstein *et al.*, 2003: 286).

3.6.1. ENERGY DISPERSIVE X-RAY ANALYSIS

X-rays generated from the beam/specimen interaction volume have energies (keV) characteristic to the elements present in the specimen, including those constituting the continuum background, which do not provide information on elemental composition

(Goldstein *et al.*, 2003: 271). The intensity ratio of characteristic X-rays collected by an energy-dispersive spectrometer is automatically processed to provide quantitative element concentration. The collected spectra were processed using the Oxford Link Isis™ Series 300 analytical software. The system uses common data processing including peak deconvolution of overlapping peaks, calculation of the apparent concentration from sample to standard intensity ratios and ZAF corrections (OIA, 1997, 2005) for atomic number of the matrix and backscattering effects (Z), X-ray absorption phenomena occurring in the specimen according to known mass absorption coefficients of elements (A), and fluorescence excitation phenomena arising from excitation of secondary X-rays (F) (Goodhew *et al.*, 2001: 201; Goldstein *et al.*, 2003: 10, 16, 404).

Energy dispersive X-ray spectroscopy has typical detection limits between 0.1-0.3wt% and is mainly used for analysis of major (>10wt%) and minor (1-10wt%) elements (Goldstein, 2003: 19). Wavelength dispersive spectrometers (WDS) have typical detection limits around 0.001-0.01 wt% due to the increased resolution of WD spectrometers (typically 8eV) as opposed to EDX (typically 600eV) (Goldstein *et al.*, 2003: 11-12, 20, 135, 355). This project does not require such low detection limits of trace elements and SEM-EDX was used for characterisation of metallic alloys and corrosion layers. The laboratory standard EDX analysis conditions were used with 35mm sample/detector distance and zero sample/detector tilt. Analysis was undertaken at 20 kV accelerating potential with 100s livetime. The system was calibrated using a set of pure elements and mineral standards supplied by Micro-Analysis Consultants Ltd, Standards-Block No. 4629 (1997).

3.6.1.1. System evaluation for composition analyses of low-tin bronzes

EDX analysis of the un-corroded bronze core of archaeological samples was conducted in multiple areas in the middle of each cross-section with 1000x magnification, with 120x96µm (11.52 mm²) field of view. The analysis area was bigger than the average crystal size to minimise compositional variations such as segregation at the grain boundaries, thus facilitating composition analyses of the average structure.

The performance of the SEM-EDX system was evaluated prior to composition analysis of the samples using a reference low-tin low-lead bronze of known composition (standard Bronze C71-34) provided by BNF Metals technology Centre, Oxford (Table 3.4). Analyses accuracy (correctness) and precision (reproducibility) (AMC, 2003) were established by calculating the relative accuracy error % (RAE%) of the analyses in relation to the reference C71-34 bronze

composition, and the relative precision error% or relative standard deviation (RSD%) of the analyses in relation to their standard deviation, based on the equations:

$$\text{(eq. 1)} \quad \text{Relative accuracy error \%} = 100 \times \frac{\text{measured value} - \text{true value}}{\text{true value}} \quad (\text{Goldstein, 2003: 466}).$$

$$\text{(eq. 2)} \quad \text{Relative Standard Deviation (RSD) \%} = 100 \times \frac{\text{Standard Deviation (SD)}}{\text{Average analyses value}} \quad (\text{Reedy and Reedy, 1988: 15;}$$

Shennan, 1997: 44; Kealey and Haines, 2002: 30).

Table 3.4 shows EDX results of 10 area analyses of the bronze standard taken at standard acquisition set up at 1000x magnification within a single analysis run. The results were normalised to 100% and compared to the reported composition of the standard and to analyses of the same standard bronze obtained by another user Mary Davies using different calibration files but the same SEM-EDX set up (MDx1000) (Table 3.4). Measurements with negative concentration values are also included to demonstrate overall quality of data. The results show satisfactory reproducibility between different analysts and a high accuracy for major elements when compared to the composition of the standard bronze. Relative accuracy error was less than 1% for Cu and varied for minor elements at concentration ranges between 1-10wt% depending on the element: approximately 5% for Sn, 2% for Zn and c.19% for Pb. Elements in trace concentrations between 0.1-1wt% showed increased accuracy error with c.18% for Fe, c.24% for Sb and a very high error for As. The spread of values for Al, P, Ni, S, Mn, As and Sb of the mean analysis is above or near the standard concentration wt% (Table 3.5) and therefore unreliable for those elements at concentrations around or below 0.1wt% in similar experimental conditions. Measurements of Fe (c. 0.2wt%) show good precision and accuracy. Measurements with better precision (RSD%) were obtained for elements above 1wt% with Cu (RSD 1.81%), Sn (5.1%), Zn (9.9%). The levels of precision and accuracy are satisfactory for the characterisation of core metal composition in this project type.

Analyses/Element	Al	P	Ni	S	Mn	As	Sb	Fe	Zn	Pb	Sn	Cu	Total
Nominal wt% bronze C71-34	0.01	0.01	0.01	0.06	0.06	0.13	0.15	0.22	1.10	2.50	7.81	87.94	99.89
Analyst: MDx1000	-0.01	0.04	-0.05	0.07	-0.06	-0.65	0.24	0.24	1.28	1.64	8.23	89.03	99.97
C71.34_x1000_1	0.02	0.02	-0.09	0.05	0.04	0.65	0.01	0.26	0.95	2.84	7.74	87.49	100.35
C71.34_x1000_2	0.04	0.00	0.00	0.11	0.14	0.01	0.14	0.20	1.15	2.71	7.78	87.73	101.46
C71.34_x1000_3	0.09	-0.04	0.09	0.14	0.12	0.41	0.13	0.24	1.05	1.94	7.32	88.50	100.07
C71.34_x1000_4	0.09	-0.02	0.02	0.14	0.18	0.74	-0.07	0.22	1.07	3.07	7.14	87.42	100.88
C71.34_x1000_5	0.02	0.00	0.02	0.03	0.09	0.42	0.06	0.22	0.96	2.97	7.94	87.26	100.04
C71.34_x1000_6	0.04	-0.02	0.00	0.19	0.16	0.46	0.24	0.30	1.32	2.28	7.39	87.66	99.90
C71.34_x1000_7	0.05	0.02	0.02	0.11	0.10	0.41	0.27	0.32	1.14	1.56	6.85	89.16	98.75
C71.34_x1000_8	0.17	0.02	0.06	0.10	0.01	0.54	0.00	0.26	1.20	3.35	6.84	87.46	97.47
C71.34_x1000_9	-0.03	-0.04	0.03	0.15	0.09	0.30	0.24	0.30	1.19	2.43	7.86	87.48	100.00
C71.34_x1000_10	0.04	0.00	0.01	0.32	0.10	1.14	0.11	0.28	1.21	6.53	7.41	82.85	101.52
Analyses mean	0.05	-0.01	0.02	0.13	0.10	0.51	0.11	0.26	1.12	2.97	7.43	87.30	100.04
min	-0.03	-0.04	-0.09	0.03	0.01	0.01	-0.07	0.20	0.95	1.56	6.84	82.85	97.47
max	0.17	0.02	0.09	0.32	0.18	1.14	0.27	0.32	1.32	6.53	7.94	89.16	101.52
Standard Deviation (SD)	0.05	0.02	0.04	0.08	0.05	0.28	0.11	0.04	0.11	1.29	0.38	1.58	1.15
Rel. Precision (RSD%)	100.0	-334.2	267.7	55.8	47.8	55.4	94.6	14.7	9.9	43.6	5.1	1.8	1.2
Rel. Accuracy Error (RAE%)	413.1	-167.5	62.8	123.9	69.4	289.8	-23.8	18.2	1.9	18.6	-4.9	-0.7	0.15
RAE% to analyst MD	-613.5	-116.9	-132.6	92.1	-269.5	-178.0	-52.3	8.5	-12.3	81.0	-9.8	-1.9	0.1

Table 3.4: Normalised wt% SEM-EDX analyses on reference bronze C71-34 standard by BNF Metals for evaluation of system performance on low-tin bronze. Negative measurement values and original totals are reported for completeness.

Element	Standard wt%	Averaged analysis	Standard Deviation (SD)	Relative Precision (RSD%)	Relative Accuracy Error (RAE %)
Al	0.01	0.05	0.05	100.0	413.1
P	0.01	-0.01	0.02	-334.2	-167.5
Ni	0.01	0.02	0.04	267.7	62.8
S	0.06	0.13	0.08	55.8	123.9
Mn	0.06	0.10	0.05	47.8	69.4
As	0.13	0.51	0.28	55.4	289.8
Sb	0.15	0.11	0.11	94.6	-23.8
Fe	0.22	0.26	0.04	14.7	18.2
Zn	1.10	1.12	0.11	9.9	1.9
Pb	2.50	2.97	1.29	43.6	18.6
Sn	7.81	7.43	0.38	5.1	-4.9
Cu	87.94	87.30	1.58	1.8	-0.7

Table 3.5: Summary of performance statistics of EDX analysis on standard bronze C71-34 by BFN Metals.

3.6.1.2. System verification for analysis of oxygen and corrosion products

With regards to quantitative EDX analysis of corrosion layers, there are three main challenges:

(a) The accurate detection of light elements such as oxygen using EDX systems (Goldstein, 2003: 319-341). The active part of the EDX detector is behind ‘window’ materials, which can absorb light elements to different degrees based on their composition and thickness. Modern Si(Li) X-ray detectors with thin or ultra-thin windows can permit detection of elements as light as beryllium ($Z>4$) and are used for the analysis of oxides (Laskin and Cowin, 2001; Goldstein, 2003: 341;392; Laskin *et al.*, 2006). The Oxford Link Pentafet 5518 EDX spectrometer used in this study has a super-thin atmosphere window (ATW2), which permits X-ray detection of elements heavier than beryllium ($Z>4$) (see Laskin and Cowin, 2001).

(b) The presence of elements that are moved or removed during measurements due to beam damage (Goldstein, 2003: 16). This can be overcome by reducing the beam current below 10keV, but it would mask identification of heavier elements, as their detection depends on X-rays collected at higher energies, which are not excited at such low beam currents. For this reason, EDX analysis was undertaken at 20 keV.

(c) The irregular surface of cross-sectioned corroded samples formed during polishing because of the hardness differences between core metal and corrosion layers (Samuels, 1985).

Scratches and irregularities increase electron backscattering and X-ray absorption and change the known X-ray to detector paths; this leads to low totals and reduction of the accuracy and precision of X-ray analysis (Goodhew *et al.*, 2001: 164); (Goldstein, 2003: 357-382;466-479). It was previously shown that the normalisation of analysis data collected from highly irregular surfaces such as powdered samples can result in acceptable accuracy and precision (Bronk and Freestone, 2001; Laskin and Cowin, 2001; Laskin *et al.*, 2006). Corrosion layers on polished samples are expected to show a smaller degree of irregularity when compared to powders supporting that EDX analyses from corrosion can provide satisfactory results.

The EDX system was verified using a wollastonite (CaSiO_3) standard (MAC No:4629), which was used for system calibration for oxygen; analyses were taken at 1000x magnification, 20kV and normal instrument set-up. EDX wt% results for oxygen show excellent accuracy (RAE 1.85%) and precision (RSD 1%) (Table 3.7, 3.7). The analysis totals are near 100% because of the flat polished surface of the wollastonite sample. Even if this may not be repeated during analyses of corroded layers, this shows the effectiveness of the system to measure oxygen with good accuracy and precision.

Element	Standard wt%	Averaged analysis	Standard Deviation (SD)	Relative Precision (RSD%)	Relative Accuracy Error %
O	41.53	42.30	0.42	1.0	1.8
Si	23.93	24.05	0.21	0.9	0.5
Ca	34.49	33.52	0.27	0.8	-2.8
Fe	0.05	0.13	0.03	21.0	164.1

Table 3.6: Summary of performance statistics of EDX analysis on wollastonite standard undertaken to evaluate system performance for the measurement of oxygen in crystalline materials.

Analyses/Elmt	O	Si	Ca	Fe	Total
Standard composition wt%	41.53	23.93	34.49	0.05	99.45
Woll1	41.73	24.27	33.87	0.13	99.61
Woll2	42.08	24.30	33.52	0.10	99.70
Woll3	41.95	24.25	33.70	0.11	98.46
Woll4	42.93	23.75	33.20	0.12	101.21
Woll5	42.27	23.98	33.64	0.11	99.98
Woll6	42.13	24.06	33.64	0.17	99.57
Woll7	43.03	23.63	33.18	0.16	99.54
Woll8	42.06	24.02	33.73	0.19	100.52
Woll9	42.01	24.18	33.70	0.11	99.86
Woll10	42.76	24.09	33.01	0.14	101.79
mean	42.30	24.05	33.52	0.13	100.02
min	41.73	23.63	33.01	0.10	98.46
max	43.03	24.30	33.87	0.19	101.79
Standard Deviation (SD)	0.42	0.21	0.27	0.03	0.89
Rel. Precision (RSD%)	1.00	0.87	0.81	21.04	0.89
Rel. Accuracy Error (RAE%)	1.85	0.50	-2.81	164.10	0.58

Table 3.7: Normalised wt% SEM-EDX analyses of wollastonite for evaluation of system performance for the detection of oxygen. The last column includes original total values.

3.6.2. SEM-EDX ELEMENTAL MAPPING

X-ray mapping provides combined information on X-ray compositional signals and SEM images to offer information on the relative spatial distribution of elements in a specimen to aid identification of phases (Goldstein *et al.*, 2003: 485-491). EDX qualitative elemental maps were collected at fine image resolution, using Speedmap in SEMQuant of the Oxford Link Isis analysis software package and are displayed in colour contrast view. EDX maps are produced by the total X-ray count of the characteristic peak of the chosen element(s) that is recorded for each pixel in the image. Low counts of X-rays from the continuum background can result in 'background induced artefacts': an element may not be present, but X-ray counts may still be recorded (*ibid.* 489, 491). For this reason, maps of elements found in trace concentrations in the samples (below around 0.1wt%) are not considered to correspond to reality and are interpreted in this study with care.

3.6.3. BACKSCATTERED ELECTRON IMAGING

Backscattered electrons are deflected from the surface of a sample into a new path and collected as BSE images. Backscattering increases with increasing atomic number (Z) at a Z^2 rate and provides the basic principle of BSE compositional contrast imaging (Goldstein, 2003: 75-76,183). The interaction volume from which BSE data is derived depends on the composition of the interaction area and the beam's energy, footprint size and the angle at which the electron beam hits the specimen (convergence angle) (*ibid.* 27; 89). BSE images were collected at 20KeV using the Maxim™ Software normally at R1 scanning frame rate with 1280x1024 pixels size and high contrast. The better quality images were obtained using shorter distances to the BSE detector than the distance that permits EDX analysis, which prohibited concurrent BSE imaging and EDX analysis. Image contrast was further enhanced using Adobe Photoshop and Gimp software to permit detailed observation of phases with similar elemental composition.

3.7. TINNING PROCEDURE FOR MODEL SAMPLES

There are several methods used for the preparation of model tinned samples to evaluate the nature of intermetallic compounds formed. In the literature, methods include electro-deposition (Hedges, 1964; Fujiwara *et al.*, 1980; ITRI, 1983; Price, 1983) and vapour-deposition of tin (Tu, 1973; Tu and Thompson, 1982), which produce uniform thin-layered

Cu/IMCs/Sn structures. These methods can be controlled to produce repeatable tinning outcomes that improve quality control of samples, but do not necessarily resemble the product of traditional tinning methods used in antiquity. Previous experimental heritage tinning work includes tinning by dipping in molten tin and by wiping molten tin on a copper or bronze surface (Tylecote, 1985; Meeks, 1986). Tylecote (1985) immersed high tin (16-18wt% Sn) bronze tokens into molten tin from room temperature after having applied ZnCl paste flux on the bronze surface. Immersion at a range of temperatures/time sets resulted successfully in growth of a thin η -Cu₆Sn₅ (1 μ m after 1 second at 234°C) or thicker layer of η -Cu₆Sn₅ (6 μ m) present with underlying ε -Cu₃Sn (1 μ m) at higher temperatures (30 sec at 285°C). Tinning by immersion is generally reported to produce relatively uniform layers (Lee and Duh, 1999; Lee and Chen, 2002; Yu *et al.*, 2005; Wang *et al.*, 2006). A systematic investigation by Meeks (1986) employed traditional tinning by fluxing with rosin and wiping tin on to a range of copper and bronze substrates (5wt%, 10wt% 20wt%Sn). This produced microstructures that were further investigated to generate examples of changes occurring during post-tinning heat treatments (or annealing) at 200, 250, 350, 450, 550 and 650°C for 2, 5 or 60 minutes (*ibid.*).

Experimental tinning in this work involved the tinning of pure copper and bronze (c.10wt% Sn) samples using both dip-tinning and traditional wiping (Davies, 1882; Fuller, 1894: 20-21; Politis, 2005; Panagiotis, 2007). Both copper and bronze samples were used to facilitate observation of intermetallic phase growth. Tin in the bronze affects the microstructural nature of IMCs due to differences in the diffusion of Cu and Sn in the bronze alloy as compared to pure copper. The dip-tinning method was employed to produce coatings on both sides of each sample to increase relative volume area and concentration of IMCs in the sample. This would permit evaluation of detection limits of IMC phases by neutron diffraction as the volume area of wipe-tinned coatings could be too thin for ToF-ND to detect. Annealing temperatures and time replicate Meeks's (1986) tinning experiments to provide a platform for comparisons of microstructures developed.

Flux is critical for removing surface oxides and increasing wettability of the tin onto the warmed substrate (Subramanian and Lee, 2003). Inorganic zinc chloride based fluxes are commonly used by modern tinsmiths (Fuller, 1894; DKL Metals Ltd, 2006) (Politis, 2005; Panagiotis, 2007), but in industry rosin-type mildly activated fluxes (RMA) are preferred (Prakash and Sritharan, 2001; Elenco Electronics, 2002; Yu *et al.*, 2005; Suh *et al.*, 2008; Zou *et al.*, 2008). High carbon concentrations at the Cu/IMC interface can develop as a result of organic fluxes that can act as a diffusion barrier for copper (Sunwoo *et al.*, 1991), but this is not commonly reported in the literature. Rosin was used in this experimental since it is more

likely to have been used in antiquity and because it is reported to be the reference standard used in industry to evaluate performance of synthetic fluxes (Srivastava *et al.*, 1989).

Materials used and tinning procedures were:

Substrates used:

- (a) A pure copper (99.9% Cu) sheet of medium hardness was cut into 20x50x3.25mm tokens. The outer surface of the copper was finely polished by the supplier.
- (b) Bronze of c.10wt% Sn was prepared using pure copper (99.9 wt% Cu) and pure tin (99.75% Sn), supplied by Goodfellow Ltd. Metals were melted in a graphite crucible and poured into preheated flat graphite moulds (13x25mm); they were left to cool to room temperature. The bronze cast tokens were annealed at 550°C for 6 hours prior to tinning in an attempt to eliminate potential tin segregation developed during casting.

Wipe-tinning procedure for copper and bronze tokens:

1. The metal token was cleaned with 50% HCl acid (32% conc. stock solution) with cotton swabs;
2. the token was heated lightly over a yellow flame of a Bunsen burner;
3. pure rosin was applied on the heated metal surface using pliers and spread on the surface whilst keeping the token near the open flame;
4. a rod of pure metal tin was passed over the metal surface and melted immediately spreading over the metal with great fluidity;
5. the molten tin was immediately wiped over the metal surface using cotton pads and excess tin was removed;
6. the process was repeated (from step 2) until the surface of the token was covered with a layer of tin;
7. the token was placed on a heat-resistant mat to cool.

Dip-tinning procedure for copper samples only:

- 1-3 as wipe-tinning.
4. The token was held with pliers in liquefied tin within a ceramic crucible for approximately 5 seconds;
 5. the token was removed from the molten tin and placed on its side to cool.

Two sets of each tinning method and substrate type were prepared prior to post-tinning thermal treatment. Residues of excess rosin flux were removed using acetone (Srivastava *et*

al., 1989) rather than by ultrasonic bath (Zou *et al.*, 2008). Annealing took place at 200°C, 250°C, 350°C, 450°C and 550°C in an electric furnace. Different growth rates and mechanisms are involved at different activation energies (Laurila *et al.*, 2005), but in general it is reported that longer aging times at the same temperature result in the growth of IMC layers (Lee and Duh, 1999). For this reason the tinned samples were annealed at each temperature for 5 or 60 minutes. Each tinned token was placed from room temperature into the furnace, which was already heated to the required temperature and then it was removed back to room temperature after 5 or 60 minutes (Table 3.8).

Experimental samples				
Wipe-tinned copper	Dip-tinned copper	Wipe-tinned bronze	Aging temperature °C	Aging time (min)
S1	S2	B5	As tinned	-
S3	S4	-	As tinned	-
S5	S6	-	250	5
S7	S8	B6	250	60
S9	S10	-	350	5
S11	S12	B7	350	60
S13	S14	-	450	5
S15	S16	B8	450	60
S17	S18	-	550	5
S19	S20	B9	550	60

Table 3.8: List of experimental tinned samples produced by wiping or dipping tin on copper and bronze substrates. Annealing temperature/time is shown per sample. Bronze substrates were annealed at 550°C for 6 hours prior to tinning.

3.8. DIFFRACTION METHODS USED IN THIS STUDY

An overview of basic principles of crystallography and comparison of different diffraction methods are presented to support the use of these methods in this study.

3.8.1. BACKGROUND AND EVALUATION OF METHODS

3.8.1.1. Basic principles

Polycrystalline materials, such as metals and several corrosion products, are composed of different crystals, each single crystal being formed by the repeating pattern of atomic units (Chapuis and Schoeni, 2006)⁷. Apart from the geometry and symmetry of a crystal, a

⁷ Details on the principles of crystallography and diffraction can be found in textbooks on physical chemistry or materials structure (Atkins and De Paula, 2006); (De Graef and Michael, 2007); this review includes information

crystalline structure is quantified by the unit cell and the distance between lattice planes. A space lattice defines the basic structure and geometrical pattern of a crystal; in two dimensions it is constructed by points that represent the locations of regularly repeating 'motifs'; in three dimensions it consists of parallel planes (Sands, 1993; Atkins and De Paula, 2006; Chapuis and Schoeni, 2006). Within this geometrical figure, a unit cell is the smallest parallelogram component from which the entire crystal structure can be constructed by using only translational displacements (IUCr, 2009), and it can be fully determined by the cell's lengths a , b and c and the angles α , β and γ between them (Atkins and De Paula, 2006; Chapuis and Schoeni, 2006; IUCr, 2009). The number of parameters that specify a unit cell varies between the seven classified crystal systems. For example, a cubic cell such as that of copper is fully characterised by $a=b=c$ and $\alpha=90^\circ$. Each lattice plane can be distinguished by the distance at which it intersects the a , b and c axes in the three dimensional grid and is normally annotated by the Miller indices, which are the reciprocals of intersection distances; these are notated as triplets of integers for an individual plane (hkl) and for a family of planes as $\{hkl\}$ (Atkins and De Paula, 2006). For example, $\{110\}$ notates all lattice planes which lie parallel to the (110) plane in a lattice and which are parallel to c axis and intersect the a and b axis of a unit cell (De Graef and Michael, 2007).

Bragg saw a crystal lattice plane as a 'semi-transparent mirror' and modelled a crystal as stacks of lattice planes that are separated by distance d_{hkl} . These reflect (diffract) radiation according to Bragg's law, when the glancing angle θ satisfies the condition: $\lambda = 2d_{hkl} \sin\theta$, where, λ is the wavelength of radiation, θ is the grazing angle that the incoming and reflected X-ray beams make with the diffracting plane arising from the $\{nh,nk,nl\}$ families of planes of a crystal, and d_{hkl} the distance between lattice planes (Atkins and De Paula, 2006).

Based on Bragg's equation it is possible to calculate the angle θ at which the crystal must be in relation to the incoming beam for diffraction to occur, or to determine the inter-planar spacing (Hammond, 2001; Hannon, 2004; Atkins and De Paula, 2006). In a diffraction pattern, each peak corresponds to a family of parallel planes in the crystal $\{hkl\}$; there are many different sets of planes in a crystal, so there are many angles at which a reflection

from sources on principles of crystallography (Hammond, 2001); (Sands, 1993); (Giacovazzo *et al.*, 2002); crystal structure analysis (Clegg *et al.*, 2001); diffraction of X-rays by crystals (Giacovazzo, 2002); X-ray and neutron crystallography (Monaco and Artioli, 2002). David *et al.*, (2002a) covers most aspects of data collection and analysis. The International Union of Crystallography provides extensive resources including an online dictionary of terms (IUCr, 2009); the Crystallography Laboratory of the Swiss Institute of Technology have useful online interactive tools (Chapuis and Schoeni, 2006).

occurs. For unit cells of known crystal systems, the distance d_{hkl} between lattice planes (hkl) are given with respect to the crystal axis, and the angles at which the {hkl} family planes give reflections can be predicted (Werner, 2002; Atkins and De Paula, 2006). For example, d_{100} spacing for a cubic structure can be calculated by $d_{hkl}^2 = a^2 / (h^2 + k^2 + l^2)$, which directly gives the unit cell size, in this case the length of a (Kockelmann *et al.*, 2004b).

3.8.1.2. Comparison of diffraction methods and instrumentation

There are two experimental methods where Bragg's law can be satisfied:

- a) when using a constant wavelength λ , i.e. monochromatic radiation, diffraction occurs at varying scattering angles 2θ (angle dispersive mode), or
- b) when white or polychromatic radiation reaches the sample at fixed 2θ angle, a reflection occurs every time Bragg's law is met (energy dispersive mode) (Kockelmann *et al.*, 2000; Kockelmann *et al.*, 2004b).

In experimental set-ups with angle dispersive diffraction geometry, samples are often rotated and the intensity of Bragg reflections is recorded as a function of the scattering angle either by a movable single detector or by position sensitive detector devices (PSD), such as a multi-wire proportional counter, a CCD camera or an image plate (Kockelmann *et al.*, 2000; Anne, 2007). CCD area detector cameras can record reflections in the accessible 2θ range simultaneously, whereas Bragg-Brentano diffractometers where the rotating detector is centred on the specimen as a function of 2θ records at selected continuous angles (Monaco and Artioli, 2002) (Figure 3.1). In the latter case, because the angle between the sample surface and the incident beam changes during the scan, the illuminated area changes on irregular samples and divergence can occur out of the plane that contains the incident and diffracted beam (defocusing of part of the sample) (Louer, 2002; Monaco and Artioli, 2002; Wessels *et al.*, 2002). Defocusing can occur on solid samples that are not absolutely flat or are slightly tilted, resulting in some asymmetry in the diffraction pattern, incorrect measurement of intensities at low angles, line broadening and an increase in reflection overlap (Louer, 2002; Wessels *et al.*, 2002). These problems can be overcome by the use of area detectors, which record Bragg reflections simultaneously, independently of their point of origin in the sample (Wessels *et al.*, 2002).

Both reflection mode, where an incident beam hits the surface of a sample, and transmission mode, where a radiation beam passes through a sample, diffractometer geometries are available with angle dispersive systems. The choice between the two depends mainly on the

sample and study type and available equipment; a conventional bench Bragg-Brentano diffractometer is most commonly used in reflection mode (Louer, 2002) (Figure 3.1).

The monochromatic radiation used in angle dispersive geometry set-ups can derive from conventional X-ray tubes such as copper (with $\text{CuK}\alpha$, with $\lambda=1.5406\text{\AA}$) or synchrotron radiation sources (SR). SR sources are high-energy electron accelerators, which produce high intensity flux radiation (10^5 more intensive than conventional sources) that covers a wide spectral range from far-infrared to hard X-rays (typically 5-50keV) depending on the source and beamline (Monaco and Artioli, 2002; Pantos *et al.*, 2002). Advantages of SR X-ray sources include the opportunity to select a monochromatic wavelength λ depending on the type of study and beamline set-up, collimation of the beam to micro-scales due to its high intensity and very fast data acquisition (milliseconds) (Kockelmann *et al.*, 2000; Louer, 2002). The high peak/background ratio obtained with synchrotron radiation permits extremely small quantities of phases and impurities to give observable diffraction peaks (Werner, 2002). The fast data collection facilitates collection of multiple data-sets, which can be averaged and further increase the resolution of minor phases in a polycrystalline material (Monaco and Artioli, 2002). Effects related to the geometry of a sample seen in conventional Bragg-Brentano diffractometers are eliminated because of the commonly employed area detectors, which record data simultaneously (Wessels *et al.*, 2002). The higher resolution of SR diffraction data can lead to sharper, better-resolved peaks, which can thus be determined more accurately for phase composition Rietveld refinements (Stephens *et al.*, 2002). These characteristics make SR diffraction techniques powerful tools for a wide range of scientific and technological applications.

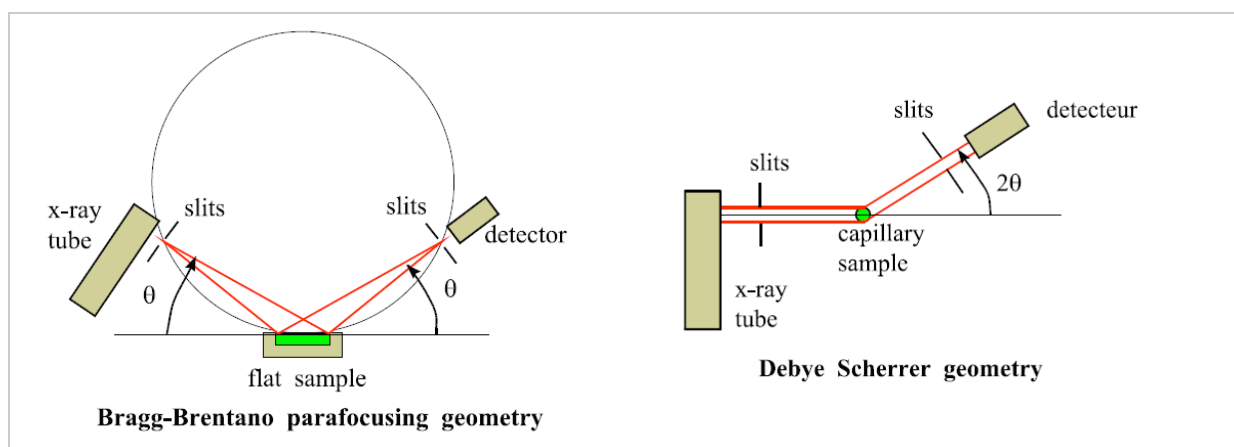


Figure 3.1: Common experimental diffractometer geometries in angle dispersive systems. Left: Bragg-Brentano parafocusing diffractometer commonly used with a flat sample, a divergent beam and in reflection mode; Right: Debye Scherrer diffractometer commonly used with thin or capillary samples, with a parallel beam and in transmission mode. Figures from Anne, 2007. For applications and limitations of the different geometries (see Louer, 2002).

The energy dispersive mode, where a polychromatic radiation beam reaches the sample at a fixed angle, is more often employed with time-of-flight neutron diffraction set-ups. Neutrons are produced either by nuclear fission in traditional reactors (a steady-state source), such as at the Institute Laue Langevin (ILL) in Grenoble, or in neutron spallation sources (pulsed sources) like the ISIS facility at the Rutherford Appleton Laboratory, UK (Monaco and Artioli, 2002). In pulsed sources, neutrons are produced in bunches because they are generated by protons that are produced by synchrotrons. Each bunch of neutrons is produced at the same time and includes neutrons of different velocities and energies (Atkins and De Paula, 2006); they scatter upon hitting a sample and are measured by the detectors at different arrival times (Monaco and Artioli, 2002). Time-of-flight geometries are often equipped with more than one detector or banks of detectors positioned at various fixed scattering angles, which cover different d-spacing regions (Kockelmann *et al.*, 2000). The detection time of each neutron corresponds to the detection time of each point of a diffraction pattern. Because neutrons exhibit wave-particle duality behaviour, the detection time (t_{hkl}) can be converted to d-spacing values when the ‘flight path’ L i.e. the distance between the source and the sample are known using the equation $d_{hkl} = (1/505.56)(t_{hkl}/L \sin\theta)$ (*ibid.*). This equation is based on Bragg’s law and on the de Broglie relation $\lambda=h/(m_n.v)$, where λ denotes the neutron wavelength, h Planck’s constant, m_n the mass of the neutron, and v its velocity (Kockelmann *et al.*, 2000).

X-ray and neutron diffraction are often complementary methods for diffraction studies because they interact with matter in different ways: X-rays are scattered by electrons; neutrons are scattered by atomic nuclei independently of the number of electrons and can penetrate deep into matter because they are free of X-ray absorption phenomena (Hill and Madsen, 2002; Ibberson and David, 2002; Hannon, 2004; Kockelmann *et al.*, 2004a; Atkins and De Paula, 2006). The ability to penetrate deep into matter, combined with the relatively large size of the neutron beam, is useful for the analysis of large volume areas (mm^3) on the walls or in the interior of objects (Kockelmann *et al.*, 2000; Rinaldi *et al.*, 2002). Collected data represent average information on an object (Rinaldi *et al.*, 2002) and are thus more representative. Although lack of spatial resolution limits its application to large analysis areas, this benefits non-destructive analyses of objects where sampling is prohibited (Kockelmann *et al.*, 2000; Kockelmann *et al.*, 2004b). For these reasons, the method has been used on heritage materials (Kockelmann *et al.*, 2000; Kockelmann *et al.*, 2001) for analysing phase composition and the manufacturing of bronzes (Siano *et al.*, 2002; Siano *et al.*, 2003; Siano *et al.*, 2004a) such as coins (Kockelmann *et al.*, 2003a; Siano *et al.*, 2004a), early Bronze Age

axes (Artioli and Dugmani, 2004; Arletti *et al.*, 2007; Artioli, 2007; Arletti *et al.*, 2008), a Greek helmet (Pantos *et al.*, 2005) and for several authentication studies (Kockelmann *et al.*, 2003b; Siano *et al.*, 2004b; Siano *et al.*, 2006; Bartoli *et al.*, 2007; Giuliani *et al.*, 2008).

The main drawback of neutron methods is the generation of radioisotopes from the interaction of neutrons with the material. This so-called ‘activation’ of an irradiated object depends on the composition of the material and the neutron flux (Kockelmann *et al.*, 2000). Activation of bronzes decays after approximately 3 days depending on the size of the irradiated volume and irradiation time (Siano *et al.*, 2002), permitting its ethical use for analysis of archaeological bronzes. Neutron diffraction data can be used for full quantitative and/or texture analysis because thermal neutrons do not cause radiation damage and analysis is not compromised by absorption of the rays by the material matrix or by the texture of the sample, as is the case with X-rays (Kockelmann *et al.*, 2004b).

3.8.1.3. Information in the diffraction pattern relevant to this study

A diffraction pattern is unique for a particular crystalline phase. Studies of heritage materials often utilise this principle, using diffraction patterns as ‘fingerprints’ to retrieve qualitative compositional information of crystalline materials (Pantos *et al.*, 2002). A diffraction pattern is much more than that, and can be used for retrieving a variety of information based on analysis of the three main peak characteristics: (i) peak position, (ii) peak-width, and (iii) its integrated intensity, all of which correspond to microstructural changes (Wang, 2006).

A shift in the peak position corresponds to dimensional changes of the grains in a material, which is a result of composition (Wang, 2006). This effect is clear in the case of homogenised α -bronze (Siano *et al.*, 2003). A shift of Bragg peaks is observed with increasing tin content because unit cell dimensions increase with tin content; in the case of α -bronze this occurs in a linear manner (Figure 3.2). Siano *et al.*’s (2003) work inputs greatly on the experimental determination of α /Sn dependence and the accurate determination of the lattice parameters (α in this case), which is required for quantitative phase analyses.

Depending on the experimental set-up, a diffraction pattern can provide quantitative information on the phases present using Rietveld refinement software such as GSAS and MAUD (Kockelmann *et al.*, 2000; Siano *et al.*, 2002). Rietveld quantitative phase analysis (wt%) is a standardless procedure, as it does not require external calibration curves, but it needs a reliable structure model (and therefore assumed chemistry) for each of the phases to be quantified (McCusker and Baerlocher, 2002; Monaco and Artioli, 2002). The method

relies on the hypothesis that each phase exhibits a unique set of diffraction peaks and that the observed intensities are proportional to the content of each phase in the polycrystalline material, although this is not generally linear (Kockelmann *et al.*, 2001). It produce quantitative analyses in good agreement (0.8wt%) with other composition analysis techniques (Siano *et al.*, 2002). Rietveld refinement can take place on laboratory or SR diffraction data, but in general refinement of neutron data is more precise because they are essentially free from systematic errors (Kockelmann *et al.*, 2000); effects such as the decrease of intensity with scattering angle, the increase of reflection overlap with increasing angle (Louer, 2002) or other X-ray scattering sensitivity factors are not present in neutron diffraction experiments (Cheetham, 2002). Overlapping peaks, clusters of peaks and preferred orientation problems can be considered in the model mathematically and largely overcome by corrections during analysis in Rietveld software (Kockelmann *et al.*, 2001, 2004b; Monaco and Artioli, 2002; Siano *et al.*, 2002; 2003; 2006).

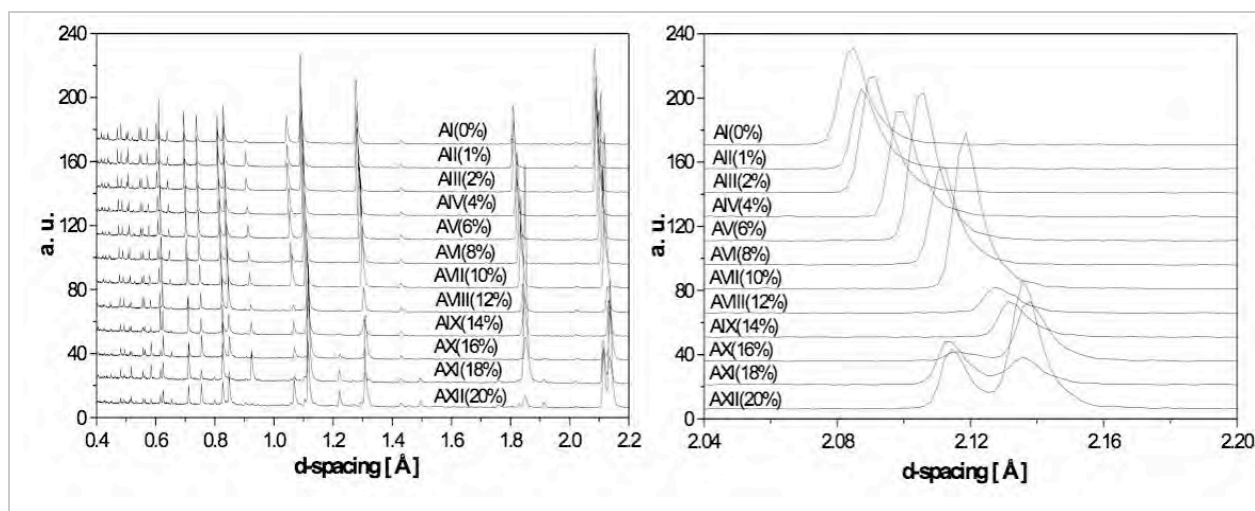


Figure 3.2: Diffraction patterns obtained using ToF-ND (ROTAX diffractometer, ISIS) showing shifting of the major copper peaks (left) due to increasing amount of Sn in the bronze alloy and detail of the shape and position of the $\{111\}$ α Cu reflection (right). The bronzes are fully homogenised. The δ -phase has a distinct diffraction pattern and appeared at 16wt% Sn content. (From Siano *et al.*, 2003).

The measured peak intensity of each phase contributes to quantitative analyses but it also shows $\{hkl\}$ plane orientation dependence (texture) because intensity depends on the number of crystal lattices that fulfil Bragg's condition. Texture or preferred orientation is the organised arrangement of crystal lattices of grains which is the result of the statistically significant preferred orientation of the grains (Vander Voort, 2004c: 24) and it is manifested by variation of Bragg peak intensity as a function of the detector angle (Kockelmann *et al.*, 2004b; Wang, 2006). If the grains in an object are oriented at random or they show equal orientation distribution, this is a texture free structure (Kockelmann *et al.*, 2000), and the

number of grains contributing to the intensity of a particular $\{hkl\}$ peak is the same for all sample orientations (Wessels *et al.*, 2002). In textured samples, in order for a $\{hkl\}$ peak of a given family of planes to be detected, diffraction data needs to be recorded from many different angles by either rotating the sample, rotating the detector or building the detector around the sample, as in the case of ToF-ND geometries and collecting data from many sample orientation positions (Kockelmann *et al.*, 2004b). The presence of intense preferred crystal orientation (or ‘strong’ texture) does not in general allow reliable phase quantification from diffraction data collected at a fixed angle (Siano *et al.*, 2003), but this can be overcome by Rietveld refinement of the averaged diffraction data collected at different angles in order to obtain an average quasi-texture-free diffraction pattern (Kockelmann *et al.*, 2004b).

Texture indicates a manufacturing process; for example, hammered specimens are characterized by the alignment of the $\{110\}$ planes with regards to the specimen surface, meaning that $\{110\}$ planes which are parallel to the surface are statistically predominant (Figure 3.3b) (Siano *et al.*, 2002). Texture analyses is thus used as a fingerprint for understanding associations between grains and degree of deformation, which is a result of the manufacturing process (Kockelmann *et al.*, 2004b; Wang, 2006) and has been used for the non-destructive characterisation of fakes in museum collections (Kockelmann *et al.*, 2003b). The distribution of grain orientation is mapped and represented in intensity pole figures of selected sets of $\{hkl\}$ reflections versus orientation angles (Tietze-Jaensch *et al.*, 1997). A pole figure is ‘*the stereographic projection that shows the distribution poles (or plane normals) of a specific crystallographic plane using specimen axis as reference axis*’ (Chin, 1985: 700). In other words, pole figures show the distribution of crystallites oriented in a certain direction with respect to the sample shape (Figure 3.3). Data is collected from a sample rotated at angle φ with x-tilt axis and one pattern is collected at each angle. Pole figures are compared to experimentally produced reference pole figures of samples with known manufacture (Kockelmann *et al.*, 2004b). Work by Siano and Kockelmann enriched such reference databases by investigating the effect of texture as a function of hardening by hammering or rolling and annealing cycles of bronzes (Kockelmann *et al.*, 2003a) (Figure 3.4). These data have been used previously to investigate texture and the working history of archaeological bronzes.

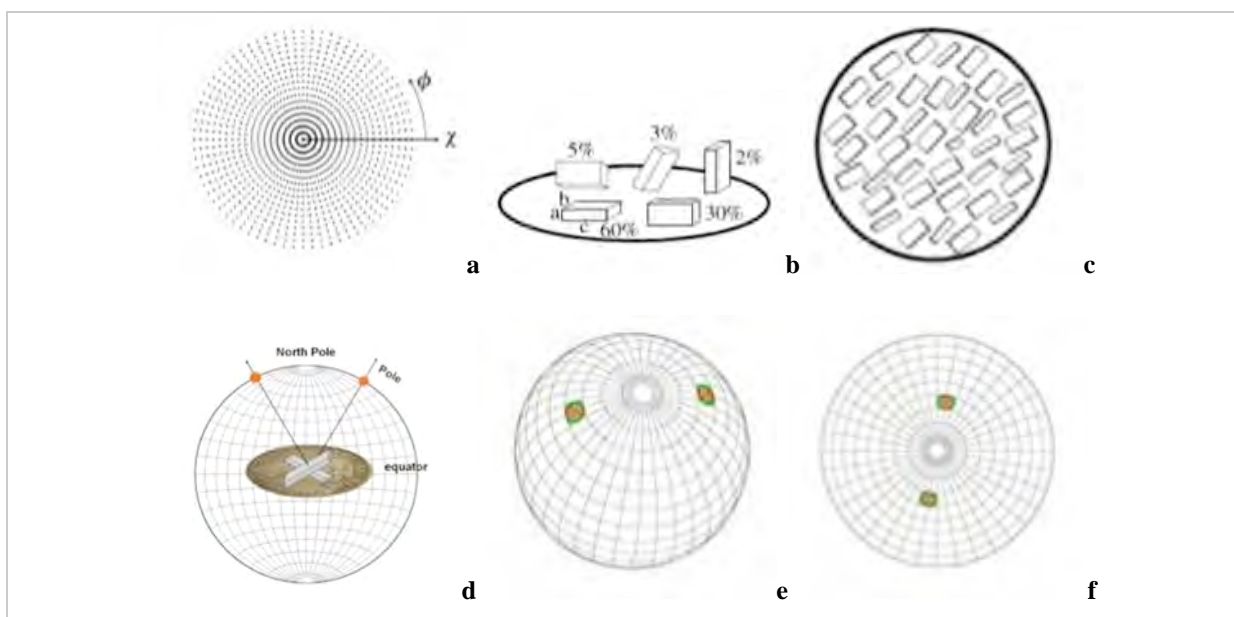


Figure 3.3: (a) Schematic representation of points in the χ (tilt axis from 0° centre to 90° perimeter) and ϕ (rotation axis) space measured to produce a pole figure for a single reflection (top view). (b) Schematic of random orientation distribution of crystallites in side view and (c) viewed from top (Wessels *et al.*, 2002). (d) Stereographic projection of pole sphere, with (e) poles marked on the equatorial plane and (f) 2-D projection of a reflection (Kockelmann *et al.*, 2004b).

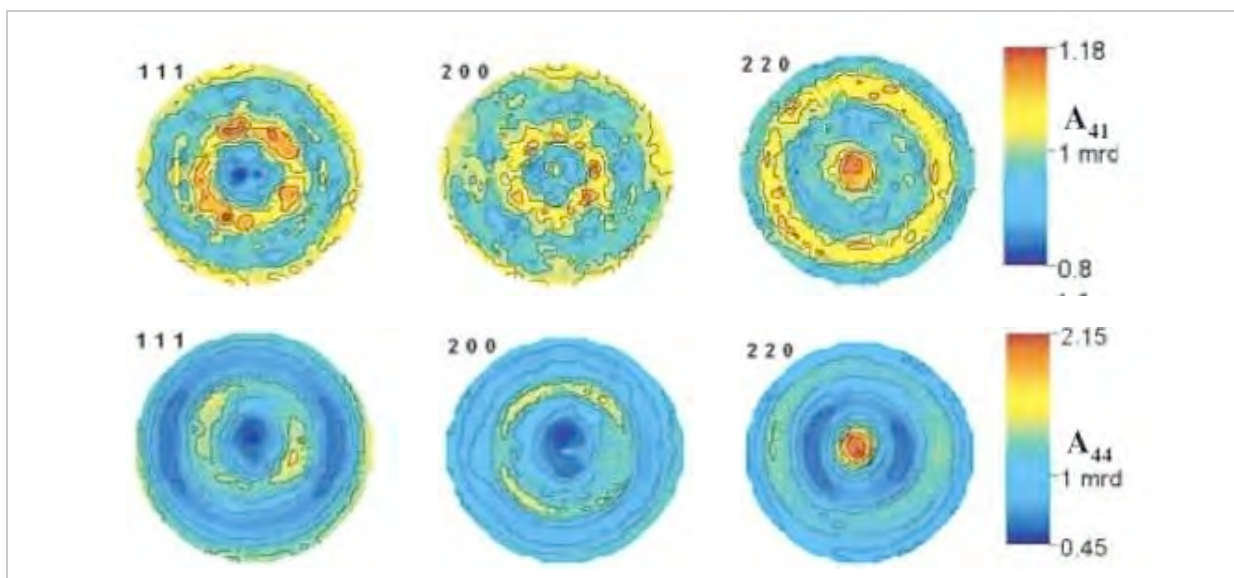


Figure 3.4: Experimental pole figures of binary (Sn 4wt%) bronze for {111}, {200} and {220} planes in multiple of random distribution (mrd). Upper row: c.8% thickness reduction by hammering. Lower row: 46% thickness reduction by hammering (from Siano *et al.*, 2006).

Information on the working history can be also retrieved by the peak-width, which provides information on the subgrain structure and measures strain fluctuation due for example to hammering (Wang, 2006). This type of analysis is possible with neutron diffraction data and is termed ‘neutron metallography’ (Siano *et al.*, 2004a). Based on analyses of simulated bronze specimens (binary alloys with 0-20wt%Sn), Siano *et al.*, (2002; 2003) showed that peak-width depends on thermal and working history. Experimental as-cast bronzes showed

(often irregular) peak broadening, annealing and recrystallisation produced narrow peaks, and subsequent cold working produced regular peaks of variable width depending on the residual stresses in the specimen (Siano *et al.*, 2006). Hammering of the cast bronzes produced significant peak broadening before annealing; subsequent annealing with slow cooling produced a strong peak-width reduction due to the partial re-crystallisation and homogenisation of the alloy. Further hammering again increased the peak-width, but to a lesser extent compared to the first hammering due to the smaller crystal grain sizes resulted by the hammering and annealing processes (Siano *et al.*, 2002).

During cold working, lattice planes which are parallel to the worked surface are compressed and perpendicular planes are stretched, which corresponds to a reduction and increase of the lattice parameter respectively; these strains are detected by the method and exhibited as peak-broadening (Siano *et al.*, 2003). The relative peak-broadening produced by hammering increases with tin-content, because increasing the tin content in the alloy results in a reduction of metal ductility, which in turn increases the strain relatively to the same degree of hammering (*ibid.*). Cold working produces characteristic peak-broadening, which is used for the qualitative assessment of neutron diffraction patterns and characterisation of archaeological bronzes (Siano *et al.*, 2003; Siano *et al.*, 2006).

This thesis employs both X-ray and time-of-flight neutron diffraction to examine specimens. The advantages and disadvantages of each method are identified and discussed in order to compare their suitability for examining tinned copper alloy. The suitability of each method is balanced against availability of the technique and the difficulties of data handling.

3.8.2. EXPERIMENTAL SET-UP AND INSTRUMENTATION

Reviewing the advantages and limitations of a range of diffraction methods shows that they can be complementary providing various types of information and quality. For this study, CuK α X-ray and time-of-flight neutron diffraction were used to evaluate the effectiveness of the methods to detect Cu-Sn intermetallics resulted from laboratory tinning. Neutron diffraction data were analysed using Rietveld refinement software to provide quantitative information on Cu-Sn phases. CuK α X-ray and SR X-ray diffraction were used to characterise crystalline compounds on the surface of selected archaeological samples. A pilot study uses neutron texture analysis of selected helmets and helmet samples to examine their composition and metallurgy in a non-destructive manner.

3.8.2.1. Time-of-flight neutron diffraction (ToF-ND)

Time-of-flight neutron diffraction analyses were undertaken at the ISIS neutron spallation source at the Rutherford Appleton Laboratory, Oxfordshire, UK, and employed for several aspects of this project:

- data collected at the ROTAX diffractometer from model and archaeological samples were used for semi-quantitative phase composition analyses of Cu-Sn intermetallic phases (beamtime RB720553);
- data collected at the General Material diffractometer (GEM) on the same material were used for quantitative phase composition analyses of Cu-Sn phases (RB720553);
- data collected at ROTAX on a small number of selected helmets and samples were used for phase composition and texture analyses, which provided non-destructive information on helmet manufacture methods (beamtime RB610547).

ISIS is an intense spallation neutron source, generating 50 intense neutron pulses every second, which is important for time-of-flight neutron diffraction instrument set-ups (Kockelmann *et al.*, 2004b). The ROTAX medium resolution diffractometer (Figure 3.5) is run as an energy-dispersive time-of-flight instrument. It is equipped with three wide-angle position sensitive detector banks around a sample chamber, which can provide information on phase compositions (Siano *et al.*, 2003) and crystallographic texture (Schifer *et al.*, 1997). The detector banks register the scattered neutrons with respect to time-of-flight (t) and position (2θ) in forward and backscattering geometry, thereby covering different d-spacing ranges: Bank 1 is in forward geometry covering a range 1-15 Å and Bank 3 is a backscattered detector bank covering 0.3-3 Å (Schafer *et al.*, 1995; Kockelmann *et al.*, 2000; Kockelmann *et al.*, 2001). The incoming polychromatic neutron beam has a wavelength range of $\lambda=0.5-5$ Å with neutron velocities (v) between 8000-800 meters per second. The flight path (L) from the neutron source is 14 m and neutron time-of-flights (t) from the source range between 2 - 20 milliseconds; based on the relation $d_{hkl} = t / (505.56 \cdot L \cdot \sin\theta)$, calculations of the collected data provide crystallographic information in d-spacing (Kockelmann *et al.*, 2000).

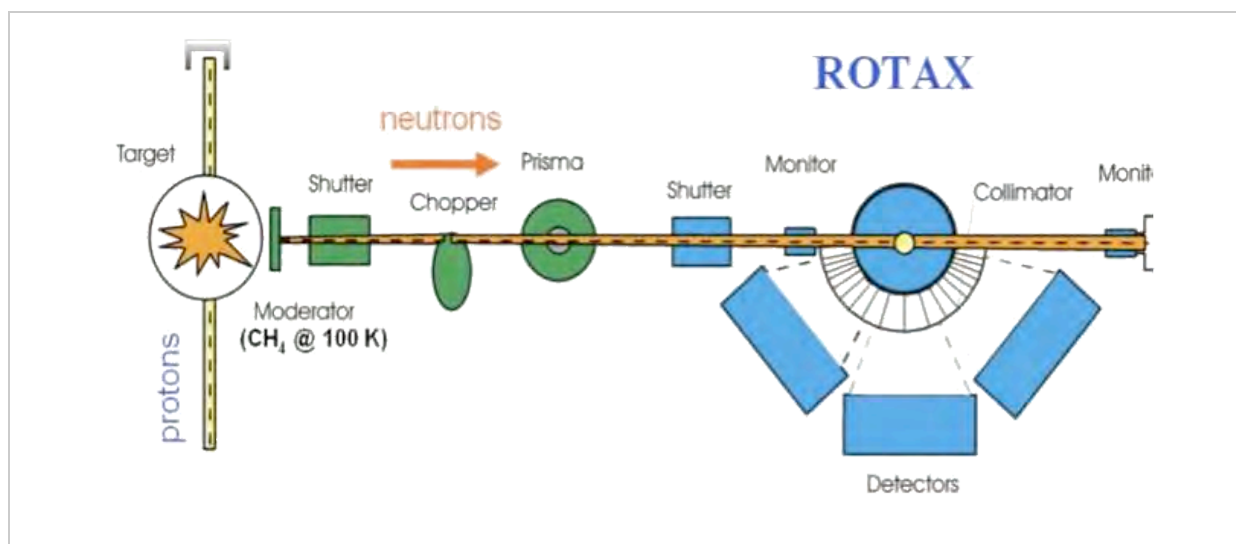


Figure 3.5: The ROTAX diffractometer at the ISIS neutron spallation source (Kockelmann *et al.*, 2004b).

The GEM diffractometer has 6 detector banks comprising about 6500 individual detectors positioned around the sample tank at fixed positions. The large number of detectors results in high resolution data that can provide faster and more accurate than ROTAX quantitative and texture analysis in a single acquisition from a stationary specimen (Kockelmann *et al.*, 2004b). GEM covers similar d-spacing ranges to ROTAX: Bank 3 covers ranges 1-8Å, Bank 4 covers 0.6-4Å and Bank 6 covers 0.2-1.6Å. GEM is 17m from the neutron source; the detectors are at distances between 1-2 m from the sample at fixed positions with regards to the specimen. Texture effects, which can be manifested as intensity differences of a diffraction line in data collected by different banks, are less significant than at ROTAX because the averaged results derive from a greater number of detector banks in this beamline. Yet, data from individual banks can be used for texture analyses and preparation of pole figures.

Two Corinthian type helmets from the National Museum of Wales (NMW4 and 6) were analysed non-destructively using time-of-flight neutron diffraction at ROTAX, to obtain information on alloy composition and texture. This provided useful information on the authentication of fragments attached to the helmet NMW2 and the work history of the helmet NMW6 (Manti and Watkinson, 2007). Each helmet was positioned individually inside the sample chamber in a vacuum, with the volume to be analysed positioned at a known distance to the incoming beam. The neutron beam footprint was 5x30 mm² or 15x20mm² in order to probe a relatively large volume and to reduce acquisition time. A strip of aluminium foil was attached to the analysis area and acted as a calibration marker. Data acquisition times were in the order of 60 minutes to reduce scattering background noise. Experimental pole figures were measured using the backscattering detector bank positioned at a 120° degrees scattering angle (Bank 3, 101° < 2θ < 143°).

Neutron diffraction is a bulk method and is not generally used to detect thin coatings or other surface material (Kockelmann *et al.*, 2000). This study aims to better understand the limits of the technique and its effectiveness as a non-destructive probe for the identification of tinning on archaeological objects. The manufacturing technique and the presence of tin coating were investigated on selected helmet samples (including PE1, OL63, PE2, OL79) and model tinned tokens at ROTAX and GEM using 15x20mm beam size with a typical acquisition time of 60 minutes. A well resolved diffraction pattern of the major phases (Cu or bronze) was normally obtained within 10 minutes. Samples were placed in vanadium pockets and positioned on the sample holder perpendicular to the beam in the vacuum sample tank; the instruments were calibrated with Y₂O₃ prior to analyses. Data collected from the many individual detector channels were used in Rietveld programs GSAS and Maud in order to determine phase compositions, provide quantitative analyses or produce pole figures of crystal orientation distributions (texture) with guidance by Dr Winfried Kockelmann.

3.8.2.2. CuK α and synchrotron radiation X-ray diffraction

An X'Pert-PRO PANalytical CuK α X-ray Bragg-Brentano diffractometer was used for the identification of crystalline compounds on selected archaeological samples and all model tinned copper and bronze tokens. The samples were placed on a silicon wafer and positioned on the sample stage, with a divergent beam footprint of 100 or 200mm²; collected 2 θ angles were between 5-130° for 20-60 minutes acquisition time, depending on the sample. Instrumental acquisition set-up was standardised for the replica samples to 100mm², 5-130° 2 θ and 20 minutes collection time in the continuous scan mode, with an average time per step of c. 20s and 0.0170° 2 θ step size. The stage was stationary when collecting data from flat fragments. A divergence slit correction⁸ was applied to the collected data, which removed background slope and standardised peak broadening due to instrumental factors (beam divergence, misalignment) (see Louer, 2002). Data was collected using X'Pert Data Collector v.2.1.1 and analysed using X'Pert HighScore v.2.1.2 search and match software, which uses the PDF2, 2005 Release ICDD library from the International Centre for Diffraction.

Selected samples were analysed using SR-XRD diffraction methods at DL10.1 and DL14.1 beamlines at the SRS Daresbury Laboratory, UK and at ID13 and ID15 at the ESRF European SR source in Grenoble, France. The high resolution and peak/background ratio obtained with

⁸ This involved the change from an automatic to a fixed divergence slit for all data (ADS to FDS) and is advised from PANalytical for better results in Rietveld analysis.

synchrotron radiation and collimation of the beam to micro-scales due to its high intensity and the very fast data acquisition times were ideal for the detection of very small amounts of intermetallic phases present in the often complex diffraction patterns of corroded archaeological samples. The variety of available instrument set-ups permitted a choice of diffraction modes (e.g. transmission or reflection), grazing angle, and X-ray beam wavelengths, which control the depth from which scattering occurs in the sample. Understanding the origins of Bragg reflections from the specimens is important when studying corroded surfaces or layered microstructures such as tin coatings (Hill and Madsen, 2002; McCusker and Baerlocher, 2002). X-ray absorption reduces the intensity of an X-ray beam when travelling through a material according to Beer's law: $I/I_0=e^{-\mu x}$, where I is the transmitted intensity, I_0 the incident intensity, x the distance travelled through matter and μ the linear absorption coefficient. μ can be substituted by the photon mass absorption coefficient (mac) which depends only on the wavelength considered because: $\mu_m=\mu/\rho$ where ρ is the materials density (g/cm^3) estimated by its specific gravity and μ the linear absorption coefficient (Monaco and Artioli, 2002).

Therefore, mass absorption coefficient (mac) provides an indication of the depth ranges from where diffraction data are collected at particular experimental set-ups. Table 3.9 shows calculated mass absorption coefficients (mac) in cm^2/g for Cu, Sn and Cu-Sn phases as a function of X-ray beam wavelength used at the different instruments and θ grazing angles, calculated using the MAC Calculator, in X'Pert HighScore software. Calculations show that tin and high-tin phases show the least penetration at 1.54Å and 0.14Å X-ray energy wavelengths due to higher photon mass absorption coefficients (mac) relative to copper. The penetration range increases with increasing X-ray beam energy (e.g. ID15) for the different phases but at 0.92Å, Cu shows elevated mac relative to tin due to the presence of the Cu (K line) X-ray absorption edge at 1.3808Å, as seen in Figure 3.6.

Phase	molecular weight	ρ density g/cm^3	CuK α : 1.5406 Å (PANalytical)			0.92 Å (DL10.1 SRS)			0.1425 Å (ID15 ESRF)		
			mac cm^2/g	penetration range μm		mac cm^2/g	penetration range μm		mac cm^2/g	penetration range μm	
				5° θ	90° θ		5° θ	90° θ		5° θ	90° θ
Cu	63.546	8.96000	52.44	4.27	49.01	101.96	2.20	25.21	0.66	339.36	3893.70
Cu ₃ Sn	309.330	8.24095	131.64	1.85	21.23	87.93	2.77	31.78	1.39	175.19	2010.13
Cu ₆ Sn ₅	974.730	7.87036	178.11	1.43	16.43	79.69	3.20	36.72	1.82	140.11	1607.51
Sn	118.690	7.30000	258.84	1.06	12.19	65.39	4.20	48.24	2.56	107.39	1232.13

Table 3.9: Calculated X-ray beam penetration range (μm) of different X-ray wavelengths in Cu-Sn phases as a function of incident angle θ (5, 90°).

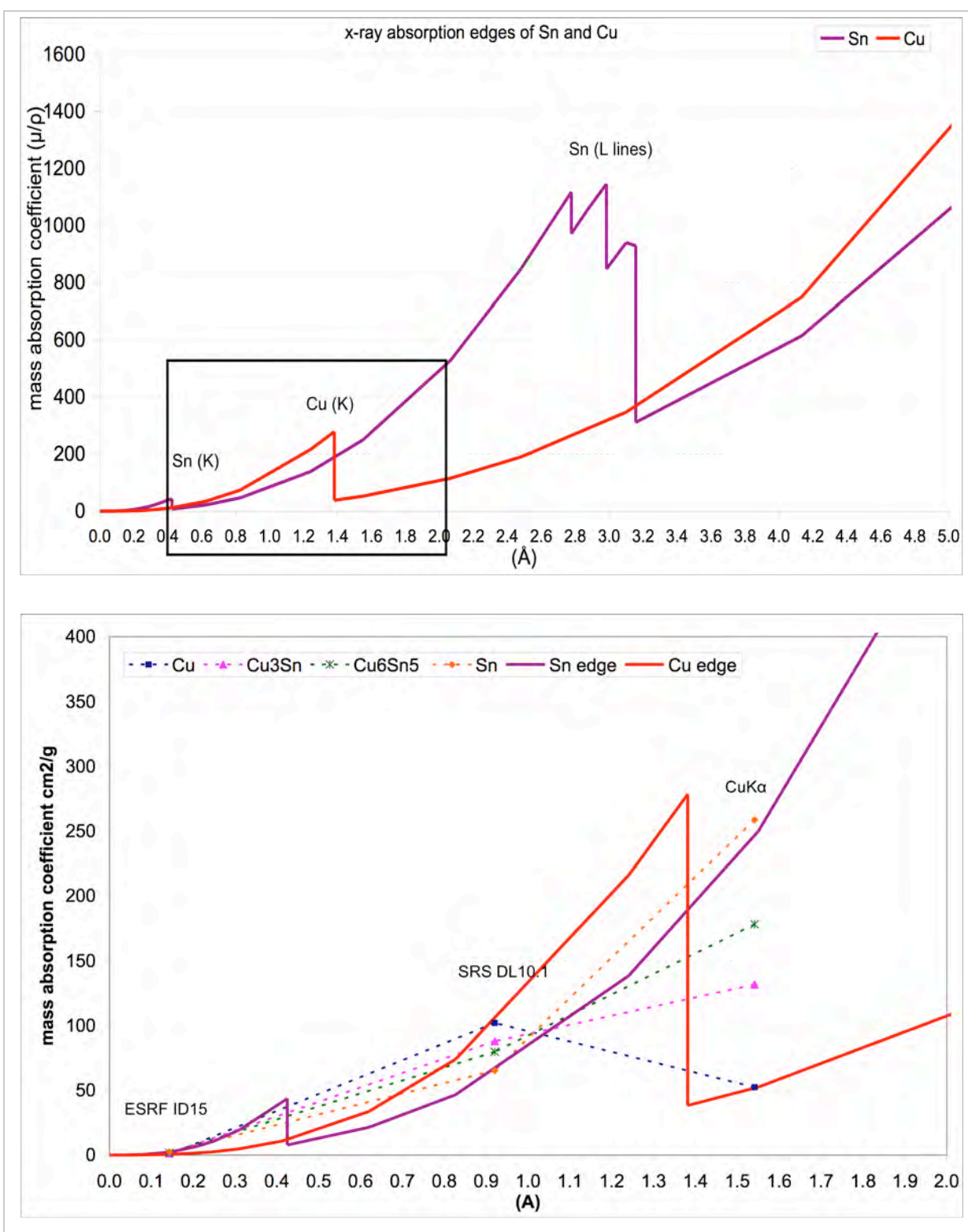


Figure 3.6: X-ray absorption edges for Cu and Sn (top) with detail (bottom), which includes calculated experimental mac for X-ray wavelengths (Å) used at ESRF, SRS and CuK α sources. This demonstrates that calculated mac values seen in Table 3.9 for SRS 10.1 beamline are due to the X-ray absorption edge of Cu(K line) at 1.3808Å(NIST, 2010), Conversion of energy to wavelength is based on $E=hc/\lambda$, $E(\text{keV}) = 12.3983/\lambda$ (Energy=Planck's constant x velocity of light / wavelength) and NASA's energy conversion tool (NASA, 2010).

At the SRS Daresbury, instrument alignments were carried out by the station scientists before use; a diffraction pattern of Al_2O_3 was normally collected for every new sample. Flat fragments and corrosion flakes from helmets PE1, OL79, OL74 and OL69 were examined in reflection geometry at beamline DL10.1, with $\lambda=0.92\text{\AA}$ wavelength and $200\mu\text{m}^2$ beam footprint. The beamline is equipped with a CCD camera detector with 3072×3072 resolution and $73.242\mu\text{m}$ pixel size. Samples were positioned at 130mm distance from the detector to increase angular resolution and were normally rotated around the φ -axis between $74\text{--}85^\circ$ to avoid preferred orientation effects and record reflections from a longer area across the sample (Figure 3.7). Multiple scans were recorded normally at 25 steps/positions by moving the stage $200\mu\text{m}$ across the sample. X-rays diffracted below the horizontal plane were obstructed by the sample and did not reach the detector.

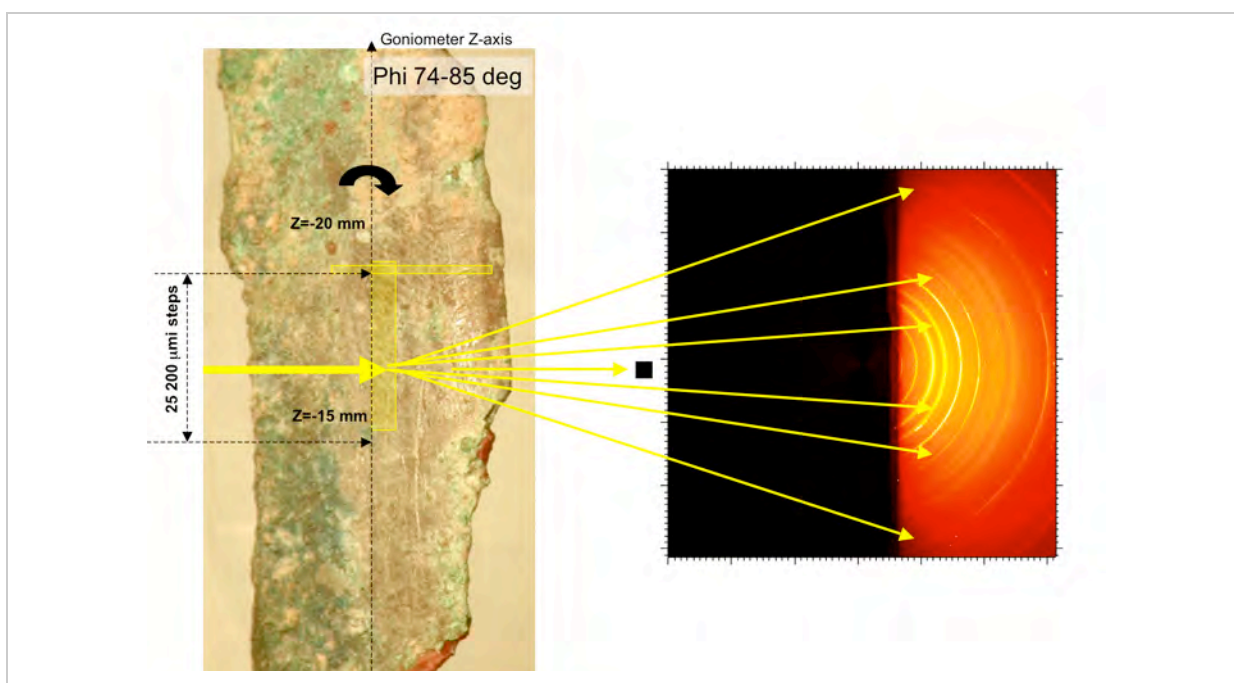


Figure 3.7: Example of sample position in reflection geometry used in SRS beamline 10.1. Data were collected between Z-15 and 20 mm and by rotating the sample between $74\text{--}85^\circ$ in the φ -axis from the large annotated yellow area. (Photo by E. Pantos)

Training at the ESRF allowed preliminary investigation of samples from helmets PE1, PE2, PE4 at ID15 and a thin cross-section from helmet PE1 at ID13, which provides a microfocused X-ray beam ($c.5\mu\text{m}$). The thin section was prepared at the School of Optometry, Cardiff University. Data were obtained by line-scanning and by mesh of line-scans (with 2.5 microns steps at 10 secs/step), which were then averaged. At ID15 data was collected with a MAR 165 CCD detector, which records images with 2048×2048 pixels/frame and $78.94\text{ }\mu\text{m}^2$ pixel size. Calibration images were taken at 71mm and 101mm distance from the detector on Al_2O_3 powder.

3.8.2.3. Data analysis

Several conversion, visualisation and analysis software programs were used throughout this study because the diffraction data deriving from different instruments are collected at different X-ray wavelengths and are in different formats. Diffraction image data from SR beamlines were converted to intensity versus 2-theta diffractograms using the Fit2D software (Hammersley). 2-theta data was converted into d-spacing using Bragg's equation and the experimental wavelength. In order to facilitate visual comparison of the relative intensities of phases on each sample, data was normalised to the maximum intensity counts of each analysis and is presented in the thesis as normalised intensity % versus d-spacing (Å).

Phase identification was undertaken using information from the Powder Diffraction Files Database (PDF02, 2005) and crystallographic databases provided by the Science and Technology Facilities Council UK (STFC) via the Chemical Database Service (CDS) which includes the Inorganic Crystal Structure Database (ICSD) and the Metal Structure Database (CRYSTMET). Phase identification is a critical but often ambiguous step, because subjective judgments and experience influence matching of experimental data to a known pattern from a database, especially when diffraction peaks strongly overlap or are hindered by the presence of a dominant major phase (David *et al.*, 2002b). The degree of difficulty increases with the complexity of the diffraction pattern, especially for identification of minor phases such as IMCs on corroded samples. Selection of an appropriate phase structures from published databases is discussed in the next chapter.

Rietveld quantitative analysis requires that a model of the correct structure is known in advance because it is a refinement process (David *et al.*, 2002a). Where information such as lattice parameters and atom positions was available in the crystallographic files (cif), this was used to calculate diffraction patterns to which the experimental patterns were fitted for quantification purposes using GSAS Rietveld analyses software package. Texture analysis was performed after or during this step because most Rietveld programs allow for refinement of peak broadening and preferred orientation parameters, and pole figures were prepared using MAUD. It is often necessary to perform this analysis step during quantitative analysis because texture effects can affect reliable quantitative phase analysis (David *et al.*, 2002a; Kockelmann *et al.*, 2004b; Billinge, 2006). Depending on the experimental set-up and the degree of texture in the examined samples, neutron phase composition Rietveld analysis reported in this text is semi-quantitative or quantitative and the relevant confidence of the results is discussed.

3.9. SUMMARY

This chapter outlined the experimental methods and workflow employed in this study. A rationale of the choice of methods was developed based on examples of their use in the literature. A review of diffraction methods provided a comparison between the various available instrumental methods and illustrated the wealth of applications in the investigation of bronzes based on the information that the diffraction pattern holds. Details of experimental set ups and instrumentation used in this study were reported.

CHAPTER 4. DEVELOPMENT AND DETECTION OF CU-SN INTERMETALLICS

4.1. INTRODUCTION

Meeks provides an important experimental overview of methods used to produce silver-coloured surfaces in antiquity (Meeks, 1986; Meeks, 1993b, 1993a). He reports extensive SEM-BSE microstructural evidence of cross-sectioned model and archaeological samples, which could be employed to identify tinning methods, indicating that η -Cu₆Sn₅ and/or ϵ -Cu₃Sn provide evidence of tinning on archaeological bronzes (Meeks, 1986). In un-corroded samples, the characteristic Sn concentration of these intermetallics aids their identification via EDX. In corroded bronzes, their characterisation via composition analyses is problematic as corrosion of bronzes can have similar Sn concentration ranges to intermetallics. Alternative analytical methodologies may offer more effective means for the detection and interpretation of these structures on corroded bronzes. The literature review in sections 2.2.3 and 2.24 indicates that diffraction analysis, which can be used to identify crystalline phases such as intermetallic phases, is undervalued despite the beneficial non-destructive character of these methods. Clear understanding of the microstructures developed during tinning and how these can be effectively detected by different analytical methods offer the starting point for identifying remaining evidence of tinning on corroded objects.

For these reasons, this chapter includes experimental work, which generates knowledge that is used to investigate surface features on helmets (Chapter 6), and which aims in particular to:

1. Revisit Meeks's microstructural evidence to identify which is the predominant intermetallic phase developed during common tinning of low-tin bronzes and copper and, then ask if this can be used as a 'marker' phase for its detection.

2. Assess whether non-destructive analysis methods such as diffraction-based methods can detect tinning with a degree of certainty to decide on the most effective method.
3. Investigate the form of evidence for tinning on a limited number of archaeological bronzes to establish similarities with the experimentally produced microstructures.

The experimental work present in this chapter includes five elements, technical details of which are found in the methodology chapter (Chapter 3). Briefly, investigations of method, physical evidence and detection of tinning were based on:

1. Observation and documentation of traditional tinning practiced by one of the last tinsmiths in Thessaloniki, Greece. This information provided technical understanding of tinning practices and the basis of laboratory experimental tinning.
2. Laboratory based tinning of copper and bronze sheets using the wiping and dipping methods following Meeks's (1986) tinning methodology to provide a basis for comparisons. Tinned tokens were exposed to a variety of annealing temperature/time sets in order to investigate changes in microstructure during thermal aging. This can reflect microstructural changes during every-day use at elevated temperatures, but its primary purpose was to build a database of microstructures to be used to evaluate the effectiveness of diffraction methods.
3. SEM-BSE was used to establish the nature of the intermetallic compounds on the model, which was then characterised by X-ray and neutron diffraction at the ISIS Neutron Spallation Source (Beamtime RB720553). This aimed to assess the efficacy of these methods for detecting thin Cu-Sn IMC layers as evidence for tinning on bronzes.
4. A small number of Roman bronzes including skillets reported to be tinned based on their silver or silver/grey appearance and context of use in antiquity, were analysed in order to compare the results from (2) and (3) to corroded tinned bronze microstructures. Discussion of these in association with current knowledge of Cu-Sn interactions will offer insight into changes that can occur during use and burial of tinned copper alloys.

4.2. MORPHOLOGICAL AND EDX ANALYSES OF TINNED TOKENS

Observation of a professional tinsmith, Mr Panagiotis, wipe-tinning a bronze tray demonstrated that experience and skill are required to achieve a uniform application of tin on a flat metal substrate. The shape of an object influences the thickness of the resulting coating;

incisions, corners, edges, or inaccessible areas show varied tin coating thicknesses. Laboratory experiments (Table 3.8) of wipe-tinning model tokens confirmed that the thickness of the tin coating varies according to the dexterity and skill of the person applying it. A fine uniform tin coating, similar to that produced by Mr Panagiotis, was achieved on a small number of wipe-tinned tokens during this experiment, because this depends, apart from skill, on the amount of tin and flux used and the temperature and length of application (Figure 4.1, S1, S3). These factors also influence the resulting thickness and physical morphology of Cu-Sn intermetallic compounds (IMCs) developed during tinning (ITRI, 1983: 58). The varied tin coating thickness produced on laboratory wipe-tinned tokens is a benefit to this study because it resulted in a range of microstructures that could be produced by different tinsmiths or developed in different areas within the same object. Dip-tinning experiments (Table 3.8) resulted in unrealistically thick tinning layers (Figure 4.1, S2, S4) and they are only discussed in the context of neutron diffraction analysis later in this chapter.

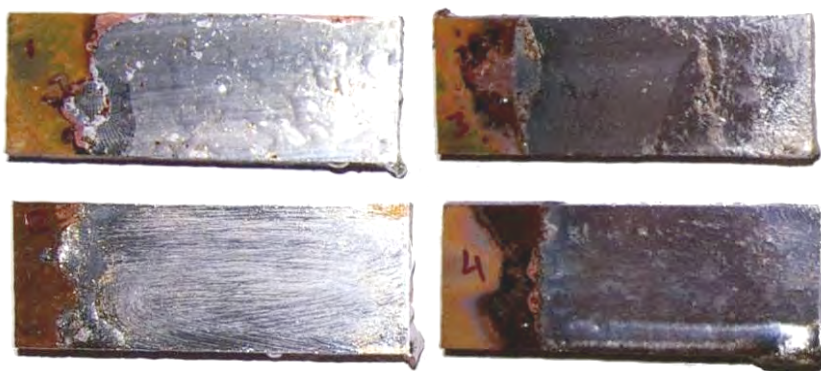


Figure 4.1: Laboratory tinned copper tokens showing a range of coating thickness produced by the wiping (left, S1, S3) and the dipping methods (right, S2, S4).

4.2.1. AS-TINNED WIPE-TINNED COPPER TOKENS

A close look at the wipe-tinned copper token S1 shows striations of the tin coating following the direction of wiping excess hot tin from the surface during tinning (Figure 4.1, Figure 4.2a). SEM-BSE imaging of the surface shows that the striations are of different relative chemical composition and morphology (Figure 4.2b). Optically, this was not easy to observe as the surface had a relatively uniform metallic tin colour with striations of slightly darker metallic tin colour. The darker areas seen in BSE are a granular or ‘scallop’ Cu-Sn intermetallic located below the tin layer, which is brighter in the BSE images. To further expose morphological details of this granular phase, surface tin was removed using 5% HCl exposing the unaffected by HCl underlying IMCs (Gagliano and Fine, 2001; Prakash and Sritharan, 2001; Kang *et al.*, 2002; Suh *et al.*, 2008). The individual IMC scallops are

separated by thin (nm scale) voids and have rounded edges with radii ranging between c. 1-4 μm (Figure 4.2c). When viewed in cross-section, this granular phase forms a thin layer (c.4 μm) at the Cu/Sn interface (Figure 4.2d). SEM-EDX from this zone in cross-section confirms that this is the $\eta\text{-Cu}_6\text{Sn}_5$ intermetallic with around 61wt% Sn.

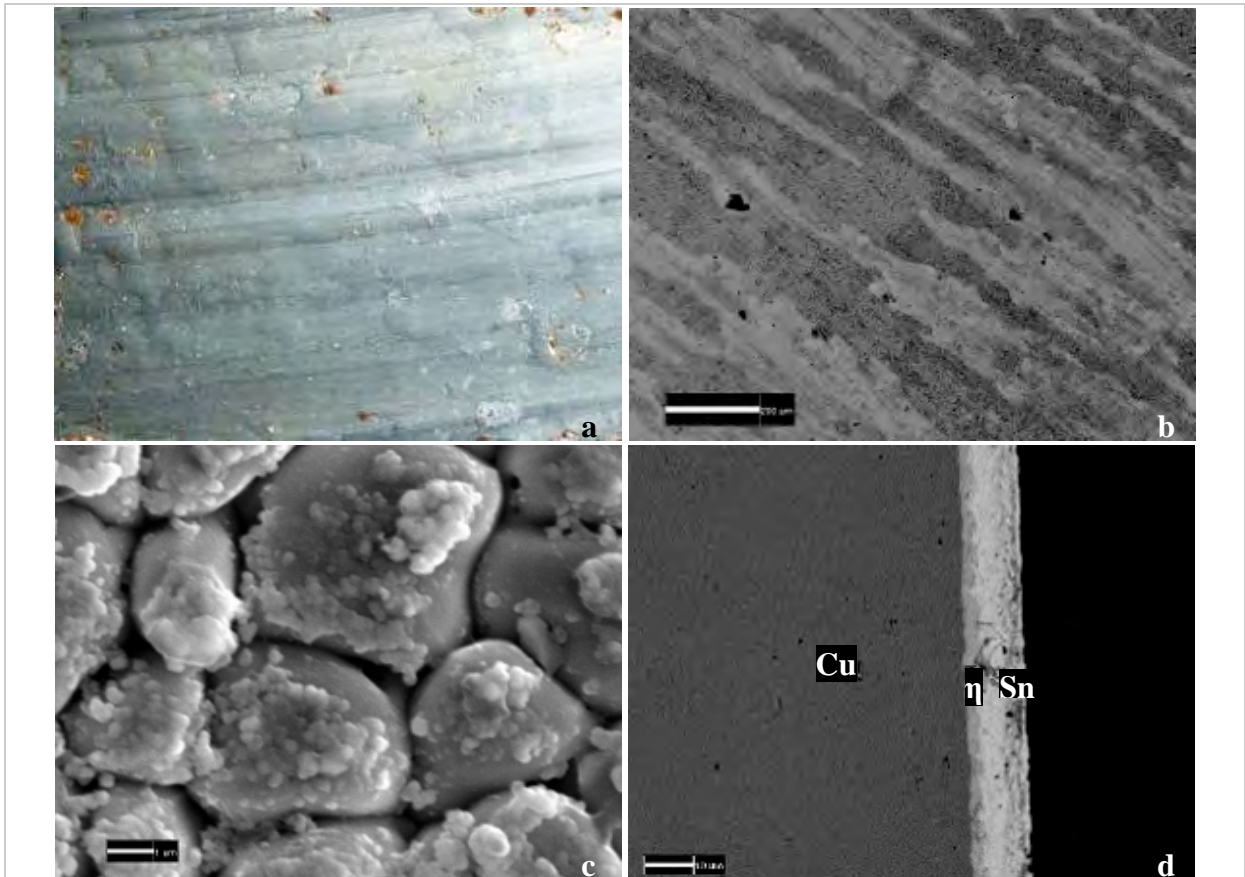


Figure 4.2: Morphology of the surface of wipe-tinned copper sample (S1). (a) Tinned surface exhibiting striations due to uneven application/wiping of tin. (b) BSE image of the same surface showing a granular surface (darker areas) under tin patches (brighter areas). (c) Plan-view BSE image of $\eta\text{-Cu}_6\text{Sn}_5$ scallops separated by intergranular channels; tin was dissolved using 5% HCl, some remnant tin is visible as particles on the top of $\eta\text{-Cu}_6\text{Sn}_5$ (the scale is 1 μm). (d) Cross-sectional BSE showing a thin (4 μm) scallopy $\eta\text{-Cu}_6\text{Sn}_5$ layer formed between the Cu substrate/Sn coating interface (scale is 10 μm).

The micromorphology observed on the wipe-tinned samples (S1 and S3) fits description of $\eta\text{-Cu}_6\text{Sn}_5$ reported in published materials science work. Gagliano and Fine (2001) showed that the $\eta\text{-Cu}_6\text{Sn}_5$ intermetallic phase grows in a scallopy (or granular) form at the Cu/Sn interface during application of melted tin. Individual $\eta\text{-Cu}_6\text{Sn}_5$ scallops are reported to grow upward from the copper surface; they are separated by small spaces or intergranular channels and have rounded tops (Gagliano and Fine, 2001; Suh *et al.* 2008) as seen in Figure 4.2c. The $\epsilon\text{-Cu}_3\text{Sn}$ phase (c.38.2wt%Sn), which is expected to be present between the Cu/ $\eta\text{-Cu}_6\text{Sn}_5$ interface based on the equilibrium phase diagram (Figure 2.2) and previous experimental work (Meeks, 1986), is not visible in the SEM-BSE images of any of the examined wiped as-tinned samples.

4.2.2. ANNEALED WIPE-TINNED COPPER TOKENS

Wipe-tinned copper tokens were annealed at 250°, 350°, 450° and 550°C for 5 or 60 minutes (Table 3.8) to investigate microstructural changes at elevated temperatures that reflect changes during every-day use and to provide a bank of microstructures for the evaluation of diffraction method in the next section. Samples were placed in an electric furnace when it had reached the required temperature, and they were removed immediately after completion of annealing time and left to cool on the bench. Individual cross-sections of these samples were not investigated prior to annealing, because they are expected to show Cu/ η -Cu₆Sn₅/Sn profiles similar to S1 and S3, which were tinned with the same method.

Results are summarised in Table 4.1 and Figure 4.5. Macroscopic optical examination of the tokens annealed at lower temperature/time sets of 250° (S5, S7) and 350° for 5 min (S9) exhibit a metallic tin colour surface, which in places has a small amount of flux (appears brown) remaining on their surface (Figure 4.5, S5, S7, S9). Tokens annealed at higher temperatures have varied thicknesses of various compounds that can be metallic tin or dark grey in colour (Figure 4.5, S11). Progressively the metallic shine is replaced by oxides (Figure 4.5, S15, S17). S19 is covered by a grey oxide layer, which is in places flaking. A scrape from the surface of S15 was confirmed by XRD as Cu₂O with a smaller quantity of CuO and a flake from S19 included Sn, SnO₂, some η -Cu₆Sn₅ and CuO due to high temperature oxidation. This oxide flake did not have any obvious metallic shine; it is interesting that η -Cu₆Sn₅ was present on the flake, indicating that detachment of this IMC from the underlying metal is possible.

Wipe-tinned copper tokens								
Sample	Thermal treatment		SEM-BSE assessment					
	Temperature	Time	coating thickness	α -CuSn	δ -Cu ₄₁ Sn ₁₁	ϵ -Cu ₃ Sn	η -Cu ₆ Sn ₅	Sn
S1	As tinned	-	11-13 μ m	-	-	-	2.2-3 μ m	9.2-10.2 μ m
S3	As tinned	-						
S5	250°C	5 min	34-36 μ m	-	-	-	2-4.5 μ m	32-33 μ m
S7	250°C	60 min	16-27 μ m	-	-	1.7-2 μ m	7.5-8.4 μ m	17-20 μ m
S9	350°C	5 min	2.2-2.5 μ m	-	-	-	?	-
S11	350°C	60 min	85-95 μ m	-	-	2.2-3.4 μ m	6.2-12 μ m	70-80 μ m (+ η crystals)
S13	450°C	5 min	40-50 μ m	-	-	2.6-3.6 μ m	18-21 μ m	24-26 μ m
S15	450°C	60 min	230-240 μ m	-	-	8.5-10.5 μ m	2-3 μ m	200 μ m (+ ϵ/η crystals)
S17	550°C	5 min	33-60 μ m	-	-	5-12 μ m	3-15 μ m	25-50 μ m
S19	550°C	60 min	80-100 μ m	2-5 μ m?	30-80 μ m	-	-	20-50 μ m

Table 4.1: Approximate thickness of metallic coating and of layers of Cu-Sn intermetallics observed in polished cross-sections of annealed wipe-tinned copper tokens as identified using SEM-BSE and EDX.

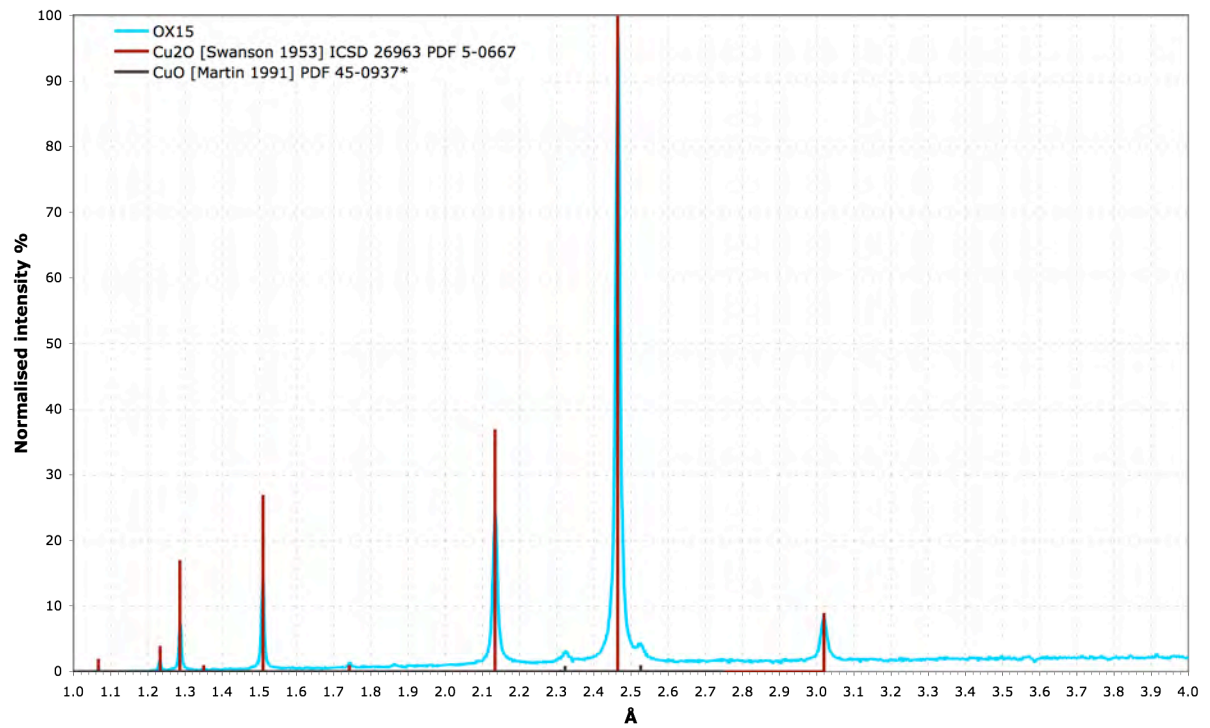


Figure 4.3: X-ray diffraction pattern from surface corrosion product developed during annealing of S15 tinned copper token at 450°C for 1 hour.

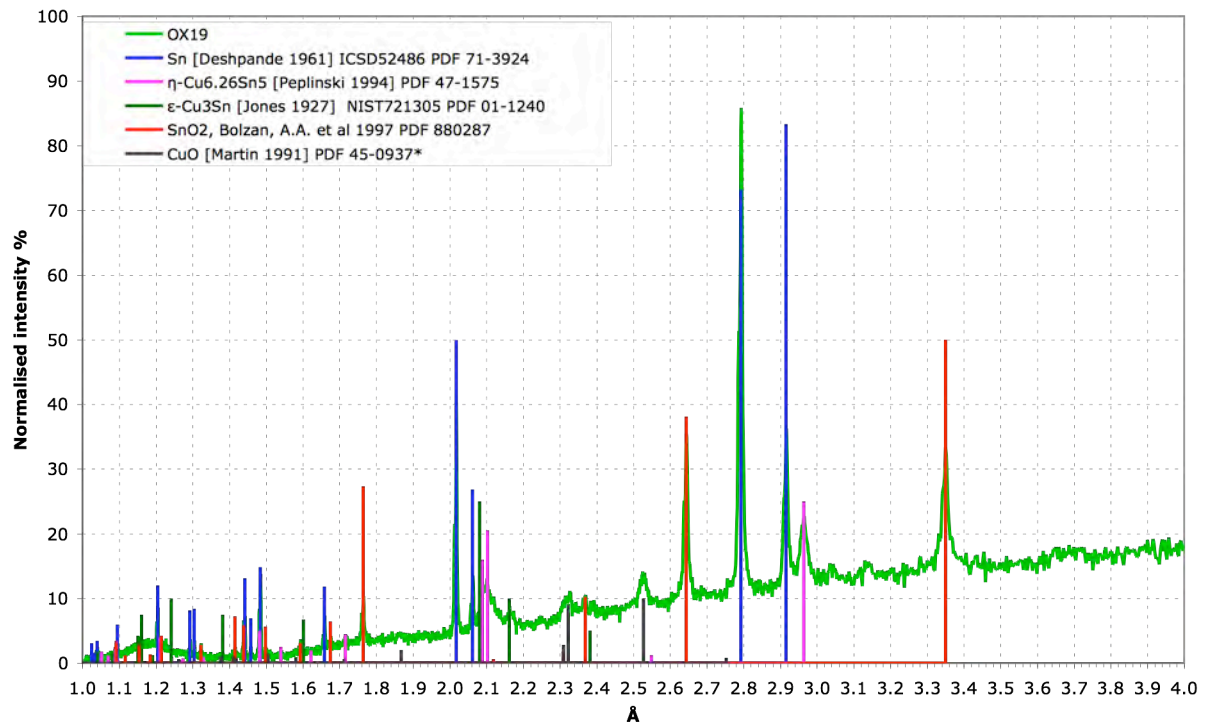


Figure 4.4: X-ray diffraction pattern from surface corrosion product developed during annealing of S19 tinned copper token at 550°C for 1 hour.

Cross-sectional SEM-BSE imaging of the annealed tokens revealed that major microstructural changes took place during annealing (Figure 4.5); the type of intermetallics, their morphology, relative quantity, and thickness changed depending on annealing temperature/time. The characteristic granular nature of η -Cu₆Sn₅ aided its identification on several samples, and phases were confirmed using EDX. The thickness of the metallic coating and other features in polished cross-sections were measured from at least three points across each feature in calibrated digital BSE images using ImageJ software (Table 4.1). The thickness of the metallic coating is taken to include intermetallics and any remaining tin.

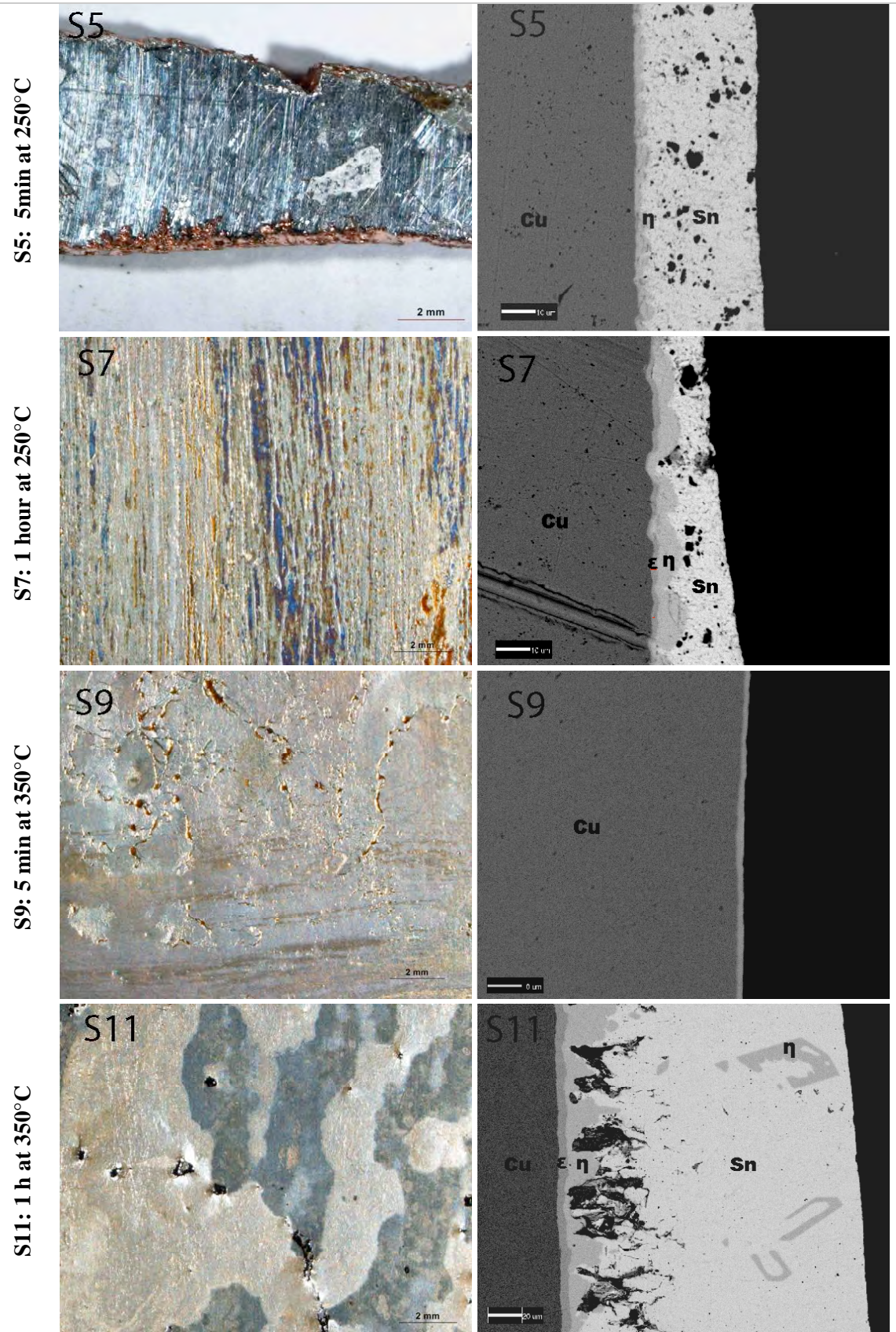
In the literature, the metallic coating formed by tinning is commonly referred to as '*tin coating*', which is imprecise, as it does not reflect the presence of intermetallics. Metallic coatings in this thesis are referred to also as *tinning coating* to avoid confusion. Overall, the coating thickness of the annealed wipe-tinned copper tokens ranges between 10-50 μm (Table 4.1). Tokens S11 (c. 85-95 μm) and S15 (c. 240 μm) have the thickest coating, which is the result of uneven application of tin during wiping leaving a considerable amount of tin on the surface (Figure 4.5, S11, S15). This is in contrast to S9, which has an extremely fine phase layer for the same reason. Variation of the original amount of tin wiped on the surface has an impact on the microstructures formed and it is discussed below.

Morphologically, **S5** (5min at 250°C) has a granular η -Cu₆Sn₅ at the Cu/Sn interface, under a thick porous Sn layer (Figure 4.5, S5). Similarly to the as-tinned samples, ϵ -Cu₃Sn is not visible in the SEM-BSE images of S5. Longer annealing at 250°C for 60min (Figure 4.5, S7) produced increasingly elongated η -Cu₆Sn₅ scallops projecting into the Sn layer and a fine (c. 2 μm) planar ϵ -Cu₃Sn layer on **S7**. The Sn layer is porous in both samples due to elevated amounts of flux used during tinning (Yu and Kim, 2008). Sample **S9** (5min at 350°C) has a very fine phase layer, which was too thin to identify using BSE or EDX (Figure 4.5, S9).

After 1 hour at 350°C the ϵ -Cu₃Sn layer is relatively planar on **S11**, situated at the Cu/ η -Cu₆Sn₅ interface (Figure 4.5, S11). η -Cu₆Sn₅ scallops are more elongated and irregular in shape and large voids are present at the η -Cu₆Sn₅/Sn interface. These so-called Kirkendall voids (or Kirkendall porosity) are associated with atomic vacancy diffusion phenomena in diffusion couples where the diffusion rates of the two species are very different (Nakajima, 1997). Long thin angular crystals of η -Cu₆Sn₅ are observed in the Sn matrix. Such rod- or whisker-shaped η -Cu₆Sn₅ in the tin matrix are reported to form by reaction of Sn with the Cu that becomes available at the top of the η -Cu₆Sn₅ scallops; the phase is forced to elongate into whisker shapes because of a gradual reduction in the available copper in the melt (Gagliano

and Fine 2001, fig.2; Laurila *et al.* 2005 fig.4). **S13** (5 min at 450°C) produced a relatively uniform thick ϵ -Cu₃Sn layer (3.4-4 μ m) (Figure 4.5, S13). Individual η -Cu₆Sn₅ scallops are joined further and form a thick and almost continuous layer, with dramatically reduced number of intergranular channels between them. Large Kirkendall voids are situated at the η -Cu₆Sn₅ / Sn interface. A number of small ‘islands’ of a different phase, identified as having in the order of 2wt% Sn by EDX analysis are present in the tin matrix near the top of η -Cu₆Sn₅.

Annealing for 1 hour at 450°C (**S15**) resulted in substantial growth of ϵ -Cu₃Sn most likely at the expense of η -Cu₆Sn₅ because in this case ϵ -Cu₃Sn starts mimicking the granular shape of η -Cu₆Sn₅ (Figure 4.5, S15). η -Cu₆Sn₅ whiskers in the Sn layer now have an ϵ -Cu₃Sn core. Kirkendall voids are found at the η -Cu₆Sn₅/Sn interface and low-tin ‘islands’ are present near these and at the bottom of the elongated crystals. Increased temperature at 550°C (**S17**, 5min) resulted in further coarsening of the ϵ -Cu₃Sn layer; the shape of the η -Cu₆Sn₅ / ϵ -Cu₃Sn elongated crystals in the Sn matrix is less clearly defined (Figure 4.5, S17). **S19** (1hour at 550°C) shows the presence of δ -Cu₄₁Sn₁₁ phase in a tin matrix, which agrees with the Cu-Sn equilibrium phase diagram (Figure 2.2). Large voids are present at the lower part of the thick δ -Cu₄₁Sn₁₁ layer. An extremely fine layer of another phase may be present at its interface with the copper substrate, however it is not clearly resolved with BSE imaging (Figure 4.5, S19). The plan-view morphology of S19 (Figure 4.6) is uncommon compared to the other samples, and may aid its identification as evidence for tinning in similar to this experiment contexts.



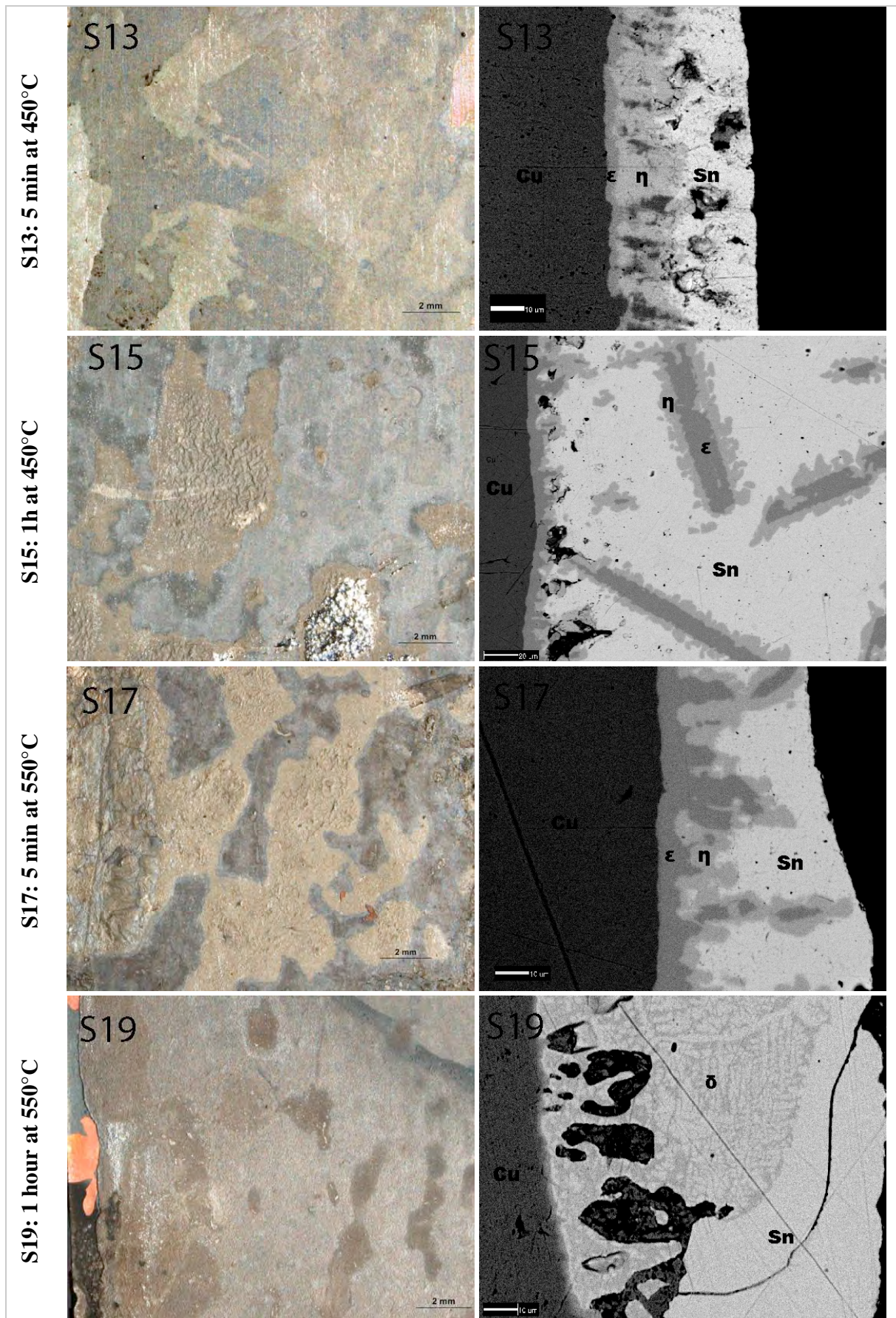


Figure 4.5: Optical micrographs of the surface of annealed wipe-tinned copper tokens (left) and cross-sectional SEM-BSE images of corresponding samples (right). Scale in BSE images is 10 μm , apart from images S11 and S15 where it is 20 μm .

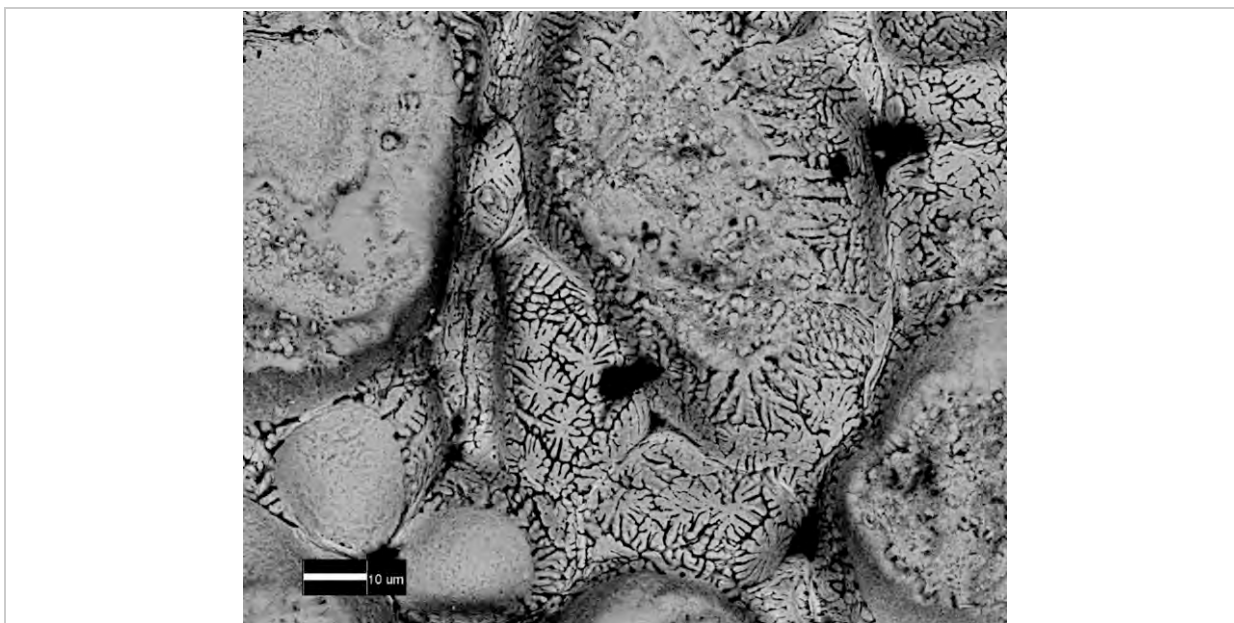


Figure 4.6: SEM-BSE image of surface on S19 in plan-view showing dendritic nature of δ -Cu₄₁Sn₁₁ below a layer of metallic tin.

Results overall show that ϵ -Cu₃Sn starts appearing at the Cu/ η -Cu₆Sn₅ interface at longer annealing time at temperatures just above the melting point of Sn. The characteristic granular nature of η -Cu₆Sn₅ is retained up to annealing for 1h at 350°C when Kirkendall voids at the η -Cu₆Sn₅ /Sn interface appear and η -Cu₆Sn₅ whiskers are present in the surplus of Sn. Further microstructural changes occur at higher temperatures, and δ -Cu₄₁Sn₁₁ is visible by SEM after annealing for 1h at 550°C when the other intermetallics seem to disappear.

4.2.3. ANNEALED WIPE-TINNED BRONZE TOKENS

As the composition of the substrate can influence the extent of intermetallic growth, in order to assess the applicability of these observations on archaeological low-tin bronzes a set of tinned bronze tokens were investigated. Bronze tokens of c. 10wt% Sn that were cast in the laboratory and homogenised for 6 hours at 500°C prior to tinning, were wipe-tinned and annealed for 60 minutes at 250°, 350°, 450° and 550°C (Table 3.8). For a broad comparison to copper tinned samples, these were at the same annealing sets to S11, S15, S17 and S19. The metallic coatings after annealing were finer than in the copper tokens ranging between c. 5-35 μ m (Table 4.2).

Sample **B6** (1h at 250°C) shows a thin ϵ -Cu₃Sn (2-2.5 μ m) under an η -Cu₆Sn₅ layer which is less granular than that developed on its equivalent annealed tinned copper sample (S7) (Figure 4.7, B6). On sample **B7** (1h at 350°), an ϵ -Cu₃Sn layer (5-10 μ m) is present between the bronze substrate and a relatively thick η -Cu₆Sn₅ (10-16 μ m) layer. Fine Kirkendall voids are

at the ϵ -Cu₃Sn/Cu₆Sn₅ interface (Figure 4.7, B7). Its annealing equivalent copper sample **S11** has a thicker overall coating but a considerably thinner the ϵ -Cu₃Sn layer (2.2-3.4 μ m) and large Kirkendall voids at the η -Cu₆Sn₅ / Sn interface. **B8** (1h at 450°C) shows a substantial ϵ -Cu₃Sn layer (c. 30 μ m) that is covered by a fine η -Cu₆Sn₅ layer (Figure 4.7, B8). The thickness of ϵ -Cu₃Sn is almost double compared to **S15** and it seems that it grew at the expense of a granular η -Cu₆Sn₅, which is evident by its slightly granular shape. At these temperatures, η -Cu₆Sn₅ can be completely transformed to ϵ -Cu₃Sn if there is sufficient annealing time (Banovic, 2007). Sn is present only locally on the surface of B8. **B9** was annealed at 550°C for an hour as S19 and shows the presence of an α + δ eutectoid structure (Figure 4.7, B9).

Overall, the IMC growth patterns in copper and bronze tinned tokens exposed to the same annealing sets are broadly similar in relation to the phases formed. The main difference between the two sets of samples is the thickness of the ϵ -Cu₃Sn layer in the bronze samples B7 and B8, which is thicker than that present at their corresponding annealed copper tokens (S11 and S15). This occurs even if the metallic coating is much thicker in the copper samples and therefore offered more tin for reaction during annealing. Kirkendall voids are substantially smaller compared to those developed on copper substrates and are observed only on B7 at the ϵ -Cu₃Sn / η -Cu₆Sn₅ interface, whereas they are at the η -Cu₆Sn₅/Sn interface in copper samples (S11). These observations indicate differences in diffusion mechanisms that take place in the Cu/Sn and bronze/Sn diffusion couples and are discussed below.

Wipe-tinned bronze tokens								
Sample	Thermal treatment		coating thickness	SEM-BSE assessment				
	Temperature	Time		α -CuSn	δ -Cu ₄₁ Sn ₁₁	ϵ -Cu ₃ Sn	η -Cu ₆ Sn ₅	Sn
B6	250°C	60 min	9-12 μ m	-	-	2-2.5 μ m	6.5-10 μ m	0-5 μ m
B7	350°C	60 min	17-33 μ m	-	-	5-10 μ m	10-16 μ m	0-10 μ m
B8	450°C	60 min	28-35 μ m	-	-	20-31 μ m	3-5 μ m	0-5 μ m
B9	550°C	60 min	5-15 μ m	?	5-15 μ m	-	-	-

Table 4.2: Approximate thickness of metallic coating and layers of Cu-Sn intermetallic compounds on annealed wipe-tinned bronze tokens.

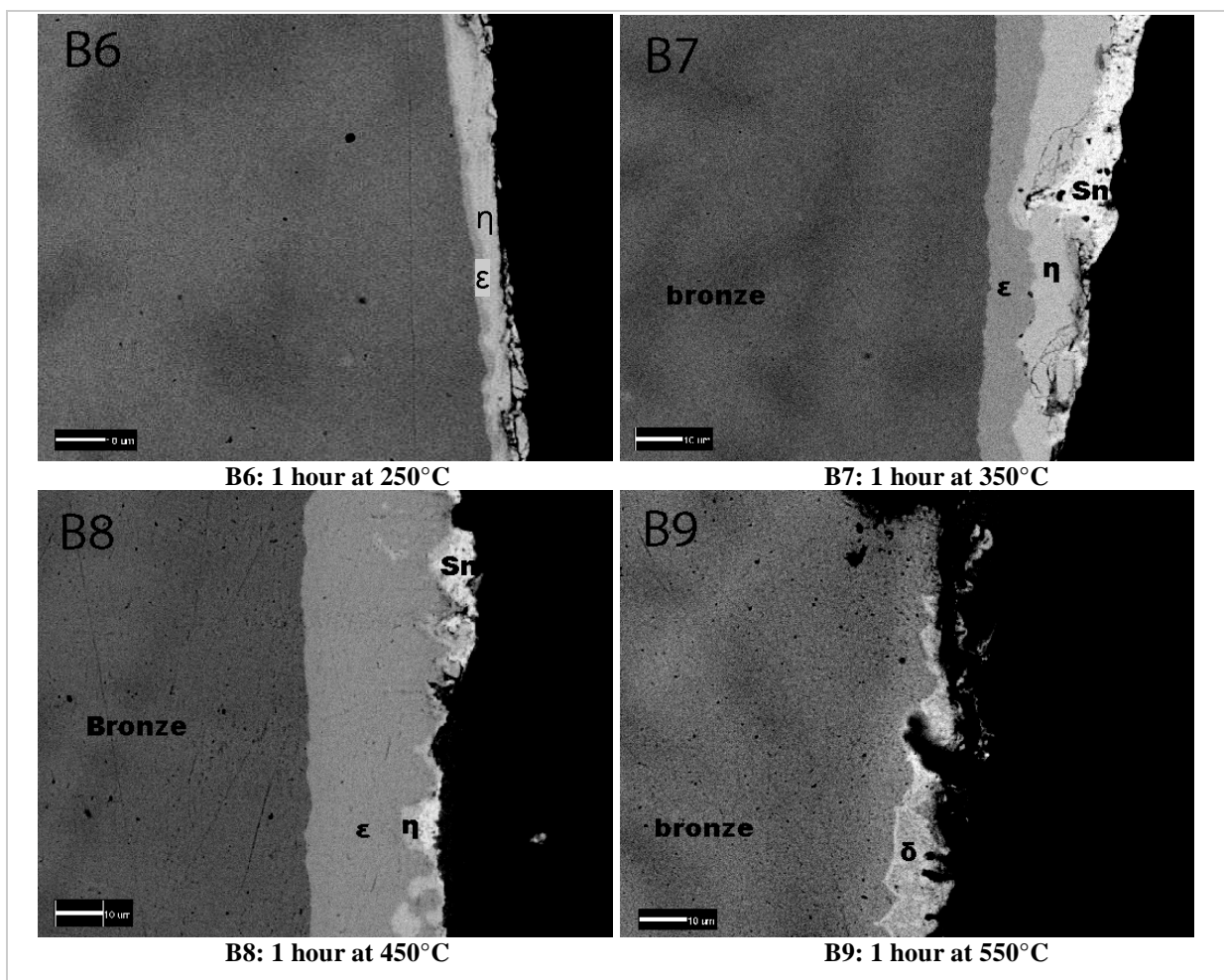


Figure 4.7: Cross-sectional SEM-BSE images of annealed wipe-tinned bronze tokens.

4.3. DIFFRACTION ANALYSES OF TINNED TOKENS

In order to evaluate the efficacy of non-destructive methods for the identification of tinning, experimental tinned copper and bronze tokens were investigated by X-ray and neutron diffraction. XRD was conducted using the PANalytical X'Pert-PRO system and time-of-flight neutron diffraction was undertaken at GEM and ROTAX diffractometers as described in section 3.8.2. Diffraction data presented in this thesis are shown as normalised intensity % (count rates) versus crystallographic d-spacing in Angstrom (\AA). Reference patterns are normally presented in 'stick' format and are scaled relative to the intensities of the major observed peaks of phases. This can provide a crude indication of the relative amount of each phase present on the samples.

Diffraction patterns were assigned to reference crystallographic structures in PDF2-2005 and ICDS databases. A literature review identified inconsistencies in the crystalline structural form of η -Cu₆Sn₅ and ε -Cu₃Sn (Table 4.3), which is noticeable in their diffraction patterns to different extents (Figure 4.8). It also revealed concerns about the transformation of the high temperature η -Cu₆Sn₅ to its stable room temperature form η' -Cu₆Sn₅ (section 2.2.4). These factors complicate accurate interpretation of the diffraction patterns necessitating a rather detailed justification of assignment of diffraction lines to reference phases. This aids discussion on the quality of the XRD and neutron diffraction data and a comparison of the effectiveness of the methods. Often reference patterns are referred to based on crystallographer rather than PDF number to ease discussion.

Phase	Database entry	Crystallographic data by	Lattice parameters
Published structures of the η-Cu₆Sn₅ phase			
Monoclinic (C2/c)			
η' -Cu ₆ Sn ₅	ICSD 106530, PDF 45-1488	Larsson <i>et al</i> 1994	a=11.022Å, b=7.282Å, c=9.827Å, $\alpha=\gamma=90^\circ$, $\beta=98.84^\circ$
η' -Cu ₆ Sn ₅	ICSD 150124	Lidin <i>et al</i> 1995	
η -Cu ₆ Sn ₅	ICSD 158248	Yu <i>et al</i> 2007	a=10.926Å, b=7.113Å, c=9.674Å, $\alpha=\gamma=90^\circ$, $\beta=99.142^\circ$
η -Cu ₆ Sn ₅	CRYSTMET 3161, PDF 65-2303	Larsson <i>et al</i> 1994,	a=11.022Å, b=7.282Å, c=9.827Å, $\alpha=\gamma=90^\circ$, $\beta=98.84^\circ$
Hexagonal (P63/mmc)			
η -Cu _{6,26} Sn ₅	PDF 47-1575	Peplinski <i>et al</i> 1994	a=b=4.206Å, c= 5.097Å, $\alpha=\beta=90^\circ$, $\gamma=120^\circ$
η -Cu ₆ Sn ₅	PDF 2-0713	Westgren	
η' (Cu ₆ Sn ₅)0.1818	ICSD 56282, PDF 71-5036	Gangulee <i>et al</i> 1973	a=b=4.192Å, c= 5.037Å, $\alpha=\beta=90^\circ$, $\gamma=120^\circ$ superstructure
η' -Cu ₆ Sn ₅	ICSD 56282, PDF 71-5036	Gangulee <i>et al</i> 1972, reported in Tu 1973	a=b=20.85Å, c=25.10Å, $\alpha=\beta=90^\circ$, $\gamma=120^\circ$ superstructure
Published structures of the ε-Cu₃Sn phase			
Orthorhombic			
ε -Cu ₃ Sn	PDF 01-1240	Jones, 1925	Cmcm
ε -Cu _{3,02} Sn _{0,98}	ICSD 103102, PDF 65-5721	Watanabe <i>et al</i> 1983	Cmcm a=5.529Å, b=47.75Å, c= 4.323Å, $\alpha=\beta=\gamma=90^\circ$
ε -Cu ₃ Sn	PDF 65-4653	Burkhardt <i>et al</i> 1959	Pmmn
ε -Cu ₃ Sn	PDF 6-0621	Isajcev	Pmmn
ε -Cu ₃ Sn	ICSD 150815	Knoedler <i>et al</i> 1966	Pnmm
Cubic (F4-3m)			
ε -Cu ₃ Sn	PDF 65-4374	Knoedler <i>et al</i> 1966	high temperature
Hexagonal (P63/mmc)			
ε -Cu ₃ Sn	ICSD 162569	Sang <i>et al</i> 2009	

Table 4.3: Summary of selected crystallographic data reported for the η -Cu₆Sn₅ and ε -Cu₃Sn phases. η' notes the room temperature structure.

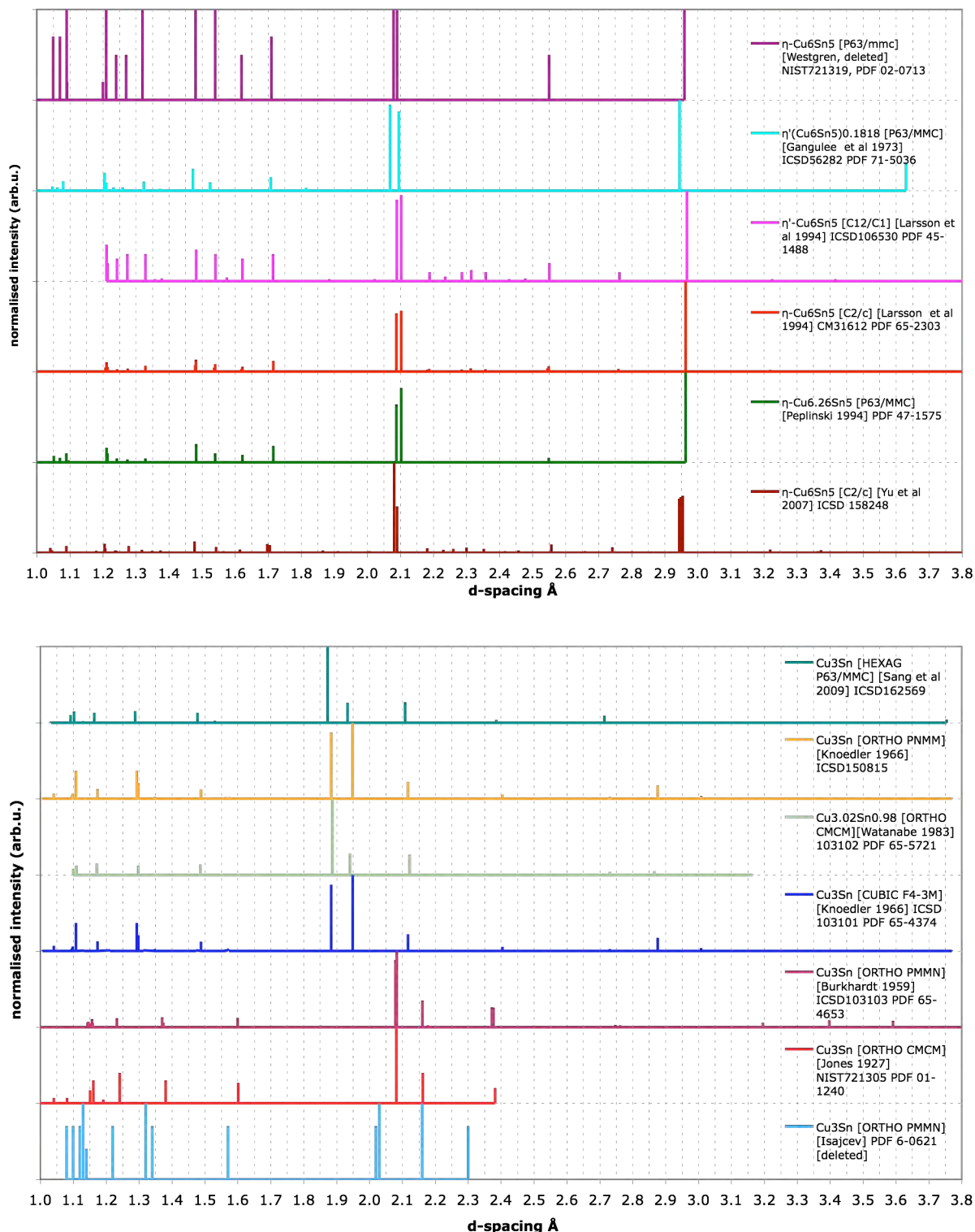


Figure 4.8: Selected reference diffraction patterns of the η - Cu_6Sn_5 and ϵ - Cu_3Sn phases. Jones's ϵ - Cu_3Sn (PDF01-1240) and Westgren's η - Cu_6Sn_5 pattern (PDF2-0713) are commonly cited in archaeological science work (e.g. Meeks, 1986, Oddy and Bimson, 1985, Qinglin and Scott, 2003)

4.3.1. X-RAY DIFFRACTION

4.3.1.1. Wipe-tinned copper tokens

XRD results are summarised in Figure 4.9 and Table 4.4. XRD patterns show a progressive change and complexity with increasing annealing temperature compared to the as-tinned copper tokens (Figure 4.9). These changes are caused by changes in the microstructure during annealing which are visible in BSE of cross-sections. All the diffraction patterns show lines of different intensities from the copper substrate (1.81, 1.28, 2.09, 1.09Å) depending on the thickness of the coating. Sn (PDF4-0673) is present to different extents on all samples apart from S19 (2.92, 2.79, 2.06, 1.66, 1.44Å, unique lines to Sn are absent) (Table 4.4).

The as-tinned tokens (**S1**, **S3**) and **S5** (5min at 250°C) and **S9** (5min at 350°C) show clear diffraction lines from η -Cu₆Sn₅, and a very small amount of ϵ -Cu₃Sn based on the relative intensity of its major diffraction lines (Figure 4.10, Figure 4.11). Westgren's η -Cu₆Sn₅ pattern (PDF2-0713), which is commonly cited in heritage science work (e.g. Oddy and Bimson, 1985; Meeks, 1986; Qinglin and Scott, 2003) fits the d-spacings but its major peaks are at 100% intensity, which does not match the experimental data. This pattern is now replaced in the PDF database by Peplinski's structure η -Cu_{6.26}Sn₅ (PDF47-1575), which has peak positions and intensity that better fit the experimental data and it was assigned to η reflections in S1, S3, S5 and S9. The tiny unassigned diffraction lines at 2.16, 2.42Å and 3.21Å in S3 and S9 do not fit d-spacings of any Cu or Sn oxides and could be from η -Cu₆Sn₅ as they are in Larsson's η -Cu₆Sn₅ pattern (PDF 65-2303). However, this pattern has additional diffraction lines, which are not present on S1, S3, S5 and S9 (2.18, 2.23, 2.28, 2.31, 2.35, 2.42 and 2.76Å) (Figure 4.10, Figure 4.11). Jones's ϵ -Cu₃Sn (PDF01-1240) best agrees with ϵ -Cu₃Sn reflections from these samples. ϵ -Cu₃Sn was not previously observed in cross-sections of S1, S3, S5 and S9 during SEM-BSE and EDX analysis (Figure 4.2, Figure 4.5).

New diffraction lines at 2.76, 3.21, 3.39Å and an increase of intensity at 1.16, 1.38, 2.16, 2.39 and 2.42Å is observed at the diffraction patterns of **S7** (1 h at 250°C), **S11** (1 hour at 350°C) and **S13** (5min at 450°C), which other than that, are similar to the previous samples (Table 4.4, Figure 4.12, Figure 4.13). These diffraction lines are present at different reference structures for ϵ -Cu₃Sn and η -Cu₆Sn₅. Burkhardt's ϵ -Cu₃Sn pattern (PDF65-4653) is similar to the one assigned to the previous samples (Jones, PDF01-1240), but it includes diffraction lines at 3.21 and 3.39Å. Diffraction lines at similar d-spacings are included in Larsson's η -Cu₆Sn₅ pattern (PDF 65-2303) (2.76, 3.23 and 3.42Å), apart from 2.16 and 2.39Å, which are unique to Burkhardt's ϵ -Cu₃Sn (PDF65-4653) and 1.38Å, which is more intense in this phase

(Table 4.4). These two structures better match the data derived from increased annealing sets. S11 may also contain a tiny amount of Cu_2O (2.47\AA , PDF 5-0667) (Figure 4.12).

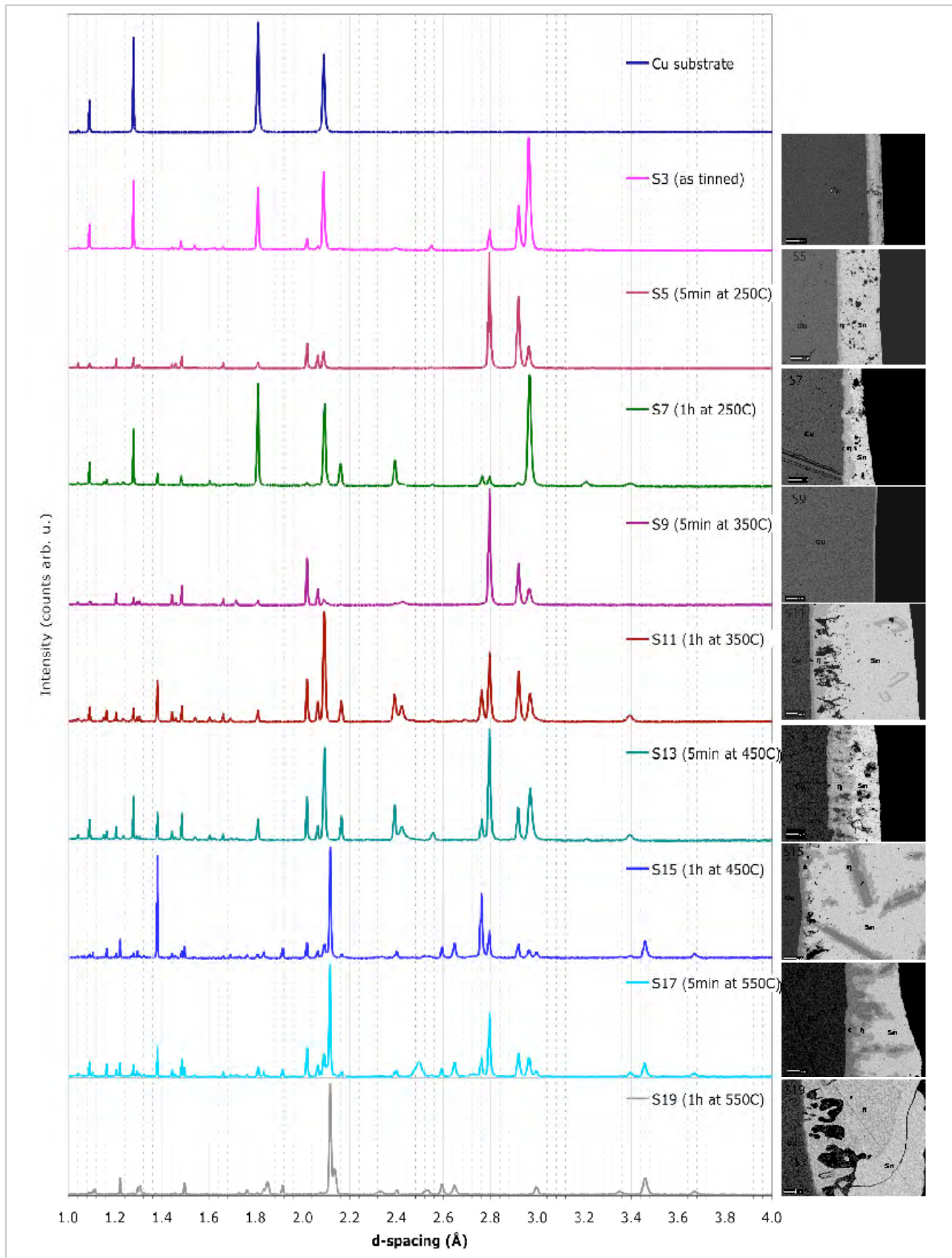


Figure 4.9: Normalised XRD patterns of as-tinned and annealed copper tinned tokens shown with BSE images of corresponding cross-sectioned samples.

S15 (1 hour at 450°C), **S17** (5 min at 550°C) and **S19** (1 hour at 550°C) show diffraction lines of different intensities from both ϵ -Cu₃Sn (PDF65-4653) and η -Cu₆Sn₅ (PDF65-2303) (Table 4.4, Figure 4.13, Figure 4.14). Overlapping of ϵ -Cu₃Sn and η -Cu₆Sn₅ lines occurs at several d-spacings (Table 4.4) and at their major reflection at 2.09Å, and makes unique assignment of peaks difficult. S15 and S17 show additional Bragg reflections that correspond to δ , which is the major phase on S19 (Figure 4.14). Several reference patterns fit this phase, for example Cu_{327.92}Sn_{88.08} (PDF30-0511) and Cu_{40.5}Sn₁₁ (PDF71-0121), Cu₃₉Sn₁₁ (PDF71-0122), Cu₄₁Sn₁₁ (PDF65-7047), which correspond to slightly different chemical compositions, but the Cu₄₁Sn₁₁ (PDF30-0510) better matched the intensity of the minor diffraction lines in the experimental data. S15 seems to have a very small amount of SnO₂ (2.65, 3.36Å, PDF88-0287), which is more dominant on S19. S19 also includes lines from an α -bronze which has a Sn content higher than c.10wt%, based on the d-spacing position of experimental reference bronze. The presence of a copper-rich phase forming ‘islands’ observed in SEM-BSE in S13 and S15 cross-sections could not be confirmed using XRD.

Normally, the intensity of the diffraction lines in a phase of a constant composition and structure is not expected to deviate compared to the reference patterns, which is normally free of crystallite preferred orientation (texture). The intensity peak height of a phase relative to other phases in a diffraction pattern can then offer information on their relative content. In these samples the peak ratio in each component including Sn, ϵ -Cu₃Sn and η -Cu₆Sn₅ changes relatively to the reference patterns and between samples. For example, the ratio of major Sn lines 2.79 and 2.92Å varies between samples and the reference pattern (Table 4.4). The intensity ratio also varies between 1.71Å/2.55Å and 2.96Å, which are assigned to η -Cu₆Sn₅, and 2.16/2.39Å, which are assigned to ϵ -Cu₃Sn. This would indicate that Sn, η -Cu₆Sn₅ and ϵ -Cu₃Sn crystallites have a preferred orientation. In the case of Sn, it is likely that texture is due to wiping the tin on the surface that resulted in striations along the tokens. As the samples were analysed mounted on a stationary stage, a change in crystal orientation could be “visible” in the diffraction pattern from sample to sample explaining the observed intensity variations. SEM-BSE showed that the granular η -Cu₆Sn₅ and all IMCs grow into Sn perpendicular to the surface. The area analysed by the X-ray beam on the samples was 20x20mm², which is large enough to be representative of all crystallite orientations in the diffracting volume. Thus, deviation of the intensity of the diffraction lines in a phase is not an artefact caused by experimental set up.

Phase	spacing Å	Sample										Reference pattern		
		S1 as-tinned	S3 5min at 250°C	S5 1h at 250°C	S7 5min at 350°C	S9 1h at 350°C	S11 5min at 450°C	S13 1h at 450°C	S15 5min at 550°C	S17 1h at 550°C	S19 1h at 550°C	Ref 1	Ref 2	
Sn	2.79	100	19	81	10	100	61	100	24	55	-	90	PDF 4-0673	
	2.92	81	39	61	4	36	44	29	12	21	-	100		
	2.79/2.92 ratio	1.2	0.5	1.3	2.5	2.8	1.4	3.4	2.0	2.6	-	0.90		
	2.06	48	5	11	3	15	18	13	7	11	-	34		
	1.66	18	4	5	2	6	8	6	3	5	-	17		
1.44	2	4	4	2	10	9	9	4	6	-	20			
η -Cu ₆ Sn ₅	2.96	42	100	18	100	13	24	44	7	17	-	100	PDF 65-2303 [Larsson]	
	2.55	11	5	1	1	1	2	7	-	1	-	6		
	1.71	22	2	-	2	4	-	2	-	1	-	12		
	2.42	3	2	-	2	2	14	12	-	-	-	1		
ϵ -Cu ₃ Sn	2.16	3	2	-	20	1	19	22	3	4	-	35	PDF 65-4653	
	2.39	5	3	-	23	2	24	32	2	4	2	26		
η and ϵ	1.16	1	1	-	7	-	11	9	8	12	-	1	η -Cu ₆ Sn ₅ [Larsson]	10 13 3 6 9 ϵ -Cu ₃ Sn [Burkhardt] PDF 65-4653
	1.38	4	3	1	11	2	36	26	88	27	1	1		
	2.76	-	-	-	9	-	28	19	56	18	-	3		
	3.21	-	1	-	4	-	1	1	-	-	-	2		
3.39	-	-	-	3	-	5	5	2	4	-	2			
Cu ₄₁ Sn ₁₁	2.11	-	-	-	-	-	-	-	48	100	100	100	PDF 30-0510	

Table 4.4: Normalised intensity % of diffraction lines at selected d-spacing (Å) characteristic of Sn, η -Cu₆Sn₅, ϵ -Cu₃Sn and δ -Cu₄₁Sn₁₁ present in the experimental data and reference diffraction patterns. η and ϵ notes peak positions where overlap of the two phases occurs. The intensity of diffraction lines at selected d-spacings from IMCs is recorded based on Larsson's η -Cu₆Sn₅ and Burkhardt's ϵ -Cu₃Sn reference patterns. The ratio of the intensity of 2.79/2.92Å is presented as indication of texture in Sn.

In as-tinned and early annealing stages, η -Cu₆Sn₅ was seen to grow into Sn in a scallopy form parallel to the surface (Figure 4.5). In S7 and S11 η -Cu₆Sn₅ becomes more elongated into Sn and an increase in ϵ -Cu₃Sn thickness is observed. This change and increase of the amount of ϵ -Cu₃Sn seen in BSE is accompanied by the increase of the intensity of 2.16Å and 2.39Å, which are unique to ϵ -Cu₃Sn (Table 4.4). S15 has whiskers in the Sn matrix formed by a thick ϵ -Cu₃Sn core and surrounded by a thin coating of η -Cu₆Sn₅ scallops (Figure 4.5). This important increase in ϵ -Cu₃Sn content is most likely reflected by the dramatic increase of its 1.38Å (88%) and 2.76Å (56%) reflections in the diffraction pattern of S15, which are minor in a texture-free sample (Table 4.4). The physical morphology of these whiskers has an impact at the intensity ratio of its diffraction lines demonstrating its texture, and the 1.38 and 2.76Å peaks could aid qualitative characterisation of the nature of the physical state of these phases. Overall, the intensity increase of ϵ -Cu₃Sn diffraction lines in S7, S11, S13, S15 and S17 that overlap with η -Cu₆Sn₅ seem to be predominantly related to the increase in the concentration of ϵ -Cu₃Sn seen in the BSE images (Table 4.4).

To support this, S1, S3, S5 and S9, where diffraction lines at 1.38, 2.76Å are very small or absent, show very small concentration of ϵ -Cu₃Sn, such that was not observed in the BSE images of S1, S3 and S5 cross-sections. S9 was fully characterised by XRD, as the very thin surface coating resulted in unsatisfactory EDX analysis for its identification. Samples S15 (1

hour at 450°C), S17 (5 min at 550°C) and S19 (1 hour at 550°C) exhibit clear diffraction lines from δ -Cu₄₁Sn₁₁, which is expected based on the equilibrium phase diagram (Figure 2.2), but the phase was not seen in the BSE images until S19. The diffraction pattern of S19 also contains evidence for an α -bronze which could not be confirmed by SEM-BSE imaging. These observations demonstrate the advantage of XRD over SEM-BSE characterisation of samples. The capacity of XRD to detect very small amount of phases on the tokens is merely a result of investigating a larger area (20x20mm in this case), than that in cross-sectioned samples. This provides a better representation of phases present. However, SEM-BSE was invaluable for the interpretation of the diffraction patterns of S7, S11, S13, S15 and S17 due to texture effects in IMC phases, making these two investigative tools complementary.

In summary, XRD and BSE results of as-tinned and annealed tinned copper tokens show that η -Cu₆Sn₅ is the major IMC formed during tinning and its characteristic scallopy form aids its microscopic identification. A very small amount of ϵ -Cu₃Sn may be formed during tinning as confirmed by XRD but this was not visible in SEM-BSE in the samples (S1, S3). Short annealing at 250°C and 350°C did not have a noticeable impact at the IMC profile (S5, S9). Longer annealing at these temperatures resulted in growth of a relatively uniform ϵ -Cu₃Sn layer and η -Cu₆Sn₅ scallops became longer projecting into the Sn layer as seen in BSE (S7, S11), and of η -Cu₆Sn₅ whiskers grew in the excess Sn matrix (S11). These changes are accompanied with Kirkendall voids and intense texture in the diffraction patterns in the IMC phases. A marked change in the diffraction patterns pointed out that Larsson's η -Cu₆Sn₅ and Burkhardt's ϵ -Cu₃Sn reference diffraction patterns are best fit for the data from annealed copper tokens. The increase of ϵ -Cu₃Sn was followed by increase of diffraction lines assigned to this phase. This seems to reach its highest concentration in S15 after annealing at 450°C for 1 hour, where η -Cu₆Sn₅ whiskers in the excess Sn matrix appear now straight and long and have a substantial ϵ -Cu₃Sn core; its surrounding η -Cu₆Sn₅ is itself scallopy. δ -Cu₄₁Sn₁₁ appears first after 1h at 450°C (S15) in the XRD patterns and it is the dominant phase at 550°C (S17, S19) in agreement with the equilibrium phase diagram, but it is not visible in BSE until S19, where an α -bronze might be in BSE images that is confirmed by XRD. A very small amount of ϵ -Cu₃Sn might be present in S19 but this cannot be confirmed by diffraction analysis of the sample.

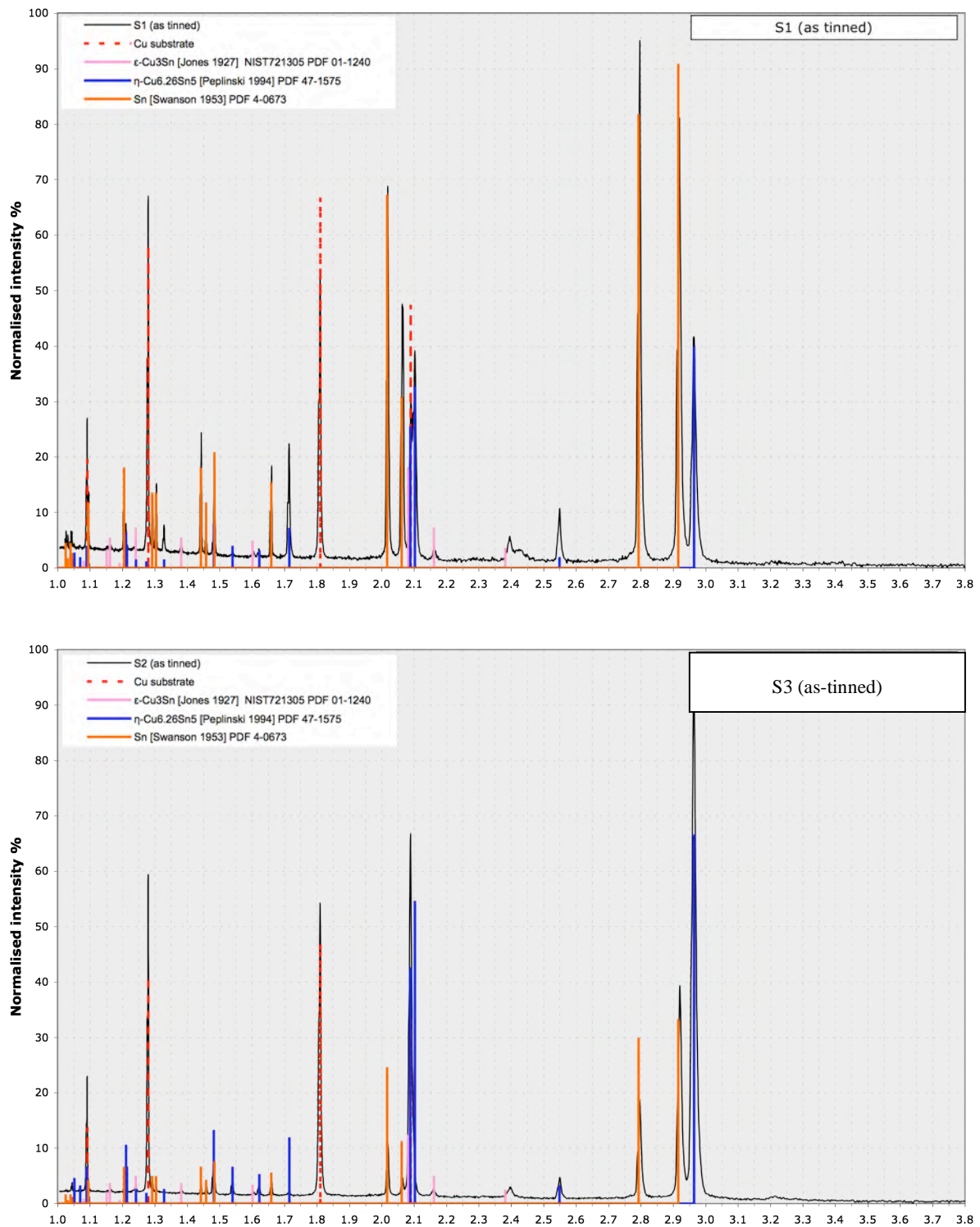


Figure 4.10: X-ray diffractograms of S1, S3 (as tinned), with stick patterns of reference structures scaled to provide a rough guide of amounts present. Normalised 100% intensity (x-axis is d-spacing in Å). η -Cu₆Sn₅, Sn and Cu are the dominant components and a very small amount of ϵ -Cu₃Sn is present.

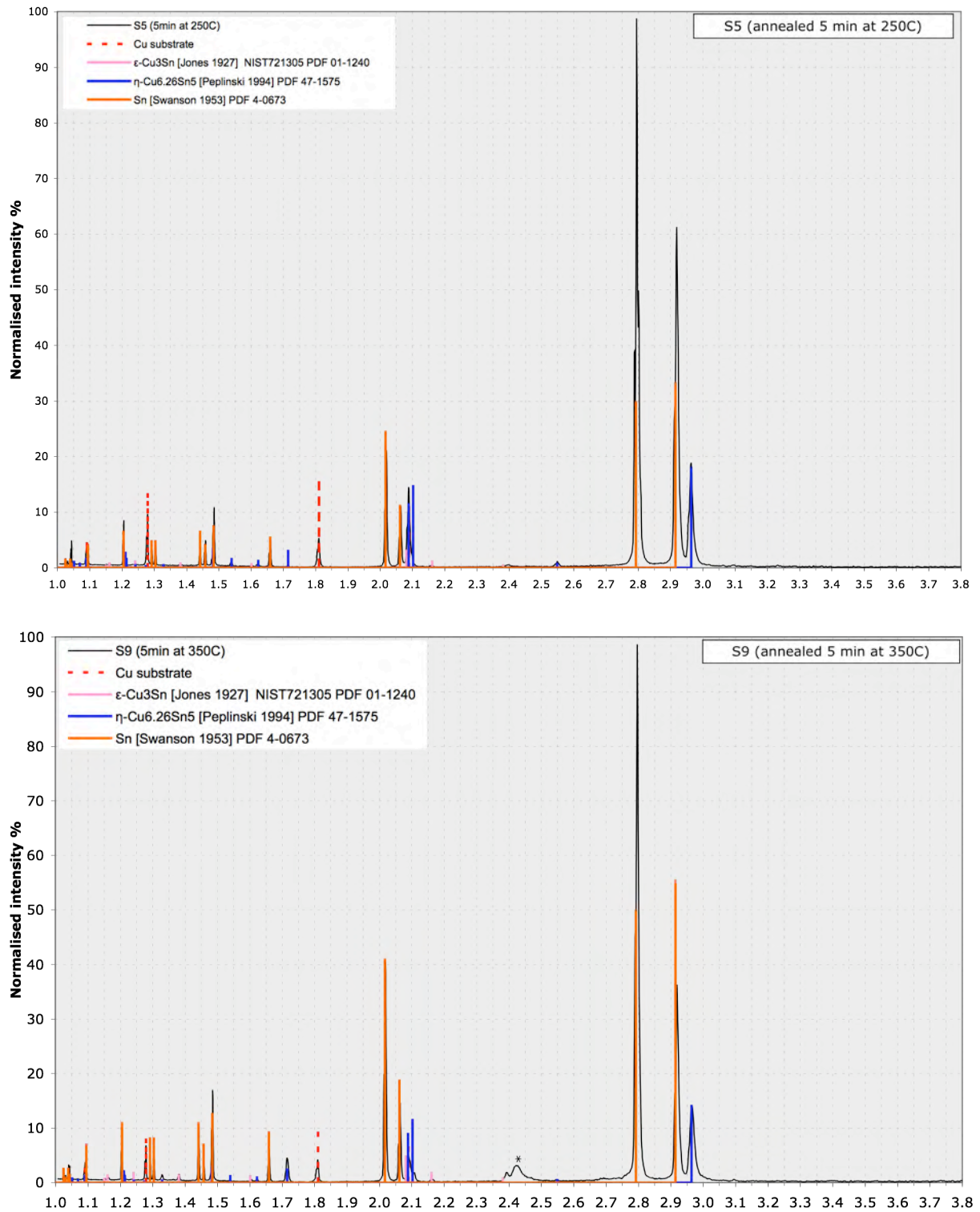


Figure 4.11: X-ray diffractograms of S5 and S9 in d-spacing Å, with assigned reference phases scaled to provide a rough guide of amounts present. Normalised 100% intensity. Sn is the main component with some η -Cu₆Sn₅.

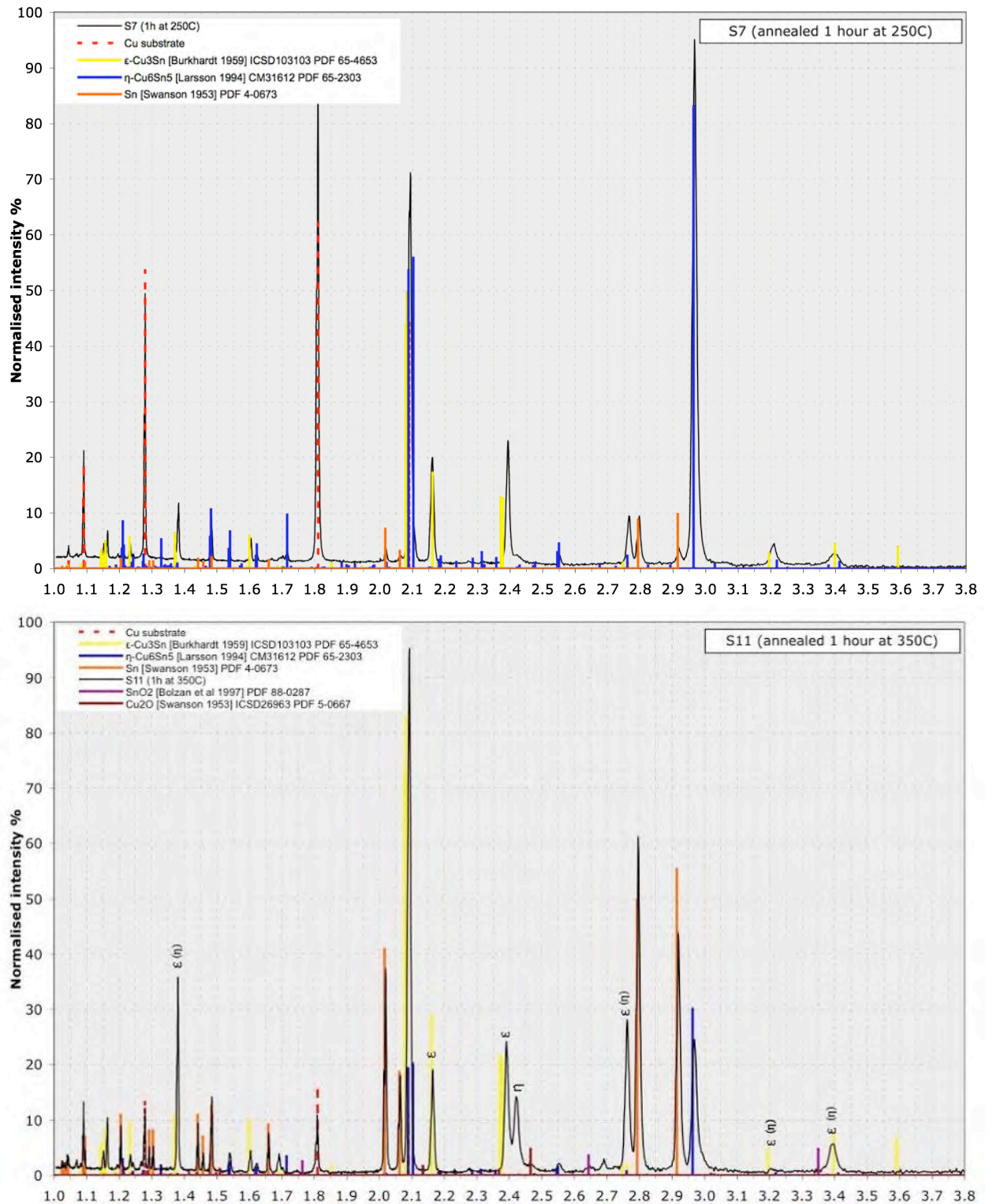


Figure 4.12: X-ray diffractograms of S7 and S11 tinned tokens in d-spacing Å. Reference structures are scaled to give an indication of relative amounts of each phase. Normalised intensity 100%. The diffraction patterns fit Larsson's η -Cu₆Sn₅ and Burkhardt's ϵ -Cu₃Sn. S7 has more η -Cu₆Sn₅ than S11 observed by the intensity of the line at 2.96 Å. Texture of η -Cu₆Sn₅ is evident by changes in the 2.42/2.96Å between the samples.

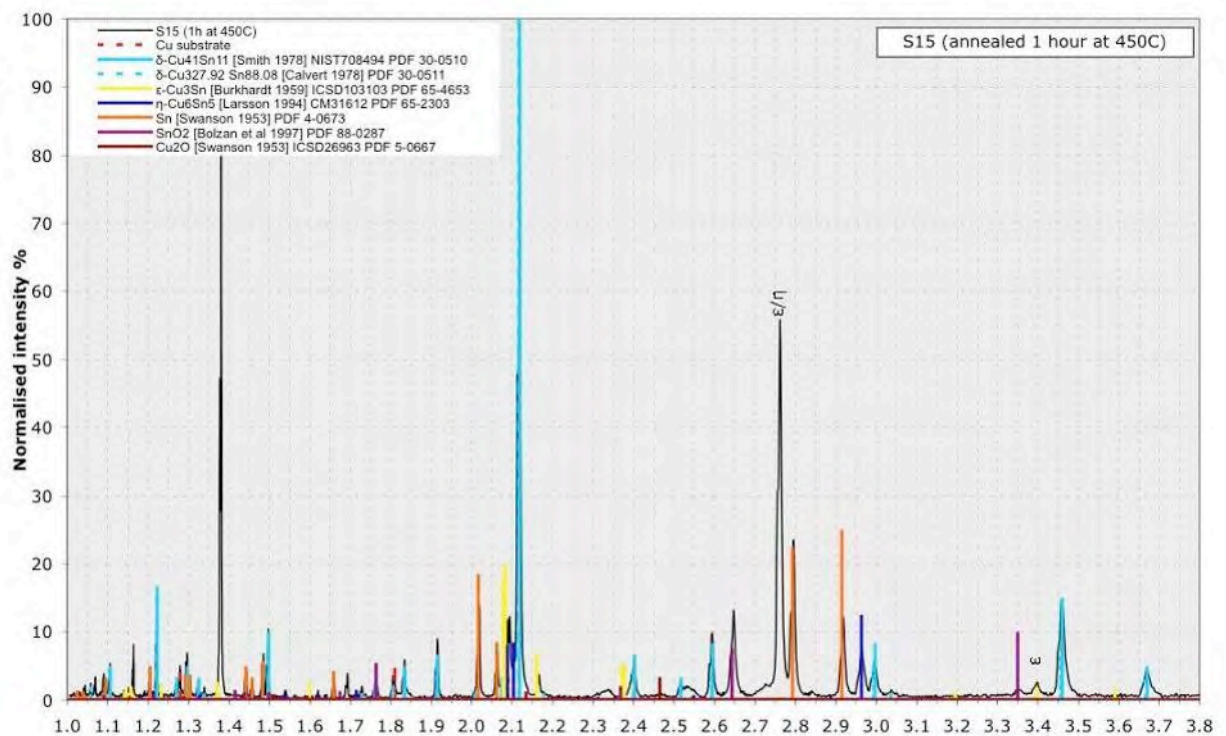
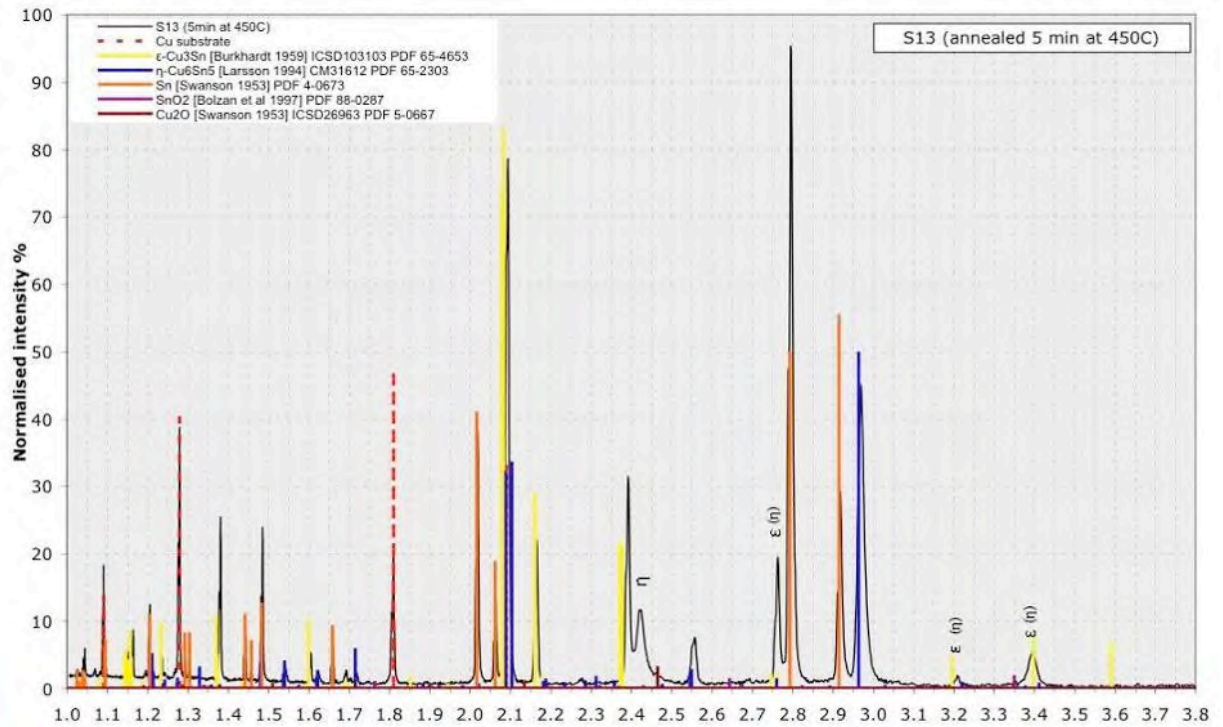


Figure 4.13: X-ray diffractograms of S13 and S15 tinned tokens in d-spacing Å. Reference structures are scaled to give an indication of relative amounts of each phase. Normalised intensity 100%. Sn is less in S15 than in S13. The unusually intense diffraction line at 1.38Å may be due to extreme crystallite preferred orientation in ϵ -Cu₃Sn.

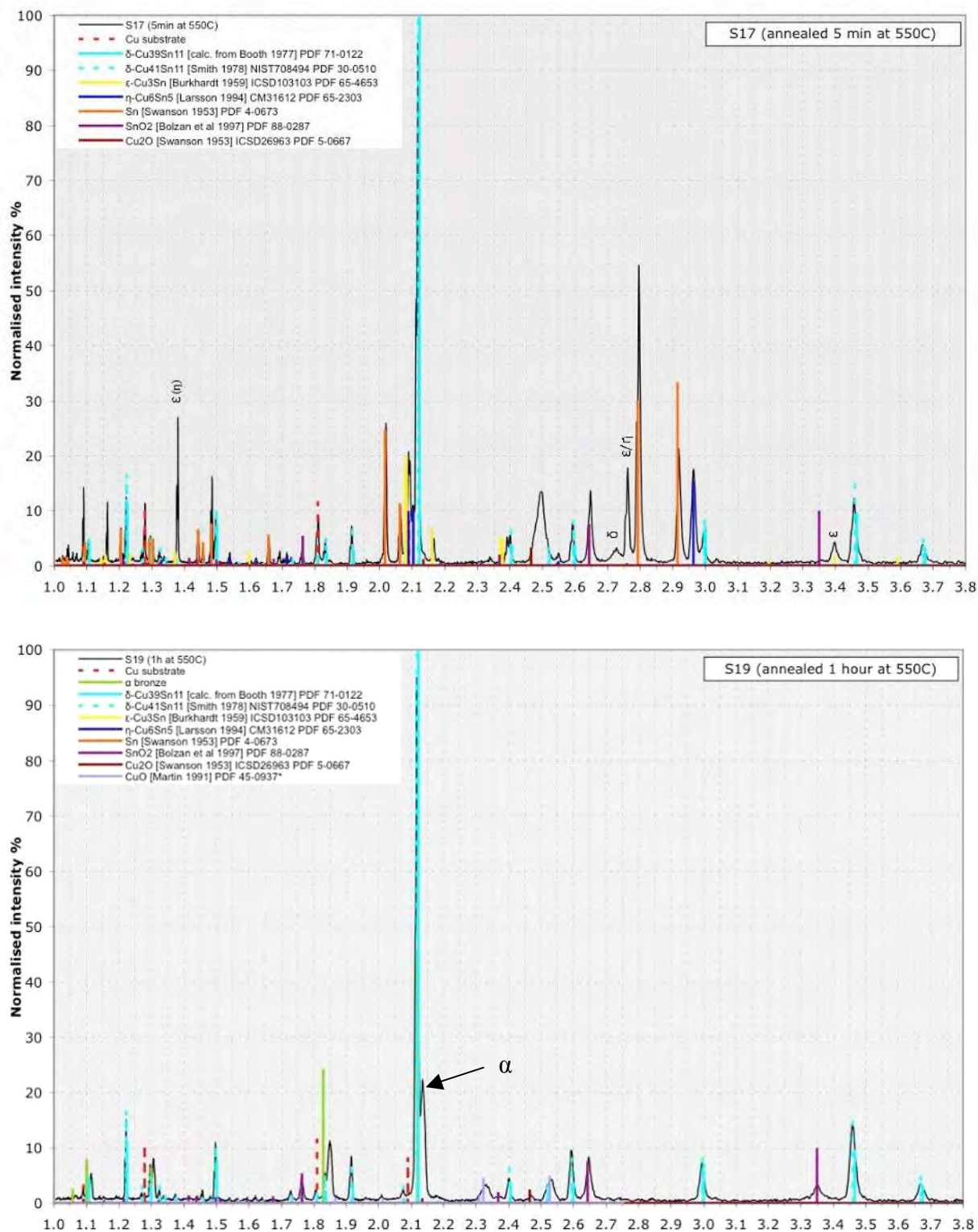


Figure 4.14: X-ray diffractograms of S17 and S19 tinned tokens in d-spacing Å. Reference structures are scaled to give an indication of relative amounts of each phase. Normalised intensity 100%. S17 shows diffraction lines from δ -Cu₄₁Sn₁₁, Sn, η -Cu₆Sn₅ and ϵ -Cu₃Sn. δ -Cu₄₁Sn₁₁ is the main phase in S19, which includes some α -bronze, a small amount of SnO₂ and perhaps a tiny concentration of ϵ -Cu₃Sn.

4.3.1.2. Wipe-tinned bronze tokens

XRD of tinned c. 10wt% bronze tokens was undertaken for B6 (1h at 250°C), B7 (1h at 350°C), B8 (1h at 450°C), and B9 (1 h at 550°C), which were annealed at the same annealing conditions to tokens S7, S11, S15 and S19 respectively. The substrate shows α -bronze diffraction lines, which are slightly shifted from those of copper due to the tin component in the bronze (Figure 4.15).

The XRD pattern of **B6** shows that the surface includes a substantial amount of η -Cu₆Sn₅, ϵ -Cu₃Sn, Sn and diffraction lines from the bronze substrate (Figure 4.16). The intensity of diffraction lines at 2.16 and 2.39Å and 1.38Å indicates a smaller concentration of ϵ -Cu₃Sn compared to its annealing equivalent **S7** (Table 4.4). This broadly agrees with BSE observations but Sn is not visible in BSE images of B6, which is present in the larger surface area analysed by XRD (Figure 4.7). **B7** includes ϵ -Cu₃Sn, Sn and η -Cu₆Sn₅ (Figure 4.17). The intensity of diffraction lines at 1.38, 2.78 and 3.39Å, which were seen to increase also in **S11**, is less in the case of B8 indicating that ϵ -Cu₃Sn shows some preferred orientation but perhaps to a lesser extent. BSE of B7 shows that ϵ -Cu₃Sn starts mimicking the granular nature of its overlying η -Cu₆Sn₅ (Figure 4.7). **B8** includes diffraction lines from ϵ -Cu₃Sn, Sn and η -Cu₆Sn₅ and oxides including Cu₂O and SnO (Figure 4.18). The intensity of lines at 1.38, 2.78Å is higher than B7, which is in agreement with BSE observations that show a thicker layer of this phase (Figure 4.7). δ -Cu₄₁Sn₁₁ is absent from the diffraction pattern of B8 in contrast to its annealing corresponding **S15** (Figure 4.13) but it is clearly present in **B9** (Figure 4.19), also seen in BSE as a $\alpha + \delta$ eutectoid structure (Figure 4.7). This is in addition to ϵ -Cu₃Sn and an increased concentration of oxides; some Sn is present, but the presence of η -Cu₆Sn₅ cannot be confirmed. The intensity of the major α -bronze diffraction line is increased. α -bronze was seen in its annealing equivalent **S19** (Figure 4.14), but its presence on B9 cannot be confirmed due to diffraction lines from the underlying bronze, which are in a similar d-spacing position.

Overall, XRD and BSE of annealed tinned bronzes show that the phases that grow during annealing occur at similar annealing temperatures as that of the tinned copper, with the exception of δ -Cu₄₁Sn₁₁ which seems to be forming at higher temperature in bronze compared to copper substrates. BSE showed that η -Cu₆Sn₅ and ϵ -Cu₃Sn exhibit broadly similar growth at low annealing temperature in bronze and in copper tinned samples. ϵ -Cu₃Sn grows into a thicker, more uniform layer in the bronze compared to copper samples in higher annealing temperatures. The intensity ratio of diffraction lines from both IMCs deviates from reference patterns in both substrates indicating texture, which seems to be less in bronze substrates and is in agreement with BSE imaging data.

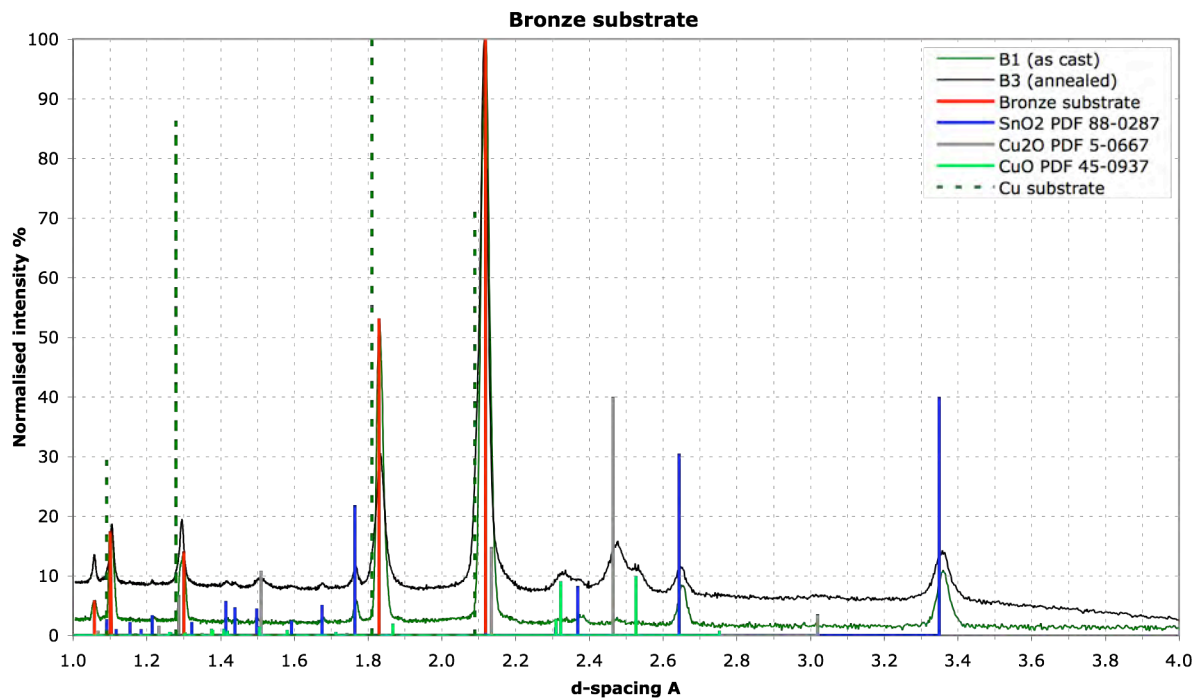


Figure 4.15: XRD diffractogram of the c. 10wt% bronze substrate used in the tinning experiment. As-cast and after annealing for 6 hours at 500°C prior to tinning. A shift in the d-spacing from the Cu values (e.g. at from 2.09 to 2.12Å) is due to the Sn content in the phase. Some other diffraction lines are from SnO₂, Cu₂O and CuO which were removed from the surface before tinning.

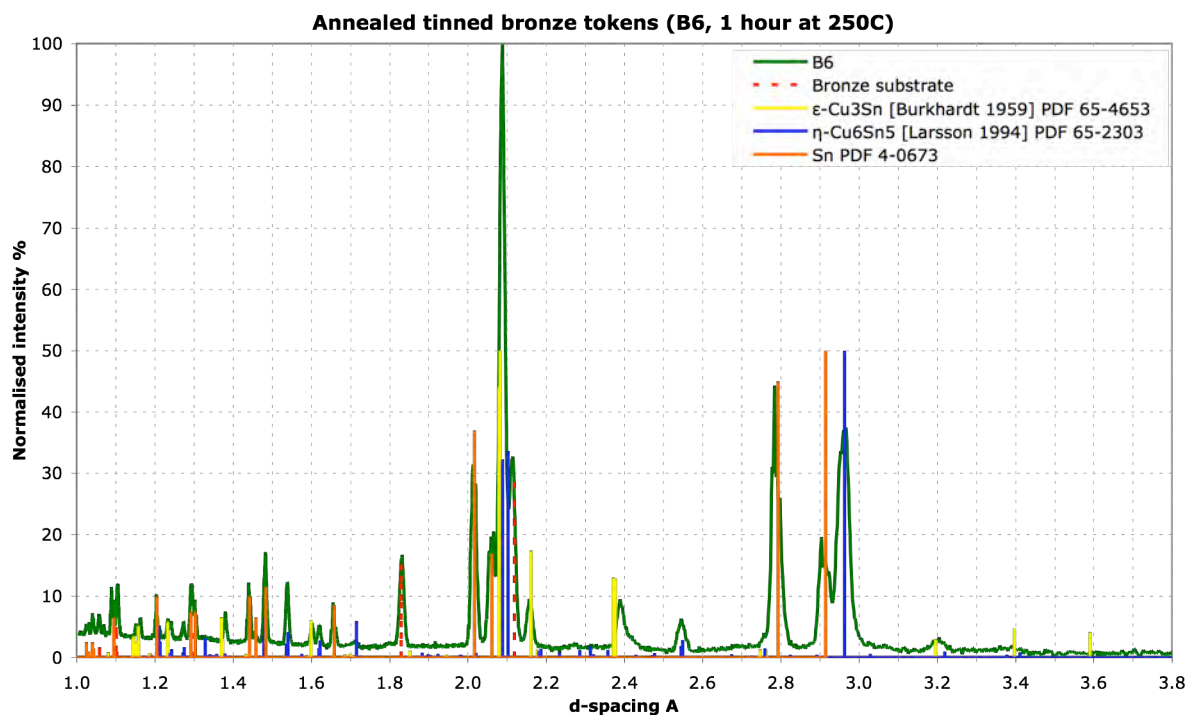


Figure 4.16: XRD pattern of B6 showing diffraction lines from Sn, η -Cu₆Sn₅ the substrate, and ϵ -Cu₃Sn.

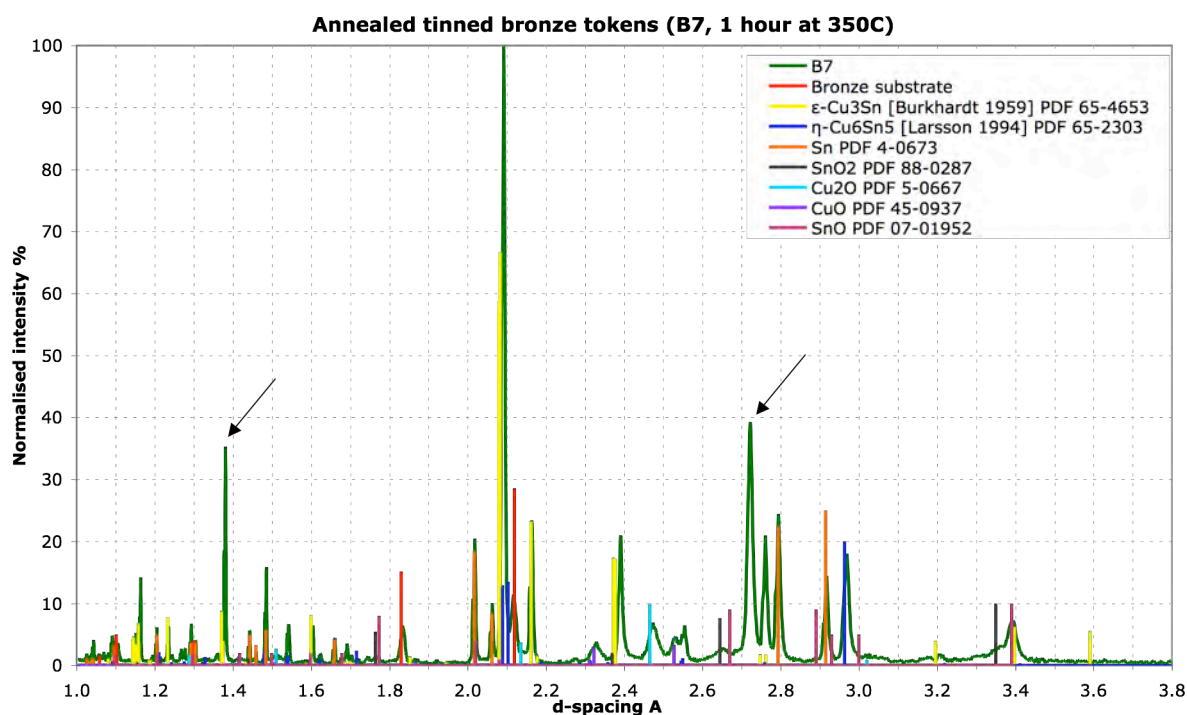


Figure 4.17: XRD pattern of B7 showing diffraction lines from ϵ - Cu_3Sn , Sn, η - Cu_6Sn_5 and small amounts of oxides. Both IMCs are textured as seen by the intensity of diffraction lines at 1.38 and 2.78 Å.

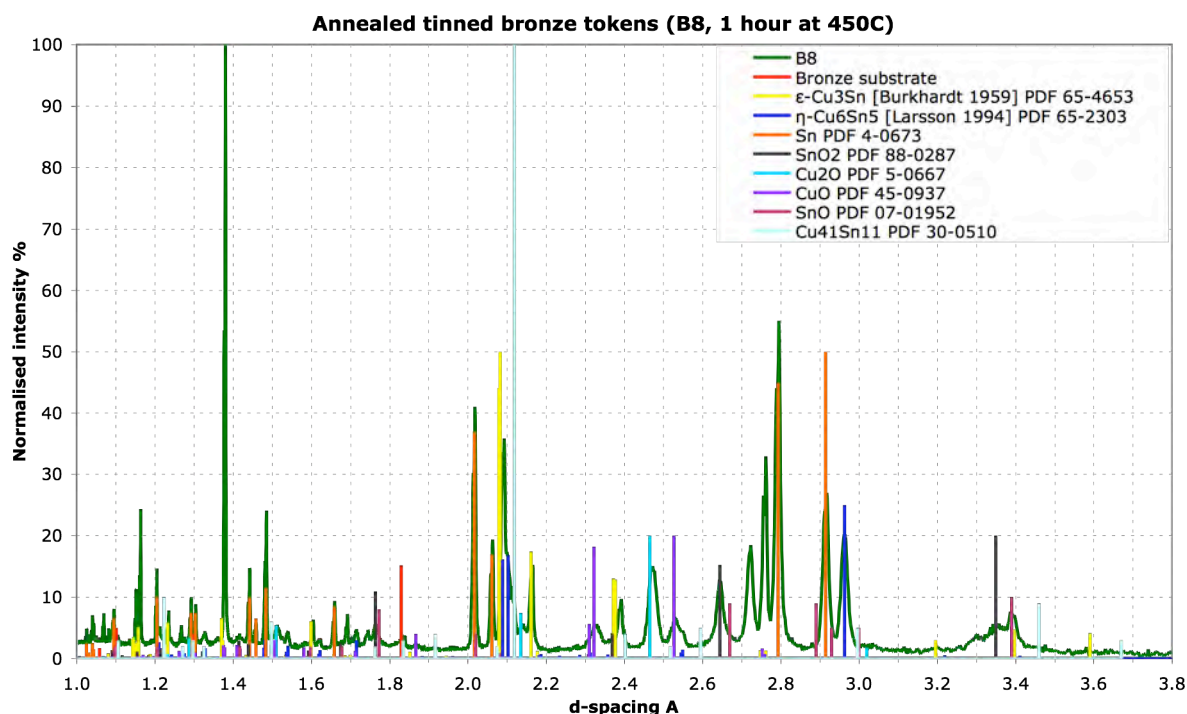


Figure 4.18: XRD pattern of B8 showing Bragg reflections from ϵ - Cu_3Sn , Sn and η - Cu_6Sn_5 and oxides including Cu_2O and SnO. δ - $\text{Cu}_{41}\text{Sn}_{11}$ is absent.

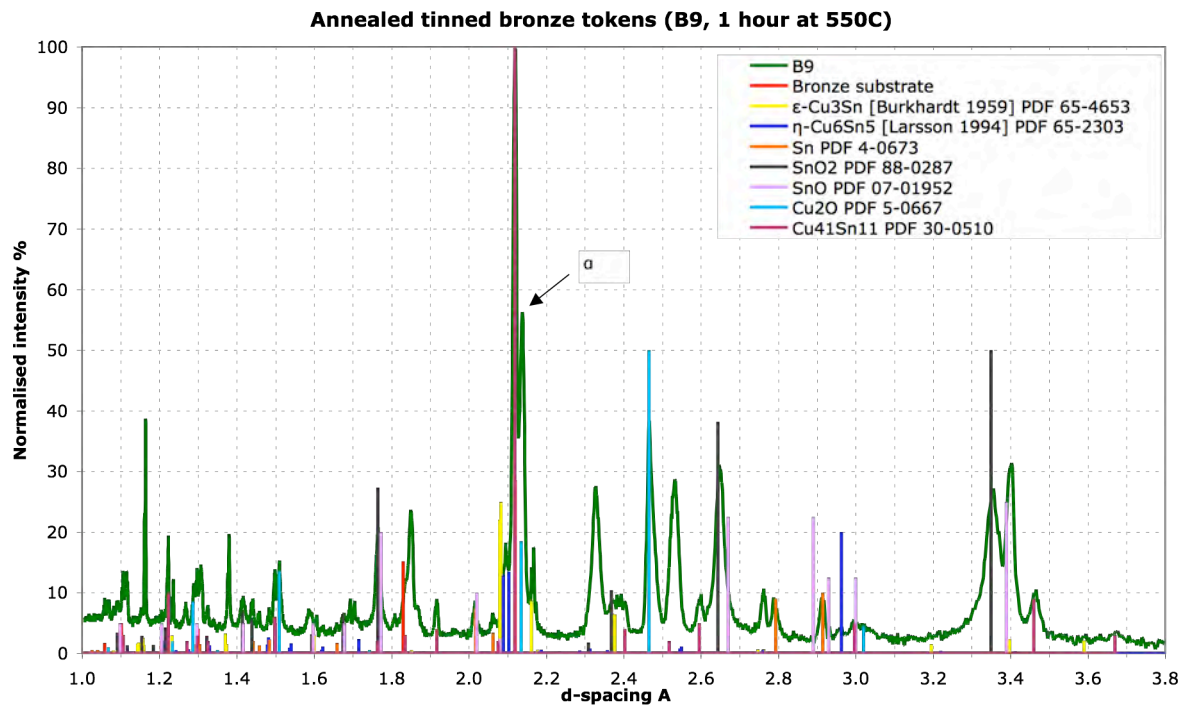


Figure 4.19: XRD pattern of B9 showing of δ -Cu₄₁Sn₁₁, ϵ -Cu₃Sn and increased concentration of oxides. Some Sn is present, but α and η -Cu₆Sn₅ cannot be confirmed.

4.3.2. TIME OF FLIGHT NEUTRON DIFFRACTION

Two sets of copper tinned tokens were analysed using time-of-flight neutron diffraction (**Error! Reference source not found.**): (a) as-tinned and annealed copper tokens tinned by the wiping method which were examined by BSE and XRD reported above, and (b) a series of as-tinned and annealed tokens tinned by the dipping method which produced thicker metal coatings (section 3.7). As neutron diffraction is a bulk analyses method, because information derives from the bulk volume rather than the surface of a sample in the beam path, there was a concern that the concentration volume of diffracting IMCs in the wipe-tinned tokens may be too small for the method to detect. The double-sided and increased metal coating thickness in dip-tinned tokens offered an opportunity to analyse sample volumes with higher IMC concentrations to assess the efficacy of the method. Rietveld analysis of the diffraction data could provide quantitative information of IMC concentrations to aid this task and preliminary results are reported below. The incident neutron beam size was in the range of 15x25mm; experimental details are in section 3.8.2.1.

The ROTAX and GEM diffractometers used have the ability to investigate crystal preferred orientation (texture) (section 3.8.1) and could validate the texture shown by XRD in Sn and

the IMC phases in the tokens which could influence the quality of the interpretation of XRD results overall. This is achieved by comparing the intensity of specific diffraction lines in data collected from different detector banks because the detectors are positioned at different fixed scattering angles with regards to the orientation of the diffracting volume in an object (Figure 3.5). Examination of neutron diffraction patterns of S15 shows that the ε -Cu₃Sn diffraction line at 2.39Å is present in GEM-bank 5 but is absent in data collected from GEM-bank 4, which is evidence of crystallite preferred orientation in this phase (Figure 4.20). XRD data from this sample showed a dramatic change in the intensity ratios of ε -Cu₃Sn diffraction lines, which validates the XRD analyses. A simple comparison of diffraction patterns does not constitute a full texture analysis in terms of pole figure determination which can be done with GEM data, but offers a good indication of the degree of texture in this phase.

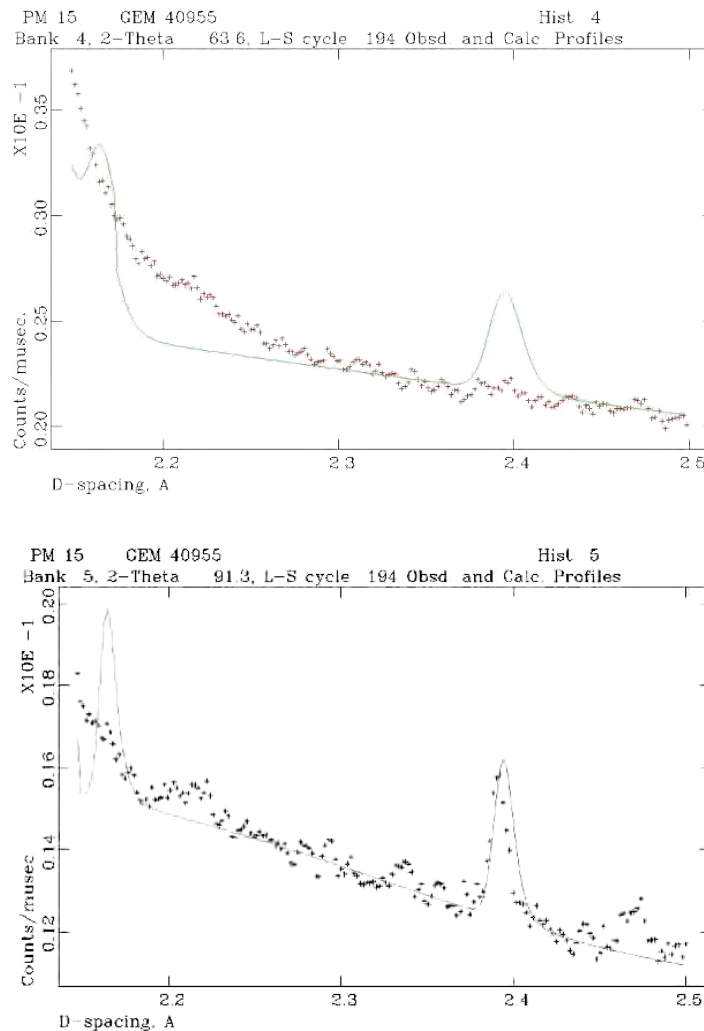


Figure 4.20: Neutron diffraction patterns of S15 collected by GEM detector banks 4 (top) and 5 (bottom), which are positioned at different fixed 2θ angles. The 2.39Å is present in diffraction data from bank 5 but is absent in bank 4, indicating crystallite preferred orientation. The line represents reference data for ε -Cu₃Sn.

Neutron diffraction patterns of analysed tokens are recorded in Figures 4.23 to 4.28 and details of annealing conditions are in (Table 3.8). The normalised intensity of the diffraction lines from IMCs is much smaller (1-2%) compared to Cu reflections deriving from the substrate, and compared to the XRD patterns of the same tokens. This is because neutrons scattered from the tokens travelled a way through the copper substrate before detection. The low intensity of IMCs influences qualitative interpretation of the diffraction patterns.

Diffraction patterns of **S1** and **S5** collected from ROTAX-bank 3 show mainly reflections from Sn (Figure 4.21). The indicative η -Cu₆Sn₅ peak at 2.96Å (PDF65-2303) is absent or hindered by the relatively high noise at this end of the pattern. A small peak may be present at 1.71Å but the evidence is not definitive. Data from the same tokens and **S9** from GEM-bank 5 (Figure 4.22) equally show the presence of Sn. Because data from GEM bank 5 are recorded up to 2.5Å, the major η -Cu₆Sn₅ peak at 2.96Å is absent and η -Cu₆Sn₅ cannot be confirmed on these tokens. Figure 4.23 shows data of **S7** and **S11** collected at GEM-bank 5. S7 includes clear reflections from ϵ -Cu₃Sn and a small amount of Sn. The intensity ϵ -Cu₃Sn peaks in S7 is higher than in S11. The presence of η -Cu₆Sn₅ could perhaps be indicated by peaks at 1.72 and 1.98Å including those annotated in Figure 4.23. Reflections from ϵ -Cu₃Sn are also visible in **S15**, which includes reflections from δ -Cu₄₁Sn₁₁ (Figure 4.24). δ -Cu₄₁Sn₁₁ is the dominant IMC phase in **S19** and includes some α solid solution phase (Figure 4.24), as revealed previously by XRD. The lattice parameter of this α -bronze is 3.69Å, which corresponds to a concentration of approximately 13wt% Sn as estimated by comparison to laboratory α -bronze standards.

Figure 4.25 and Figure 4.26 show diffraction patterns of dip-tinned copper samples compared with wipe-tinned copper tokens reported above. The increased thickness of dip-tinned samples resulted in higher intensity reflections from Sn, ϵ -Cu₃Sn and δ -Cu₄₁Sn₁₁ making easier assignment of phases to individual major reflections. Assigned peaks are annotated on the diffraction patterns (Figure 4.25, Figure 4.26). Despite the higher intensity of phases in the diffraction patterns of the dip-tinned tokens, which resulted in unambiguous identification of Sn, ϵ -Cu₃Sn, δ -Cu₄₀Sn₁₁ and α -bronze, the lack of evidence for the presence of η -Cu₆Sn₅ on samples which are previously shown to have a substantial η -Cu₆Sn₅ content is surprising.

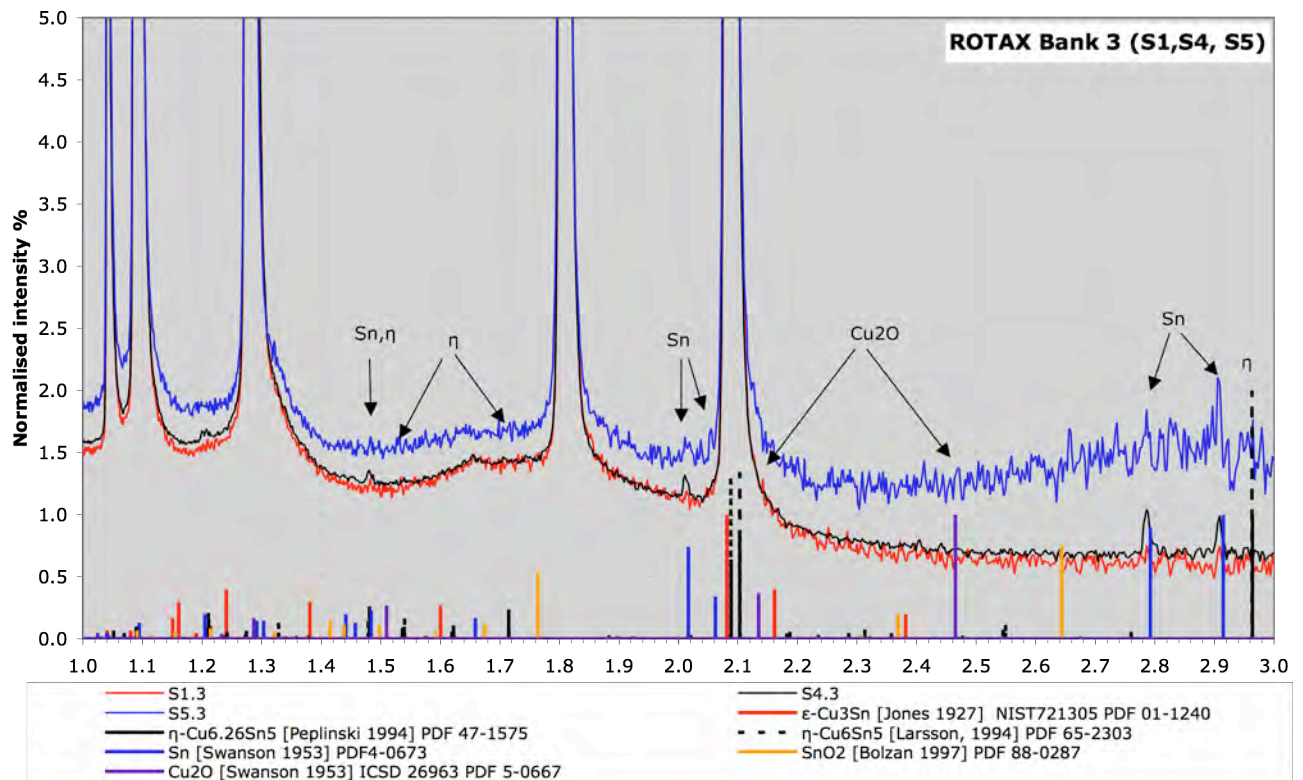


Figure 4.21: Diffraction patterns of S1, S4 and S5 of data collected at ROTAX bank 3.

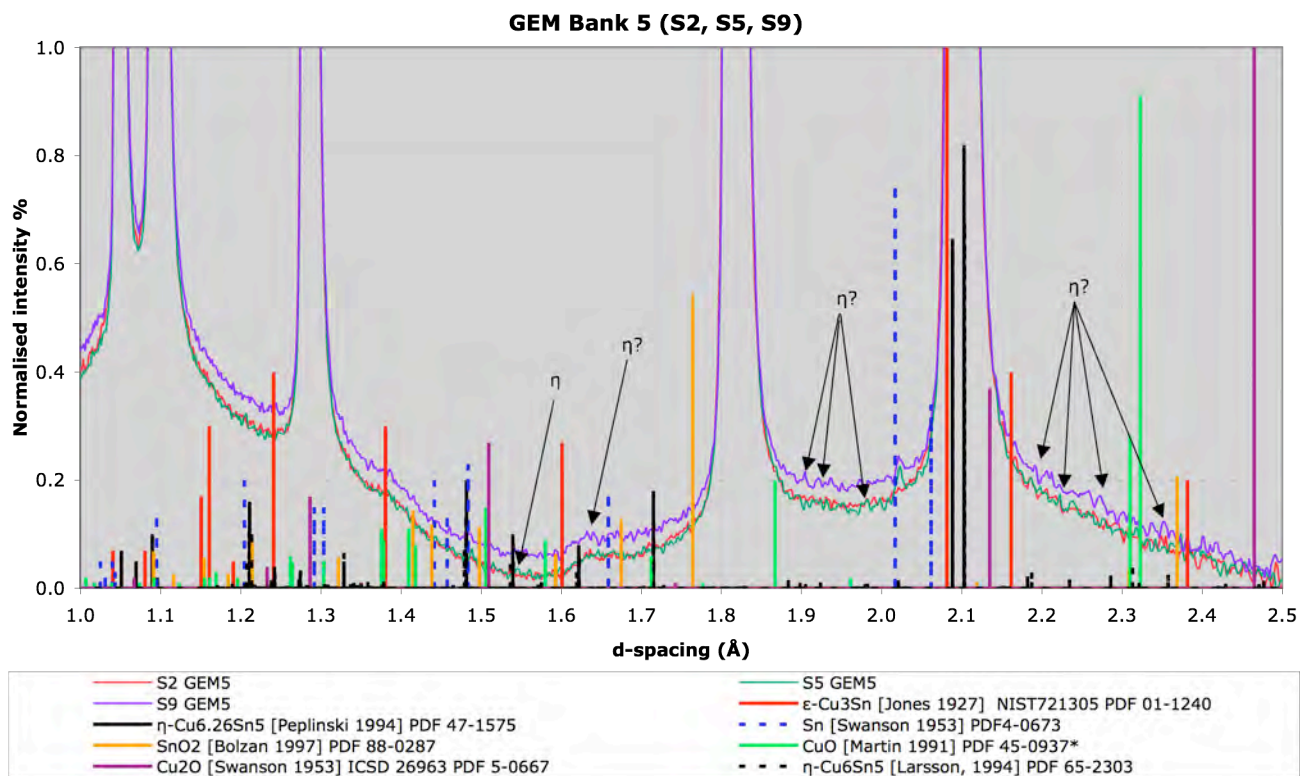


Figure 4.22: Diffraction patterns of S2, S5, S9 of data collected from GEM bank 5.

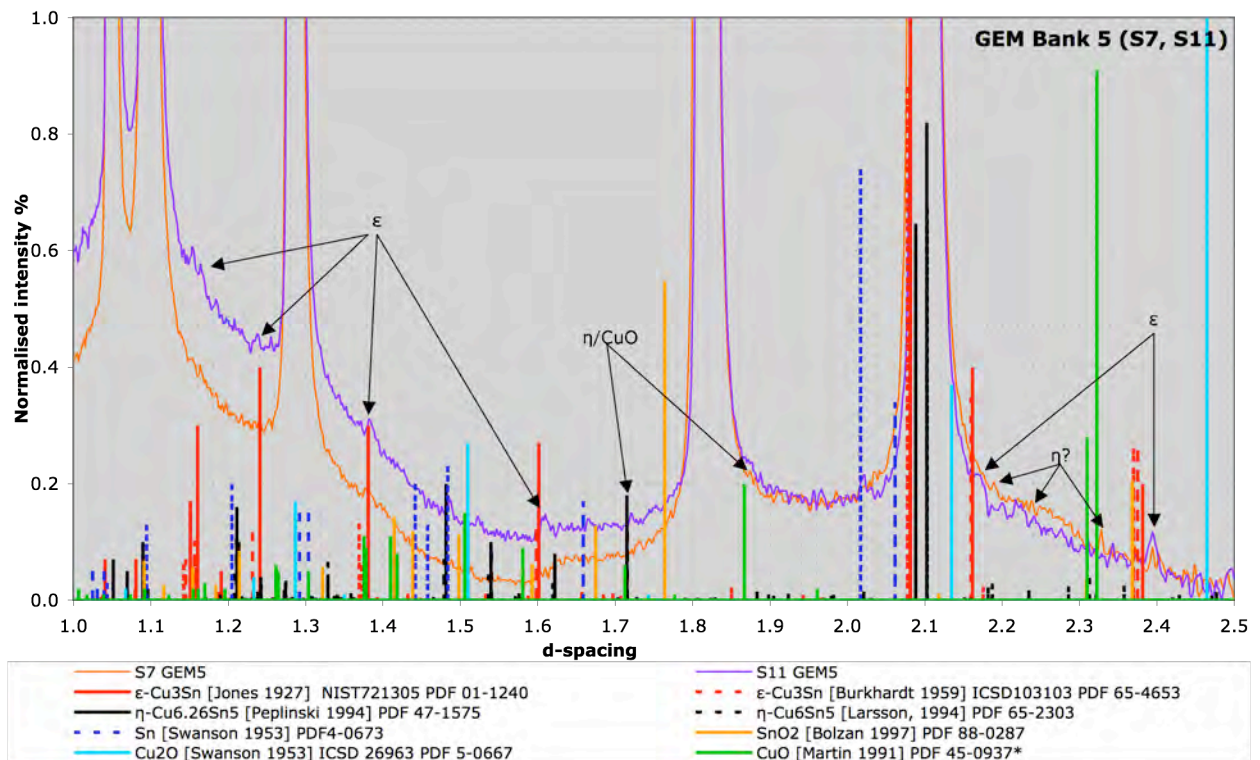


Figure 4.23: Diffraction patterns of S7 and S11 of data collected at GEM-bank 5.

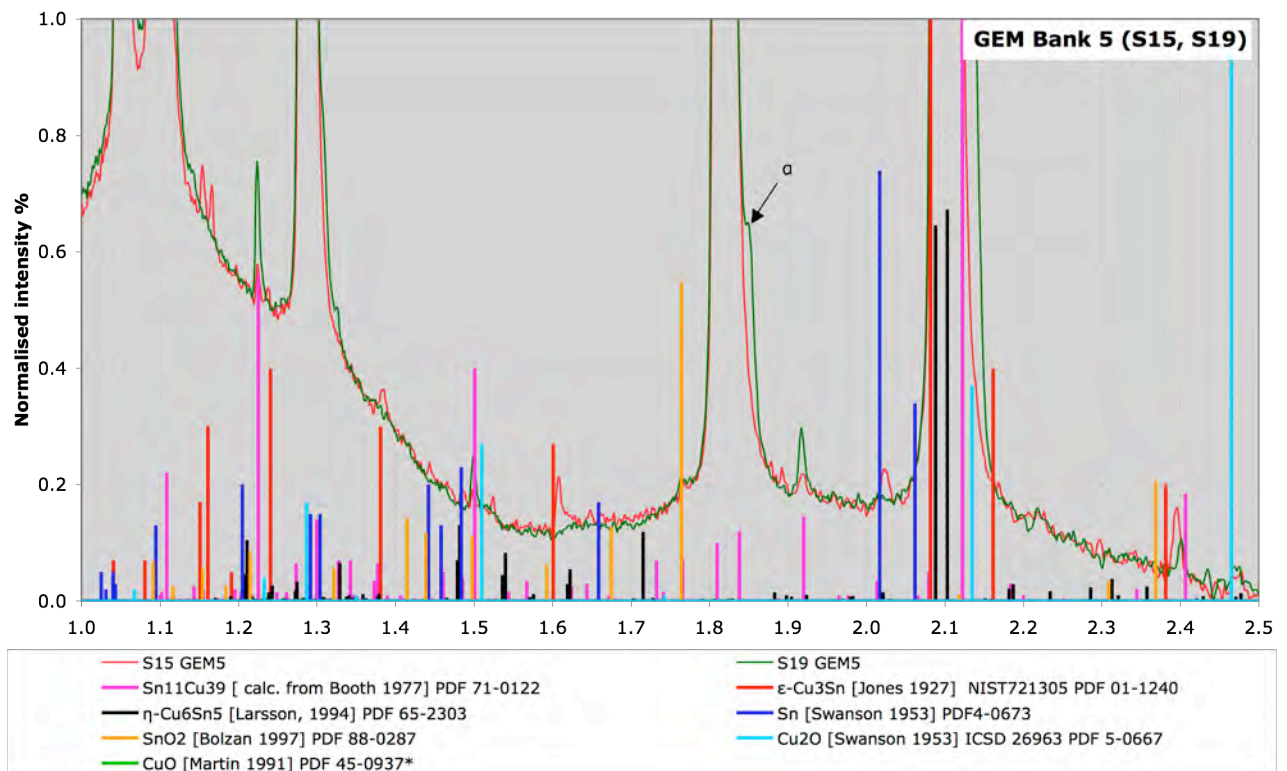


Figure 4.24: Diffraction patterns of S15 and S19 of data collected from GEM-bank 5.

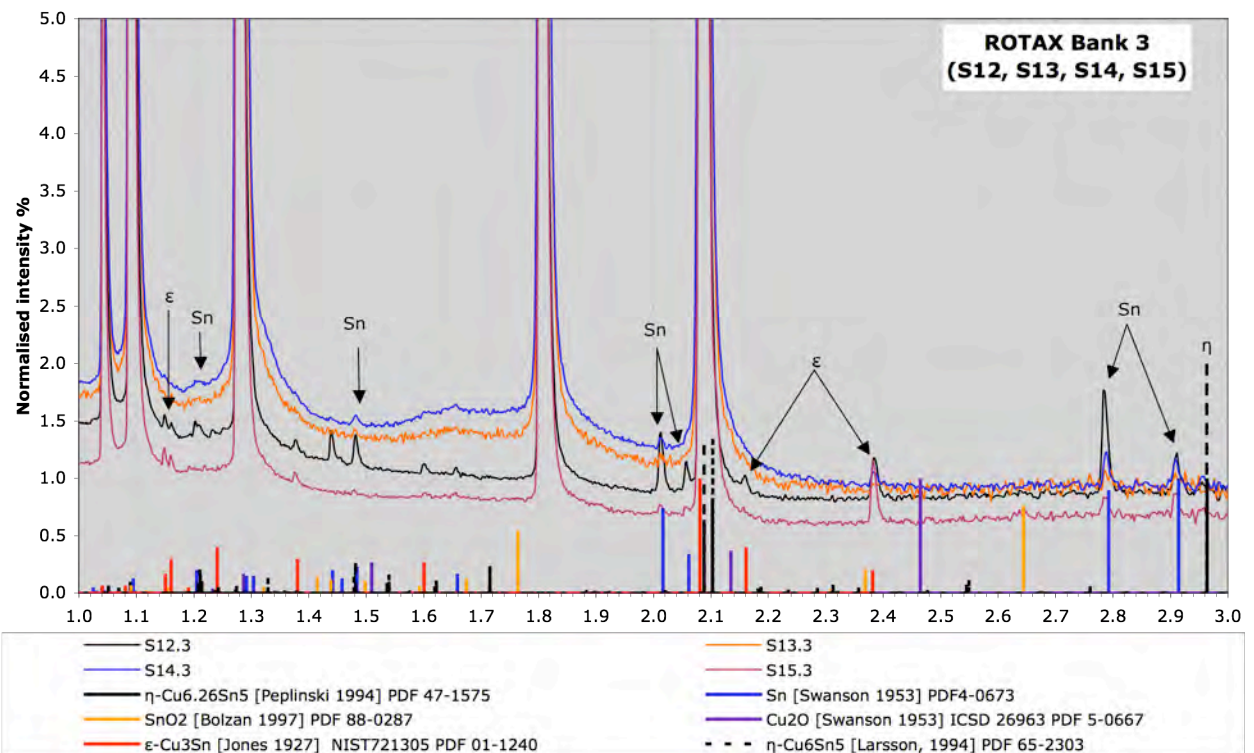


Figure 4.25: Diffraction patterns of S12, S13, S14 and S15 of data collected from ROTAX-bank 3.

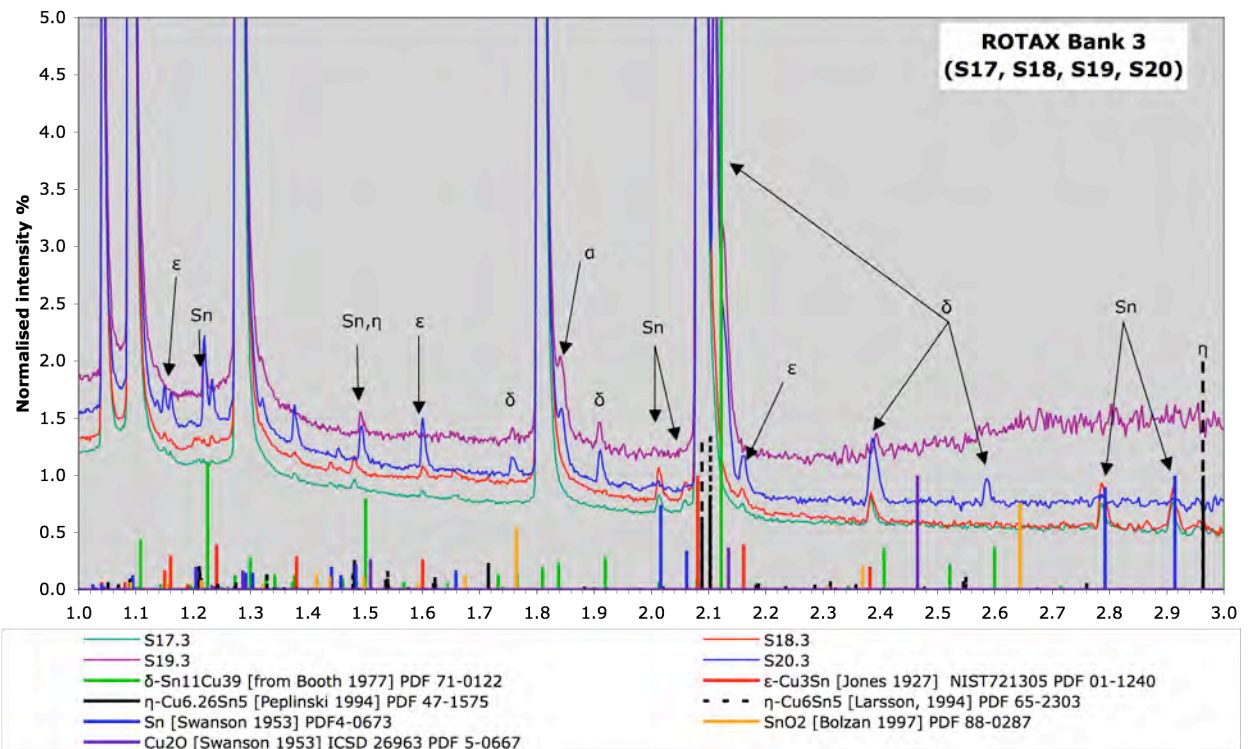


Figure 4.26: Diffraction patterns of S17, S18, S19 and S20 of data collected from ROTAX-bank 3.

Data were scrutinised using GSAS Rietveld phase composition analysis to validate qualitative interpretation of the diffraction patterns, investigate the presence of η -Cu₆Sn₅ and provide an indication of the relative concentration of phases. This was performed by averaging data collected from several banks of GEM and from ROTAX bank 3 and using published crystal structure models (η -Cu₆Sn₅ ICSD 158248, ϵ -Cu₃Sn ICSD 1-3102, PDF65-5721, δ -Cu₄₀Sn₁₁ CRYSTMET AL4034, ICSD 800). Data collected at GEM are more reliable due to the large number of detectors surrounding the sample considerably reducing texture effects and providing lower detection limits due to its higher resolution and count rates. Texture effects were taken into account during GSAS analyses of data from ROTAX-bank 3. Results are in Table 4.5.

wipe-tinned copper	Sample	S1	S3	S5	S7	S9	S11	S13	S15	S17	S19
	Phase	As tinned	As tinned	250°C 5 min	250°C 60 min	350°C 5 min	350°C 60 min	450°C 5 min	450°C 60 min	550°C 5 min	550°C 60 min
ROTAX wt% semi-quantitative	Sn	n.d.	1.20	n.d.	n.d.	-	-	0.50	0.60	1.70	n.d.
	η -Cu ₆ Sn ₅	n.d.	n.d.	n.d.	n.d.	-	-	n.d.	n.d.	n.d.	n.d.
	ϵ -Cu ₃ Sn	n.d.	n.d.	n.d.	0.20	-	-	0.20	1.00	1.20	0.40
	δ -Cu ₄₁ Sn ₁₁	n.d.	n.d.	n.d.	n.d.	-	-	n.d.	n.d.	n.d.	2.20
	α -CuSn	n.d.	n.d.	n.d.	n.d.	-	-	n.d.	n.d.	n.d.	1.00
dip-tinned copper	Sample	-	S4	-	-	S10	S12	S14	S16	-	S20
	Phase	As tinned	As tinned	250°C 5 min	250°C 60 min	350°C 5 min	350°C 60 min	450°C 5 min	450°C 60 min	550°C 5 min	550°C 60 min
ROTAX wt% semi-quantitative	Sn	-	0.70	-	-	0.10	3.60	0.60	2.00	-	n.d.
	η -Cu ₆ Sn ₅	-	n.d.	-	-	n.d.	n.d.	n.d.	n.d.	-	n.d.
	ϵ -Cu ₃ Sn	-	n.d.	-	-	n.d.	2.20	0.50	1.00	-	4.00
	δ -Cu ₄₁ Sn ₁₁	-	n.d.	-	-	n.d.	n.d.	n.d.	n.d.	-	6.00
	α -CuSn	-	n.d.	-	-	n.d.	n.d.	n.d.	n.d.	-	1.00
wipe-tinned copper	Sample	S1	S3	S5	S7	S9	S11	S13	S15	S17	S19
	Phase	As tinned	As tinned	250°C 5 min	250°C 60 min	350°C 5 min	350°C 60 min	450°C 5 min	450°C 60 min	550°C 5 min	550°C 60 min
GEM wt% quantitative	Sn	-	-	0.39	n.d.	weak	0.01	-	0.36	-	n.d.
	η -Cu ₆ Sn ₅	-	-	n.d.	n.d.	n.d.	n.d.	-	n.d.	-	n.d.
	ϵ -Cu ₃ Sn	-	-	n.d.	n.d.	n.d.	0.60	-	0.93	-	<0.5
	δ -Cu ₄₁ Sn ₁₁	-	-	n.d.	n.d.	n.d.	n.d.	-	n.d.	-	1.30
	α -CuSn	-	-	n.d.	n.d.	n.d.	n.d.	-	n.d.	-	0.58

Table 4.5: Semi-quantitative wt% phase composition analyses of tokens analysed at ROTAX-bank 3 and quantitative wt% phase composition analysis of tokens analysed at GEM. The remaining wt% composition is copper and trace amounts of oxides. The incident neutron beam size was c. 15x25mm and the thickness of the copper tokens 3.25mm. α -bronze observed on S19 is of c. 13wt% Sn.

GSAS analysis results show that both diffractometers have some ability to detect ϵ -Cu₃Sn to about 0.5 wt%, δ at c. 1 wt% and α -bronze at c. 0.5wt% fraction of the diffracting volume in tokens which appear to be at the limit of detection of these phases at GEM. Results show that ϵ -Cu₃Sn is present in S19, which was not definitive in XRD data due to the complexity of the XRD pattern due to the complex nature of the X-ray diffraction pattern. GSAS refinement did not reveal any η -Cu₆Sn₅ on any of the tokens confirming the qualitative assessment of the

neutron diffraction patterns. Its absence from the neutron diffraction patterns is surprising. This shows that the different IMC phases have very different volume detection limits for neutron diffraction and there is no obvious reason why this should be the case (Kockelmann, *pers. com.*). Understanding why η -Cu₆Sn₅ was not detected by neutron diffraction, despite being present in substantial quantities in several samples, requires further investigation and is beyond the scope of this thesis.

In summary, as η -Cu₆Sn₅ is the major phase on as-tinned copper and bronze tokens neutron diffraction method cannot effectively be used to identify tinning on archaeological bronzes. This inability of neutron diffraction to detect η -Cu₆Sn₅ must be contrasted with its increased sensitivity to detect small concentrations of ε -Cu₃Sn, δ and α -bronze by the high resolution diffractometer GEM, which may be present on archaeological tinned bronzes exposed to heat, depending on the thickness of the metal coating and its volume fraction on an object. Considering these limitations, neutron diffraction can be a useful non-destructive diffraction method for analysis of archaeological tinned bronzes. XRD shows advantage over neutron diffraction in this context of application.

4.4. INVESTIGATION OF ROMAN BRONZES

A major impediment to the identification of tinning on archaeological artefacts is likely to be the effect of corrosion of Cu-Sn phases and of the copper alloy substrates (section 2.2). This section reports analysis from a small number of selected Roman objects (Table 4.6, Figure 4.27), which were reported to be tinned due to their silver or silver/grey colour surface. This examines the nature of evidence for tinning on archaeological bronzes and compares this to the results from the tinning experiment. SEM-EDX from these surfaces in cross-sectioned samples will provide the bank of data used to investigate the helmets in the next chapter.

Code	Object	Excavation	Date	Museum	Samples
BG	Harness fitting	Brecon Gaer Roman fort (metal detected)	1-2 nd c. AD	National Museum of Wales	BG1 to BG2
MB	Skillet	Manorbier	1 st c. AD	National Museum of Wales	MB1 to MB3
CER	Skillet	Unknown	Roman	Ceredigion museum, Aberystwyth	CER1 to CER2
BOV	Decorated collar – sample from riveted plate	Boverton, Vale of Glamorgan	2 nd c. AD	National Museum of Wales 2007.19H/1	BOV

Table 4.6: List of Roman objects investigated.

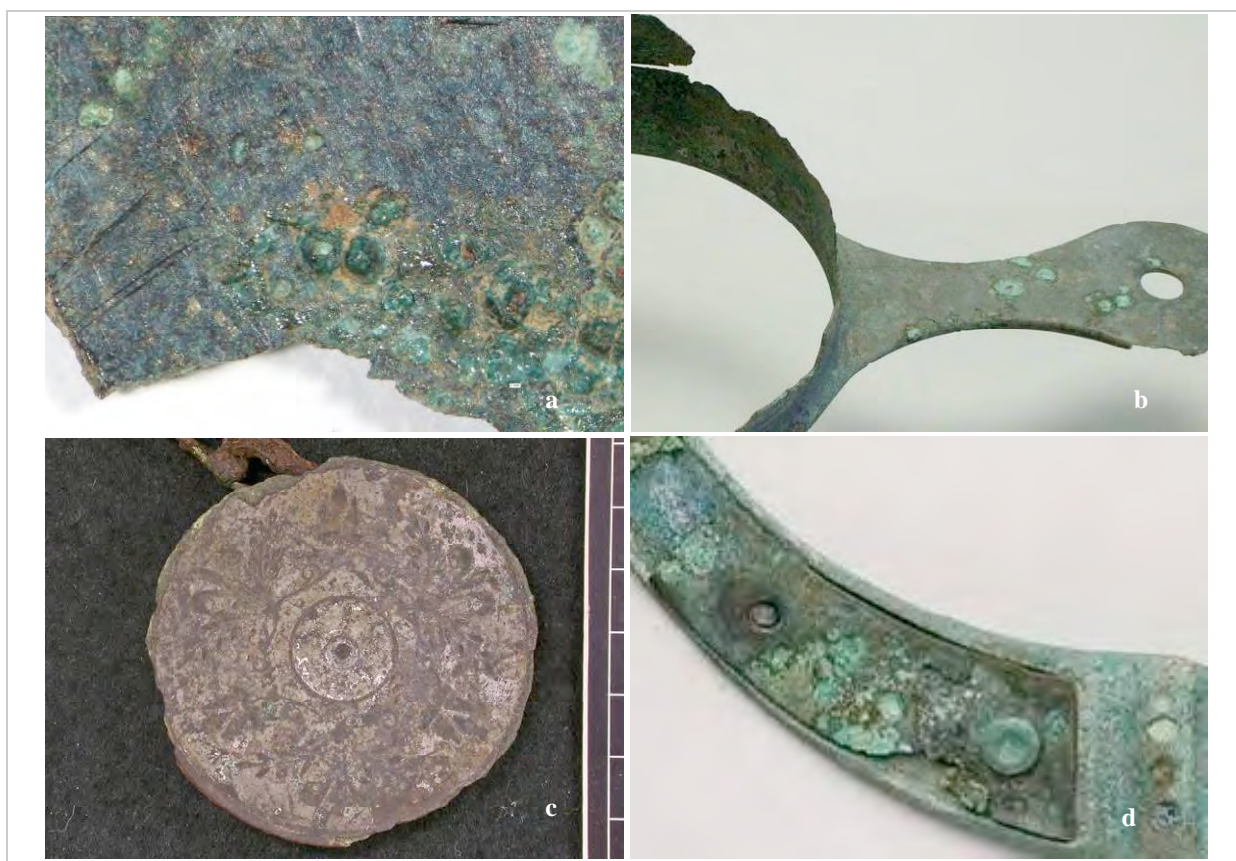


Figure 4.27: Roman objects investigated. (a) fragment from Manorbier skilnet (MB); (b) Ceredigion skilnet (CER); (c) Brecon Gear harness fitting (BG); (d) Boverton collar (BOV).

Examination of the manufacture of these objects was undertaken prior to investigating the presence of any $\eta\text{-Cu}_6\text{Sn}_5$ and $\varepsilon\text{-Cu}_3\text{Sn}$ as manufacture could influence interpretation of the results. The thicknesses of the rim, handle and the designs of the bases of the two skilnets (MB and CER) indicate that they were cast. Their bodies are significantly thinner than the rest of the object and the presence of uniform circular lines observed there indicate that the body of the skilnets was thinned by turning on a lathe (Craddock and Lang, 1983). This suggests that different areas of the skilnets have different work histories. Samples taken from the body of the Manorbier skilnet show slip lines present in recrystallised bronze grains (Figure 4.28, MB1) suggesting that several mechanical and annealing cycles took place leaving the item in the work-hardened state. Samples from the Ceredigion skilnet were removed from areas closer to the rim and base and exhibit a dendritic microstructure, the appearance of which is enhanced by corrosion of the α -bronze (Figure 4.28, CER1). Samples from both skilnets have small lead inclusions, which are relatively larger in the case of the Ceredigion skilnet.

The extremely thin low-tin bronze plate from the Boverton collar shows evidence of work hardening and extensive corrosion (Figure 4.28, BOV) and the sample from the surface of the Brecon Gear harness fitting (BG) has a corroded microstructure with lead inclusions and areas

of unusually shaped α -bronze. Thus, none of the samples is a high Sn bronze, which could include phases to influence interpretation of analysis.

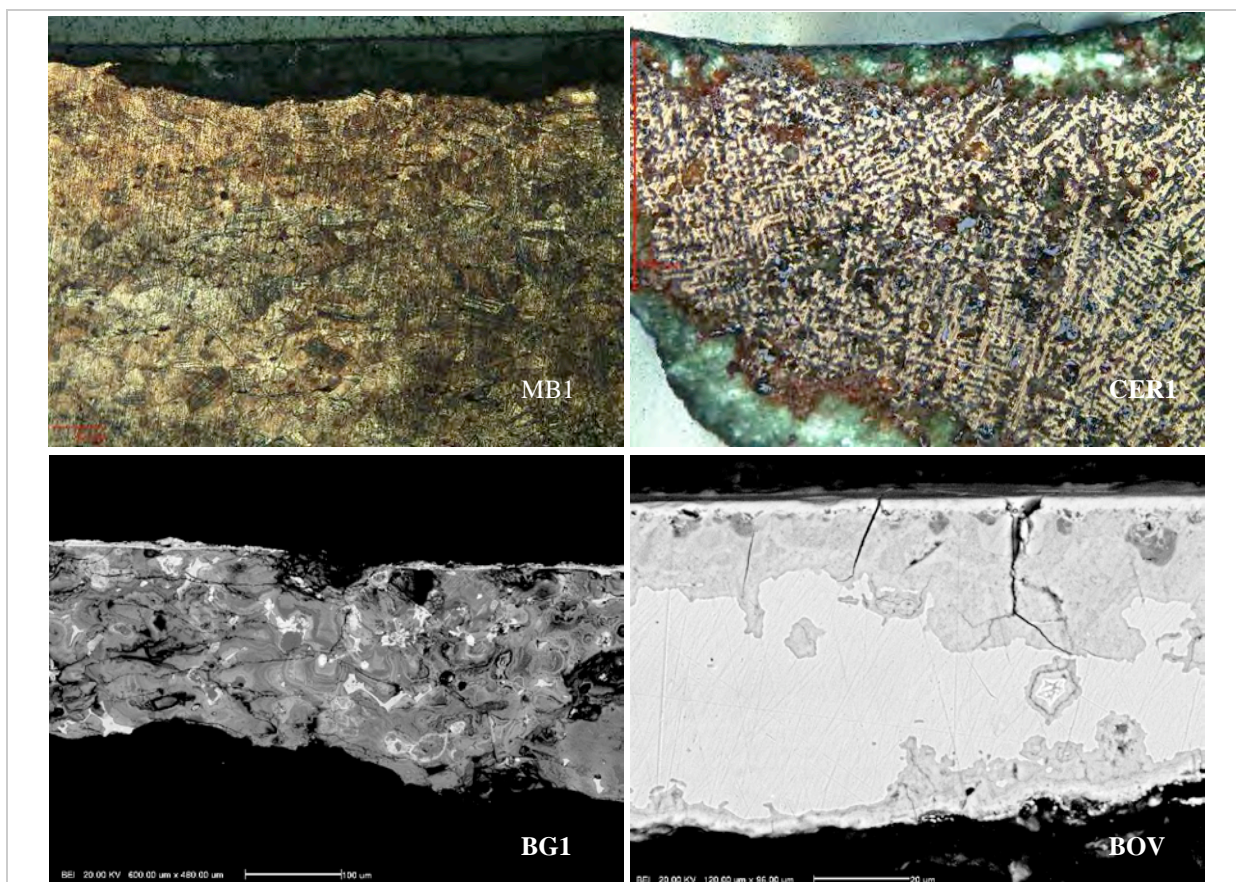


Figure 4.28: Micrographs of cross-sectioned samples showing evidence of manufacture. MB1 (skillet): annealed and work hardened microstructure. CER1 (skillet): corroded cast dendritic microstructure. BG1 (harness): corroded microstructure with lead inclusions and areas of unusually shaped α -bronze. BOV (collar): wrought microstructure. Samples are polished but not etched.

4.4.1. X-RAY DIFFRACTION ON THE SURFACE OF SAMPLES

X-ray diffraction was undertaken directly on the surface of small fragments from the Ceredigion skillet (CER1), the Manorbier skillet (MB1 to 3) and the Brecon Gaer harness fitting (BG1, BG2). Experimental details are in section 3.8.2.2. The XRD patterns of fragments from the BG harness fitting (Figure 4.29) and the Ceredigion skillet are dominated by the presence of η -Cu₆Sn₅. The diffraction lines seem to fit better Larsson's high temperature η -Cu₆Sn₅ structure (PDF 65-2303) similar to the annealed tinned tokens discussed in the previous section. Samples from the Brecon Gaer harness fitting also include a small amount of malachite, cassiterite, and perhaps a tiny amount of ϵ -Cu₃Sn based on its very low intensity peak at 2.16Å (Figure 4.29).

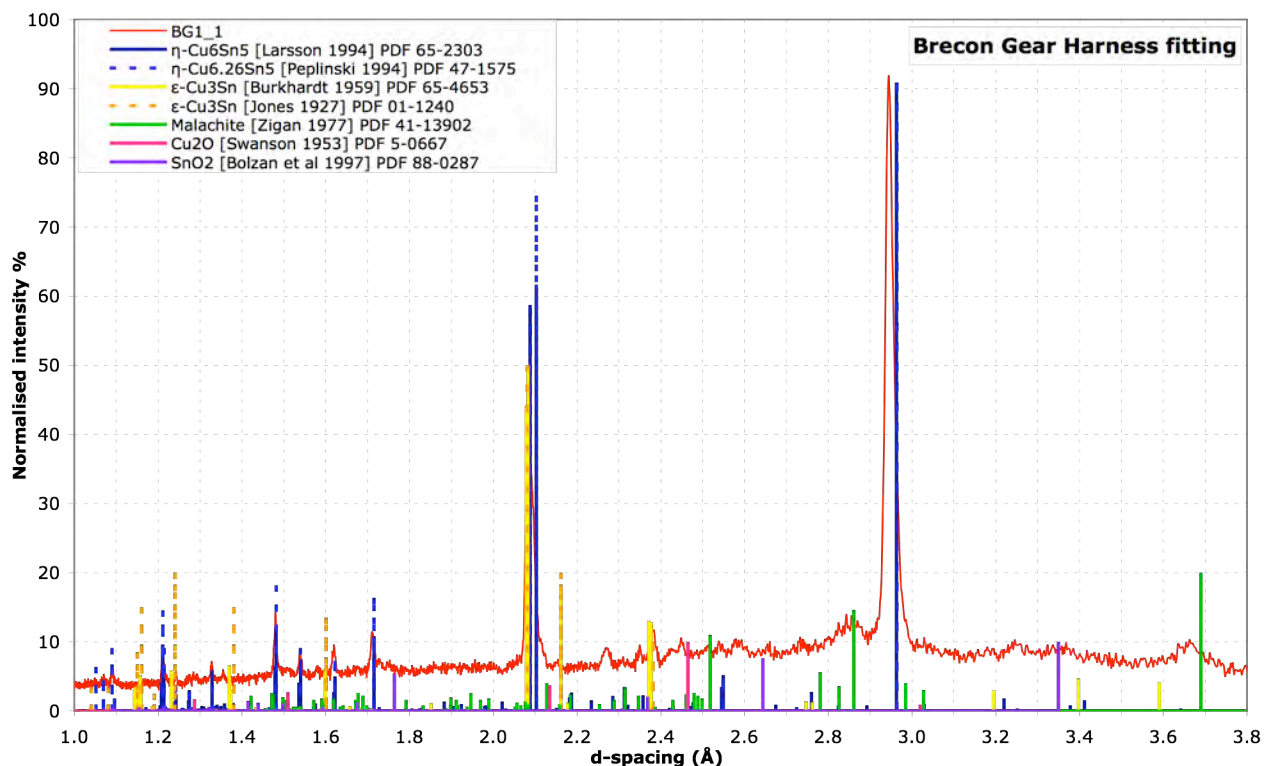


Figure 4.29: XRD pattern of fragment BG1 from the Brecon Gaer harness fitting. The pattern is dominated by η -Cu₆Sn₅ (PDF 65-2303). Alternative reference diffraction patterns are provided for comparison.

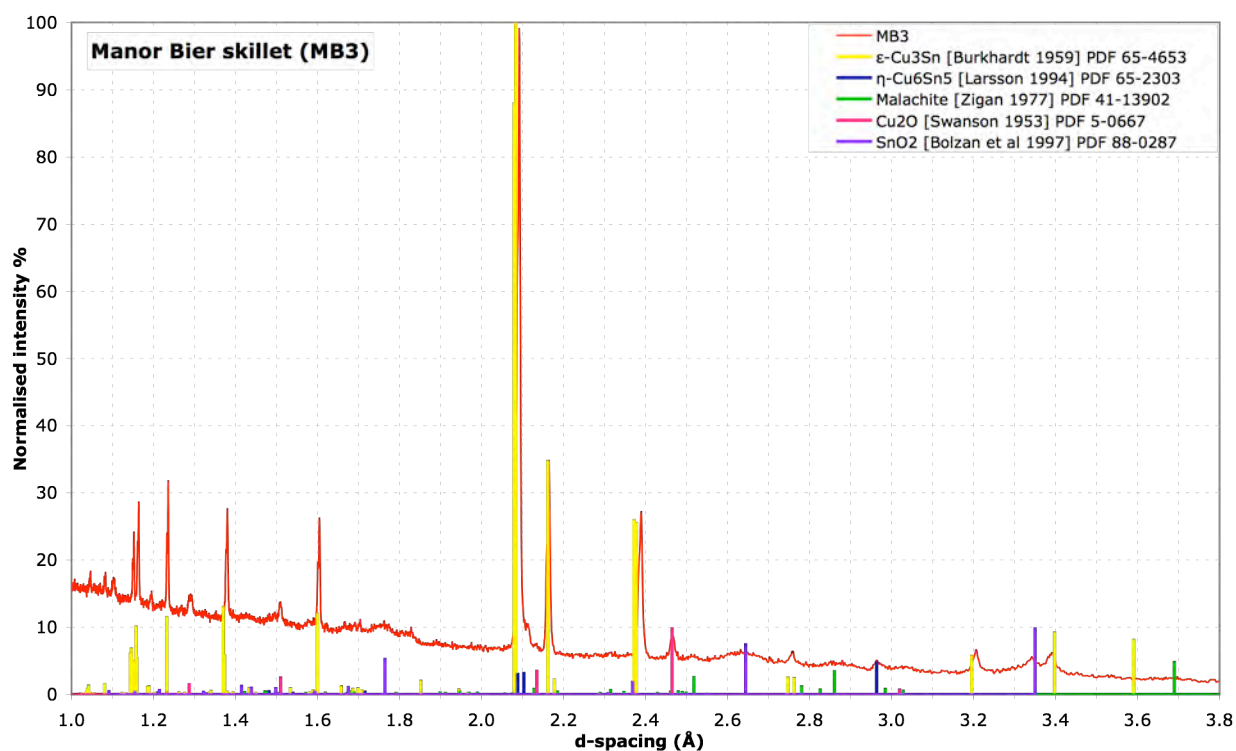


Figure 4.30: XRD pattern of fragment MB3 from the Manorbier skillet. Burkhardt's ϵ -Cu₃Sn dominates the pattern.

Out of the three fragments examined from the Manorbier skillet, only MB3 shows evidence of an IMC, Sn or Sn oxides. There are clear reflections from ϵ -Cu₃Sn, along with a small amount of cassiterite and an elevated concentration of cuprite (Figure 4.30). The diffraction pattern fits better Burkhardt's ϵ -Cu₃Sn structure (PDF 65-4653), which was previously assigned to annealed, rather than as-tinned, tinned tokens. η -Cu₆Sn₅ is absent from the XRD pattern. Detection of ϵ -Cu₃Sn in one out of three analysed samples indicates that its preservation may be patchy on the object. Sn is absent from the samples (2.92, 2.79, 2.06, 1.66 Å PDF4-0673).

4.4.2. SURFACE AND CROSS-SECTIONAL EXAMINATION

Surface and cross-sectional SEM-BSE examination of samples from the Ceredigion skillet shows the presence of a granular Sn-rich surface layer (c. 1 μ m), which is situated in an inhomogeneous tin and oxygen rich corrosion zone (Figure 4.32). These resemble η -Cu₆Sn₅ scallops developed during experimental tinning (Figure 4.2) and its presence on CER1 and CER2 was shown by XRD. This was not distinguished in BFPM examination using up to x500 magnification. Some lead compounds seen in the EDX map of the cross-section are locally on the top of the scallops and are the result of corrosion of the lead inclusions in the leaded bronze of the cast body seen in BSE and BFPM images (Figure 4.28). XRD indicated that a tiny amount of ϵ -Cu₃Sn may perhaps be present but a layer of ϵ -Cu₃Sn is not observed under the granular layer of η -Cu₆Sn₅. None of the Roman samples was etched before analysis.

A similar characteristic scallopy η -Cu₆Sn₅ layer (c. 1 μ m) is found on the surface of BG1 from the Brecon Gaer harness fitting (Figure 4.33), where XRD evidenced the presence of η -Cu₆Sn₅ (Figure 4.29). The EDX map shows that the η -Cu₆Sn₅ scallops are locally covered by lead compounds, which are the result of corrosion of the alloy of the body. This object is a cast leaded copper alloy with decorative plating on one side, the upper part of which was sampled. In cross-section, the sample shows a heavily corroded microstructure with unusually shaped remnants of metallic α -bronze and lead /phosphorus compounds (Figure 4.33). XRD indicated that a tiny amount of ϵ -Cu₃Sn may be present but a layer of ϵ -Cu₃Sn is not observed under the granular η -Cu₆Sn₅.

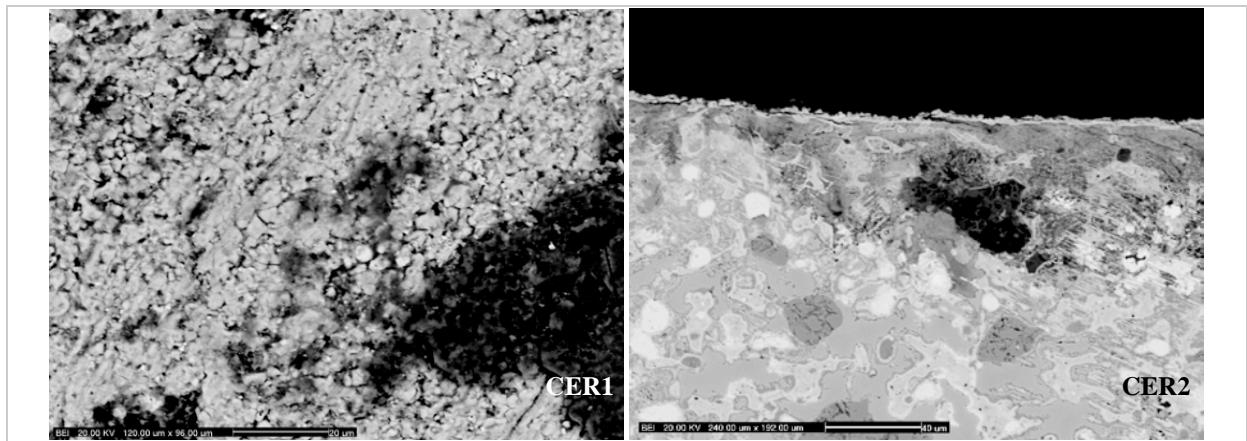


Figure 4.31: SEM-BSE images of samples from Ceredigion skillet. CER1: plan-view BSE image showing Cu_6Sn_5 scallops. CER2: BSE image showing scallops on the surface of the polished section. Unetched samples.

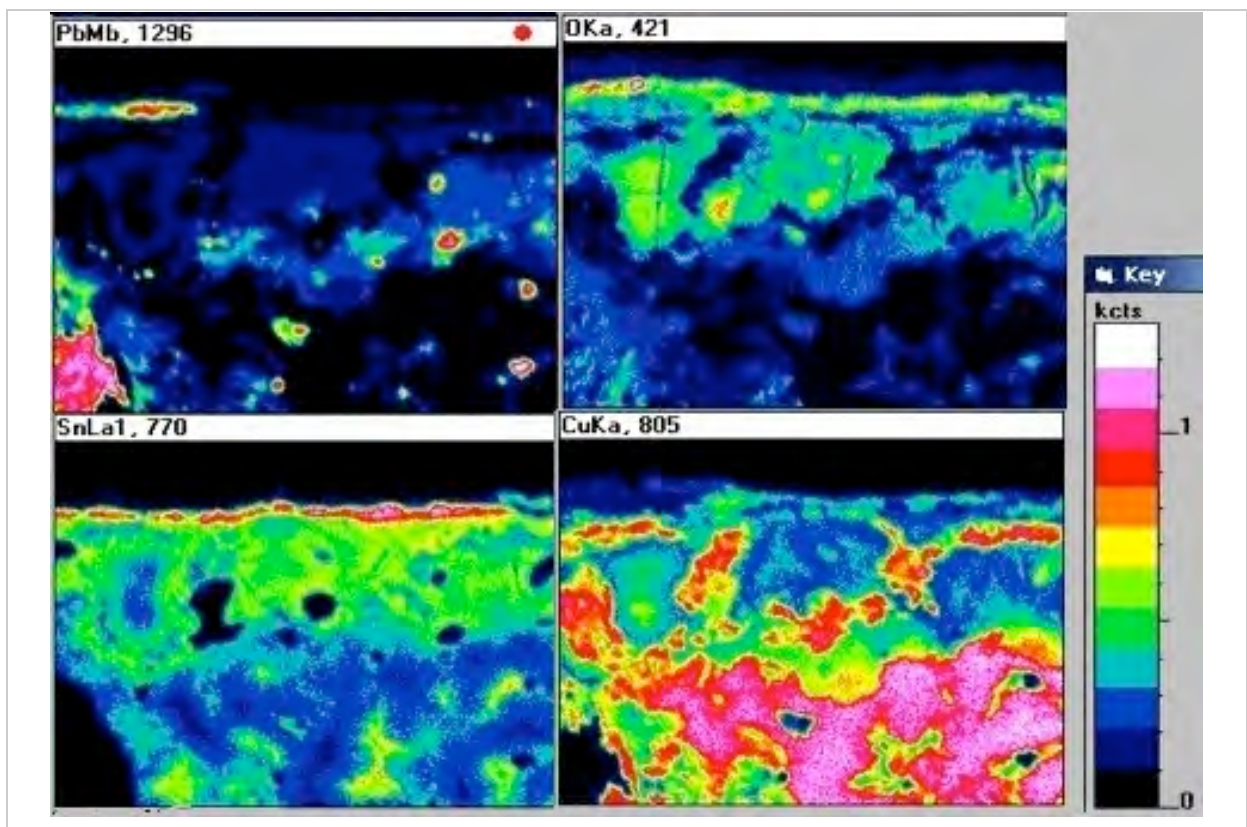


Figure 4.32: EDX maps of $\text{PbM}\beta$, $\text{OK}\alpha$, SnLa and $\text{CuK}\alpha$ X-ray lines of CER2 polished section seen above. The key indicates the counts of $\text{PbM}\beta$. Unetched polished sample naturally corroded.

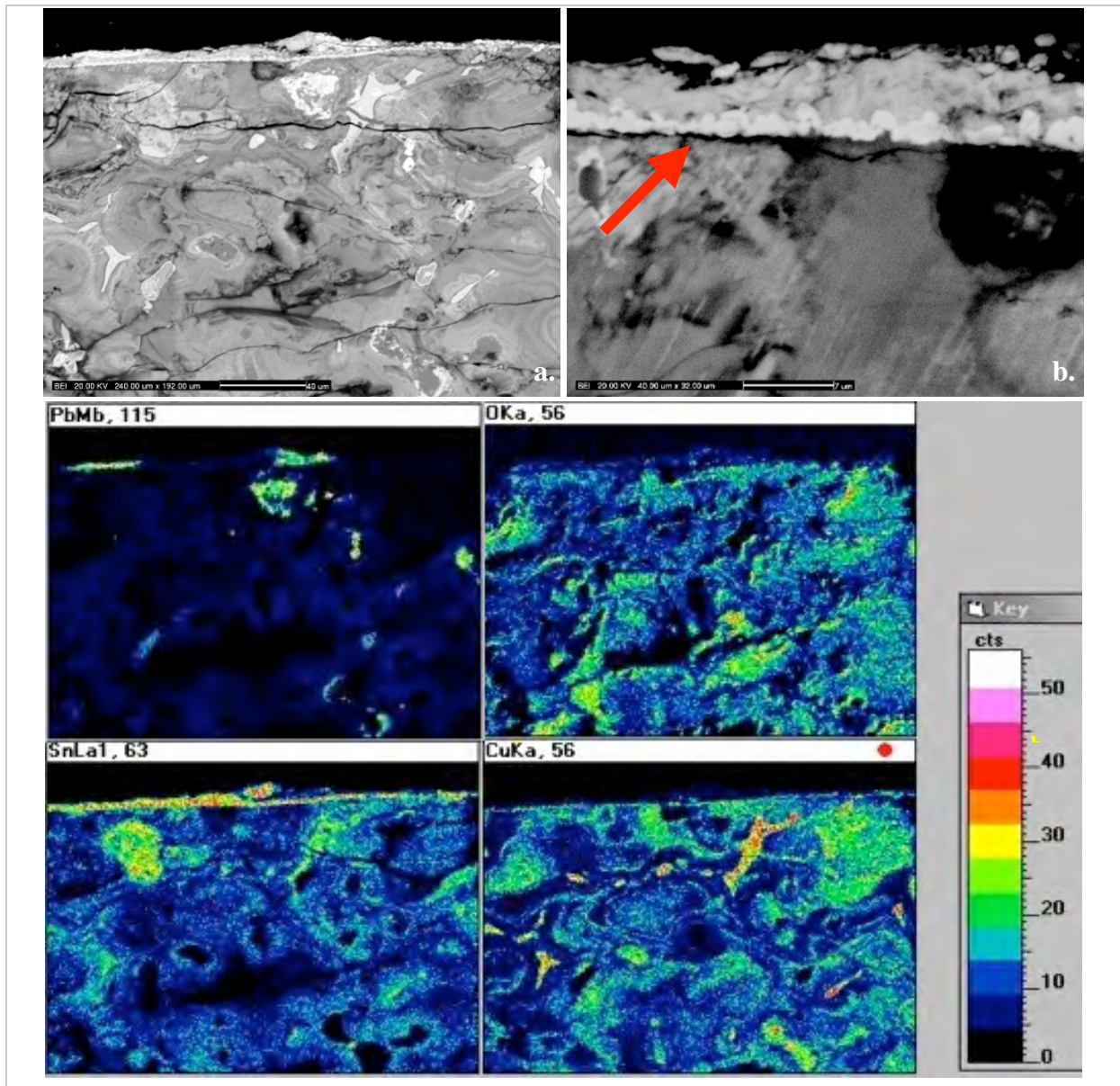


Figure 4.33: Cross-sectional SEM-BSE images and EDX map of sample from the Brecon Gear harness fitting. (a) BSE image showing general condition and Cu_6Sn_5 scallops on the surface below corrosion deposits. (b) BSE in high magnification showing detail of scallop layer. EDX maps showing elemental distribution of $\text{PbM}\beta$, $\text{OK}\alpha$, $\text{SnL}\alpha$ and $\text{CuK}\alpha$. The key indicates the counts of $\text{CuK}\alpha$. Unetched polished section.

A very flat thin localised Sn-rich layer is observed on samples from the MB skillet, which is distinguished from its underlying corrosion only in high image contrast in BSE (Figure 4.34, c). Sample MB3 where XRD showed clear evidence of $\epsilon\text{-Cu}_3\text{Sn}$ has a slightly darker (black/grey) colour at the outer part of its corrosion profile seen in BSE (Figure 4.34, b), compared to the other two examined samples. In plan-view, the sample exhibits evidence of polishing marks (Figure 4.34, a), which are reported in the literature to be preserved on the corroded surface of low-tin bronzes (Piccardo *et al.*, 2007). These observations demonstrate that it is difficult to distinguish a thin $\epsilon\text{-Cu}_3\text{Sn}$ layer on the surface of a corroded low-tin

bronze based on BSE or BFPM imaging. In fact, it would have been impossible without using XRD. If this is a result of mounting an unrepresentative section of the fragment, it is unknown. XRD analyses derived from a larger analysis area (incident beam footprint 20x20mm) than that mounted in cross section, and the patchy preservation of ϵ -Cu₃Sn was shown by the low success rate (1/3) of finding it on the three examined samples. Nevertheless, the presence of ϵ -Cu₃Sn manifests that the object was tinned.

Cross-sectioned sample BOV shows a very flat uniform thin (c. 1 μ m) Sn-rich layer in the outer part of its corrosion profile (appears brighter), and shows small round voids at its interface with its underlying corrosion in BSE (Figure 4.34, d). Voids in the form of Kirkendall voids were previously seen in annealed experimental tinned tokens (Figure 4.5, Figure 4.7). If these voids in BOV were present due to Kirkendall diffusion, their presence could manifest tinning. However, this sample was already mounted in cross-section when collected for analyses and surface XRD was not possible to confirm the presence of IMCs.

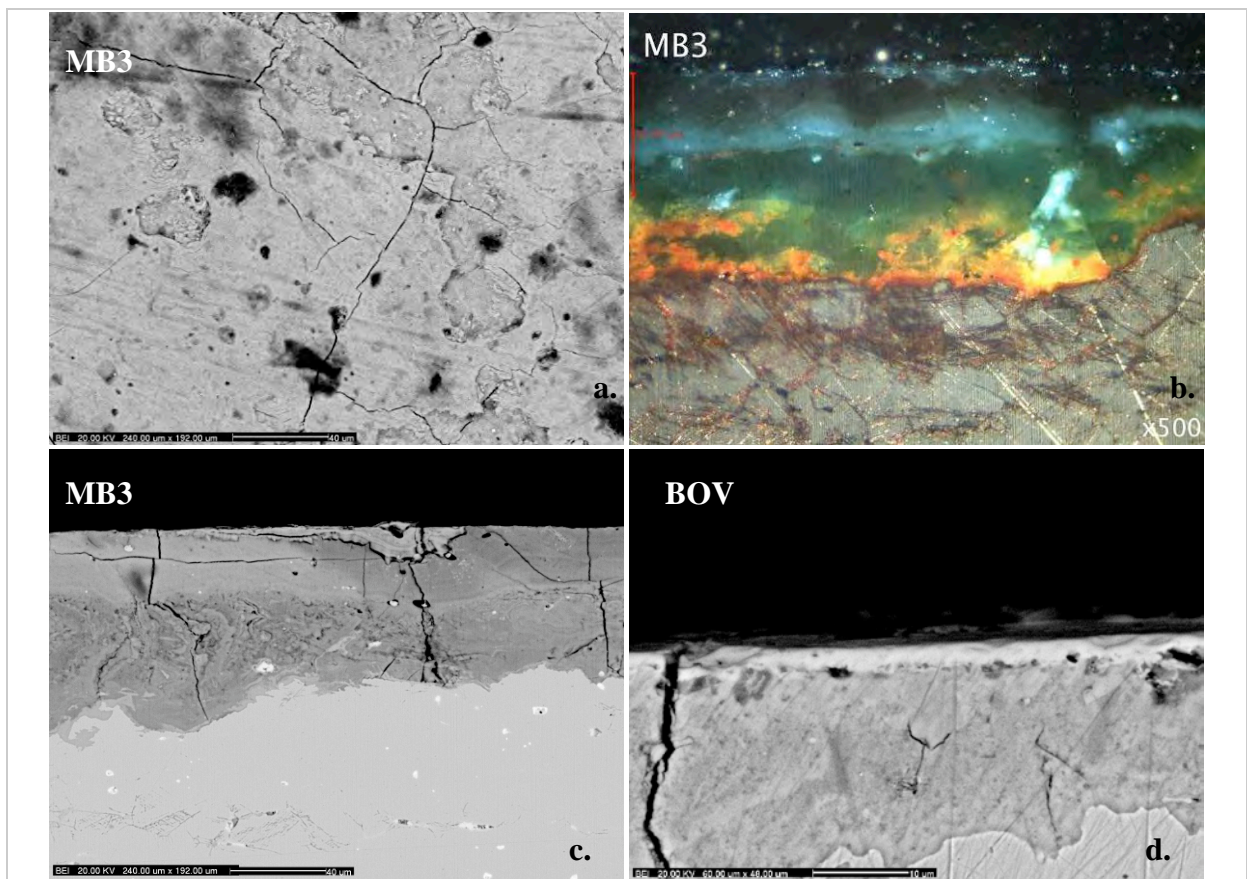


Figure 4.34: Plan and cross-sectional SEM-BSE and BFPM images of samples from Manorbier skillet and Boverton collar. (a) plan-view BSE image of the surface of showing polishing marks preserved on a very fine non-metallic corroded surface. (b) BFPM image of MB3 cross-section showing the full corrosion profile and a darker black/grey colour at the upper part of the corrosion profile. (c) BSE of MB3 cross-section showing thin patchy tin-rich outermost corrosion surface. (d) BSE of BOV cross-section showing tin-rich layer with voids at its interface with its underlying corrosion.

In summary, analysis of the Roman objects shows evidence that:

- η -Cu₆Sn₅ has a scallopy form similar to that grown on as-tinned experimental tokens, and can be preserved on archaeological objects (Ceredigion skilket, Brecon Gear harness fitting). The form of η -Cu₆Sn₅ is characteristic and can be used as a criterion for its identification.
- η -Cu₆Sn₅ can be detected by X-ray diffraction (PDF 65-2303) on archaeological bronzes as seen in published work (Oddy and Bimson, 1986) and its diffraction pattern seems to fit better the high temperature rather than its room temperature transformation.
- Where η -Cu₆Sn₅ was found, it was the main IMC and ε -Cu₃Sn was absent or its presence could not be determined definitively by XRD. This is in broad agreement with experimental tinning results in this thesis where a tiny amount of ε -Cu₃Sn was present in some as-tinned tokens and which was detected only by XRD. Thus, η -Cu₆Sn₅ can act as an indicator of as-tinned structures. On the side, this indicates that the Ceredigion skilket and the BG harness fitting were not exposed to heat during their use, because ε -Cu₃Sn grows substantially at higher temperatures or during annealing.
- Metallic Sn was absent from the diffraction patterns and η -Cu₆Sn₅, when observed, was not covered by a metallic Sn layer.
- ε -Cu₃Sn was only detected by XRD, and only in 1 out of 3 fragments from the Manorbier skilket. Evidence of ε -Cu₃Sn shows that the Manorbier skilket was tinned and it would have likely been exposed to heat during its use to aid growth of this phase.
- A thin layer of ε -Cu₃Sn alone cannot be easily identified using BFPM or BSE. In this instance, XRD has a clear advantage over these methods.
- Based on this evidence, 3 out of the 4 objects examined were tinned. Small voids in section from the Boverton collar may resemble Kirkendall voids like those observed in the experimental annealed tokens, but the evidence is insufficient to support tinning on this sample.

How these findings fit the broader understanding of IMC development and previous work by Meeks (1986) is discussed below.

4.4.3. SEM-EDX COMPOSITION ANALYSIS

Corrosion mechanisms of Cu-Sn intermetallics in the burial environment are unknown (section 2.2.5) and a systematic investigation is necessary to further our understanding, as it

would affect their characterisation via composition analysis. SEM-EDX spot analyses were undertaken on the η -Cu₆Sn₅ scallops present in cross-sectioned samples BG1, CER1 and CER2, at the outermost corrosion layer in MB3, sample which showed XRD evidence of ε -Cu₃Sn, and on deposits present just above the η -Cu₆Sn₅ scallops or the flat surface in MB3. Investigation of MB3 includes analysis from the inner and outer part of the corrosion zone below the outermost surface. BOV was not further investigated at this stage, as the presence of IMCs was not confirmed on its surface. Analysis took place in the normal equipment conditions reported in section 3.6.1. A minimum of three spot analyses was taken from each area of interest; results are in Table 4.7. Table 4.8 shows the same analysis results in wt% and at% normalised excluding elements other than Cu, Sn and O, and normalised as Cu+Sn=100% to show the impact of normalisation at the numerical values. The table includes nominal Cu, Sn, O concentrations of IMCs and tin oxides for reference.

Analyses code	Analysis area	O	Cu	Sn	Al	Si	P	S	Cl	Ca	Cr	Fe	Zn	As	Ag	Pb	Sum of other than Cu, O, Sn	
Brecon Gear fitting	BG1_Deposit Above Cu ₆ Sn ₅	22.1	5.1	39.2	0.1	0.8	1.0	0.2	0.4	0.2		3.5	0.8	3.1	1.0	22.4	33.6	
	BG1_Dep_1	Above Cu ₆ Sn ₅	26.5	4.2	41.0	0.1	0.8	1.3	0.1	0.1		6.4	0.7	2.4	0.3	16.1	28.3	
	BG1_Dep_2	Above Cu ₆ Sn ₅	18.4	4.4	35.2	0.2	0.6	1.1	0.2	0.6	0.1	0.1	1.9	0.8	4.2	0.6	31.5	42.0
	BG1_Dep_3	Above Cu ₆ Sn ₅	21.3	6.6	41.5	0.2	0.9	0.7	0.4	0.5	0.3		2.3	0.8	2.8	2.0	19.5	30.6
	BG1_Sn On Cu ₆ Sn ₅	14.7	24.3	47.6	0.1	0.6	0.3		0.1				1.7	1.2	1.3	0.1	8.8	14.1
	BG1_Sn_2	On Cu ₆ Sn ₅	8.7	28.6	50.8	0.1	0.5	0.1		0.1			0.8	1.3	0.9	0.1	8.6	12.5
	BG1_Sn_3	On Cu ₆ Sn ₅	18.5	20.2	45.9		0.6	0.4					1.9	1.1	1.9	0.1	10.3	16.2
	BG1_Sn_4	On Cu ₆ Sn ₅	16.9	24.1	46.1	0.1	0.6	0.4					2.4	1.1	1.2	0.1	7.6	13.6
	Ceredigion skillet	CER1_2Sn On Cu ₆ Sn ₅	8.2	37.9	49.3	0.1	0.2		0.1	3.1			0.1	0.1	0.2	0.5	0.5	4.8
		CER1_2Sn_1	On Cu ₆ Sn ₅	13.4	28.4	52.6		0.2	0.1	0.1	3.9		0.1	0.2	0.6	0.4	0.3	5.9
CER1_2Sn_2		On Cu ₆ Sn ₅	4.3	44.4	47.2	0.1	0.2			2.5	0.1	0.2			0.3	0.9	4.2	
CER1_2Sn_3		On Cu ₆ Sn ₅	6.8	41.0	48.0	0.1	0.2		0.1	3.0		0.2		0.1	0.7	0.3	4.4	
CER1_3Sn On Cu ₆ Sn ₅		24.4	13.1	54.1	0.1	0.2	0.1	0.1	3.4			0.1	0.2	0.4	1.5	2.3	8.4	
CER1_3Sn_1		On Cu ₆ Sn ₅	23.7	14.1	56.8	0.1	0.1		0.1	2.2			0.1	0.2	0.5	0.6	1.5	5.4
CER1_3Sn_2		On Cu ₆ Sn ₅	24.8	14.1	51.5	0.2	0.2	0.3	0.1	3.2			0.2	0.5	1.4	3.4	9.5	
CER1_3Sn_3		On Cu ₆ Sn ₅	24.6	11.1	54.1	0.1	0.2	0.1	0.1	4.9			0.1	0.2	2.4	2.0	10.2	
CER1_Sn On Cu ₆ Sn ₅		18.6	29.6	46.5	0.1	0.2	0.2		1.5				0.1	0.1	0.2	0.7	2.2	5.2
CER1_Sn_1		On Cu ₆ Sn ₅	23.6	13.8	54.4	0.2	0.2	0.2	0.1	2.8			0.1	0.1	0.5	1.1	3.0	8.2
CER1_Sn_2		On Cu ₆ Sn ₅	29.9	15.8	47.5	0.2	0.2	0.5	0.1	1.5			0.1	0.1		0.7	3.4	6.8
CER1_Sn_3		On Cu ₆ Sn ₅	2.4	59.3	37.5		0.1	0.1		0.1			0.1			0.2	0.1	0.7
CER2_2Sn On Cu ₆ Sn ₅		21.7	17.7	54.6	0.1	0.2	0.1	0.1	3.6				0.1		0.4	0.3	1.4	6.3
CER2_2Sn_1		On Cu ₆ Sn ₅	22.0	20.1	53.3	0.1	0.2		0.1	3.1					0.2	0.2	0.8	4.7
CER2_2Sn_2	On Cu ₆ Sn ₅	24.5	16.5	52.3	0.1	0.3	0.1		2.7			0.2		0.6	0.5	2.5	7.0	
CER2_2Sn_3	On Cu ₆ Sn ₅	18.5	16.5	58.3		0.2	0.1	0.1	5.0			0.1		0.2	0.3	1.0	7.0	
Manorbier skillet	MB3_L2O Deposit	26.3	27.0	26.8	0.2	1.6	2.4	0.1	0.6	0.4		0.3	1.8	1.8		10.8	19.8	
	MB3_L2O_1	Deposit	25.6	22.7	28.4	0.1	1.1	2.4	0.3	0.3	0.3	0.3	2.3	2.2		13.9	23.3	
	MB3_L2O_2	Deposit	31.1	27.0	25.0	0.1	1.4	2.2		0.3	0.3	0.1	1.7	1.4		9.2	16.8	
	MB3_L2O_3	Deposit	22.1	31.3	27.0	0.3	2.3	2.6		1.1	0.5	0.3	1.5	1.7		9.2	19.5	
	MB3_L2Oi Outermost	15.2	31.6	41.7		0.3	2.1		0.1	0.3		0.2	1.0	1.5		5.9	11.4	
	MB3_L2Oi_1	Outermost	8.6	36.6	45.2	0.1	0.3	1.7		0.1	0.3	0.3	1.1	1.5		5.0	10.3	
	MB3_L2Oi_2	Outermost	8.1	36.2	43.6		0.2	2.4		0.1	0.5	0.2	1.0	2.1		6.3	12.7	
	MB3_L2Oi_3	Outermost	28.7	22.1	36.4	0.3	2.5	0.1	0.1	0.2	0.1	0.2	1.1	1.3		7.1	12.8	
	MB3_LO Outer	30.5	24.6	35.6	0.1	0.7	2.1		0.2	0.2		0.2	1.0			4.7	9.2	
	MB3_LO_1	Outer	30.5	24.7	35.5	0.1	0.8	2.2		0.1	0.2	0.3	1.1			4.5	9.2	
	MB3_LO_2	Outer	31.1	24.2	35.7	2.1		0.2	0.2		0.3	0.1	0.9		0.7	4.6	9.0	
	MB3_LO_3	Outer	29.8	25.0	35.6	2.1	0.1	0.2	0.2	0.1	0.1	0.1	1.0		0.7	5.1	9.7	
	MB3_LI Inner	31.1	32.3	28.8		0.9	1.7		0.1			0.1	0.5	0.5		3.8	7.6	
	MB3_LI_1	Inner	31.1	30.4	30.4		0.7	2.2		0.2		0.2	0.4			4.4	8.1	
	MB3_LI_2	Inner	29.6	33.9	28.5	0.1	0.9	1.7	0.1	0.1		0.1	0.5	0.8		3.7	8.0	
MB3_LI_3	Inner	32.6	32.7	27.6		0.9	1.2		0.1			0.6	0.7		3.4	7.0		

Table 4.7: Results of EDX wt% analyses from η -Cu₆Sn₅ scallop and areas of interest in the corrosion profiles of cross-sectioned samples from the Brecon Gaer harness fitting and the Ceredigion and Manorbier skillets. Values below the detection limit of each element are removed from the table.

		Normalisation: Cu+Sn+O=100			Cu+Sn=100		Cu+Sn+O=100			Cu+Sn=100		
Analyses code	Analysis area	O	Cu	Sn	Cu	Sn	O	Cu	Sn	Cu	Sn	
		wt%	wt%	wt%	wt%	wt%	at%	at%	at%	at%	at%	
BG1_Deposit	Above Cu₆Sn₅ (Sn oxide)	33.2	7.6	59.1	11.4	88.6	77.1	4.4	18.5	19.4	80.6	
BG1_Dep_1	Above Cu ₆ Sn ₅ (Sn oxide)	36.9	5.8	57.2	9.3	90.7	80.1	3.2	16.7	16.0	84.0	
BG1_Dep_2	Above Cu ₆ Sn ₅ (Sn oxide)	31.7	7.6	60.7	11.2	88.8	75.8	4.6	19.6	19.0	81.0	
BG1_Dep_3	Above Cu ₆ Sn ₅ (Sn oxide)	30.7	9.5	59.8	13.6	86.4	74.6	5.8	19.6	22.8	77.2	
BG1_Sn	On Cu₆Sn₅	17.0	28.0	55.0	33.8	66.2	54.0	22.4	23.5	48.8	51.2	
BG1_Sn_2	On Cu ₆ Sn ₅	9.9	32.4	57.6	36.0	64.0	38.4	31.6	30.0	51.2	48.8	
BG1_Sn_3	On Cu ₆ Sn ₅	21.9	23.8	54.3	30.5	69.5	62.2	17.1	20.8	45.1	54.9	
BG1_Sn_4	On Cu ₆ Sn ₅	19.4	27.7	52.9	34.3	65.7	57.9	20.8	21.3	49.4	50.6	
CER1_2Sn	On Cu₆Sn₅	8.6	39.8	51.7	43.5	56.5	33.6	39.2	27.3	59.0	41.0	
CER1_2Sn_1	On Cu ₆ Sn ₅ (ETA)	14.2	30.1	55.7	35.0	65.0	48.5	25.8	25.6	50.2	49.8	
CER1_2Sn_2	On Cu ₆ Sn ₅ (ETA)	4.5	46.3	49.2	48.5	51.5	19.7	51.2	29.1	63.7	36.3	
CER1_2Sn_3	On Cu ₆ Sn ₅ (ETA)	7.1	42.8	50.1	46.0	54.0	28.8	43.7	27.4	61.4	38.6	
CER1_3Sn	On Cu₆Sn₅	26.6	14.3	59.1	19.5	80.5	69.7	9.4	20.9	31.2	68.8	
CER1_3Sn_1	On Cu ₆ Sn ₅	25.0	15.0	60.0	19.9	80.1	67.9	10.2	21.9	31.8	68.2	
CER1_3Sn_2	On Cu ₆ Sn ₅	27.4	15.6	56.9	21.5	78.5	70.3	10.1	19.6	33.9	66.1	
CER1_3Sn_3	On Cu ₆ Sn ₅	27.4	12.3	60.3	17.0	83.0	70.9	8.0	21.0	27.7	72.3	
CER1_Sn	On Cu₆Sn₅	19.7	31.3	49.1	38.9	61.1	57.6	23.1	19.4	54.4	45.6	
CER1_Sn_1	On Cu ₆ Sn ₅	25.7	15.0	59.3	20.2	79.8	68.6	10.1	21.3	32.1	67.9	
CER1_Sn_2	On Cu ₆ Sn ₅	32.1	17.0	51.0	25.0	75.0	74.2	9.9	15.9	38.3	61.7	
CER1_Sn_3	On Cu ₆ Sn ₅ (EPSILON?)	2.4	59.8	37.8	61.2	38.8	10.6	66.8	22.6	74.7	25.3	
CER2_2Sn	On Cu₆Sn₅	23.1	18.8	58.1	24.5	75.5	64.7	13.3	22.0	37.7	62.3	
CER2_2Sn_1	On Cu ₆ Sn ₅	23.1	21.1	55.8	27.4	72.6	64.2	14.8	21.0	41.4	58.6	
CER2_2Sn_2	On Cu ₆ Sn ₅	26.3	17.7	56.0	24.0	76.0	68.7	11.6	19.7	37.1	62.9	
CER2_2Sn_3	On Cu ₆ Sn ₅	19.9	17.7	62.5	22.1	77.9	60.7	13.6	25.7	34.6	65.4	
MB3_L2O	Deposit	32.8	33.7	33.5	50.2	49.8	71.6	18.5	9.9	65.3	34.7	
MB3_L2O_1	Deposit	33.4	29.5	37.1	44.3	55.7	72.9	16.2	10.9	59.8	40.2	
MB3_L2O_2	Deposit	37.4	32.5	30.1	51.9	48.1	75.4	16.5	8.2	66.9	33.1	
MB3_L2O_3	Deposit	27.5	38.9	33.6	53.7	46.3	65.8	23.4	10.8	68.4	31.6	
MB3_L2Oi	Outermost	17.1	35.7	47.1	43.1	56.9	52.7	27.7	19.6	58.6	41.4	
MB3_L2Oi_1	Outermost (EPSILON?)	9.5	40.5	50.0	44.7	55.3	36.1	38.5	25.4	60.2	39.8	
MB3_L2Oi_2	Outermost (EPSILON?)	9.2	41.2	49.6	45.4	54.6	35.1	39.5	25.4	60.8	39.2	
MB3_L2Oi_3	Outermost	32.9	25.3	41.8	37.7	62.3	73.3	14.2	12.5	53.1	46.9	
MB3_LO	Outer	33.6	27.1	39.3	40.9	59.1	73.5	15.0	11.6	56.4	43.6	
MB3_LO_1	Outer	33.6	27.2	39.2	41.0	59.0	73.5	15.0	11.5	56.5	43.5	
MB3_LO_2	Outer	34.2	26.5	39.2	40.4	59.6	74.1	14.5	11.4	55.8	44.2	
MB3_LO_3	Outer	32.9	27.7	39.4	41.3	58.7	72.8	15.4	11.7	56.8	43.2	
MB3_LI	Inner	33.7	35.0	31.2	52.9	47.1	72.1	18.9	9.0	67.7	32.3	
MB3_LI_1	Inner	33.9	33.1	33.0	50.0	50.0	72.6	17.9	9.5	65.2	34.8	
MB3_LI_2	Inner	32.2	36.8	31.0	54.3	45.7	70.5	20.3	9.2	68.9	31.1	
MB3_LI_3	Inner	35.1	35.2	29.7	54.3	45.7	73.2	18.5	8.3	68.9	31.1	
Phase	Name	O	Cu	Sn	Cu	Sn	O	Cu	Sn	Cu	Sn	
		wt%	wt%	wt%	wt%	wt%	at%	at%	at%	at%	at%	
IMC	Cu₃Sn	Epsilon	0.0	62.3	37.7	62.3	37.7	0.0	75.5	24.5	75.5	24.5
	Cu₅Sn	Epsilon	0.0	60.5	39.5	60.5	39.5	0.0	74.1	25.9	74.1	25.9
	Cu₆Sn₅	Eta	0.0	39.8	60.3	39.8	60.3	0.0	55.2	44.8	55.2	44.8
	Cu₆Sn₅	Eta	0.0	38.9	61.1	38.9	61.1	0.0	54.3	45.7	54.3	45.7
Corrosion	SnO	Stannous oxide	11.9	0.0	88.1	0.0	100.0	50.0	0.0	50.0	0.0	100.0
	SnO₂	Cassiterite (IV)	21.2	0.0	78.8	0.0	100.0	66.7	0.0	33.3	0.0	100.0
	SnO₂ 2 at% Cu	Stannic oxide	21.7	2.6	75.7	3.3	96.7	66.7	2.0	31.3	6.0	94.0
	SnO₂ 7 at% Cu	Stannic oxide	23.0	9.6	67.4	12.5	87.5	66.7	7.0	26.3	21.0	79.0
	SnO₂.2(H₂O)	Dihydrated Stannic Oxide	35.0	0.0	65.0	0.0	100.0	80.0	0.0	20.0	0.0	100.0
	SnO₂.H₂O	Hydrated Stannic Oxide	28.8	0.0	71.2	0.0	100.0	75.0	0.0	25.0	0.0	100.0

Table 4.8: wt% and at% EDX composition analyses of surface features in cross-sections of Roman samples normalised excluding elements other than Cu, Sn, O and normalised excluding elements other than Cu and Sn. The nominal composition of selected Sn oxides and IMCs is presented for comparison. Interpretation of data is included in parenthesis.

Analyses of η -Cu₆Sn₅ scallops deviates from its nominal concentration (Table 4.8) with decreased Sn and Cu concentration due to oxidation, and eventually the loss of a substantial amount of Cu from the IMC and compositions towards SnO₂.2H₂O (Figure 4.35). Analysis from scallops on CER1 with the least oxygen concentration (CER1_2Sn) show Cu

concentration closer to the nominal η -Cu₆Sn₅ value, compared to its Sn content that is considerably less than in η -Cu₆Sn₅ indicating that Sn oxidation has taken place in preference to Cu oxidation. Recent laboratory corrosion experiments using modern low-tin bronzes in aqueous solutions show that the oxidation rate of Sn is higher than that of Cu during the initial early corrosion stage, a trend which is gradually reversed and the rate of Cu dissolution becomes higher than that of Sn (Chunchun and Julin, 2003; Satovic *et al.*, 2009). If during corrosion of the IMCs Cu dissolution and Sn oxidation take place, it would thus be likely that Sn oxidation took place at an early stage of corrosion followed by Cu dissolution from the IMC phase. Assuming that the analyses are collected from areas on η -Cu₆Sn₅ that exhibit different degrees of corrosion, data would provide snapshots of the impact of corrosion on the chemical composition of the intermetallic. Data indicate that Sn concentration decreases faster than Cu compared to nominal concentrations at low O concentrations (below 20at% O), and Sn oxidation occurs at an early stage of this phase. Sn concentration continues to decline in conjunction with a faster Cu dissolution heading towards the composition of SnO₂.2H₂O (Figure 4.35). At an early corrosion stage, Sn oxidation may predominate against copper dissolution from η -Cu₆Sn₅, which slows down in a later stage in agreement with published work (Chunchun and Julin, 2003).

The composition of a fine deposit just above η -Cu₆Sn₅ scallops in BG1 where a small concentration of SnO₂ was detected by diffraction (Figure 4.30) has an EDX composition similar to SnO₂.2H₂O. Analyses from the same sample, from an area on η -Cu₆Sn₅ scallops (or at least thought to be), shows compositions close to ϵ -Cu₃Sn, but with less Cu due to oxidation. It is likely that the spot analysis was on a zone of ϵ -Cu₃Sn film, which was not distinguished in the BSE. XRD indicated that a tiny amount of ϵ -Cu₃Sn may be present in this sample but its presence was not definitive. Metallic Sn was not found in the profiles.

Overall, compositional data from intermetallics on the Roman bronzes align within the ϵ -Cu₃Sn - η -Cu₆Sn₅ - SnO₂.2H₂O region in the Cu-Sn-O at% ternary plot, and the more oxidation had taken place the more similar the composition becomes heading towards SnO₂.2H₂O. Despite the small number of samples examined, which is in no way statistically viable, this compositional region is distinctively different from analyses of areas within the corrosion profile (MB3), which are characterised by a smaller amount of Sn and Sn/Cu ratio in their patinas. Composition from the profile of MB3 is within published compositional ranges for corroded low-tin bronzes exhibiting Type I corrosion (Robbiola and Hurtel, 1997; Dorigo *et al.*, 1998). It would appear that it is possible to detect residues of intermetallic compounds by EDX but this may be very 'hit and miss' according to location of the analysis.

Also, corroded areas of intermetallics with altered compositions are difficult to assign to the actual intermetallic based on compositional data. It may be possible with many further analysis to link specific composition ranges to corroded intermetallics. Until more data is available, EDX alone shows limitations for detecting tinning and XRD has a clear advantage over elemental analyses.

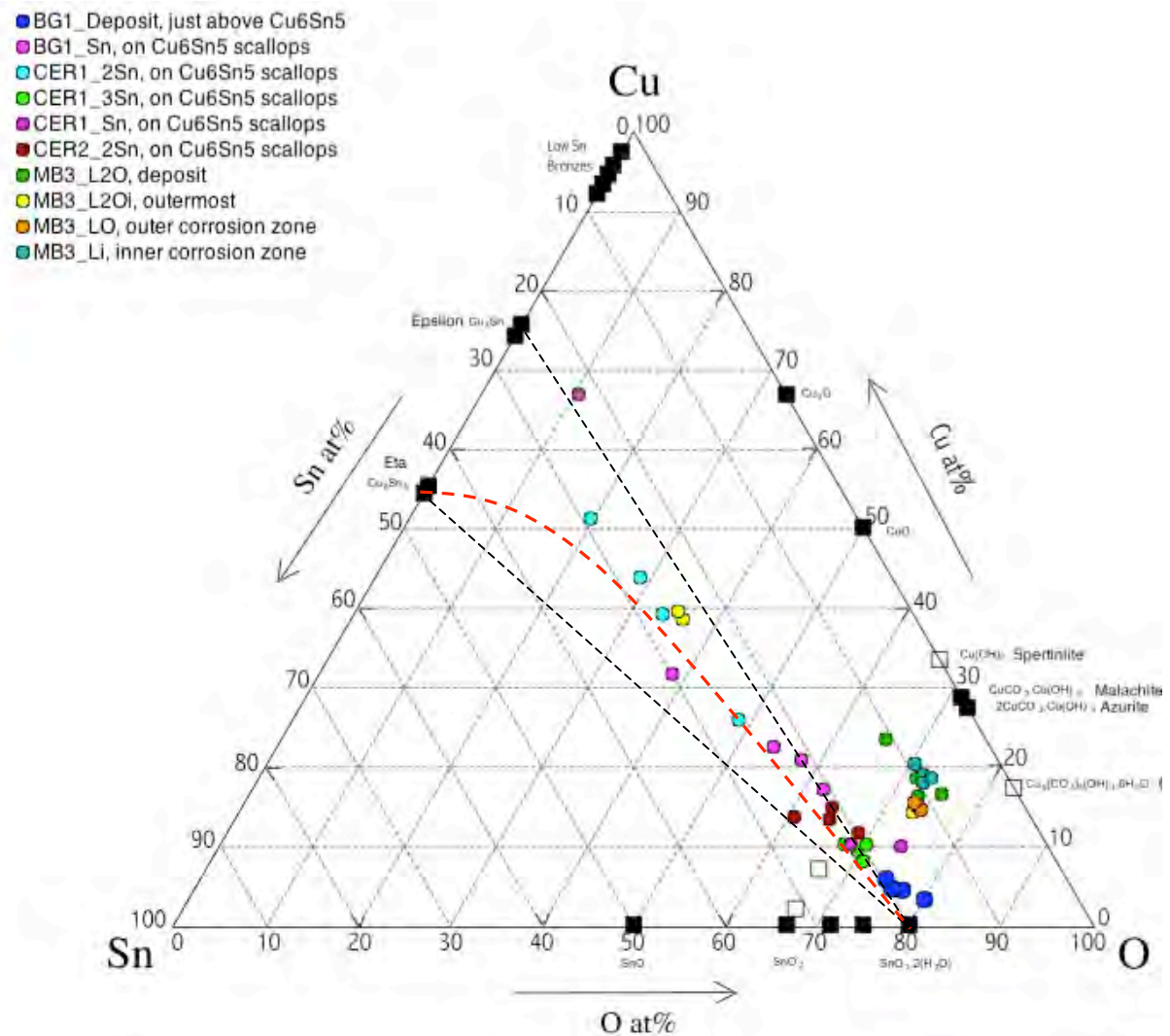


Figure 4.35: Cu-Sn-O ternary diagram of at% EDX composition analyses results from different areas in the analysed Roman samples. Each point in the graph represents individual spot analysis.

Interestingly, analysis of this small number of Roman objects detected η -Cu₆Sn₅ on cast bronzes, while ϵ -Cu₃Sn or a complete absence of an intermetallic was observed on wrought samples. Substrate texture is important for the growth of η -Cu₆Sn₅ during tinning, and η -Cu₆Sn₅ scallops show a preferred orientation towards given planes in the copper substrate (Wang *et al.* 2009). Such crystal orientation preferences and texture could perhaps be significant during the development of intermetallics on low-tin bronzes in relation to their manufacture. This could influence their preservation. A literature review (section 2.2.5)

showed that analysis which reports IMCs derives predominantly on objects likely to be cast (Oddy and Bimson, 1985; Meeks, 1993b, 1993a). Exceptions are a wrought Bronze Age vessel (Ryndina, 2009) and a wrought low-tin bronze shield (Born, 2007), but these unfortunately do not provide diffraction analyses data. If the frequency of reported IMCs on archaeological tinned bronzes reflects the distribution of object types that are tinned, then this could give an indication of the preservation rates on different substrates. More work is required to examine this hypothesis, including a systematic investigation of the type and distribution of tinned objects in antiquity.

4.5. GENERAL DISCUSSION AND CONCLUSIONS

4.5.1. IMC GROWTH AND CHANGES BY HEAT

4.5.1.1. Phases formed during tinning and the nature of η -Cu₆Sn₅

Experimental tinning results are generally comparable with previous experiments by Meeks (1986) that the identification of η -Cu₆Sn₅ and ε -Cu₃Sn is strong evidence of tinning, but differ in the extent to which ε -Cu₃Sn appears on the surface of as-tinned samples. The granular nature of η -Cu₆Sn₅ and the dominance of this phase in the as-tinned bronzes have been previously neglected. Results here showed that during wipe-tinning, η -Cu₆Sn₅ is the first and major phase that forms at the Cu(solid)/Sn(liquid) interface on both copper and bronze substrates. This agrees with theory, where η -Cu₆Sn₅ is reported to be the first phase that forms during tinning (Tu, 1973) due to the fast diffusion (1-3 seconds) of Cu into the melted Sn (Bader *et al.*, 1995; Banovic, 2007). This fast diffusion rate is also the reason for the characteristic scallopy shape of this phase (Gagliano and Fine, 2001; see also Suh *et al.* 2008). The thickness of the developed η -Cu₆Sn₅ layer depends on availability of tin and the temperature and length of application (Laurila *et al.* 2005). Expected growth of the ε -Cu₃Sn phase at the Cu/ η -Cu₆Sn₅ interface is, in general, associated with longer reaction times or annealing at temperatures around 240-330°C for tinned copper substrates (Bader *et al.*, 1995). ε -Cu₃Sn was not observed in as-tinned wipe-tinned copper and bronze samples using BSE imaging and appears after 1 hour annealing at 250°C (S7, B6). XRD detected a very small amount of ε -Cu₃Sn in some of the as-tinned experimental and possibly in archaeological samples in association to η -Cu₆Sn₅ (Figure 4.10, Figure 4.11) showing that ε -Cu₃Sn could be formed during tinning but it is normally very thin to be detected by BSE.

The η -Cu₆Sn₅ layer on low-tinned bronzes was observed here to be less scallopy (shorter nodules) than on as-tinned copper samples, due to a reduction in the diffusion rate of Cu atoms from the bronze in the melted Sn (Hayashi *et al.*, 1997; Kao, 1997). Yet, their shape is still characteristic to aid identification of η -Cu₆Sn₅. Slightly thicker ε -Cu₃Sn layers grow on tinned bronzes as compared to copper during annealing at elevated temperatures (at or above 350°C) (Figure 4.7).

Literature shows that the original number of η -Cu₆Sn₅ scallops is also related to the roughness of the substrate surface; the rougher the surface the more crystals are formed (Gagliano and Fine, 2001; Lee and Chen, 2002). A relationship between the crystallographic orientation of η -Cu₆Sn₅ and Cu is reported to exist; the (240) η -Cu₆Sn₅ plane is aligned with the {110}Cu family of planes during formation of the intermetallic compound (Wang *et al.*, 2009). It is therefore possible that substrates with preferred crystal orientations can influence the nature of η -Cu₆Sn₅ that grows during tinning. It is unknown how the heavily hammered structure of low-tin bronzes, commonly found in antiquity with evidence of directional working and crystallite preferred orientation, would influence the growth of IMCs growth compared to as-cast bronzes.

The characteristic manifestation of η -Cu₆Sn₅ was typically observed at magnifications higher than 500x (around 1000x) during this experiment, in areas not covered by tin. This, in conjunction with knowledge that η -Cu₆Sn₅ is the first and dominant phase that forms during tin coating, is important for the visual non-destructive detection of tinning practices. Analyses of tinned archaeological samples showed that η -Cu₆Sn₅ scallops can be preserved (Figure 4.32) and used as a visual marker IMC for the detection of tinning on archaeological samples.

Comparison of these findings to microstructures developed using other tinning methods such as mercury tinning would provide information on the physical nature of developed phases and the possibility to discriminate between different tinning methods using surface observations and XRD. Work by Qinglin and Scott (2003) showed that η -Cu₆Sn₅ readily forms during mercury tinning at a variety of application and heat treatment temperatures. It would be interesting to know if the physical form of this η -Cu₆Sn₅ phase is similarly granular in form. Polishing of a tinned object is suggested to remove η -Cu₆Sn₅, but this has not been experimentally verified nor how polishing could affect its granular nature. These are all aspects that require further investigation.

4.5.1.2. Transformations by heat: post-tinning

Post-tinning heat-treatment experiments above the melting point of Sn showed a variety of developed microstructures generally similar to those published by Meeks (1986, fig.8). Results showed that ϵ -Cu₃Sn grows in a generally planar form at the Cu/ η -Cu₆Sn₅ interface during annealing of copper and bronze substrates. At elevated annealing temperatures ϵ -Cu₃Sn grows at the expense of the η -Cu₆Sn₅ scallops mimicking their scallopy form and it is covered by a thin layer of η -Cu₆Sn₅ until it is all consumed (at 550°C). Growth of ϵ -Cu₃Sn on the bronze tokens resulted in slightly thicker layers (B7, B8), than those on copper substrates at the same annealing time because of the slower diffusion rates of the diffusing species at the bronze (solid)/Sn(liquid) interface (Hayashi *et al.*, 1997; Kao, 1997) because the Sn-Cu alloy melt is already saturated with copper (Laurila *et al.*, 2005).

Details of the growth and diffusion mechanisms within ϵ -Cu₃Sn and η -Cu₆Sn₅ are not fully understood and several mechanisms are proposed in the literature. ϵ -Cu₃Sn is generally reported to grow by reaction of Cu with η -Cu₆Sn₅ at the ϵ/η interface at temperatures above the melting point of tin. Growth of ϵ -Cu₃Sn and η -Cu₆Sn₅ can be simultaneous and is reported to be at a parabolic rate (square root of time) at temperatures above 80°C (Lee and Duh, 1999; Gagliano and Fine, 2001; Laurila *et al.*, 2005). Growth of ϵ -Cu₃Sn is also reported to be at the expense of η -Cu₆Sn₅ because ϵ -Cu₃Sn grows faster than η -Cu₆Sn₅ at higher temperatures (Bader *et al.*, 1995; Lee and Chen, 2002). It seems that the latter has taken place in the experimental samples here, where the increasingly thicker ϵ -Cu₃Sn layer mimics the shape of the gradually thinner η -Cu₆Sn₅ nodules suggesting that it grew at the expense of η -Cu₆Sn₅ and at a rate faster than the growth rate of η -Cu₆Sn₅.

At 350°C and above (S13, S15, S17), the intergranular channels between the η -Cu₆Sn₅ scallops is reduced affecting the shape of η -Cu₆Sn₅ scallops. Growth of η -Cu₆Sn₅ scallops is attributed to the diffusion of copper through the spaces that are present between the η -Cu₆Sn₅ grains; copper diffuses from there and reacts with the molten Sn to form more η -Cu₆Sn₅ (and more elongated nodules) (Bader *et al.*, 1995). The increase in the diameter of the η -Cu₆Sn₅ grains observed at this annealing times is attributed to the dissolution of smaller IMC grains into the liquid solder, which contributes to further growth of neighbouring grains (Wu *et al.*, 2004; Banovic, 2007; Suh *et al.*, 2008). Such phenomena lead to the narrowing of the space between the η -Cu₆Sn₅ grains, which inevitably slows down diffusion through the intergranular channels and further growth, due to reduction of the copper available for diffusion into the melt (Gagliano and Fine, 2001). Gagliano and Fine (2001) showed that

complete closure of the intergranular channels can take place after 10 minutes reaction at 275°C, but this was not observed in the samples examined here. Further diffusion of copper into the molten tin can take place over increased reaction times through the η -Cu₆Sn₅ and ϵ -Cu₃Sn layers themselves, which increases growth of these layers until all liquid tin is exhausted (Banovic, 2007).

The formation of Kirkendall voids at the Cu₆Sn₅ /Sn interface was observed predominantly at annealed copper samples and at a smaller extent at the Cu₃Sn/Cu₆Sn₅ interface of annealed bronze samples, due to loss of mass that takes place because of unbalanced diffusion rates between Cu and Sn within the different phases (see Appendix3). Observation of such voids on archaeological objects would indicate that fast diffusion rates took place during tinning or post-tinning use. Kirkendall voids could influence the mechanical properties of tinning layers during use and polishing potentially resulting at their mechanical loss or affecting corrosion of these layers.

Extensive annealing at higher temperatures (B9, 550°C, 1 hour) results in the formation of a surface layer of δ -Cu₄₁Sn₁₁, in agreement with previous work. XRD identified that this phase was present on copper samples after 1h at 450°C (S15) in the XRD patterns and it is the dominant phase at 550°C (S17,S19) in agreement with the equilibrium phase diagram. In BSE this was not visible until S19, where an α -bronze might be in BSE images but is confirmed by XRD, showing the value of this method. Some α -bronze is present at 1h at 450°C.

XRD analysis of a wrought low-tin bronze Roman sample showed that ϵ -Cu₃Sn can be present on the surface alone without any η -Cu₆Sn₅. Objects such as skillets, would be exposed to post-tinning heat treatment if the objects were used in antiquity. It is interesting that analysis of two Roman skillets revealed the presence of granular η -Cu₆Sn₅ on sample deriving from cast areas of one object and ϵ -Cu₃Sn on this deriving from wrought areas of the body of the other skillet. It is not possible to know the extent to which the different skillets were used in antiquity and their thermal history. If their thermal history was similar, one could argue that it is likely that all η -Cu₆Sn₅ was removed from the body area due to extensive polishing in antiquity, leaving behind a thin layer of ϵ -Cu₃Sn. In this case, one would expect to observe some ϵ -Cu₃Sn under η -Cu₆Sn₅, which is not the case. If the objects were exposed to post-tinning thermal treatment, ϵ -Cu₃Sn would be expected to have been developed under η -Cu₆Sn₅ and it is not in the case of the Ceredigion skillet.

Literature reports that the role of texture on the substrate may affect growth and orientation of η -Cu₆Sn₅ grains. This can indicate that manufacturing (casting and the degree of hammering)

may be important for the growth of intermetallics, which may perhaps somehow be linked to preservation of these phases on archaeological low-tin bronzes. A brief literature review, where the presence of intermetallics was confirmed with analysis, indicates that research focuses mainly on cast archaeological objects. Could this be a coincidence or could this be the result of complex mechanisms involving preservation of η -Cu₆Sn₅ on cast objects? This is yet to be discovered and a systematic work on archaeological objects is required.

Although, not shown experimentally here, it is important to note that further changes can take place at the Cu-Sn couple at temperatures below the melting point of Sn and as low as -2°C due to solid state diffusion phenomena (Tu, 1973). Tu (1973) demonstrated that η' -Cu₆Sn₅ forms at room temperature and it continues to grow linearly in time due to diffusion of Cu atoms into Sn (Tu, 2007: 80). This growth eventually stops when all tin is consumed to form η' -Cu₆Sn₅. Annealing at room temperature for a year did not result in the growth of ϵ -Cu₃Sn, which only grew at the Cu/ η' - Cu₆Sn₅ interface at temperatures above 60°C (Tu, 2007:75). If solid state diffusion phenomena had taken place in antiquity these would be manifested by lack of Sn, further growth of η' -Cu₆Sn₅ and above 60°C subsequent growth of ϵ -Cu₃Sn. An extensive growth of ϵ -Cu₃Sn was not observed on the Roman tinned tokens, and such solid state diffusion phenomena do not seem to have affected the archaeological structures.

4.5.2. THE CRYSTALLINE NATURE OF IMCS AND DIFFRACTION METHODS

Preferred crystallite orientation (texture) was evidenced on all tinned and annealed samples to different extents. This gave information on the nature of the IMCs but heavily influenced the processes of assigning reference diffraction patterns to the experimental data. This work followed the intensity of characteristic diffraction lines, which broadly corresponded to the imagery BSE information on the relative quantity and physical shape of η -Cu₆Sn₅ and ϵ -Cu₃Sn.

Texture of the copper substrate and of η -Cu₆Sn₅ and ϵ -Cu₃Sn phases bedevilled the least-squares fits of known structures to the measured diffraction patterns collected on ROTAX during Rietveld quantitative analysis. For reasons that are yet to be understood, but are beyond the scope of this thesis, η -Cu₆Sn₅ was surprisingly not detected using TOF-ND in this experiment. Even so, neutron diffraction at GEM was shown to have a great capacity to detect ϵ -Cu₃Sn and α -CuSn at concentrations as low as 0.5wt% and δ around 1wt%. X-ray diffraction was extremely useful for the detection of all phases on experimental and

archaeological bronzes, which often were not seen in BSE or EDX analysis. XRD shows a clear advantage for the non-destructive characterisation of tinned archaeological bronzes.

The X-ray diffraction patterns from as-tinned samples seemed to match better the hexagonal (P63/mmc) high temperature η -Cu_{6.26}Sn₅ (PDF 47-1575), but some unassigned very small peaks and the clear additional peaks at diffraction patterns from annealed samples showed that η -Cu₆Sn₅ on these samples must be of a monoclinic (C2/c) structure (PDF 65-2303). This was also found on Roman tinned bronzes (Ceredigion skillet and Brecon Gear harness fitting). Both structures are the high temperature η -Cu₆Sn₅ structure rather than the room temperature transformation η' -Cu₆Sn₅ of the phase. This finding is significant as it supports the hypothesis that such equilibrium transformation does not occur, because during cooling from tinning there is not enough time for equilibrium to be achieved (Laurila *et al.*, 2005). Finding this on archaeological objects offers significant evidence to support this. This is also important for the characterisation of archaeological samples, because understanding the crystal nature of the phase can assist the accurate identification of the phase by diffraction and offer technical details on the tinning method. The possible presence of a metastable Cu-rich phase on the annealed copper samples offers information beyond the relevancy of this study and a hypothesis on its role is found in Appendix 3.

4.6. SUMMARY

Theory and literature indicate that the identification of η -Cu₆Sn₅ and ε -Cu₃Sn offer strong evidence of tinning. SEM examination of experimental tokens shows a systematic development of IMCs during tinning and with time and temperature during annealing. η -Cu₆Sn₅ forms first and is the characteristic predominant phase. Its characteristic scallopy form aids its identification via surface observation at high magnifications (c. 700x) and can be used as a visual ‘marker’ that manifests tinning. This was confirmed by examination of Roman objects. When the phase is covered by metallic tin on un-corroded samples, local application of a tin-dissolving agent can reveal the η -Cu₆Sn₅ granules to promote identification of the phase. Increased temperature and time forms ε -Cu₃Sn at the bronze/ η -Cu₆Sn₅ interface. It is shown that this layer is slightly thicker on bronzes at lower annealing temperatures and becomes much thicker at elevated temperatures. The presence of a distinct layer of ε -Cu₃Sn manifests that the object was exposed to elevated heat. On archaeological objects examined here, where ε -Cu₃Sn is the predominant phase in XRD, it was found in isolation and η -Cu₆Sn₅

was absent. XRD showed an advantage over neutron diffraction because of the limited success of neutron diffraction to detect η -Cu₆Sn₅. The low detection limits of other phases including ϵ -Cu₃Sn and δ makes this a powerful non-destructive tool in other areas of heritage science work. Corrosion of IMCs complicates identification of these phases by composition analyses, but preliminary works indicates that this may be possible in the future. More systematic analysis of archaeological tinned bronzes is necessary. This chapter has provided valuable information on identification methods of tinning, which will underpin the investigation of surfaces of helmets investigated in this study.

CHAPTER 5. MANUFACTURE AND TYPOLOGY OF HELMETS

5.1. INTRODUCTION

The fabrication method and alloy composition of helmets are important in understanding surface treatments and corrosion because metallurgy and bronze composition affect the visual appearance of the helmets in antiquity (see section 2.2.3) and corrosion during burial (section 2.2.2). Manufacturing methods are linked to typological and chronological sequences of helmets. Technical observations derived from helmets from dated excavation contexts make it possible to date helmets of unknown provenance, such as those commonly found in museum collections or those from archaeological sites that have no datable archaeological contexts. Information on dating and archaeological context was unavailable for several helmets in this study. For these reasons, this chapter reviews established typologies for Illyrian and Corinthian type helmets and provides a summary of their technological evolution. The typological/chronological sequences followed are mainly these of Pflug (1988a; 1988b; 1988c; 1988d; 1988e) and Kunze (1958, 1961, 1967). This provides the technical framework for placing the 58 helmets included in this thesis into archaeological context using visual observation of their technical features and scientific analyses of removed samples (Table 3.2). Technical description of individual helmets is provided in Appendix 1.

Scientific investigation of technology and manufacture was supported by x-radiography (of 17 helmets) and non-destructive neutron texture analyses of limited number of helmets undertaken at GEM and ROTAX diffractometers at ISIS neutron spallation source. The composition and microstructure of cross-sectioned samples from 36 helmets, which were selected for further examination of their surface, were investigated using scanning electron microscopy energy dispersive X-ray analysis (SEM-EDX), backscattered electron imaging

(BSE) and metallography using polarised light microscopy. Experimental methodology and instrumentation are reported in Chapter 3.

5.2. PUBLISHED HELMET TYPOLOGIES AND DATE SEQUENCES

5.2.1. DISTRIBUTION AND DATING OF GREEK HELMETS

Current understanding of the typological development and chronology of Greek helmets is based on the distribution and observation of physical types, mainly compiled by Kukahn (1936) and Kunze (1958, 1961, 1967), who published material excavated in Olympia, and significant additions made by Snodgrass (1964, 1967) and Pflug (1988a; 1988b; 1988c; 1988d; 1988e). More recent contributions include Jarva (1995) on Archaic armour and Dintsis (1986) on Hellenistic helmets, whilst Moustaka (2000) provides an interesting discussion on the origins of the Illyrian helmet. These works are focused mainly on the stylistic evaluation of helmets predominantly from excavations in Olympia, links to artistic depictions of helmets on dated pottery and helmets from dated excavation contexts in Greece, the Balkans, and *Magna Grecia* in southern Italy. Helmet types are named after the distribution of early find spots (i.e. provenience) and naming does not reflect helmet origins (i.e. provenance⁹) or production workshops. Such is the case for most Greek helmets. The Illyrian type, for example, is named after first discoveries of this type in Illyria (nowadays Albania), although scholars agree that its origins lie in Peloponnesus (Snodgrass, 1964: 18-20; Pflug, 1988b) or in northern Greece, region of Macedonia (Moustaka, 2000) .

The large numbers of helmets retrieved from panhellenic sanctuaries, such as those at Olympia (Zeus), Isthmia (Poseidon) and Delphi (Apollo), has contributed immensely to the development of helmet typologies and the history and technology of weapons. There, Greeks dedicated arms taken as booty from their Greek or other enemies and in later periods their own weapons (Snodgrass, 1967: 48). These helmets are often found with their cheek-pieces and nose-guard bent, evidence for the end of their use and dedication to the Gods (Jackson, 1992; see discussion in Whitley, 2011). It is now clear that enormous numbers of arms could be dedicated in sanctuaries: Herodotus (8.274-5) records 2000 shields at the temple of Apollo

⁹ According to Rapp (1999) the term *provenience* means the precise location where an artefact was recovered, and *provenance* is the locality of the artefact, site, quarry, mine, deposit or coherent and bounded geological feature that is the origin of the artefact's raw material. In this text, provenance is used in a broader sense as the place of production, rather than the origins of the raw materials, unless otherwise stated.

dedicated by the Phocians (in Whitley, 2008); the Archaic temple at Isthmia had received over 200 helmets by 470 BC (Jackson, 1992), and about 860 helmets have been found so far in Olympia (Frielinghaus, 2007; Whitley, 2011). At Olympia, arms are mainly found buried in wells or in the stadium walls, where they were disposed of after their dedication at the sanctuary. Unless helmets carry datable inscriptions of dedication, difficulties with dating such material are obvious, as these artefacts were used as dedications for an unknown length of time and then they were discarded. The archaeological context from which helmets are excavated thus has no actual chronological association (see also Snodgrass, 1967: 13) constituting a major problem for the development of a tight typological/chronological sequence and provenance of Greek helmets. Uncertainties on the length of the use of a helmet before deposition¹⁰ and if helmets were passed from father to son or from brother to brother in later periods (Snodgrass, 1967: 59) further complicate chronological associations.

It may be possible that in the Athenian army helmets were passed on but this practice contradicts the hypothesis that armour was made to fit. Technically, one cannot easily enlarge the size of a helmet, which is already very thin-walled. During the Archaic period in northern Greece, this surely is not the case, as the local burial customs necessitated the burial of the armour with the deceased, resulting in a single owner and consequently offering more secure dating sequences based on the associated pottery or other grave goods. The Archaic period burials excavated within the broader region of Macedonia, Ochride and by the Thermaikos gulf, such as Thermi, Aghios Athanasios, Nea Myhaniona, and Sindos, Nea Philadelphia, Aghia Paraskevi and Archontiko near Pella helmets from which are studied here, demonstrate similar burial traditions (Misailidou-Despotidou, 2003:31) (Figure 5.1). Male warriors were buried with all their offensive and defensive weapons (Sismanidis, 1987), including gold items such as masks and breastplates; decorative gold leaf strips originally attached onto clothes, helmets, shields, swords and spears; jewellery; and other objects, such as bronze and clay vessels, clay figurines, faience objects and metal cart models (Chrysostomou and Chrysostomou, 2001).

¹⁰ When looking at earlier helmets of the Mycenaean period and the Dark Ages, Snodgrass (1967: 32) notes that an example of the boar's tusk helmet from Kallithea was found in a context dated two centuries after the main period of use of this type of helmet. For Snodgrass, this explains the survival of this old-fashion helmet type in the Iliad, where Homer describes a similar type helmet that Meriones gives to Odysseus (X:261-5, cited in Snodgrass, 1967: 32). Interestingly, this helmet was owned by six different people before it was given to Odysseus, the first time being stolen and then given as a valuable gift (Ο μ ἦ ρ ο υ Ι λ ι ᾶ δ α : 10.266-271).

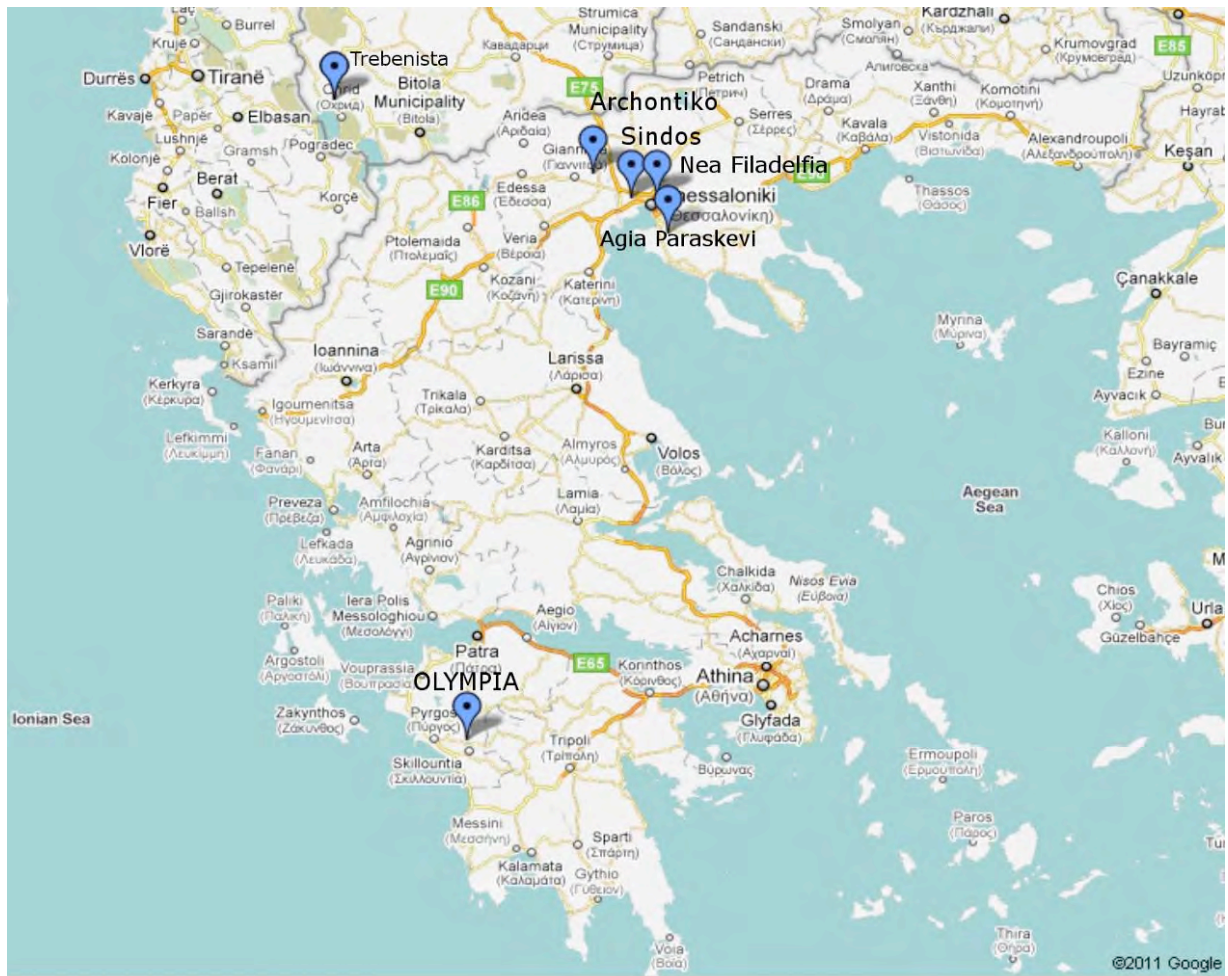


Figure 5.1: Map of part of Greece showing places mentioned in this text.

The Archaic burials excavated at Archontiko revealed grave goods of an outstanding aesthetic and social value dated from the first half of the 6th c. BC to the beginning of the 5th c. BC (Chrysostomou and Chrysostomou, 2000, 2001; Chrysostomou and Chrysostomou, 2002; Chrysostomou and Chrysostomou, 2003). This extraordinarily rich cemetery is associated with a settlement built in the centre of Bottiaia, one of the most important urban centres in the region until the end of the 5th c. BC, when Pella became the new capital of the Macedonian kingdom (around 410 BC) (Chrysostomou and Chrysostomou, 2001). Similar finds were unearthed at Aghia Paraskevi (excavated by K. Sismanidis) and Nea Philadelphia (excavated by V. Misailidou-Despotidou). Misailidou-Despotidou dates the Archaic parts of Aghia Paraskevi cemetery from the second quarter of the 6th c. to the first half of the 5th c. BC (575-450 BC, but 570-500 BC according to Sismanidis (Sismanidis, 1987)). Nea Philadelphia mainly dates from the mid 6th c. to the second quarter of the 5th c. BC (550-475BC) (Misailidou-Despotidou, 2003:33). This period is defined as Middle and Late Archaic Period (*ibid.* 24). Both cemeteries belonged to settlements in the vicinity of Thessaloniki, at a short distance from the Thermaikos gulf (Figure 5.1). Sismanidis (Sismanidis, 1987, 1988) argues

for a relatively large population because of the large number of graves (more than 400 were excavated in 1987) dated to within a short 70 year span. Sindos (excavated by Aik. Despini), dated to a similar period, is the first excavated cemetery of a richness comparable to other cemeteries at Thermaikos and Trebenista (or Trebenische) (Vokotopoulou *et al.* 1985; Pflug, 1988a). There is a lot of pottery from southern and eastern Greece which permits the dating of the graves (Misailidou-Despotidou, 2003). However, there are problems of anachronism, such as aryballoi dated to 575-550 BC which at Sindos were found in graves dated to 540 BC (Vokotopoulou *et al.*, 1985) 245-246). The same type aryballoi were found at the West cemetery of Archontiko (Chrysostomou and Chrystostomou, 2002) complicating precise dating of individual graves.

During the Archaic period, people living in the colonies, ports or mainland Macedonia had cultural links with the Aegean and the south of Greece, especially during the first decades of the 6th c. BC, with documented links to Corinth, Attica, Ionia and Egypt (Chrysostomou and Chrysostomou, 2002). The large production centres in these regions directly influenced production in Macedonia, especially regarding pottery, metals and coinage (Misailidou-Despotidou, 2003). There is evidence for the growth of local metal workshops in the north of Greece (Chrysostomou, *pers. com.* 2002), leading Moustaka (2000) to advocate a local Macedonian production of the late Illyrian type helmet (after the mid 6th c. BC), the earliest examples of which are found in Sindos. During this period, there is a marked increase in mobility of Greek warriors, growth of professionalism and employment of mercenaries (Sage, 1996: xix), which would involve transportation of helmets and widening of the geographical distribution of helmet types. Apart from some artistic evidence on pottery, there is little evidence about the organisation of armour manufacture (see 5.8.2). Snodgrass (1967: 64) notes that especially for the period starting with the introduction of the hoplite, '*the marked growth of regionalism allowed for considerable local variations in the style of his various equipment, especially the helmet*'. Despite the observed regional stylistic developments, such as the Apulian-Corinthian helmets, scientific evidence to support geographical distribution and growth of regional helmet workshops is absent. Overall, these factors influence understanding of their distribution and the accuracy of current helmet typology/chronology, which is 'stylistic' based rather than it is derived from a clearly and closely datable sequence of archaeological deposits.

5.2.2. HELMET TYPOLOGY AND TECHNOLOGICAL EVOLUTION

The technologies employed for the manufacture of Greek helmets evolve since their first occurrences, and continue during the entire Archaic period (end 8th – mid 5th c. BC) and

beyond. Developments in manufacturing methods are accompanied by changes in form and decoration and reflect technological progress in metalworking (Pflug, 1988b). In addition to an ‘organic’ evolution based perhaps on functional criteria, there is noticeable regional variation of finds responsible for the parallel development of sub-forms and type variants (Snodgrass, 1967). Marked changes in the shape and appearance of helmets, associated with technological changes, include the use of cast parts, the degree of hammering or the use of foil/plated decoration.

Apart from few fragmentary Mycenaean examples, the earliest finds of Greek metal helmets date to the end of the Geometric period (late 8th c. BC) (Snodgrass, 1967). This period sees the development of three most likely contemporaneous variants of the *kegelhelm* (Figure 5.2), which is a cone-shaped type with cheekpieces and it is composed of five metal sheets that are riveted together (for the development of the types see Pflug, 1988a). Pflug (1988a) sees the *kegelhelm* as an independent invention of Greek craftsmen originating in Peloponnesus, although some stylistic influence from Assyria is evident (see Snodgrass, 1967: 43; Dezcö, 1998). It remains unclear if these ‘oriental’ style Geometric helmets were produced in Argos, as has been suggested (Pflug, 1988a).

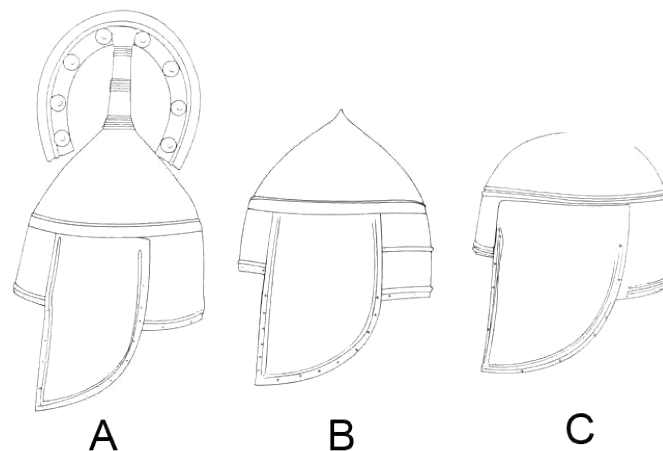


Figure 5.2: Variants of the *Kegelhelm* (Geometric Helmet) (Pflug, 1988a).

The Illyrian and Corinthian types predominate during the Archaic period in Greece and are seen as independent developments after the turn of the 8th c. BC (Pflug, 1988b). The Corinthian type in particular has influenced the modern idea of the ancient Greek helmet, which is seen as a heroic attribute (Pflug, 1988c). For these reasons, and due to the abundance of material evidence, the study focuses on these two types. A review of their technological evolution is presented below, primarily based on Snodgrass (1964, 1967), Pflug (1988a,b,c,d,e) and Kunze (1961, 1967).

5.2.2.1. The Illyrian type

The Illyrian type helmet has a rectangular face opening and characteristic crest-track on the crown. The crest-track has parallel ridges running lengthwise over the crown and functions as a support for the attachment of an organic crest¹¹ and for increasing the mechanical stability/strength of the crown (Snodgrass, 1967: 52; Pflug, 1988b). The equally balanced distribution of Illyrian and Geometric helmets in the western Peloponnesus and the striking parallels in shape support the idea that the Illyrian helmet is an independent development deriving from the *Kegelhelm* (Snodgrass, 1964: 18-20; Pflug, 1988b), although connections to an earlier Cretan open-faced helmet have been made (Kunze, 1958; Hoffmann, 1972). Evidence as to when the transition from *Kegelhelm* to Illyrian helmets took place is ambiguous. The leading hypothesis is that it starts at the turn of the 8th c. BC, with the earliest example being a helmet made in two halves discovered in a grave in Kalavryta approximately dated to the first half of the 7th c. BC (Snodgrass, 1964: 57; Kunze, 1967). The development of the Illyrian helmet is parallel to the Corinthian type. Three phases are identified based on technological and stylistic changes (Figure 5.3).

Helmets of the Early Phase (Type I), both variants A (in one piece) and B (in two pieces), consist of an evenly hammered thin bronze sheet. The edge around the helmet is strengthened by a bulge and carries a row of rivets, perhaps for the attachment of the now disintegrated helmet lining¹² (Pflug, 1988b). A row of rivets is also found on other contemporary defensive weapons. The distance between the rivet-holes changes systematically through time, a characteristic potentially significant for dating (Jarva, 1995: 65-72). Lack of significant numbers of excavated helmets of the different variations means that helmets of this phase cannot be put in a clear chronological order and a clear transition to the middle phase is not detectable (Pflug, 1988b).

The Middle Phase (Type II) starts with depictions of the Illyrian type on pottery in the last quarter of the 7th c. BC. It has a curved profile and consists of a thin hammered bronze sheet. The crest-track on the crown becomes more noticeable due to ridges that are more elevated.

¹¹ Pictorial evidence shows that an organic crest was stretched over the crown and hooked (with metal pins) into holes at the end of the crest track. Material evidence of a crest is not reported in the archaeological literature.

¹² Material evidence of organic parts of a helmet, such as the inner padding or lining, organic decoration under the rivet row found at some helmets or the crest track is extremely rare. Pseudomorphic evidence of leather used as lining is reported in a mid-6th c. BC bronze-decorated iron Bandhelm helmet from Sardis (Greenewalt and Heywood, 1992). A fibrous felt-like material is reported on an Illyrian type helmet at Harvard (HUAM 1972.55, McNamara, 2002). Felt as a lining material is first mentioned in the *Iliad* (X:265).

The walls of the crown curve slightly inwards at the sides, making it a stylistically independent element. The wide neckguard curves outwards and is visually distinguished from the cheekpieces; this is enhanced by the deep side cuts near the ear areas, which separate the neckguard from the cheekpieces. The presence of these 'side cuts' develops parallel to the Corinthian helmet and predominates since the 7th c. BC. Engraved decoration is rare. The only decoration on the Illyrian helmets of the Middle Phase consists of a row of wide-headed rivets situated around the edge of the helmet. Material evidence supports the attachment of an organic component (bone or ivory) for decorative purposes (Manti unpublished, Helmet A2002 G194, Pella). It is suggested that more elaborated examples would have silver rivet heads similar to Corinthian examples (Pflug, 1988b). The distribution of Type II reflects the expanding trade of Greek cities in the Adriatic Sea (Illyria and SW Balkans), resulting in the development of new variants, which may indicate the development of new workshops or better trade networks (*ibid.*).

Most excavated Illyrian type helmets date to the Late Phase. They are characterised by a solid, thick metal sheet and a less curvy form with an almost horizontal neckguard. The cheekpieces are visually separated from the neckguard by either deep side cuts (Type III A) or rounded ear openings (Type III B) (Pflug, 1988b). The former is influenced by the contemporary Corinthian types and the latter, which is relatively rare, by the Chalkidian types. This influence becomes stronger in the 5th c. BC (Figure 5.4) (Kunze, 1967). The general uniformity in shape during this phase (especially Type III A.2) is seen as evidence of an organised production geared towards making large numbers of helmets (*ibid.*).

The late phase Illyrian Type III A has three main variants: (1) with rivet row around the edge; (2) with punched decoration around the edge imitating rivets; and (3) with no edge decoration (Moustaka, 2000). According to Pflug, the transition from variant 1 to 2 may be connected to requirements for faster production and to the increased thickness of the metal sheet used, which would make the drilling of rivet-holes more time consuming (Pflug, 1988b). Variant 3 is seen as an independent group with its own line of development because of its main distribution around Thessaloniki (e.g. Sindos, Mikro Karabournaki) and Trebenista (second half of 6th c. BC) (*ibid.*). Examples of decoration include engraving and the use of silver foil (Type III A.1), such as on the helmet in the British Museum (Hockey *et al.*, 1992) and on display in Olympia. Macedonian coins depict 5th c. kings wearing Illyrian type III A.2 helmets (Snodgrass, 1967: 116; Pflug, 1988c; Moustaka, 2000). This, and the distribution of this type support a local production in Illyria itself or the broader Macedonian region in northern Greece (Moustaka, 2000).


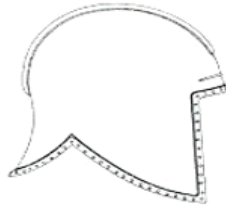



Phase I - Early form	End of 8th – 3rd quarter of the 7th c. BC	c. 735-625 BC	<p>Type I</p>  <p>Variant A Helmet in two parts riveted together perpendicularly</p>
			<p>The horizontal edge of the forehead runs parallel to the neckguard. Oval or stretched profile. The crown is semicircular in profile and continues without interruption into pointed cheekpieces of varied shapes. Drilled holes may be present at the edge of the cheekpieces although this is more common in later types. Often the main ridge of the crest-track is flanked by two smaller ones. There is a strengthening bulge at the rim and a row of rivets at the rim border.</p> <p>Variant B Helmet in one part</p>
Phase II - Middle Form	Last quarter of the 7th – mid 6th c. BC	c. 625-550 BC	<p>Type II</p>  <p>Variant A With bulge at the rim</p>
			<p>The walls curve slightly inwards at the sides of the crown, making the crown a more independent element. A wide neckguard curves outwards and is separated from the cheekpieces by deep cuts near the ear. There is a more distinguishable crest-track with elevated ridges and a row of rivets around the rim.</p> <p>Variant B Without rim-bulge; from first half of the 6th c. BC, co-exists with variant A</p>
Phase III - Late Form	Mid 6th – 4th c. BC	c. 550 BC onwards	<p>Type III A</p>  <p>Variant 1 With rivets around the edge</p>
			<p>A less curvy form with clear stylistic separation of the cheekpieces from the neckguard and an almost horizontal neckguard.</p> <p>Variant 2 With punched rivet row (edge decoration)</p>
			<p>Variant 3 (Macedonian Group) With smooth edge (no rivets)</p> 
			<p>Type III B</p>  <p>Variant 1 With rivets</p>
<p>As Type IIIA, but with ear openings. Influenced by the Chalkidian type.</p> <p>Variant 2 With punched edge decoration</p>			

Figure 5.3: Illyrian type helmets: summary of typological and chronological development. Based on information in Pflug 1988e, Snodgrass 1967, Kunze 1967, Moustaka 2000, figures from Moustaka, 2000.

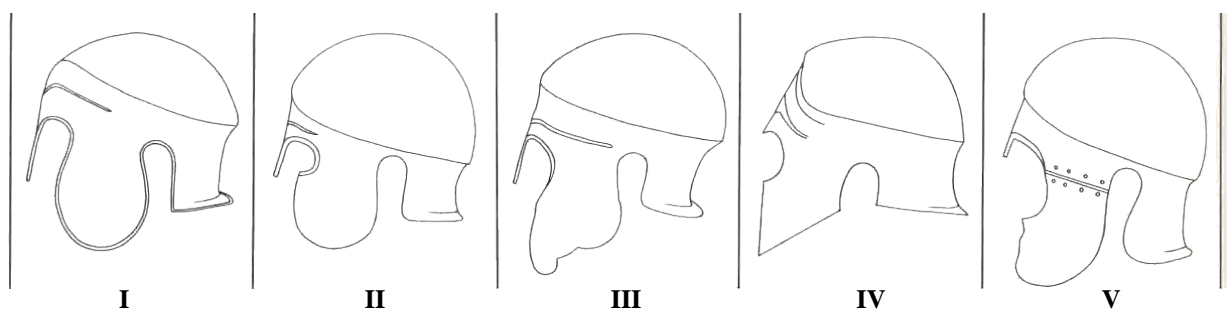


Figure 5.4: Chalkidian type helmet variants. This type starts appearing in the mid 6th c. BC. Although Kunze (Kunze, 1994) places its origins at Chalkis, Euboia (and named it accordingly), its distribution focuses on *Magna Grecia*, hence arguing for a southern Italian origin. Figure from (Pflug, 1988d).

5.2.2.2. The Corinthian type

The Corinthian type helmet covers the head completely. The only openings are around the eyes and mouth, giving it a mask-like appearance (Pflug, 1988c). Just like other helmets named after Greek cities, the helmet from ‘Corinth’ is claimed to have a Peloponnesian origin and was soon produced at several places in Greece and *Magna Grecia* (Kunze, 1961). This could explain the growth of numerous variants that make it difficult to fully understand the development of this type (Pflug, 1988c). Scholars agree on three main developmental phases, although terminology and chronology of subgroups vary between researchers. Figure 5.5 summarises the main developmental characteristics and subgroups, based on Snodgrass (1964), Pflug (1988d) and Kunze (1961), and information from Benton (1943), Hencken (1971) and Jackson (2004).

During the Early Phase (Type I), helmets have straight sides and back and are robust in both style and technology (Pflug, 1988c). Like the early Illyrian helmet, Corinthian helmets are made in one part (Type I A) or two parts (Type I B). Early variants have an embryonic nose guard (Snodgrass, 1964). Small holes around the rim can be present, but decoration would be based on the attachment of a plume, as evidenced from depictions on decorated pottery. Since the first half of the 7th c. BC, the helmet is more voluptuous, shorter at the neck and has a visual distinction between the front and the back (Pflug, 1988c). Less commonly, a crest-track is present on the crown, an influence from the Illyrian type (Kunze, 1961).

The Middle Phase (Type II), starting in the second half of the 7th c. BC, sees an extraordinary plethora of shapes, styles, and quality both in mainland Greece and *Magna Grecia*. Helmets of this period are heavy, seem to have a polished surface and are characterised by very precise execution (Pflug, 1988c). In typological terms, the most important aspect is the shape of the crown, which can be (1) rounded or (2) with a slight kink just below the crown, making it more distinct. This type is generally adopted towards the mid of the 6th c. BC and continues to

develop into the next phase (Pflug, 1988c). A further element of subdivision is the presence of a 'side gusset' between the neckguard and the cheekpieces, which can be (3) a stepped lateral gap or (4) a pointy/triangular gusset. Helmets with wide pointy gussets (i.e. 4) are seen from the second quarter of the 7th c. BC, whilst the last examples with stepped lateral gaps (i.e. 3) were made around the second quarter of the 6th c. BC. Both forms (1 and 2) can be found with pointy gussets or a stepped lateral gap (elements 4 and 3 respectively) (Snodgrass, 1964). Characterisation based on these features makes grouping of helmets difficult; for this reason, helmets examined for this thesis are annotated with numbers 1-4 to indicate the presence of each feature. The Myros Group, which develops around the mid 7th c. BC and dominates until the second quarter of the 6th c. BC, is a heavy chunky cast helmet with characteristic rim decoration and stepped gusset (Kunze, 1961). The considerable thickness of the metal promoted embossing rather than hammering of the edge rim (Pflug, 1988c). A combination of round form, pointy cuts, rim decoration, embossed eyebrows and decoration on the forehead defines the Lotus Flower Group (*ibid.*). Eyebrows become more pronounced on helmets from Puglia (first third of 6th c. BC), which continue until the development of the Apulian-Corinthian type which prevails during 600-566 BC.

The Late Phase (Type III) sees a plastic separation of the crown created by a more pronounced kink; this is used until the end of the helmet's development. The noseguard becomes thinner and longer and there is a variety of cheekpiece shapes. Two main groups are defined based on the shape of the kink at the front over the forehead. This can be lambda-shaped (Λ -shaped), as in the Lamia and Hermione Groups that emerge simultaneously around 530 BC, or V-shaped, which predominates in southern Italy from the third quarter of the 6th c. BC (Pflug, 1988c). Helmets of this phase show a tendency towards lighter armour. The crown and sides are generally very thin and the helmet has a fraction of its former weight. Helmet-smiths achieved the necessary rigidity of the increasingly thin sheet by including ridges and stepped ridges at the edges. The decreased protection granted by the sometimes amazingly thin sheet of the crown was counterbalanced by a new kind of kinked shape, eventually resulting in a pronounced kink forming a central ridge at the front of the crown. The end product of these technological innovations was a light helmet with a plastically detached crown and elastic cheek-pieces which allowed the wearer flexibility (Pflug, 1988c).

Compositional data and metallurgical studies of Corinthian type helmets overall are scarce and summarised in section 2.1.4 and Table 5.7 in section 5.8.3.



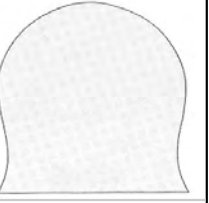





<p>Early Phase I</p>	<p>Early to mid 7th c. BC c. 700-650 BC</p>	<p>Features</p> <p>By the 1st half of the 7th c. BC, helmets become curvier and have a shorter neckguard, which is increasingly visually separated from the cheekpieces.</p> <p>Early transition style: Corinthian helmet with crest-track and small embryonic noseguard. Main style: they fall steeply at the back, exhibit small side gusset, neckguard curves very slightly outwards, low eyeholes.</p>	<p>Variant A Helmet in one piece</p>  <p>Variant B Helmet in two pieces</p> 
<p>Middle Phase II</p>	<p>Second half of 7th c. – mid 6th c. BC c. 650-550 BC</p>	<p>Features</p> <p>Defined separation of the neckguard and cheekpieces by 'side cuts', which progressively move towards the centre of the sides; the voluminous crown increasingly becomes an independent element. The forehead and noseguard are heavier, the noseguard longer. The Lotus Flower Group with protruding eyebrows combines styles 2 and 3.</p> <p>During the 6th c. it continues to develop with more prominent plastic division of the crown from the rest of the helmet</p>	<p>Form of Crown</p> <p>1. Rounded Crown</p>  <p>2. With angular kink at the crown</p>  <p>Type of sides cuts</p> <p>3. with stepped gap e.g. the Myros Group, (650-550 BC)</p>  <p>4. with pointy gusset (650-500 BC)</p> 
<p>Late Phase III</p>	<p>Mid 6th c. BC onwards c. 550 BC onwards</p>	<p>Features</p> <p>The defining elements are the separation of the crown and the general move to lighter armour; helmets are lighter in weight and style. The angular kink/stepped crown predominates. Two main groups are based on the type of gusset on the forehead; they exist simultaneously from c. 530 BC for more than 50 years.</p>	<p>Λ-shape gusset</p> <p>V-shape gusset (since the 3rd quarter of 6th c. BC, predominantly found in southern Italy)</p> <p>Hermione Group Lamia Group</p>  

Figure 5.5: Stylistic development of Corinthian Helmets. Images from Pflug, 1988d, drawings Kunze, 1961

5.3. STYLISTIC CATEGORISATION OF INVESTIGATED HELMETS

The review of published helmet typologies reveals that a plethora of forms were adopted since the first appearances of the bronze helmet, which can be associated to technological changes. Early helmets are constructed of joint sheets of bronze. Solid one-piece bronze helmets replace this practice by the mid 7th c. BC. Stylistic and technical features show that the degree of hammering and casting employed on a helmet varies between different periods and helmet types. The tendency to move from heavy chunky helmets (e.g. Myros Group) to thinly hammered light helmets (e.g. Late Phase III) is indicated for Corinthian types. Shaping by hammering would involve cycles of annealing. The mode of hammering and the final production step affect bronze hardness and flexibility. Typological evolution could have been the result of technical innovations for adapting to faster production and lightweight protection. Whether these technological choices are related to surface finishes and corrosion is yet to be examined.

A broad typological and chronological classification of the investigated helmets (Table 5.1) was established based on the review of published stylistic associations summarised in Figure 5.3 and Figure 5.5, because typological evolution of helmets is linked to technological changes, which could impact surface finishes and corrosion. This also places the examined helmets in a broader archaeological context. Subgrouping of Corinthian helmets was complex, because stylistic criteria currently used to define subgroups require refinement. Especially in the case of subgrouping Phase II Corinthian type helmets, criteria such as the profile of the crown or the shape of the side gusset is confusing, as these features can co-exist on a helmet. Yet, a combination of these criteria is not identified in the literature as to form an independent stylistic category or subgroup. Typological characterisation of the Illyrian type helmets was easier to follow, but there are disagreements regarding the sequence and chronology of helmets from Sindos (Vokotopoulou *et al.*, 1985; Pflug, 1988b; Moustaka, 2000) which influences the overall categorisation of the Phase III Illyrian subgroups. More inconsistencies were identified during the course of typological characterisation of the helmets, but a further or an exhaustive discussion of typology and chronology is beyond the remit of this thesis. Further details on individual helmets are in Appendix 1 and some are included in publications mentioned earlier. Those from the National Museum of Wales and the Ashmolean Museum are published in Joubert (1923) and Vickers (1981; 2002) respectively.

Type	Phase	Variant	Museum/ Excavation	Acc. No.	Excavation	Archaeological Context	Helmet or Context Date	Helmet Code	Typology Code	
Attic	Attic 550-475 BC	-	Arch.Mus. Pella	A2002G189	Archontiko	Field Taousanidi, pit grave 189, 14/6/2002	550-475 BC (Chrysostomou 2003)	PE4	ATT	
Chalkidian	III	-	Arch.Mus. Olympia	B5239	Olympia	Not available	-	OL79	CH_III	
	V	-	Arch.Mus. Olympia	B7080	Olympia	Not available	-	OL66	CH_V	
Corinthian	(I) Early 700-650 BC	A	Arch.Mus. Olympia	ab34	Olympia	Not available	-	OL17	COR_IA*	
				ab64	Olympia	Not available	-	OL21	COR_IA	
				B2608	Olympia	Not available	-	OL29	COR_IA	
				B2648	Olympia	Not available	-	OL31	COR_IA*	
				B10534	Olympia	Not available	-	OL41	COR_IA*	
				Nat.Mus. Wales	47.409_cat36	Unknown	De Walden Collection	-	NMW11	COR_IA
					47.409_7.26	Unknown	De Walden Collection	-	NMW2	COR_IA
		47.409_7.39	Unknown		De Walden Collection	-	NMW5	COR_IA		
		47.409_7.40	Unknown		De Walden Collection	-	NMW6	COR_IA		
		A with crest	Arch.Mus. Olympia	B10527	Olympia	Not available	-	OL69	COR_IA.crest	
			Nat.Mus. Wales	47.409_7.36	Unknown	De Walden Collection	-	NMW4	COR_IA.crest	
		(II) Middle 650-550 BC	1.3.	Nat.Mus. Wales	47.409_7.33	Unknown	De Walden Collection	-	NMW3	COR_II.1.3
				1.3. Myros	Arch.Mus. Olympia	B9805	Olympia	Not available	-	OL27
	B10528		Olympia			Not available	-	OL58	COR_II.1.3.Myros	
	B6131		Olympia			Not available	-	OL65	COR_II.1.3.Myros*	
	B6960		Olympia			Not available	-	OL80	COR_II.1.3.Myros*	
	Nat.Mus. Wales		47.409_7.24			Unknown	De Walden Collection	-	NMW1	COR_II.1.3.Myros
	1.4.		Arch.Mus. Olympia	B7073	Olympia	Not available	-	OL44	COR_II.1.4.	
				B1501	Olympia	Not available	-	OL46	COR_II.1.4.*	
				B10526	Olympia	Not available	-	OL57	COR_II.1.4.*	
				Nat.Mus. Wales	47.409_7.41	Unknown	De Walden Collection	-	NMW7	COR_II.1.4.
	47.409_7.42		Unknown		De Walden Collection	-	NMW8	COR_II.1.4.		
	1.4. Myros		Nat.Mus. Wales	NMW_877	Unknown	De Walden Collection	-	NMW9	COR_II.1.4.Myros	
	1.4. with crest/nose		Arch.Mus. Olympia	B10518	Olympia	Not available	-	OL_B10518	COR_II.1.4.crest/nose*	
				B4150	Olympia	Not available	-	OL68	COR_II.1.4.crest/nose*	
	2.4. with edge bulge		Arch.Mus. Olympia	B4411	Olympia	Stadium, North Wall, Well 13 (in	-	OL49	COR_II.2.4.edge*	
				B4698	Olympia	Not available	-	OL50	COR_II.2.4.edge	
		B6550		Olympia	Not available	-	OL53	COR_II.2.4.edge		
		B5178		Olympia	Stadium, North Wall, Well 23,	-	OL75	COR_II.2.4.edge*		
Pitt Rivers		1884.32.16		Unknown	Unknown	-	PR1	COR_II.2.4.edge		
(III) Late 550 BC onwards		2.4. V with eyebrows		Arch.Mus. Olympia	B4799	Olympia	Not available	-	OL70	COR_III.2.4.V
				Arch.Mus. Olympia	B5177	Olympia	Not available	-	OL63	COR_III.2.4.V.Lotus
	Arch.Mus. Olympia		B5070	Olympia	Stadium, North Wall, Well 21, 17/10/1960	-	OL71	COR_III.2.4.Λ.edge*		
B5167		Olympia	Stadium, North Wall, Well 21, 17/10/1960	-	OL73	COR_III.2.4.Λ.edge*				
B5176		Olympia	Stadium, North Wall, Well 14, 2/12/1959	-	OL74	COR_III.2.4.Λ.edge*				

Type	Phase	Variant	Museum/ Excavation	Acc. No.	Excavation	Archaeological Context	Helmet or Context Date	Helmet Code	Typology Code
Etruscan	Etruscan	-	Pitt Rivers	1884.32.15	Unknown	Unknown	-	PR4	ETR
Illyrian	(I) Early 735-625 BC	B	Arch.Mus. Olympia	B3348	Olympia	Not available	-	OL4	IL_IB
		(II) Middle 625-550 BC	A	Arch.Mus. Pella	A2002G194	Archontiko	Field Taousanidi, pit grave 194, 10/7/2002	550-475 BC (Χρυσσοστόμου, 2003)	PE2
	A with forehead ridge		Arch.Mus. Thessaloniki	MΘ16405	Aghia Paraskevi	T322, 8/3/1990	575-550 BC (Σισμανίδης, 1987)	AP4	IL_IIA (forehead)
				MΘ16423	Aghia Paraskevi	T325, 8/3/1990	575-550 BC (Σισμανίδης, 1987)	AP5	IL_IIA (forehead)
	(III) Late 550 BC onwards	A.1	Arch.Mus. Olympia	B7170	Olympia	Not available	-	OL11	IL_IIIA1
				B4821	Olympia	Not available	-	OL5	IL_IIIA1*
				B5115	Olympia	Not available	-	OL9	IL_IIIA1*
			Arch.Mus. Pella	A2001G10	Archontiko	Field Taousanidi, pit grave 10, orygmata 3, 24/6/2001	550-475 BC (Χρυσσοστόμου, 2003)	PE1	IL_IIIA1*
				A2001G9	Archontiko	Field Taousanidi, pit grave 9, orygmata 2, 24/6/2001	550-475 BC (Χρυσσοστόμου, 2003)	PE3	IL_IIIA1
			Arch.Mus. Thessaloniki	MΘ8563	Sindos	T111	430 BC (Βοκοποπούλου, 1985)	S9	IL_IIIA1*
		Fitzwilliam	GR.B.5	Unknown	Unknown	-	FZ2	IL_IIIA1	
		A.2	Arch.Mus. Thessaloniki	MΘ16603	Aghia Paraskevi	T349, 8/10/1990	575-550 BC (Σισμανίδης, 1987)	AP6	IL_IIIA2*
				MΘ23115	Nea Philadelphia	Not available	550-450 BC (Μισσηλίδου-Δεσποτίδου, 2003)	NF5	IL_IIIA2*
		A.3	Arch.Mus. Olympia	BE58	Olympia	Not available	-	OL13	IL_IIIA3*
	Arch.Mus. Thessaloniki			MΘ9119	Aghia Paraskevi	T14	575-550 BC (Σισμανίδης, 1987)	AP1	IL_IIIA3*
			MΘ8561	Sindos	T E1	425-420 BC (Μουστάκα, 2000)	S1	IL_IIIA3	
	Nat.Mus. Wales		47.409_cat27	Unknown	De Walden Collection	-	NMW10	IL_IIIA3	
B.1	Arch.Mus. Olympia	B4667	Olympia	Not available	-	OL78	IL_IIB1		

Table 5.1: Details and typological sequence of helmets included in this thesis. * notes helmets within a subgroup that are almost identical.

Figure removed for copyright reasons.

Figure 5.6: Investigated Corinthian type helmets presented according to their stylistic grouping.

Figure removed for copyright reasons.

Figure 5.7: Investigated Illyrian type helmets presented according to their stylistic grouping.

5.4. MACROSCOPIC EVIDENCE OF SHAPING AND DECORATION

A general qualitative assessment of shape, wall and noseguard thickness and weight of the Corinthian helmets agrees with broad technical changes cited in the published typologies, and facilitates characterisation of the typology/chronology of the helmets examined. For example, some helmets in the Corinthian-Myros group are characteristically thick and heavy and are reported in the literature to be cast due to their thickness; Late Phase III Corinthian helmets are characteristically lightweight with thin walls and are described to be heavily hammered to shape. Macroscopic technical observation of 58 and the x-radiography of 17 helmets (Table 5.2) were undertaken to provide bulk evidence of manufacture prior to metallography and to preliminarily examine if hammering and/or casting were employed for the shaping of different subgroups of helmet types through time as indicated by their typological grouping.

Type	Phase	Variant	Museum/ Excavation	Archaeological Context	Acc. No.	Helmet or Context Date	Helmet Code			
Corinthian	(I) Early 700-650 BC	A	Nat.Mus. Wales, Unknown	De Walden Collection	47.409_7.26	-	NMW2			
					47.409_7.39	-	NMW5			
	47.409_7.40				-	NMW6				
	47.409_cat36				-	NMW11				
		A with crest	Nat.Mus. Wales, Unknown	De Walden Collection	47.409_7.36	-	NMW4			
	(II) Middle 650-550 BC	1.3.	Nat.Mus. Wales, Unknown	De Walden Collection	47.409_7.33	-	NMW3			
					1.3. Myros	Nat.Mus. Wales, Unknown	De Walden Collection	47.409_7.24	-	NMW1
					1.4.	Nat.Mus. Wales, Unknown	De Walden Collection	47.409_7.41	-	NMW7
								47.409_7.42	-	NMW8
1.4. Myros					Nat.Mus. Wales, Unknown	De Walden Collection	NMW_877	-	NMW9	
Illyrian	(II) Middle 625-550 BC	A with forehead ridge	Arch.Mus.Thessalonikis, Aghia Paraskevi	T322, 8/3/1990	MΘ16405	575-550 BC (Σισμανίδης, 1987)	AP4			
	(III) Late 550 BC onwards	A.1	Arch.Mus.Thessalonikis, Sindos	T111	MΘ8563	430 BC (Βοκοτοπούλου et al, 1985)	S9			
						575-550 BC (Σισμανίδης, 1987)	AP6			
		A.2	Arch.Mus.Thessalonikis, Aghia Paraskevi	T349, 8/10/1990	MΘ16603	550-450 BC (Μισσηλίδου- Δεσποτίδου, 2003)	NF5			
						Not available	MΘ23115	425-420 BC (the grave, Μουστάκα, 2000)	S1	
		A.3	Arch.Mus.Thessalonikis, Sindos	T E1	MΘ8561					
		Nat.Mus. Wales, Unknown	De Walden Collection	47.409_cat27	-	NMW10				
	Arch.Mus.Thessalonikis, Aghia Paraskevi	T14	MΘ9119	575-550 BC (Σισμανίδης, 1987)	AP1					

Table 5.2: Details of x-radiographed helmets.

5.4.1. EVIDENCE OF CASTING: CORINTHIAN TYPE HELMETS

Optical evidence of casting includes metal shrinkage and cast decoration, features which are predominantly evident on Corinthian helmets of the Middle Phase II (c.650-550 BC) (e.g. OL80, OL68). A thick noseguard, which in one case is c. 6.5 mm thick (NMW1, Corinthian-

Myros) is in itself evidence of casting, and often carries cast decorative features such as ridges (e.g. OL_B10518) or further fine quality punched decoration (Figure 5.8, a, b, OL68). Metal shrinkage due to casting is observed on the noseguard of helmet OL68 (Middle Phase II) (Figure 5.8, c) and a dendritic bronze microstructure is observed with naked eye on the thick crown of helmet OL80 (Corinthian-Myros) (Figure 5.8, d). In fact, the presence of dendritic microstructure indicates that OL80 is entirely cast and left in the as-cast state without further work hardening or annealing. Work hardening and annealing would have changed the dendritic as-cast bronze microstructure and resulted in homogenisation of the bronze. Observation of helmets from the Corinthian-Myros group did not reveal visible evidence of hammering on the crown and upper parts of the cheekpieces. However, the crown of other Myros helmets (NMW1, NMW9) is noticeably thinner than their noseguard and rims, which is observed even during basic visual examination. Assuming that the difference in thickness within a helmet is evidence of thinning due to hammering, this indicates that a combination of casting followed by hammering could have been employed for shaping these helmets.



Figure 5.8: Examples of cast features on helmets. (a) Cast noseguard and decoration (OL_B10518). (b) Cast and punched decoration on noseguard (OL68). (c) Casting shrinkage and crude filing marks at the back of noseguard (OL68). (d) Dendritic microstructure on the crown of OL80 (Myros group) emphasised by corrosion.

A small number of x-radiographed Corinthian type helmets including the Myros NMW1 and NMW9 confirm that areas of a helmet such as the crown were subjected to different degrees of hammering between helmets; some helmets also show evidence of moderate hammering at the cheekpieces (Figure 5.9). The degree of hammering varies within different areas of a helmet. The extent of hammer blows is manifested by the uneven thickness of the bronze sheet seen in the X-rays as variation in density (Lang, 1997: 41), which is distinct from corrosion. An unusual circular feature and very crude changes in thickness are observed at the crown of NMW2 (Figure 5.9). The circular feature is a result of past restoration that employed soldering of pieces that were not original to the helmet, and which was not detected prior to x-radiography. NMW3 (Early Phase I), and NMW5 and NMW8 (Middle Phase II, contemporaneous to Myros) seem to have been subjected to relatively intense hammering (Figure 5.9), and have a thin noseguard, which in other examples from these periods can be as thin or less than 0.1cm (e.g. OL44, OL_B6777).

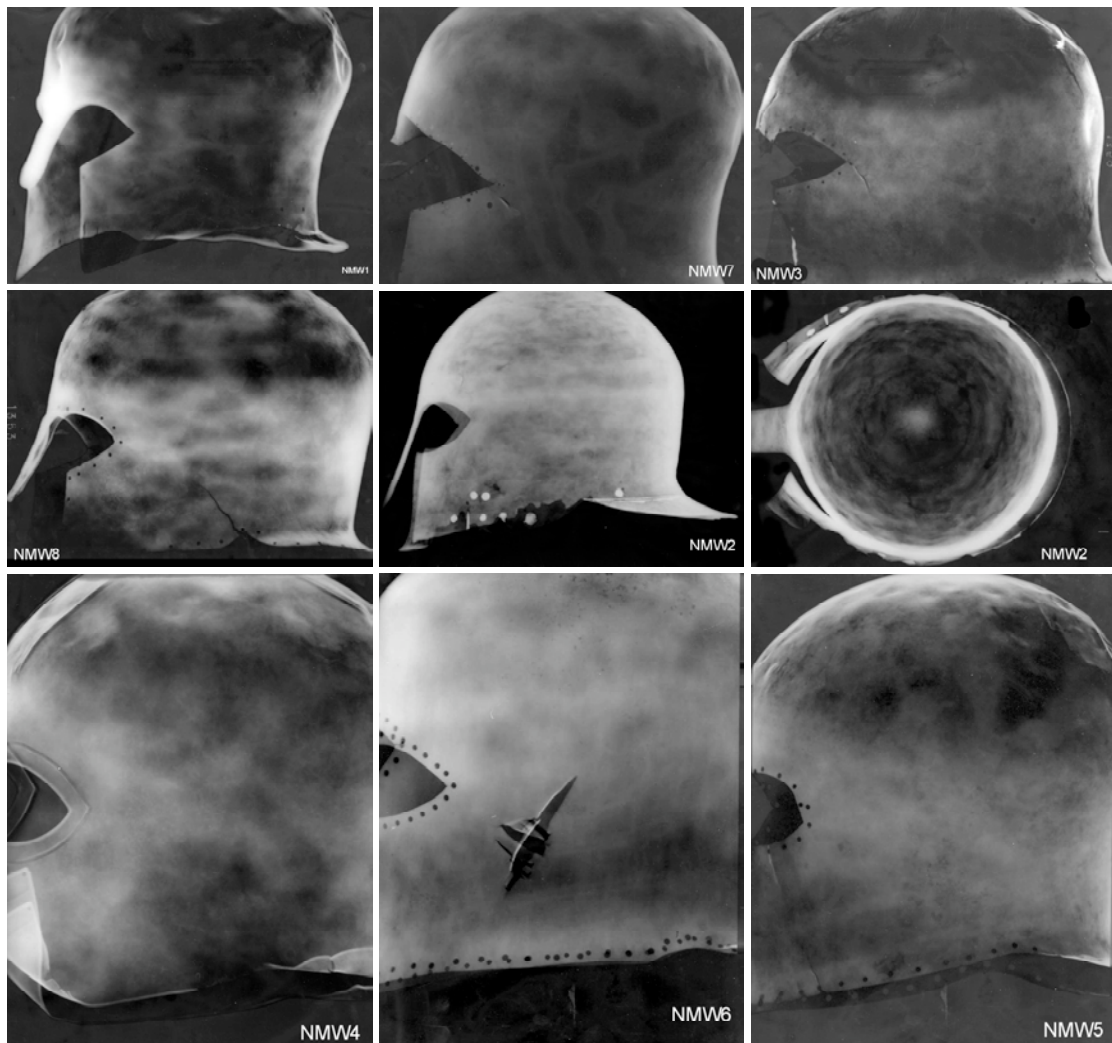


Figure 5.9: X-Radiographs of selected Corinthian type helmets.

Investigation shows that shaping of Corinthian type helmets of different or even the same stylistic variant involved an abundance of techniques such as hammering, casting or both employed on the same helmet. The examined Corinthian-Myros helmets show evidence for shaping by casting alone (OL80), and indications that a degree of hammering was employed followed casting (NMW1, NMW9). Samples from two other Corinthian-Myros helmets (OL27 and OL58) were selected for metallographic examination to further investigate if more helmets of the Myros group were formed entirely by casting without any apparent work hardening as is the case of OL80.

5.4.2. EVIDENCE OF HAMMERING: ILLYRIAN TYPE HELMETS

Evidence of hammering for shaping and decoration is most often observed at the inner of helmets, when not covered by thick corrosion deposits. For example, shaping of the Illyrian helmet PE2 involved the use of tool with a rectangular tip as evidenced from the c. 3 mm¹³ wide rectangular tool-marks on the inner of the right cheekpiece and crest-track ridge of the helmet (Figure 5.10). The Illyrian type helmet is thought to be shaped entirely by hammering (Snodgrass, 1967), and the majority of the helmets with clear visible evidence of hammering here are of the Illyrian type (Figure 5.10a,b). Overall, hammering was employed from the inner side of the helmets for shaping, for raising ridges at the edge of a helmet, for the formation of the crest-track at the crown of Illyrian types (e.g. helmets AP5, PE2). Traditionally, the metal being raised rests on a soft material such as a piece of hardwood, sandbag or pitch for securing the piece *in situ* to withstand blow, but in the case of punching designs, this is done on a hard bed to offer resistance to the punch impact (Untracht, 1969:89; 96). The uniform and precise hammering of the crest-track, which is especially observed on the Illyrian type of the Late Phase III, may suggest that hammering out of the crest-track ridges was undertaken in a mould or on a shaped anvil. Only helmet PE2 has tool marks at the outer side of the high ridge at the crest-track, indicating that it was formed by hammering from both the inner and the outer side. Literature suggests that hammering of the edges of a helmet leading to its thickening (bulge) is an organic process during the raising process (Pflug, 1988c) because it improves rigidity and resistance to shock, which helps retention of shape during hammering (Untracht, 1969:248).

¹³ Measurement was taken from calibrated digital image using ImageJ software.



Figure 5.10: Examples of hammering work on helmets. (a) Hammering tool marks at the inner side of cheekpiece of Illyrian type helmet PE2. The tool used was approximately 3mm wide and was applied on the surface in a relatively regular manner. The ridge found at the edge is hammered out from the inner side of the helmet. (b) Hammering marks formed during working of the edge (AP5). (c) Tool marks at the outer side of high ridge on the crown of helmet (PE2). (d) Cheekpiece in the shape of the head of a ram shaped by the *repoussé* technique (OL79). (e) Inner side of *repoussé* decoration on cheekpiece (OL78).

Helmets OL78 (Illyrian III B.1) and OL79 (Chalkidian III) show *repoussé* decoration on their cheekpieces in the shape of a ram's head (Figure 5.10, c, d). *Repoussé* work involves the use of shaped punches and a hammer to raise portions of metal sheet into relief from the back, and it is often combined with chasing (hammering from the front) (Untracht, 1969:93; 97). *Repoussé* and chasing tools are often similar, and are worked with hammer blows held at different angles. Punched decoration is achieved with the use of punch or stamping tools that

have sharply engraved designs at their end, creating a raised imprint of the design from a single blow (*ibid.* 89). An example of this technique is seen on OL68, which carries precisely punched row of decorative circles at the edge of the noseguard (Figure 5.8, b). Other examples show a careless punching of rim decoration, including on helmet FZ2 and where the punched designed is not aligned in a straight line (Table 5.1, Appendix 1).

X-radiography of the crown of selected Illyrian type helmets from Sindos, Aghia Paraskevi and Nea Philadelphia which belong to a more tight chronological period, showed evidence of distinctive hammering styles (Figure 5.11). Helmet S9 suffers from substantial corrosion. Helmets AP6 and NF5, which are of the same stylistic subgroup (Late Phase III, A.2) show distinct relative crude hammering occurring in a concentric manner (Figure 5.11, AP6, NF5), whereas helmets AP1 (Late Phase III, A.3) and AP4 (Middle Phase II, A with forehead) show a much finer hammering execution and an overall hammering style. Hammering in a concentric manner is typical for hammered bowl-shaped bronze artefacts (Craddock, 2009: 158). Fine voids visible in the X-rays of these helmets are likely to be pitting corrosion rather than casting porosity because of their spatial distribution. Both AP1 and AP4 are excavated from the same cemetery and are dated to the same period (575-550 BC, Sismanidis, 1987), but they are assigned to different typological groups based on published stylistic rather than strictly technological criteria. In this case, the similarities in hammering style could be a more effective grouping factor compared to stylistic observations to provide information on production workshops.

Helmet S1 (Late Phase III A.3), which was found in a grave dated to later context 425-420 BC (Moustaka, 2000) shows evidence of casting porosity on the crown and cheekpieces, which is in agreement with the unusually thick walls and heavy weight of this late Illyrian type helmet (Figure 5.12). Casting porosity is unlikely to be found on well-wrought and annealed objects (Lang, 1997:41). Due to the pristine condition of the helmet, a sample could not be taken to examine its metallurgy, which would verify these observations.

So far, literature supports that Illyrian type helmets are shaped entirely by hammering. This is based on the x-radiography and metallography of a small number of helmets in isolated studies (Hoffmann, 1972; Smith, 1972; Hockey *et al.*, 1992; McNamara, 2000). Evidence of casting porosity in helmet S1 is significant as it is the first documented example of a cast Illyrian type helmet and it provides new evidence to understand the technologies involved in their making. X-radiography in this case demonstrates that manufacturing evolution of the Illyrian type helmet is more complex than is currently thought.

A systematic scientific investigation is necessary to reveal manufacturing details that can be placed in a chronological and geographical context. This relatively small number of examples demonstrates the value of x-radiography in understanding manufacturing styles that could provide technological evidence to form the basis for the identification of production workshops of different helmet types in the Archaic period Greece.

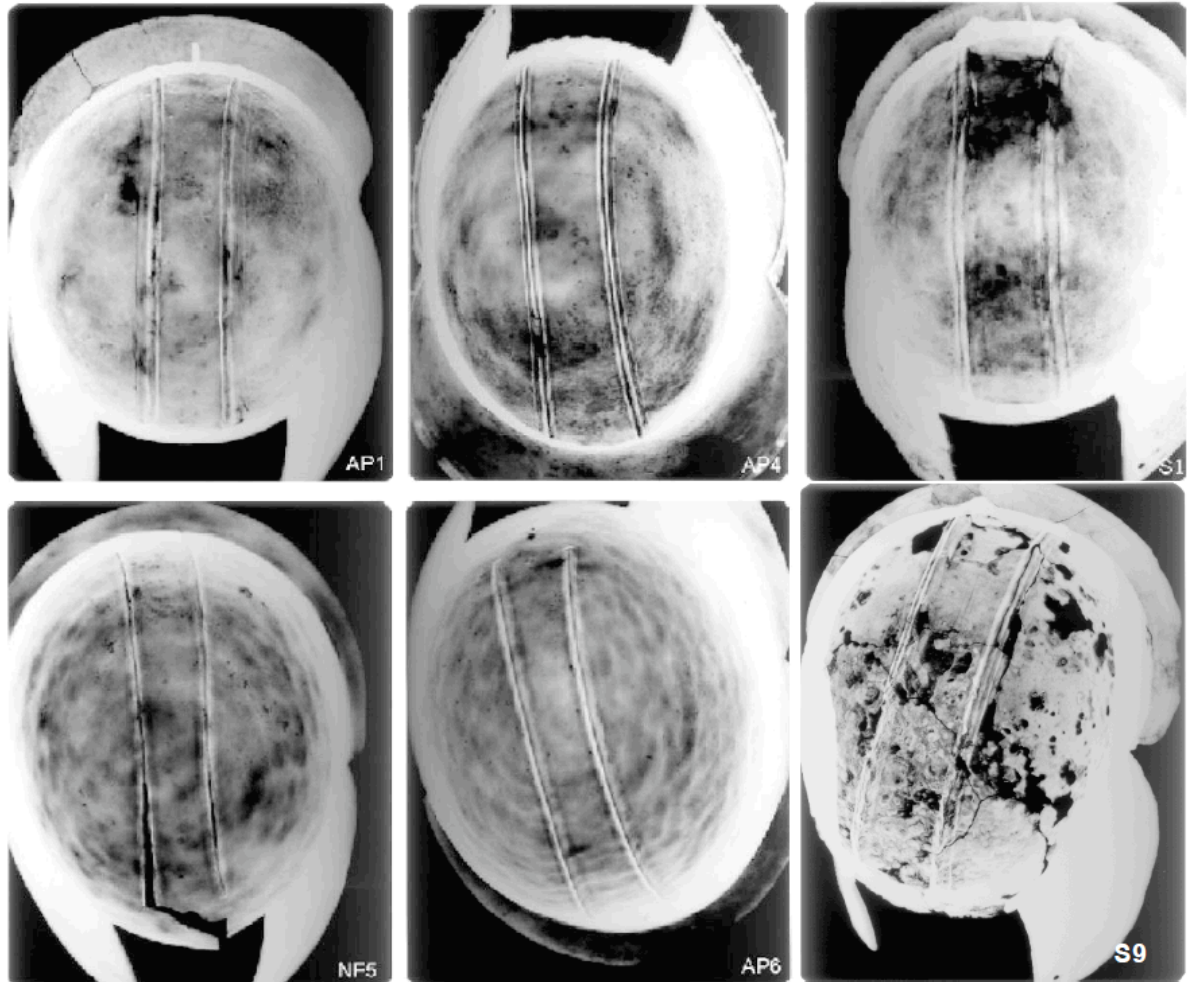


Figure 5.11: X-radiographs of the crown of selected Illyrian type helmets.

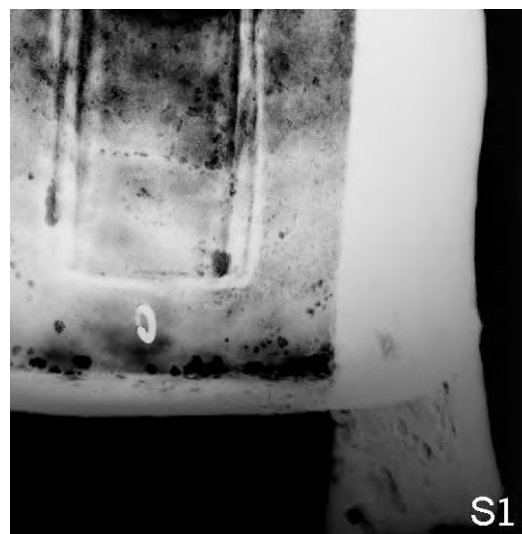


Figure 5.12: X-radiograph of Illyrian Type helmet S1 showing casting porosity

5.5. THICKNESS AND POSITION OF SAMPLES ON HELMETS

Macroscopic examination demonstrated that sample position on a helmet is critical regarding the metallurgical information they carry, because a combination of casting and hammering was in cases employed or because the degree of hammering may differ within a helmet. For example, samples from the noseguard of Late Phase III Corinthian type helmets may not be representative of the bulk shaping method of a helmet, because the crown is often much thinner likely due to hammering. Samples were thus not removed from noseguards because they do not represent the bulk shaping method of a helmet. Sampling positions were controlled predominantly by the principle of minimal visual change and the condition of each helmet, and were removed from a range of areas (Table 5.3), including the cheekpieces (x4 samples), the crest-track (x4), the crown (x12), the neckguard (x7), the side (x3) and a small number of loose fragments from unknown positions (x5). Such sampling strategy of arbitrary sample locations provides a relatively random statistical population (Reedy and Reedy, 1988) and can be used to detect broad technical changes in helmet shaping through time. Due to the rarity of Illyrian type helmets from the Early Phase I and Middle Phase II, only a small statistically insignificant number of samples were available; this limits comprehensive understanding of its manufacturing development over time.

The thickness of each sample was measured from polarised microscopic digital images of mounted polished cross-sections using ImageJ software; at least three measurements were taken along each section and were averaged (Table 5.3). The thickness of the samples varies greatly between helmets ranging $170\text{-}1150 \pm 10\mu\text{m}$. The thinnest sample derives from the crown of Late Corinthian OL70 and the thickest from the side of Corinthian-Myros helmet OL27. Plotting the thickness against position of samples from Corinthian type helmets, irrespective of their variant/chronology, shows that there is no systematic relationship between sample position and its thickness (Figure 5.13). This further supports the arbitrary nature of the examined samples.

Results show a systematic change in thickness observed through the evolution of the Corinthian type helmets. The thickness of samples from Corinthian type helmets declines in time, with the exception of OL27 Myros helmet in the Middle Phase (II), which shows elevated thickness (Figure 5.14, left). A similar trend is marginally seen at samples of the Illyrian type but it cannot be verified due to the small number of samples from Phase I and II (Figure 5.14, right). Results confirm literature and macroscopic observation of a trend to lightweight thinner Corinthian type helmets over time.

Type/Phase	Typology Code	Sample	Position on Object	Av. Thick. (um)
Attic	ATT	PE4.3	neckguard , upper	790
Etruscan	ETR	PR4.1	side , lower	805
Chalkidian				
III	CH_III	OL79.1	unknown , loose fragment	540
V	CH_V	OL66.2	crown , middle back	565
Corinthian				
(I) Early	COR_IA	OL21.1	neckguard , lower part	500
		OL29.1	crown , top	600
	COR_IA*	OL17.1	cheekpiece , right, middle	550
		OL31.1	crown	850
		OL41.1	cheekpiece , right	600
COR_IA.crest	OL69.1	crown , top, by the high ridge	800	
(II) Middle	COR_II.1.3.Myros	OL27.1	side	1150
		OL58.1	unknown , loose fragment	800
	COR_II.1.4.	OL44.1	neckguard , left	380
	COR_II.1.4.*	OL46.1	neckguard , top	840
		OL57.1	unknown , loose fragment	510
	COR_II.2.4.edge	OL50.1	crown , rear	330
		OL53.1	neckguard , upper left	760
		PR1.1	crown , front	550
	COR_II.2.4.edge*	OL49.1	crown , rear	275
		OL75.2	crown	625
(III) Late	COR_III.2.4.V	OL70.1	crown , middle back	170
	COR_III.2.4.V.Lotus	OL63.1	unknown , loose fragment	175
	COR_III.2.4.Λ.edge*	OL71.1	side , right	300
		OL73.1	neckguard , upper	350
		OL74.1	unknown , loose fragment	565
Illyrian				
(I) Early	IL_IB	OL4.2	crown , top	910
(II) Middle	IL_IIA	PE2.2	crest-track , middle small ridge	700
		AP4.2	crest-track , high ridge	240
	IL_IIA (forehead)	AP5.1	neckguard , lower part	230
(III) Late	IL_IIIA1	OL11.1	cheekpiece , right, middle	500
		PE3.1	crown , top, by the high ridge	n.m.
	IL_IIIA1*	OL5.1	crown , upper left	350
		OL9.2	crest-track , left ridge, back	650
		PE1.1	crest-track , high ridge	320
	IL_IIIA3*	OL13.1	cheekpiece , right, low part	400
	IL_IIIB1	OL78.1	crown , front, lower	420

Table 5.3: Details of the position and thickness of samples removed from 36 helmets for metallurgical investigation and examination of surface finishes. Average section thickness ($\pm 10\mu\text{m}$).

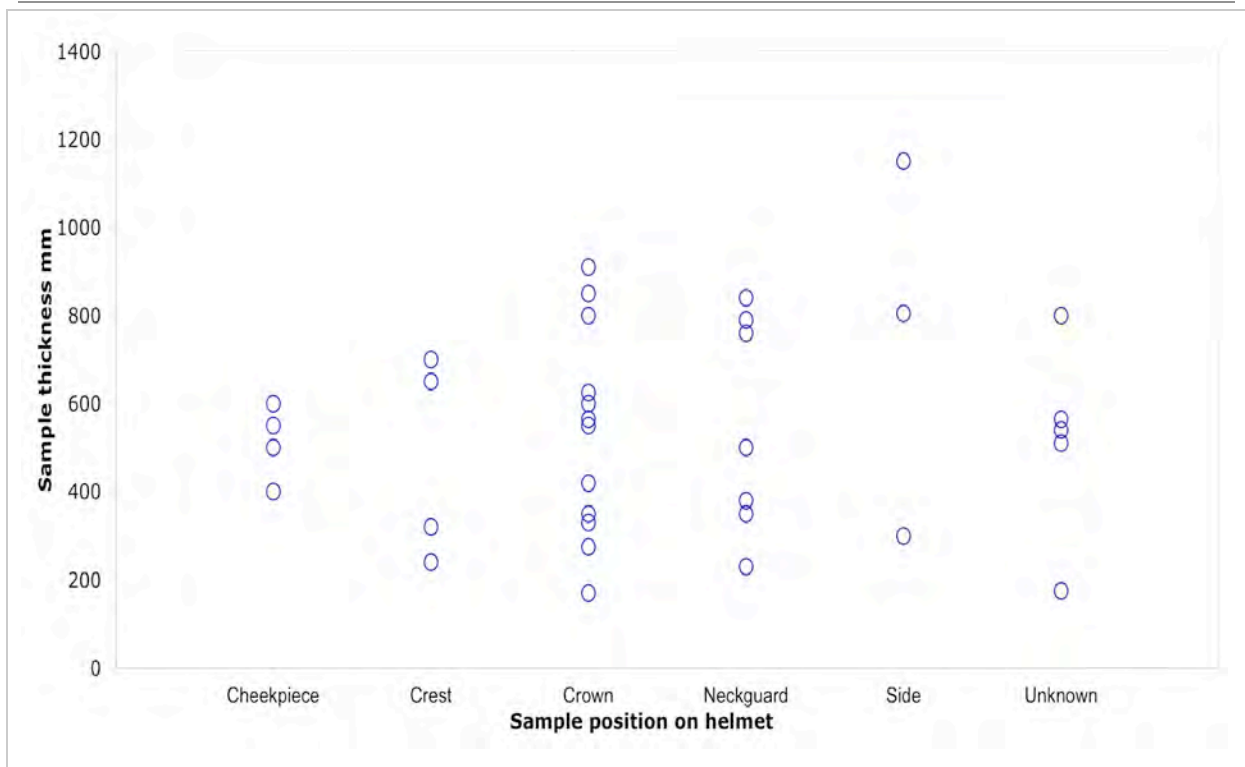


Figure 5.13: Graph showing sample position of individual samples and their average thickness (μm). Details of plotted data are found in Table 5.3. The plot shows that sample thickness does not strictly depend on their position on a helmet.

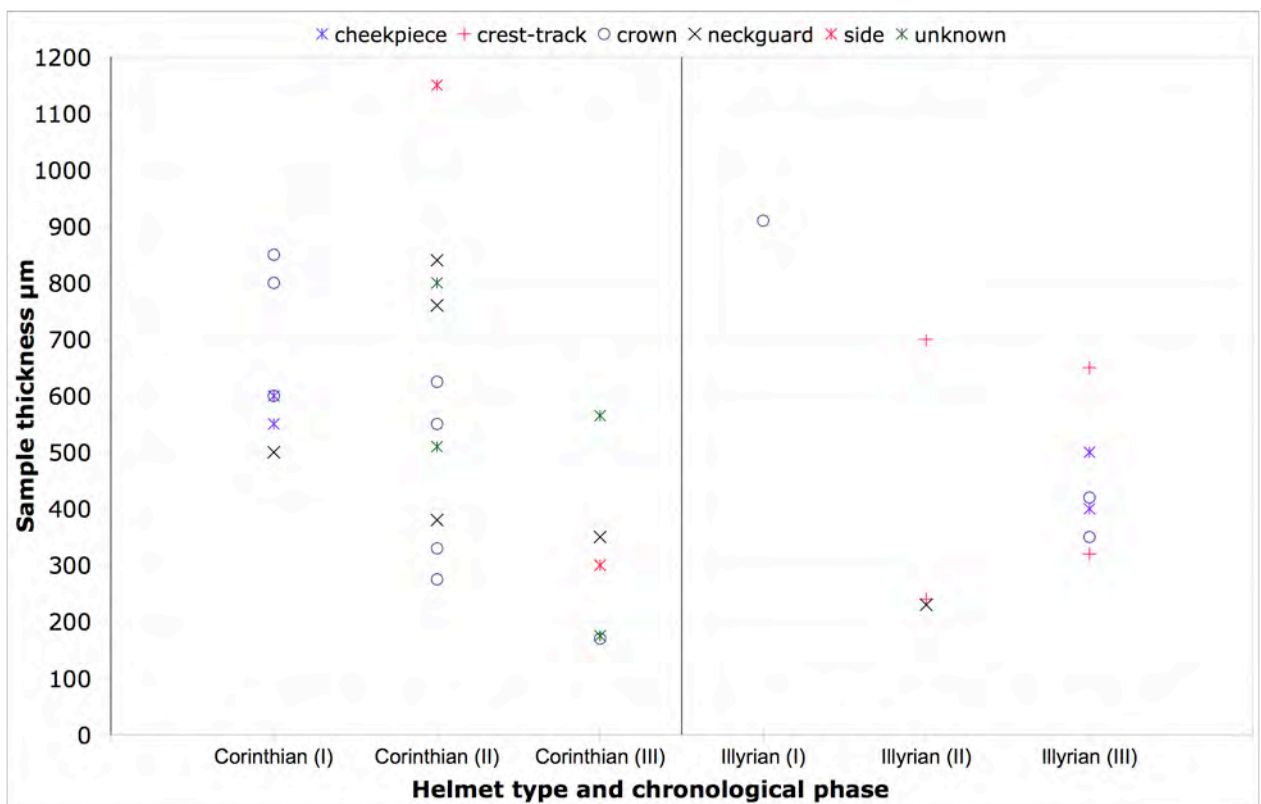


Figure 5.14: Graph showing sample thickness as a function of helmet type and chronological phase. Left: Corinthian helmets showing trend to move from thicker to thinner helmets, with the exception of a Myros Group outlier in the Middle Phase II. Right: Illyrian type helmets follow a similar broad trend, but interpretation is hindered by the small number of samples from Phase I and II.

5.6. METALLOGRAPHIC INVESTIGATION OF MANUFACTURE

Metallurgical investigation of helmet manufacture was undertaken using polarised microscopy on mounted cross-sectioned etched samples and, non-destructively using time-of-flight neutron diffraction on a small number of helmets (NMW2, NMW11) and helmet fragments (OL79, OL63, PE1, PE2). During hammering, secondary phases and inclusions in the bronze become elongated and align in the direction of the metal flow (Hosford, Jonas, Leslie, 1985: 686), and the bronze grains align to a preferred crystallographic orientation even if the initial grains are oriented at random (Hu, 1985: 693). Texture, describes this preferential alignment of the crystalline lattice of the grains in a metal and short annealing at low temperatures that results in recovery stage only has little change in texture (Chin, 1985: 700). Texture analysis can therefore provide an indication of the degree of cold hammering (see section 3.8.1.3). Neutron diffraction analysis thus aimed at the non-destructive characterisation of selected intact helmets and evaluation of the degree of hammering via texture analyses of the diffraction patterns (Manti and Watkinson, 2007). Experimental details are reported in sections 3.4 and 3.8.2.1 respectively.

5.6.1. POLARISED MICROSCOPY AND SEM-EDX MAPPING

The majority of samples have small inclusions in the bronze, which in most cases are elongated to the direction of hammering (Table 5.4). Larger inclusions tend to be dissolved by etching suggesting that they are Cu_2O (cuprite) inclusions, while the very fine thin elongated or round inclusions are black in BFPM and un-affected by etching indicating that are particles of CuS (Figure 5.15). A small amount of sulphur in the bronze further provides an indication on the type of ore used (e.g. chalcopyrite). Elongation of inclusions supports that the sampled helmet areas where intensively hammered.

Several helmet samples exhibit a fibrous microstructure due to intensive directional hammering, which is evident by the presence of corrosion bands in the core of samples parallel to the surface of the helmet (OL9.2, OL11.1, OL29.1, OL69.1, PE1.1, PR1.1). This banding is revealed either naturally by corrosion (Figure 5.16, a) or due to preferential chemical attack after metallographic etching (Figure 5.16, b) (Scott, 1991:9; Bailey, 1982:30). SEM-EDX mapping of PE1.1 shows bands depleted in tin relative to the rest of the bronze, a feature that is not revealed by metallographic etching likely due to insufficient etching (Figure 5.17). Such uneven banded distribution of tin can be the result of intensive hammering and may explain the preferential banded corrosion observed in other samples (Figure 5.16). This

indicates that extensive hammering can result in banding of alloying elements, which in turn can affect corrosion of the core, and possibly the surface appearance of a sample. In a published example, banding due to intensive hammering of a 10 wt% Sn Greek bronze shield (5th c. BC) was interpreted to be the reason for the fine white/grey cassiterite layer present on the surface (Colacicchi-Alessandri and Ferretti, 2002). Evaluation of hammering and annealing processes is hence important as they could affect corrosion processes and the appearance of corroded low-tin bronze.

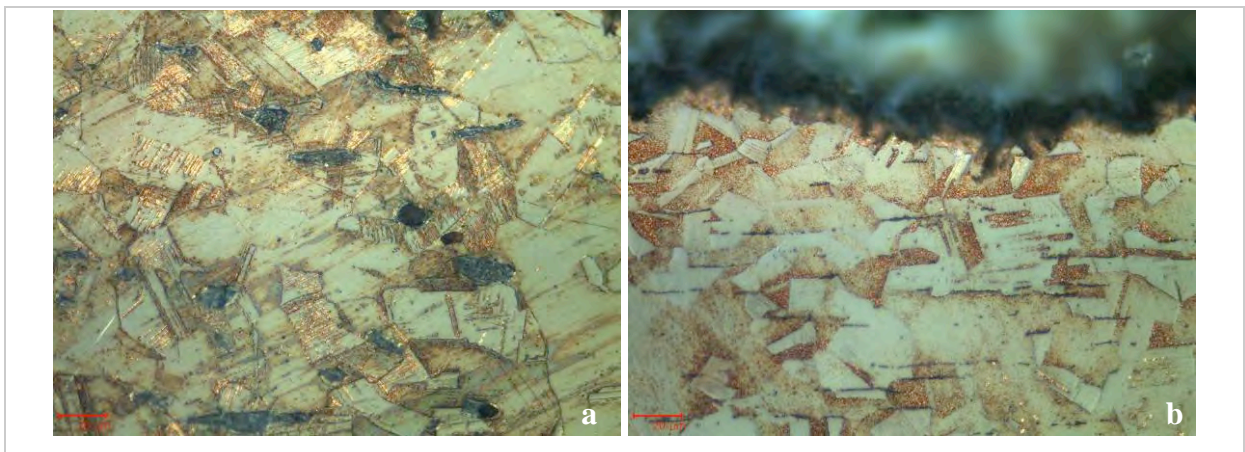


Figure 5.15: BFPM images of etched cross-sections showing types of inclusions present in the bronze. (a) Large roundish and elongated inclusions in OL78.1. (b) Fine elongated inclusions in OL71.1.

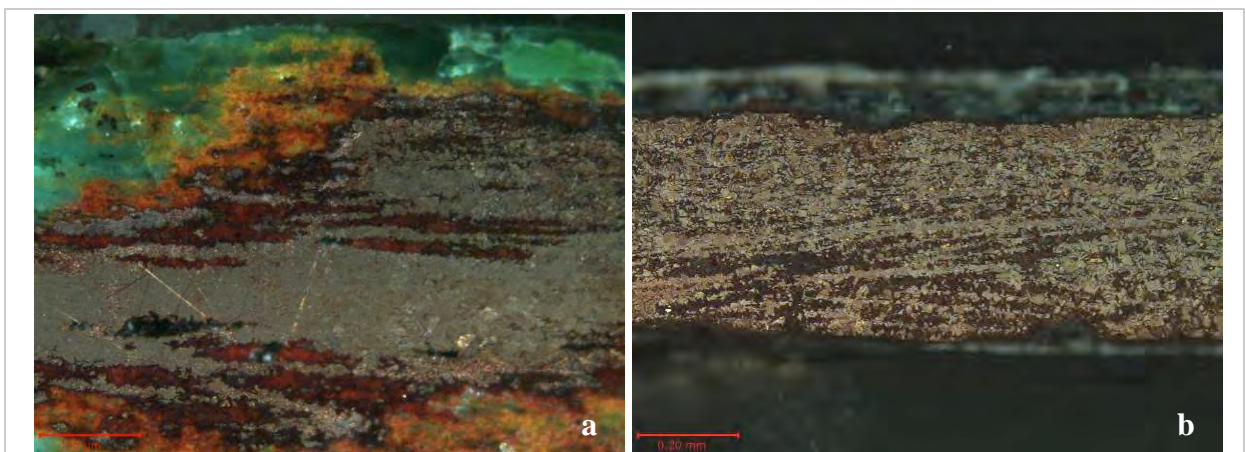


Figure 5.16: Bright field polarised (BFPM) images showing examples of fibering or banding in the core of cross-sectioned samples due to extensive directional working. (a) OL11.1 showing cuprite bands parallel to the surface of the helmet. (b) PR1.1 with exposed banding after metallographic etching.

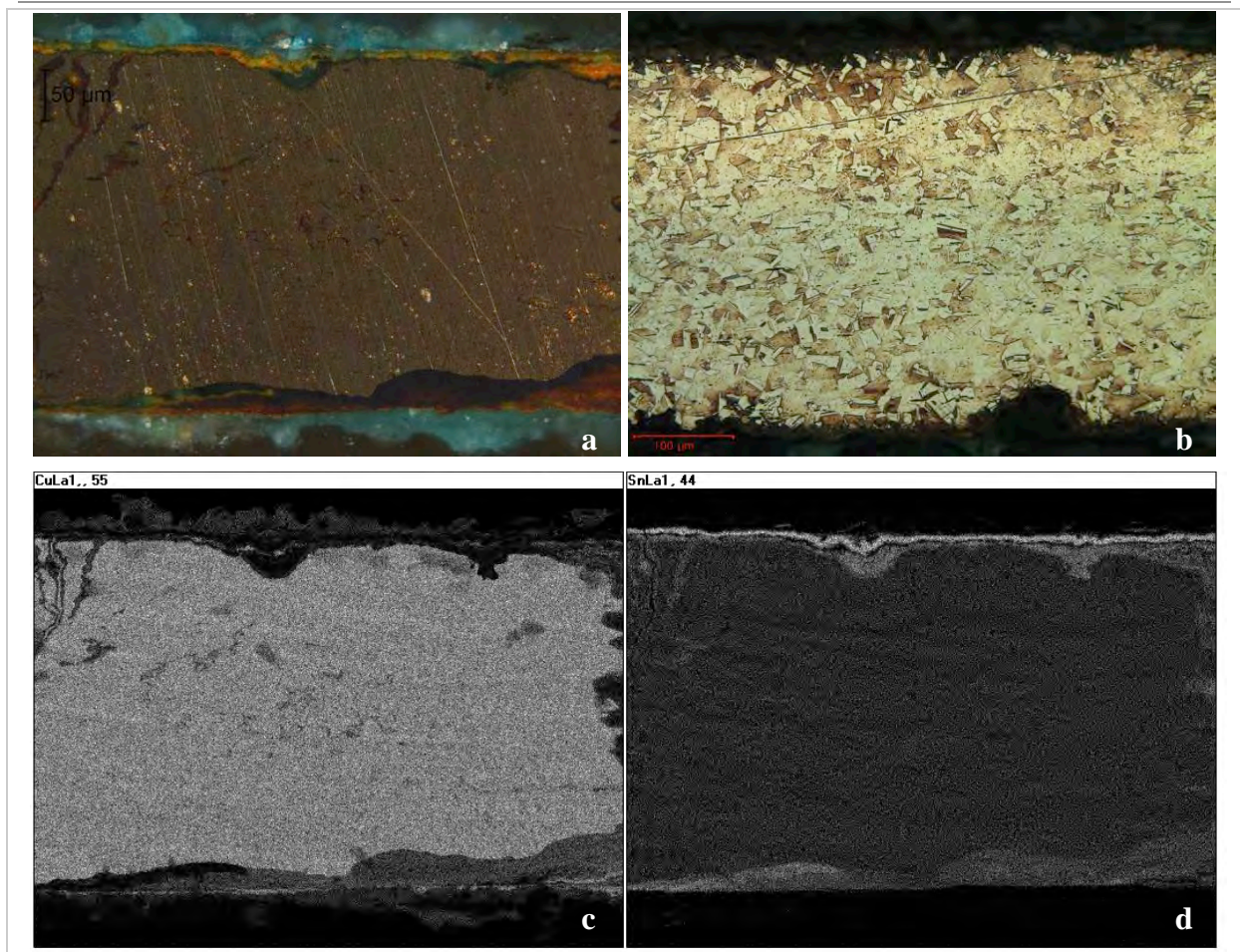


Figure 5.17: Cross-sectioned sample PE1.1 showing uneven compositional distribution due to extensive hammering. (a) BFPM image of polished section. (b) BFPM image after etching revealing a worked and annealed microstructure but not fibering. (c) SEM-EDX map for CuLa. (d) SEM-EDX map for SnLa showing directional bands depleted of tin.

5.6.2. TIME-OF-FLIGHT NEUTRON DIFFRACTION AND TEXTURE ANALYSIS

Texture analysis of non-destructive time-of-flight neutron diffraction data collected from a small number of helmet samples was undertaken using published experimental reference materials (Siano *et al.*, 2006). Pole figures show evidence of bronze crystallite preferred orientation (Figure 5.18) OL79.1 has a weaker texture compared to PE2.1 and PE1.1, which show moderate texture due to hammering (Kockelmann, *pers. com.*). This confirms the hypothesis above that the uneven banded distribution of Sn observed at the core of PE1.1 is the result of intensive hammering (Figure 5.17). The higher crystallite randomisation seen in the pole figure of OL79.1 could also be the result of recrystallisation occurring during annealing of a heavily worked microstructure. Further analyses and characterisation of the peak shape in the neutron diffraction pattern is required to determine if the piece was annealed at its final manufacture stage and is underway. Analyses of the peak shapes of selected neutron diffraction patterns (Figure 5.19), which was based on published calibration

curves (Siano *et al.*, 2006), shows that helmet NMW2 was left in the as-cast state. NMW6 has much narrower diffraction peaks indicating a much higher degree of homogenisation. Both helmets lack characteristic micro-strain broadening signature imparted by a final hardening step. This indicates that annealing was the last stage of manufacture of NMW6.

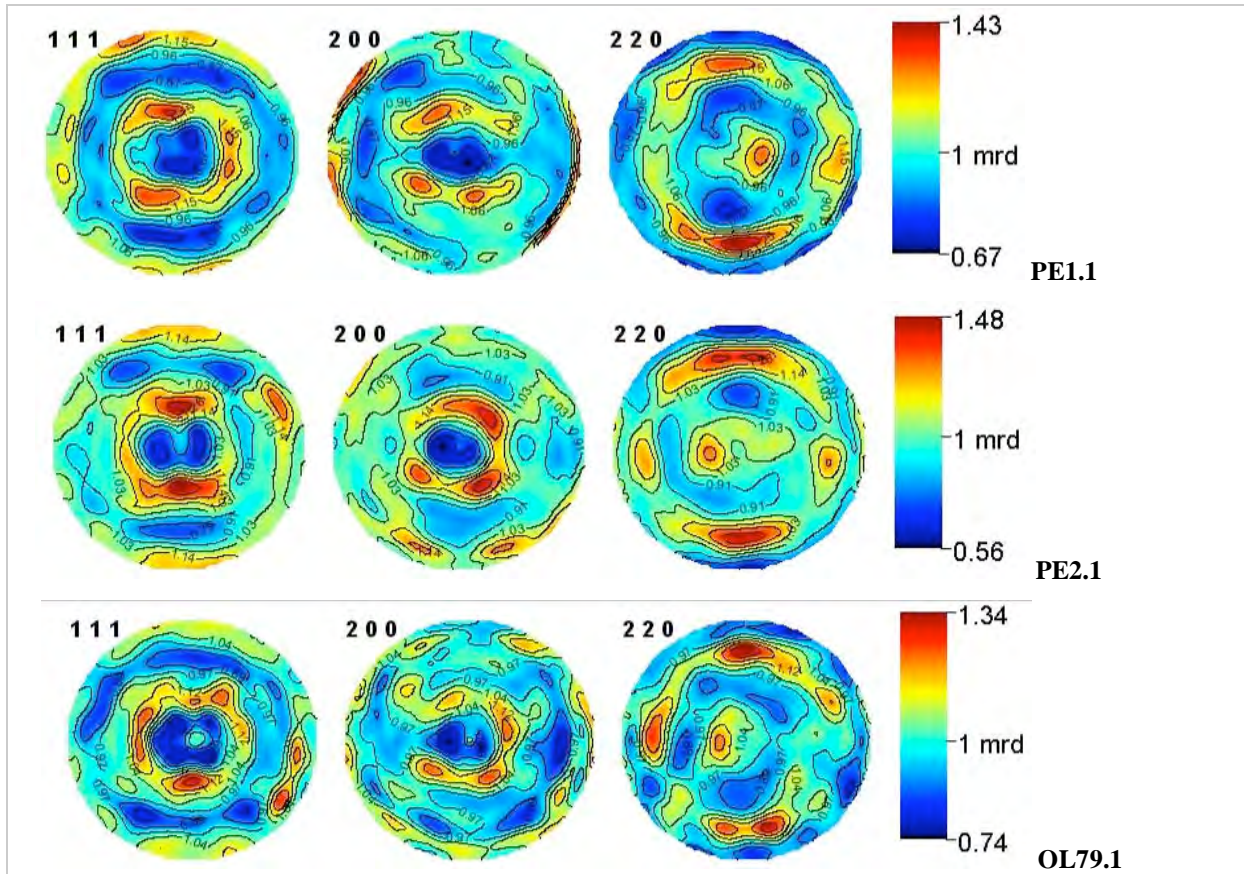


Figure 5.18: Pole figures of PE1.1, PE2.1 and OL79.1 in multiples of random distribution (mrd) showing grain orientation distribution typical of a compressed hammered texture. Data collected at GEM (Figures and analyses by W. Kockelmann).

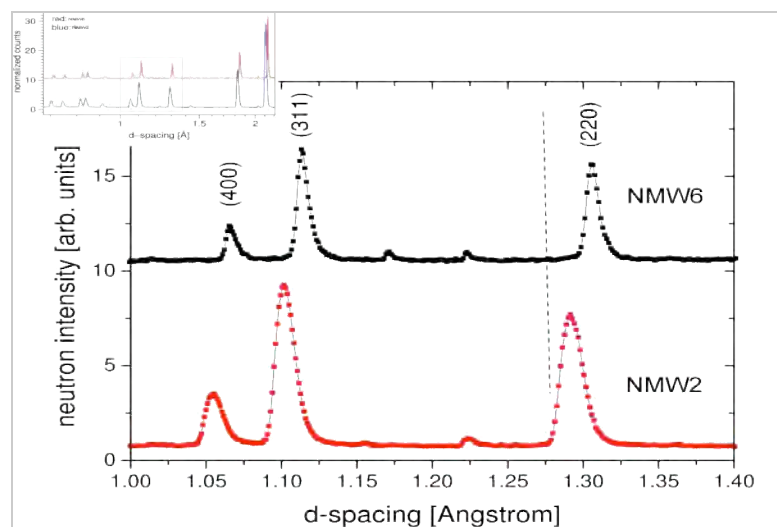
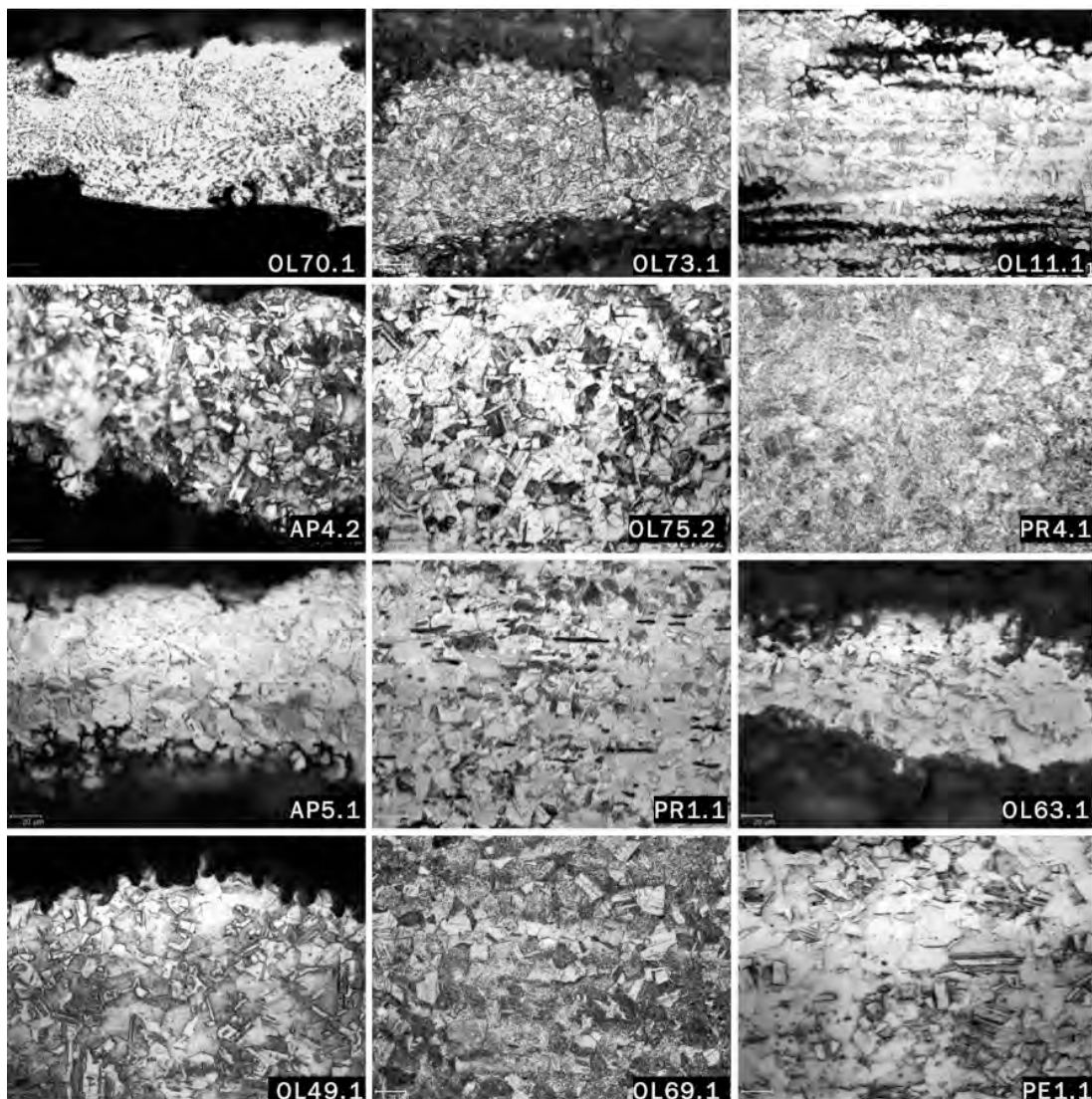


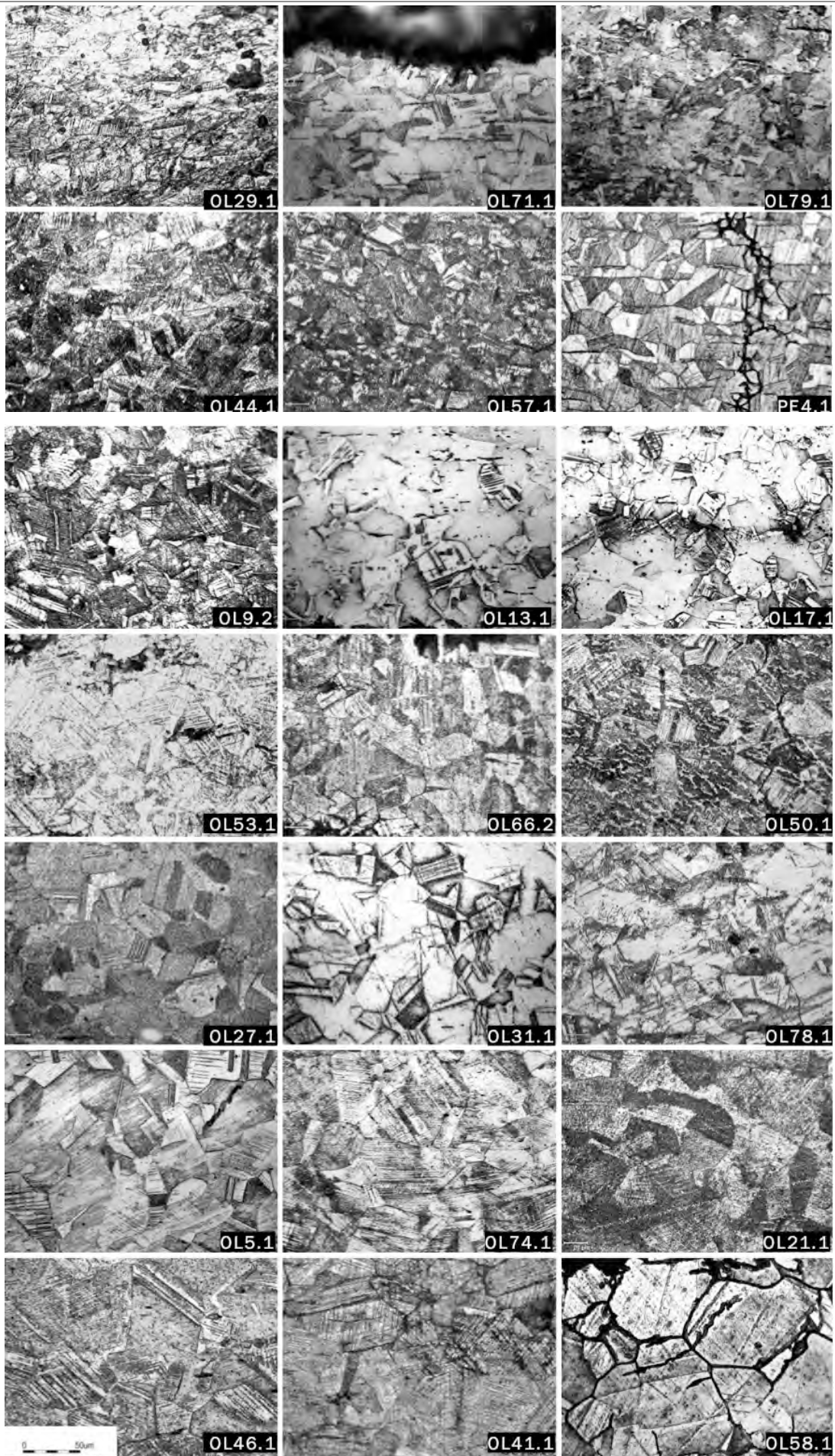
Figure 5.19: Neutron diffraction pattern for NMW2 and NMW6. NMW6 reflections are shifted to higher d-spacing due to its higher tin content, and both are shifted when compared to copper (dashed line). Characteristic peak broadening for NMW2 shows that the alloy was left in the as-cast state and NMW6 in the annealed state. Data collected at ROTAX diffractometer bank (Analysis by W. Kockelmann).

5.6.3. MICROSCOPY OF ETCHED CROSS-SECTIONS

Etched cross-sections exhibit recrystallised grains that contain twinning, which is a typical microstructure of a worked and annealed microstructure (Figure 5.20), including samples OL31.1 and OL27.1 from Corinthian-Myros helmets suspected to be as-cast. Samples are of highly homogenised α -bronze as no other secondary phases are observed. Slip lines are present to differing extents in all samples (Table 5.4). The degree of visible slip lines depends on the degree of etching, but their presence can provide an indication for the relative degree of cold working. The presence of twinned grains in these homogenised α -bronzes is clear evidence that the samples were cold worked and annealed. Identifying the final production step is more challenging because of the presence of straight twinning and extensive slip lines in the same sample. Literature is contradictory to what the simultaneous presence of straight twins and slip lines indicates and is discussed in detail below.

Figure 5.20: (below) Microscopy images of polished cross-sections shown in increasing grain size; taken at the same magnification (x500).





Sample	Typology Code	Position group	Grain size (um) <	Twins	Slip lines	Inclusions, other features	Fibering
OL21.1	COR_IA	neckguard	60	straight	High	fine elongated and round inclusions	
OL29.1	COR_IA	crown	30	slightly bent?	High	large roundish and elongated inclusions, some small round, banding	fibering (etched sample)
OL17.1	COR_IA*	cheekpiece	40	straight	Medium	fine roundish inclusions	fibering (at the edge, etched)
OL31.1	COR_IA*	crown	50	straight	Low	not observed inclusions	
OL41.1	COR_IA*	cheekpiece	70	slightly bent?	High	fine elongated inclusions in grain	
OL69.1	COR_IA.crest	crown	20	straight	Medium	fine elongated inclusions, banding, preservation of strain in corrosion	fibering (etched sample)
OL27.1	COR_II.1.3.Myros	side	50	straight	Low	fine elongated and roundish inclusions, corrosion banding	fibering ? (etched, x20)
OL58.1	COR_II.1.3.Myros	unknown	70	straight	Low	not observed inclusions, beautiful intergranular corrosion	
OL44.1	COR_II.1.4.	neckguard	30	straight	High	not observed inclusions	
OL46.1	COR_II.1.4.*	neckguard	70	straight	High	fine roundish inclusions	
OL57.1	COR_II.1.4.*	unknown	30	slightly bent?	High	not observed inclusions	
OL50.1	COR_II.2.4.edge	crown	40	straight	Medium	not observed inclusions	
OL53.1	COR_II.2.4.edge	neckguard	40	straight	High	not observed inclusions, corrosion banding	fibering (cuprite)
PR1.1	COR_II.2.4.edge	crown	20	straight	Medium	fine elongated inclusions, corrosion banding	fibering (etched sample)
OL49.1	COR_II.2.4.edge*	crown	20	straight	Medium	fine roundish inclusions	
OL75.2	COR_II.2.4.edge*	crown	15	straight	Medium	not observed inclusions, corrosion banding	fibering ? (etched, x20)
OL70.1	COR_III.2.4.V	crown	5	straight	High	very fine structure	
OL63.1	COR_III.2.4.V.Lotus	unknown	20	straight	High	fine elongated inclusions	
OL71.1	COR_III.2.4.Λ.edge*	side	30	bent and straig	Medium	fine elongated inclusions	
OL73.1	COR_III.2.4.Λ.edge*	neckguard	10	straight	High	fine roundish inclusions	
OL74.1	COR_III.2.4.Λ.edge*	unknown	60	slightly bent?	High	fine roundish inclusions	
OL4.2	IL_IB	crown	40	straight	High	large roundish inclusions (cuprite?)	
PE2.2	IL_IIA	crest-track	30	straight	High	acicular features (polishing effect?)	
AP4.2	IL_IIA (forehead)	crest-track	15	straight	Low	fine roundish inclusions	
AP5.1	IL_IIA (forehead)	neckguard	15	slightly bent?	High	not observed inclusions	fibering ? (etched, x20)
OL11.1	IL_IIIA1	cheekpiece	15	straight	Medium	fine elongated inclusions, corrosion banding	fibering (cuprite)
OL5.1	IL_IIIA1*	crown	60	straight	Medium	not observed inclusions	
OL9.2	IL_IIIA1*	crest-track	30	straight	High	elongated inclusions, corrosion banding	fibering (at the edge, etched)
PE1.1	IL_IIIA1*	crest-track	20	bent and straig	Medium	fine elongated inclusions	fibering (EDX map)
OL13.1	IL_IIIA3*	cheekpiece	40	straight	Medium	fine elongated and roundish inclusions	
OL78.1	IL_IIIB1	crown	50	straight	Medium	large roundish and elongated inclusions (cuprite? Etched)	
PR4.1	ETR	side	15	inconclusive	inconclusive	not observed inclusions	
PE4.3	ATT	neckguard	30	straight	High	fine elongated inclusions	
OL79.1	CH_III	unknown	30	straight	High	fine elongated inclusions/some dispersed fine round particles	
OL66.2	CH_V	crown	40	straight	High	not observed inclusions	

Table 5.4: Summary of microscopical observations in cross-sectioned samples presented by helmet type. Notice that the Myros helmets exhibit slip lines only in a few grains.

5.6.4. BRONZE GRAIN SIZE OF ETCHED CROSS-SECTIONS

The bronze grain size, visible after etching, was measured from digital microscopic images using common counting techniques (Section 3.5). The average grain size varies among samples between 5 -70 μm (Table 5.4). Plotting grain size against the thickness of a sample reveals a broad marginal relationship between these two factors (Figure 5.21). This relationship is more evident when considering helmet types and broad chronological development. It appears that the grain size tends to decline through time in the case of the Corinthian type helmets; the Late Phase (III) Corinthian helmets have smaller grain sizes (Figure 5.22). The small number of Illyrian Phase I and II samples limits interpretation of the data but a general indication for the opposite trend may be observed (Figure 5.22).

Results show that the trend for thinner Corinthian type helmets through their development is accompanied by a reduction in grain size. The final grain size in the bronze is controlled by two factors: the degree of hammering and the conditions of annealing (temperature and length of heat treatment), because the more intensive the hammering the smaller the grain size upon recrystallisation during annealing. Prolonged annealing at temperatures that aid grain recrystallisation would result in further grain growth and an increase of grain size (Davis, 2001). A change in grain size over time can reflect a change in the final production step and overall degree of hammering. The final grain size has a notable impact on the mechanical performance of the final product because the strength of the bronze increases with reducing grain size (Ashby and Jones, 2006:166). Hence, such shift towards smaller grain sizes in the Corinthian type helmets may have been a deliberate technological choice in their manufacture.

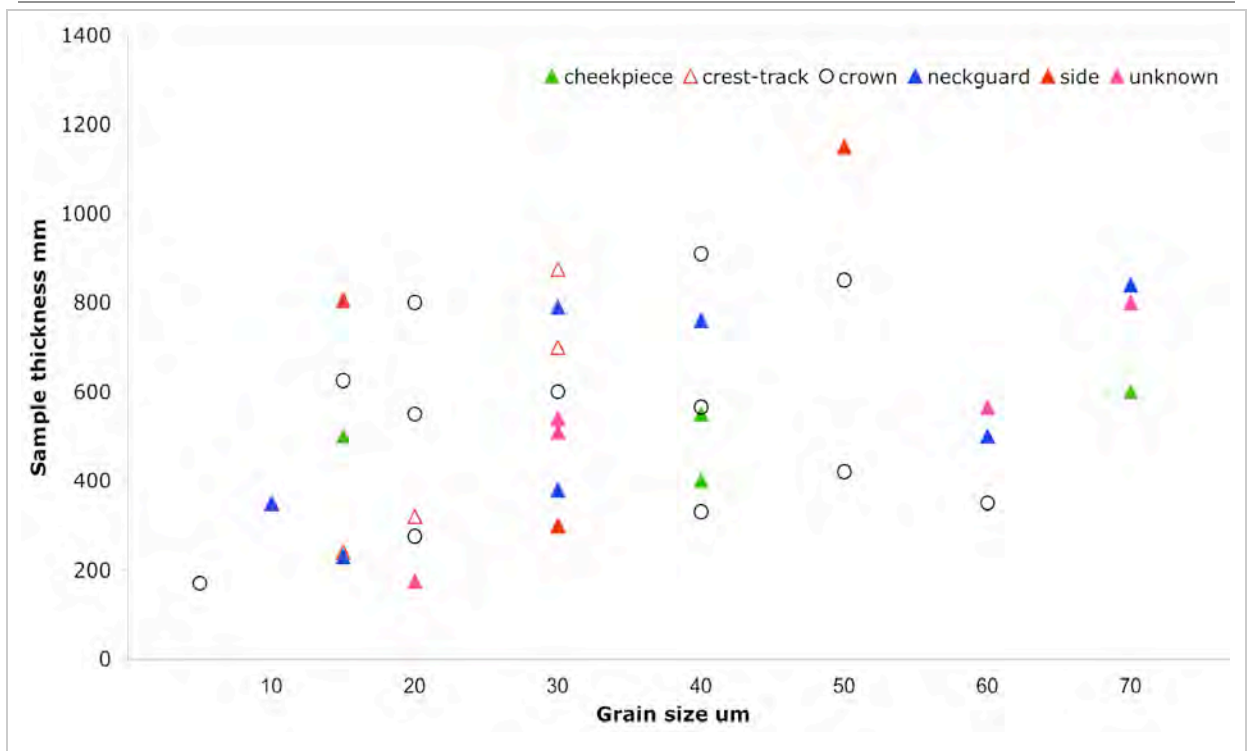


Figure 5.21: Graph showing the approximate size of homogenised bronze grains (μm) in the samples as a function of their thickness (μm).

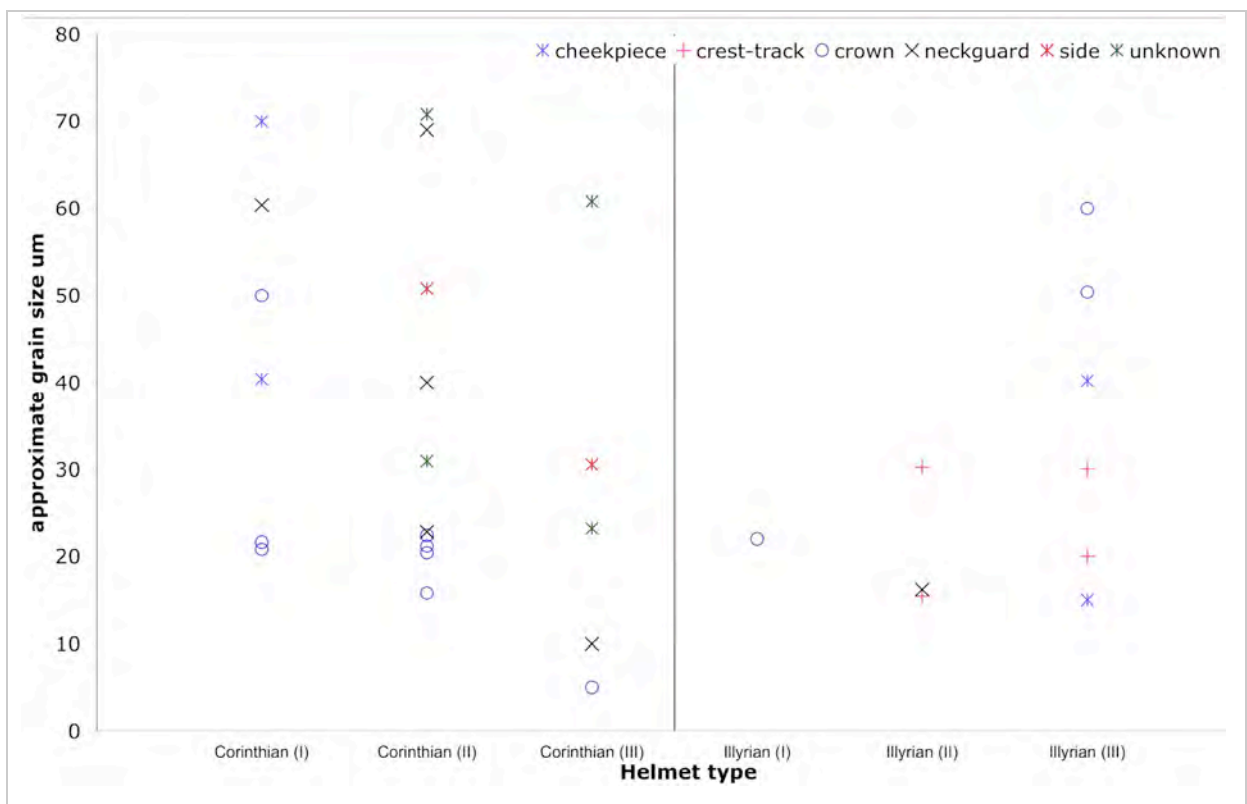


Figure 5.22: Graph showing the approximate bronze grain size (μm) in samples as a function of helmet type and chronological phase.

5.6.5. DISCUSSION OF METALLOGRAPHIC RESULTS

Investigations of the grain size and of the final production step of the helmets provide information on the mechanical performance of the helmets and could contribute to understanding corrosion phenomena. A discussion of what constitutes evidence of cold deformation and annealing is necessary to provide the basis for interpreting the microstructures observed at the etched cross-sections.

Hammering involves the shaping of the metal via plastic deformation of the grains under the action of a stress, and occurs by the movement of dislocations that are present in the atomic structure of the alloy (John, 1972:64). With applied force, dislocations move through a crystal along crystallographic planes (slip planes) (Hosford *et al.*, 1985: 684). As plastic deformation proceeds, the density of dislocations increases and their distribution becomes less uniform (Hosford, Jonas, Leslie, 1985: 685). There is a limit to cold deformation because of the presence of grain boundaries, which become barriers to the further movement of dislocations (John, 1972: 64). To overcome this barrier and to continue shaping, more force is required. This means that the material is strengthened during cold working and the more the working the more force is required to continue deforming the bronze (*ibid.*). Grain size is an important factor of the strength of the final material because the smaller the grain size, the more grain boundaries present in the specimen, the more barriers are therefore present to inhibit movement of dislocations, resulting in a stronger material. Reduction in grain size and thickness by cold working increases the tensile strength of a given solid solution in a reproducible quantitative manner (Davis, 2001: 66; fig.63). This indicates that the helmets exhibiting smaller grain size would be stronger but more brittle, a change that is observable through the developmental phases of the Corinthian type helmets (Figure 5.22).

The type and density of dislocations depends on the crystal structure of the alloy (Barrett, 1985:719). Generally, the crystal planes on which slip takes place are those with the highest degree of atomic packing; in face-centred cubic alloys such as bronze, the {110} planes contain the greatest atomic packing density and constitute the most active slip systems (with 12 possible slip planes) (Davis, 2001:446; John, 1972:62). Therefore, slip may be occurring simultaneously on several intersecting planes and the dislocations may interfere with one another's movement during hammering increasing the strength of fcc solid solution alloys faster than other alloys (John, 1972:64). Dislocations produced during hammering have high strain energy (Ashby and Jones, 2006:58), due to the mechanical energy stored in them (Hu, 1985:693). Dislocations are microscopically visible from their preferential etching in polished

specimens and appear as long straight slip or strain lines on the slip planes of individual grains (Hosford, Jonas, Leslie, 1985: 685; Barrett, 1985:719). These lines are observed to differing extent¹⁴ in all etched samples investigated in this thesis (Figure 5.20).

Annealing affects the existence of slip lines and final grain size thus influencing the hardness and ductility of the final product. Annealing is used to relieve stress in work-hardened specimens and re-establishes ductility by removing strain and increasing grain size. This involves microstructural transformations to achieve a lower energy state and occurs in three stages: recovery, recrystallisation and grain growth (Hu, 1985:693). It depends on alloy type, grain size, degree of preceding plastic deformation, and annealing conditions (temperature and time) that can be designed to produce the optimum combination of ductility and strength in the final product. During recovery, structural changes occurring include the eradication and rearrangement of dislocations, formation and growth of subgrains, and the formation of recrystallisation-nuclei energetically capable of further growth (Hu, 1985:693). These changes result in the reduction or removal of strain hardening without any visible change of the overall shape of the grain boundaries (ASM, 1985: recovery). Structural changes at this stage can become microscopically observable if the density of dislocations is considerably reduced and rearrangement of dislocations occurs (Hu, 1985:693). Sufficiently high annealing temperature can initiate recrystallisation, which involves the nucleation and growth of new strain-free grains; this occurs at the expense of sub-grains that coalesce leading to the formation of new grains (Hu, 1985:694; Ashby and Jones, 2006:58). The recrystallisation temperature depends on the alloy composition and degree of work hardening; the more the hardening the less the recrystallisation temperature (John, 1972:64). If the initial grains are strongly textured, normal grain growth may be inhibited (Hu, 1985:697). Prolonged annealing results in the growth of the grain size (Hu, 1985:697). The annealing time and temperature can be selected so that upon completion of recrystallisation, further or no further grain growth takes place depending on the required outcome (ASM, 1985: recrystallised grain size; Davis, 2001:244; fig.3).

During recrystallisation, work-hardened face-centred cubic metals undergo characteristic twinning in their grains (Barrett, 1985: 719). Recrystallisation is accommodated by the formation of mirror-image orientations across particular planes (across the {111} planes in the [112] direction) within a crystal (John, 1972:64; Davis, 2001:446). This means that

¹⁴ Some effects of under-polishing (for example OL63.1) or over etching (OL57.1) (Samuels, 1985: 35) do not seem to compromise evidence of fabrication for the degree of interpretation required for this study.

twinning crystals have portions of different orientations with respect to the rest of the crystal, which is microscopically visible in etched samples as parallel bands exhibiting different colour (Barrett, 1985:719). This is because twin boundaries are low energy defects and corrode less actively than grain boundaries (Barrett, 1985:719); grain boundaries have higher dissolution potential because of severe localised deformation and accumulation of impurities (ASM, 1985: grain boundary etching).

The presence of annealing twins is observed in all helmet samples (Figure 5.20) and is evidence that the metal was mechanically deformed prior to annealing (Davis, 2001:446; Bailey, 1982:32). If additional cold working took place after this annealing or annealing was the final stage of manufacture can be deduced from the nature of the twinning and the presence or absence of slip lines. The majority of the helmets show a combination of straight twinning and extensive slip lines (Table 5.4). Interpretation of these microstructures is complicated because there is a contradiction related to the effect of cold working on the presence of slip lines and the nature of twinning. In summary it is reported that:

- The presence of straight twinning in grains normally indicates that annealing was the final stage of manufacture (Bailey, 1982:32).
- The presence of strain lines is evidence of residual strain introduced upon cold working and indicates that the metal was left in the cold work state (Bailey, 1982:32; 1984:27)
- Cold working after annealing of a wrought bronze is manifested primarily by the bending of twins; slip lines are visible after extensive cold-working.

Limited post-annealing cold working would result in the bending of twins because deformation may need to be relatively severe before strain lines are shown up by ordinary etching solutions (Bailey 1966:27). Examples of progressive cold reduction of the thickness of a Cu5Zn brass (fcc solid solution) show that 5% cold work reduction by rolling is efficient for bending the twins (no strain is visible); 40% reduction results in bent twins and intense strain (slip lines); further cold working results in increasing fibrous texture and elongation of the grains (Davis, 2001:244, fig.3; p409, fig. 69). This indicates that if helmets were left in the wrought state, the presence of slip lines should be accompanied by bent twins rather than straight twins and slip lines as is the case here.

- Cold working after annealing of a wrought bronze is manifested primarily by the presence of slip lines; bending of the twins becomes visible only after extensive cold-working. This directly contradicts the evidence reported above.

Northover (*pers. com.*) in unpublished work has shown that in fcc solid solution alloys cold working of less than 5% thickness reduction does not result in visible strain lines because they are not etched by etching solutions. At around 10% reduction significant slip lines start to appear in the grains, with families of slip lines intersecting one grain; at 20-25% reduction bending of twinning is visible and, above 25% thickness reduction grain elongation starts to become visible. These phenomena are quantitative and reproducible for fcc solid solution alloys (*ibid.*), but no other published information was retrieved on the topic to confirm this. It is reasonable to assume that the formation of visible slip lines would require less energy compared to bending the twins, because slip lines are dislocations that involve movement of a smaller number of atoms. A further indication to support that slip lines require less energy to form than bending the twins is that line dislocations require less energy to be rearranged or eradicated and occurs at the recovery stage of annealing, whereas twinning starts with recrystallisation at a later annealing stage.

- The combined presence of straight twinning and slip lines indicates hot working.

Examples include an early arsenical bronze (Ryndina 2009, fig 5) and a brass Roman coin which showed straight and bent twins in grains with extensive strain lines a result of hot striking of the cast billet (Scott, 1991:97, fig. 125). The presence of inclusions in the bronze, such as in the case of the helmets (Figure 5.15), is claimed to be characteristic of hot worked copper alloy specimens (Bailey, 1982:31). Hot working of bronze in antiquity is disputed due to limitations in workability (Northover, *pers. com.*). In addition, the generation of dislocations during hot working is slightly compensated by the simultaneous thermally activated recovery process (Hosford, Jonas, Leslie, 1985: 690), indicating that the extensive slip lines present on the helmet samples (Figure 5.20) are not a result of hot working.

- The presence of slip lines is the result of insufficient annealing.

A short annealing period may not be sufficient to eliminate heterogeneity and stresses in the metal (Scott, 1991:7;89). This is possible during short annealing at low temperatures where specimens may only recover without going into the next stage of recrystallisation (Hu, 1985:694). Microstructural changes during the first stages of annealing (recovery) may not be apparent in optical microscopy unless if the density of dislocations is considerably reduced and rearrangement of dislocations occurs (*ibid.* 693).

Based on this evidence, it seems more reasonable that the co-existence of straight twins and extensive slip lines indicates that the helmets were subjected to cycles of cold working and

annealing, with a final step of cold working. This final step of cold working was not extensive enough to bend the twinning in the grains, or to produce a visible elongation of the grains. A final very short annealing cycle at low temperature, which prevented recrystallisation, is possible if it did not result in microscopically evident changes. In cases where only a small number of grains include slip lines, it is likely that moderate hammering took place followed by a short stage of annealing (Corinthian-Myros helmets OL27, OL58; and OL31, AP4, Table 5.4). Diffraction line broadening is sensitive to changes during the first stages of annealing (Hu, 1985:693). Neutron diffraction data indicated that NMW6 was fully homogenised due to hammering and annealing cycles and it was left in the annealed state (Figure 5.19). Helmet NMW2 was left in the as-cast state and x-radiography confirms this (Figure 5.11, NMW2). A final hardening step (cold working) is absent from both helmets contrary to helmet PE1.1, PE2.1 and OL79.1 which showed significant and moderate cold work hardening respectively.

Results must be viewed within the context of the typology and chronology of the helmets examined. Thickness of the samples and grain size demonstrate that sample thickness and grain size (Figure 5.22) are reduced during the evolution of the Corinthian type through centuries. These observations combined with information from visual observations and x-radiography indicate that although the degree of hammering varies between different areas of a helmet (Figure 5.9) the extent of hammering increases with time to produce thinner, lighter and stronger but more brittle Corinthian type helmets. A final annealing step is observed on an early Corinthian type helmet (NMW6), which is thicker and heavier than the later types. One of the examined Corinthian-Myros helmets is made entirely by casting (OL80) where a combination of casting and hammering was employed for the rest. This, and the single example of a cast Illyrian type helmet (S1) demonstrate that the technical development of helmet making in time may be more complex than currently thought.

5.7. SEM-EDX ANALYSIS OF COPPER ALLOY COMPOSITION

Metallographic analysis showed that the helmet samples are homogenised α -bronzes with a grain size between 5-70 μm . SEM-EDX analyses were undertaken by probing an area (120x96 μm), which is larger than the grain size in order to provide average compositional data by including grain boundaries where potential elemental segregation occurs. Details on the experimental conditions, equipment set ups and performance of SEM-EDX are discussed in section 3.6.1.1.

Table 5.5 shows averaged normalised 100wt% analysis of data collected from three or more areas on the polished cross-sectioned samples. The data are edited by setting negative concentration values to zero, after which normalisation took place (AMC, 2001b, 2001a). Two or more samples from each of the helmets AP5, OL4, OL57, PE1 and PE2 were analysed in order to assess compositional variation within a helmet.

Overall, SEM-EDX shows that helmets are of low-tin bronze ranging between c. 5-14wt%, with only trace concentration of impurities notably Pb, Fe, Ni, Al and Si. The bronze alloys used were pure with a very low concentration of impurity elements. The maximum wt% concentrations of each trace element is at Al 0.11% (± 0.04), Si 0.18% (± 0.03), Fe 0.54% (± 0.06), Ni 0.33% (± 0.09), Zn 0.06% (± 0.15), S 0.13% (± 0.07), Sb 0.2 (± 0.16), As 0.4% (± 0.27), and Pb 1.3% (± 0.32); uncertainty was calculated as the average value of statistical sigma% for each element at each analyses. Zn is at concentrations below the detection limits of the method (similarly to Bi, Au, Mn which are not shown here). Table 5.5 notes in green concentrations above sigma% for each element.

Results show that all helmets have traces of Si and Fe, few include detectable (by the method) levels of Al, and a very small number of helmets include traces of Ni and Pb. Ni shows consistency within groups of samples such as those from helmets excavated from Aghia Paraskevi (AP4, AP5), which have the highest Ni and lowest Sn concentrations. This indicates that helmets from this cemetery may have a different chemical signature, which could be characteristic to contribute to investigations of helmet manufacture workshops.

The spread of values between analysis taken from different areas within a sample (Table 5.5) changes between sample and element but is generally small. Of greater interest here, is the spread of Sn concentration in a sample and between samples from the same helmet. Understanding the degree of Sn variation within a helmet aids understanding of Sn microsegregation from casting or hammering. Northover (1991) suggests that variation of the tin content within a helmet is caused by a slight segregation in the original blank, which was not entirely removed during hammering. In the case of the helmets of this thesis, deviation of Sn concentration is small both within individual samples, and within helmets (Table 5.6, AP5, OL57, PE2). OL4 shows slightly higher Sn variation and PE1 shows the greatest, because as previously seen by SEM-EDX mapping, tin is unevenly distributed in bands (Figure 5.17), due to intensive hammering as confirmed by texture analyses of PE1 (Figure 5.18). For this reason, it is likely that some minor spread of Sn values within or between samples of the same helmet is the result of extensive hammering rather than residual segregation in the original cast blank which was not entirely removed by hammering.

Sample	Al	Al SD	Si	Si SD	S	S SD	Fe	Fe SD	Ni	Ni SD	Cu	Cu SD	As	As SD	Sn	Sn SD	Sb	Sb SD	Pb	Pb SD
AP4.2		0.01	0.07	0.04		0.01	0.08	0.03	0.33	0.06	94.2	0.2		0.09	5.0	0.1		0.17		0.15
AP5.1		0.01	0.09	0.03		0.04	0.13	0.04	0.30	0.08	93.9	0.1		0.17	5.0	0.1		0.14	0.32	0.30
AP5.2	0.11	0.04	0.07	0.00		0.03	0.10	0.02	0.28	0.05	93.9	0.4	0.38	0.08	4.9	0.1		0.08		0.11
OL11.1	0.05	0.01	0.10	0.03		0.02	0.10	0.01		0.02	92.3	0.7		0.14	6.5	0.4		0.06	0.68	0.37
OL13.1		0.03	0.08	0.03		0.02	0.35	0.03		0.08	89.4	0.5		0.23	9.8	0.1		0.11		0.25
OL17.1		0.00	0.07	0.02		0.03	0.08	0.02		0.03	89.0	0.3		0.10	9.6	0.3		0.16	0.92	0.20
OL21.1		0.03	0.06	0.00		0.01	0.12	0.01		0.06	88.8	0.2		0.25	10.8	0.2		0.13		0.23
OL27.1		0.01	0.18	0.09		0.04	0.18	0.01		0.03	86.7	0.2	0.30	0.06	12.3	0.1		0.04		0.18
OL29.1		0.02	0.09	0.01		0.02	0.13	0.05		0.01	91.4	0.6		0.08	7.8	0.2	0.16	0.07		0.12
OL31.1		0.03	0.11	0.04		0.04	0.35	0.03		0.04	88.4	0.4		0.08	10.7	0.2		0.08		0.14
OL4.1		0.02	0.09	0.02		0.01	0.16	0.05		0.02	85.4	0.5		0.22	13.8	0.1		0.01		0.21
OL4.2	0.10	0.02	0.09	0.01		0.01	0.13	0.04		0.02	85.9	0.1		0.18	13.5	0.1		0.05		0.09
OL41.1		0.02	0.10	0.02	0.11	0.09	0.30	0.09		0.01	88.0	0.6		0.05	11.2	0.6		0.08		0.28
OL44.1	0.10	0.02	0.10	0.03		0.03	0.16	0.02		0.05	89.6	0.2	0.28	0.08	9.1	0.3		0.09	0.50	0.21
OL46.1	0.04	0.02	0.12	0.01		0.05	0.13	0.03		0.02	90.8	0.6		0.18	8.7	0.2		0.10		0.54
OL49.1		0.02	0.10	0.04		0.04	0.29	0.02		0.02	86.6	0.3		0.07	12.8	0.0		0.12		0.07
OL5.1	0.05	0.02	0.09	0.03		0.05	0.15	0.02	0.10	0.08	88.7	0.9		0.28	10.7	0.4		0.18		0.39
OL50.1		0.02	0.08	0.01		0.05	0.11	0.05		0.10	89.2	0.5		0.06	10.4	0.2		0.17		0.33
OL53.1		0.01	0.15	0.04		0.02	0.25	0.04	0.21	0.04	89.3	0.1		0.15	9.7	0.1		0.05		0.15
OL57.1		0.05	0.08	0.02		0.04	0.30	0.05	0.11	0.04	88.9	0.3		0.20	10.3	0.2		0.12		0.10
OL57.2		0.03	0.13	0.02		0.01	0.28	0.04	0.14	0.05	89.2	0.5		0.08	10.1	0.1		0.05		0.20
OL58.1		0.02	0.10	0.02		0.01	0.10	0.04		0.02	89.3	0.7		0.06	10.0	0.3		0.15		0.22
OL63.1		0.02	0.17	0.01		0.02		0.04	0.10	0.02	88.1	0.5		0.06	11.3	0.0		0.11		0.10
OL66.2		0.04	0.09	0.00		0.07	0.20	0.04		0.05	89.1	0.6	0.43	0.16	10.0	0.3		0.02		0.16
OL69.1	0.09	0.02	0.07	0.01		0.06	0.08	0.02	0.12	0.07	90.0	0.2		0.08	9.1	0.3		0.21	0.40	0.15
OL70.1		0.01	0.13	0.02		0.04	0.10	0.02	0.11	0.03	91.3	0.3		0.06	8.0	0.2	0.19	0.06		0.42
OL71.1		0.02	0.10	0.02		0.03		0.05		0.06	89.0	0.3		0.07	10.8	0.2		0.15		0.23
OL73.1	0.06	0.04	0.12	0.02		0.02	0.19	0.04	0.11	0.06	88.6	0.2		0.01	10.5	0.2		0.12		0.15
OL74.1		0.02	0.07	0.02		0.06	0.16	0.04		0.02	86.9	0.4		0.17	12.7	0.1		0.15		0.16
OL75.2		0.01	0.10	0.01		0.05		0.03		0.02	88.6	0.5		0.10	11.1	0.1		0.15		0.30
OL78.1	0.08	0.01	0.09	0.01		0.03	0.17	0.03	0.12	0.11	85.4	0.6		0.22	13.8	0.4		0.66		0.10
OL79.1		0.03	0.10	0.02		0.05	0.54	0.03		0.03	87.7	0.4		0.20	11.4	0.1		0.05		0.18
OL9.2		0.01	0.14	0.01		0.01	0.26	0.01		0.03	88.6	0.3		0.02	10.5	0.4		0.09	0.33	0.25
PE1.1	0.04	0.01	0.05	0.02		0.02	0.08	0.06		0.04	89.6	0.2		0.02	9.9	0.1		0.15		0.14
PE1.1ii		0.01	0.17	0.03		0.11	0.06	0.02		0.06	84.2	0.5		0.15	14.2	1.0		0.26	1.29	0.11
PE1.2	0.06	0.01	0.10	0.02		0.04	0.06	0.03		0.04	89.8	0.5		0.18	9.9	0.2		0.13		0.33
PE2.1	0.04	0.00	0.06	0.02		0.04	0.36	0.03		0.02	88.3	0.1		0.19	11.0	0.1		0.08		0.24
PE2.2	0.40	0.40	0.06	0.02		0.02	0.35	0.02		0.07	88.0	0.7		0.05	10.5	0.1		0.07	0.34	0.27
PE4.3		0.02	0.07	0.01	0.13	0.08	0.17	0.04	0.10	0.06	89.7	0.5		0.14	9.3	0.1		0.05		0.23
PR1.1		0.01	0.08	0.02		0.09	0.08	0.04		0.03	92.6	0.5		0.11	6.6	0.1		0.03		0.29
PR4.1		0.03	0.11	0.00		0.04		0.05		0.05	90.3	0.4		0.07	9.1	0.6		0.04		0.17
Sigma %	0.04		0.03		0.07		0.06		0.09		0.44		0.27		0.15		0.16		0.32	

Table 5.5: Averaged normalised wt% SEM-EDX analysis of core metal composition. The table includes spread of values (STDEV) between analyses taken at different areas within each sample. Only concentrations above sigma % for each element are shown (green). The maximum values for each column are in bold. Measured Zn, Sb, Au, Bi, Ag, S and P were below the detection limit.

Helmet sample	Sn wt%	SD within sample
AP5.1	5.03	0.12
AP5.2	4.88	0.09
SD within helmet		0.08
OL4.1	13.78	0.07
OL4.2	13.45	0.10
SD within helmet		0.16
OL57.1	10.29	0.16
OL57.2	10.09	0.11
SD within helmet		0.10
PE1.1	9.94	0.06
PE1.1ii	14.19	1.03
PE1.2	9.87	0.16
SD within helmet		0.03
SD within helmet (incl. PE1.1ii)		2.02
PE2.1	11.00	0.15
PE2.2	10.49	0.15
SD within helmet		0.26

Table 5.6: Standard deviation of Sn wt% concentration in helmets AP5, OL4, OL57, PE1 and PE2, and their corresponding samples.

5.8. GENERAL DISCUSSION AND CONCLUSIONS

5.8.1. TECHNICAL EVOLUTION OF THE ILLYRIAN & CORINTHIAN TYPES

SEM-EDX analysis results of samples removed from 37 helmets showed that they are made of low-tin bronze (c. 5-14wt% Sn). Low-tin bronze alloys can be used for casting or wrought manufacturing processes. In this case, the bronze microstructure was homogenised after cycles of hammering and annealing into α -bronze solid solution as evidenced by the presence of equiaxed grains that contain twinning (Figure 5.20). Cross-sections lack any evidence of $\alpha+\delta$ eutectoid expected to be present in room temperature at as-cast or poorly homogenised bronze (Cuthbertson, 1960; Scott, 1991: 123) (Figure 5.23). Only one Corinthian-Myros helmet (OL80) exhibited a dendritic microstructure at the top of its crown, which was macroscopically observed on the helmet (Figure 5.8, d). This indicates that the silver/grey appearance seen on some helmets cannot be the result of corrosion of phases in a cast microstructure (section 2.2.5), but could be influenced from intensive hammering of the low-tin bronze (sections 5.6.1, 5.6.2).

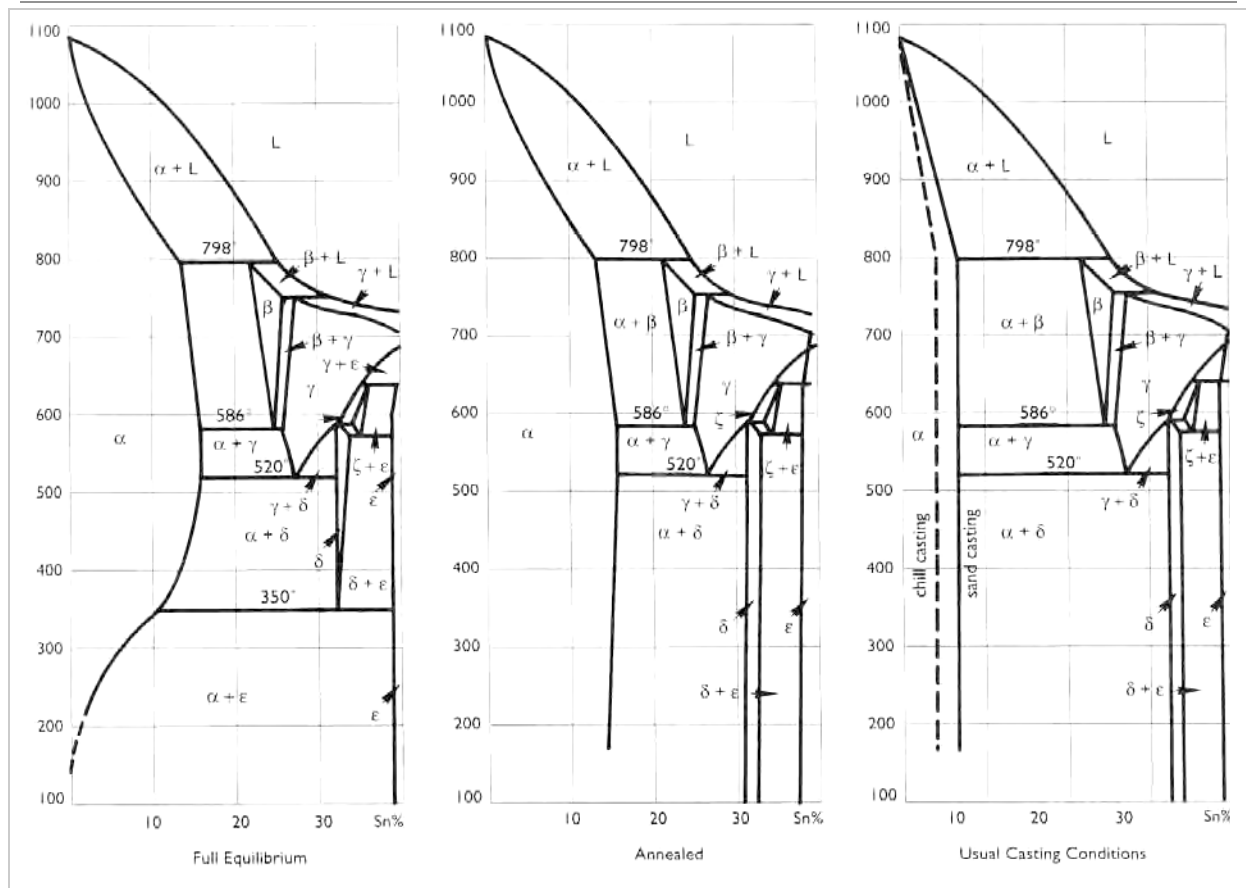


Figure 5.23: Part of the Cu-Sn phase diagram showing phases formed under different working conditions including full thermodynamic equilibrium, annealing and usual casting conditions where full equilibrium is not achieved (image from Scott, 1991: 123). The α solid solution is present in annealed low-tin bronzes (up to c. 14wt%) at room temperature.

That all cross-sections show evidence for a homogenised α -bronze contrasts with the macroscopic observations of technological features on a number of Middle Phase II Corinthian type helmets. There was evidence of casting shrinkage and finely executed cast decoration (e.g. OL68) (Figure 5.8) and clear evidence of a dendritic microstructure (OL80, crown Figure 5.8, d). Casting is a more prominent feature for the Myros stylistic subgroup of Middle Phase II Corinthian helmets, which are thicker and heavier than their successors or other helmet variants of the same period. These features have supported in the literature the hypothesis that the Myros style helmets were made by casting (Pflug, 1988a). Metallographic analysis of OL27.1 (side) and OL58.1 (unknown position) samples from Myros style helmets showed that although relatively thick (800-1150 μ m) they are work hardened and annealed, and exhibit slip lines in only a small number of grains (Table 5.4). These results agree with x-radiography of other Myros-style helmets (NMW1, NMW9) (Figure 5.9) and indicate that not all Corinthian-Myros helmets are entirely cast; some were shaped by further hammering and annealing.

This, combined with neutron diffraction analyses of an Early Phase I Corinthian helmet (NMW6, Figure 5.19), which shows macroscopic evidence of casting but was worked and left in the annealed state, support Swaddling's (1987) hypothesis that Early I and Middle Phase II Corinthian type helmets were formed using a roughly pre-formed cast that was further shaped by hammering. This hypothesis was developed during investigation of an extraordinary thick (c. 9mm) forerunner of the Myros style helmet that was previously assumed to be cast due to its thickness but metallography revealed evidence of annealing (*ibid.*). Microstructural changes upon working and annealing obscure evidence of a pre-formed cast blank (Swaddling, 1987; Scott and Podany, 1990). The frequent examples of Middle Phase II Corinthian type helmets with thick noseguards and finely executed cast decoration, which would perhaps require only further refinement by filing and polishing (Figure 5.8), suggest that the use of a fine pre-formed rather than a roughly pre-formed cast blank is more likely for these particular helmets. The entirely cast Myros style helmet (OL80) indicates that a fine casting method was in place to produce finely executed helmets. This fineness in casting could be achieved by the lost wax method, but experimental casting would be necessary to confirm this hypothesis. This method has only been proposed for Etruscan type helmets with a knob at the top of the crown; they could be made either by casting the knob and a roughly shaped helmet in an open mould, or by producing the whole helmet by the lost wax method, before further working and polishing it (Born, 1991).

Analyses of the Myros style helmets further demonstrates that helmets with similar stylistic features, which typologically belong in the same group/variant, may not necessarily share common manufacturing technology. Caution thus should be exercised when generalising technical observations based on stylistic criteria alone. Overall, the Corinthian type helmet is subject to different work histories through its chronological development. Irrespective of the sampling site on a helmet, thickness of the Corinthian helmets decreases in time, except for some of the Myros style (Middle Phase II) (Figure 5.14). This trend is accompanied by smaller grain sizes, resulting from more intensive hammering and the lack of a final annealing step to produce grain growth in Late Phase III (Figure 5.22). A final step of cold working was previously detected in a small number of Late Phase III Corinthian type helmets, where the excellence of hammering skills was reflected by the small variation in wall thickness (0.75-1.5 mm) (Blyth, 1988, 1993). Analyses support that there was a shift towards thinner, lightweight, stronger, but more brittle helmets. Similarly, increasing tin content increases the hardness of the α -bronze but reduces the percentage elongation before fracture (Davis, 2001:43; fig.29) making the material stronger but more brittle. Results broadly indicate that the Sn concentration tends to increase during the evolution of the Corinthian type (Figure

5.24), suggesting again a shift towards stronger helmets. Results are in agreement with macroscopic observations and, hardness measurements of the crown of Corinthian type helmets that showed a gradual shift toward harder helmets reaching its pick at the Late Phase III (Blyth, 1977). Examining other areas of helmets confirms Blyth's overall analysis from one area of helmets. This change may reflect a gradual change in the performance requirements of the Corinthian type helmet, and provide evidence of technological innovation.

A shift from thicker to thinner helmets is only marginally indicated for the Illyrian type helmets (Figure 5.14). Contrary to the Corinthian type helmets, they seem to have increasing grain size over time (Figure 5.22), despite indications of intensive hammering (Figure 5.20). Similarly, data do not support an increase of tin concentration over time to produce stronger helmets. Trends observed here are uncertain due to the small number of samples from the Early I and Middle Phase II Illyrian type helmets. Neutron texture analysis (Figure 5.18) and metallography (Figure 5.20) showed that Illyrian type helmets were subject to differing extents of hammering, possibly with a final cold work-hardening. A final cold work hardening is previously reported for two Illyrian type helmets, which was more extensive than that of the (two) Corinthian type helmets (McNamara, 2000).

X-radiography demonstrated that the degree of hammering, which is concentric, can vary within and among helmets (Figure 5.11) but it was successfully used to discriminate between different hammering styles from associated archaeological contexts. Helmets AP6 and NF5 (Late Phase III A.2), show distinct crude hammering relatively to the finer hammering of AP1 (Late Phase III A.3) and AP4 (Middle Phase II A with forehead), which are from the same period and place but assigned to a different typological group. In this case, the similarities in hammering style could be a more effective grouping factor than stylistic observations for information on production workshops. Similarly, the characteristic low tin concentration in helmets from this site (AP4 and AP5), which also show an elevated concentration of trace elements such as Ni (Figure 5.24), suggest a distinctive chemical signature that could be used to aid characterisation of helmet workshops over time.

Hammering is also evidenced by tool marks present on several helmets (Figure 5.10). In cases where the helmet was made entirely by hammering, this could have been achieved using a relatively thin circular cast sheet, which was shaped by raising or by sinking (Untracht, 1969:93). Both may be used on the same object and raising hammers may be used on the outside at early stages of work (*ibid.* 433). The raising process involves hammering of the metal from the inside against an anvil (Craddock, 2009: 158) and requires various smoothly

polished anvils whose design depends on the shape of the work (Untracht, 1969:247;249). The uniform and precise hammering of the crest-track observed on Late Phase III Illyrian type helmets can suggest that hammering of the crest-track ridges was undertaken in a mould or on a shaped anvil. It is most likely that wrought helmets were raised in this way from a single sheet of metal. This process involves repeated cycles of hammering and annealing followed by planishing with finer hammers to consolidate the surface; the piece would be finished by filing and planing or scraping before polishing (Untracht, 1969:433; Craddock, 2009:158).

Due to lack of evidence to support other theories, the Illyrian type helmets have been thought to be shaped by hammering (Snodgrass, 1967). Indications of casting porosity in the x-radiograph of an unusually thick Late Phase III Illyrian type helmet (Figure 5.12, S1) provide new evidence. This indicates that the technical development of the Illyrian type helmet may be more complex than currently thought. Overall, the large number of helmets investigated in this study aid broad understanding of manufacturing technologies of helmets and points out that metallurgical evidence must be viewed within the chronological context of helmets.



Figure 5.24: Sn wt% concentration of samples plotted against chronological phase of helmet type. Left: Corinthian type helmets exhibiting a slight trend for increasing tin content at the Late Phase III. Right: Illyrian type helmets showing clustering of Sn composition based on provenience (green, Aghia Paraskevi) or stylistic subgroup (red).

5.8.2. ARTISTIC EVIDENCE OF HELMET MANUFACTURE TECHNIQUES

The most important evidence of plastic art for the making of helmets derives from a late 8th-7th c. BC bronze figurine of a bronze-smith hammering a Corinthian type helmet on a high 'rod'-anvil exhibited in Metropolitan Museum of Art (Snodgrass, 1967) (Figure 5.25). The *sphyrelaton* or hammering technique is supported by pictorial artistic evidence on Archaic period pottery, especially during 540-470 BC, when the scene of the making of Achilles's new weapons by Hephaistos found in Iliad (Sigma rhapsody) becomes a favourite pottery painting theme (Chatzidimitriou, 2005) (Chatzidimitriou, 2005: 58). Although there are considerations related to the validity of datable information based on representation of this anachronistic theme, and other issues related to artistic 'licence' (see Snodgrass, 1982; Pflug, 1988), it is broadly recognised that Archaic pottery paintings can provide important information on metal working practices and in particular the making of armour and helmets (Chatzidimitriou, 2005: 58).



Figure 5.25: Cast Bronze statuette of helmet maker, late 8th-early 7th c. BC, Metropolitan Museum (from Mattusch, 1988:34)

Figure 5.26 shows pottery paintings that represent several steps of helmet making and provide information on the types of tools used in their making during the Archaic period. According to Chatzidimitriou (2005:77), the earliest depiction of helmet making on pottery is from the pyxis of Thaliarhos (Figure 5.26c, 520-500 BC), where a young man shapes a Corinthian type helmet. Based on the shape of the crown, this helmet could be allocated to the Late Phase III, material evidence of which starts to appear after around 550BC. This indicates that the pictorial evidence is only slightly anachronistic or contemporaneous to the helmet style, giving evidence for the value of pictorial art in understanding the technology of the period.

At the pyxis of Thaliarhos, the hammer-smith uses a hammer with a long handle attached on one side, which most likely is made of wood (*ibid.* 61), and with a long, thin slightly curved

hammerhead attached at the end. This type of hammer was most likely used for the making of raised ridges on the crown or the final shaping of a helmet because its length permits the smith to reach areas that could not be normally reached (*ibid.* 63). The positioning of the smith's body implies that he did not apply great force for hammering. Light hammers which have a highly polished slightly convex surface, are commonly used to planish or finish a hammered metal object in order to remove tool marks that occurred during the raising of an object from a flat sheet (Untracht, 1969: 247). This process requires great skills and the maximum metal-to-anvil contact (*ibid.* 249) similar to the angle of the helmet seen in the pyxis of Thaliarhos that indicates the hammer seen in the pyxis is for planishing and that the scene represents the planishing step of helmet manufacture. The famous kylix of the Foundry (not shown here) shows six different hammer types, the long thin ones being used for light hammering (Chatzidimitriou, 2005:62), similar to those seen in Figure 5.26c.



Figure 5.26: Evidence of helmet manufacture from Greek vase paintings. (a) Man hammering metal. From red-figure kylix, c. 500 BC. Staatliche Museen Berlin, No 1980.7. (b) Nude helmet-smith works on helmet with rasp. Notice the tools hanging on the wall. Red-figure kylix, 480 BC. Ashmolean Museum, Oxford, No 518. (c) Nude helmet-smith hammering helmet. Red-figure pyxis of Thaliarhos 520-500 BC. Petit Palais, Paris, No 382. (d) Hephaestus hammering Achilles helmet in the presence of Thetis who holds decorated shield. Red-figure kylix, 490-480 BC. Staatliche Museen Berlin, No 2294. (e) Hephaestus polishes Achilles shield in the presence of Thetis. Notice the helmet and tools at the background. Red-figure amphora, 490-480 BC. Museum of Fine Arts, Boston, No 13.188. (f) Young man working on a greave using saw. Red-figure kylix, 515-510 BC. Museo Archeologico Nazionale, Florence, No PD117. Images from Chatzidimitriou, 2005.

The smith in Figure 5.26a applies great force to the hammering of the metal sheet that he holds with pliers and hammers using a rectangular flat-head hammer which looks very robust. This can provide indication for a hammer used for early stages of hammering to shape. Figure 5.26d shows Hephaestus himself holding two-head hammer with flat and rounded heads in the vicinity of a heavily decorated helmet overlooked by Thetis, (*ibid.* 62) that shows similarities to what could be described as a ball-head hammer (Untracht, 1969:84). The smith would have employed all of his senses during this process. During hammering bronze becomes hard and annealing is necessary to restore the metal to the favourable working condition and to continue shaping (Bailey, 1982:30; Untracht, 1969:246). Skilled craftsmen recognise this moment from the sound of the hammer blow, which becomes more high-pitched when the metal needs annealing (Untracht, 1969:246). Overheating during annealing holds the danger of destroying the favourable working qualities of the metal; this is based on judgements on the colour of the metal, which is why annealing is often undertaken in a dark area (*ibid.* 246).

Even if the above pictorial evidence refer mostly to the making of Late Phase III Corinthian type helmets, which are thinner than their predecessors, it is clear that different types of hammers would be employed for different reasons during different steps of manufacture. Close examination of helmets in this thesis showed evidence for the use of a small hammer, which left oblique c. 3mm width marks on the bronze of Illyrian type helmets. These could be marks of a light hammer, such as a planishing hammer used at the final manufacture steps. Hammer blows seen in the x-radiographs of selected helmets did not provide sufficient information to indicate the type of hammer used. Further investigation of tool marks using SEM or by taking silicone rubber impressions of the surface could support understanding of metal working tools such as hammers or decorative punch marks used (Mortimer and Stoney, 1997) for the making and decoration of helmets.

Finishing would include cleaning and polishing of the surface and related to both hammered and cast pieces. In Figure 5.26e Hephaistos is most likely holding a piece of pumice for polishing Achilles' decorated shield; Figure 5.26b shows a young man using a tool likely to be a rasp (or strigil) which is used in a slight angle on the surface of the bronze helmet; and, in Figure 5.26f, man uses a type of saw to clean off unwanted edges before polishing the greave (Chatzidimitriou, 2005:64-65). Apart from the (most likely painted) decoration on the shields and helmets seen on this pottery, these latter three scenes provide important information on the final steps of helmet manufacture. There are no recorded pictorial representations of casting or annealing helmets or of tinning.

5.8.3. A NOTE ON HELMET WORKSHOPS

It is possible to discriminate between different hammering styles using x-radiography (Figure 5.11) and the chemical alloy composition may vary between stylistic groups of helmets excavated from different locations (Figure 5.24). This indicates potential to identify relationships between manufacture, helmet provenience, and typological variation, which would be invaluable in investigations of production workshops. Identification of helmets' origin and locality of manufacture is essential for understanding control of resources for producing military equipment within the Archaic period Hellenic world. The current use of 'location-name' terminology, which reflects the early discoveries and distribution of helmets, may be a convenient way to describe helmet typological associations but it does not indicate the place of their production. This nomenclature hinders understanding of the broad picture of helmet production in Greece and the distribution and control of military equipment. Currently helmets are named based on stylistic similarities" and their production is inferred by their distribution in the archaeological record; for example, subgroups of the Late Phase (III) Corinthian type helmets are thought to be made in *Magna Grecia* based on their distribution. Corinth is regarded as the major helmet producer in mainland Greece, but scientific evidence is required to demonstrate that other polis-states did not produce "Corinthian" type helmets.

Trace element composition could aid interpretation of helmet production. The two helmets from Aghia Paraskevi had the lowest Sn wt%, and the highest trace concentrations of Ni (Table 5.5). Trace element fingerprinting and/or Pb isotope analyses are commonly used methods to understand trade patterns and routes that may relate to social stratification, economic organisation and use of technology (Rapp, 1999). Both methods have been encountered with scepticism based on methodological and instrumental considerations (Chippindale, 1994; Muhly, 1995; Pernicka, 1999), and the methods are often seen as complementary (Pernicka *et al.*, 1990). Chemical fingerprinting can provide information to investigate (a) links between objects of distinct typology or archaeological context, and/or (b) links between objects and a known copper ore. The latter is more challenging and has its basis on the assumption that (i) each ore has a homogeneous and unique chemical signal, (ii) the process of smelting does not affect the composition of the final product, and (iii) recycling of scrap metal did not take place for the making of the final product (Craddock, 1976).

Pernicka's work (1990, 1999) convincingly shows that object categorisation can be achieved using trace element analyses with methods such as laser ablation inductive plasma mass spectroscopy that has sufficient low detection limits to detect heterogeneity between samples

(Craddock, 2009: 139) (AMC, 2008). A number of chalcophilic elements remain as impurities after smelting of the ore (S, Zn, As, Se, Ag, Cd, In, Sn, Sb, Te, Au, Hg, Ti, Pb, Bi) and their relative concentration profiles, rather than the actual amounts, are important for provenance studies (Pernicka, 1999). The concentration of some trace elements is directly related to smelting temperatures notably Ni where copper with or without Ni can be produced from the same ore depending on the smelting temperature (*ibid.*). Some volatile elements, such as Sb and As can be lost to different extents in the roasting process and other impurities such as Fe, S, Mo, Co, Ni and Pb during further refinement. Fe and S concentrations in the final object can therefore reflect the efficiency of smelting and purification process that took place (*ibid.*).

The detection limits required for this analysis cannot be attained by SEM-EDX, and were outside the scope of this study. Published analyses of Greek helmets using electron probe microanalyses (Northover, 1991) and flameless atomic absorption spectroscopy (Craddock, 1977) can be used to illustrate further that helmets can have distinctive chemical signatures (Table 5.7). Northover (1991) successfully analysed several samples from two different helmet fragments to demonstrate that they did not belong to the same helmet (Fitzwilliam, GR.2.1893 a and b). Even if the tin alloy was quite similar and tin concentration varied within each fragment, the concentration of the principle trace elements was different (As, Fe, Co, Bi and Ni), and reasonably homogeneously distributed across each fragment. That the two fragments are from different helmets is confirmed by stylistic observation of the decoration of the rim (*personal observation*). This example and the analysis undertaken in this thesis demonstrate the prospect for further chemical analyses and investigations that aim towards identification of helmet production workshops.

Museum / Acc. No.	Helmet Type / Date c. BC	Cu	Sn	Pb	Ag	Fe	Sb	Ni	Co	As	Bi	Zn	Au	Cd
Ashmolean Museum, Craddock 1971; 1977														
1881.90 (ASH2)	Corinthian, 7-6th c.	88.50	11.80	0.00	0.03	0.08	0.00	0.00	0.05	0.02	0.10	0.00	0.00	0.00
1885.464 (ASH1)	Illyrian, (Scythian), 5th c. BC	89.00	9.50	0.00	0.00	0.10	0.02	0.00	0.12	0.00	0.50	0.00	0.00	0.00
1963.3?	?, 7th c. BC	91.00	8.50	0.20	0.00	0.13	0.04	0.08	0.04	0.01	0.20	0.00	0.00	0.00
G478 (ASH3)	Apulo-Corinthian, 4th c. BC	90.00	9.70	0.08	0.00	0.14	0.05	0.07	0.06	0.03	0.20	0.01	0.00	0.00
British Museum, Craddock 1971; 1977														
BM.2818	?, 6-5th c. BC	86.00	10.20	0.03	0.96	0.45	0.01	0.00	0.04	0.00	1.00	0.00	0.00	0.00
BM.2820	Myros, 5-4th c. BC	92.00	7.50	0.14	0.00	0.10	0.00	0.00	0.20	0.10	0.30	0.00	0.00	0.00
BM.2837	Myros, 6th c. BC	89.00	9.50	0.03	0.15	0.50	0.03	0.05	0.14	0.80	0.80	0.00	0.00	0.00
BM.2821	Myros, 5-4th c. BC	92.00	7.10	0.08	0.00	0.10	0.03	0.15	0.08	0.00	0.19	0.06	0.00	0.00
National Museum Wales, Craddock 1971; 1977														
A877 (NMW9)	Corinthian, 7-6th c.	90.00	9.90	0.02	0.00	0.15	0.04	0.05	0.05	0.10	0.15	0.00	0.00	0.00
Fitzwilliam Museum, Northover, 1991														
GR.2a.1893 (FZ5)	Corinthian	91.42	7.99	0.02	0.00	0.15	0.08	0.00	0.04	0.05	0.19	0.03	0.08	0.01
GR.2b.1893 (FZ6)	Corinthian?	90.75	7.81	0.02	0.01	0.31	0.06	0.01	0.31	0.37	0.29	0.01	0.08	0.02

Table 5.7: Collection of published composition (wt%) analyses of Greek bronze helmets using flameless atomic absorption spectroscopy (Craddock 1971, 1977) and electron probe microanalyses (Northover, 1991; Blyth, 1993).

5.9. SUMMARY

This chapter investigated the typology and manufacturing techniques of 58 Greek helmets (8-4th c. BC) using a range of analytical techniques. Apart from a single example of as-cast Corinthian type helmet, metallography demonstrated that all other helmets exhibit various degrees of cold working and annealing. Results show that not all helmets of the Corinthian-Myros style were made entirely by casting as it was previously thought, but a combination of casting followed by hammering was also employed. The use of a pre-formed cast blank that was hammered into shape was previously supported (Swaddling, 1987), but new data show that the Myros style helmets would have been finely executed. This means that stylistic subgrouping of helmets does not necessarily reflect a common manufacturing technology.

Extensive hammering was evidenced by elongation of inclusions, fibering and texture in the bronze. Neutron diffraction texture analyses proved to be an important method for the non-destructive metallurgical characterisation of the helmets. Section thickness and grain size measurements confirmed a trend for thinner helmets and revealed generally smaller grain sizes through the stylistic development of the Corinthian type. A move from thicker to thinner and more intensely hammered helmets will produce a change in the mechanical performance of the helmets: thin hammered helmets would be stronger, lightweight but more brittle. Analyses independently confirm hardness measurements of Corinthian type helmets, which was not previously combined with compositional data (Blyth, 1977:78,79). This change can reflect a gradual change in the performance requirements of the helmet, and can provide evidence of technological innovation in the ancient world. X-radiography of Illyrian type helmets showed the value of this method in characterising hammering styles, which could be used to differentiate between production workshops. It also revealed casting porosity in a single example, making this the first reported cast Illyrian type helmet. Elemental composition analyses of these helmets showed that this has potential for grouping helmets to identify production workshops. More work is required to understand technological change in the making of helmets. This would add to the current typological/chronological sequences, which now show limitations because they are primarily based on stylistic criteria rather than on technological features revealed by scientific analyses.

That cross-sectioned samples are of α -bronze (5-14 wt% Sn) is significant for investigation of surface appearance because this demonstrates that the silver or black surface seen on some helmets cannot be due to casting or corrosion of phases in a cast microstructure. A small number of samples and published work indicate that the degree of hammering could influence the surface appearance and corrosion of archaeological bronze, which is examined next.

CHAPTER 6. SURFACE FINISHES, TINNING AND CORROSION OF HELMETS

6.1. INTRODUCTION

A discussion of artistic representations of helmets on pottery supported the hypothesis that decoration of helmets could be achieved by engraving, painting or plating (section 2.1.3). Arguments against decoration by artificially induced coloured corrosion patina or overpainting are based on ancient references to the regular cleaning and protection of armour, which could lead to removal of this type of decoration (section 2.2.1). Archaeometric evidence of plating on bronze helmets is rare. A prime example of an Illyrian type helmet at the British Museum (GR1914.4-8.1) has silver rivets at the rim, a very thin silver foil applied onto the bronze with tin solder and silver foil *repoussé* decoration attached to the cheekpieces with a calcite based adhesive (Hockey *et al.*, 1992; La Niece, 1993). In the case of another Illyrian helmet, analysis of which is included in this thesis (PE2), gold leaf decoration was applied on the bronze using a layer of birch pitch adhesive (Manti and Watkinson, 2008). Evidence supports the use of gold leaf decoration for funerary purposes in burial customs of northern Greece (e.g. Archontiko, Aghia Paraskevi) that become more common in the mid to late Archaic period. The only reported tin-plated helmet known to the author is a 5th c. BC Greek helmet in the British Museum (GR1856.12-26.616), and is thought to be the earliest tin plated museum object from the Mediterranean (Meeks, 1986; Meeks, 1993b). These few published examples of decorative technological choices could reflect the social significance of plating and the status of the wearer in the Archaic period. Further scientific investigation is necessary to evaluate the existence and distribution of plated helmets to support discussion on technological innovation and the social significance of helmet plating.

Identification of tinning on corroded archaeological bronzes is complicated as a silver/grey, black finish can be the result of corrosion of low-tin bronzes such as the examined helmets (section 2.2.2). Original tool marks can be preserved in fine corrosion patinas that occur via the internal oxidation of tin and the dissolution of copper from the surface to produce surface tin enrichment expressed by the copper dissolution factor equation f_{Cu} (Robbiola *et al.*, 1998a; Piccardo *et al.*, 2007; Robbiola *et al.*, 2008). The presence of extraneous elements is reported to be significant for the colour of the corrosion patina, which could be, bright grey, green, or blue, with blue patinas showing the largest amounts of extraneous elements (Robbiola *et al.*, 1998a). In the case of chromium, its unusual presence in black patinas on low-tin bronzes is thought to be important for the patina colour and there are hypotheses supporting intentional surface treatment (Han Rubin *et al.*, 1988). Other black patinas on low-tin bronzes are rarely found to be predominately composed of cassiterite and are more common on black high tin archaeological bronzes (section 2.2.2). Note that the word patina in this thesis refers to natural or artificial corrosion surfaces that preserve evidence of the original bronze surface, in other words mark the limits of original surface onto which copper-based compounds can be deposited due to corrosion in the burial (Figure 2.1).

Robbiola *et al.*, (1998a) produced a milestone work for understanding of corrosion mechanisms of low-tin archaeological bronzes. His data derived from the non-destructive SEM-EDX analysis of 16 small Bronze Age objects positioned at the SEM with no sample removal, using an estimated electron beam penetration of c. 1.5 μ m (KeV not reported) (*ibid.*). Evaluation of microstructures in cross-section and the 450 reported EDX analyses of features in corrosion profiles were based on 3 samples (No.1 bar-ingot 4.8wt% Sn; No.12 pin 10.1wt% Sn and No.24 pin 13.1 wt% Sn). The objects were first cast but further shaped by hammering and annealing as they exhibited a homogenous recrystallised grain structure and numerous deformed copper sulphide inclusions but only a few mechanical twins (*ibid.*). This was an excellent work but more data from cross-sectioned samples is necessary to extend and confine understanding of corrosion mechanisms that produce fine patinas seen on archaeological low-tin bronzes. To do this, 36 helmets were selected to study surface finishes, patination, and tinning (Table 6.1).

Type / Phase	Typology Code	Sample	Sn wt%	Sn SD	Thickness, Av. (um)	Position on Object
Attic						
Attic	ATT	PE4.3	9.3	0.1	790	neckguard, upper
Chalkidian						
III	CH_III	OL79.1	11.4	0.1	540	unknown, loose fragment
V	CH_V	OL66.2	10.0	0.3	565	crown, middle back
Etruscan						
Etruscan	ETR	PR4.1	9.1	0.6	805	side, lower
Corinthian						
(I) Early	COR_IA	OL21.1	10.8	0.2	500	neckguard, lower part
		OL29.1	7.8	0.2	600	crown, top
	COR_IA*	OL17.1	9.6	0.3	550	cheekpiece, right, middle
		OL31.1	10.7	0.2	850	crown
		OL41.1	11.2	0.6	600	cheekpiece, right
COR_IA.crest	OL69.1	9.1	0.3	800	crown, top, by the high ridge	
(II) Middle	COR_II.1.3.Myros	OL27.1	12.3	0.1	1150	side
		OL58.1	10.0	0.3	800	unknown, loose fragment
	COR_II.1.4.	OL44.1	9.1	0.3	380	neckguard, left
	COR_II.1.4.*	OL46.1	8.7	0.2	840	neckguard, top
		OL57.1	10.3	0.2	510	unknown, loose fragment
	COR_II.2.4.edge	OL50.1	10.4	0.2	330	crown, rear
		OL53.1	9.7	0.1	760	neckguard, upper left
		PR1.1	6.6	0.1	550	crown, front
	COR_II.2.4.edge*	OL49.1	12.8	0.0	275	crown, rear
		OL75.2	11.1	0.1	625	crown
(III) Late	COR_III.2.4.V	OL70.1	8.0	0.2	170	crown, middle back
	COR_III.2.4.V.Lotus	OL63.1	11.3	0.0	175	unknown, loose fragment
	COR_III.2.4.Λ.edge*	OL71.1	10.8	0.2	300	side, right
		OL73.1	10.5	0.2	350	neckguard, upper
		OL74.1	12.7	0.1	565	unknown, loose fragment
Illyrian						
(I) Early	IL_IB	OL4.2	13.5	0.1	910	crown, top
(II) Middle	IL_IIA	PE2.2	10.5	0.1	700	crest-track, middle small ridge
		IL_IIA (forehead)	AP4.2	5.0	0.1	240
		AP5.1	5.0	0.1	230	neckguard, lower part
(III) Late	IL_IIIA1	OL11.1	6.5	0.4	500	cheekpiece, right, middle
		PE3.1	9.9	0.5	n.a.	crown, top, by the high ridge
	IL_IIIA1*	OL5.1	10.7	0.4	350	crown, upper left
		OL9.2	10.5	0.4	650	crest-track, left ridge, back
		PE1.1	9.9	0.1	320	crest-track, high ridge
		PE1.2	9.9	0.2	n.a.	crest-track, ridge
	IL_IIIA3*	OL13.1	9.8	0.1	400	cheekpiece, right, low part
IL_IIIB1	OL78.1	13.8	0.4	420	crown, front, lower	

Table 6.1: List of helmet cross-sectioned samples analysed showing sample position, thickness, chronology and bulk Sn wt% concentration with corresponding deviation (SD). The surface of these samples was investigated in plan view before mounting and polishing to examine surface finishes and tinning.

Helmets were chosen on the basis that they had a fine smooth silver/grey, black, blue, or green corrosion surface or that exhibited minor or no post-excavation cleaning. The small number of analysed samples compared to the number of accessed helmets is a result of inappropriate cleaning methods used in the past, which stripped the surface of corrosion. Samples were removed from non-chemically stripped helmets and from representative uncleaned areas, which were covered by soil where possible. Analyses of helmets included in this chapter was designed to investigate:

- a. Remains of tinning;

- b. evidence of polishing or intentional patination, in order to explore surface finishes on helmets practiced during the Archaic period;
- c. the nature of silver/grey and black or other colour fine corrosion surfaces (or patinas), in order to further understanding of corrosion mechanisms responsible for the formation of such patinas.

Analyses included SEM-BSE morphological examination of the surface of samples (Table 6.1) supported by XRD and SR-XRD before mounting and polishing and physicochemical characterisation of corrosion profiles using SEM-BSE, EDX maps and SEM-EDX elemental composition of features in the corrosion profiles in the polished sections (Table 3.1).

6.2. GENERAL ASSESSMENT OF HELMET APPEARANCE

The general surface appearance of the helmets was qualitatively evaluated based on macroscopic observation of the nature of corrosion deposits and the colour of the exposed underlying fine corrosion layer (patina) on each helmet and their samples. This broadly related the condition of individual samples to that of the bulk helmet surface, although this was not always possible. A small number of representative corrosion deposits were analysed using CuK α or SR-XRD to confirm their nature. The blue deposit found on several samples is azurite $\text{Cu}_3(\text{CO}_3)_2(\text{OH})_2$ (Figure 6.1) and the dark green/green deposit malachite $\text{Cu}_2(\text{CO}_3)(\text{OH})_2$ (Figure 6.2).

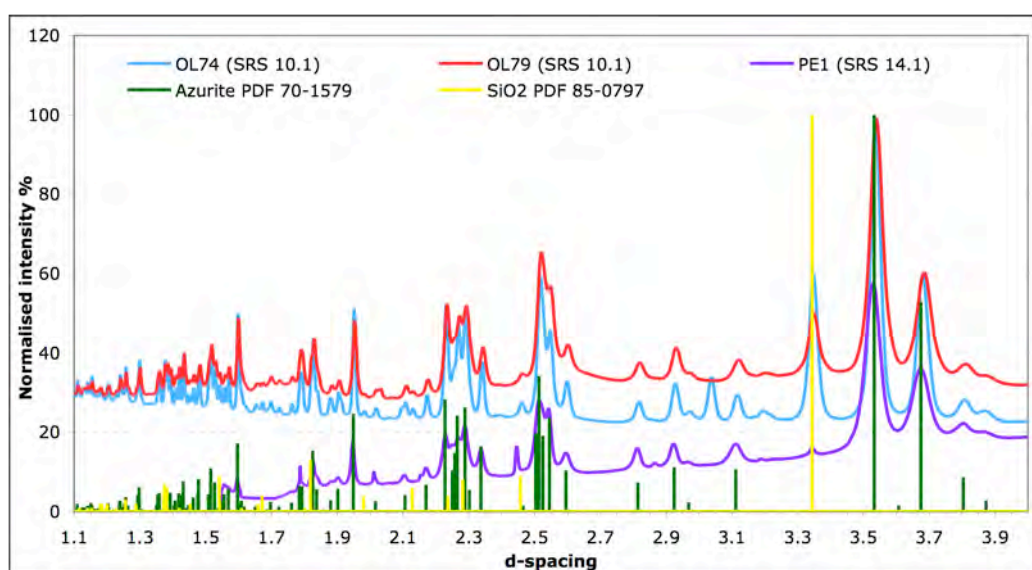


Figure 6.1: Diffraction patterns of corrosion deposits from helmets OL74, OL79 and PE1 confirming the presence of azurite. SR-XRD, SRS 10.1, $\lambda=0.92\text{\AA}$, corrosion flakes analysed in reflection geometry. SRS 14.1, $\lambda=1.488\text{\AA}$, corrosion powder samples analysed in transmission geometry.

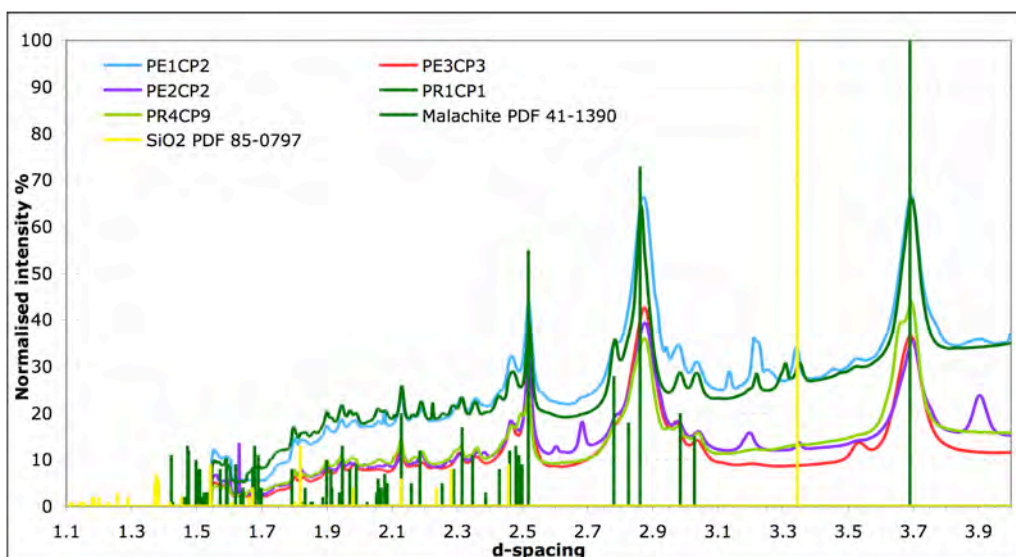


Figure 6.2: Selected diffraction patterns of powder corrosion samples from helmets PE1, PE2, PE3, PR1 and PR4 confirming the presence of malachite. SRS beamline 14.1, $\lambda=1.488\text{\AA}$, in transmission geometry.

Based on qualitative assessment of relative abundance of azurite/malachite deposits, the physical nature of malachite and the nature of the underlying corrosion patina, the helmets were broadly placed in 5 categories (Table 6.2):

1. Helmets in Group A exhibit localised voluminous malachite pustules with areas of smooth grey or black patina. Helmets OL5 and OL31 from this group have azurite deposits in the inner side of the helmets. This may also have been present on the outer surface but could have been removed during mechanical cleaning which is evidenced by the absence of soil on the outer side. The characteristic malachite morphology is used to consider these helmets as an individual group.
2. Group B includes helmets with predominantly azurite deposits and a fine black or grey patina, which is largely free of deposits on several helmets. Helmet PE1 is included in this group based on its sample having an exposed grey/silver surface with mainly azurite deposits whereas the rest of the helmet is predominantly covered by malachite.
3. Helmets in Group C are largely covered by both azurite and malachite deposits and exhibit a black, brown or green patina. Sample OL4.2 is not indicative of the bulk helmet condition.
4. In Group D, malachite is more abundant relative to azurite, which is located on a black or green surface with several areas of red patina. Several helmets of Group C and D have been mechanically cleaned (including OL4.2, OL63, OL57, OL41, OL44) and assessment is predominantly based on the samples, which do not show evidence of cleaning. OL58 exhibits voluminous corrosion.

5. Group E includes helmets with areas of exposed dark or red patinas covered by malachite, which is in most cases voluminous (e.g. PE4, AP4, AP5, PR1).

This preliminary macroscopic assessment revealed malachite deposits predominantly cover the patina of a helmet and a finer patina is more frequently observed on helmets where azurite predominates. The exposed patina is finer in groups where azurite is predominant and, in several cases, appears black or grey (Group B). With increasing malachite deposits the patina appears dark red (Group E). Group A shows distinct malachite corrosion pustules with a fine grey/black patina and is considered a special corrosion case. These observations suggest that fine black or grey and red/brown patinas can be related to different burial corrosion processes favouring the formation of azurite or malachite deposits.

Helmet Group	Predominant corrosion deposit	Surface finish colour	Helmet	Sample
Group A	Malachite - pustules	Black	OL31	OL31.1
		Black/grey	OL5	OL5.1
		Grey	OL27	OL27.1
Group B	Azurite	Black	OL74	OL74.1
			OL75	OL75.2
			OL79	OL79.1
		Grey	PE1	PE1.1
		Soiled	OL13	OL13.1
Group C	Azurite / Malachite	Black	OL4	OL4.2
			OL78	OL78.1
		Black/grey	OL73	OL73.1
		Brown	OL49	OL49.1
			OL50	OL50.1
			OL57	OL57.2
			OL63	OL63.1
		Green	OL71	OL71.1
			OL70	OL70.1
			OL9	OL9.2
		Blue	OL66	OL66.1
OL66	OL66.1			
Group D	Malachite / Azurite	Black/red	OL21	OL21.1
			OL41	OL41.1
			OL44	OL44.1
		Green	OL58	OL58.1
		Green/Red	OL29	OL29.1
			OL53	OL53.1
Group E	Malachite	Black/red	AP4	AP4.2
			AP5	AP5.1
		Green/Red	OL11	OL11.1
			OL69	OL69.1
			PE2	PE2.2
			PE4	PE4.3
			PR1	PR1.1
PR4	PR4.1			

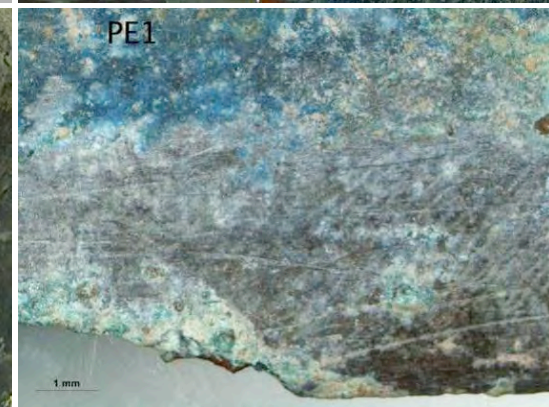
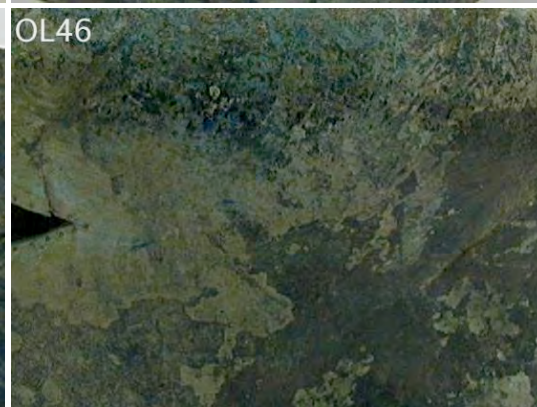
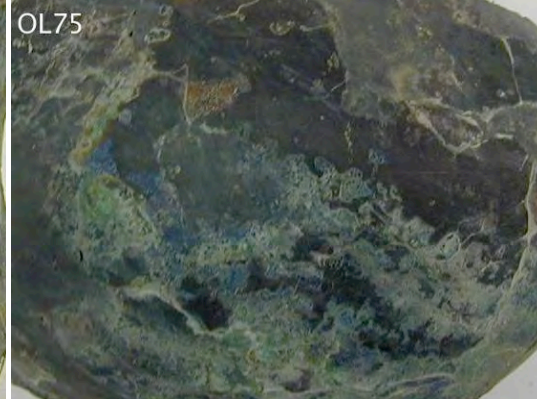
Table 6.2: Groups of helmets based on the relative abundance of azurite and/or malachite established by macroscopic observation. Note that the red patinas are encountered with malachite deposits and black or grey patinas are predominantly found in the presence of azurite.

Figure 6.3: (next page) Details of the surface corrosion and colour of helmets investigated. Note that samples from OL46 and OL13 are covered by blue deposits and the pictures shown here may not be representative of the selected samples.

Group A

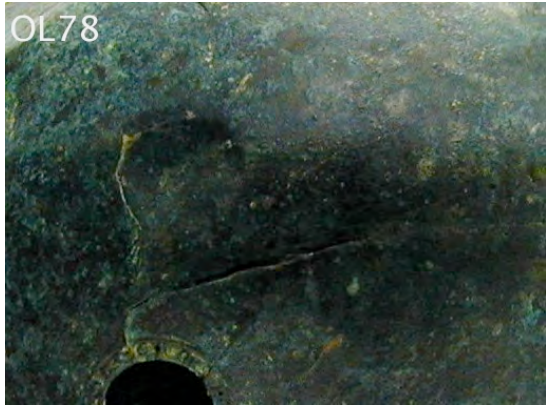


Group B



Group C

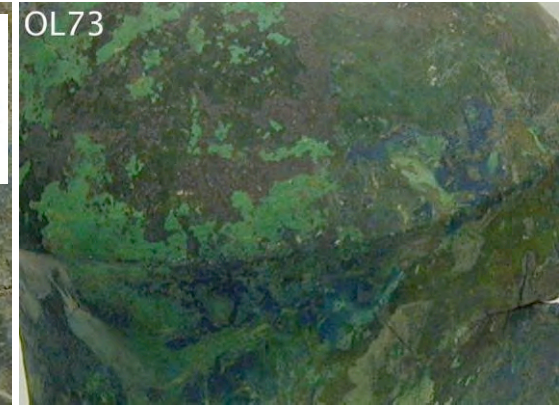
OL78



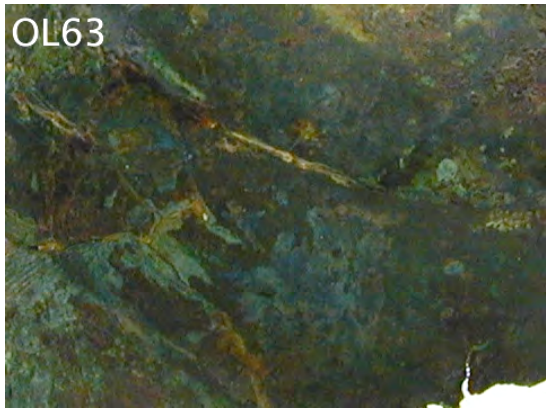
OL4



OL73



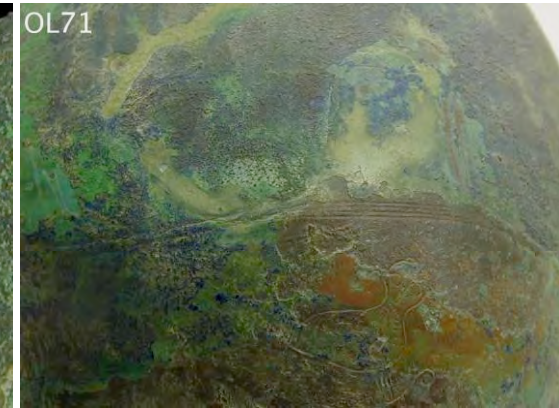
OL63



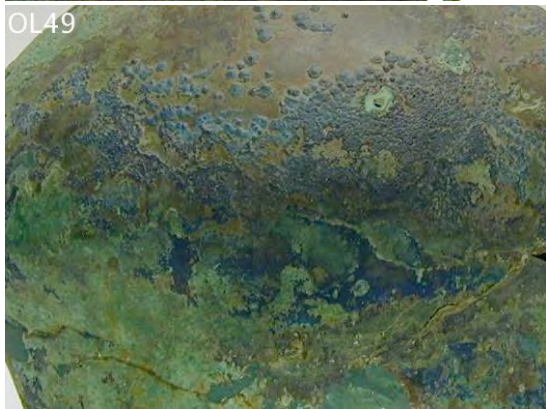
OL57



OL71



OL49

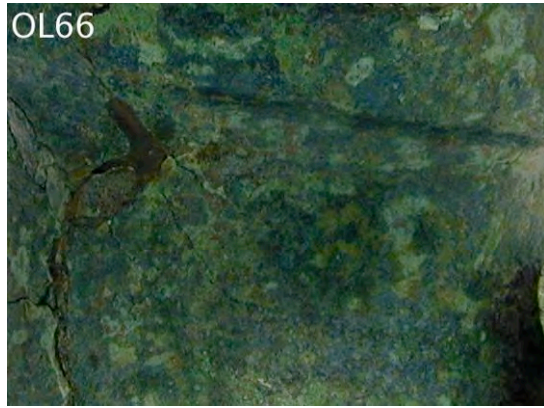
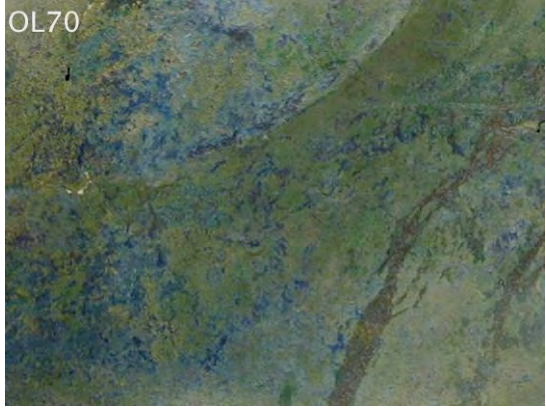


OL50

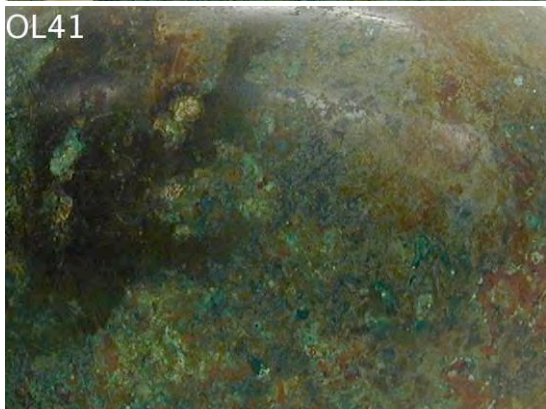
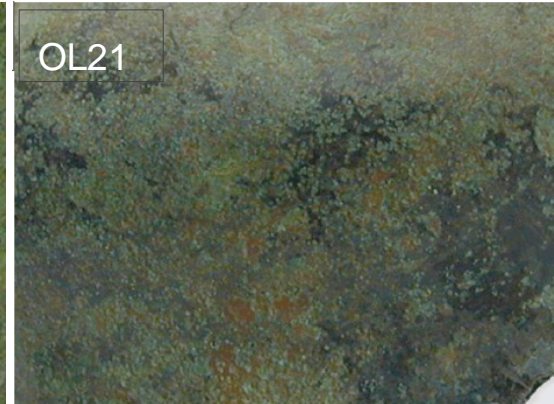
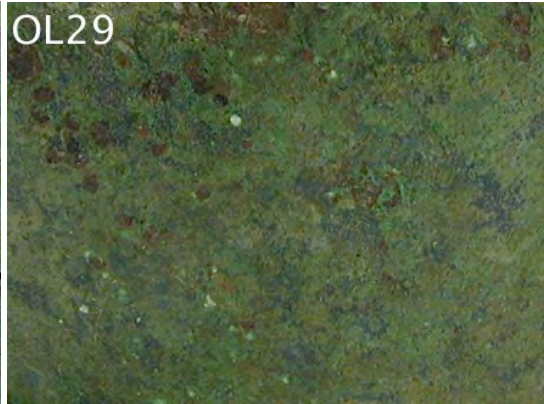


OL9



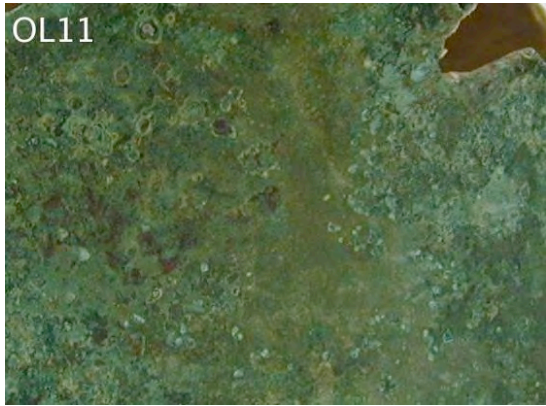


Group D

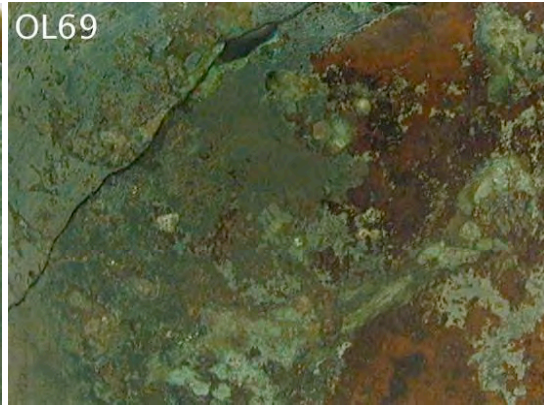


Group E

OL11



OL69



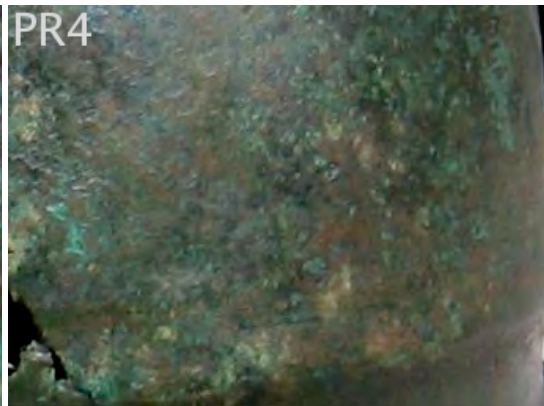
PE2



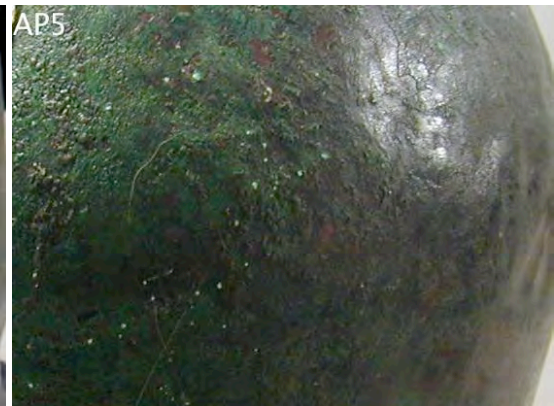
PE4



PR4



AP5



PR1



AP4



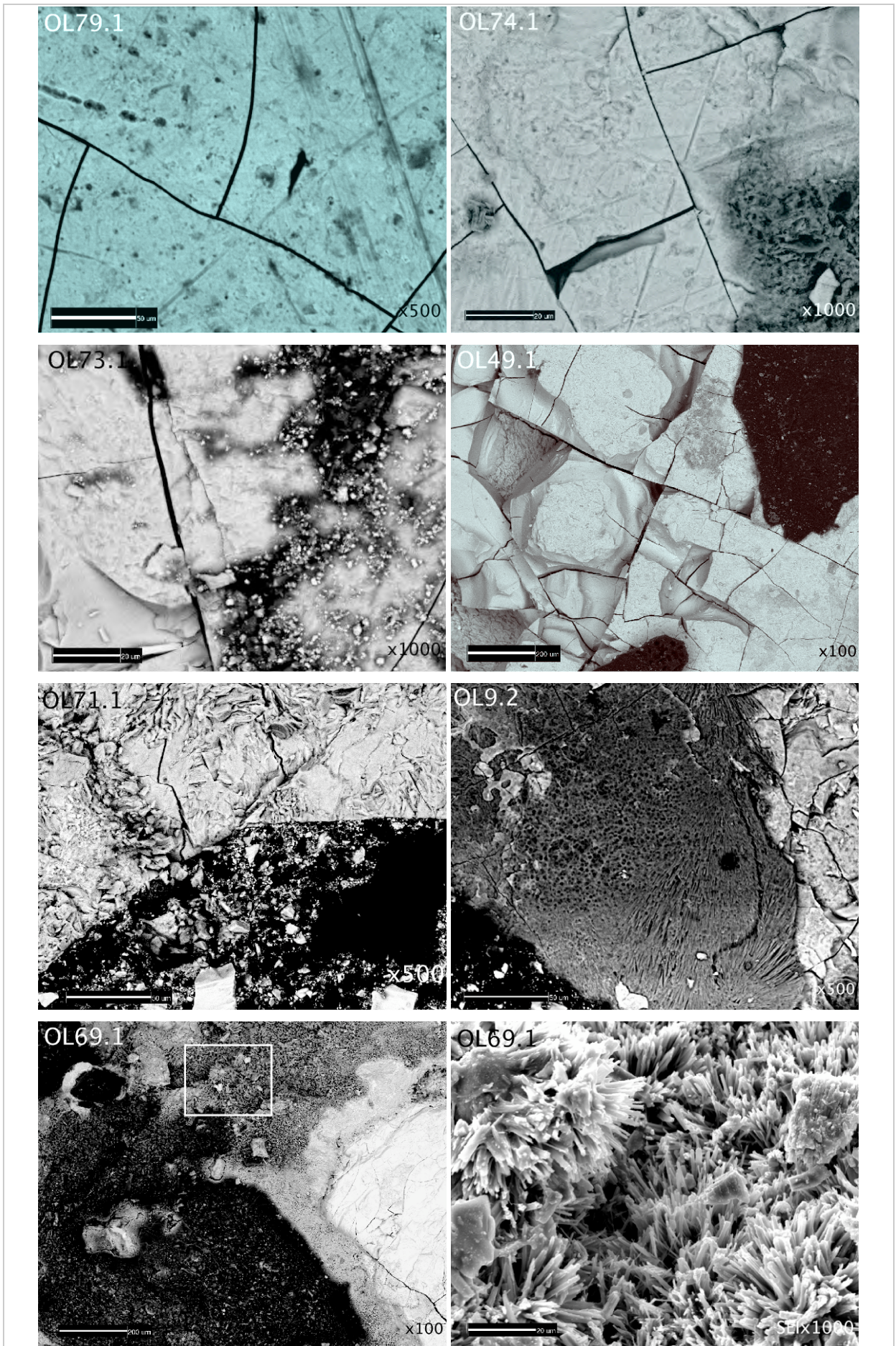
6.3. INVESTIGATION OF POLISHING MARKS AND TINNING

6.3.1. PLAN-VIEW SEM-BSE EXAMINATION OF UN-MOUNTED SAMPLES

6.3.1.1. Evidence of polishing marks

SEM-BSE examination of the surface of un-mounted samples (Table 6.1) revealed a smooth corroded surface (patina) that is visible when not covered by corrosion deposits (Figure 6.4). The condition of the surface patina seems to be related to the nature of the corrosion deposit. An extremely smooth but cracked patina preserving polishing marks offers a ‘marker of original of surface’ (MOS) and is seen when it is free of corrosion deposits (Figure 6.4, OL79.1, OL74.1). This patina is pitted in cases where spiky (Figure 6.4, OL73.1) or flat compact corrosion (Figure 6.4, OL49.1) deposits are present. The removal of flat compact deposits can cause destruction of the MOS (Figure 6.4, OL71.1, malachite green deposit) or expose polishing marks on the patina, which are also imprinted at the underside of the compact deposit (Figure 6.5, OL74.1, azurite deposit confirmed by SR-XRD, Figure 6.1). OL9.2 shows a layered corrosion deposit composed of an exterior flat compact and an inner fibrous corrosion deposit (Figure 6.4, OL9.2). The patina in this case mimics the fibrous nature of the corrosion with which it is in direct contact. Thicker corrosion deposits composed of several layers are predominantly on samples from Group E obscuring the MOS (e.g. Figure 6.4, OL69.1). The exterior layers of these deposits often have a spiky ‘sea-urchin’ appearance, which is most likely malachite. Overall, 11 of the examined helmets were covered by corrosion deposits obstructing close observation of their MOS and evidence of tinning (Table 6.3).

Figure 6.4 (next page): Plan-view BSE images showing characteristic conditions of MOS and types of corrosion deposits. OL79.1: MOS in superb condition with minor cracking. OL74.1: fine MOS with minor pitting covered by spiky corrosion deposit. OL73.1: pitted MOS covered by spiky corrosion and soil deposits. OL49.1: fine MOS with extensive pitting disfiguring evidence of polishing; covered by flat compact deposit. OL71.1: flat corrosion deposit covering surface, which is damaged in uncovered areas. OL9.2: flat layer of fibrous corrosion situated between a flat compact corrosion layer and porous MOS that resembles the fibrous nature of the deposit. OL69.1: general view of layered corrosion deposits on damaged MOS; detail of ‘sea-urchin’ corrosion deposit on the same sample. Scale is 200µm at x100, 50µm at x500 and 20µm at x1000 magnification.



Plan-view BSE observation at high magnifications reveals that twelve helmets exhibit evidence of polishing marks at the MOS (Table 6.3, Figure 6.6). The width of the polishing marks varies: OL29, OL46, OL73 and OL74 show the thinnest grooves some of which are less than $1\mu\text{m}$ thick (Figure 6.5, d). Apart from the grooves observed on OL74.1, for the majority of samples grooves are parallel to each other indicating that polishing was directional. Samples PR4.1, OL31.1 and OL11.1 show crude scratches unlikely formed from polishing and probably due to post excavation cleaning (Figure 6.6, PR4.1). OL70.1 is thoroughly covered by deposits apart from the edge where polishing marks are present. AP5.1 has a flat smooth surface in a small exposed area but polishing marks are not observed perhaps due to examination of an unrepresentative area. Overall, polishing marks are detected mainly on the surface of samples from helmets in Group A and B (Table 6.3) because they are relatively free of corrosion deposits or deposits only cover them locally.

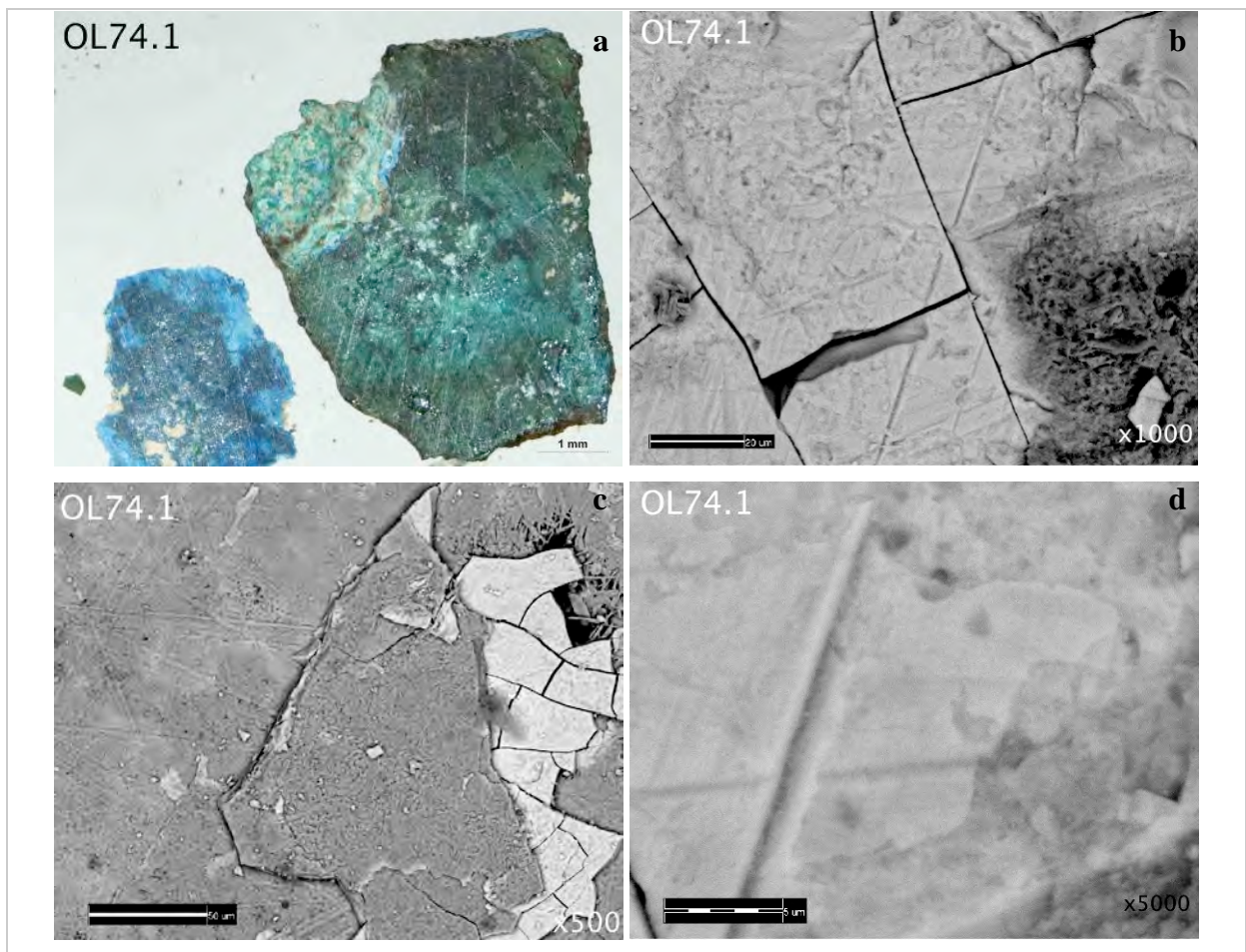


Figure 6.5: Images showing the condition and polishing marks on helmet OL74. (a) Optical image showing detached corrosion deposit from the surface; the flake is composed of azurite as confirmed by diffraction. (b) BSE image of the MOS of the patina that preserves polishing marks. (c) Detail of the underside of the azurite deposit flake, which shows imprints of polishing marks. (d) BSE in high magnification showing detail of fine groove (less than $1\mu\text{m}$ width) created by polishing. Scale is $50\mu\text{m}$ at $\times 500$, $20\mu\text{m}$ at $\times 1000$ and $5\mu\text{m}$ at $\times 5000$ magnification.

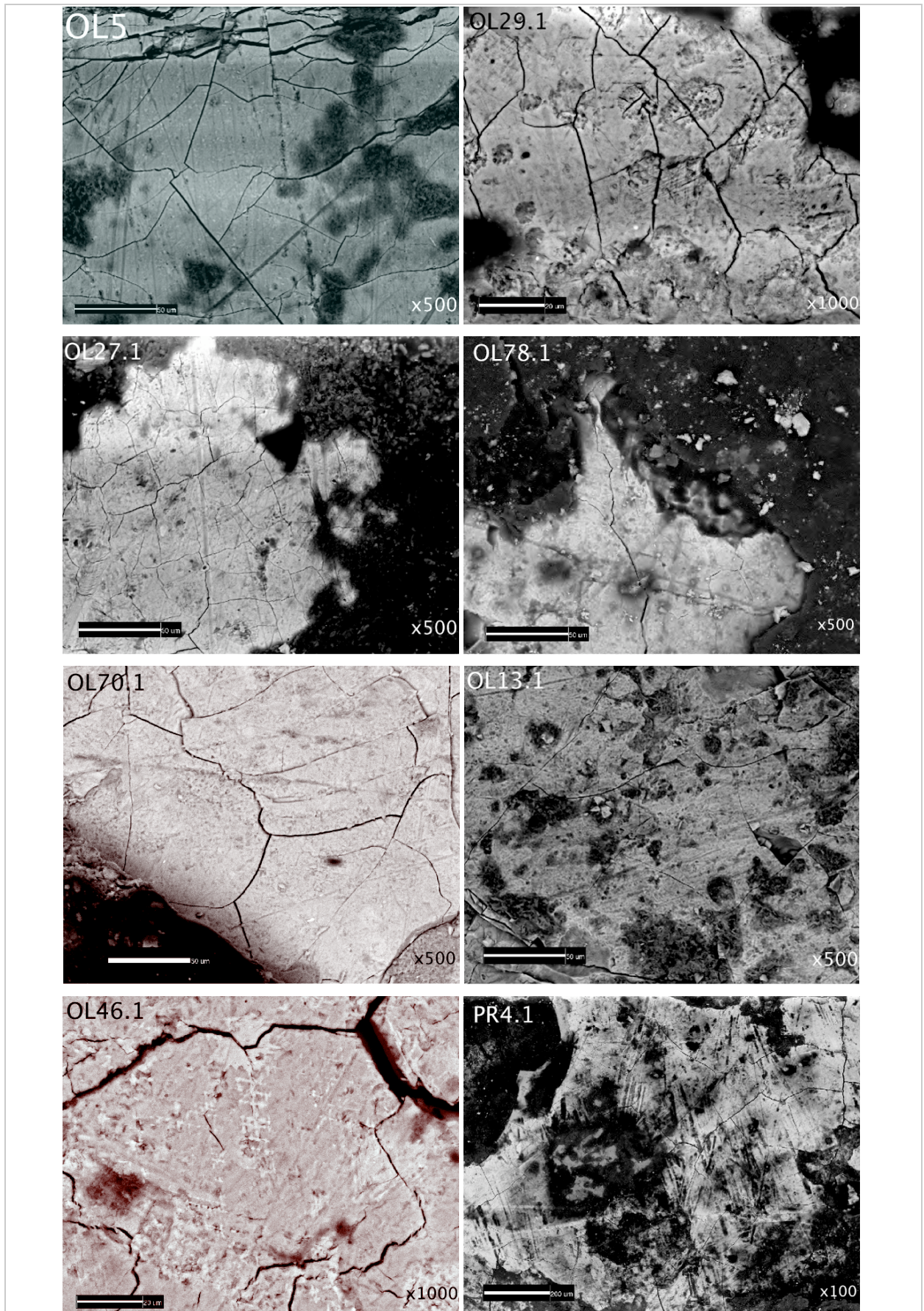


Figure 6.6: SEM-BSE images of the surface of helmet samples showing polishing marks preserved on the marker of original surface at the patina / corrosion deposit interface. PR4.1: scratches on the surface due to post excavation cleaning. Scale is 200µm at x100, 50µm at x500 and 20µm at x1000 magnification.

Polishing marks	Appearance Group	Predominant deposit	Patina Colour	Sample
Yes	Group A	Malachite - pustules	Black/grey	OL5.1
			Grey	OL27.1
	Group B	Azurite	Black	OL74.1
				OL75.2
				OL79.1
			Grey	PE1.1
			Soiled	OL13.1
	Group C	Azurite / Malachite	Black	OL78.1
			Black/grey	OL73.1
			Green	OL70.1
Group D	Malachite / Azurite	Green/Red	OL29.1	
No	Group E	Malachite	Black/red	AP5.1
Obscured	Group C	Azurite / Malachite	Black	OL4.2
			Brown	OL50.1
				OL57.2
				OL63.1
	Group D	Malachite / Azurite	Blue	OL66.1
			Black/red	OL44.1
			Green	OL58.1
	Group E	Malachite	Green/Red	OL53.1
			Black/red	AP4.2
			Green/Red	OL69.1
Damaged	Group C	Azurite / Malachite	Brown	OL49.1
			OL71.1	
			Green	OL9.2
	Group D	Malachite / Azurite	Black/red	OL21.1
			OL41.1	
Post depositional	Group A	Malachite - pustules	Black	OL31.1
	Group E	Malachite	Green/Red	OL11.1
			PR4.1	
Not examined	Group E	Malachite	Green/Red	PE2.2
				PE4.3

Table 6.3: Results of SEM-BSE investigation of polishing marks on the surface of helmet samples.

6.3.1.2. Evidence of tinning

The samples not covered by deposits exhibit smooth patinas with preserved polishing marks (Table 6.3). Hence, none of these samples shows physical evidence of a granular η -Cu₆Sn₅ on their exposed patina. A flat thin layer of ε -Cu₃Sn has no obvious physical characteristic to aid its identification (section 4.4). BSE imaging of the surface of helmet samples showed that the majority of exposed patinas are of a relatively uniform composition. OL13.1 and PE1.1 have patches of a phase with a higher average atomic number (brighter areas in BSE) as compared to the rest of their patina (Figure 6.7). This could be the result of localised corrosion or due to remains of a flat ε -Cu₃Sn and these cases are examined further with SR-XRD analyses directly employed on the surface of the sample.

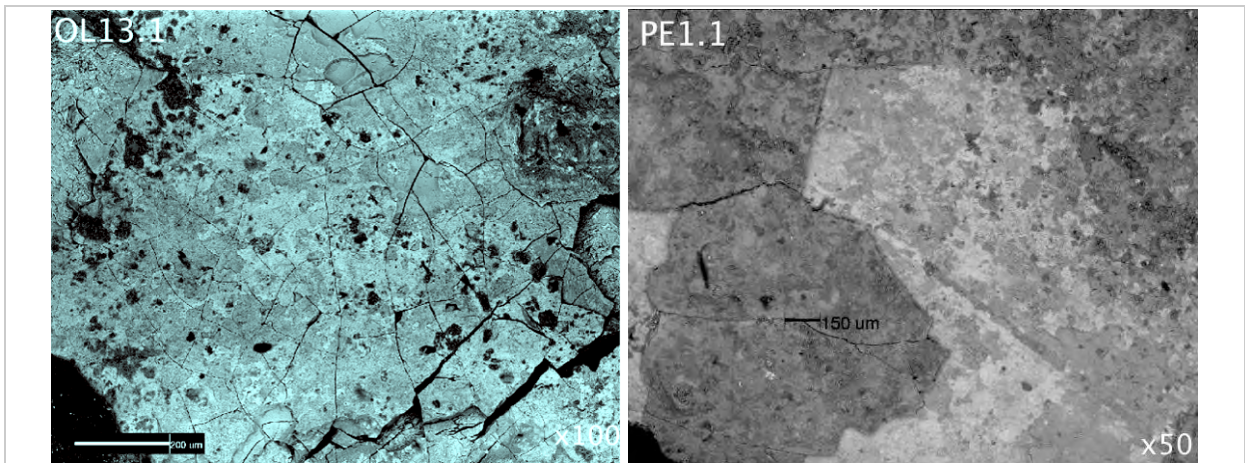


Figure 6.7: SEM-BSE images of the surface of OL13.1 and PE1.1 showing localised uneven composition in their patinas; patches of higher average atomic number are observed.

Tinning remains (if present) could be hidden under corrosion deposits that limit their detection. Analyses of tinned Roman cross-sectioned samples in Chapter 4 showed that η - Cu_6Sn_5 scallops are located at the limit of the original bronze surface (MOS) from where they elongate into the corrosion deposit (e.g. as found on the silver/grey green surface on Ceredigion skilnet, Figure 4.33). ϵ - Cu_3Sn existed within the patina that marked the limits of the original bronze. Identifying the interface between patina | ϵ - Cu_3Sn was difficult because of the extremely thin and planar nature of ϵ - Cu_3Sn observed on as-tinned bronzes (e.g. as on fine black-green layer on MB3 skilnet, where ϵ - Cu_3Sn was detected by diffraction Figure 4.34). The sequence in which intermetallics would be expected, if tinning had taken place, is:

un-corroded bronze | patina | sharply defined MOS, ϵ - Cu_3Sn | η - Cu_6Sn_5 | corrosion deposit.

Strict definition of the terms ‘marker of original surface’ and ‘patina’ should include any intermetallics because they would form a new surface boundary that marks the original shape of the object. To facilitate discussion, both terms here refer to the physical features that define the shape of the underlying corroded bronze. All samples were further investigated in cross-section to examine the presence of intermetallics at the interface between the marker of original surface and corrosion deposits.

6.3.2. CROSS-SECTIONAL EXAMINATION OF THE PATINA | DEPOSIT INTERFACE

6.3.2.1. Morphology of the marker of original surface (MOS)

Mounted polished cross-sectioned samples were examined using bright-field polarised microscopy (BFPM) and SEM-BSE to investigate the patina | corrosion deposit interface for the presence of Cu-Sn intermetallics. Evaluation of the nature of this interface can contribute

to discussions of corrosion mechanisms. The nature of this marker varies between samples (Table 6.4, Figure 6.8). The majority of samples exhibit an extremely straight and sharply defined boundary which marks the original surface (MOS) at the patina | corrosion deposit interface (SMOS=Sharply defined Marker of Original Surface) that preserves polishing marks whereas only a few exhibit a less clearly defined boundary at the patina | deposit interface (BMOS=Broadly defined Marker of Original Surface) (Table 6.4). Exception to this is OL70.1, which shows evidence of polishing but a BMOS surface. This sample is thoroughly covered by deposits apart from the edge where polishing is present. Cracking and lamination of the outer part of the patina in OL63.1, is likely to be the result of aging of the patina and disrupts what could have been a SMOS. Aging of corrosion layers is previously reported to take place in advanced corrosion manifested by cracking and splitting (Robbiola *et al*, 1998, fig. 11). In a small number of samples, the nature of the MOS varied between helmet sides or even within the same side. Characterisation reported here is based on several BFPM and BSE images of features mainly at the outer helmet side (Figure 6.18, Figure 6.22, Figure 6.24).

MOS	Helmet Group	Predominant deposit	Polishing marks	Helmet	
SMOS	Group A	Malachite - pustules	Yes	OL27.1	
				OL5.1	
			Post depositional	OL31.1	
	Group B	Azurite	Yes		OL13.1
					OL46.1
					OL74.1
					OL75.2
					OL79.1
					PE1.1
	Group C	Azurite / Malachite	Yes		OL73.1
					OL78.1
			Obscured	OL4.2	
				OL50.1	
				OL66.1	
	Group D	Malachite / Azurite	Yes		OL29.1
				Obscured	OL53.1
	Group E	Malachite	Post depositional	PR4.1	
			Obscured	PR1.1	
			No	AP5.1	
n.a.			PE2.2		
			PE4.3		
BMOS	Group C	Azurite / Malachite	Yes	OL70.1	
	Group E	Malachite	Obscured	AP4.2	
SMOS (aged)	Group C	Azurite / Malachite	Obscured	OL63.1	
	Group D	Malachite / Azurite	Obscured	OL44.1	
SMOS (aged fibrous)	Group C	Azurite / Malachite	Damaged	OL9.2	
Damaged	Group C	Azurite / Malachite	Obscured	OL57.2	
			Obscured	OL58.1	
	Group D	Malachite / Azurite	Damaged	OL21.1	
				OL41.1	
	Group E	Malachite	Post depositional	OL11.1	
		Obscured	OL69.1		

Table 6.4: Quality of the marker of original surface (MOS) on helmets. SMOS denotes a sharply defined marker of the original surface and BMOS a broadly defined MOS.

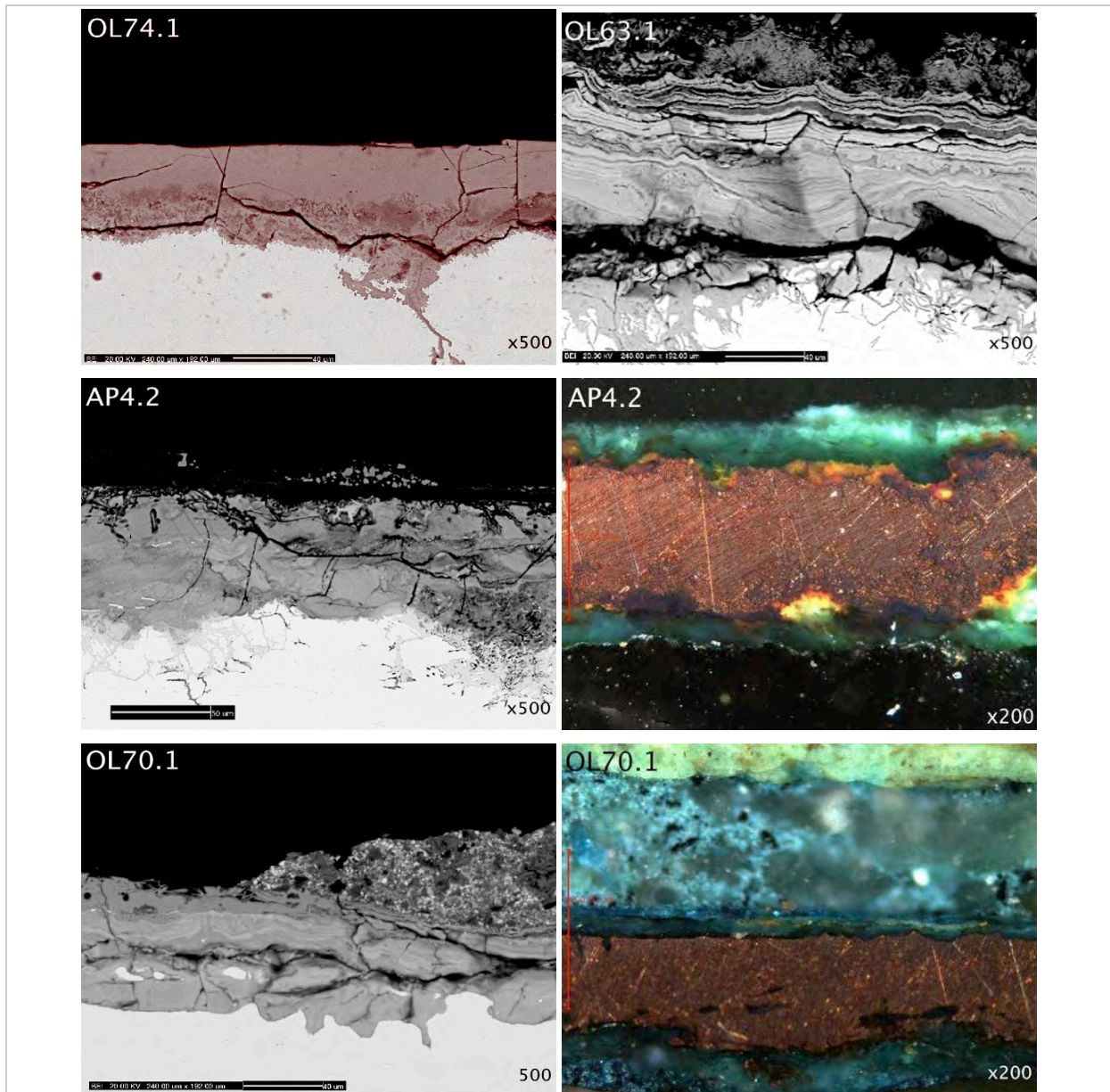


Figure 6.8: BSE and BFPM images showing characteristic qualities of the marker of original surface at the patina | corrosion deposit interface. OL74.1: sharp MOS (SMOS) with no corrosion deposit. OL63.1: heavily cracked and banded patina (SMOS-aged) covered with brown/red spiky corrosion deposit. AP4.2: broadly defined MOS (BMOS) under malachite deposits. OL70.1: broadly defined MOS (BMOS) under spiky azurite deposits. Scale is 40 μ m in BSE images apart from AP4.2 where is 50 μ m.

6.3.2.2. Unusual features at the patina|deposit interface: searching for η -Cu₆Sn₅

A small number of cross-sections with thick deposits of malachite and/or azurite exhibit an unusual microstructure just above the limit of the original bronze surface; this appears brighter in BSE relative to its underlying patina (Figure 6.9). It may indicate the presence of higher density intermetallics that were hidden under the corrosion deposits during plan-view investigation. BFPM and EDX mapping demonstrate that this bright (in BSE) compound is cuprite rather than a tin-rich phase (Figure 6.11; Figure 6.12). Investigation of cross-sections failed to reveal any evidence of a granular η -Cu₆Sn₅.

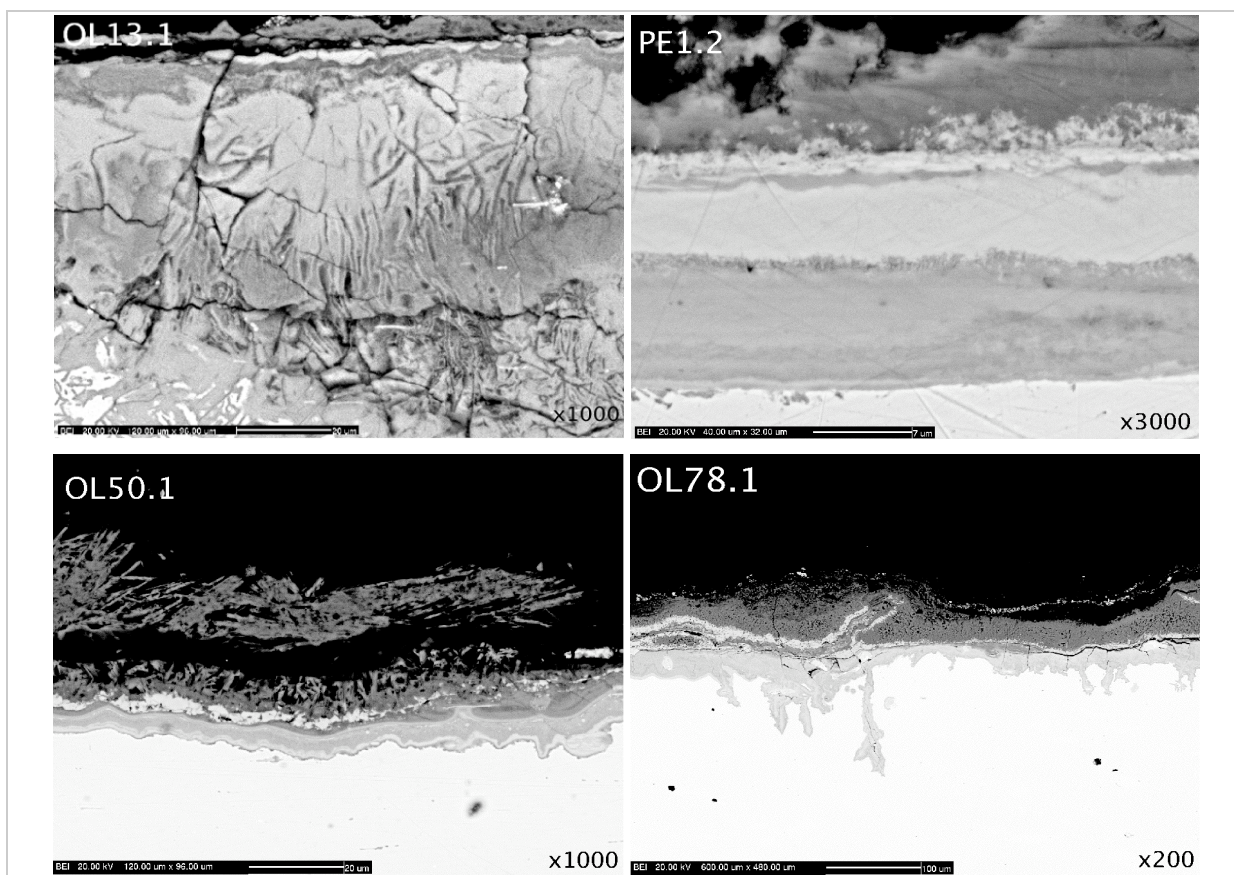


Figure 6.9: BSE images showing in the corrosion deposits unusual compound with higher average atomic number relatively to its underlying corrosion that marks the limit of the original bronze surface. Scale is 100 μ m at x200, 20 μ m at x1000 and 7 μ m at x3000.

The distribution of a cuprite surface layer could indicate an association with azurite deposits (OL50.1, OL13.1, OL74.1 inner, Figure 6.10, Figure 6.11) but it is also visible in cases where the sample is covered by malachite deposits (Figure 6.12, OL78.1 inner). Cuprite surface layers are observed on helmets with increased amounts of corrosion deposits. At high magnifications, it becomes evident that this cuprite layer forms the basis of numerous, extremely fine, straight needle-like crystals that elongate from the patina upwards. Each individual crystal is cuprite red at its base and gradually changes into azurite or malachite. This change is visible in BFPM and EDX of OL78.1, where the cuprite base of single needle-like crystals is depleted in oxygen (Cu_2O , 11.18 at% O by stoichiometry) and their outer part is increased in oxygen to form malachite or azurite (38.63 and 40.17 at% O respectively) (Figure 6.12). The orientation of individual needles in ‘spiky’ azurite (OL50.1) is not as easy to distinguish as in the case of malachite (OL78.1), where crystals develop into a ‘sea-urchin’ shape similar to those seen in plan-view on OL69.1 (Figure 6.4). In one case, such ‘sea-urchin’ shaped malachite crystal is present directly onto the green patina and a cuprite base is absent (OL44.1, Figure 6.13). This sample exhibits a thick, layered corrosion patina and absence of a cuprite base may be due to advanced corrosion.

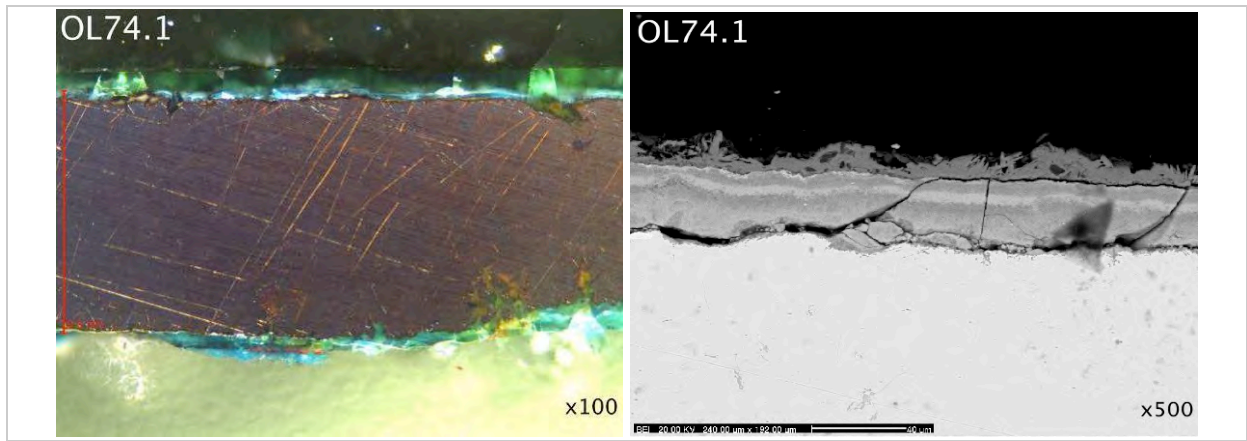


Figure 6.10: BFPM and BSE showing spiky azurite deposit with cuprite base. OL74.1 inner helmet side.

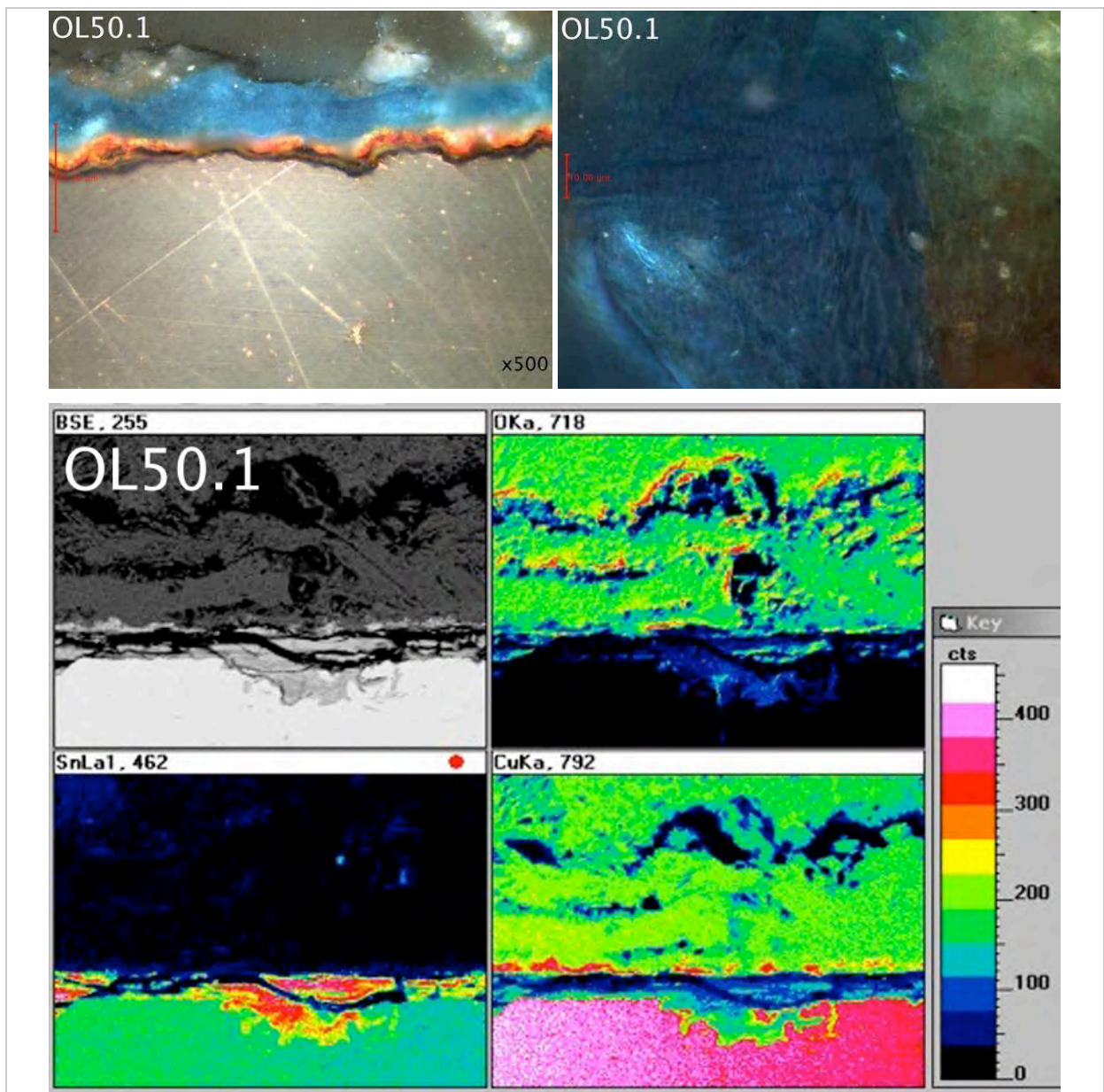


Figure 6.11: BFPM, BSE images and EDX maps of OK α , SnL α and CuK α , showing spiky azurite crystal formation onto cuprite layer. The key notes X-ray counts for SnL α . Sample OL50.1.

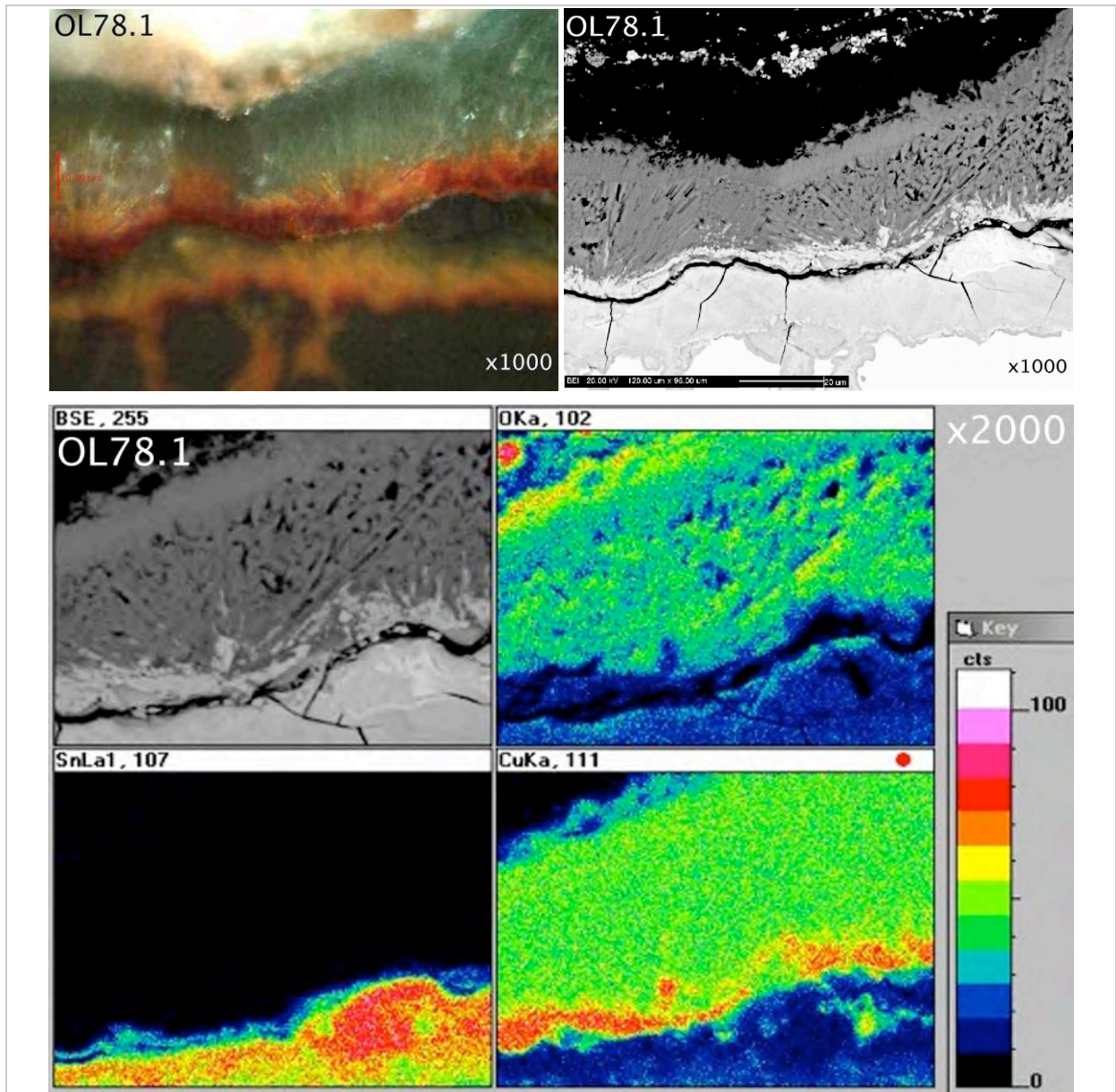
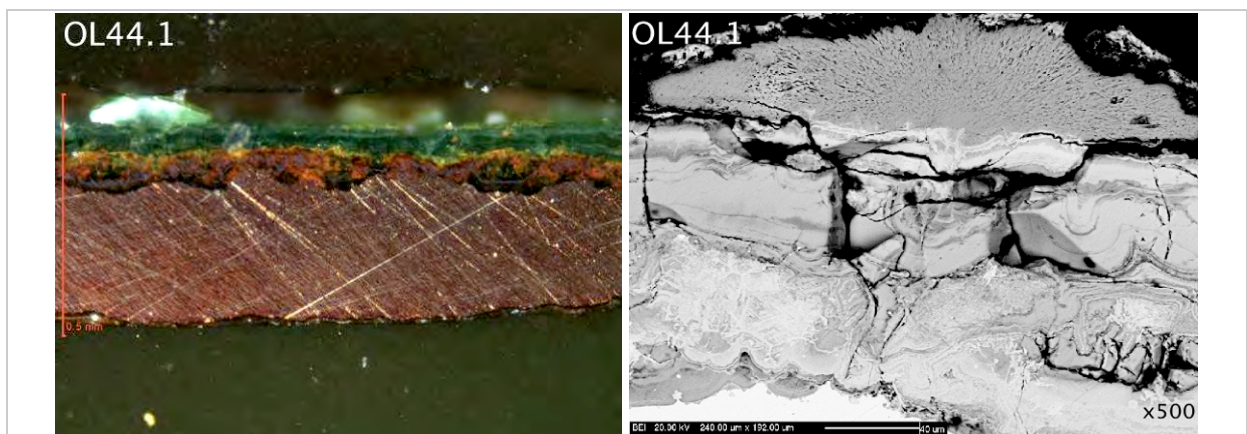


Figure 6.12: BFPM, BSE images and EDX maps of $OK\alpha$, $SnLa$ and $CuKa$, showing ‘sea-urchin’ shaped spiky malachite crystals elongating from spiky cuprite layer. The key notes X-ray counts for $CuKa$. Sample OL78.1 inner helmet side.



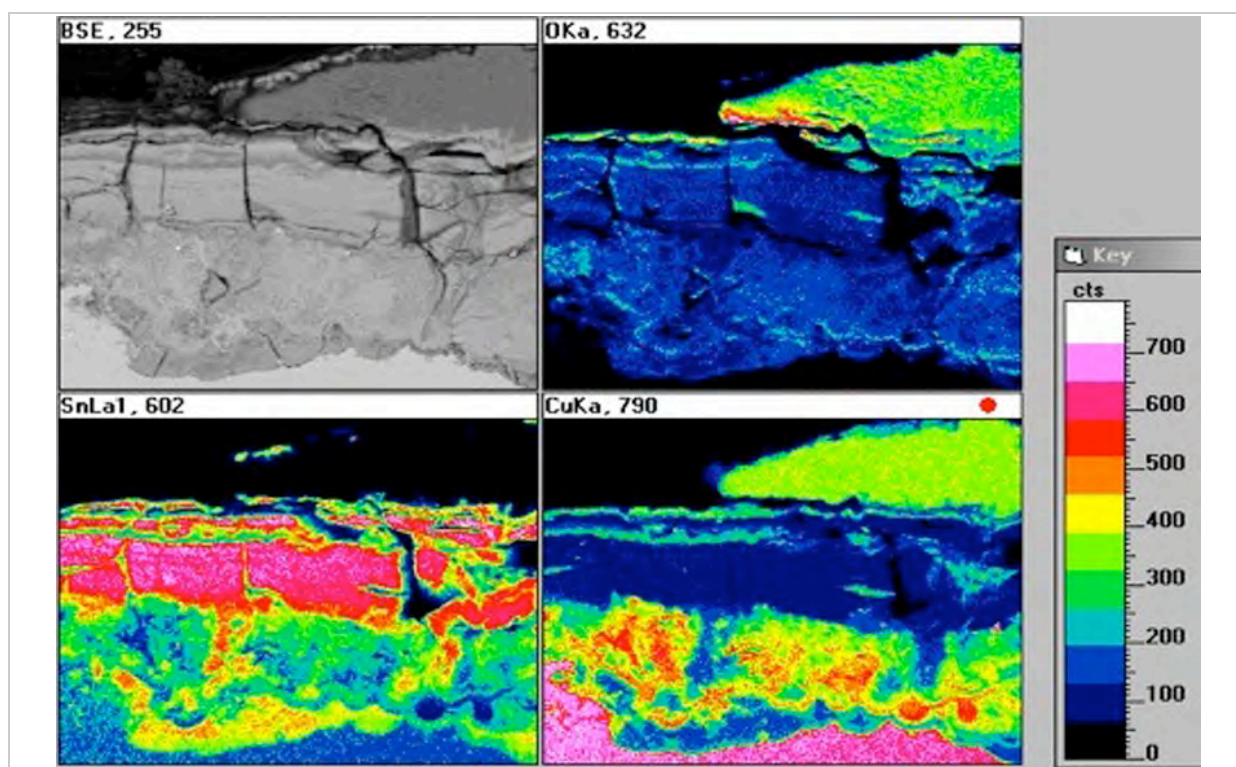


Figure 6.13: BFPM and BSE images and EDX maps of OK α , SnL α and CuK α showing ‘sea-urchin’ shaped spiky malachite crystal directly formed onto green patina. The key notes X-ray counts for CuK α . Sample OL44.1.

This type of sea-urchin shaped malachite has not been previously reported on archaeological bronzes, but it has been observed in corrosion experiments with water pipes in stagnated water (Merkel *et al.*, 2002; Vargas *et al.*, 2009; Vargas *et al.*, 2010). There, sea-urchin shaped malachite crystals were perfectly round, suggesting crystallites formed from a single nucleation point at low nucleation rates (Merkel *et al.*, 2002). The individual crystallites in sea-urchin malachite on OL78.1 have a distinct cuprite base which changes into malachite (Figure 6.12). As copper carbonates require more oxygenated environments for their formation (Cu₂O 33.3at% O, malachite 50at% O, azurite 53at% O, see also Eh/pH diagram in Figure 6.32Figure 6.37, it is likely that the upper parts of the crystals had more access to oxygen during their formation. Equally, the lower parts had restricted access to oxygen supply but a greater supply of Cu⁺ ions from the underlying corroding substrate permitting Cu₂O formation. Formation of such sea-urchin shaped crystals requires space and therefore their growth must have been spatially unrestricted. None of these structures is related to the presence of Cu-Sn intermetallics.

6.3.2.3. Characteristically straight fine patinas: searching for ϵ -Cu₃Sn

Examination of 36 cross-sectioned helmet samples and close observation of unusual features demonstrate that a granular η -Cu₆Sn₅ is absent from all samples. Absence of a flat fine ϵ -

Cu₃Sn layer is yet to be confirmed. Fragments from OL79, PE1, and OL74 exhibit very distinctive fine, uniform black, silver/grey and silver/green colour patinas that preserve polishing marks. These were further investigated for the potential presence of a very fine ϵ -Cu₃Sn layer.

EDX mapping shows that the black patina on OL79.1 exhibits a distinct thin outermost layer just below the SMOS limit, which has a non-uniform interface with the lower part of the patina; this outermost layer has a higher oxygen and tin content relative to the rest of the patina and could indicate the presence of a corroded ϵ -Cu₃Sn (Figure 6.14). However, evidence drawn from experimental and tinned Roman samples (Chapter 4) showed that the ϵ -Cu₃Sn has a relatively uniform and planar morphology at its interface with the bronze or its underlying patina. Based on this, it is more likely that the outermost layer seen on OL79.1 is a result of corrosion; a corroded layer of ϵ -Cu₃Sn would be expected to exhibit a more uniform interface with its underlying patina. The c. 2 μ m thick outer layer in PE1.1, which exists below the SMOS, appears copper-rich orange/yellow in BFPM (Figure 6.15). In other areas across the sample, this gives its place to an outer layer depleted of copper but rich in oxygen and tin (Figure 6.15, SEM-EDX map). The interface with its underlying corrosion is straight but has small round features (Figure 6.16), similar to those observed in the Roman collar (Figure 4.34,d) that could indicate the presence of Kirkendall voids, if this were a corroded ϵ -Cu₃Sn.

SR-XRD was undertaken to clarify the nature of the surface features seen on these samples (Figure 6.17). OL74.1 was additionally analysed to examine the nature of its fine green/grey patina and provide data to understand its composition. Analysis took place in reflection geometry collecting data directly from the patina in areas free from corrosion deposits (see section 3.8.2.2). Results show that both the black (OL79.1) and grey (PE1.1) patinas consist predominantly of azurite. The green/grey patina on OL74.1 is comprised of both azurite and malachite. Silica is present in OL74.1 and OL79.1 and a small amount of silica and cuprite is detected in PE1.1. None of the samples show Bragg reflections that could be assigned to cassiterite or a Cu-Sn intermetallic. Small peaks present at 2.39 Å and 3.19 Å in the diffraction patterns of OL74.1 and OL79.1, which could be attributed to ϵ -Cu₃Sn, are from azurite, because the major peak for ϵ -Cu₃Sn at 2.09 Å is absent. The very small peak at 2.09 Å, which could be attributed to ϵ -Cu₃Sn at the diffraction pattern of PE1.1 is more difficult to interpret, due to overlap with reflections from azurite and mainly cuprite, a small amount of which is present on the sample. No other diffraction peaks associated to ϵ -Cu₃Sn are visible in this diffraction pattern. Cassiterite is also absent from the diffraction pattern. If the presence of an amorphous or poorly crystalline hydrated stannic oxide is present, for example SnO₂.2H₂O

this is not confirmed because such compound is not reported to be found as a naturally occurring mineral (see section 2.2.5). Composition analyses could aid the characterisation of the corrosion surface (section 6.4.2).

If an extremely small amount of ϵ -Cu₃Sn is present on PE1.1, this cannot be objectively confirmed by diffraction because of overlapping of the major ϵ -Cu₃Sn with peaks from cuprite in the sample. The marked difference of the condition of the patina between the inner and outer helmet side (Figure 6.15) cannot be used alone as evidence to support tinning of this helmet because a similar variation of the condition between the two helmet sides is encountered in other samples. This discovery of the small, potentially, Kirkendall voids is significant (Figure 6.16) but one would be reluctant to assign these features to Kirkendall voids with a degree of certainty based on only two samples, especially when the presence of intermetallic compounds cannot be verified by diffraction. In the context of corrosion, Kirkendall vacancy diffusion is reported to result in the physical shift of the position of cationically formed oxide scales at high temperatures, without leading necessarily to the formation of voids, and occurs because diffusion in ionic solids is several orders of magnitude slower than that in molten metallic materials (Pieraggi, 2010). Based on the point defect model of vacancy diffusion, similar mass transport phenomena that produce passivating corrosion films can take place in aqueous environments (Macdonald and Urquidi - Macdonald, 1990), such as the burial. Mass transport in the burial is a complex process due to the numerous variables present. It can be assumed that uncommon local conditions may permit a very fast interdiffusion of species via a vacancy exchange mechanism to take place to form voids, but for samples PE1.1 and BOV the presence of voids cannot readily be ascribed to corrosion phenomena due to the limited evidence available and their occurrence remains enigmatic.

In relation to the colour of the patinas, the diffraction analysis shows that the black surface on OL79.1 does not involve the formation of cassiterite, which was not detected by diffraction. If an extremely small amount of ϵ -Cu₃Sn is present on PE1.1, this cannot be confirmed due to peak overlap with cuprite.

Analyses indicate the colour of the exposed patina is the result of corrosion. Tinning was not verified on any helmet samples, but they show clear evidence of fine polishing. Further investigation of cross-sectioned samples and EDX composition analysis aims to characterise the nature of silver/grey and black or other colour fine corrosion patinas, and to investigate possible corrosion mechanisms for their formation.

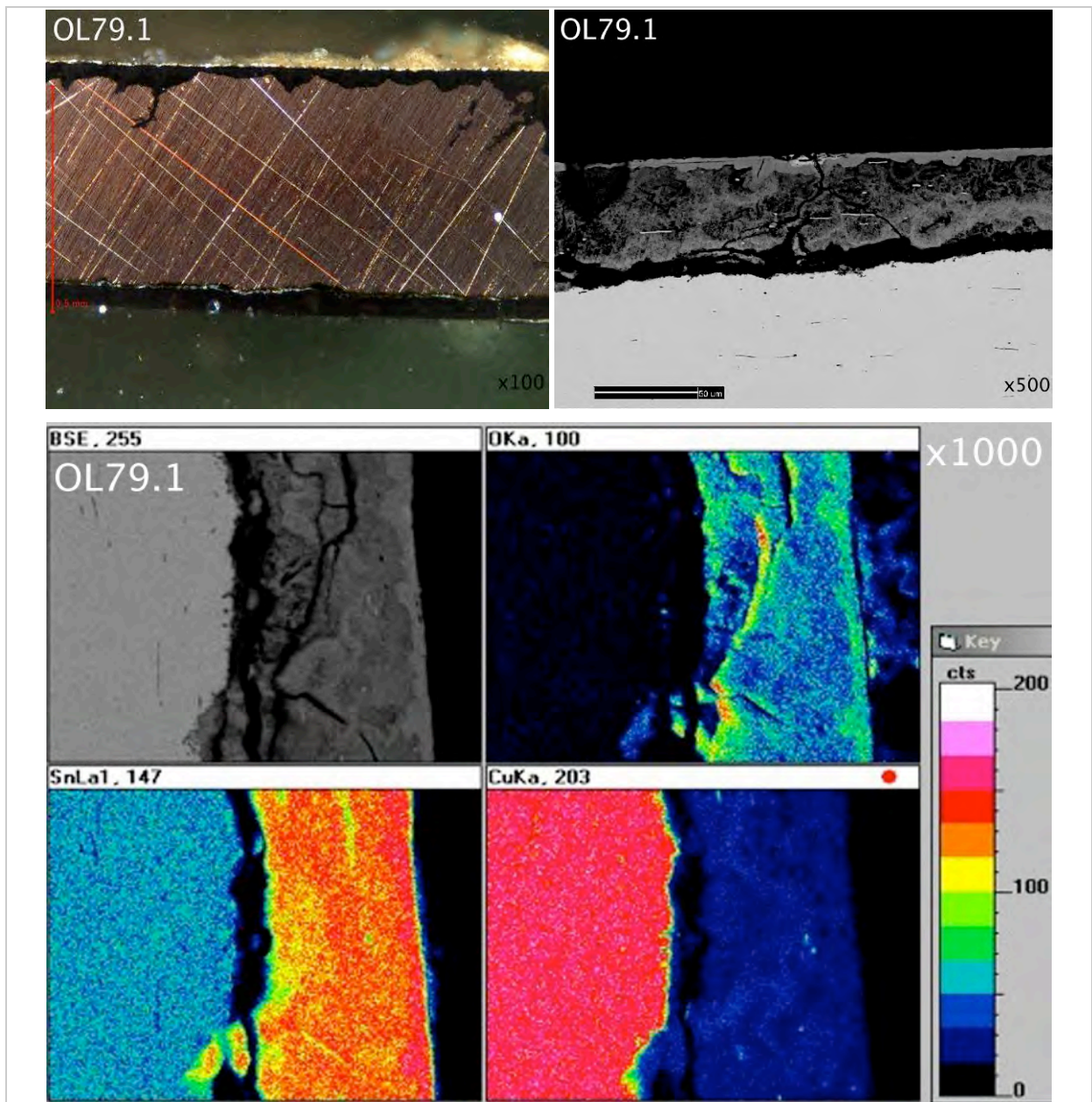


Figure 6.14: BSE and SE images showing a sharp black corrosion patina with a distinct outermost layer in OL79.1 cross-section. SEM-EDX map of OK α , SnL α and CuK α shows spatial distribution of elements in patina. The key notes X-ray counts of CuK α .

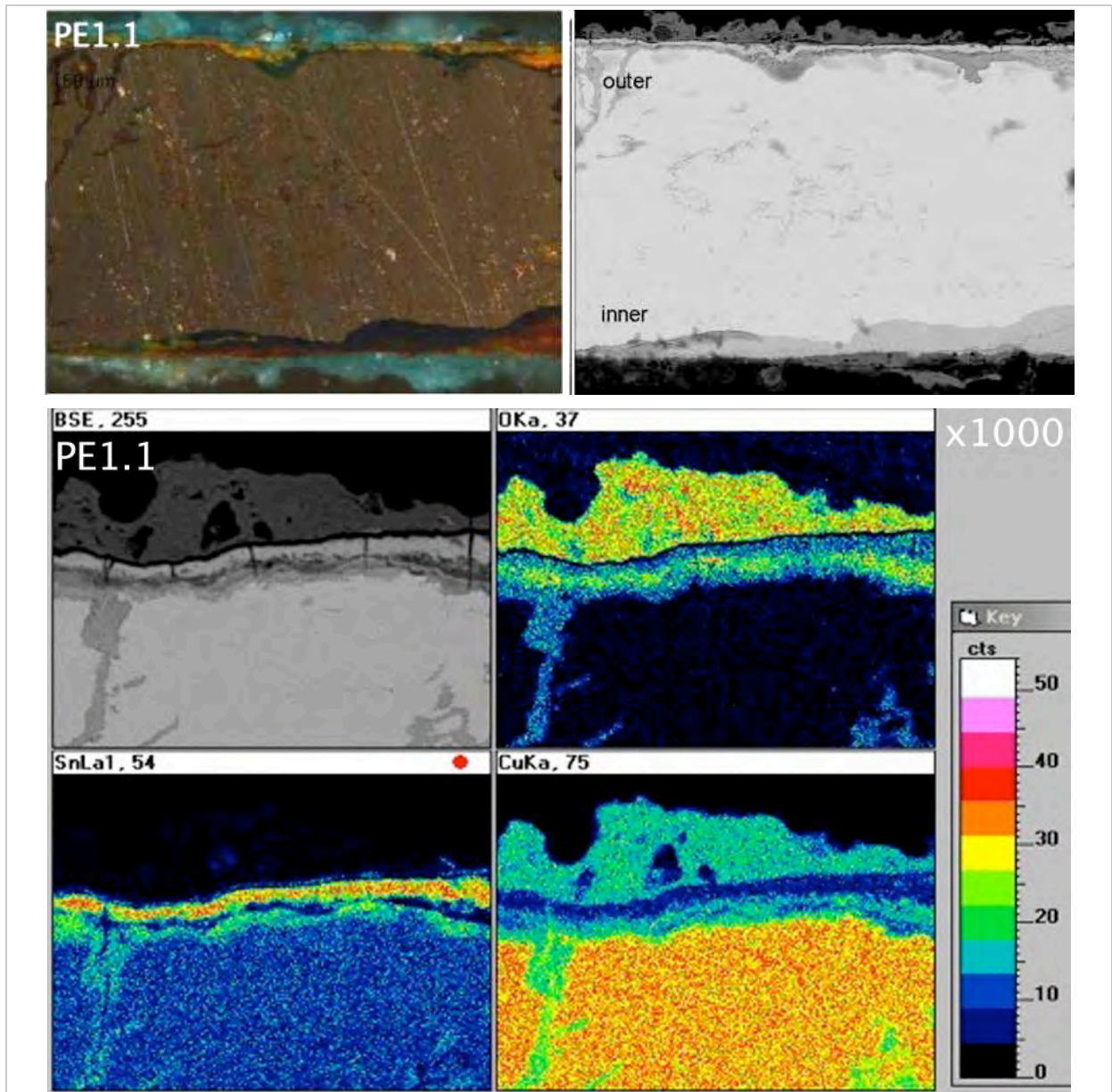


Figure 6.15: BSE and SE images showing the nature of the grey/silver patina in PE1.1 in cross-section. SEM-EDX map of OK α , SnLa and CuKa shows spatial distribution of elements in patina. The patina appears orange/yellow in BSE but it is richer in Sn than in Cu. The key notes X-ray counts of SnLa.



Figure 6.16: BSE detail of the c. 2 μ m thick tin-rich layer in PE1.1 showing small voids at its interface with the underlying corroded bronze. Scale is 2 μ m.

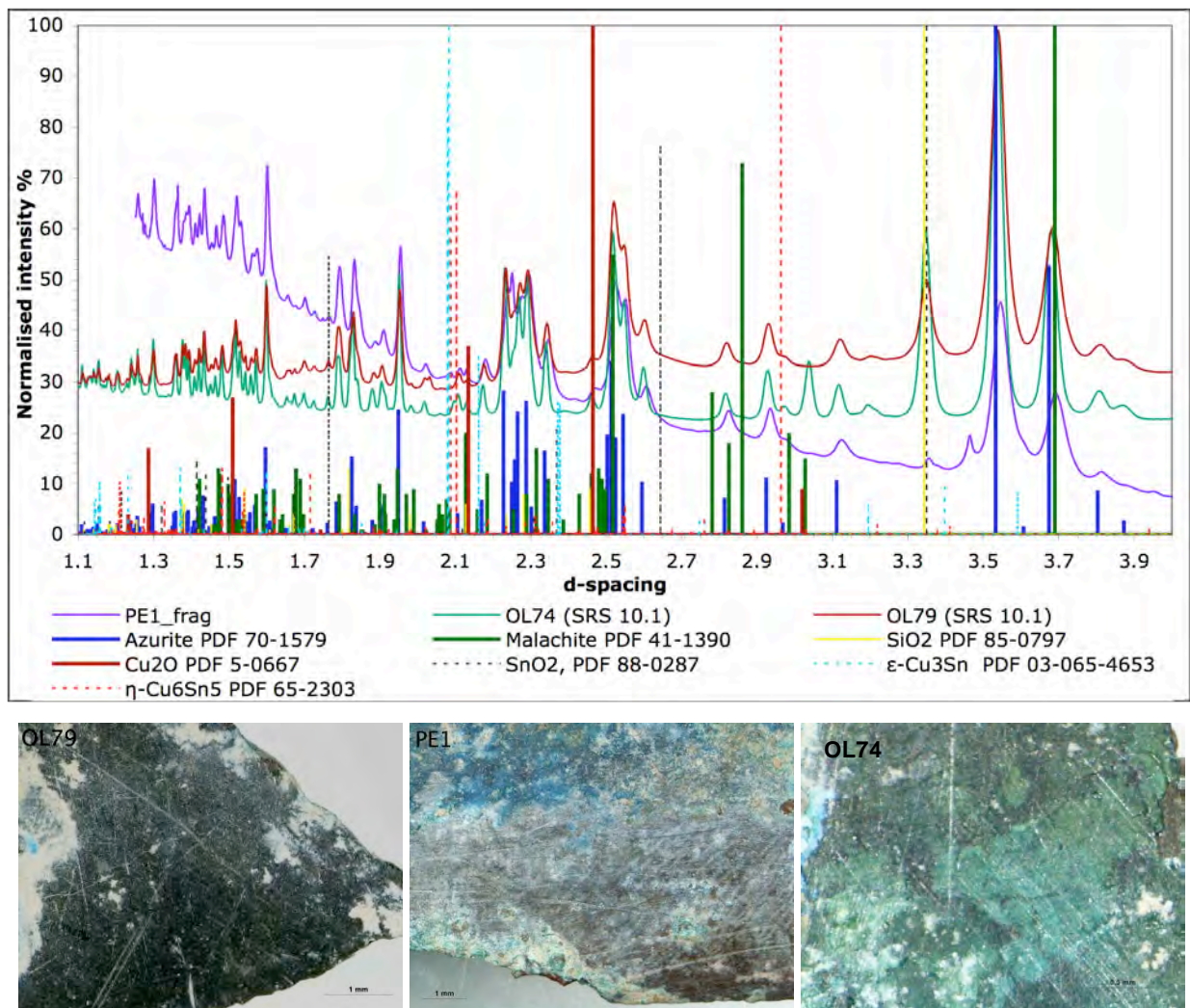


Figure 6.17: SR-X ray diffraction patterns of surface of fragments from helmets OL79, PE1 and OL74 that exhibit a fine smooth black, grey and green/dark grey patinas respectively. The patinas of OL79 and PE1 are composed predominantly of azurite and, OL74 both of malachite and azurite. Silica is present in OL74 and OL79 and a small amount in addition to cuprite is in PE1. SRS, beamline 10.1, $\lambda=0.92\text{\AA}$, analysed in reflection geometry.

6.4. INVESTIGATION OF CORROSION PATINA PROFILES

6.4.1. MICROSCOPIC CHARACTERISATION OF CORROSION PROFILES

6.4.1.1. Criteria of characterisation

The profile of the patinas and the nature of the bronze/patina interface were examined to investigate the formation of patinas that preserve polishing. The corrosion profiles show a number of physicochemical qualities that aid their characterisation; these include the number of corrosion zones seen in the corrosion profile below the marker of original surface (MOS) and the presence or absence of an inner cuprite zone at the patina/bronze interface (Table 6.5).

With the exception of two samples that have a single fine corrosion layer (Corrosion Profile 1, Figure 6.18), cross-sections exhibit two main corrosion zones below the marker of the original surface. Several of the samples with two corrosion zones exhibit a characteristic cuprite red and/or orange/yellow inner corrosion zone visible in BFBM, the lower limit of which interfaces with the bronze (Corrosion Profile 3, Figure 6.24). The colour of the outer corrosion zone, the upper limit of which is the MOS, varies from light to dark green in these samples. Several samples that do not have an inner red/yellow zone (Corrosion Profile 2, Figure 6.22) have a fibrous microstructure or an unusual chemical distribution of major elements. A small number of samples include areas of banding at their outer corrosion zone, which are specified here as *bands* and are regarded to be part of a broader inner or outer corrosion zone or layer. The words *corrosion zone* and *layers* are used here interchangeably to signify broad corrosion zones parallel to the MOS. A small number of samples exhibit dramatically different conditions at the two helmet sides (outer, inner) (e.g. OL78.1, OL70.1) or slightly different conditions within the same helmet side. In summary, the corrosion profiles of cross-sections were categorised according to the criteria:

Corrosion Profile 1 (CP1): samples that exhibit a single, relatively uniform corrosion zone between the marker of original surface (MOS) and the bronze metal.

Corrosion Profile 2 (CP2): samples that exhibit two corrosion zones (outer and inner) and are free of cuprite or orange/yellow compounds at the inner corrosion zone. Two subgroups were defined based on the morphology of the inner layer and the extent of corrosion deposits covering the surface:

CP2.1: samples with characteristic fibrous microstructure mainly present at the inner zone. The outer part of the patina is black, blue or light green/blue in colour and it is not covered extensively by deposits;

CP2.2: samples that do not exhibit a fibrous microstructure, although they can have intergranular corrosion filaments in the bronze, but are covered extensively by corrosion deposits and there may be minor patches of cuprite-red in other areas of the sample (e.g. inner helmet side).

Corrosion Profile 3 (CP3): includes samples with cuprite present at the inner corrosion zone. Two subgroups were defined based on the extent of red-cuprite and/or orange yellow inner zone and the presence or absence of ‘ghost’ slip lines preserved in the inner corrosion zone:

CP3.1: samples with a thin or localised inner zone of red, orange/yellow inner compounds with no evidence of slip lines;

CP3.2: samples with a thick distinctive cuprite or orange/yellow inner zone, which preserves extensive evidence of slip lines.

Characteristic features of samples in groups CP2.1 and CP3.2 are very distinct and categorisation of the samples within these groups was straightforward. Group CP2.2 was difficult to differentiate from CP3.1. Primary criterion for the distinction between the two groups was the presence or absence of azurite as a corrosion deposit and the green/blue patina observed at samples of CP2.2, which is different to the green patina seen in CP3.1. Hence, CP2.1 and CP3.1 can be considered as an intermediate mixed group between the clearly defined CP2.1 and CP3.2.

Corrosion	Bronze / inner interface	Inner layer	Outer layer	MOS	Patina colour	Sample	
1	Flat-uniform	-	Uniform	SMOS	Black	OL31.1	
					Grey	OL27.1	
2.1	Flat-non uniform	Fibrous	Banded	Damaged	Brown	OL57.2	
			Uniform	SMOS	Black	OL74.1	
	Flat-uniform	Fibrous	Uniform	SMOS	Black	OL79.1	
					Black	OL71.1	
	Intra-granular / filaments	Fibrous	Fibrous	SMOS	SMOS (aged fi	Green	OL9.2
					SMOS	Black	OL75.2
				Non-uniform	SMOS	Soiled	OL13.1
						Uniform	SMOS
	2.2	Flat-non uniform	Uniform	Uniform	SMOS	Brown	OL73.1
						Soiled	OL46.1
Flat-non uniform		Uniform	Uniform	SMOS	Black	OL4.2	
					Blue	OL66.1	
Flat-uniform		Uniform	Banded	BMOS	Green	OL70.1	
					Green	OL78.1	
Intra-granular / filaments		Uniform	Banded	SMOS (aged)	Brown	OL63.1	
			Non-uniform	SMOS	Brown	OL50.1	
3.1		Flat-non uniform	Uniform	Non-uniform	BMOS	Black/red	AP4.2
					Damaged	Green	OL58.1
	Green/Red					OL11.1	
	Flat-uniform	Uniform	Non-uniform	SMOS	Black/red	AP5.1	
				SMOS	Green/Red	PR1.1	
				SMOS	Grey	PE1.1	
				SMOS	Green/Red	PR4.1	
3.2	Intra-granular / strain	Slip-lines	Banded	SMOS (aged)	Black/red	OL44.1	
			Slip-lines	Damaged	Black/red	OL21.1	
					Black/red	OL41.1	
				SMOS	Green/Red	OL69.1	
			SMOS	Green/Red	OL29.1		
					OL53.1		
			PE4.3				
Uniform	SMOS	Green/Red	PE2.2				

Table 6.5: Summary of microstructural details in corrosion profiles.

6.4.1.2. Corrosion Profile 1: one corrosion layer

Samples OL27.1 and OL31.1 are characterised by a single thin corrosion layer, which preserves a sharp marker of original surface (SMOS) (Figure 6.18). The patina is relatively uniform in composition as observed in the BSE. Soil deposits are present on both samples, but corrosion deposits are absent.

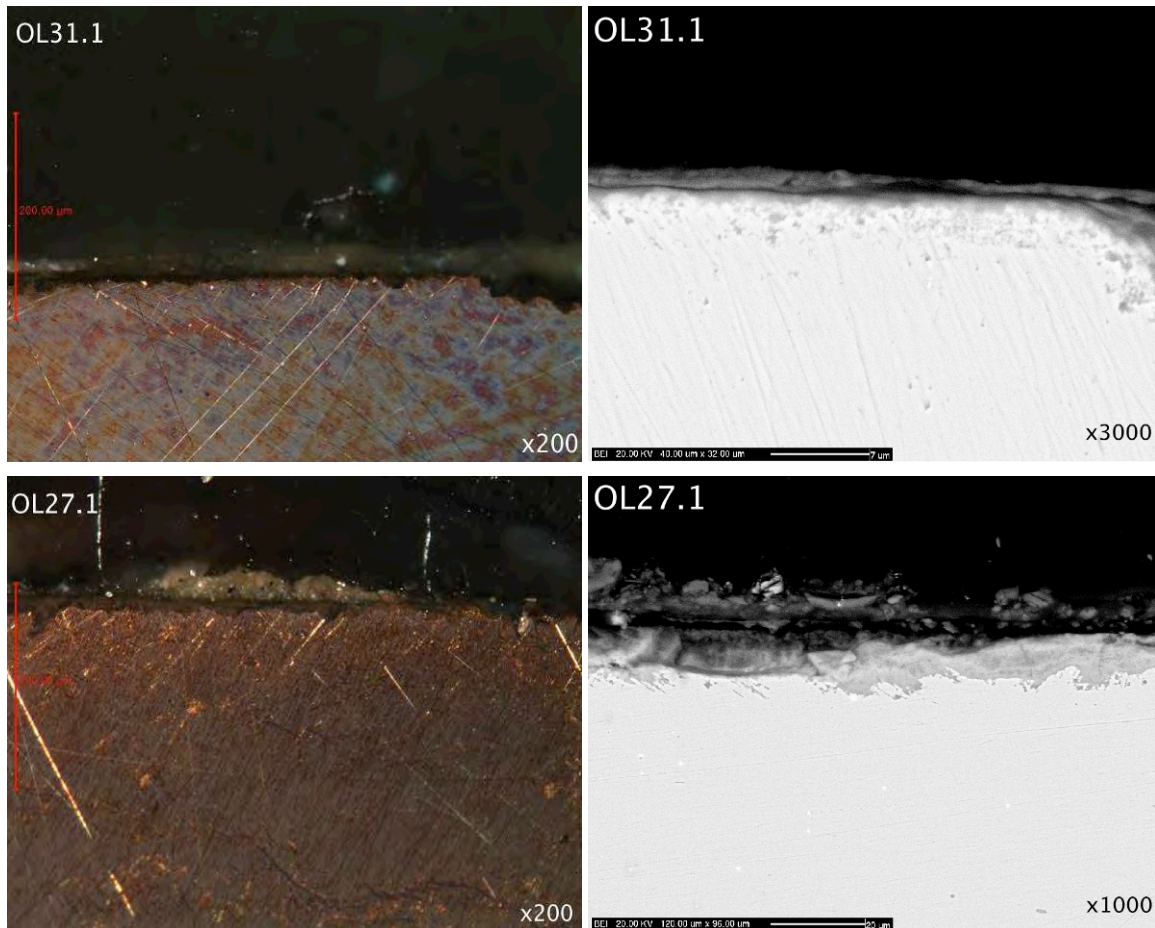


Figure 6.18: BFPM and BSE images of cross-sectioned samples that exhibit relatively uniform single layer patina characteristic of *Corrosion Profile 1* group.

6.4.1.3. Corrosion Profile 2: absence of a distinct red/yellow inner zone

Samples in Corrosion Profile 2 (CP2) are free of a cuprite red or orange/yellow copper zone at the inner corrosion zone (Figure 6.22). Close examination shows that several samples in this group exhibit a fibrous microstructure at the inner zone, which is characterised by extremely fine long filaments (<1µm), elongated mainly perpendicularly to the bronze, and are separated in places by fine gaps that increase porosity in the layer (Figure 6.19). Additionally, most exhibit fine corrosion filaments also exhibit fine intra-granular corrosion filaments that elongate into the bronze (Figure 6.22, Table 6.5). OL74.1 and OL79.1 exhibit only minor intra-granular corrosion of this type at the bronze/inner corrosion interface and the bronze/patina interface is in general flat.

Samples OL73.1 and OL13.1 exhibit similar network of intra-granular corrosion at the bronze/inner zone interface, but they have a network of thicker fibre-like or ‘root-like’ features, made visible because of their different composition in BSE. SEM-EDX mapping shows that these ‘roots’ are rich in Cu and O, and appear red-orange in BFPM images (Figure 6.20). Such fine or thicker fibre-like microstructural system as observed in the inner corrosion zone has not been previously reported in the literature.

Due to the characteristic nature of the fibrous inner zone, this group of samples is defined as a distinct subgroup Corrosion Profile CP2.1. The physical morphology of the outer layer of samples in CP2.1 varies as it can be fibrous (OL71.1, OL9.2), or exhibit a banded (OL57.2, OL63.1) or a non-uniform composition (OL13.1, OL75.2). In most samples, the outer zone is uniform and compositionally distinct relative to the inner corrosion zone (e.g. OL46.1, OL5.1, Figure 6.21). Several samples preserve a fine MOS (SMOS) that was discussed earlier including features at the patina / corrosion deposit interface discussed in section 6.3.2 (OL79.1, OL13.1, OL74.1). Overall, the outer corrosion zone is enriched in tin and depleted of copper relative to the inner zone (Figure 6.21). The overall colour of the patina profiles tends to be uniform within individual samples and varies from black, dark green to light blue/green in BFPM (Table 6.5).

Samples that do not exhibit a fibrous and cuprite-based inner microstructure form a subgroup Corrosion Profile CP2.2. OL50.1, OL66.1 and OL70.1 show only very small localised areas of cuprite which are not representative of the average condition of the samples, hence they are included in this group. Note that categorisation of OL78.1 is based on the outer side of the helmet; the inner side shows an inner layer of cuprite and does not fit the criteria of this category (Figure 6.12). The inner zone in samples of this subgroup is relatively uniform and has a compact often non-uniform interface with the bronze (Table 6.5). OL50.1 shows some intra-granular corrosion. The outer layer is physically and chemically uniform or banded, and carries a SMOS, apart from OL70.1 where the MOS is broadly defined (BMOS). Samples in this subgroup are covered with several layers of corrosion deposits, with cuprite formed onto the SMOS in several cases (e.g. OL50.1) examined earlier (section 6.3.2). The colour of the corrosion profile overall ranges from dark green to dark blue/green (Table 6.5).

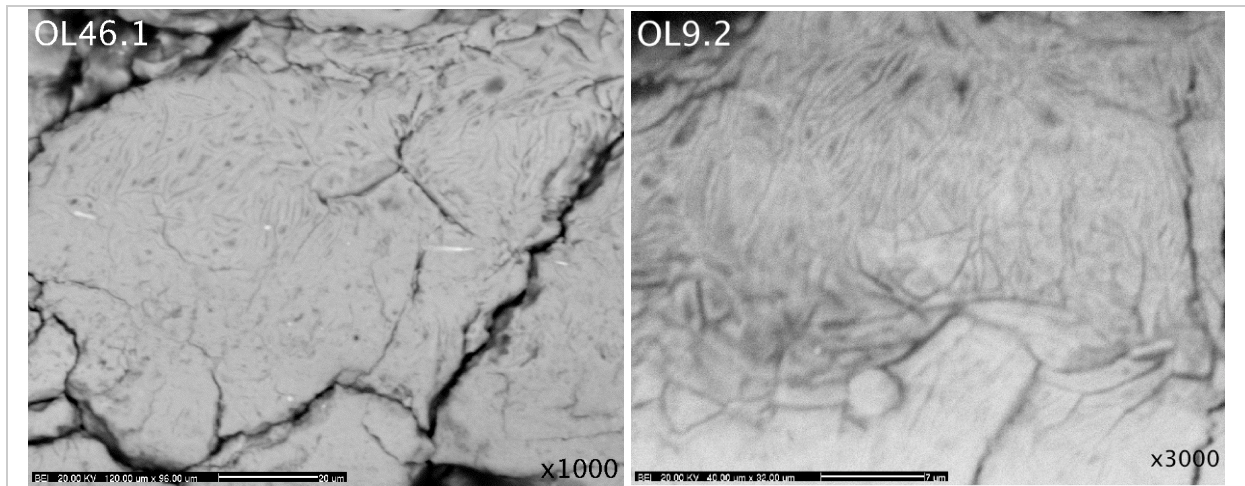


Figure 6.19: BSE images in high magnification showing extremely fine fibre-like corrosion feature at the inner corrosion zone near the bronze/corrosion interface.

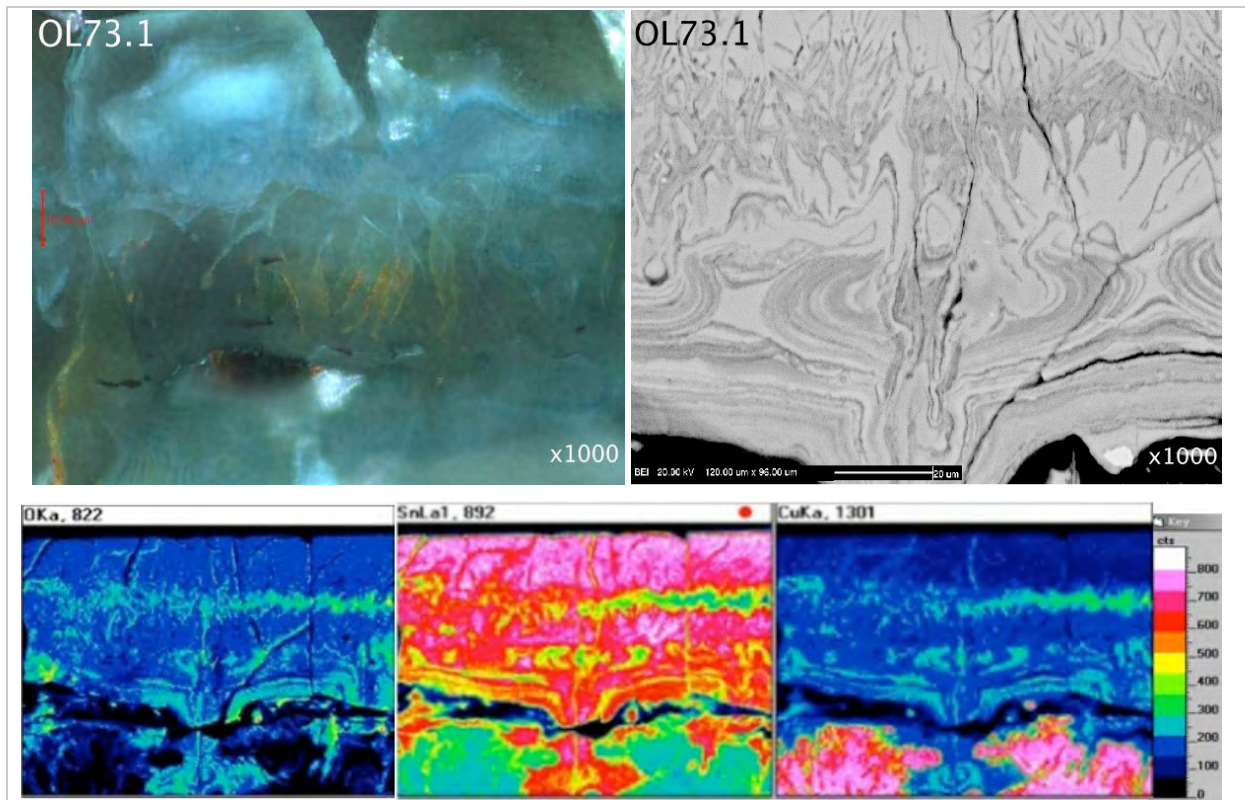


Figure 6.20: Analysis images of OL73.1 showing uniform outer layer with increased Sn concentration relatively to the inner corrosion zone. Characteristic filaments rich in Cu and O are present at the inner corrosion zone and appear yellow / orange in BFPM. Top left: BFPM image showing watercolour patina with orange/red filaments. Top right: BSE showing the overall nature of the patina. Bottom: SEM-EDX maps at x500 magnification of $OK\alpha$, $SnL\alpha$ and $CuK\alpha$. The key notes X-ray counts for $SnL\alpha$.

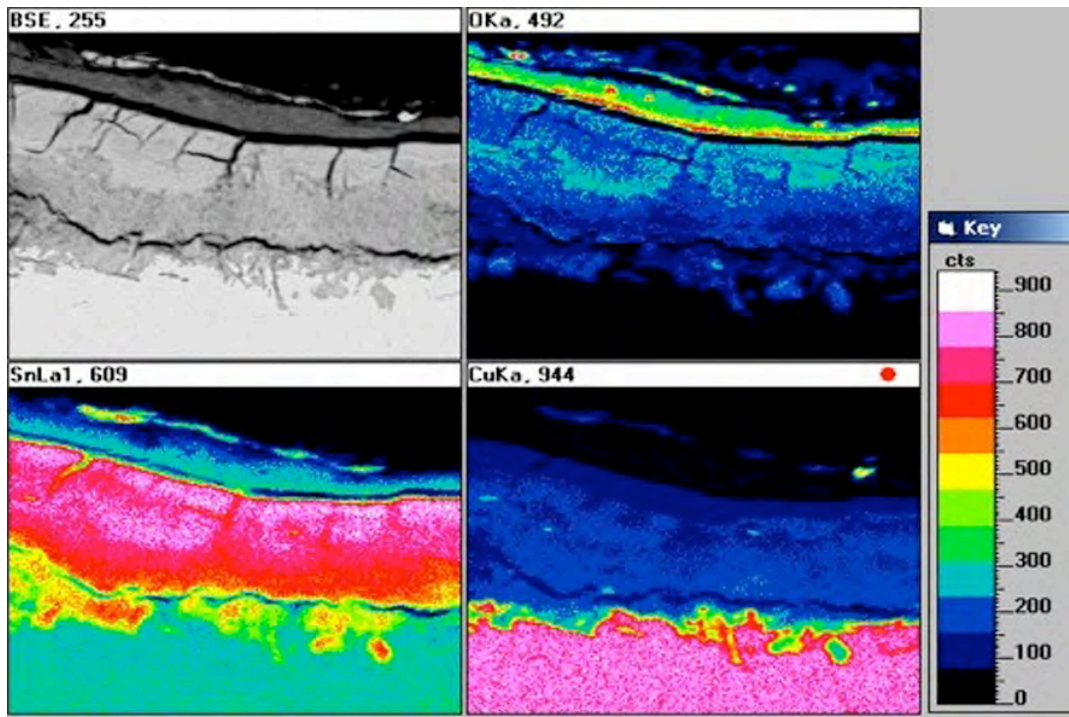
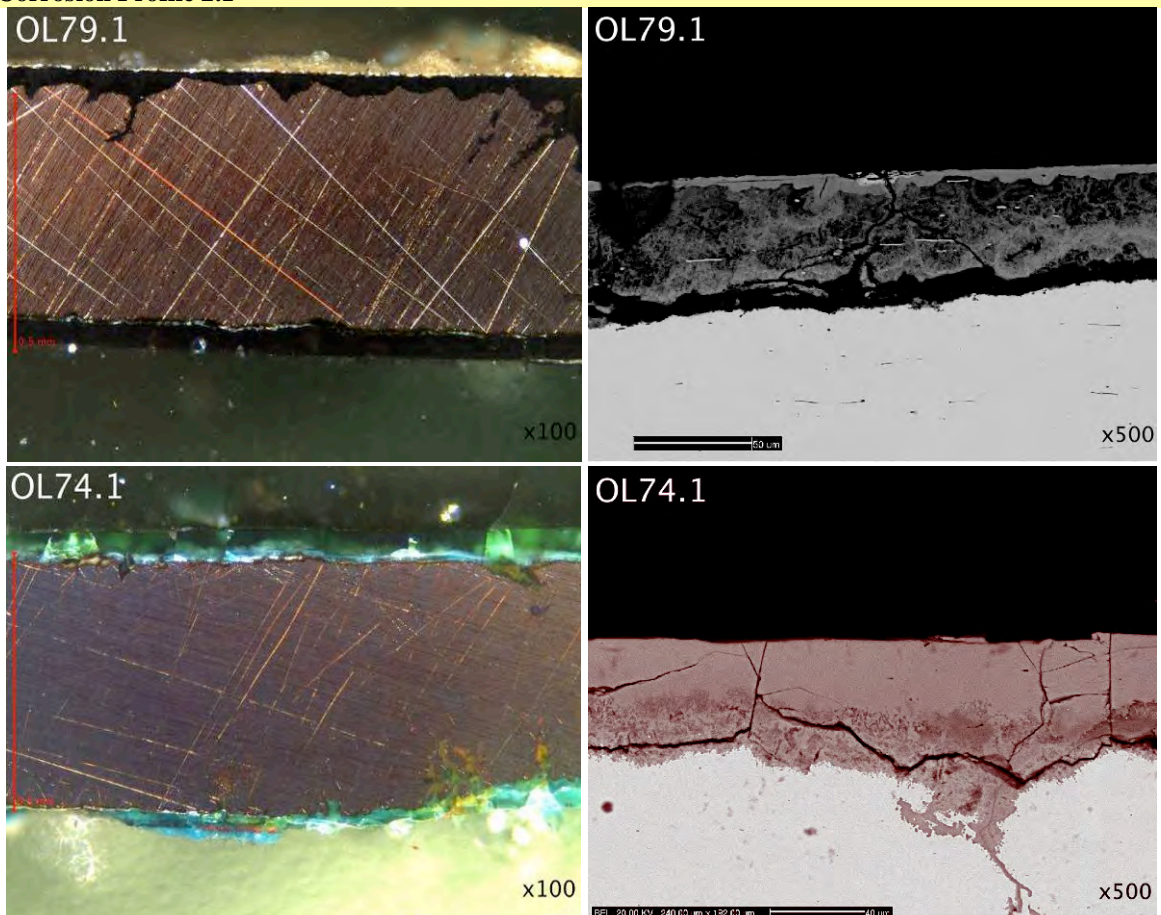
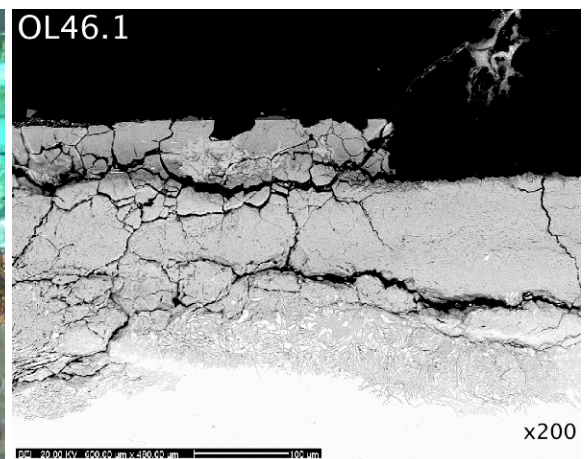
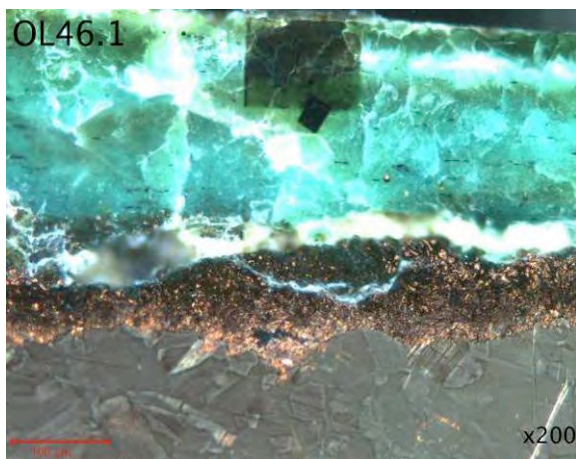
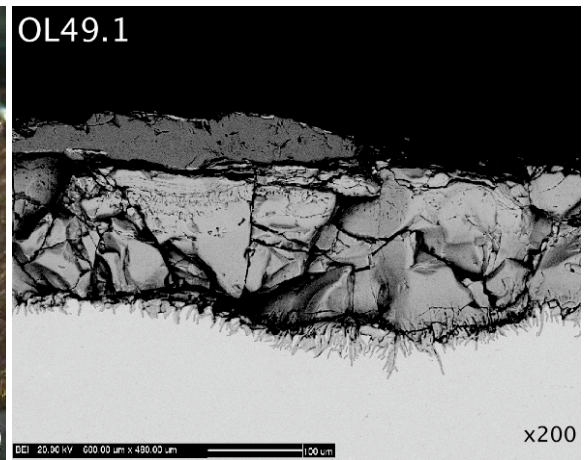
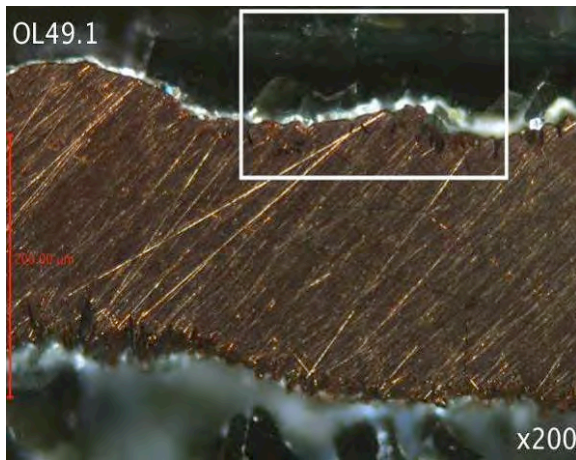
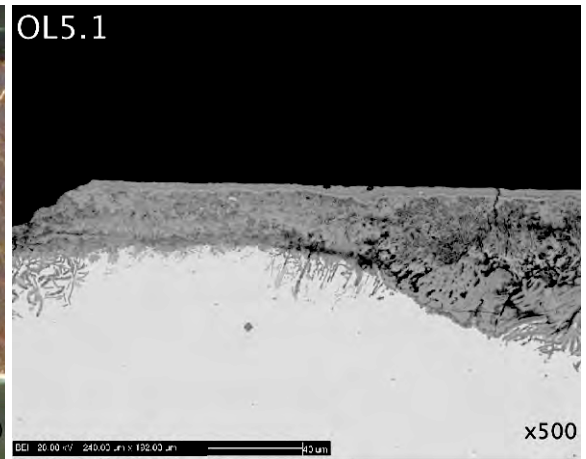
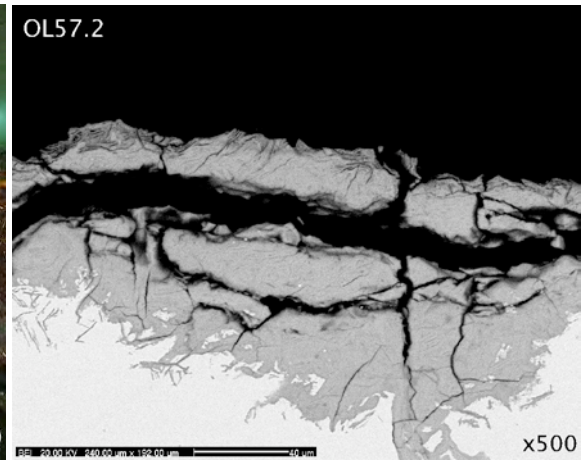
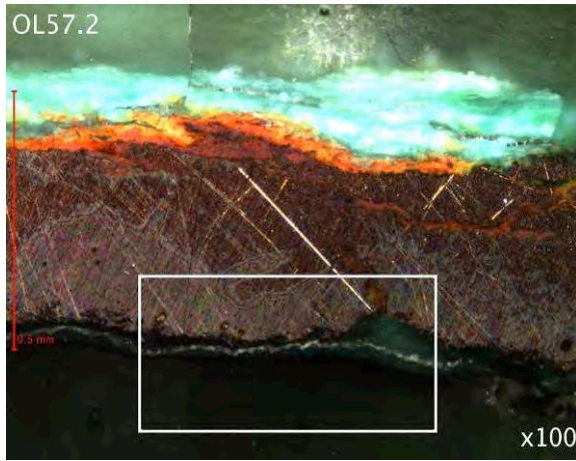


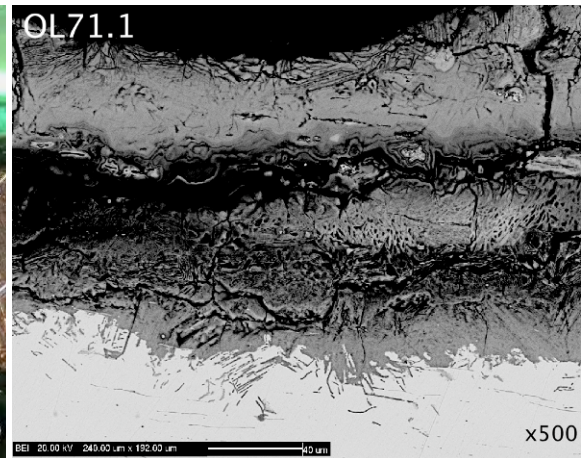
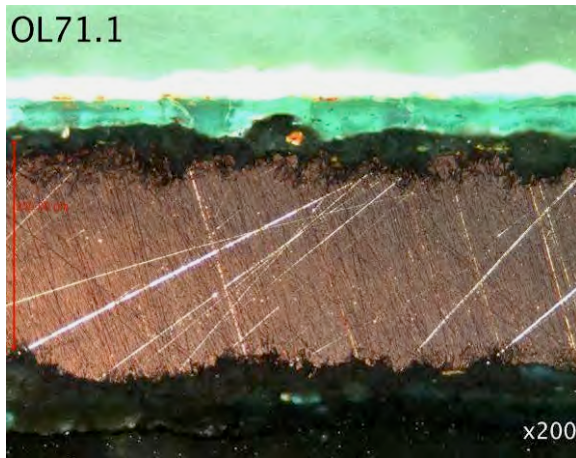
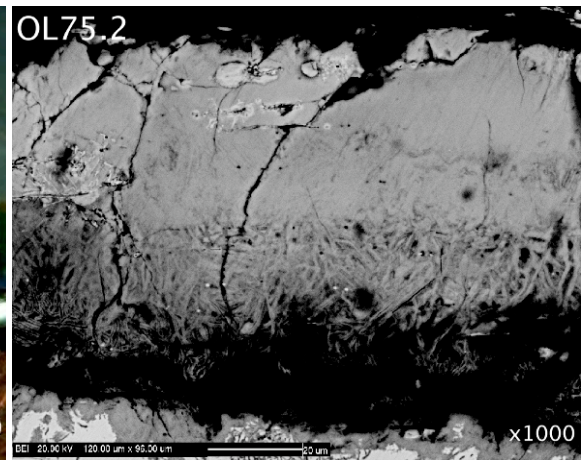
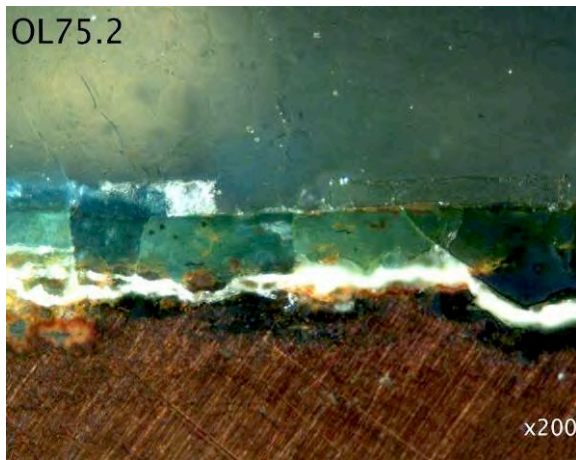
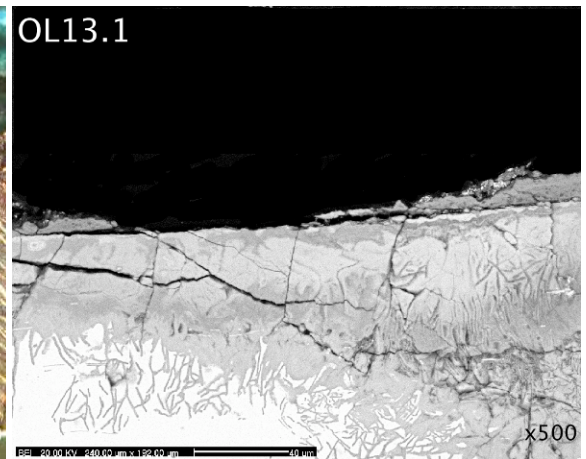
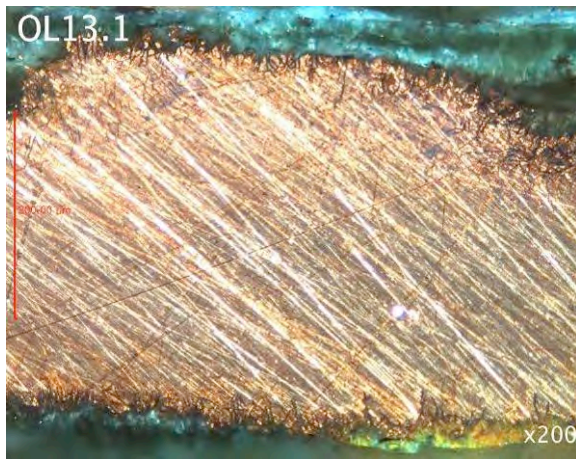
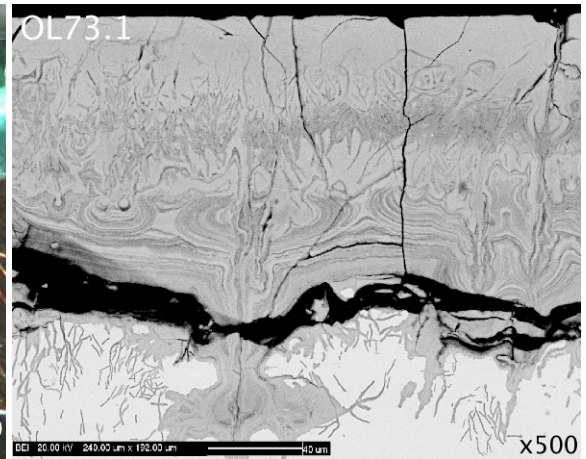
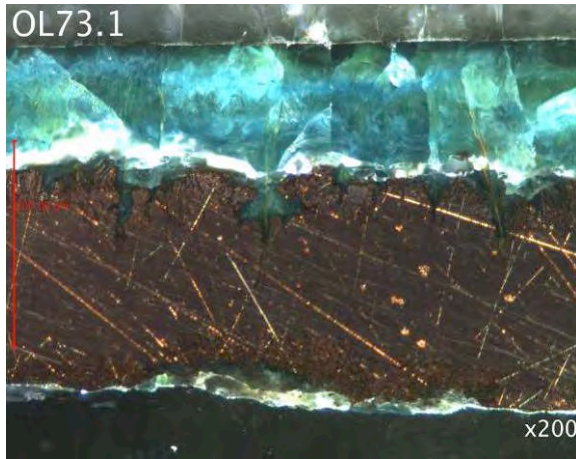
Figure 6.21: SEM-EDX map of OKa, SnLa and CuKa showing Sn-enrichment of the outer corrosion zone relatively to the inner, which has more Cu. OL5.1, x1000 magnification. The key notes CuKa X-ray counts.

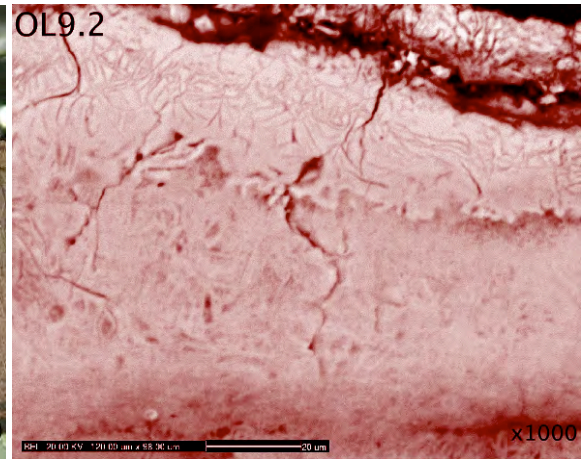
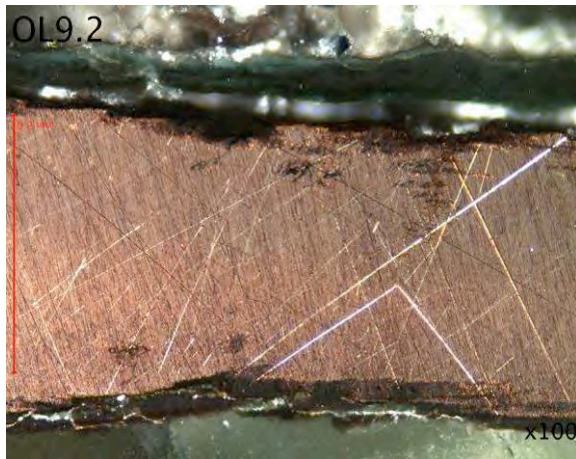
Figure 6.22: (next pages) BFPM and BSE images of cross-sectioned samples in Corrosion Profile 2 which exhibit two corrosion zones and the inner zone is free of cuprite or orange/yellow compounds.

Corrosion Profile 2.1

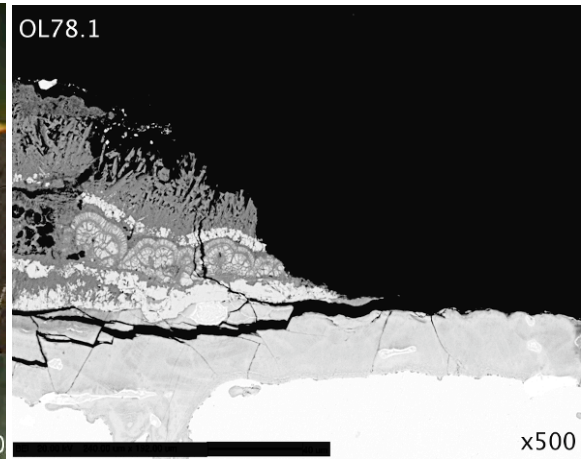
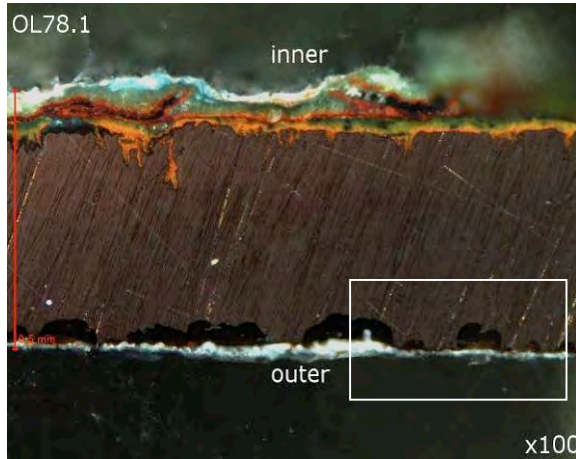
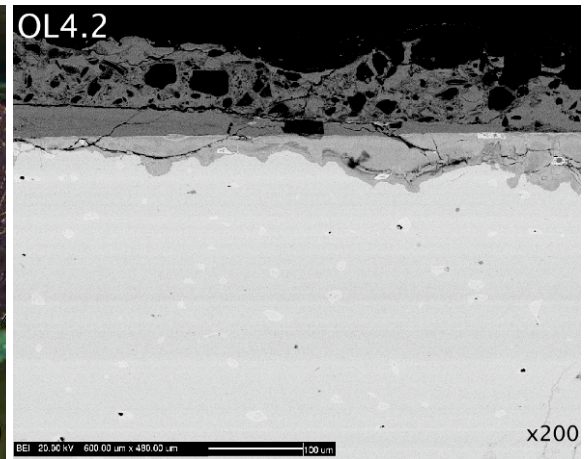
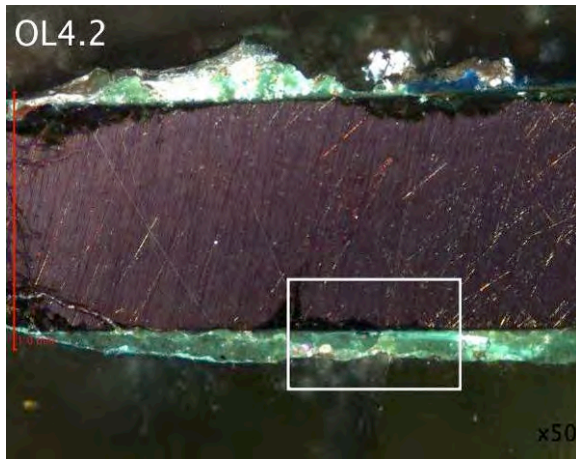
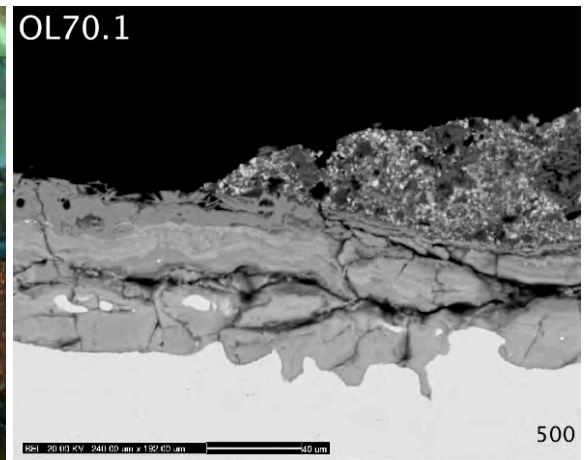
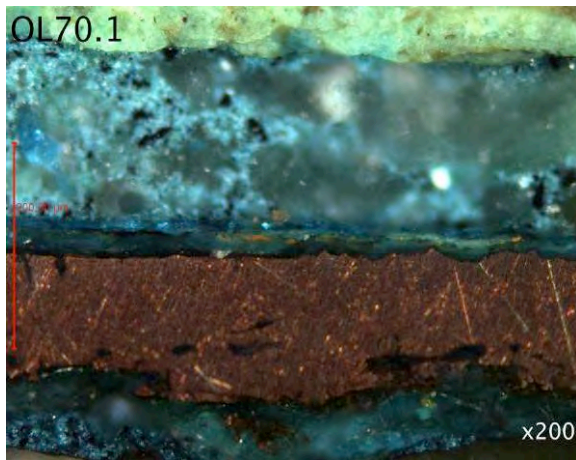


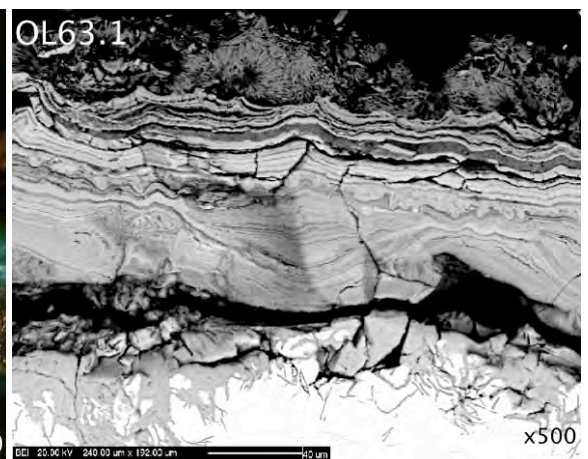
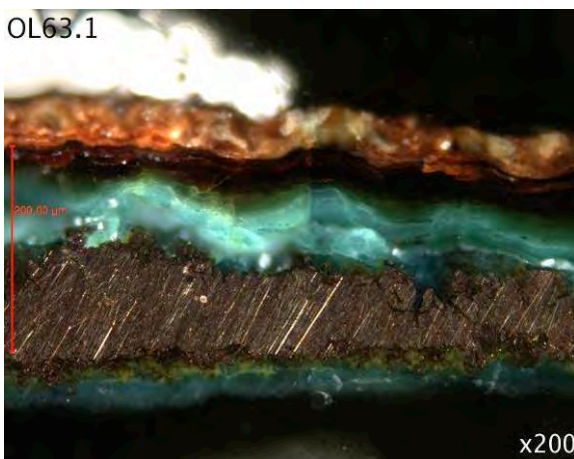
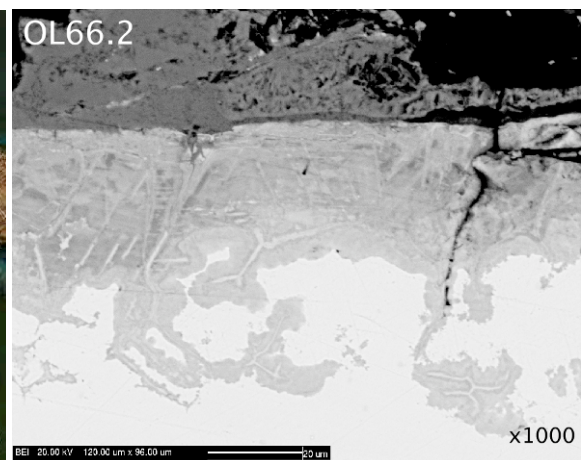
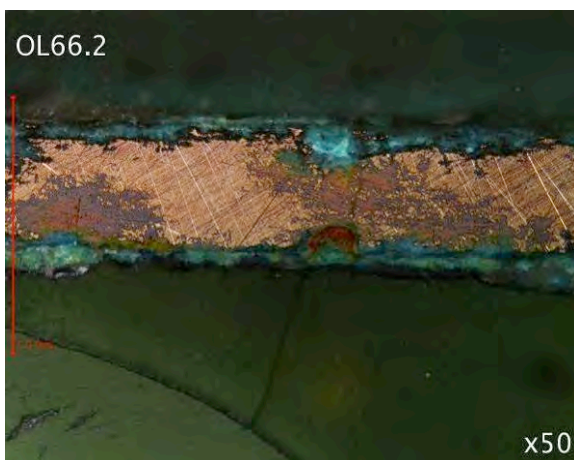
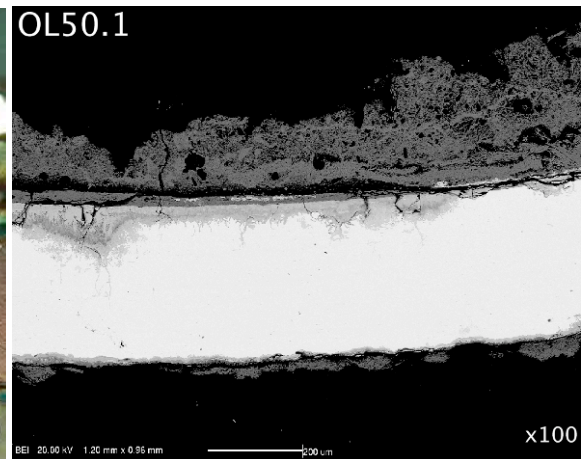
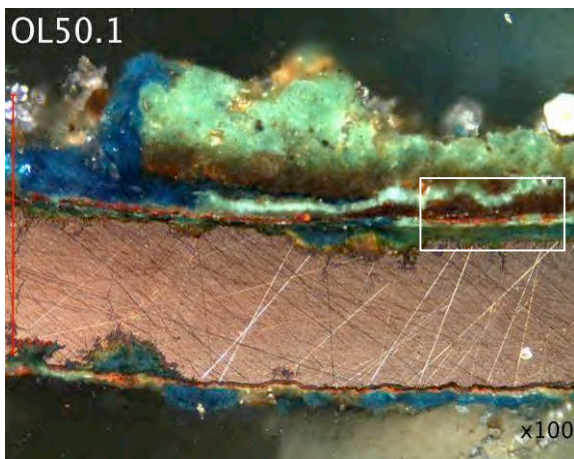
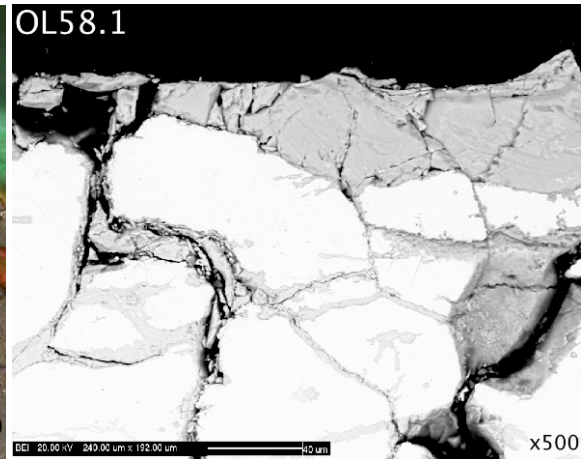
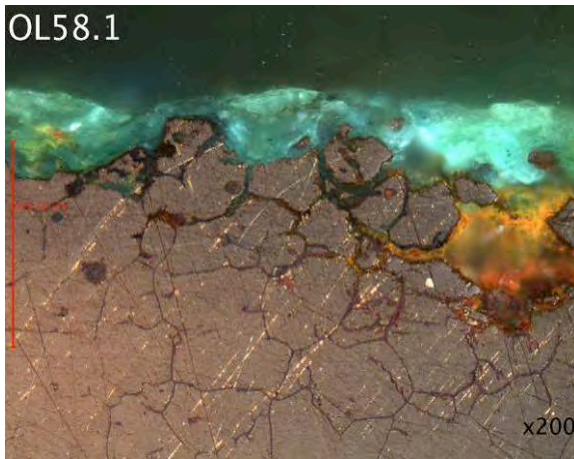






Corrosion Profile 2.2





6.4.1.4. Corrosion Profile 3: with red/orange-yellow inner zone

Samples in Corrosion Profile 3 (CP3) have a cuprite red and/or orange/yellow present at the inner corrosion zone that is overlaid by a green outer corrosion zone. In several samples, the cuprite layer includes extremely fine straight lines that are parallel or cross each other in batches and each batch seems to have a different orientation (Figure 6.23) These lines resemble slip lines observed in strained, work-hardened α -bronze grains seen in the metallic bronze (section 5.6.3). This shows that cuprite can preserve the metallographic structure of the bronze in the form of pseudomorphs, via an *in situ* corrosion mechanism. Characteristically, evidence of strain stops at the inner/outer corrosion zone interface where green outer corrosion zone starts (Figure 6.23, OL21.1, OL41.1). Samples that demonstrate evidence of slip-lines are subgrouped as Corrosion Profile 3.2 (Table 6.5).

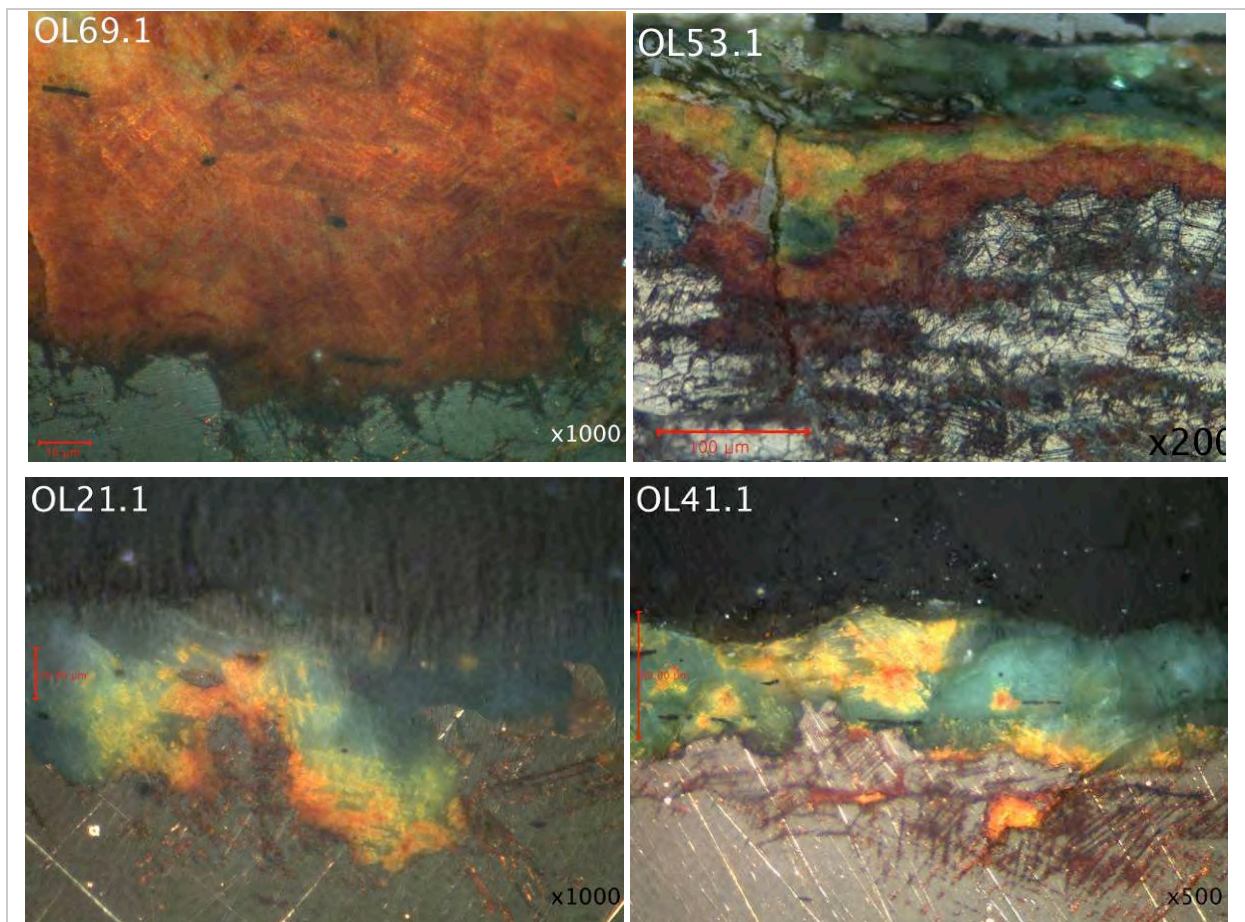


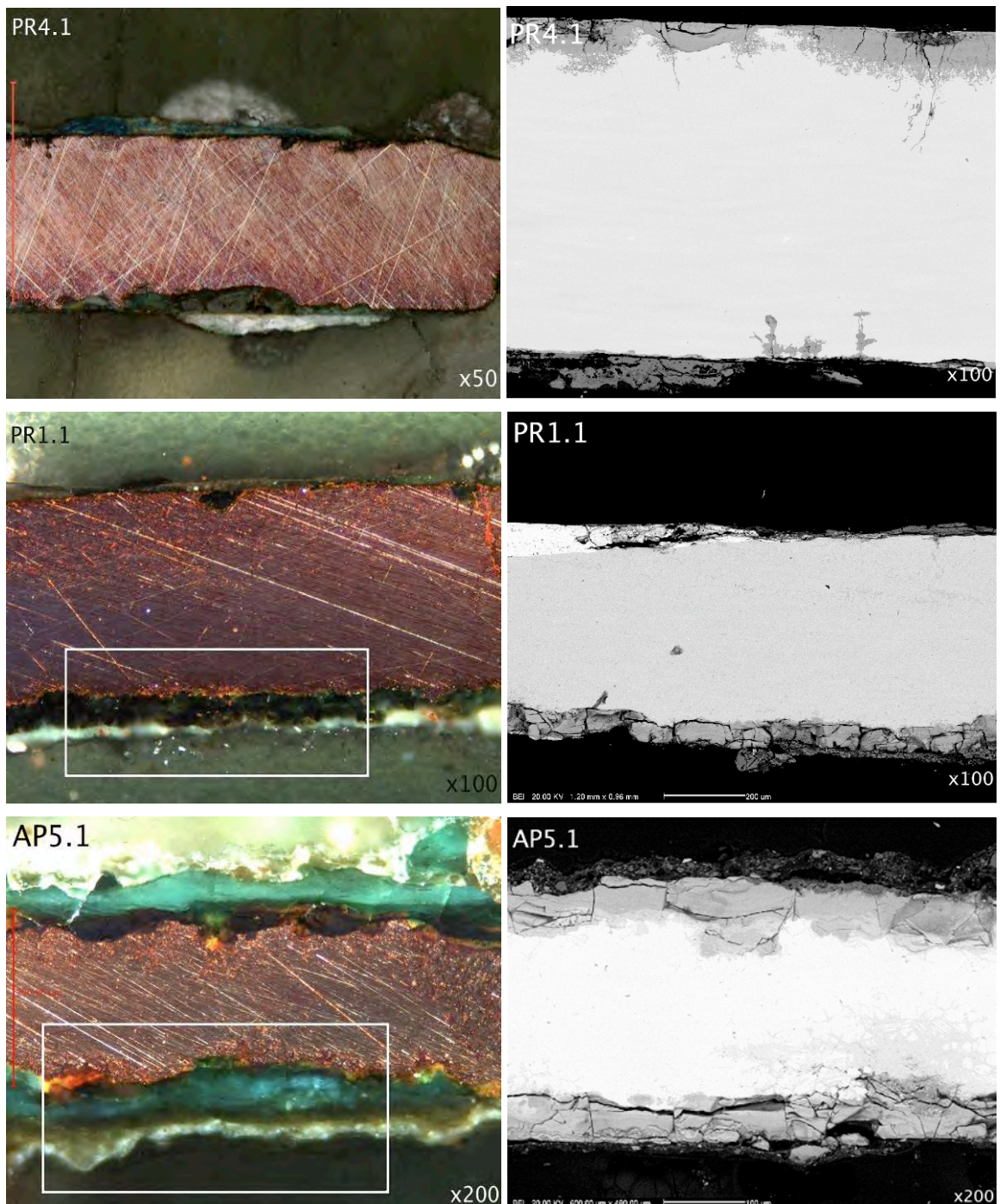
Figure 6.23: BFPM images showing cuprite and/or orange yellow compounds forming an inner corrosion zone. OL69.1: detail showing fine straight filaments pseudomorphs of slip lines. OL53.1: partially etched sample showing slip lines in the strained work-hardened α -bronze grains continuing into the cuprite zone. OL21.1 and OL41.1: detail showing cuprite slip line pseudomorphs changing into orange/yellow colour as they elongate into the green/blue outer corrosion zone where they are no longer visible in BFPM images.

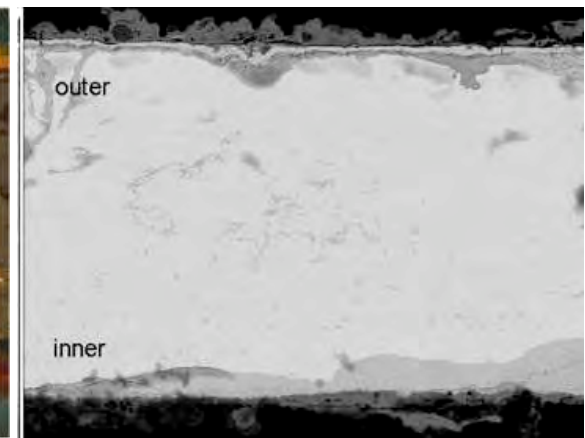
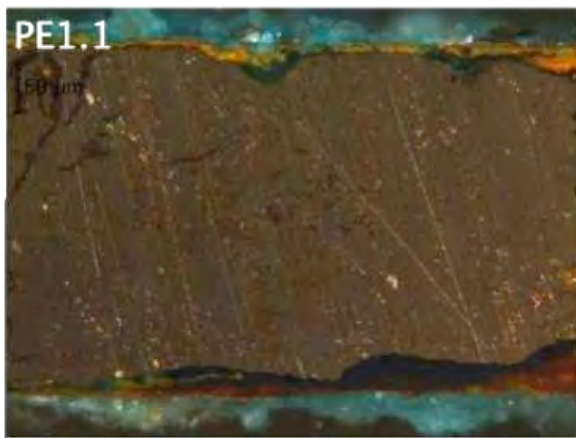
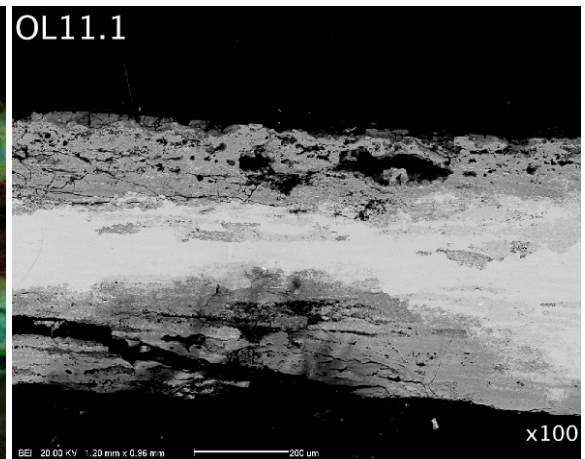
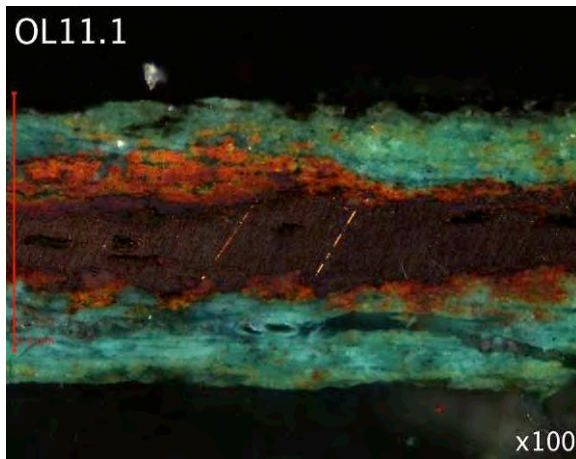
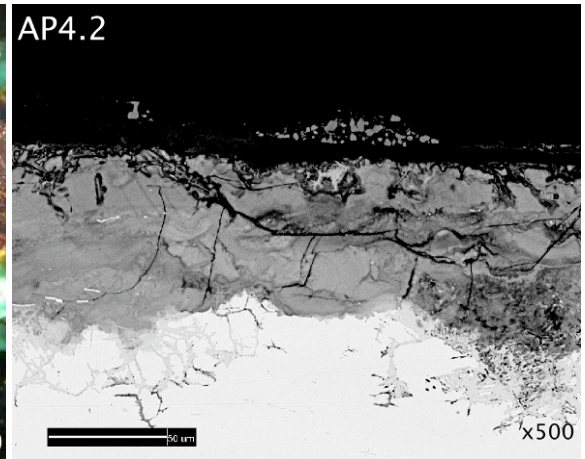
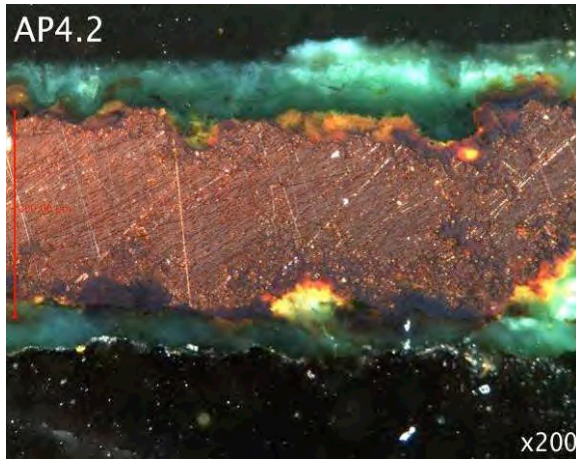
A small number of samples have a thinner localised inner cuprite zone, which does not show clear evidence of slip-lines (Corrosion Profile 3.1). OL11.1 is in an advanced corrosion state.

Apart from PE1.1, the outer zone in samples of this subgroup has a non-uniform chemical distribution (AP4.2, AP5.1). The majority of samples in CP3 are from helmets that show predominance of malachite at a macro scale and exhibit a green/red surface patina colour. The colour of the outer zone varies in BFPM between different tones of green. Sample PE1.1 is an outlier sample in this group because it shows a fine grey/silver patina which was discussed above (section 6.3.2).

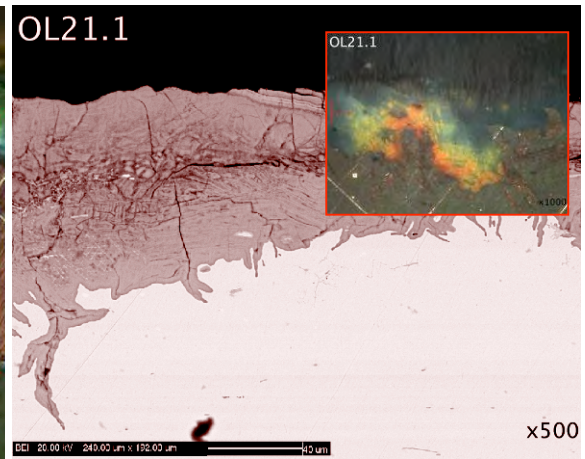
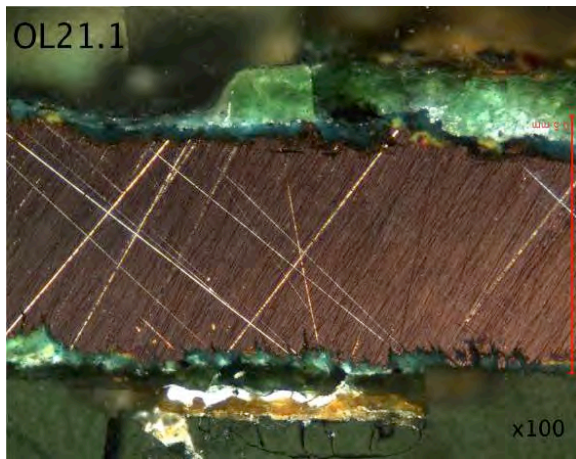
Figure 6.24: (next pages) BFPM and BSE images of cross-sectioned samples in *Corrosion Profile 3* which exhibit two corrosion zones and the inner zone is composed of cuprite or orange/yellow compounds.

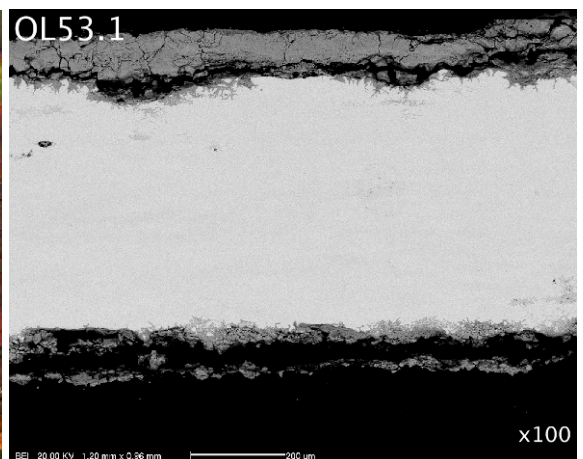
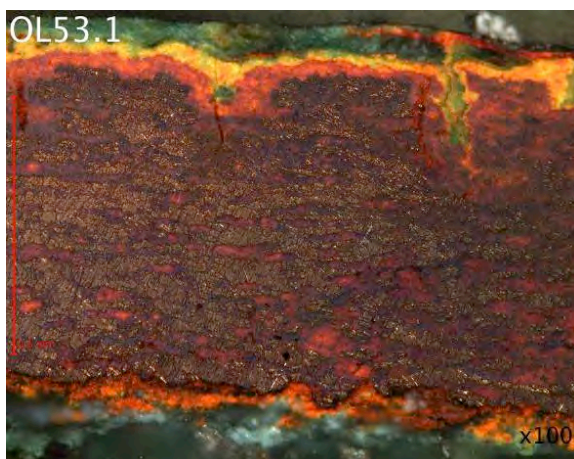
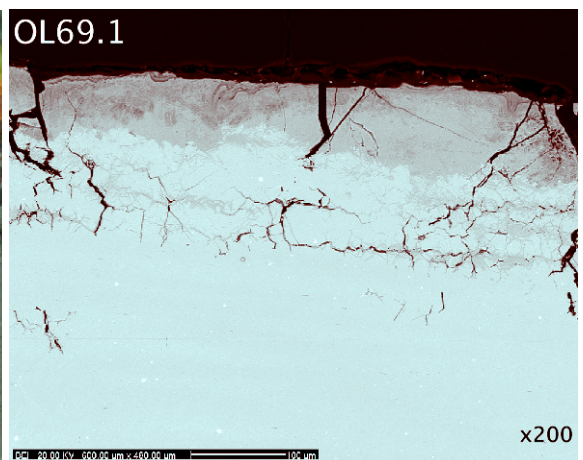
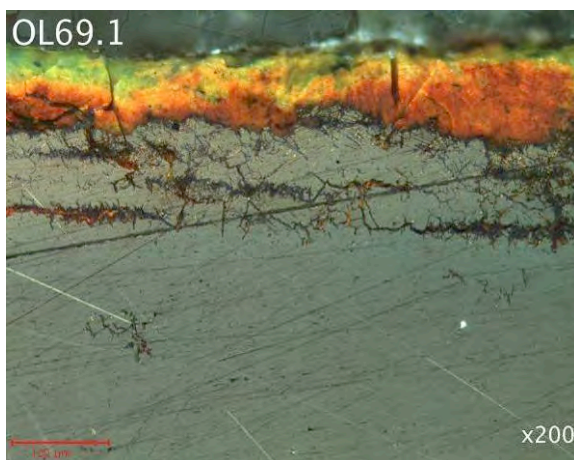
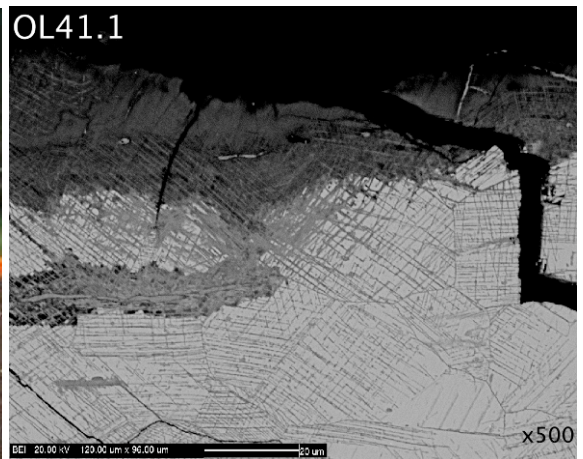
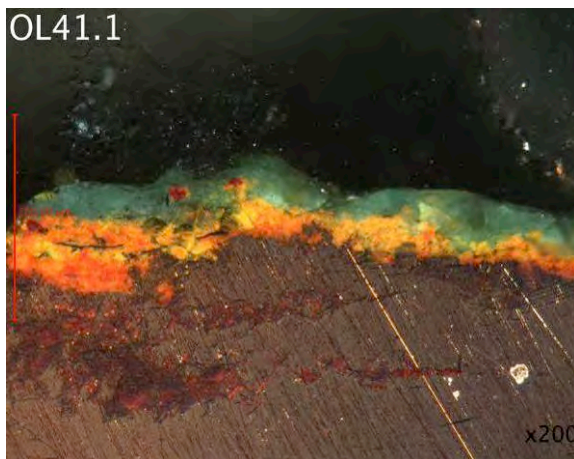
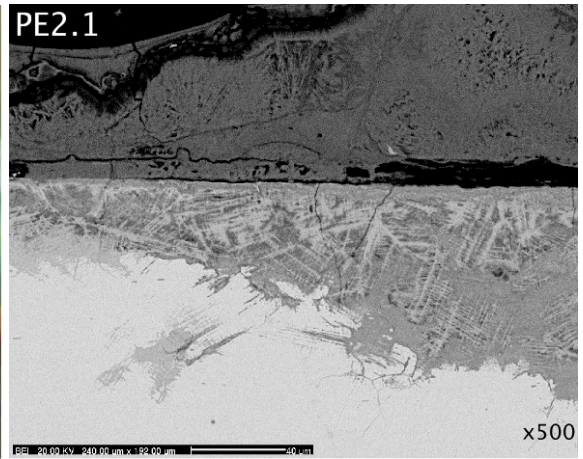
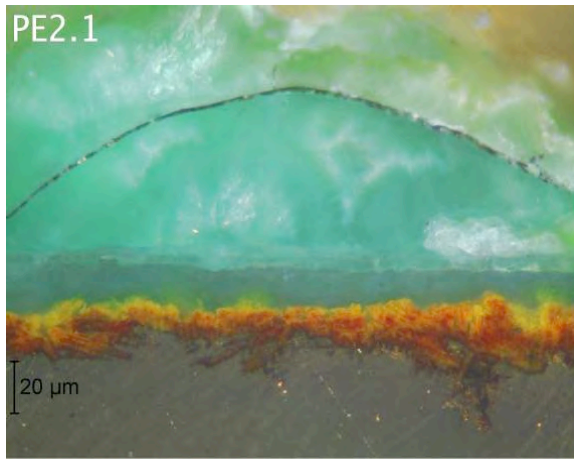
Corrosion Profile 3.1

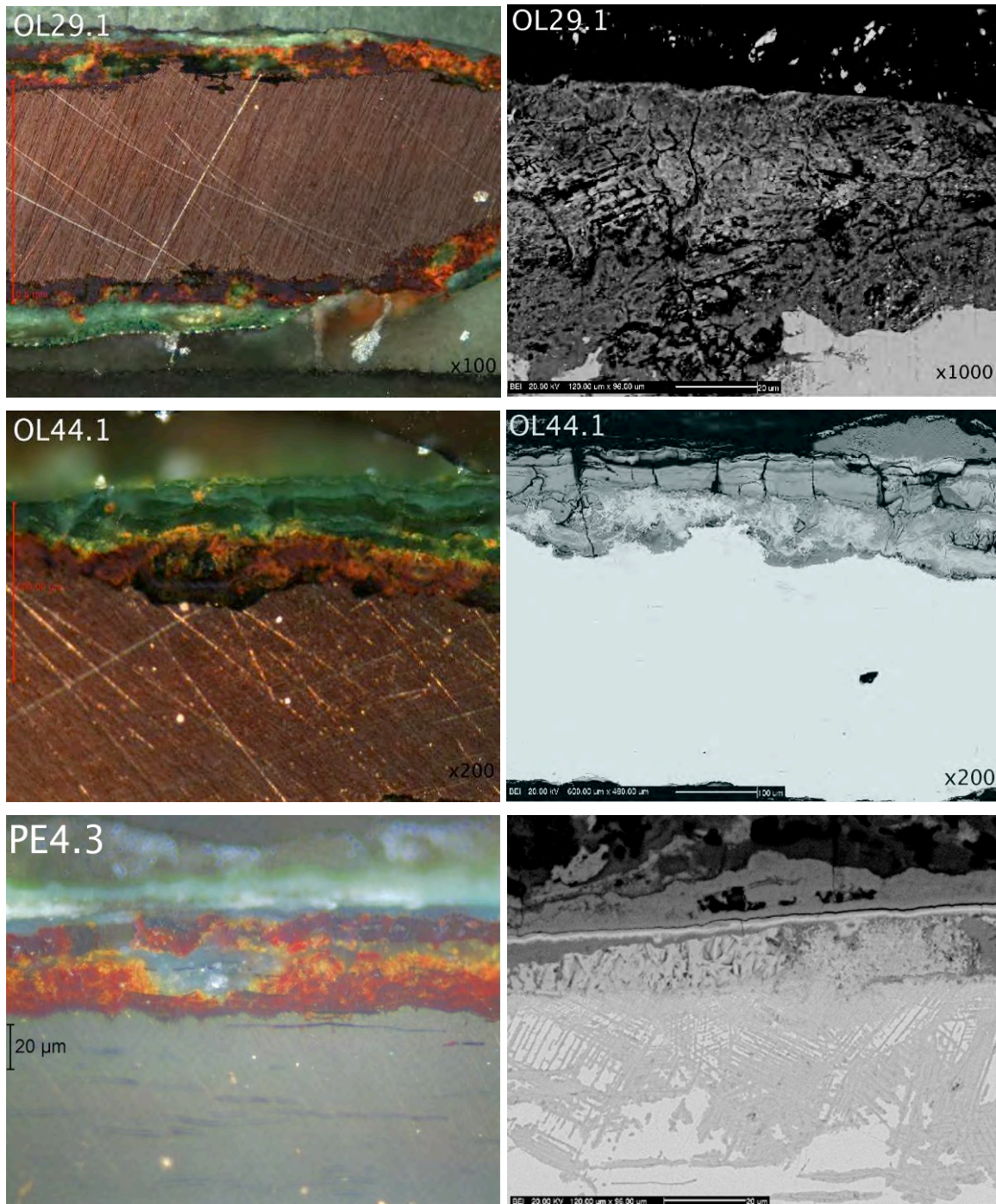




Corrosion Profile 3.2







6.4.2. SEM-EDX COMPOSITION ANALYSES

The elemental composition of the corrosion profile in polished cross-sectioned samples was determined using spot SEM-EDX analysis or area analysis at 1000x magnification. Experimental conditions and SEM-EDX performance are discussed in section 3.6.1. Analysed areas of interest include outer (annotated as _LO) and inner (_LI) corrosion zones in the corrosion profile, features just below the marker of original surface at the outermost part of the outer corrosion zone ('outermost' zone), green and blue copper carbonate deposits (_LD)

and cuprite red zones ($_Lcup$). Inhomogeneous structures such as corrosion filaments (annotated as 'roots') or banded structures ('band') that were thick enough to be analysed are mentioned explicitly. Table 6.6 shows averaged normalized wt% analyses of data collected from three or more areas within each area of interest at the outer side of a helmet. The table includes the sum of elements other than Cu, Sn and O, these are Al, Si, P, S, Cl, Ca, Cr, Fe, Zn, which are noted as Total Soil Elements (TSE). Al, Si, P, S, Cl and Fe are regularly reported in the corrosion layers of archaeological bronzes and are normally encountered as contaminants from the mass transfer of soil constituents into the corrosion layers during burial (Tylecote, 1979; Scott, 1985; Robbiola and Hurtel, 1997). Fe and Zn may be present as trace or Zn as alloying element but in the case of the helmet samples examined in this thesis the concentration of Zn was negligible in the bulk alloy (Table 5.5). Thus, the presence of these elements in the corrosion layers would be due to the burial conditions and in this case are included in TSE. The counts of $CK\alpha$ gave a useful indication of the presence of copper carbonates during analysis, but carbon was excluded from quantitative analysis because of the limitations related to measuring with accuracy carbon using EDX on carbon coated polished samples. Data were normalised to 100% and the sum of TSE is presented to facilitate discussion (Table 6.6). The same data is presented in wt% and at% normalised excluding elements other than Cu, Sn and O ($Cu+Sn+O = 100\%$), because these were used for preparation of ternary plots (Table 6.7). All other plots presented below are based on values seen in Table 6.6.

Before normalisation of the results, the few negative values of trace concentrations of soil elements were set to zero (AMC, 2001b, 2001a). The average sigma% value for each element shown in Table 6.6 corresponds to the averaged experimental error for each individual analysis estimated by the Oxford Link Isis analysis software; data below the experimental error are not shown in the table. The spread of values (noted as 'dev.')

for data collected within an area of interest in each sample was calculated based on the standard deviation equation in MS Excel© to provide an indication of the chemical homogeneity of the analysed area. The inhomogeneous nature of the areas analysed make evaluating analyses precision difficult, as the spread could merely be due to the inhomogeneous nature of the samples. Banded areas show the maximum spread of values within an analysis area; in more uniform samples, the precision is often impressive, especially in the case of Si and O. Average deviation for Cu, Sn, and O is c. 2wt%, with the maximum being c. 10wt%; O wt% deviates the least (Table 6.6). Individual minor and trace elements show in general a good average standard deviation of about 0.1 wt%, and that of their total amount (TSE) averages at 5wt%.

Analyses from the outer corrosion zone of OL31.1 have the highest TSE concentration (higher than 10wt%) due to unusually high P content. Only few samples show unusually high Ca, P and Fe concentrations. In general, standard deviation of analysis of major elements is below c.10wt%; only a few samples have a spread above 10wt% in cases where the analysed areas were very thin or very close to the metallic bronze and are excluded (OL70_LO and LI, OL46.1_LI, PR4_LI).

According to Robbiola's corrosion model of archaeological low-tin bronzes (Robbiola *et al.*, 1998a), internal oxidation phenomena produce preferential dissolution of Cu and surface enrichment of Sn in the corrosion profile. Sn enrichment is said to be a function of the original Sn content in the bronze alloy and it is expressed by the copper dissolution factor f_{Cu} which is calculated from atomic weight composition fractions using eq.3 assuming that Sn dissolution is negligible during corrosion in the binary alloy.

(eq. 3) $f_{Cu} = 1 - [(Cu_{patina}/Sn_{patina}) / (Cu_{bronze}/Sn_{bronze})]$, copper dissolution factor, calculated assuming that $Cu_{bronze} + Sn_{bronze} = 1$ (Robbiola *et al.*, 1998a).

This equation can be also be written as eq. 4, which could be described as a Sn enrichment factor, similarly assuming that Sn dissolution from the corrosion layer is negligible, as well as other elements in the binary bronze alloy.

(eq. 4) $f_{Cu} = 1 - [(Sn_{bronze} / Cu_{bronze}) / (Sn_{patina} / Cu_{patina})]$

To compare the analyses included in this thesis to published work and independently examine the role of the original bronze composition in the corrosion process, f_{Cu} was calculated for each analysis and is included in Table 6.7. Robbiola *et al.* (1998a), do not state if they normalised their data or how it was normalised prior to calculating f_{Cu} . To address this, calculations of the f_{Cu} used a variety of normalisation types including $Cu+Sn+O+TSE=100\%$, $Cu+Sn+O=100\%$ and $Cu+Sn=100\%$. Calculations took place for both fractions, atomic and weight % values. In all cases, the resulting f_{Cu} values were identical for all types of data normalisation. This shows that the f_{Cu} is a rather solid factor that can be calculated from any type of normalised data. Hence, the f_{Cu} results presented in this thesis can be compared to published data.

Table 6.6: (next page) Normalised wt% SEM-EDX analysis of areas of interest in the outer helmet side of cross-sectioned samples. The table includes spread of values (STDEV) between analyses taken at different areas within each analysed area of interest. The table includes the total of elements other than O, Cu and Sn, which are noted as Total Soil Elements (TSE). Concentrations of individual soil elements that are below the detection method are excluded from the table.

Sample	Analyses code	Zone / sigma%	O		Cu		Sn		TSE	Al		Si		P		S		Cl		Ca		Cr		Fe		Zn		
			0.24	dev.	0.34	dev.	0.23	dev.		0.04	dev.	0.05	dev.	0.04	dev.	0.03	dev.	0.03	dev.	0.08	dev.	0.05	dev.	0.07	dev.	0.15	dev.	
AP4.2	AP4.2_LO	Outermost	21.5	6.6	52.3	0.9	20.1	4.8	6.1			0.59	0.12	3.27	0.31	0.08	0.02	0.10	0.06	1.66	0.52			0.36	0.04			
	AP4.2_L2O	Outer	34.0	0.6	48.7	0.2	15.5	0.7	1.9			0.67	0.13	0.18	0.06	0.25	0.06	0.10	0.00	0.39	0.08			0.23	0.06			
	AP4.2_L2I	Inner	17.3	0.8	68.4	1.3	12.2	0.5	2.1			0.28	0.07			0.47	0.05	1.10	0.06					0.12	0.02			
AP5.1	AP5.1_LO	Outer	30.7	0.3	32.63	3.53	26.0	4.0	10.6			0.64	0.02	5.88	0.26	0.23	0.00	1.40	0.07	2.08	0.08			0.34	0.03			
	AP5.1_L2O	Outer	36.2	3.3	43.2	4.0	16.5	0.4	4.1			1.11	0.52	1.57	0.14	0.28	0.03	0.20	0.12	0.68	0.03			0.23	0.05			
	AP5.1_L2I	Inner	16.8	0.4	68.3	3.1	12.4	2.8	2.5			0.33	0.06	0.24	0.22	0.66	0.16	0.90	0.06	0.14	0.05			0.24	0.02			
	AP5.1_LI	Inner	34.7	2.4	40.4	2.4	16.1	2.0	8.8	0.04	0.03	0.64	0.10	5.06	1.29	0.29	0.05	1.10	0.12	1.26	0.56			0.32	0.10			
OL13.1	OL13.1_LO	Outermost	26.4	0.8	25.6	11.6	43.0	10.2	5.0	0.09	0.04	2.16	0.38	0.63	0.11					0.73	0.01	0.05	0.03	1.21	0.37			
	OL13.1_Lid	Inner root_	18.9	1.2	45.2	1.9	31.4	0.5	4.5	0.05	0.05	1.92	0.14	0.41	0.03	0.06	0.02	0.10	0.00	0.80	0.09	0.08	0.01	1.11	0.20			
	OL13.1_LII	Inner root_	32.2	1.2	20.8	2.0	41.1	3.1	5.9	0.08	0.04	3.46	0.06	0.51	0.04	0.09	0.01	0.10	0.07	0.79	0.03			0.91	0.00			
	OL13.1_LR	Inner root_	31.7	7.7	35.3	12.9	28.4	4.1	4.6	0.06	0.03	2.35	0.69	0.52	0.05	0.05	0.03	0.10	0.06	0.63	0.27	0.05	0.02	0.80	0.09			
OL21.1	OL21.1_LO	Outer	31.6	0.7	15.0	0.7	47.5	1.1	5.9	0.07	0.04	4.04	0.25	0.11	0.05	0.33	0.01	0.10	0.00	0.74	0.06			0.45	0.06			
	OL21.1_LI	Inner	36.1	0.4	23.8	0.5	34.7	0.4	5.4			3.62	0.09	0.21	0.04	0.22	0.03	0.30	0.06	0.53	0.07			0.39	0.03			
	OL21.1_L2O	Outer	32.1	2.1	16.4	0.5	45.6	1.8	6.0	0.07	0.02	4.24	0.04	0.13	0.03	0.31	0.03			0.68	0.05			0.43	0.08			
OL27.1	OL27.1_LO	Outer	30.1	3.9	20.4	0.6	43.2	3.1	6.2	0.09	0.03	2.80	0.32	1.22	0.14	0.05	0.02	0.20	0.12	1.18	0.09			0.63	0.02			
	OL27.1_L2O	Outer	30.8	4.4	22.5	1.5	41.6	2.9	5.0			1.72	0.24	1.44	0.15	0.04	0.02			0.99	0.05	0.13	0.08	0.58	0.05			
OL31.1	OL31.1_LO	Outer	33.2	1.2	16.0	0.5	36.4	0.5	14.4	0.07	0.01	1.85	0.17	4.62	0.20	0.15	0.04	0.10	0.00	3.03	0.11	0.05	0.05	4.51	0.93			
OL4.2	OL4.2_LO	Outermost	27.4	3.1	30.6	4.8	38.4	3.0	3.5	0.07	0.09	1.54	0.60	0.42	0.14	0.06	0.02	0.07	0.06	0.45	0.14			0.86	0.12			
	OL4.2_LD	Deposit	33.6	0.7	65.5	0.8			0.7	0.06	0.04	0.08	0.02	0.15	0.05	0.04	0.04	0.10	0.06	0.11	0.02			0.13	0.04			
OL41.1	OL41.1_LO	Outer	34.6	0.9	18.8	2.9	40.4	3.2	6.2	0.18	0.05	2.47	0.14	0.54	0.01	0.18	0.07	0.10	0.06	0.75	0.08	0.07	0.02	1.78	0.17			
	OL41.1_LI	Inner	31.4	0.9	36.6	1.2	28.4	1.0	3.5			1.67	0.10	0.64	0.08	0.05	0.05	0.10	0.00	0.29	0.09			0.65	0.10			
OL44.1	OL44.1_LO	Outer	32.7	1.1	14.9	1.6	46.6	1.6	5.9	0.10	0.01	3.18	0.02	0.29	0.02	0.05	0.00			1.13	0.09	0.42	0.09	0.75	0.05			
	OL44.1_LI	Inner	18.1	2.8	66.2	5.0	14.3	1.9	1.3			0.62	0.23			0.06	0.02	0.07	0.06	0.17	0.07	0.06	0.07	0.26	0.03			
OL46.1	OL46.1_LO	Outer	33.9	3.6	15.0	1.8	43.5	1.8	7.6	0.10	0.03	3.19	0.19	1.05	0.08	0.70	0.12	0.10	0.00	0.79	0.14	0.49	0.13	0.92	0.10	0.3	0.1	
	OL46.1_L2O	Inner root	16.8	4.0	46.9	9.8	31.7	5.0	4.6	0.05	0.02	1.17	0.55	1.16	0.27	0.04	0.05	0.10	0.06	1.27	0.11	0.11	0.03	0.64	0.09			
	OL46.1_LI	Inner	39.0	0.1	22.5	0.6	31.6	0.6	6.9	0.09	0.03	3.16	0.04	1.63	0.08	0.18	0.05	0.10	0.00	0.85	0.04	0.29	0.06	0.57	0.05			
	OL46.1_LD_1	Deposit	31.7		66.1				2.3	0.34		0.84		0.16						0.57				0.32				
OL49.1	OL49.1_LO	Outer	32.3	0.6	11.7	0.0	48.9	1.0	7.0			3.75	0.11	0.09	0.02	0.07	0.03	0.10	0.00	0.70	0.01	1.45	0.43	0.84	0.07			
OL5.1	OL5.1_LO	Outer	28.0	3.4	15.8	1.1	45.9	2.3	10.4	0.23	0.01	3.99	0.16	0.27	0.01	0.19	0.01	0.10	0.00	1.05	0.03	0.29	0.04	0.58	0.09	3.7	0.1	
	OL5.1_LI	Inner	32.9	1.6	20.8	1.9	40.0	0.3	6.3	0.11	0.02	2.66	0.19	0.24	0.04	0.13	0.03	0.10	0.00	0.67	0.09	0.12	0.03	0.46	0.05	1.9	0.2	
OL50.1	OL50.1_LO	Outer	33.6	0.6	34.3	2.6	27.0	1.1	5.1			2.48	0.06	0.22	0.03	0.16	0.05	0.10	0.00	0.43	0.03			1.63	0.73			
	OL50.1_LI	Inner	21.9	2.2	39.5	4.5	33.1	4.5	5.5			2.50	0.29	0.24	0.03	0.48	0.68	0.10	0.15	1.11	0.16	0.32	0.23	0.75	0.47			
	OL50.1_LD	Deposit	37.7	1.7	61.2	1.7			1.0			0.07	0.07							0.11	0.01			0.54	0.07			
OL53.1	OL53.1_LO	Outer	31.0	5.1	20.4	2.3	40.4	2.8	8.3			3.54	0.56	1.17	0.14	0.22	0.13	0.10	0.00	1.27	0.07	0.70	0.06	1.24	0.47			
	OL53.1_L2O	Outer	36.5	0.9	19.6	0.5	36.0	0.5	7.9			3.88	0.07	1.17	0.02	0.04	0.02			1.18	0.14	0.46	0.06	1.12	0.09			
	OL53.1_LO_cup	Inner cuprite	10.9	1.1	88.0	1.2	0.3	0.0	0.8	0.06	0.03							0.50	0.29					0.11	0.05			
	OL53.1_LI	Inner	30.4	3.7	29.2	7.5	35.1	8.2	5.2			1.47	0.31	0.72	0.13	0.09	0.04	0.10	0.00	0.62	0.11			2.11	0.30			
OL57.2	OL57.2_L2O	Outer	32.5	2.5	14.5	0.6	42.3	2.5	10.8	0.16	0.03	3.99	0.20	1.88	0.06	0.23	0.03	0.10	0.00	1.56	0.09	0.61	0.24	2.10	0.19			
	OL57.2_L2I	Inner	30.0	0.6	23.4	0.2	38.8	0.2	7.9			2.73	0.27	1.52	0.20			0.30	0.06	1.22	0.12	0.77	0.14	1.24	0.06			
OL58.1	OL58.1_LO	Outer	33.9	3.2	40.1	3.1	23.4	1.2	2.6	0.04	0.02	0.44	0.20	0.76	0.25	0.75	1.23			0.30	0.03			0.24	0.22			
	OL58.1_L2Ob	Outer band	34.1	1.9	39.7	1.4	23.5	2.6	2.7	0.04	0.04	0.14	0.03	0.77	0.17			0.10	0.10	0.23	0.03	0.33	0.10	0.90	0.38	0.2	0.2	
	OL58.1_L2O	Outer	34.2	0.8	36.2	1.8	26.6	1.6	3.0			0.85	0.17	0.99	0.31	0.08	0.05			0.52	0.10			0.22	0.10	0.3	0.1	
OL66.1	OL66.1_LO	Outer	31.1	5.7	40.1	3.9	24.5	5.7	4.3			1.44	0.30	1.25	0.34					0.77	0.12			0.76	0.22			
	OL66.1_Lcup	Inner cuprite	12.2	0.9	87.5	0.8			0.2																			

Sample	Analyses code	Zone / sigma%	O		Cu		Sn		TSE	Al		Si		P		S		Cl		Ca		Cr		Fe		Zn	
			0.24	dev.	0.34	dev.	0.23	dev.		0.04	dev.	0.05	dev.	0.04	dev.	0.03	dev.	0.03	dev.	0.08	dev.	0.05	dev.	0.07	dev.	0.15 dev.	
OL69.1	OL69.1_L2I	Inner	17.5	0.3	64.4	1.3	16.4	0.9	1.6	0.06	0.01	0.49	0.08					0.80	0.06					0.19	0.29		
	OL69.1_LI	Inner	30.0	0.5	45.2	1.0	22.6	0.7	2.2	0.08	0.02	0.90	0.04	0.10	0.01	0.06	0.02	0.10	0.21	0.09	0.03			0.89	0.05		
OL70.1	OL70.1_LO	Outermost	9.8	2.5	58.1	4.1	28.6	3.3	3.5			1.40	0.32	0.24	0.12	0.16	0.00			1.04	0.15	0.10	0.09	0.44	0.13		
	OL70.1_LI	Inner	13.7	1.1	48.6	3.2	33.5	3.8	4.2			2.01	0.25	0.61	0.10	0.05	0.03	0.10	0.07	0.83	0.41	0.12	0.09	0.43	0.07		
	OL70.1_LD	Deposit	34.5	0.3	62.9	0.8	1.5	0.7	1.0	0.09	0.06	0.42	0.15	0.10	0.04	0.04	0.01			0.27	0.04			0.11	0.09		
OL71.1	OL71.1_LO	Outer	34.7	0.2	10.3	0.3	47.0	0.4	8.1	0.24	0.04	4.50	0.02	0.05	0.01	0.22	0.03	0.10	0.00	1.19	0.08	1.67	0.21	0.13	0.03		
	OL71.1_LI	Inner	36.1	0.4	19.8	0.4	38.8	0.4	5.4	0.08	0.00	3.42	0.18	0.05	0.02	0.08	0.02	0.10	0.06	0.78	0.12	0.77	0.03	0.12	0.05		
OL73.1	OL73.1_LO	Outer	30.2	0.7	17.0	0.4	47.0	0.7	5.8	0.11	0.02	3.53	0.03	0.05	0.00	0.09	0.03			0.56	0.01	0.81	0.16	0.61	0.09		
OL74.1	OL74.1_L-band	Outer band	25.5	2.0	21.4	0.9	47.1	1.3	6.0	0.05	0.03	3.72	0.08	0.30	0.02	0.08	0.02	0.10	0.00	1.02	0.02	0.30	0.07	0.41	0.02		
	OL74.1_LO	Outer	34.7	1.0	14.9	0.4	44.2	0.8	6.2	0.10	0.01	3.92	0.10	0.12	0.11	0.06	0.00	0.10	0.06	0.94	0.08	0.51	0.07	0.47	0.02		
	OL74.1_LI	Inner band	31.1	1.0	33.2	1.2	31.6	1.6	4.1			2.58	0.06	0.19	0.02			0.10	0.00	0.70	0.05	0.11	0.05	0.35	0.08		
	OL74.1_cpd	Deposit	35.3	2.3	62.5	2.7			2.0	0.31	0.12	0.91	0.44	0.07	0.05			0.07	0.06	0.29	0.03			0.24	0.06		
OL75.2	OL75.2_LO	Outer	36.9	0.2	11.2	0.4	44.5	0.4	7.4	0.11	0.03	3.95	0.01	0.14	0.01	0.13	0.03	0.10	0.00	1.13	0.02	1.53	0.20	0.27	0.09		
	OL75.2_L2O	Outer	27.2	0.2	16.0	1.0	49.9	0.2	6.9	0.12	0.02	3.16	0.04	0.20	0.03	0.04	0.01	0.10	0.06	0.96	0.09	0.08	0.03	2.12	0.80		
OL78.1	OL78.1_L2O	Outer	33.8	1.2	13.6	1.7	44.6	0.4	8.0	0.35	0.08	2.52	0.09	0.93	0.05	0.09	0.06	0.10	0.06	1.12	0.03	1.28	0.27	1.54	0.42		
OL78.1	OL78.1_LO	Outer	32.5	0.3	30.9	0.5	32.8	0.7	3.8	0.05	0.00	1.10	0.07	0.33	0.03	0.13	0.01	0.20	0.00	0.38	0.07			1.63	0.13		
	OL78.1_cup	Inner cuprite	10.7		88.7				0.4									0.10						0.20			
	OL78.1_LI	Inner	21.8	0.7	53.0	0.4	23.7	0.4	1.4	0.09	0.03	0.53	0.04			0.04	0.03	0.30	0.00	0.23	0.09			0.24	0.05		
	OL78.1_carb	Deposit	34.6		58.4				7.0	1.67		3.78		0.07		0.11				0.48				0.85			
OL79.1	OL79.1_LO	Outer	31.0	0.7	13.2	0.4	45.7	0.6	10.0	0.13	0.01	3.80	0.11	0.93	0.00	0.05	0.01			1.88	0.01	0.74	0.15	2.50	0.18		
	OL79.1_L2O	Outer	33.3	0.4	20.7	0.3	39.6	0.1	6.4	0.06	0.01	2.67	0.04	0.51	0.01	0.05	0.03			1.05	0.14	0.29	0.11	1.67	0.14		
	OL79.1_LI	Inner	32.8	0.5	16.5	0.6	42.9	0.3	7.8	0.13	0.01	3.07	0.13	0.68	0.02					1.35	0.10	0.74	0.04	1.81	0.12		
OL9.2	OL9.2_LO	Outer	32.7	0.5	9.7	0.2	49.4	0.1	8.2	0.30	0.06	4.33	0.11	0.07	0.04	0.28	0.03	0.10	0.06	1.30	0.04	0.82	0.12	1.01	0.06		
	OL9.2_LI	Inner	34.4	0.9	8.8	0.2	48.1	0.7	8.7	0.33	0.01	4.65	0.04	0.06	0.03	0.23	0.01			1.22	0.04	1.07	0.07	1.03	0.08		
PE1.1	PE1.1_LO	Outer	29.5	1.1	24.4	3.7	43.9	3.5	2.2	0.08	0.02	0.88	0.35	0.30	0.37	0.15	0.05			0.37	0.16			0.26	0.12		
	PE1.1_LI	Inner	20.1	0.7	55.7	1.0	22.3	1.4	1.8	0.04	0.01	0.83	0.16	0.39	0.06	0.08	0.01	0.20	0.00	0.11	0.07			0.09	0.07		
PE1.2	PE1.2_LO	Outer cuprite	19.1	0.4	63.3	0.3	16.4	0.3	1.1	0.05	0.00	0.33	0.02			0.11	0.01	0.40	0.06					0.13	0.02		
	PE1.2_LI	Inner	24.3	6.5	44.6	3.8	28.2	3.2	2.9			1.80	0.68	0.35	0.06	0.10	0.01	0.10	0.00	0.30	0.05			0.15	0.03		
PR1.1	PR1.1_LO	Outer	31.4	2.2	34.0	0.9	28.2	1.9	6.3	0.04	0.03	1.21	0.13	0.88	0.10	0.63	0.05	2.00	0.29	1.13	0.10			0.17	0.11	0.3	0.1
	PR1.1_LI	Inner	21.5	2.3	46.3	0.5	25.6	1.6	6.5	0.04	0.02	1.07	0.06	0.91	0.02	0.73	0.05	1.80	0.14	1.47	0.10			0.16	0.04	0.4	0.0
PR4.1	PR4.1_L2O	Outermost	25.4	2.5	37.5	1.9	31.4	0.6	5.7	0.06	0.01	1.07	0.03	0.65	0.12	0.18	0.02	0.37	0.06	0.56	0.10			2.80	0.45		
	PR4.1_LI	Inner band	14.3	1.3	41.1	1.8	40.0	2.9	4.7	0.07	0.02	1.94	0.10	0.37	0.05	0.45	0.02	0.30	0.00	1.09	0.14			0.44	0.02		
	AVERAGE		28.6	1.7	36.1	2.0	33.2	1.9	5.1	0.14	0.03	2.12	0.17	0.79	0.11	0.19	0.06	0.29	0.05	0.83	0.09	0.49	0.10	0.77	0.14	1.0	0.1
	MAX		39.0	7.7	88.7	12.9	49.9	10.2	14.4	1.67	0.12	4.65	0.69	5.88	1.29	0.75	1.23	2.00	0.29	3.03	0.56	1.67	0.43	4.51	0.93	3.7	0.2
	MIN		9.8	0.1	8.8	0.0	0.3	0.0	0.2	0.04	0.00	0.07	0.01	0.05	0.00	0.04	0.00	0.07	0.00	0.09	0.01	0.05	0.01	0.09	0.00	0.2	0.0

Sample	Analyses code	Corrosion zone	O	Cu	Sn	O	Cu	Sn	f _{Cu}
			Cu+Sn+O=100 wt%			Cu+Sn+O=100 at%			
AP4.2	AP4.2_LO	Outermost	22.9	55.7	21.4	57.5	35.2	7.2	0.86
	AP4.2_L2O	Outer	34.6	49.6	15.8	70.3	25.4	4.3	0.83
	AP4.2_L2I	Inner	17.6	69.9	12.5	47.8	47.7	4.6	0.70
AP5.1	AP5.1_LO	Outer	34.4	36.5	29.1	72.4	19.4	8.3	0.93
	AP5.1_LI	Inner	38.0	44.3	17.7	73.7	21.6	4.6	0.87
	AP5.1_L2O	Outer	37.7	45.0	17.2	73.4	22.1	4.5	0.86
	AP5.1_L2I	Inner	17.2	70.0	12.8	47.1	48.2	4.7	0.71
OL13.1	OL13.1_LO	Outermost	27.8	27.0	45.2	68.3	16.7	15.0	0.93
	OL13.1_LR	Inner root_	33.2	37.0	29.8	71.4	20.0	8.6	0.86
	OL13.1_LII	Inner root_	34.2	22.1	43.7	74.9	12.2	12.9	0.94
	OL13.1_Lid	Inner root_	19.8	47.3	32.9	54.8	33.0	12.3	0.84
OL21.1	OL21.1_LO	Outer	33.6	15.9	50.5	75.6	9.0	15.3	0.96
	OL21.1_LI	Inner	38.2	25.1	36.7	77.2	12.8	10.0	0.92
	OL21.1_L2O	Outer	34.1	17.4	48.5	75.7	9.8	14.5	0.96
OL27.1	OL27.1_LO	Outer	32.1	21.8	46.1	73.4	12.5	14.2	0.93
	OL27.1_L2O	Outer	32.5	23.7	43.8	73.2	13.5	13.3	0.93
OL31.1	OL31.1_LO	Outer	38.8	18.7	42.5	78.8	9.6	11.6	0.95
OL4.2	OL4.2_LO	Outermost	28.4	31.8	39.9	68.0	19.2	12.9	0.88
	OL4.2_LD	Deposit	33.9	66.0	0.2	67.1	32.9	0.0	
OL41.1	OL41.1_LO	Outer	36.8	20.1	43.1	77.2	10.6	12.2	0.94
	OL41.1_LI	Inner	32.6	38.0	29.5	70.7	20.7	8.6	0.84
OL44.1	OL44.1_LO	Outer	34.7	15.8	49.5	76.5	8.8	14.7	0.97
	OL44.1_LI	Inner	18.4	67.1	14.5	49.4	45.4	5.3	0.53
OL46.1	OL46.1_LO	Outer	36.7	16.3	47.1	77.8	8.7	13.5	0.97
	OL46.1_LI	Inner	41.9	24.2	33.9	79.7	11.6	8.7	0.93
	OL46.1_LD_1	Deposit	32.4	67.6	0.0	65.6	34.4	0.0	
	OL46.1_L2O	Inner root	17.7	49.2	33.2	51.2	35.9	13.0	0.86
OL49.1	OL49.1_LO	Outer	34.7	12.6	52.7	77.2	7.1	15.8	0.96
OL5.1	OL5.1_LO	Outer	31.2	17.6	51.2	73.4	10.4	16.2	0.96
	OL5.1_LI	Inner	35.1	22.2	42.7	75.6	12.0	12.4	0.94
OL50.1	OL50.1_LO	Outer	35.4	36.1	28.5	73.2	18.8	7.9	0.85
	OL50.1_LI	Inner	23.2	41.9	35.0	60.3	27.4	12.3	0.86
	OL50.1_LD	Deposit	38.0	61.8	0.2	70.9	29.0	0.1	
OL53.1	OL53.1_LO_cup	Inner cuprite	11.0	88.7	0.3	33.0	66.9	0.1	
	OL53.1_LO	Outer	33.7	22.2	44.0	74.5	12.4	13.1	0.95
	OL53.1_LI	Inner	32.1	30.8	37.1	71.6	17.3	11.1	0.91
	OL53.1_L2O	Outer	39.6	21.3	39.1	78.8	10.7	10.5	0.94
OL57.2	OL57.2_L2O	Outer	36.4	16.2	47.4	77.6	8.7	13.6	0.96
	OL57.2_L2I	Inner	32.5	25.4	42.1	73.0	14.3	12.7	0.93
OL58.1	OL58.1_LO	Outer	34.8	41.2	24.0	71.9	21.4	6.7	0.81
	OL58.1_L2Ob	Outer band	35.0	40.8	24.2	72.1	21.2	6.7	0.81
	OL58.1_L2O	Outer	35.3	37.3	27.5	72.9	19.4	7.7	0.85
OL66.1	OL66.1_LO	Outer	32.5	41.9	25.6	69.9	22.7	7.4	0.82
	OL66.1_Lcup	Inner cuprite	12.2	87.7	0.1	35.6	64.4	0.1	
OL69.1	OL69.1_LI	Inner	30.7	46.2	23.1	67.5	25.6	6.9	0.80
	OL69.1_L2I	Inner	17.8	65.5	16.7	48.7	45.1	6.2	0.60
OL70.1	OL70.1_LO	Outermost	10.2	60.2	29.7	34.7	51.6	13.6	0.82
	OL70.1_LI	Inner	14.3	50.7	35.0	44.9	40.2	14.8	0.87
	OL70.1_LD	Deposit	34.9	63.6	1.5	68.3	31.3	0.4	
OL71.1	OL71.1_LO	Outer	37.7	11.2	51.1	79.6	5.9	14.5	0.97
	OL71.1_LI	Inner	38.1	20.9	41.0	78.0	10.7	11.3	0.94
OL73.1	OL73.1_LO	Outer	32.1	18.0	49.9	74.0	10.5	15.5	0.96
OL74.1	OL74.1_LO	Outer	37.0	15.9	47.2	78.1	8.5	13.4	0.95
	OL74.1_LI	Inner band	32.5	34.6	33.0	71.2	19.1	9.7	0.85
	OL74.1_L-band	Outer band	27.2	22.7	50.1	68.5	14.4	17.0	0.93
	OL74.1_cpd	Deposit	36.0	63.8	0.1	69.1	30.8	0.0	
OL75.2	OL75.2_LO	Outer	39.8	12.1	48.1	80.7	6.2	13.1	0.97
	OL75.2_L2O	Outer	29.2	17.2	53.6	71.7	10.6	17.7	0.96
OL78.1	OL78.1_L2O	Outer	36.8	14.8	48.5	78.2	7.9	13.9	0.95
OL78.1	OL78.1_LO	Outer	33.7	32.1	34.1	72.7	17.4	9.9	0.85
	OL78.1_LI	Inner	22.1	53.8	24.1	56.8	34.8	8.3	0.63
	OL78.1_cup	Inner cuprite	10.7	89.0	0.3	32.3	67.6	0.1	
	OL78.1_carb	Deposit	37.2	62.8	0.0	70.2	29.8	0.0	
OL79.1	OL79.1_LO	Outer	34.5	14.7	50.8	76.5	8.2	15.2	0.96
	OL79.1_LI	Inner	35.5	17.9	46.6	76.7	9.7	13.6	0.95
	OL79.1_L2O	Outer	35.6	22.1	42.4	75.9	11.9	12.2	0.93
OL9.2	OL9.2_LO	Outer	35.7	10.6	53.8	78.3	5.8	15.9	0.98
	OL9.2_LI	Inner	37.7	9.7	52.7	79.8	5.1	15.0	0.98
PE1.1	PE1.1_LO	Outer	30.1	25.0	44.9	70.9	14.8	14.3	0.94
	PE1.1_LI	Inner	20.5	56.8	22.7	54.2	37.7	8.1	0.72
PE1.2	PE1.2_LO	Outer cuprite	19.4	64.0	16.6	51.3	42.7	5.9	0.57
	PE1.2_LI	Inner	25.0	45.9	29.0	61.8	28.5	9.7	0.82
PR1.1	PR1.1_LO	Outer	33.6	36.3	30.1	71.8	19.6	8.7	0.91
	PR1.1_LI	Inner	23.0	49.6	27.4	58.7	31.8	9.4	0.87
PR4.1	PR4.1_L2O	Outermost	26.9	39.8	33.3	65.0	24.2	10.8	0.88
	PR4.1_LI	Inner band	15.0	43.1	41.9	47.6	34.5	17.9	0.90

Table 6.7: SEM-EDX weight and atomic % composition analyses of areas of data presented in Table 6.6 normalised as Cu+Sn+O=100%. The last column includes the copper dissolution factor or tin enrichment factor $f_{Cu} = 1 - [(Cu_{patina}/Sn_{patina}) / (Cu_{bronze}/Sn_{bronze})]$ using bronze composition data in Table 5.5.

6.4.2.1. Relationships between Cu, Sn, O, TSE and f_{Cu} in corrosion profiles

The EDX data from the corrosion profiles show relationships between the relative concentrations of Cu, Sn, O and total soil elements (TSE) (Figure 6.25). The inner corrosion layers tend to have smaller amount of oxygen, tin and total soil elements relatively to the outer zone of the corrosion profile, which is enhanced in Sn, O, and TSE depending on morphological profile (discussed below) (Table 6.6). Looking at the results in bulk, the decreasing amount of Cu from the corrosion profile is clearly related to the increasing concentration of Sn, O and TSE (Figure 6.25a, b, c). The concentration of Sn increases with increasing TSE and O (Figure 6.25d, e). The plot of TSE and O at% shows great scatter between the data points, yet indicates the trend for TSE to increase with increasing O (Figure 6.25f).

Because of these relationships, plotting the TSE/O ratio (extraneous elements) against Sn/Cu (alloying elements) at% can be used to characterise the chemical nature of the corrosion profile and points of unusual TSE content can be identified (Figure 6.26). The Sn/Cu ratio lies between 0.1-2.8 and was calculated to facilitate discussion of results. An assessment of the numerical data based on the ratios of Sn/Cu, TSE/Sn, TSE/Cu, Cu/O and Sn/O (Table 6.8) aided identification of outliers. The majority of the analyses have Sn>TSE at% and O at% concentration higher than Cu at% (O>Cu at%). Sn at% outweighs TSE at% at the great majority of analyses (Sn>TSE at%) (Table 6.8). The few samples where the opposite relationship exists (TSE>Sn at%) are copper carbonate deposits (OL4.2, OL50.1, OL70.1) and analysis from AP4.2 and AP5.1 where Cu is higher than TSE at% (Cu>TSE>Sn at%). The outer corrosion zone of OL31.1 has uncommon TSE composition (c. 14wt% and TSE>Sn at%) and it is unrepresentative to the bulk of the samples. Analysis from areas of cuprite (OL53.1, OL66.1) and the outmost corrosion zone on OL70.1 are the only where Cu at% outweighs O at% (Cu>O at%) indicating the unrepresentative nature of analyses from OL70.1. In relation to the Sn/Cu ratio, the range between 0.7 and 1.2 is arbitrarily taken to indicate an approximate equal Sn \approx Cu concentration in order to accommodate compositional variation within the analysed area of interest in individual samples. Thus, Sn>Cu when the ratio is higher than 1.2 and Cu>Sn when the ratio is less than 0.7 (Table 6.8).

The f_{Cu} value, which provides an indication of the relationships between the Sn content in the corrosion relative to the original bronze increases with increasing Sn concentration in the patina as expected because Sn/Cu is part of the f_{Cu} equation (Figure 6.26). A few analyses have high f_{Cu} at low Sn/Cu ratio (<0.7) deviating and are discussed later.

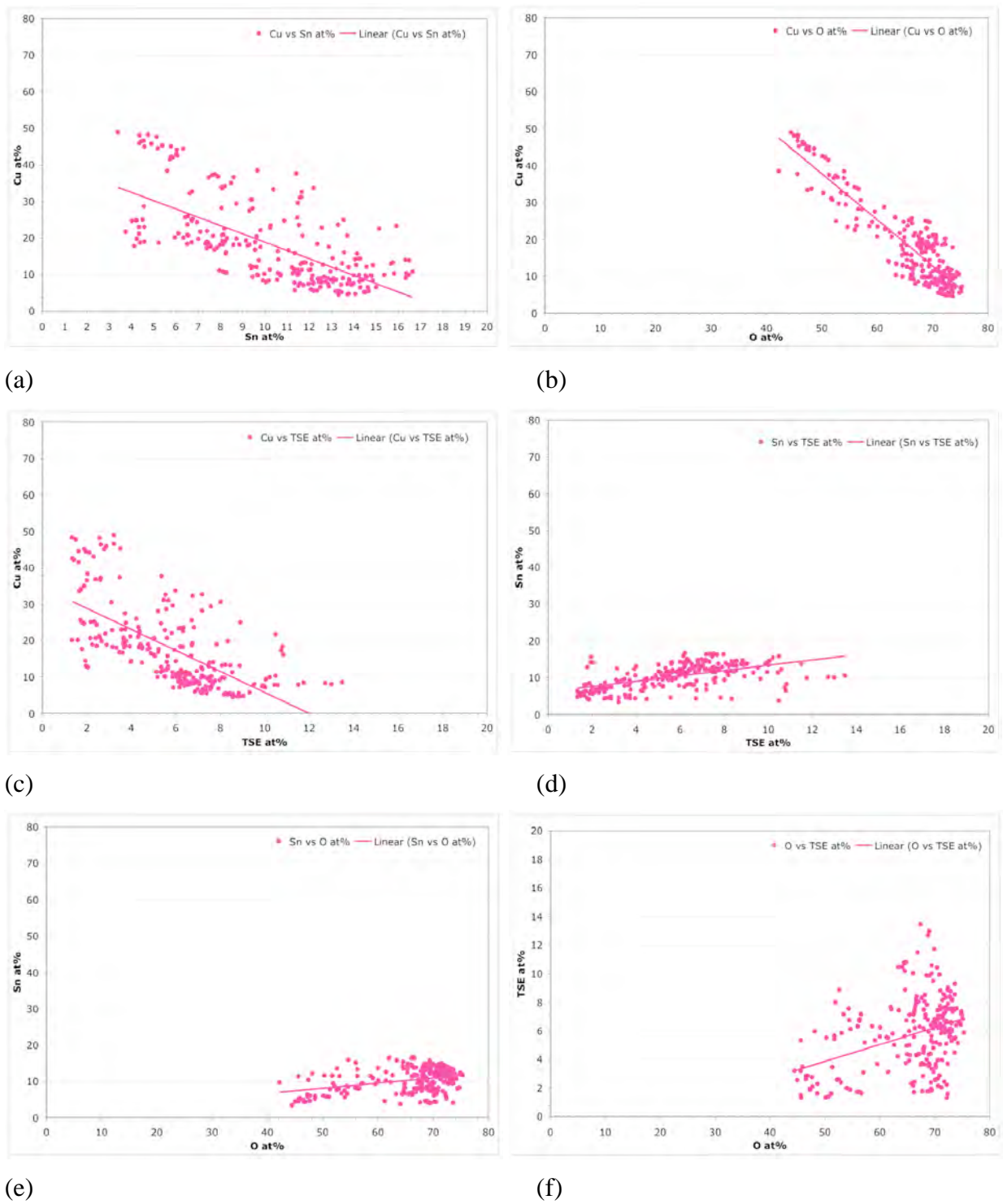


Figure 6.25: Scatter plots of all analyses data (Table 6.6) in atomic % showing relationships between Cu, Sn, O and total soil elements (TSE) in the corrosion profiles. Plots include analyses from areas of interest within the corrosion profile of both inner and outer helmet sides.

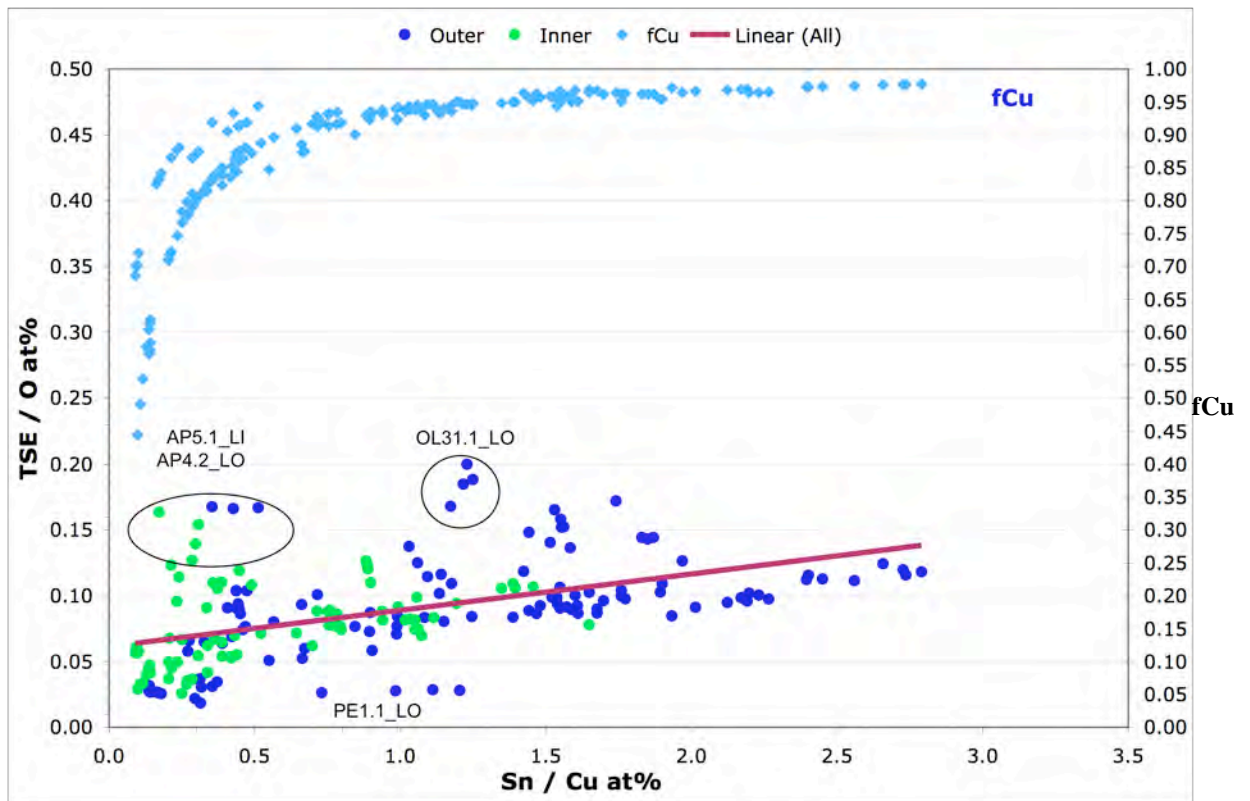


Figure 6.26: Scatter plot of Sn/Cu and TSE/O at% ratios of analyses from the outer and inner corrosion zones in corrosion profiles. It shows trend for TSE to increase with increasing Sn. The f_{Cu} increases with increasing Sn in the corrosion profile, but some samples show a high f_{Cu} at low Sn/Cu. Marked is analysis from samples with uncommonly high amount of total soil elements.

Cu>O at%	TSE>Sn at%	TSE>Cu at%	Sn>Cu at%	Sn/Cu at% ratio	O>Sn wt	Corrosion zone	Sample	Analyses code					
Cu>O	Sn>TSE	Cu>TSE	Cu>Sn	<0.7 Cuprite	Sn>O O>Sn	Outermost	OL70.1	OL70.1_LO					
						Cuprite inner	OL53.1	OL53.1_LO_cup					
							OL66.1	OL66.1_Lcup					
O>Cu	Sn>TSE	Cu>TSE	Cu>Sn	0.7-1.2	O>Sn Sn>O	Outer	OL53.1	OL53.1_L2O					
						Inner	OL21.1	OL21.1_LI					
						Outermost	OL13.1	OL13.1_LO					
							OL4.2	OL4.2_LO					
						Outer	OL27.1	OL27.1_LO					
							PE1.1	PE1.1_LO					
						Inner	OL53.1	OL53.1_LI					
							OL57.2	OL57.2_L2I					
						O>Sn	O>Sn	O>Sn	<0.7	O>Sn	Outermost	OL58.1	OL58.1_L2Ob
											Outer	AP4.2	AP4.2_L2O
												OL50.1	OL50.1_LO
												OL58.1	OL58.1_L2O
													OL58.1_LO
												OL66.1	OL66.1_LO
												PE1.2	PE1.2_LO
			PR1.1	PR1.1_LO									
			Inner Root	OL13.1	OL13.1_LR								
			Inner	AP4.2	AP4.2_L2I								
				OL41.1	OL41.1_LI								
				OL44.1	OL44.1_LI								
				OL69.1	OL69.1_L2I								
					OL69.1_LI								
				PE1.1	PE1.1_LI								
			PE1.2	PE1.2_LI									
			PR1.1	PR1.1_LI									
			Sn>Cu	Sn>Cu	Sn>Cu	>1.2	Sn>O	Sn>O	Outer	OL21.1	OL21.1_LO		
										OL44.1	OL44.1_LO		
										OL46.1	OL46.1_LO		
										OL73.1	OL73.1_LO		
										OL74.1	OL74.1_LO		
OL79.1	OL79.1_LI												
Outermost	OL27.1	OL27.1_L2O											
	Outer	OL41.1							OL41.1_LO				
	OL53.1	OL53.1_LO											
Inner Root	OL13.1	OL13.1_LII											
	Inner	OL5.1							OL5.1_LI				
OL71.1	OL71.1_LI												
Outer	OL49.1	OL49.1_LO											
	OL5.1	OL5.1_LO											
	OL57.2	OL57.2_L2O											
	OL71.1	OL71.1_LO											
	OL75.2	OL75.2_LO											
	OL78.1	OL78.1_L2O											
	OL79.1	OL79.1_LO											
	OL9.2	OL9.2_LI											
	OL9.2_LO												
TSE>Sn	Cu>TSE	Cu>Sn	Deposit	O>Sn	O>Sn	Deposit	OL4.2	OL4.2_LD					
							OL50.1	OL50.1_LD					
							OL70.1	OL70.1_LD					
			<0.7			O>Sn	O>Sn	<0.7	O>Sn	Outermost	AP4.2	AP4.2_LO	
										Outer	AP5.1	AP5.1_LO	
										Inner	AP5.1	AP5.1_LI	
										Outer	OL31.1	OL31.1_LO	
TSE>Cu	Sn>Cu	0.7-1.2	Sn>O	Sn>O	Sn>O	Outer							

Table 6.8: Pivot table showing relative abundance of elements and Sn/Cu at% ratio groups of analyses from areas of interest at the outer helmet side in cross-sectioned samples. Based on averaged data normalised as Cu+Sn+O+TSE=100%.

Soil elements introduced in the corrosion profiles increase with decreasing Cu and increasing O and Sn at% concentrations. Si is by far the most abundant soil element detected at 1 at% in high Cu concentrations increasing to around 6 at% at the lowest Cu (and highest Sn) content concentrations (Figure 6.28). Soil elements include Fe, P, Ca, S and Cr, and a small number of samples have low concentrations of Cl (0.1 at%). Figure 6.27 shows that the concentrations of Al and Cr is relatively constant for up to around 12at% Sn (14at% Cu), but then rapidly increases for samples that exhibit more advanced Cu dissolution ($\text{Cu} < \text{c. } 14\text{at}\%$). This sudden increase is not observed for Ca, Fe and Si, which is more gradual. This may reflect entry of soil elements relative to the Cu and Sn content of the corrosion layer. Si and Fe may enter the patina in the early stages of oxidation. Alternatively, this may reflect that Cr is associated with enhanced copper dissolution.

Cr is rarely reported on archaeological patinas. Its presence has been associated with black patinas on Chinese bronzes but its existence due to intentional surface treatment is debated (section 2.2.2). Cr present in the patinas could have been introduced from the soil during burial. Chromium exists in the environment in the trivalent Cr_{III} or hexavalent Cr_{VI} form and its natural source are chromite minerals (FeCr_2O_4). Relatively high levels of Cr often occur naturally in Greek waters due to their passage through chromite deposits (Karavoltzos *et al.*, 2008) that occur widely in Greece. Occurrences include at Domokos, Vourino at Volos (Moore and Fairbridge, 1997: 315), Rodiani (Augustithis, 1995: 98), Pindos mountains (Economou-Eliopoulos and Vacondios, 1995), Vavdos at Chalkidiki (Christodoulou and Hirst, 1985), Peloponnesus and the Aegean islands (Karavoltzos *et al.*, 2008). Despite lack of geochemical information from Olympia, where the majority of the helmets were unearthed, Peloponnesus has similar geology with the mainland Greece and it would be expected that chromite minerals be encountered there too. A chemical study of bones from the nearby Hellenistic site of Asine, showed that they had substantial concentrations of Cr, which was attributed to contamination from the soil (Edward *et al.*, 1984).

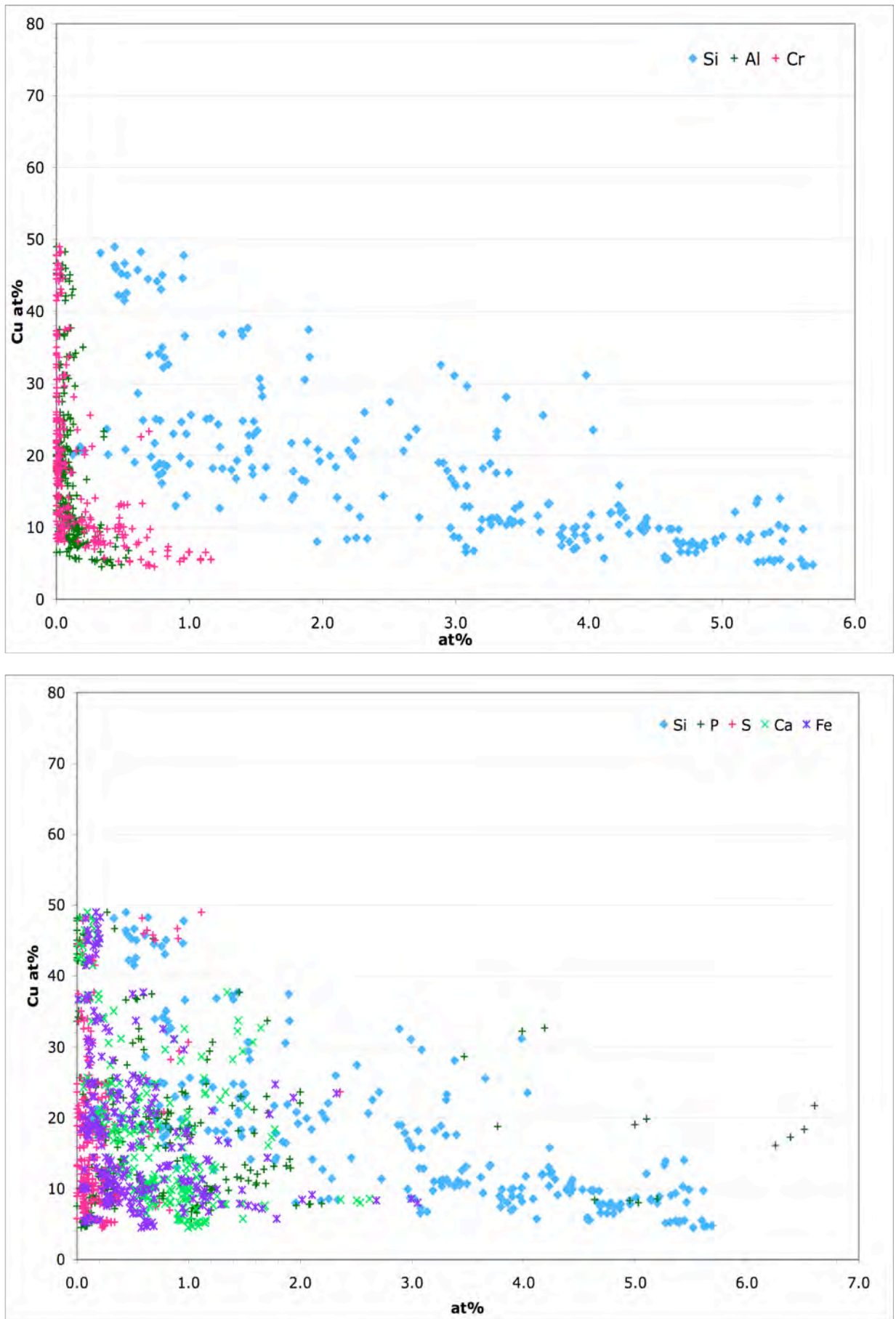


Figure 6.27: Scatter plots showing relationship of soil elements with Cu.

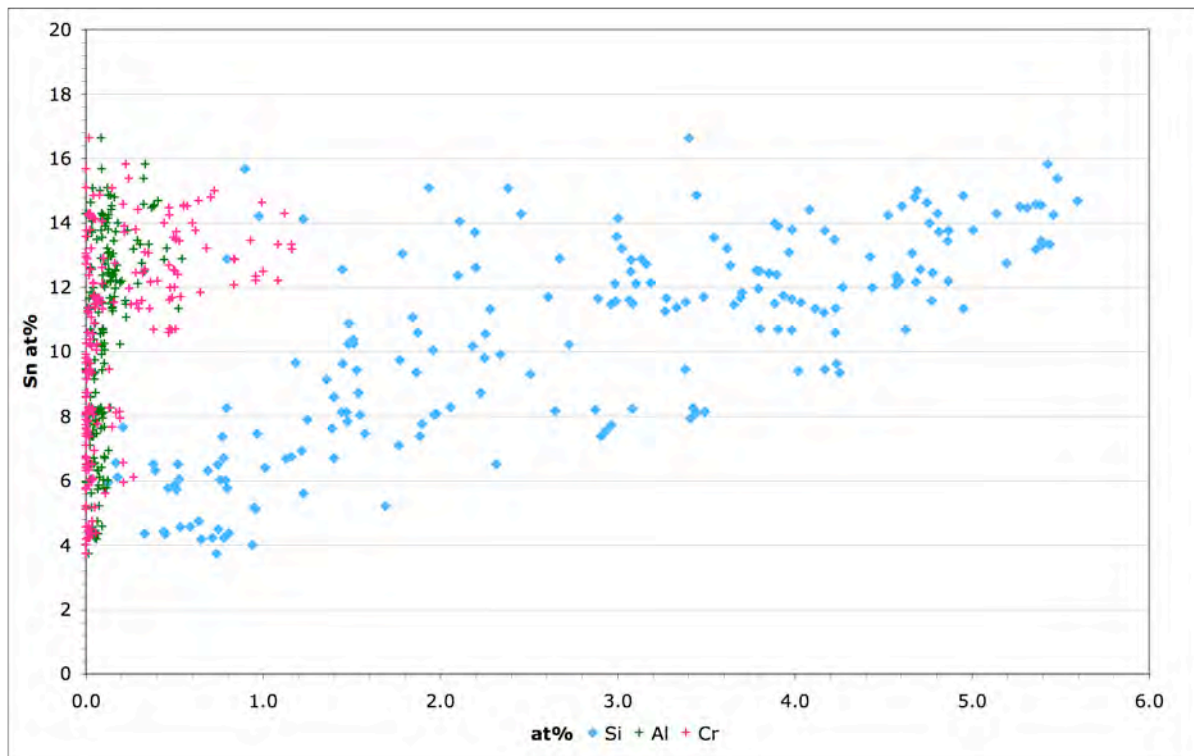


Figure 6.28: Scatter plot showing relationship of Si, Al and Cr to Sn at% in the bulk analysis results.

6.4.2.2. Cu, Sn, O and TSE variation in and between corrosion profiles

Analysis shows that the outer corrosion zone tends to have elevated Sn, O and TSE at% and Sn/Cu ratio compared to the inner corrosion zone of the same sample (Table 6.9). The Cu-Sn-O ternary diagram of analyses from the outer side of helmet samples shows that the outer corrosion zone in the profile clusters either towards the composition of $\text{SnO}_2 \cdot 2\text{H}_2\text{O}$ or towards that of copper carbonates. Data from the inner zone are scattered between Cu_2O and higher O at% and lower Cu at% concentrations. Analysis of the results based on the physical characteristics of the corrosion profile shows correlation between these and the Sn/Cu ratio in the profile (Table 6.9).

Samples exhibiting a fibrous microstructure and a very fine surface finish (CP2.1) tend to have the maximum Sn concentrations ($\text{Sn}/\text{Cu} > 1.2$). In the Cu-Sn-O at% ternary plot (Figure 6.30), data from the outer and inner corrosion layers from samples with CP2.1 profile show Cu-O-Sn at% composition near $\text{SnO}_2 \cdot 2\text{H}_2\text{O}$ below 12at% Cu. Due to the fineness of the corrosion profiles clustered there, this region can be described as 'stability region'. The inner and outer corrosion zone of this group is chemically more uniform than other groups.

The outer corrosion layers from CP3.2 samples cluster in a similar high-Sn region but, in contrast, data from the inner corrosion zone scatter between regions of cuprite and high Sn, due to their inner cuprite-rich corrosion zone. Samples which exhibit Corrosion Profile 2.2 or

3.1, which were identified as an intermediate mixed group between the very distinct CP2.1 and CP3.2, exhibit the least Sn ($\text{Sn}/\text{Cu} < 0.7$). They tend to have more O wt% than Sn wt% and in the Cu-Sn-O at% ternary diagram cluster near the area of the plot where the composition of copper carbonates lies. Samples in these groups show a broad uneven surface, and this region in the ternary plot can be described as ‘mineralisation region’. The $\text{CK}\alpha$ X-ray line gave a good indication for carbonates, but it was not quantitatively measured. The only samples with microstructural profiles in these groups that have a high Sn/Cu ratio is OL78.1. Overall, with the exception of 3 samples, corrosion profiles of similar physical characteristics tend to have similar Cu, Sn, O at% concentration and variation in their profile.

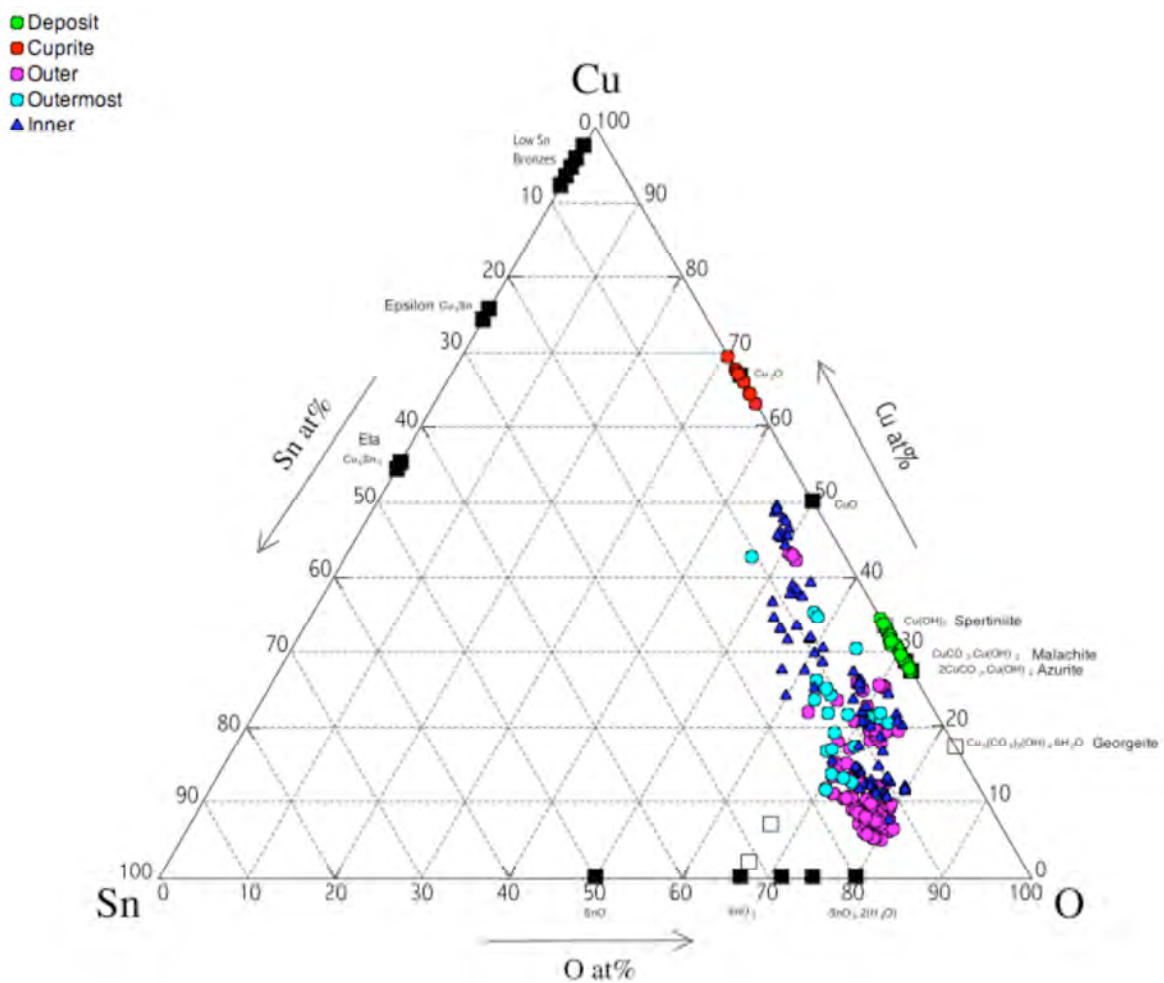


Figure 6.29: Cu-Sn-O at% ternary plot of all EDX data. It shows that the outer part of the patina can reach stability (plot area near $\text{SnO}_2 \cdot 2\text{H}_2\text{O}$) or mineralization (plot area near copper carbonates).

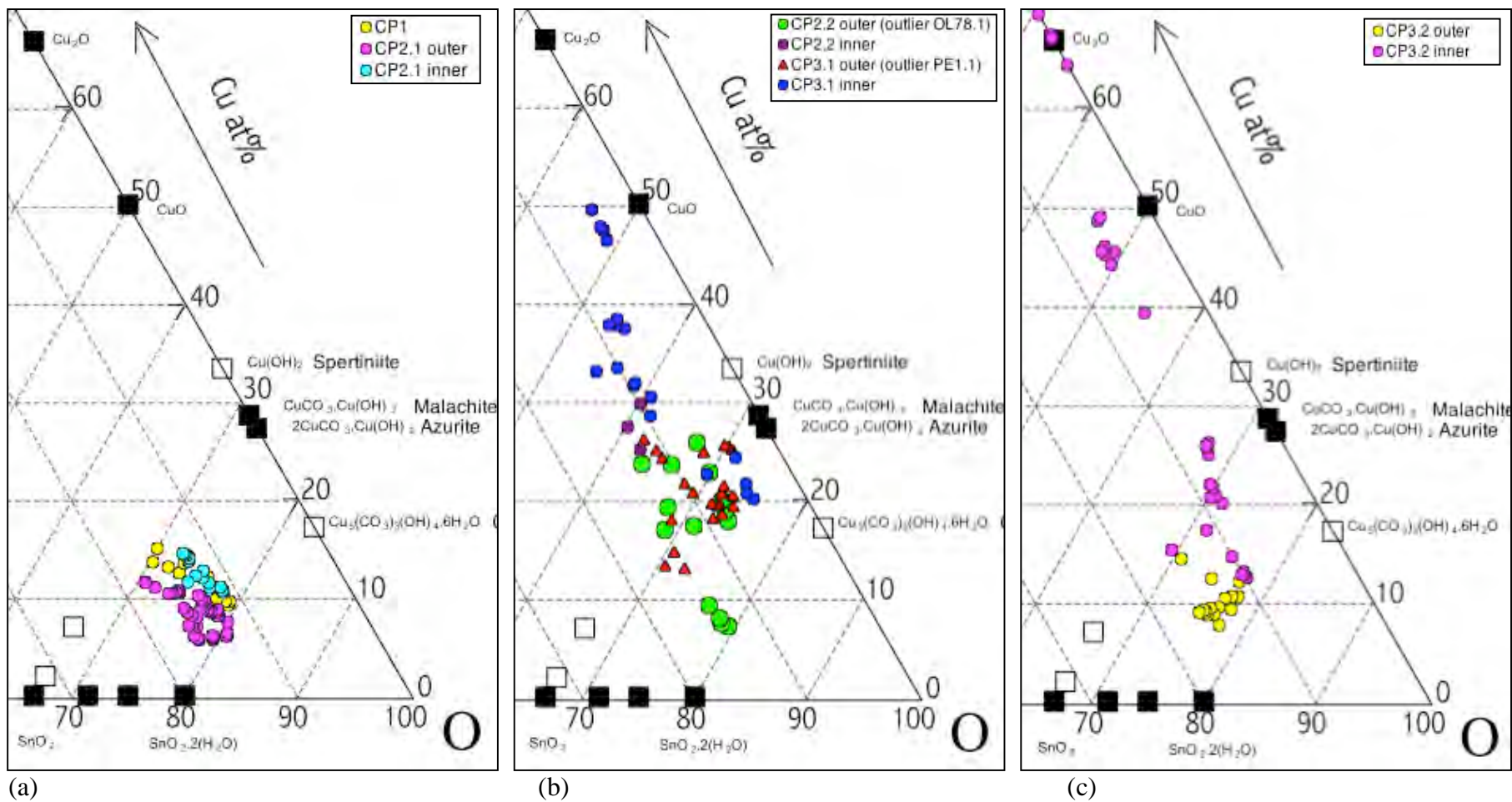


Figure 6.30: Detail of Cu-Sn-O at% ternary plots showing analysis data from the inner and outer corrosion zones of samples with different physical microstructures. (a) Corrosion profiles CP1 and CP2.1. (b) Corrosion profiles CP2.2 and CP3.1. (c) Corrosion profile CP3.2.

Sn/Cu at%	Sn/Cu at%	TSE/Sn at%	TSE/Cu at%	O/Sn wt%	Analyses code	Corrosion zone	fCu	TSE at%	Si at%	Cr at%	Cor. Profile			
>1.2	Sn>Cu	Sn>TSE	TSE>Cu	Sn>O	OL49.1_LO	Outer	0.96	7.2	4.7	1.0	2.1			
					OL5.1_LO	Outer	0.96	10.0	5.4	0.2	2.1			
					OL71.1_LO	Outer	0.97	8.2	5.4	1.1	2.1			
					OL75.2_LO	Outer	0.97	7.1	4.6	1.0	2.1			
					OL78.1_L2O	Outer	0.95	7.5	3.1	0.8	2.2			
					OL79.1_LO	Outer	0.96	9.9	4.8	0.5	2.1			
					OL9.2_LO	Outer	0.98	8.6	5.4	0.6	2.1			
					OL57.2_LO	Outer	0.96	10.6	4.9	0.4	2.1			
					Cu>TSE	Sn>O	OL21.1_LO	Outer	0.96	6.8	5.1	0.0	3.2	
					OL44.1_LO		Outer	0.97	6.2	4.0	0.3	3.2		
					OL46.1_LO		Outer	0.97	7.7	3.9	0.3	2.1		
					OL73.1_LO		Outer	0.96	6.4	4.6	0.6	2.1		
OL74.1_LO	Outer	0.95	6.5	4.7	0.3		2.1							
0.7-1.2	Sn>Cu	Sn>TSE	Cu>TSE	Sn>O	OL41.1_LO	Outer	0.94	5.9	3.0	0.0	3.2			
					OL53.1_LO	Outer	0.95	8.5	4.4	0.5	3.2			
					TSE>Sn	TSE>Cu	Sn>O	OL31.1_LO	Outer	0.95	12.7	2.2	0.0	1
	Cu>Sn	Sn>TSE	Cu>TSE	Sn>O	OL13.1_LO	Outermost	0.93	5.6	3.0	0.0	2.1			
					OL27.1_LO	Outer	0.92	5.3	2.2	0.1	1			
					PE1.1_LO	Outer	0.94	1.9	1.0	0.0	3.1			
<0.7	Cu>Sn	Sn>TSE	Cu>TSE	Sn>O	OL4.2_LO	Outer	0.88	3.9	2.1	0.0	2.2			
					OL70.1_LO	Outermost	0.82	5.4	2.7	0.1	2.2			
					PR4.1_LO	Outer	0.88	5.5	1.5	0.0	3.1			
					O>Sn	AP4.2_LO	Outer	0.83	1.8	0.8	0.0	3.1		
					OL50.1_LO	Outer	0.85	4.8	2.9	0.0	2.2			
					OL58.1_LO	Outer	0.81	2.6	0.5	0.0	3.1			
				TSE>Sn	Cu>TSE	O>Sn	OL66.1_LO	Outer	0.82	4.3	1.8	0.0	2.2	
							PR1.1_LO	Outer	0.91	6.3	1.5	0.0	3.1	
							AP5.1_LO	Outer	0.93	10.7	0.8	0.0	3.1	
							Zone B	Sn>Cu	Sn>TSE	Cu>TSE	Sn>O	OL5.1_LI	Inner	0.94
OL71.1_LI	Inner	0.94	5.5	4.0	0.5	2.1								
Cu>Sn	Sn>TSE	Cu>TSE	Sn>O	OL57.2_LI	Inner	0.93	8.1					3.5	0.5	2.1
O>Sn				OL21.1_LI	Inner	0.92	5.6					4.2	0.0	3.2
				OL46.1_LI	Inner	0.93	6.6					3.4	0.2	2.1
Zone C	Cu>Sn	Sn>TSE	Cu>TSE	Sn>O	OL13.1_Lid	Inner root_	0.84	5.7	3.0	0.1	2.1			
					OL50.1_LI	Inner	0.86	6.7	3.7	0.3	2.2			
					OL53.1_LI	Inner	0.91	4.9	1.9	0.0	3.2			
					PE1.1_LI	Inner	0.72	2.4	1.2	0.0	3.1			
					PR1.1_LI	Inner	0.87	7.6	1.5	0.0	3.1			
					O>Sn	AP4.2_LI	Inner	0.70	2.6	0.4	0.0	3.1		
						OL13.1_LR	Inner root_	0.86	4.7	2.9	0.0	2.1		
						OL41.1_LI	Inner	0.84	3.7	2.1	0.0	3.2		
				OL44.1_LI		Inner	0.53	1.6	0.9	0.0	3.2			
				TSE>Sn	Cu>TSE	O>Sn	OL69.1_LI	Inner orange	0.60	2.1	0.8	0.0	3.2	
OL69.1_LI1	Inner green	0.80	2.2				1.1	0.0	3.2					
					AP5.1_LI	Inner	0.87	8.3	0.7	0.0	3.1			

Table 6.9: Pivot table showing analysis from the outer and inner corrosion zones in corrosion profiles grouped by Sn/Cu ratio. Highlighted are $f_{Cu} < 0.94$, $TSE < 6at\%$, $Si < 3at\%$ and $Cr > 0.1 at\%$. The majority of analysis from samples with Corrosion Profile 2.1 have high Sn/Cu, f_{Cu} , Cr and Si content.

Pivot table Table 6.9 shows that analyses with high Sn/Cu ratio have the highest f_{Cu} values and TSE concentrations. Samples in CP2.1 and CP3.2 are those exhibiting the highest f_{Cu} values (>0.94) and apart from samples PE1.1 and OL41.1 they all have Cr content higher than 0.1at%. The amount of TSE generally increases with increasing Sn in the patina, its Sn/Cu ratio and f_{Cu} . Exception to this general trend is PE1.1, which shows high Sn/Cu ratio and high f_{Cu} but has relatively small amount of soil elements including Si. BFPM colour observations

of the outer part of the patina in cross sections indicate that the dark green or black patinas have increased TSE and Cr and this may contribute to their dark colour. Patina profiles with low TSE content also have absence of Cr and appear lighter in colour (blue or green). PE1.1, which is the only sample with the least TSE and high f_{Cu} has a silver/grey surface.

6.4.2.3. Relationships between corrosion profiles and corrosion deposit

Analysis of the EDX results based on the physicochemical characteristics of the corrosion profile and macroscopic surface observations show that a correlation exists between the nature of the profiles and coverage from azurite or malachite deposits (Table 6.10, Table 6.11). When azurite is the dominant deposit (Group B and C), fibrous features dominate their corrosion profile (CP2), and for malachite (Group D and E) an inner cuprite red orange/yellow zone is predominant (CP3). The colour of the patina is black or dark green/blue (CP2) and increasingly red/brown or red with increasing amount of malachite deposits (CP3). As malachite tends to cover the surface more extensively, polishing marks are observed mainly on samples associated with azurite (Group B and C). CP3.1 in Group E exhibits the least fine patinas, which in cross sections are uneven and have a low Sn content ($Sn/Cu < 0.7$). Samples in Group D exhibit fine brown patinas and have a CP3.2 microstructure which is characterised by an inner layer of cuprite and higher Sn content in their outer corrosion zone. This inner layer offers the brown/red patina colour in macroscopic surface observations. Half of the samples in Group C are covered by extensive corrosion deposits and exhibit a CP2.2 microstructure with a lower Sn content ($Sn/Cu < 0.7$), whereas the other half exhibit a fibrous microstructure CP2.1 with high Sn content ($Sn/Cu > 1.2$) at the outer corrosion zone. All samples in Group B where azurite is the dominant corrosion deposit have a CP2.1 fibrous microstructure and high Sn content ($Sn/Cu > 1.2$). This group also has the highest Cr and Si content which may be significant for the colour of the patina or corrosion mechanisms. Since azurite and malachite can develop in different burial environments, corrosion profiles can be the outcome of different corrosion mechanisms. Results are summarised in Table 6.12.

Deposit	Cor. Profile	Composition in outer zone	Sn/Cu ratio
Azurite	CP2.1	Sn>TSE>Cu at% and Sn>O wt%	>1.2
Azurite/Malachite	CP2.2	Cu>Sn>TSE at% and O>Sn wt%	<0.7
Malachite	CP3.1	Cu>Sn>TSE at% and O>Sn wt%	<0.7
Malachite/Azurite	CP3.2	Sn>Cu>TSE at% and Sn>O wt%	0.7-1.2, or >1.2

Table 6.10: Summary of observations with regards to predominant deposit, physical nature of corrosion profiles and chemical composition in the outer corrosion zone.

Predominant deposit (macro)	Appearance Group	Corrosion Profile	Sn/Cu at%	Analyses code	Sn>Cu at%	TSE>Sn at%	TSE>Cu at%	O>Sn wt%
Malachite - pustules	Group A	1	>1.2	OL31.1_LO	TSE>Sn	Sn>Cu	TSE>Cu	Sn>O
			0.7-1.2	OL27.1_LO	Sn>TSE	Cu>Sn	Cu>TSE	Sn>O
Azurite	Group B	2.1	>1.2	OL5.1_LO	Sn>TSE	Sn>Cu	TSE>Cu	Sn>O
			>1.2	OL46.1_LO	Sn>TSE	Sn>Cu	Cu>TSE	Sn>O
			>1.2	OL74.1_LO	Sn>TSE	Sn>Cu	Cu>TSE	Sn>O
			>1.2	OL75.2_LO	Sn>TSE	Sn>Cu	TSE>Cu	Sn>O
		>1.2	OL79.1_LO	Sn>TSE	Sn>Cu	TSE>Cu	Sn>O	
Azurite / Malachite	Group C	2.1	0.7-1.2	PE1.1_LO	Sn>TSE	Cu>Sn	Cu>TSE	Sn>O
			>1.2	OL49.1_LO	Sn>TSE	Sn>Cu	TSE>Cu	Sn>O
			>1.2	OL71.1_LO	Sn>TSE	Sn>Cu	TSE>Cu	Sn>O
			>1.2	OL73.1_LO	Sn>TSE	Sn>Cu	Cu>TSE	Sn>O
			>1.2	OL9.2_LO	Sn>TSE	Sn>Cu	TSE>Cu	Sn>O
		>1.2	OL57.2_LO	Sn>TSE	Sn>Cu	TSE>Cu	Sn>O	
		2.2	>1.2	OL78.1_L2O	Sn>TSE	Sn>Cu	TSE>Cu	Sn>O
			<0.7	OL4.2_LO	Sn>TSE	Cu>Sn	Cu>TSE	Sn>O
			<0.7	OL50.1_LO	Sn>TSE	Cu>Sn	Cu>TSE	O>Sn
			<0.7	OL66.1_LO	Sn>TSE	Cu>Sn	Cu>TSE	O>Sn
<0.7	OL70.1_LO		Sn>TSE	Cu>Sn	Cu>TSE	Sn>O		
Malachite / Azurite	Group D	3.1	<0.7	OL58.1_LO	Sn>TSE	Cu>Sn	Cu>TSE	O>Sn
			>1.2	OL21.1_LO	Sn>TSE	Sn>Cu	Cu>TSE	Sn>O
		3.2	>1.2	OL44.1_LO	Sn>TSE	Sn>Cu	Cu>TSE	Sn>O
			0.7-1.2	OL41.1_LO	Sn>TSE	Sn>Cu	Cu>TSE	Sn>O
Malachite	Group E	3.1	<0.7	AP4.2_LO	Sn>TSE	Cu>Sn	Cu>TSE	O>Sn
				AP5.1_LO	TSE>Sn	Cu>Sn	Cu>TSE	O>Sn
				PR1.1_LO	Sn>TSE	Cu>Sn	Cu>TSE	O>Sn
				PR4.1_LO	Sn>TSE	Cu>Sn	Cu>TSE	Sn>O

Table 6.11: Pivot table showing analysis results from the outer corrosion zone (outer helmet side only) with corresponding chemical and physical corrosion profile (CP1 to CP3.2) and appearance group assigned based on macroscopic observation of the predominance of malachite or azurite.

6.4.2.4. The f_{Cu}

Results show that burial environments favouring either azurite or malachite formation can produce high tin content corrosion layers that preserve a fine marker of original surface (CP 2.1 and 3.2). Robbiola's work suggests that the relative amount of Sn in the corrosion patina is a function of the Sn content in the bronze alloy expressed as the f_{Cu} factor (Robbiola *et al.*, 1998a). The calculated f_{Cu} values from the outer corrosion zone of cross-sections increases with increasing Sn content in the patina and in the alloy. To support this, AP5.1, AP4.2 and PR1.1 (CP3.1) have low Sn and f_{Cu} in the outer corrosion zone and low Sn content in the alloy (below 5at%). Despite broad agreement with Robbiola, some anomalies exist. OL50.1, OL58.1, OL66.1 (CP2.2) show lower than anticipated Sn/Cu and f_{Cu} for their original Sn content as a guide (Figure 6.31). They all exhibit elevated TSE/O at% content and have thick corrosion deposits. It may be possible that burial environment could influence the relative Sn concentration by corrosion of the patina itself. Nevertheless, burial conditions that favoured formation of azurite and a CP2.1 fibrous corrosion profile have fine patinas with higher Sn content and f_{Cu} .

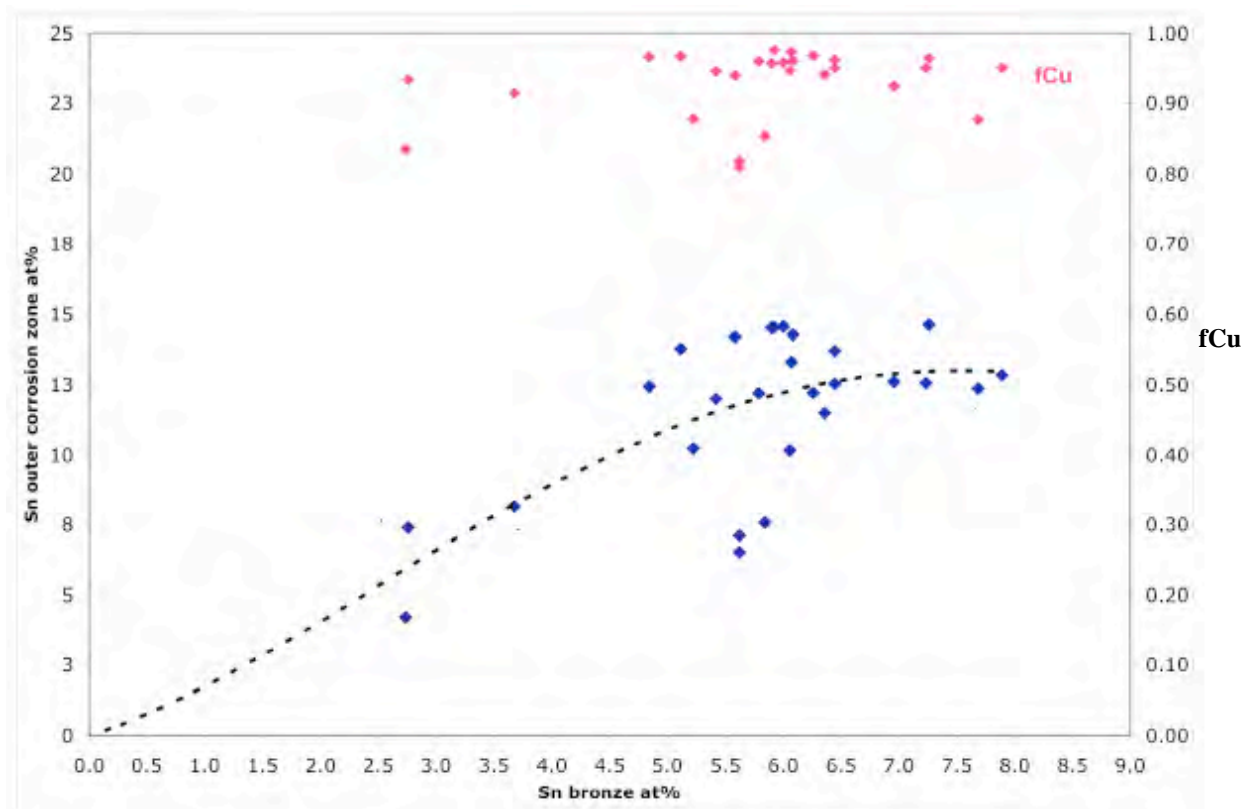


Figure 6.31: Scatter plot of Sn at% in the bronze alloy substrate and Sn at% in the outer corrosion layer in cross sections. The corresponding f_{Cu} is included for reference. Calculations based bronze composition data in Table 5.5, corrosion profiles in Table 6.6 and $f_{Cu} = 1 - [(Cu_{patina}/Sn_{patina}) / (Cu_{bronze}/Sn_{bronze})]$.

Appearance Group	Predominant deposit (macro)	Corrosion Profile	Sn/Cu at% ratio	fCu	TSE at%	Si at%	Cr at%	Polishing marks	Patina colour (macro)	Colour of analysed layer	Analyses code		
Group A	Malachite - pustules	1	0.7-1.2	0.92	5.3	2.2	0.1	Yes	Grey	Black	OL27.1_LO		
				0.95	12.7	2.2	0.0	Scratches	Black	Black	OL31.1_LO		
		2.1	>1.2	0.96	10.0	5.4	0.2	Yes	Black/grey	Black	OL5.1_LO		
Group B	Azurite	2.1	>1.2	0.95	6.5	4.7	0.3	Yes	Black	Green/Blue	OL74.1_LO		
				0.96	9.9	4.8	0.5	Yes	Black	Black	OL79.1_LO		
				0.97	7.7	3.9	0.3	Yes	Soiled	Green/Blue	OL46.1_LO		
				0.97	7.1	4.6	1.0	Yes	Black	Dark Green	OL75.2_LO		
		3.1	0.7-1.2	0.94	1.9	1.0	0.0	Yes	Grey	Green	PE1.1_LO		
Group C	Azurite / Malachite	2.1	>1.2	0.96	6.4	4.6	0.6	Yes	Black/grey	Green/Blue	OL73.1_LO		
				0.96	10.6	4.9	0.4	Obscured	Brown	Dark Green	OL57.2_LO		
				0.96	7.2	4.7	1.0	Damaged	Brown	Dark Green	OL49.1_LO		
				0.97	8.2	5.4	1.1	Damaged	Brown	Dark Green	OL71.1_LO		
				0.98	8.6	5.4	0.6	Damaged	Green	Dark Green	OL9.2_LO		
		2.2	>1.2	0.95	7.5	3.1	0.8	Yes	Black	Black	OL78.1_L2O		
					<0.7	0.82	4.3	1.8	0.0	Obscured	Blue	Green/Blue	OL66.1_LO
						0.85	4.8	2.9	0.0	Obscured	Brown	Green/Blue	OL50.1_LO
						0.88	3.9	2.1	0.0	Obscured	Black	Green	OL4.2_LO
Group D	Malachite / Azurite	3.1	<0.7	0.81	2.6	0.5	0.0	Obscured	Green	Green/Blue	OL58.1_LO		
		3.2	>1.2	0.96	6.8	5.1	0.0	Damaged	Black/red	Green/Blue	OL21.1_LO		
				0.97	6.2	4.0	0.3	Obscured	Black/red	Green	OL44.1_LO		
		0.7-1.2		0.94	5.9	3.0	0.0	Damaged	Black/red	Green	OL41.1_LO		
				0.95	8.5	4.4	0.5	Obscured	Green/Red	Dark Green	OL53.1_LO		
Group E	Malachite	3.1	<0.7	0.83	1.8	0.8	0.0	Obscured	Black/red	Green	AP4.2_LO		
				0.88	5.5	1.5	0.0	Scratches	Green/Red	Green	PR4.1_LO		
				0.91	6.3	1.5	0.0	Obscured	Green/Red	Dark Green	PR1.1_LO		
				0.93	10.7	0.8	0.0	No	Black/red	Dark Green	AP5.1_LO		

Table 6.12: Summary of physical and key chemical characteristics of investigated samples and helmets. Highlighted are fCu>0.94, TSE>6at%, Si>3at% and Cr > 0.1 at%.

6.5. GENERAL DISCUSSION AND CONCLUSIONS

6.5.1. CORROSION PROFILES AND THE BURIAL ENVIRONMENT

The burial environments where the helmets were found are unknown. Data indicate that the corrosion profile of patinas is related the abundance of azurite or malachite deposited on their surface (Figure 6.33). Investigation showed that most helmets covered predominantly by azurite exhibit black or silver/grey patinas, while those covered by malachite have a red-cuprite or red/green patina. These differences are characteristic in cross-sections, which have: (a) fine black patinas with a fibrous microstructure associated with azurite (CP2.1); (b) even patinas with an inner cuprites/cuprite rich zone, which appear red/brown macroscopically (CP3.2); (c) uneven patinas, which are associated to extensive coverage from malachite and azurite (CP2.2, CP3.1). The corrosion profiles have broadly similar trends of Cu, O, Sn and TSE composition, with Cr and Si being characteristic to corrosion profile groups. Increased Cr and Si are associated with fine, fibrous dark patinas (CP2.1). A discussion on the role of Cr and Si in the development of fine smooth corrosion profiles (like CP2.1) is below (section 6.5.1.1). As malachite and azurite develop under different burial conditions, depending on the amount of dissolved CO₂, pH, temperature, dissolved ions and other factors (Figure 6.32), data indicate that corrosion profiles are a result of different mechanisms in the burial. These mechanisms and an attempt to explain the role of particular soil elements are discussed below according to characteristic corrosion profile, and are compared to corrosion models proposed by Robbiola.

In general, there is a tendency for Sn-bronzes with higher Sn content to have higher f_{Cu} and Sn/Cu in their outer patina. These results agree with Robbiola's work, which supports that the Sn/Cu content in the patina is a function of the Sn/Cu in the alloy. However, there were cases where α -bronzes with higher Sn content (Sn>10wt%) exhibited a low f_{Cu} and Sn/Cu in their patina. This could indicate that although there is a tendency for high Sn α -bronzes to develop an increased Sn patina relatively to α -bronzes with less Sn, this is not an absolute condition because unusually high or low TSE and O can affect the relative Sn/Cu concentration of the patinas (which in turn impacts the f_{Cu}). Overall, the f_{Cu} provides a viable indication of the relative Sn enrichment of patinas on low-tin bronzes, but this can be affected by unusual amounts of oxygen or TSE, which would have an impact on the Sn/Cu of the patina and therefore on the calculation of f_{Cu} equation.

Patinas with high Sn (and f_{Cu}) content at the outer side of the helmet preserve a fine marker of the original surface and polishing marks, observed in plan view. Helmets with predominantly

azurite deposits were covered less by corrosion deposits, which allowed better observation of polishing marks. These have previously been reported in the literature observed in Sn-rich patinas on α -bronzes (Robbiola et al, 1998) and low-tin bronzes with $\alpha+\delta$ cast microstructure (Robbiola *et al.*, 2001), which exhibit a Robbiola's Type I even corrosion surface.

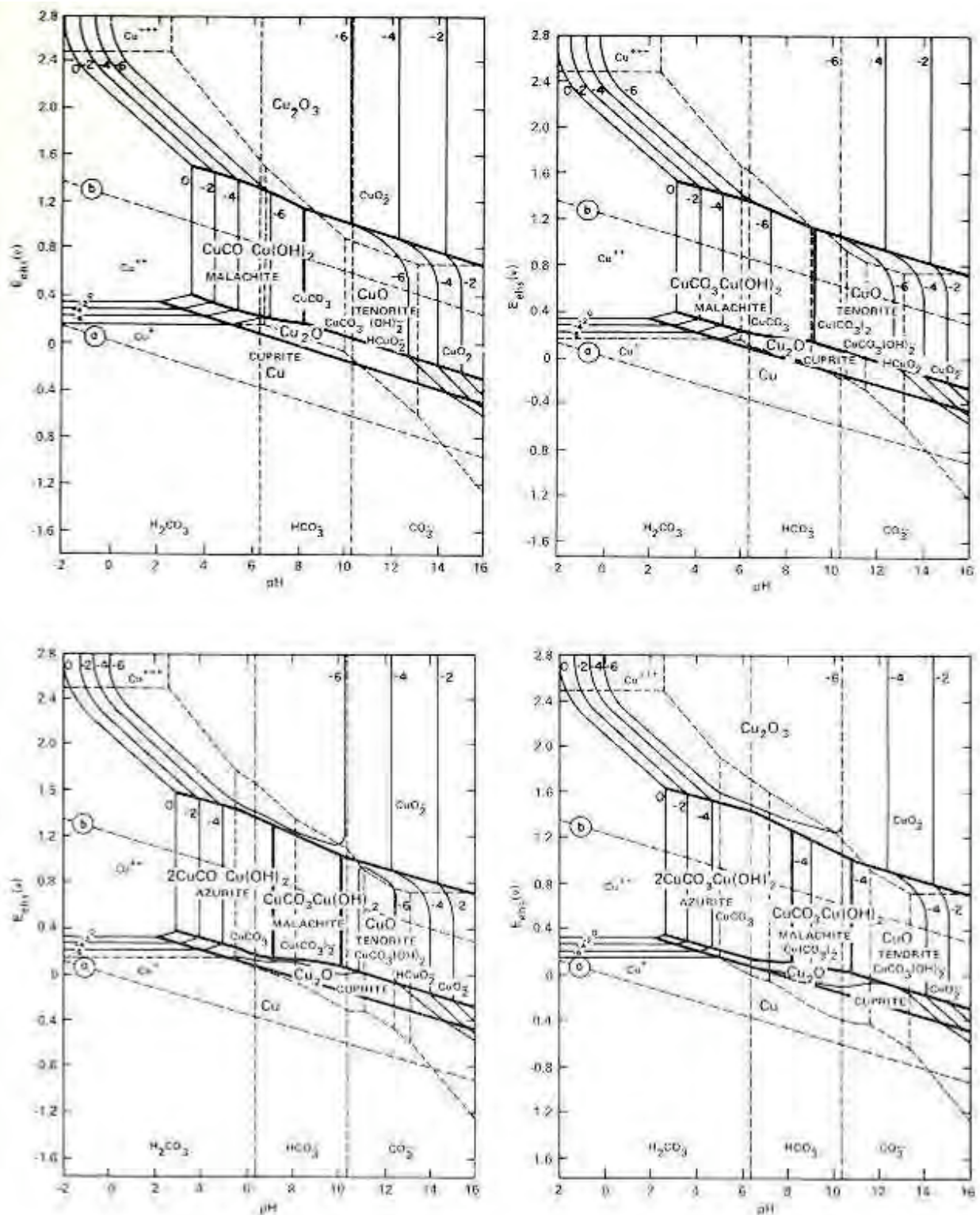


Figure 6.32: Equilibrium potential – pH diagrams for the Cu-CO₂-H₂O ternary system at 25°C. (a) 10⁻³ molal CO₂ total dissolved (44ppm). (b) 10⁻² molal CO₂ total dissolved (440 ppm). (c) 10⁻¹ molal CO₂ total dissolved (4400 ppm). (d) 1 molal CO₂ total dissolved (44,000 ppm) (Pourbaix, 1977).

Robbiola *et al.*, (1998a) characterised the corrosion structure of archaeological bronzes mainly based on the preservation of the marker of the original surface as, Type I for even or ‘noble’ corrosion surfaces that preserve original surface features and Type II which includes uneven or coarse or ‘vile’ patinas. There are several deviations from these proposed microstructural models described in Robbiola *et al.*, (1998a), but the outer part of the patina is Sn-rich in both types and have a high Sn/Cu ratio because of selective dissolution of copper, which is connected to internal oxidation of the bronze. The two types are a result of different corrosion mechanisms. According to this model, corrosion growth in Type I structures proceeds inward, with oxygen and hydroxyl anions migrating inwards and copper cations migrating outwards controlling the corrosion process (Figure 6.33). This protective tin-rich layer forms over a large range of applied anodic potential in open circuit conditions, and due to the fact that it grows into the alloy. Its formation is clearly related to a movement of oxygen anions through it, but further investigations are necessary to determine precisely if the process is under control of interfacial reactions or controlled by cationic (Cu cations) or anionic oxygen migration. In Type II structures, corrosion growth proceeds outwards, resulting in the loss of the marker of original surface; copper cations migrate from the bronze surface to the aqueous environment, whilst anions migrate inwards and control the corrosion mechanism (Robbiola *et al.*, 1998a; Piccardo *et al.*, 2007) (Figure 6.34).

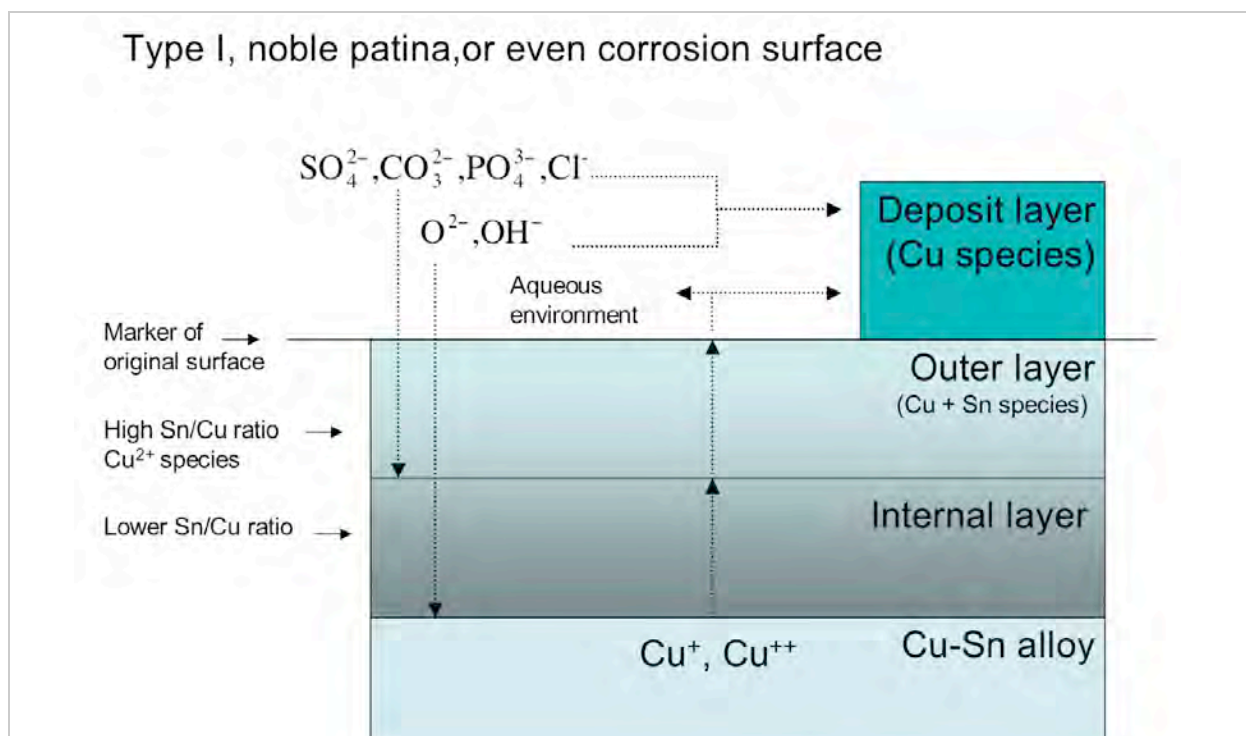


Figure 6.33: Schematic of Type I corrosion structure according to Robbiola’s corrosion model, which results in even or noble patinas that grow inwards and preserve the marker of the original surface. The outer part of the patina has a high Sn/Cu ratio, which is lower at the inner corrosion zone (Robbiola *et al.*, 1998a). Diagram redrawn from Piccardo *et al.*, (2007).

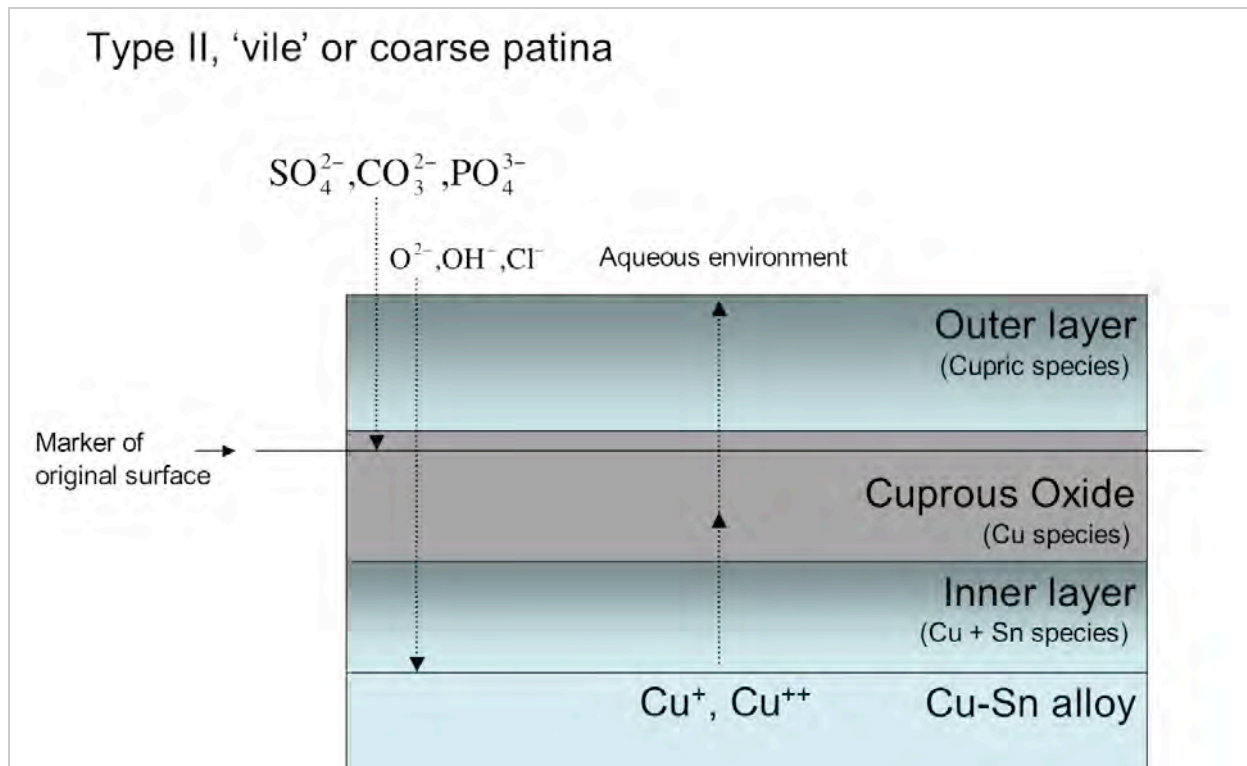


Figure 6.34: Schematic of Type II corrosion structure according to Robbiola's corrosion model, which results in 'vile' or coarse patinas that grow outwards and do not preserve the marker of the original surface. Characteristic to this corrosion type is the presence of an inner cuprite or cuprite-rich corrosion zone (Robbiola *et al.*, 1998a). Diagram redrawn from Piccardo *et al.*, (2007).

6.5.1.1. Fine black patinas associated with azurite deposits

Results are in broad agreement with corrosion models proposed by Robbiola and co-workers, especially in terms of preservation of the marker of the original surface. Samples predominantly covered by azurite exhibit a fine dark patina, which preserves the marker of the original surface and has characteristics similar to those seen in Type I structures (Figure 6.35). The majority of the samples in this group show characteristic fibrous microstructure and are free of an inner cuprite-rich zone. In one case (OL73.1) the individual fibres or 'filaments' are of different Cu-Sn-O content to the bulk of the patina and appear orange/yellow in BFPM gradually changing into the colour of the bulk patina (Figure 6.20). These filaments may act as channels (or paths) for the mass transport of migrating species. The orange/yellow areas of the filaments have a lower oxygen and increased copper concentration relative to the bulk of the patina, which agrees with previous findings that orange/yellow corrosion sites are a mixture of cuprite and hydrated SnO_2 oxides (Piccardo *et al.*, 2007).

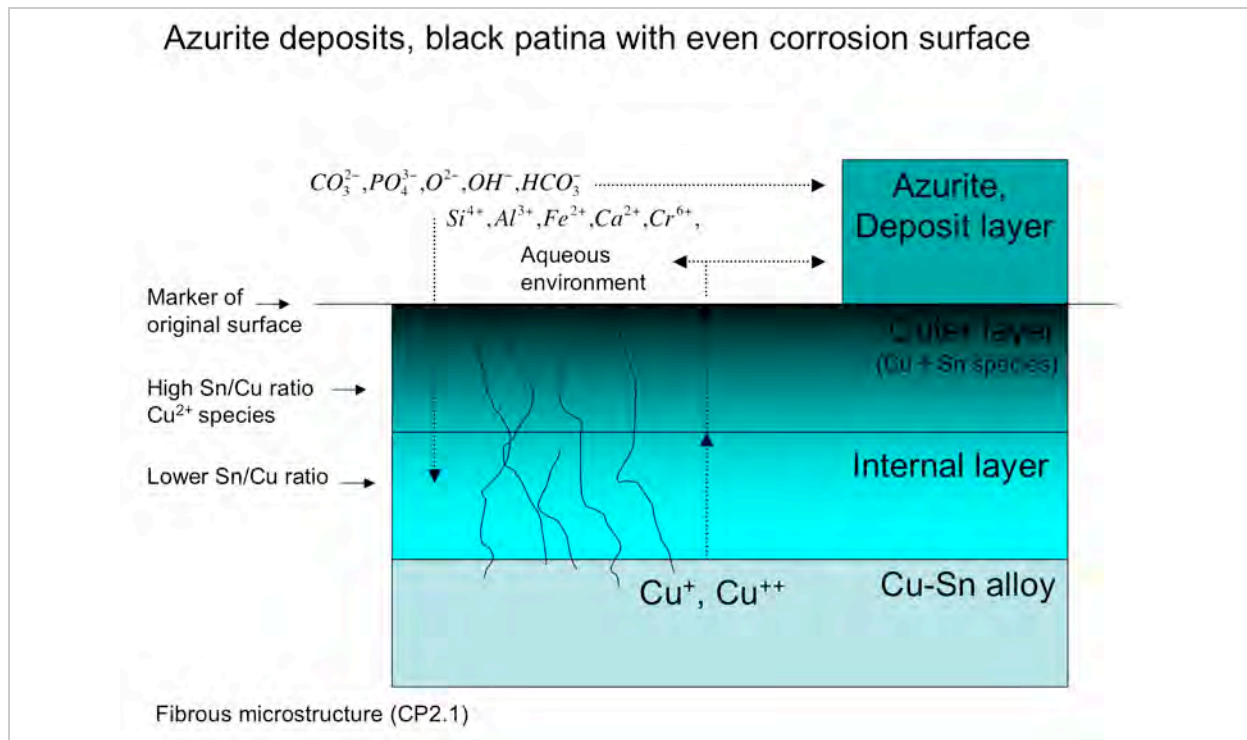


Figure 6.35: Schematic of corrosion profile CP2.1 which preserves a fine corrosion surface and the marker of the original surface. The surface is free of corrosion deposits or associated to the predominance of azurite deposits. The structure fits criteria of Robbiola's Type I corrosion structure. The outer part of the patina is rich in soil elements and has a higher Sn/Cu relatively to the inner corrosion zone.

Previous work on the electrochemical behaviour of synthetic low-tin bronzes has demonstrated the impact of the oxidation of Sn in the dissolution of copper and the formation of uniform patinas. Oxidation of Sn to Sn(II) oxide takes place early in corrosion at a lower potential than the oxidation of Cu (Sidot *et al.*, 2006; Satovic *et al.*, 2009). Sn oxidation is followed by the formation of a Cu(I) oxide rich phase and Cu(II) species; then Sn-enrichment occurs in the outer corrosion layer because of the dissolution and relative loss of copper compared to tin, which remains in the patina due to the low solubility and high stability of tin species (Robbiola *et al.*, 1998b; Satovic *et al.*, 2009). Analysis has shown that the outer part of the patina is composed of a mixture of Cu²⁺ compounds and sparingly crystalline SnO₂·2H₂O (Piccardo *et al.*, 2007). The low solubility of hydrated Sn compounds against a wide range of pH conditions, results in the formation of a physical and chemical barrier against the corrosive environment encouraging negligible rates of corrosion (Britton, 1952:11; Robbiola & Hurtel, 1997; Robbiola *et al.*, 1998a).

Uniform corrosion can occur in various conditions: when the metal surface is in direct contact with the environment and the anodic and cathodic reactions control kinetics; in stagnant liquids or soils with restricted oxygen flow or the solution has low conductivity; and when the conductive properties of a passive corrosion film control corrosion rate (Frankel and Cottis,

2010). Initially, metal ions released during oxidation either enter solution or remain on the surface without passing into solution to form a new solid phase. Once first corrosion layers (atomic scale) have been formed, oxide film growth occurs via transport of metal cations or oxide anions (or both) through the oxide layer until a steady state is reached (Burstein, 2010). The ionic and electronic properties of the corrosion film are important and with sufficient electronic conductivity corrosion itself can act as an electrode for electrochemical reactions (Payer *et al.*, 1995).

Formation of noble patinas is related to movement of oxygen anions through it (Robbiola *et al.*, 1998b). The point defect model for steady state growth of passive corrosion films (Macdonald and Urquidi - Macdonald, 1990) identifies that mobile metal cations lead to metal dissolution and mobile oxide anions lead to passivity via a logarithmic film growth (Burstein, 2010). During dry oxidation at high temperatures, it is well understood that oxide film growth occurs via ionic migration through the corrosion film which takes place due to migration of anionic or cationic vacancies or interstitially in the crystalline structure of an oxide (Pieraggi, 2010). Macdonald's experiments explain that migration of ions during aqueous corrosion occurs via the migration of anion and cation vacancies in the growing oxide crystal lattice in contact with a solution (Macdonald and Urquidi - Macdonald, 1990), assuming that the oxide film is crystalline but contains many crystal point defects. Where the concentration of point defects is large enough, the film may be regarded as amorphous (Lin *et al.*, 1981). In the case of inward corrosion growth, corrosion is controlled by the availability of anion vacancies in the corrosion film (Pieraggi, 2010). Inward film growth on a single metal is generally observed in p-type semiconductor oxide films, which are positive carriers and act as an acceptor to satisfy the vacancy defects in their structure (Pieraggi, 2010). Passivity requires the rapid formation of an oxide film at high potential, the slow dissolution of metal ions through the film, and a low ionic (not necessarily electron) conductivity within the oxide (Burstein, 2010).

These theories and experimental models can explain the formation of fine black patinas observed in samples exhibiting a CP2.1 corrosion profile, which are associated with azurite deposits. However, corrosion is affected by several factors including solution composition, water flow conditions, pH, potential, and temperature. Precise understanding of corrosion becomes more complicated when considering the role of the soil elements, which may be released in the solution. It was previously shown the majority of samples with fine black/dark patinas that grow inwards (CP2.1) are associated with azurite deposits, have high contents of Sn/Cu, O and soil elements (TSE) especially Si and Cr. The precise way in which ions from

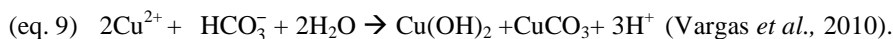
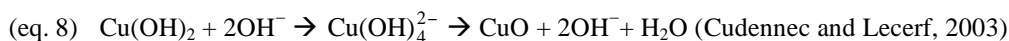
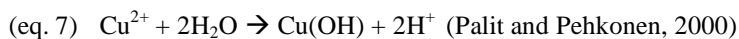
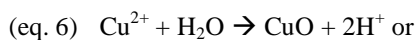
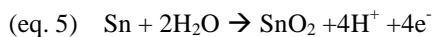
soil constituents migrate into the corrosion profile and their impact on enhancing stability on archaeological bronzes is not yet experimentally researched. Laboratory corrosion experiments using synthetic bronzes often use Na₂SO₄ solutions (Robbiola *et al.*, 1998b; Sidot *et al.*, 2006; Satovic *et al.*, 2009).

Chromate ions act as oxidising agents or a source of insoluble films by formation of Cr₂O₃ (Cr_{III}) or as spinel with the metal oxide of the substrate deposited onto the metal surface (Frankel and Cottis, 2010). A crystalline chromium based compound was not identified on the helmet samples by diffraction but analyses showed that measurable Cr concentrations appear in the corrosion profiles at advanced oxidation and Cu dissolution stage. Chromate compounds may be in an amorphous state or adsorbed by other compounds (Adriano, 2001:321). Research shows that chromates in the aqueous environment accelerate the cathodic reaction of several metals in acidic conditions (Frankel and Cottis, 2010) acting as a corrosion inhibitor if solid compounds are formed. Acceleration of the cathodic half reaction at an early point could have resulted in the faster anodic dissolution of Cu leaving in place a Sn-rich patina.

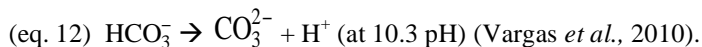
Cr_{III} compounds are highly insoluble but they can oxidize to highly soluble Cr_{VI} depending on surrounding ions (Reyes-Gutiérrez *et al.*, 2007) and the pH of the solution (Stepniewska *et al.*, 2001). Adsorption of Cr_{VI} in the form of CrO₄²⁻ increases in acidic conditions on compounds with exposed hydroxyl groups on their surfaces due to protonation of any hydroxyl compounds and because adsorption is favoured by positively charged surfaces at low to natural pH: mineral-OH + H⁺ + CrO₄²⁻ → mineral-OH₂⁺ - CrO₄²⁻ (Adriano, 2001: 322). There is plenty of opportunity for the chromate ion to be adsorbed into the corrosion patina in the burial environment during corrosion. The formation of a metastable Cu(OH)₂, the role of which is unclear for the CuO formation (eq. 5-8, next page) could offer opportunity for Cr adsorption onto OH⁻ already in the corrosion profile. Analysis showed that measurable Cr starts occurring in samples with Si content greater than about 3 at%. Silicon has high solubility in the aqueous environment and high affinity for oxygen in acidic pH. It is possible that at an early stage, Si⁴⁺ was adsorbed onto OH⁻ or O⁻ present in the patina, in turn facilitating adsorption of the chromate ion as a next step.

These reactions require acidic to neutral conditions. There are three main arguments to supporting a slightly acid burial for formation of fine black azurite associated patinas. First, the equilibrium Eh-pH diagram of the Cu-CO₂-H₂O system (Figure 6.37, b) shows that azurite

is stable at acidic to neutral pH. Second, formation of corrosion products releases hydrogen ions in the solution decreasing locally the pH (eq. 5-10) (Vargas *et al.*, 2010).



Third, the form of dissolved carbonate in a solution impacts the pH and the cathodic reaction (Vargas *et al.*, 2010). Dissolved carbonate must exist chiefly as H_2CO_3 in strong acid solutions, as HCO_3^- in some intermediate range (eq. 11) and as CO_3^{2-} in basic solutions (eq. 12) (Krauskopf and Bird, 1995: 37). Assuming that the system behaves as a closed system, the form in which carbonate is in water depends on pH.



Low pH favours the presence of H_2CO_3 , which continuously provides hydrogen ions in the water (Vargas *et al.*, 2010). Increased availability of hydrogen ions, due to the increased dissolved carbonate in acidic conditions enhances the uptake of oxygen and metal dissolution. This is because the system provides H^+ to assist the cathodic half reaction (Vargas *et al.*, 2009,2010). In turn, this induces a reduction in the amount of dissolved oxygen due to oxygen consumption by copper corrosion (Sobue *et al.*, 2003).

Based on this data it is possible that acceleration of the cathodic reaction due to the presence of chromate ions and/or the amount of dissolved carbonate in a mildly acidic aqueous environment, produced accelerated Cu dissolution at an early stage and the formation of a stable Sn-rich patina where soil elements were incorporated at different rates and stages. This hypothesis needs to be tested experimentally to determine its worth.

6.5.1.2. Fine red/brown patinas associated with malachite deposits

A fine corrosion surface (Type I) existed in corrosion profiles covered predominantly by malachite deposits with inner red cuprite or orange/yellow cuprite-rich corrosion interfacing the bronze (Figure 6.36). Macroscopically, the exposed patina when not covered by deposits

is red/brown in colour. This deviates from Robbiola's categorisation and lies somewhere between Type I and Type II structures: the cuprous layer which is present only in Type II structure, here is present in contact with the bronze and the sample exhibits a fine rather than coarse patina.

The surface is covered locally mainly by malachite corrosion deposits, and the underlying patina is red/brown in macroscopic observations. The outer part of the patina is rich in soil elements and has a high Sn/Cu. The inner corrosion zone is cuprite-rich (orange/yellow) and/or composed entirely of cuprite. Cuprite preserves slip lines as pseudomorphic metallurgical evidence of the bronze microstructure. This could fit Robbiola's Type II structure, due to the presence of an inner cuprite zone, but samples in this group show a fine corrosion surface.

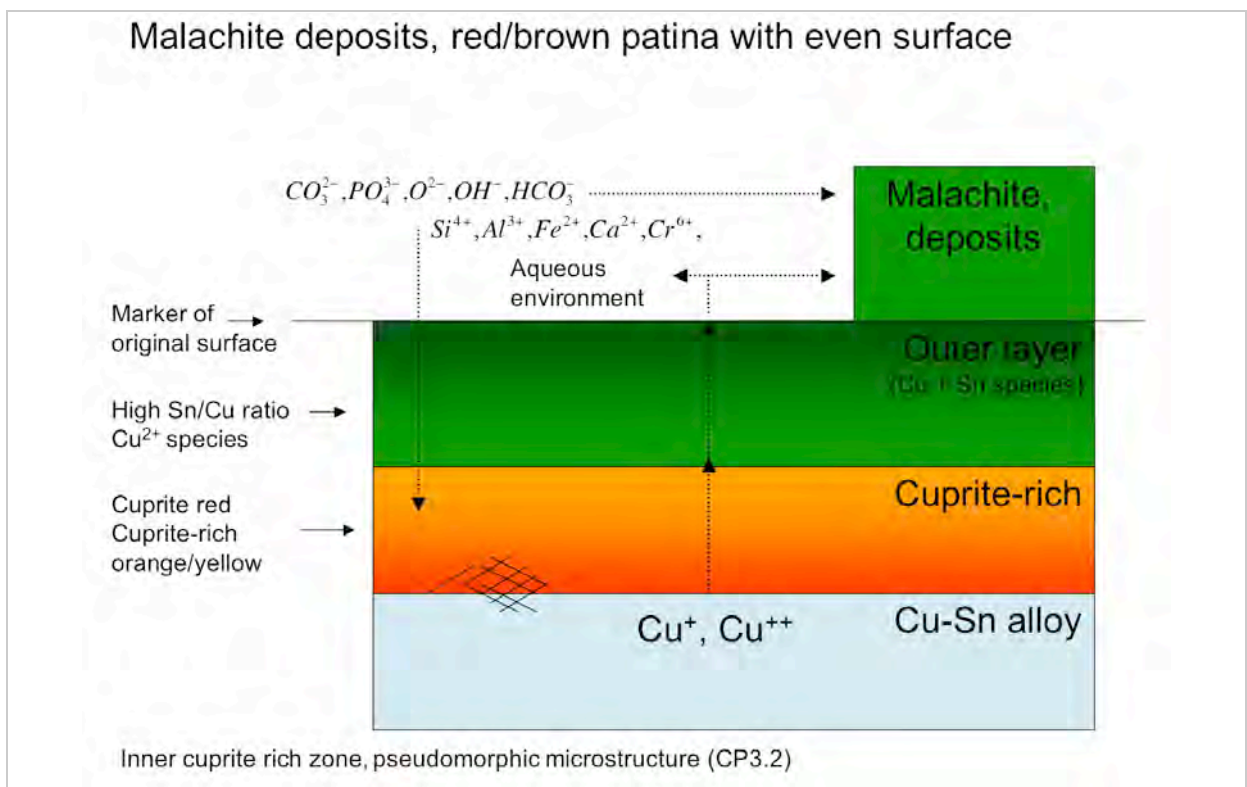


Figure 6.36: Schematic of corrosion profile CP3.2, which preserves a fine corrosion surface and the marker of the original surface.

As both this corrosion profile (CP3.2) and the black/azurite related fine patinas (CP2.1), can have a high Sn/Cu ratio and preserve the marker of the original surface, differences between them centre on the presence or absence of the inner cuprous layer and the predominance of azurite or malachite deposits. The equilibrium Eh/pH diagram of the Cu-CO₂-H₂O system (Figure 6.37, a) indicates that malachite is stable at low concentrations of dissolved carbonate in acidic to neutral pH. Copper carbonates have about 50-53 O at% in their structure whereas

cuprite only 33.3 O at%. By contrast, cuprite has 66.7 at% Cu and copper carbonates about 20 at% Cu. It is therefore logical to assume that formation of copper carbonates requires more oxidising conditions than that of cuprite. This is in agreement with the Eh/pH diagram, where in acidic to neutral conditions stability of cuprite occurs in a wider Eh range, which is in less oxidising conditions than that required for the formation of malachite. Thus, formation of an inner cuprite layer in conditions that favour malachite formation, could be explained based on the availability or supply of oxygen to the inner corrosion zone. In conditions that favour the formation of azurite the Eh range of cuprite stability is not as wide as in conditions that favour malachite, and azurite is stable down to less oxidising conditions than malachite (Figure 6.37,b, red line). This could explain the absence of an inner cuprite zone in conditions that favour azurite formation.

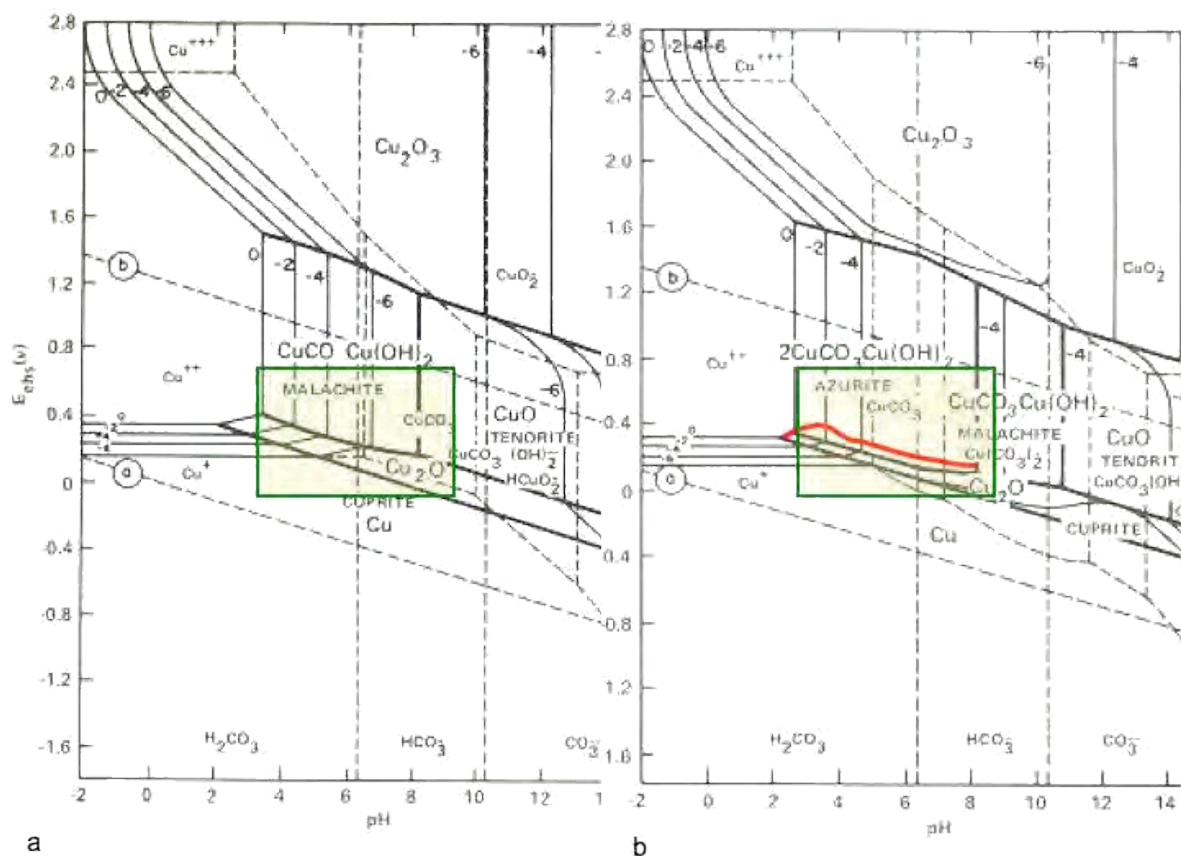


Figure 6.37: Equilibrium potential – pH diagrams for the Cu-CO₂-H₂O ternary system at 25°C. (a) 10⁻³ molal CO₂ total dissolved (44ppm). (b) 1 molal CO₂ total dissolved (44,000 ppm). (Adopted from Pourbaix, 1977).

It is possible that the fine Sn-rich outer corrosion layer had a reduced anionic conductivity, which restricted migration of OH⁻, O⁻ or HCO₃⁻ to the inner zone. This could explain the elevated copper content at the inner zone, showing less copper oxidation (and hence dissolution) has taken place here than in the outer zone. Whether cuprite forms from the

reaction of copper ions with metallic copper ($\text{Cu}^{2+} + \text{Cu}^0 + 2\text{OH}^- \rightarrow \text{Cu}_2\text{O} + \text{H}_2\text{O}$), or directly as $\text{Cu} + \text{H}_2\text{O} \rightarrow \text{Cu}_2\text{O} + \text{H}^+ + \text{e}^-$, or whether cuprite precipitates from an oversaturated solution is not clear (Merkel *et al.*, 2002) or forms via the transformation of other species ($2\text{CuO} + 2\text{H}^+ + 2\text{e}^- \rightarrow \text{Cu}_2\text{O} + \text{H}_2\text{O}$ or $2\text{Cu}(\text{OH})_2 + 2\text{H}^+ + 2\text{e}^- \rightarrow \text{Cu}_2\text{O} + 3\text{H}_2\text{O}$) (Kunze *et al.*, 2004) is not clear. This could depend on the local redox conditions and the ability of cuprite itself for mass transport (Payer *et al.*, 1995). BFPM of the cross sections shows that oxidation in this zone follows slip lines in the strained bronze crystals, which are the result of intense cold work during manufacture, and that the layer is a pseudomorph of the original microstructure. It is therefore more likely that the formation of cuprite in this case is the result of a direct reaction with metallic copper from the bronze rather than the result of precipitation from a supersaturated solution. Recent works have shown that the copper crystal orientation may impact the nature of the formed cuprite layer, which can have epitactic relationships to the underlying copper, maintaining defined crystallographic orientations (Kunze *et al.*, 2004). This indicates that both the environment and the crystal orientation in the bronze due to texture would have had an impact on the formation of stable epitactic cuprite inner layer.

EDX analysis showed that the red cuprite zone does not contain Sn, unlike the orange/yellow compounds, which contain Sn, Cu and O. These compounds were shown by Piccardo *et al.*, (2007) to be a mixture of cuprite and hydrated Sn oxides. This raises questions about the way in which the original Sn content from the bronze is removed from the cuprite zone during its formation. A hypothesis to explain this phenomenon is that local conditions favour the slow dissolution of Sn, which migrates out from this layer into the burial environment. Kinetics play a prominent role in epitaxial growth of oxide films (Markov, 1996). It may be that growth of the cuprite zone was very slow and the Eh/pH local conditions favoured slow dissolution of Sn and transport of Sn ions from the layer. Slower corrosion rates could be attributed to a reduced amount of dissolved carbonate in the solution producing consumption of dissolved oxygen at the early stages of corrosion in the closed system. This contributes to explaining restricted access to oxygen to the inner zone and the consequent formation of cuprite.

Migration of Sn and Cu species from the inner zone would depend on kinetic factors and the conductive properties of cuprite, which is pH dependant (Wang *et al.*, 2010). In basic and alkaline environments cuprite acts as an acceptor to satisfy the Cu vacancy defects in its structure (p-type semiconductor), but in very strong acids ($\text{pH} < 2$) it behaves as a donor due to formation of different types of vacancies in its structure (n-type semiconductor) and at about pH 4 it shows an amphoteric relationship (Wang *et al.*, 2010). Hence, the conductive

properties of the cuprite and kinetic factors would be important in the mass transport of Sn species from this zone. This theory could be tested by experiment.

6.5.1.3. Uneven or coarse patinas that grow outwards

Uneven corrosion surfaces are few and are observed on samples covered by extensive mixtures of either azurite and malachite (CP2.2) or malachite alone (CP3.1) (Figure 6.38). These corrosion profiles broadly fit the Type II structures described by Robbiola, but they do not exhibit a distinct inner cuprite and/or orange/yellow zone. Their corrosion profile is often non-uniform or banded (CP2.2). A thin or localised inner cuprite-rich area is observed at sections with malachite deposits and the inner helmet side of sample OL78.1. Corrosion growth of this structure is outwards, resulting in the partial or complete destruction of the marker of the original surface, depending on the sample area examined. Overall, at the outer helmet side, the marker of the original surface can still be broadly defined.

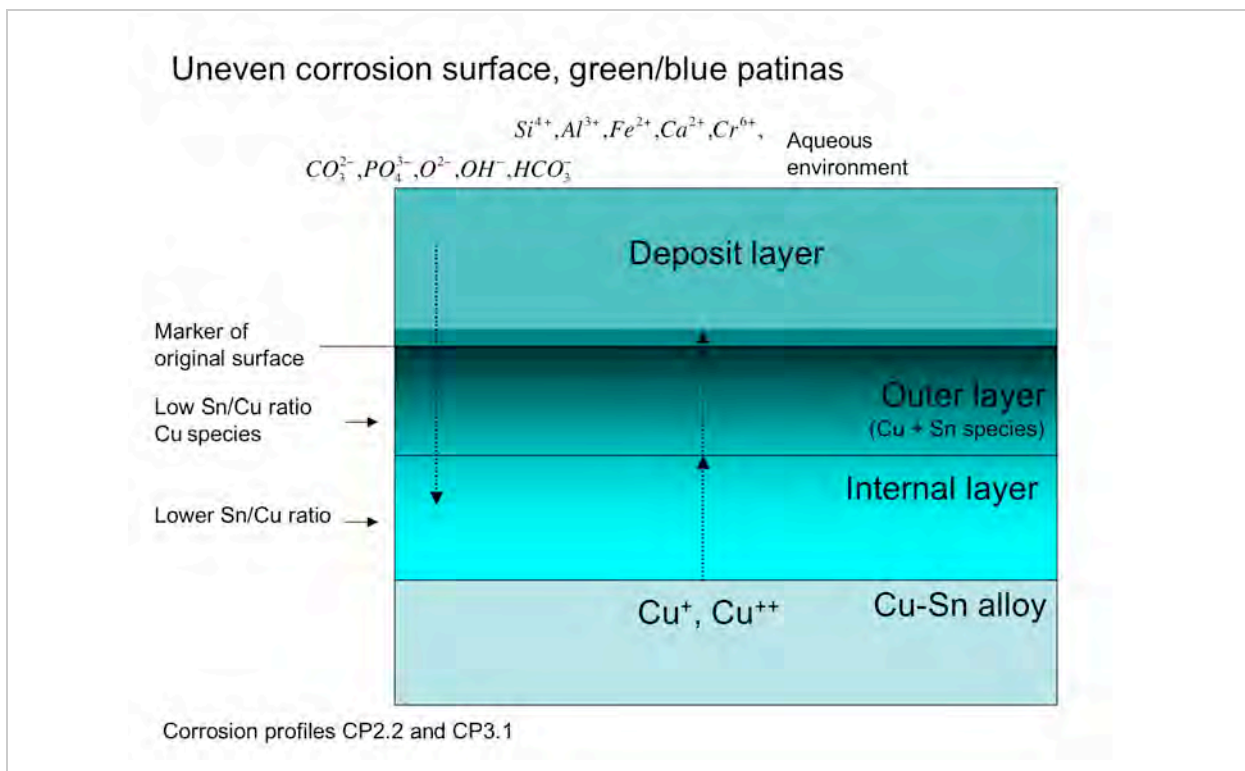


Figure 6.38: Schematic of corrosion profiles CP2.2 and CP3.1 which do not preserve a fine corrosion surface and the marker of the original surface is only broadly defined. The surface is covered extensively mainly by malachite and/or azurite corrosion deposits.

The outer corrosion layer of these profiles is Sn rich but to a lesser degree than the profiles discussed above, and this is reflected in lower Sn/Cu and f_{Cu} . In some cases, the low f_{Cu} is due to the low Sn content in the alloy (<5 at%) (CP3.1). The low Sn/Cu ratio and relatively high Cu content at the outer part of the corrosion surface, may be evidence that dissolution and oxidation is not as extensive as for fine black patinas. According to Robbiola *et al.*, (1998a),

copper cations migrate from the bronze surface to the aqueous environment, whilst anions migrate inwards and control the corrosion mechanism. Based on the point defect theory, outward film growth on a single metal is generally observed in negative carrier (n-type) semiconductor oxide films that act as donors (release e^-) (Pieraggi, 2010). Surface corrosion films in this case are formed cationically, and the growth is controlled by the mobility of metal cations (Pieraggi, 2010). This could be evidenced by the relatively low sum of soil elements incorporated in the corrosion profile, when compared to the fine black patinas.

It is unclear what produces such uneven corrosion surfaces. Their formation would be influenced by phenomena such as diffusion (movement under a concentration gradient), migration (movement under an electric field gradient) or convection (natural or forced solution flow) that take place in the burial conditions at the bronze/soil interface (Scott and John, 2010). It is possible that the extensive corrosion deposits also influence their formation, as copper carbonate deposits ‘act as sinks’ for dissolved Cu^{2+} (Merkel *et al.*, 2002). More work is necessary to understand details of the processes involved.

6.5.2. IDENTIFICATION OF TINNING BASED ON EDX DATA: A COMPARISON OF DATA FROM HELMET PATINAS AND ROMAN TINNED BRONZES

EDX analyses of thin intermetallic layers on corroded bronzes presents technical difficulties due to the impact of the surrounding copper corrosion. $\eta-Cu_6Sn_5$ was not present on the helmet samples, and detection of $\varepsilon-Cu_3Sn$ using imaging and diffraction methods was not successful. EDX data collected from $\eta-Cu_6Sn_5$ scallops cross-characterised by XRD found on Roman bronzes (Table 4.7) indicated that oxidation and Cu dissolution from this phase could have taken place during burial (Figure 4.35), because of the reduction in the Cu at% concentration relative to its increased O at% content. Identification of the $\varepsilon-Cu_3Sn$ by EDX was hampered by the thin flat nature of the phase and its scarce preservation on the worked areas of the Roman skilllets. The hypothesis that $\varepsilon-Cu_3Sn$ cannot be identified using compositional data developed in Chapter 4 was based on information from published numerical data but this can now be tested using the new data derived from the investigation of the corrosion layers on helmets.

The Cu-Sn-O at% ternary plot (Figure 6.39) shows all data collected from corrosion profiles of helmet samples, data collected from $\eta-Cu_6Sn_5$ scallops and other surface features on Roman bronzes, previously seen in Figure 4.35. Data collected from the $\eta-Cu_6Sn_5$ scallops have elevated Sn at% concentrations relative to data collected from the surface of helmet samples. Analyses from $\eta-Cu_6Sn_5$ scallops occupy a distinct region in the Cu-O-Sn at%

ternary plot (Figure 6.39, red line) with a tendency to cluster near the $\text{SnO}_2 \cdot 2\text{H}_2\text{O}$ region in the ternary plot. This indicates that the phase can corrode into the di-hydrated form of cassiterite. The small number of data from suspected $\epsilon\text{-Cu}_3\text{Sn}$ areas shows marginally a similar tendency (Figure 6.39, green line) occupying compositional ranges from metallic $\epsilon\text{-Cu}_3\text{Sn}$ to $\text{SnO}_2 \cdot 2\text{H}_2\text{O}$ but more data is required to verify that.

Analyses from helmet samples with a high Sn/Cu previously described as fine inward growing ‘noble’ patinas (section 6.5.1.1) cluster near the wider chemical region of $\text{SnO}_2 \cdot 2\text{H}_2\text{O}$ in the ternary plot, but do not reach the actual composition of $\text{SnO}_2 \cdot 2\text{H}_2\text{O}$ (Figure 6.39). The plot shows locations of SnO_2 and SnO_2 with 2 at% and 7 at% Cu (Figure 6.39, white rectangulars) as potential corrosion products, because literature suggests that Cu^{2+} ions can be substituted into the $\text{Sn}_{(\text{iv})}$ oxide lattice (Piccardo *et al.*, 2007, references therein). None of the analyses show a chemical composition near this composition.

Data from the outer part of uneven, outward growing coarse helmet patinas concentrate near the composition area of copper carbonates in the Cu-Sn-O at% plot. The data from the inner red-orange-yellow corrosion zones included in the plot is in agreement with analyses collected from the two samples published in Piccardo *et al.*, 2007 (fig. 14.12), related to the elevated Sn and O at% in the corrosion. As data cluster in distinct regions of the Cu-Sn-O at% ternary plot, it can be a useful tool for interpreting EDX data from objects with suspected tinning (Figure 6.40). The composition of noble patinas (e.g. CP2.1) is characteristic and different to that of uneven corrosion surfaces as seen above. This can be the first step to developing a discrimination ternary plot, similar to those used in earth sciences for the interpretation of geochemical data. Tinning is expected to result in $\eta\text{-Cu}_6\text{Sn}_5$ and this has a specific concentration on the Cu-Sn-O at% diagram. Corroded $\eta\text{-Cu}_6\text{Sn}_5$ may follow the concentration profile indicated by the analysis of the tinned Roman bronzes which follow a trend defined by the red line in Figure 6.40. More EDX data collected from intermetallics and especially from $\epsilon\text{-Cu}_3\text{Sn}$, would provide the firm boundaries for chemical regions within which this phase can exist on archaeological objects. This ‘discriminant’ ternary plot provides a significant aid for the characterisation of tinning and corrosion on archaeological low-tin bronzes.

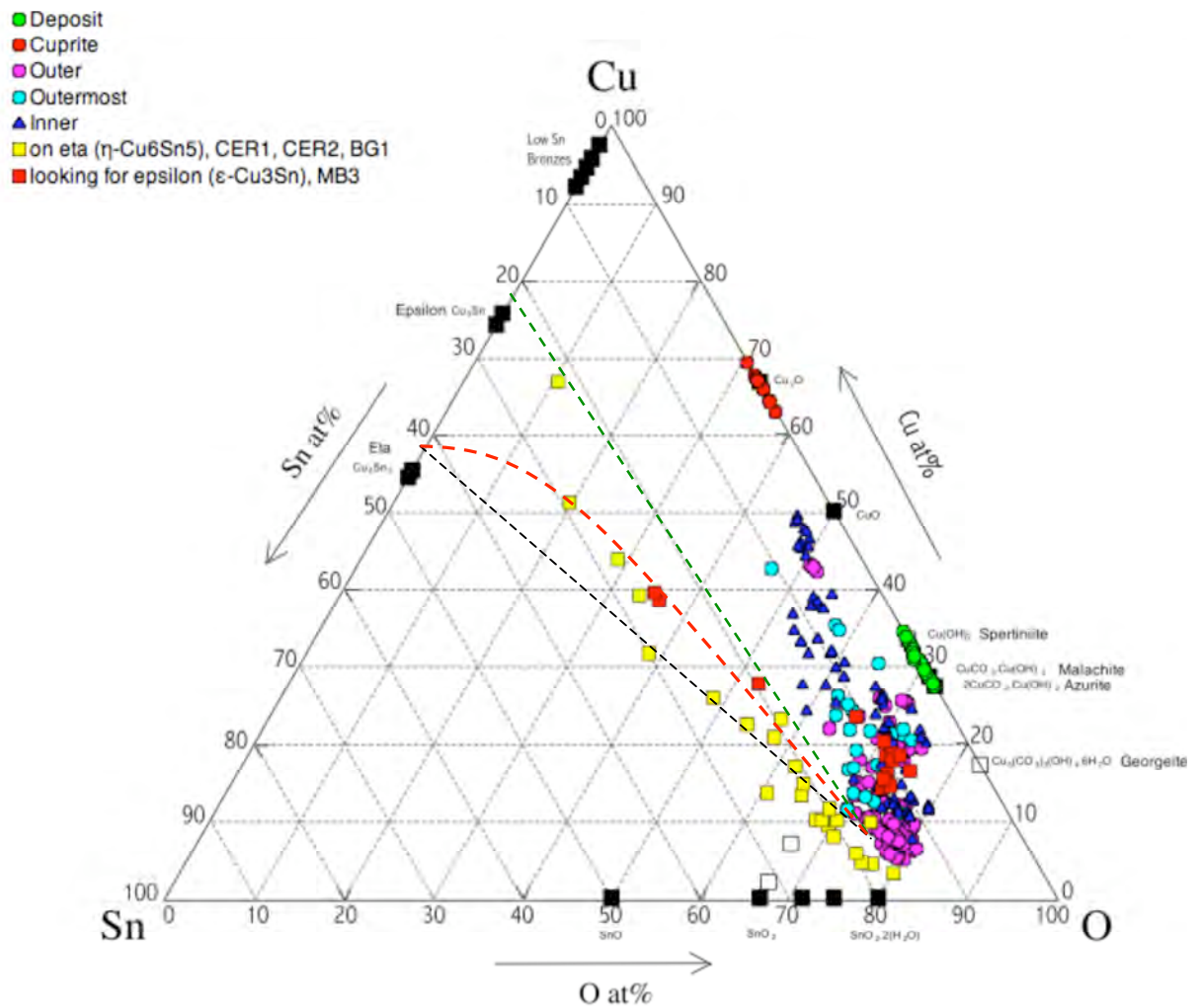


Figure 6.39: Cu-Sn-O at% ternary plot of EDX analyses data collected from corrosion profiles in helmet samples. The yellow data points are collected from η -Cu₆Sn₅ scallops and areas suspected to be ϵ -Cu₃Sn in sections of tinned Roman bronzes (section 4.4.3, Figure 4.35). The blue and green dotted lines denote trends for hypothetical changes in composition for the mineralization of η -Cu₆Sn₅ into SnO₂·2H₂O (Lower line blue) and ϵ -Cu₃Sn to SnO₂·2H₂O respectively.

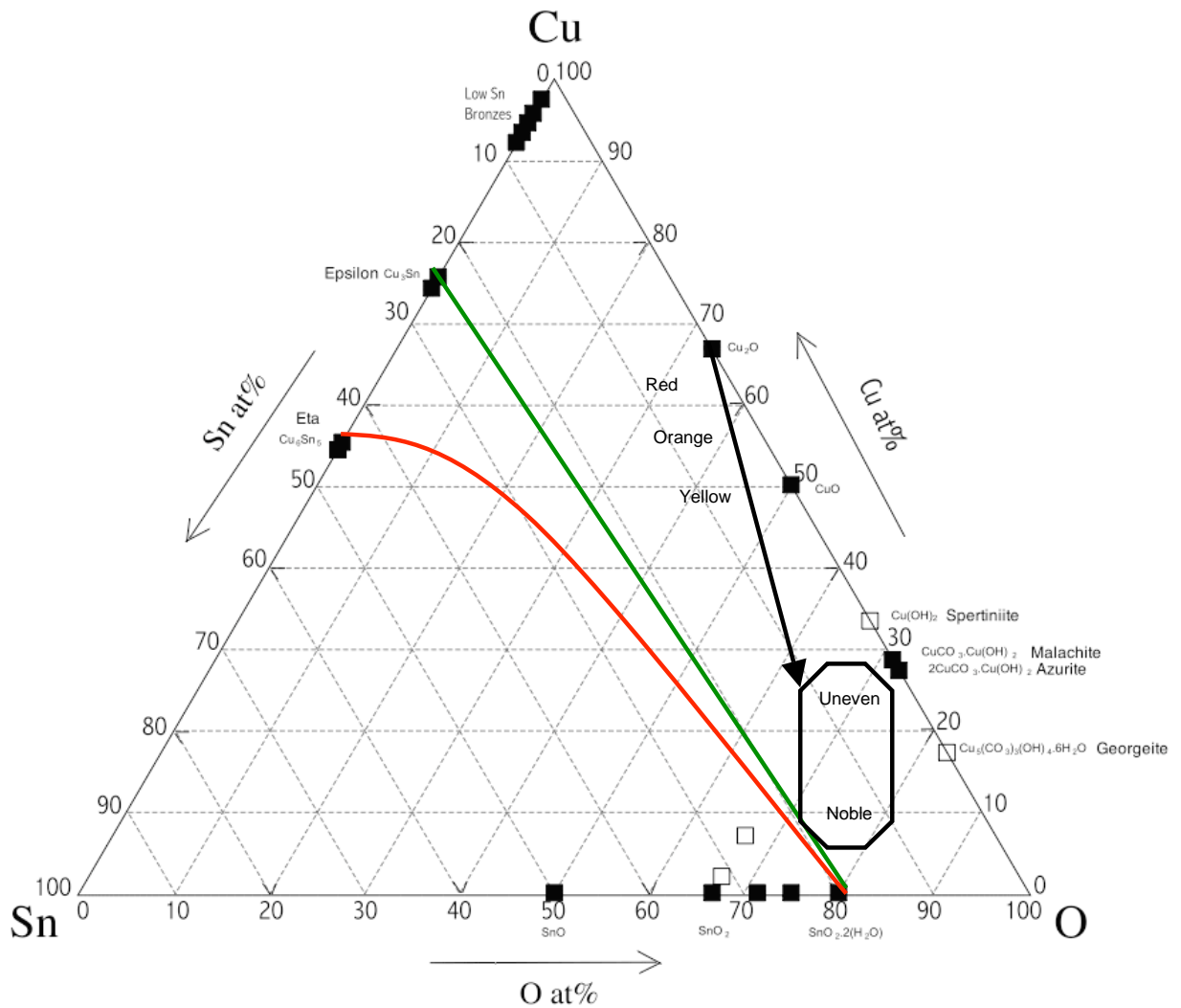


Figure 6.40: Cu-Sn-O ternary plot for EDX at% analyses with annotated characteristic compositional regions for the discrimination between intermetallics and high-Sn corrosion on low-tin archaeological bronzes. The graph notes compositional regions as indicated from analyses from η -Cu₆Sn₅ scallops (red line), ϵ -Cu₃Sn (green line), high-Sn fine ‘noble’ patinas, uneven patinas, and red-orange-yellow areas at the inner corrosion zone in corrosion profiles.

6.5.3. A NOTE ON METALLURGY AND ITS IMPACT ON CORROSION

Due to lack of data and the complexity of interactions between metallurgical structure, environment and mechanical stress it is difficult to know which of these variables has a significant impact on the corrosion behaviour of metals (Cottis, 2010; Macdonald and Engelhardt, 2010). Examples in the literature indicate that slight changes in composition and addition of particular elements to alloys, even at trace concentrations, can have a great impact on the corrosion resistance of an alloy. For example, even a small addition of As to a brass

alloy (c. 0.04%) will reduce the susceptibility to dezincification, as will additions of Sn, Sb and P (Frankel and Cottis, 2010). Data from this thesis for very low-tin bronzes ($\text{Sn} < 5\text{at}\%$) are in broad agreement with Robbiola's proposal that the Sn/Cu ratio in the patina is a function of Sn/Cu of the original bronze.

Hammering, grain size and residual strain can affect the degree of corrosion because they influence distribution and microsegregation of alloying metals and impurity elements. For example, in strain areas more compounds are precipitated (ASM, 1985: strain etching) and grain boundaries are in general susceptible to localised corrosion caused by anodic dissolution (Engelberg, 2010). These phenomena are clearly more enhanced in inhomogenous as-cast microstructures which may lead to more uneven surfaces or pitting. It is hypothesised that stresses and strain may lead to a higher degree of atomic disorder at grain boundaries increasing the driving force for anodic dissolution. Large regions with clusters of low energy boundaries such as twins can impede the growth of intergranular corrosion. Although stress and strain at grain boundaries likely play a secondary role for intergranular corrosion, they can be responsible for enhanced diffusion pathways (Engelberg, 2010).

Filaments observed in corrosion profile CP2.1, which includes several examples of intragranular corrosion at the patina/bronze interface, may be evidence for enhanced diffusion due to extensive cold working and hammering of the helmets. Preservation of slip lines in cases of an inner cuprite layer (CP3.2) offer clear evidence of extensive cold work. Oxidation appears to follow the pattern of slip lines that may offer pathways for diffusion. Crystallographic relationships are important, even if they may only influence the first nanometers of the oxide formation, because its nature in early stages of corrosion influence its semiconductor properties, which in turn influence diffusion of ionic species through the layer.

Another example of the possible impact of cold working on the helmets is the grain size. Cycles of cold hammering and annealing resulted in progressively smaller grain sizes through the chronological development of the Corinthian type helmet. Data indicates a broad correlation between the thickness of the patina and the thickness of the sample (Figure 6.41) or the grain size in the bronze (Figure 6.42). If sufficient further data is available, especially in relation to texture and crystal orientation of the underlying bronze it may be possible to better understand the precise nature of the complex corrosion mechanisms of low-tin bronzes that take place in the burial.

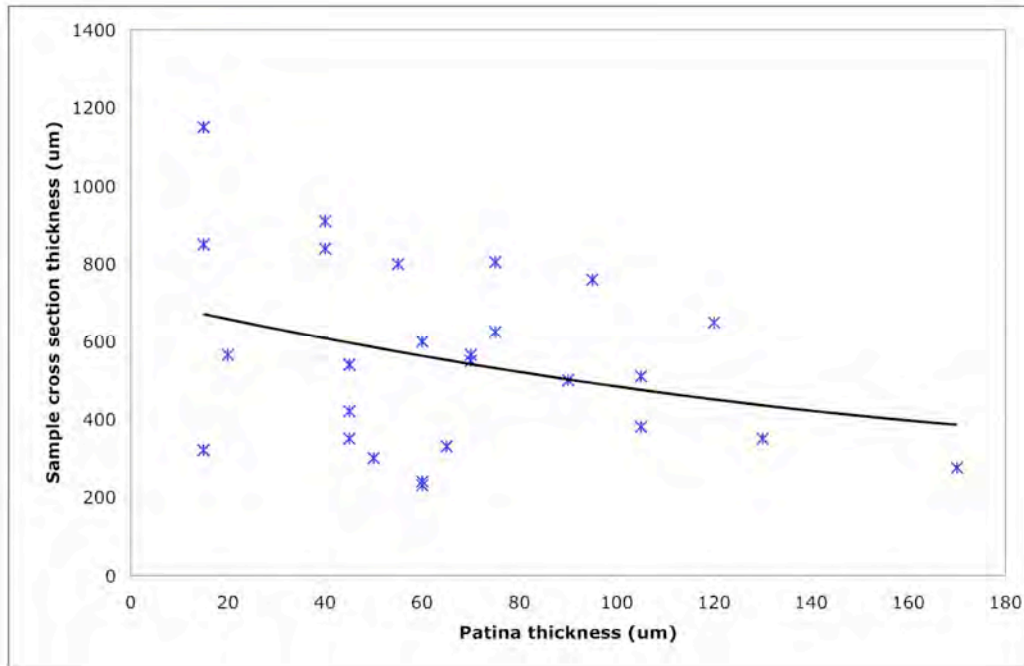


Figure 6.41: Scatter plot showing relationship of the thickness of the cross section (includes patina) and the thickness of the patina (μm).

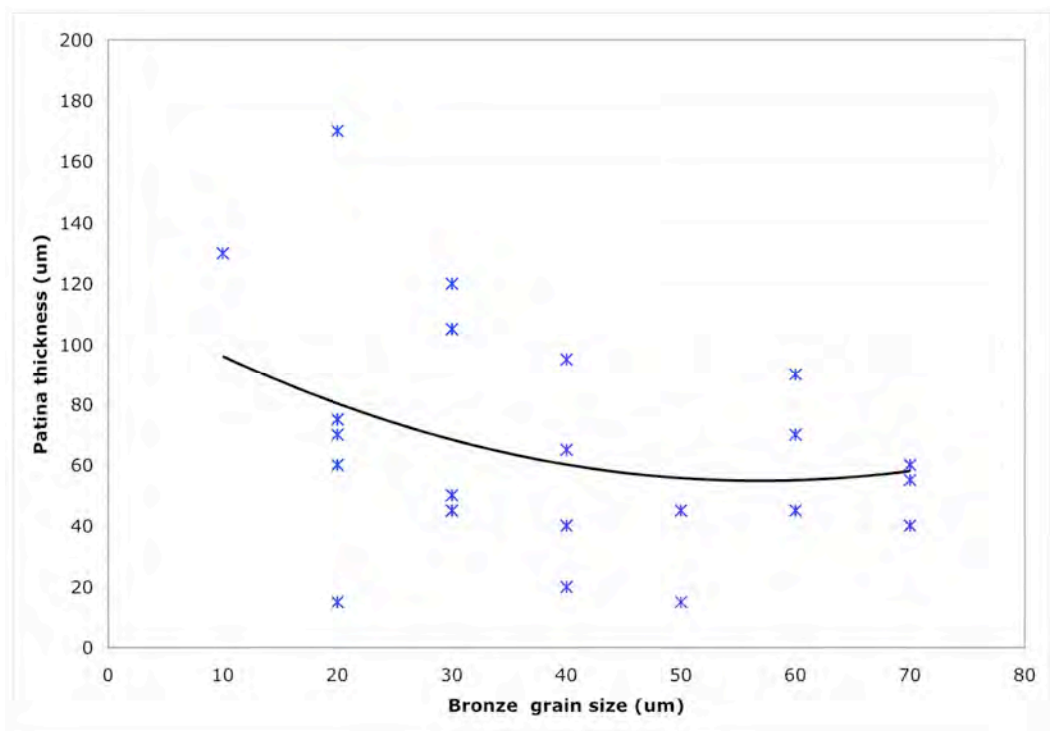


Figure 6.42: Scatter plot showing relationship of the thickness of the patina in cross sections (μm) and the grain size (μm) of the underlying bronze.

6.5.4. SURFACE FINISHES ON HELMETS

It was not possible to identify evidence of tinning on the helmets. Rather, there is clear evidence that the helmets were polished to a high shine finish, using a method which resulted in polishing marks of finer than 1 μm . A finely ground polishing material such as pumice or an earth oxide could have been used for polishing. The only known tin plated helmet remains the 5th c. BC Greek helmet held at the British Museum (GR 1856.12-26.616) (Meeks, 1986; Meeks, 1993b). Future research would include access to this helmet and close examination to investigate details of the surface finish. Overall, plating of helmets appears to be scarce and for helmets from Archontiko and the broader Thermaikos gulf, gilding is associated only with funeral practices. This data suggest that helmet smiths did not employ tinning as a means to harden the surface of the helmets until at least the 5th c. BC. Hardening of helmets was achieved by extensive hammering and annealing, and thinning of the sides, as it was demonstrated by the metallurgical analysis of Corinthian type helmets, which revealed an evolution in metallurgical practices through time.

6.6. SUMMARY

Analysis included in this chapter was designed to investigate the nature of the surfaces on helmets. Plan view SEM-BSE observations showed no evidence of a granular intermetallic but revealed polishing marks on helmets in areas not covered by corrosion deposits. BFPM and SEM-BSE of cross sections revealed characteristic microstructures with distinct chemical profiles examined by EDX composition analyses. A discussion based on current literature offered proposed mechanisms of the formation of these profiles and pointed out differences based on the predominance of malachite or azurite deposits. Comparison of the composition of corrosion patinas and of analyses collected from areas associated with intermetallics, was useful to establish the basis for a Cu-Sn-O at% ternary plot to facilitate future researchers for the characterisation of suspected tinned low-tin bronzes. A preliminary analysis of data and current literature point out to the impact of the metallurgical history and crystal orientation of the original bronze on corrosion. More data collection is necessary to further understand this impact.

CHAPTER 7. SUMMARY AND FUTURE WORK

7.1. RESEARCH OUTCOMES AND CONTRIBUTION

This research was designed to provide scientific research into surface finishes of Greek helmets during the Archaic period (end 8th – mid 5th c. BC), with a review of what comprises evidence for tinning from new experimental data and with insight into methodology for its efficient detection. It was anticipated that results would contribute to understanding the formation of grey/silver or black patinas on archaeological low-tin bronzes. The work was divided in two main experimental parts: a. what comprises evidence of tinning and evaluation of the efficacy of methods for their characterisation; b. examination of the surface finishes of helmets, and understanding of corrosion phenomena that may lead to silver/grey, black or fine patinas based on evidence on the helmets and current literature.

In total, 154 helmets were studied, 107 of which were sampled and 58 included in the thesis for investigation of their manufacture and 36 cross-sections for study of their surface finishes. Detailed technological investigation of the selected helmets provided a means for linking metallurgy and manufacture to helmet types. X-radiography, scanning electron microscopy, and light and neutron metallography were successfully used to investigate the manufacture and the chemical and structural nature of the bronze substrate to better study surface corrosion and tinning. Examination provided evidence on working methods such as casting, degree of hammering and the final work state which influence the mechanical properties of the objects. Neutron diffraction texture analysis offered a great deal of information on crystallographic microstructure, and therefore working methods, in a non-destructive manner on selected intact helmets. The rationale on the choice of this method has been discussed elsewhere (Manti and Watkinson, 2007). It was possible to show that a wealth of metallurgical techniques was employed on the making of helmets, which developed gradually in time. Not all Corinthian-

Myros style helmets are formed entirely by casting, but a combination of casting and hammering was often employed. This supports hypothesis for the use of a pre-formed cast blank that was hammered into shape (Swaddling, 1987), and adds that in several cases this would have been finely executed. The Corinthian type helmet shows an obvious evolution and moves towards thinner and harder helmets, which was achieved by extensive cold working and a reduction in the bronze grain size. This trend was not as evident for helmets of the Illyrian type. Analysis points out limitations of typological/chronological sequences, which are primarily based on stylistic criteria rather than technological features revealed by scientific analyses. Analyses must be viewed within the chronological context of helmets. The chemical composition of the bronze used varies at helmets of different provenience (e.g. Aghia Paraskevi) and analysis pointed out the possibility for future work on an attempt to investigate provenience, helmet composition, and typology based on trace element analysis.

Previous research reports that low-tin archaeological bronzes can exhibit a silver/grey colour surface as a result of corrosion during burial (Dorigo *et al.*, 1998; Robbiola *et al.*, 1998a). This can be problematic because compositional data from surface corrosion can be of similar Sn concentration to the ϵ -Cu₃Sn intermetallic formed during tinning. Meeks's experimental work (1985) on tin-plating methods could be employed to identify tinning methods, but these now need to be viewed in association with current knowledge of Cu-Sn interactions. A review of what comprises evidence of tinning on low-tin bronzes in the light of recent scientific advances was therefore necessary prior to investigating archaeological samples or evaluating the efficiency of selected analytical methods for their detection. This part of the project aimed in particular to: identify which is the predominant intermetallic phase developed during common tinning practices, which would evidence tinning; assess whether non-destructive analysis methods such as diffraction-based methods can detect tinning with a degree of certainty; and, investigate the form of evidence for tinning on archaeological bronzes. This was achieved by observation and interview of a traditional tinsmith to gain understanding of the relevant skills required; laboratory tinning and preparation of copper and bronze tokens; annealing of tinned tokens at different temperature/time to widen the range of microstructures developed at the Cu/Sn interface; analyses of the microstructures. Analyses of the replica tokens included plan-view and cross sectional morphological observations using SEM-BSE, and X-ray and neutron diffraction analyses which was followed by a detailed evaluation of the efficacy of the methods to detect Cu-Sn intermetallics. Results were then compared to data collected from a small number of selected Roman bronzes, which were highly likely to be tinned due to the context of their use (skillets) and their surface appearance.

Meeks's findings (1986) showed that the presence of η -Cu₆Sn₅ and/or ε -Cu₃Sn indicate tinning. This experimental section proved useful in understanding the nature of this evidence. The η -Cu₆Sn₅ intermetallic has a characteristic granular structure that was observed on both experimental and archaeological samples at high magnifications during plan view or in cross sectional SEM examination. The granular nature of this phase was previously neglected, making these findings significant for the non-destructive identification of tinning on small objects. This is the dominant phase developed during tinning and it can be considered as a 'marker' phase when investigating suspected tinned archaeological bronzes. Only a fine planar layer of ε -Cu₃Sn developed on as-tinned copper and bronze tokens at the substrate/ η -Cu₆Sn₅ interface and it was shown that this phase grows at higher temperatures or during longer annealing times. The lone presence of ε -Cu₃Sn on archaeological bronzes may indicate that tinning took place at longer higher temperatures, or that the object was subject to high temperatures during its use.

ε -Cu₃Sn was challenging to detect on archaeological samples using either microscopic observation (SEM-BSE and BFPM) or chemical analysis (SEM-EDX) probably due to its thinness and its scarce preservation. In this case, XRD proved a very powerful analysis tool, being the only method able to confirm the presence of the phase on one sample. XRD has the advantages of collecting data from a large surface area, and ε -Cu₃Sn produces a clear diffraction pattern. It is noticeable that samples where η -Cu₆Sn₅ was present did not show any evidence of an underlying ε -Cu₃Sn phase, reinforcing η -Cu₆Sn₅ as the key phase to characterise tinning. A discussion on solid state diffusion phenomena, the presence of Kirkendall voids on experimental samples, and the increased occurrence of tinning evidence on as-cast bronzes rather than on homogenised bronzes, raised questions on the preservation of these intermetallics during burial. This was further supported by EDX compositional data collected from intermetallics in the Roman bronzes, which indicated that a degree of oxidation must take place during burial. Evidence indicates that oxidation of Sn from the Cu-Sn intermetallics must take place at an early stage, followed by copper dissolution during further oxidation stages; EDX data from areas suspected to be heavily corroded are close to SnO₂.2H₂O composition. However, the number of archaeological samples examined was too small to proceed with general conclusions on the preservation or corrosion of intermetallics. More data collected from tinned archaeological bronzes is necessary to further understand the corrosion behaviour of intermetallic phases during burial.

Detailed examination of the annealed experimental tokens identified Kirkendall voids, the possible presence of a metastable phase which could support theoretical phenomena of

diffusion, and methodological concerns as that the experiment did not provide sufficient time for the high temperature η -Cu₆Sn₅ to transform to the room temperature η' -Cu₆Sn₅. Identification of intermetallic phases using diffraction methods was undertaken using published data in crystallographic databases. Both Cu₆Sn₅ and Cu₃Sn were reported in databases with a range of different crystallographic structures. This could influence accurate Rietveld quantitative analyses of the neutron diffraction data aimed at evaluating the efficacy of the diffraction methods used and determining detection limitations for the two intermetallics. Bibliographic research and best matches to data collected from archaeological and experimental tinned samples showed that the high temperature η -Cu₆Sn₅ fitted best the intermetallic on both the experimental and archaeological samples. This may indicate that transformation of the high to the room temperature structure of Cu₆Sn₅ is in reality uncommon. This may have implications on the theoretical understanding of these phases, and practical implications during phase matching of diffraction data.

Evaluation of diffraction data collected from laboratory tinned copper tokens using CuK α XRD and time-of-flight neutron diffraction (TOF-ND) undertaken at ISIS neutron spallation source (beamtime RB610547 in 2006 and RB720553 in 2008) showed that XRD as a surface technique has an advantage over TOF-ND, which is a bulk method. The potential of this method for the identification of tinning on low-tin bronzes was investigated due to the non-destructive nature of the method and because the efficiency of the method in detecting tinning is not previously investigated. Semi-quantitative Rietveld analysis of the diffraction data showed a great sensitivity of TOF-ND to detect the δ -phase (c. 1 wt%) and ϵ -Cu₃Sn but was unsuccessful in detecting η -Cu₆Sn₅. These results require further analysis and investigation to understand possible reasons of why this may be the case. The X-ray diffraction pattern of data from replica samples was complex due to the contemporaneous presence of Sn, Cu, η -Cu₆Sn₅, ϵ -Cu₃Sn and at higher annealing temperatures the δ -phase. The growth of extensive η -Cu₆Sn₅ followed by a wavy ϵ -Cu₃Sn, and the formation of isolated elongated crystals in the Sn matrix had an impact in the diffraction pattern demonstrating clear evidence of texture. These were extreme cases of elongated crystals formed due to excess amount of Sn during tinning, and it is not expected that cases of this kind would be encountered on archaeological samples. XRD on archaeological samples, proved overall a powerful tool for the investigation of suspected tinned bronzes.

Knowledge obtained from the experimental part that focused on the microstructure and detection evidence of tinning using SEM-EDX, BFPM, SEM-BSE and diffraction methods, was utilised to investigate the surface of helmets. Samples that were not covered by corrosion

deposits showed evidence of polishing marks preserved in a fine corrosion patina. Investigation did not reveal evidence of Cu-Sn intermetallics suggesting that none of the helmets was tinned. One helmet sample exhibiting a fine silver/grey colour surface, showed very fine round voids at the patina/bronze interface, which resemble Kirkendall voids. It could be possible that these are preserved evidence of voids developed during tinning, but it was not possible to confirm the presence of intermetallics and the patina had a moderate Sn/Cu ratio. It is possible that the observed voids are the result of a diffusion process during corrosion. This is the first time that such voids are reported in archaeological samples, and examination of more samples could aid understanding of their formation. Some other unusual features at the outermost part of the patina, observed using SEM-BSE in cross section, were shown to be unusual surface cuprite formation associated with the development of 'sea-urchin' shaped copper carbonate corrosion deposits. These structures are composed of fine filaments that change gradually from cuprite red to copper carbonate and may aid understanding of diffusion and migration phenomena that take place during burial.

The helmet cross-sections show distinct corrosion profiles that aided their characterisation. These were fine black patinas with a fibrous corrosion profile that are associated with predominance of azurite corrosion deposits, and samples with red/brown patinas and an inner cuprite or cuprite-rich layer associated with the presence of malachite deposits. Both these groups could have a high Sn/Cu ratio at their outer part of the patina, which aided preservation of the marker of the original surface, or could have a low Sn/Cu ratio which did not, or only aided preservation of a broadly defined marker of original surface. Results broadly agree with works by Robbiola who first proposed a systematic model of copper dissolution from the bronze and the development of tin-rich patinas on low-tin archaeological bronzes. EDX analysis of the helmets indicated that the tin content in the original bronze has a significant impact on the Sn/Cu ratio of the patina, but it was not possible to show that a linear relationship exists between the Sn content in the patina and the original bronze. Evidence showed that black patinas have elevated content of soil elements (including chromium), whereas silver/grey patinas have the least. Red/brown patinas are due to an underlying inner cuprite/cuprite-rich corrosion zone.

Based on thermodynamic information drawn from relevant Eh-pH diagrams it was possible to develop a rationale on the formation of the two characteristic corrosion profiles (fibrous or with inner cuprite/cuprite rich zone), which preserved fine patinas and the marker of the original surface. Recent work has showed that the amount of dissolved inorganic carbon in the electrolyte solution is important for corrosion as it has an impact on the corrosion rates

and enhances copper dissolution due to the production of H^+ ions during the formation of corrosion, which assists the cathodic half reaction. It is proposed that the fine black patinas, which are associated with azurite were formed via a fast early corrosion stage which lead to *in situ* oxidation of Sn and the extensive dissolution of copper. The fibrous microstructure, or filaments may be evidence of paths for faster inward ionic migration of O^- , OH^- , HCO^- . The presence of chromium may be important in the development of these fine patinas by enhancing oxidation processes likely at an early corrosion stage. Cr is associated with elevated amount of Si from the soil. Results indicate that the role of soil elements is important in the formation of stable or noble patinas, but this fact is often neglected. More experimental data collected from laboratory corrosion tests on low-tin bronzes are required to aid understand of the precise mechanisms that take place during corrosion.

The formation of an inner cuprite or cuprite rich zone in samples exhibiting a red/brown patina overlaid by malachite deposits, and which was not present in those samples with azurite deposits, was explained based on the Eh/pH diagram. Cuprite is stable in a wider Eh range in aqueous environments that favour malachite, so its existence can be explained by restricted access to oxygen and a smaller degree of dissolved copper from this region.

Plotting EDX data in the ternary Cu-Sn-O at% plot aided interpretation of the results. Noble patinas have composition which is situated near that of $SnO_2 \cdot 2H_2O$ (but never reach it). Samples with an uneven corrosion surface have a lower Sn/Cu and their composition is similar to copper carbonates indicating mineralization. The ternary plot becomes more useful by adding compositional data of intermetallics from the Roman bronzes. Discrimination becomes more difficult towards the $SnO_2 \cdot 2H_2O$ region, but corroded intermetallics have a slightly higher Sn/Cu content, which is not as evident when examining the numerical data. Because of the distinct chemical regions they cover, it is possible to use this plot for the interpretation of compositional data taken from the surface of suspected tinned objects, provided oxygen concentration is also measured. The importance of measuring oxygen to fully evaluate corroded structures and to avoid erroneous interpretations is self-evident. More data is required to populate the plot to better understand the chemical composition of corroded intermetallics. It is hoped that this plot will be useful for analysts working on low-tin bronzes, to aid identification of tinning and corrosion.

Overall, this thesis offered the opportunity to review knowledge on tinning structures, process, which identified characteristic morphologies that aid the identification of Cu-Sn intermetallics, and to expand current understanding on the corrosion processes involved for the development of fine patinas, by adding on Robbiola's models. At a practical level, new

information on methodological aspects and the effectiveness of the methods used can aid other researchers to employ appropriate methodologies. A significant outcome of this work is the development of a discriminant plot that could aid interpretation of compositional data from the surface of suspected tinned bronzes, in cases where oxygen is measured.

7.2. FUTURE WORK

This thesis pointed out several interesting research avenues that require further work and in places where only noted in passing and are summarised below:

- a. Detailed technological examination of the rest of the sampled helmets would provide a statistically significant number of samples to assess variability of metallurgical styles employed for the manufacture of different helmet types. Chemical characterisation of helmets via trace element analysis in association with typological characteristics could aid characterisation of production workshops. This would contribute to discussions on the extent to which nomenclature of helmet types is associated with the locality of their production (Kunze, 1958; Snodgrass, 1964:18-20) and to understanding economic and military power in the Archaic period.
- b. More experimental work is necessary to better understand corrosion behaviour of low-tin bronzes in the presence of dissolved inorganic carbon. Data currently derive from research on the corrosion of copper pipes. The effects of soil elements and chromium on the oxidation of bronzes is important to investigate due to its passivating action aiding formation of noble patinas. The role of silicon in the corrosion of low-tin bronzes is unknown and its potentially passivating role is yet to be explored.
- c. The influence of the crystalline nature of low-tin bronzes on their corrosion is unknown. Literature indicates that cuprite can have an epitactic relationship with the underlying bronze, which in turn can affect corrosion. The degree of hammering and its impact on corrosion requires further exploration.
- d. Investigation of more archaeological and experimental tinned samples is necessary to understand corrosion mechanisms of Cu-Sn intermetallics phases.

REFERENCES

- Abbaschian R., Abbaschian L. and Reed-Hill E.R. (2010). Physical Metallurgy Principles. 4th SI edn. Stamford, USA: Cengage Learning.
- Adriaens A. and Demortier G. (2004). COST Actions G1 and G8: Eu Programs on the Use of Radiation in Art and Archaeometry. *Nuclear Instruments and Methods in Physics Research Section B: Beam Interactions with Materials and Atoms* 226 (1-2), 3-9.
- Adriaens A., Degriigny C. and Cassar J. (eds.), (2005). Benefits of Non-Destructive Analytical Techniques for Conservation. Papers from a COST Action G8 Workshop Held in Kalkara, Malta, on 8 January 2004 Luxembourg: COST Office.
- Adriano D. (2001). Trace Elements in Terrestrial Environments. 2nd edn. NY: Springer-Verlag.
- AMC (2001a). Measurement of near Zero Concentration: Recording and Reporting Results That Fall Close or Below the Detection Limit. *The Analyst* 126, 256-259.
- AMC (2001b). What Should Be Done with Results Below the Detection Limit? Mentioning the Unmentionable. . *Analytical Methods Committee Technical Briefs (Royal Society of Chemistry)* 5.
- AMC (2003). Terminology - the Key to Understanding Analytical Science. Part 1: Accuracy, Precision and Uncertainty. *Analytical Methods Committee Technical Briefs (Royal Society of Chemistry)* 13.
- AMC (2008). Test for 'Sufficient Homogeneity' in a Reference Material. *Analytical Methods Committee Technical Briefs (Royal Society of Chemistry)* 17 A.
- Anheuser K. (1996). An Investigation of Amalgam Gilding and Silvering on Metalwork. DPhil Thesis. Oxford: University of Oxford, Faculty of Physical Sciences.
- Anheuser K. (2000). Amalgam Tinning of Chinese Bronze Antiquities. *Archaeometry* 42 (1), 189-200.
- Anne M. (2007). Crystallography and Diffraction Techniques for Cultural Heritage Materials. Presentation Delivered at the HSC5: Synchrotron Radiation and Neutrons for Cultural Heritage Studies. The European Synchrotron Radiation Facility (ESRF), Grenoble, 7 to 13 October 2007
- Arletti R., Cartechini L., Giovannini S., Rinaldi R., Kockelmann W. and Cardarelli A. (2007). Neutron Diffraction Study of Bronze Age Tools from Second Millennium BC Dwellings in Italy. *Il Nuovo Cimento C* 30 (1), 21-26.
- Arletti R., Cartechini L., Rinaldi R., Giovannini S., Kockelmann W. and Cardarelli A. (2008). Texture Analysis of Bronze Age Axes by Neutron Diffraction. *Applied Physics A: Materials Science & Processing* 90 (1), 9-14.

- Artioli G. and Dugmani M. (2004). Crystallographic Texture Analysis: Applications in Mineralogy and Archaeometry. *Periodico di Mineralogia* 73 (3), 5-16.
- Artioli G. (2007). Crystallographic Texture Analysis of Archaeological Metals: Interpretation of Manufacturing Techniques. *Applied Physics A: Materials Science & Processing* 89 (4), 899-908.
- Ashby M.F. and Jones D.R.H. (2006). Engineering Materials 2: An Introduction to Microstructures, Processing and Design. 3rd edn. Oxford: Butterworth-Heinemann (Elsevier).
- ASM (1985). Terms and Definitions. In ASM (ed.), Metallography and Microstructures, Metals Handbook, Volume 9, 9th Edition. Ohio: American Society for Metals, 1-19.
- Atkins P. and De Paula J. (2006). Atkins' Physical Chemistry. 8th edn. Oxford: Oxford University Press.
- Augustithis S.S. (1995). Atlas of the Textural Patterns of Ore Minerals and Metallogenic Processes. Berlin: De Gruyter.
- Bader S., Gust W. and Hieber H. (1995). Rapid Formation of Intermetallic Compounds Interdiffusion in the Cu-Sn and Ni-Sn Systems. *Acta Metallurgica Et Materialia* 43 (1), 329-337.
- Bailey A.R. (1982). The Role of Microstructure in Metals : An Introductory Volume. 3rd edn., Annotated Metallographic Specimens. Special Series. Exercises in Materials Science. Betchworth: Metallurgical Services.
- Bailey A.R. (1984). Introductory Practical Metallography : A Basic Course of Microstructures with 37 Specimens. 2nd edn., Annotated Metallographic Specimens, Special series. Betchworth, Surrey: Metallurgical Services.
- Banovic S. (2007). Microstructural Characterization and Mechanical Behavior of Cu–Sn Frangible Bullets. *Materials Science & Engineering A* 460, 428-435.
- Barrett C.S. (1985). Crystal Structure of Metals. In ASM (ed.), Metallography and Microstructures, Metals Handbook, Volume 9, 9th Edition. Ohio: American Society for Metals, 706-720.
- Bartoli L., Siano S., Kockelmann W., Santisteban J., Miccio M. and Marinis G.D. (2007). Non-Destructive Characterisation of a Villanovan Sword Using Time-of-Flight Neutron Diffraction. *Il Nuovo Cimento C* 30 (1), 21-26.
- Benton S. (1943). The Dating of Helmets and Corselets in Early Greece. *The Annual of the British School at Athens* XL (Session 1939-1940), 78-82.
- Bertholon R. (2001). The Location of the Original Surface, a Review of the Conservation Literature. Metal 2001, Proceedings of the ICOM Committee for Conservation Metals Working Group, 167-179.
- Billinge S. (2006). Structure Determination and Phase Analysis by the Use of Neutron Diffraction. *JOM Journal of the Minerals, Metals and Materials Society* 58 (3), 47-51.
- Blyth P.H. (1977). The Effectiveness of Greek Armour against Arrows in the Persian War (490-479 B.C.): An Interdisciplinary Enquiry. PhD Thesis. Reading: University of Reading,
- Blyth P.H. (1988). Cold-Working in Ancient Greek Helmets. In(ed. Jones J.E.). Aspects of Ancient Mining and Metallurgy, 1988, Acta of a British School at Athens Centenary Conference, University College of North Wales, Bangor, 1986. 151-154.
- Blyth P.H. (1993). Metallurgy of Two Fragmentary Archaic Greek Helmets. *Historical Metallurgy* 27, 25-36.

- Borchhardt J. (1972). Homerische Helme : Helmformen Der Ägäis in Ihren Beziehungen Zu Orientalischen Und Europäischen Helmen in Der Bronze- Und Frühen Eisenzeit. Mainz am Rhein: Römisch-Germanisches Zentralmuseum Mainz. and P. von Zabern.
- Born H. (1990). Patinated and Painted Bronzes: Exotic Technique or Ancient Tradition? , Small Bronze Sculpture from the Ancient World., Papers delivered at a Symposium organised and held at the J. Paul Getty Museum. Malibu, California: J. Paul Getty Museum, 179-196.
- Born H. (1991). Zur Herstellung Der Etruskischen Bronzehelme Mit Scheitelknauf (on the Manufacturing Technique of Etruscan Bronze Helmets with Knobs). *Archäologisches Korrespondenzblatt* 21 (1), 73-78 (Abstract).
- Born H. (1993). Multi-Coloured Antique Bronze Statues. In Craddock P.T. and La Niece S. (eds), Metal Plating and Patination : Cultural, Technical and Historical Developments. Oxford ; Boston: Butterworth-Heinemann, 19-29.
- Born H. (2007). Archaischer Silberglanz Verzinnte Schildbänder Und Schildbugel Aus Olympia - Ein Vorbericht. *Da Altertum* Band 52 (4), 241-256.
- Britton S.C. (1952). The Corrosion Resistance of Tin and Tin Alloys. Greenford, Middx: Tin Research Institute.
- Bronk H. and Freestone I.C. (2001). A Quasi Non-Destructive Microsampling Technique for the Analysis of Intact Glass Objects by SEM/EDXA. *Archaeometry* 43 (4), 517-527.
- Burstein G.T. (2010). Passivity and Localised Corrosion. Chapter 2.02. In Cottis R.A., Graham J.M., Lindsay R., Lyon S.B., Richardson J.A., Scantlebury J.D. and Scott F.H. (eds), Shreir's Corrosion 4th edn., Vol. 2. Amsterdam: Elsevier, 731-752.
- CDS, (2010). The Chemical Database Service. Science and Technology Facilities Council UK (STFC), <http://cds.dl.ac.uk/>
- Chao B.H., Zhang X., Chae S. and Ho P.S. (2009). Recent Advances on Kinetic Analysis of Electromigration Enhanced Intermetallic Growth and Damage Formation in Pb-Free Solder Joints. *Microelectronics Reliability* 49 (3), 253-263.
- Chapuis G. and Schoeni N. (2006). 'E-Crystallography Course : An Interactive Course', Lausanne, Laboratoire de Cristallographie, Swiss federal Institute of technology in Lausanne (EPFL), <http://lcr.epfl.ch/page37341.html> (Dec 2009).
- Charbonneaux J. (1962). Greek Bronzes. trans. Watson K. London: Elek Books.
- Chase W.T. (1977). What Is the Smooth Lustrous Black Surface on Ancient Bronze Mirrors ? In Brown B.F. (ed.), Corrosion and Metal Artefact : A Dialogue between Conservators and Archaeologists and Corrosion Scientists, NBS special publication 479. Washington: National Bureau of Standards, 191-203.
- Chase W.T. (1994). Chinese Bronzes: Casting, Finishing, Patination, and Corrosion. In Scott D.A., Podany J. and Considine B.B. (eds), Ancient & Historic Metals : Conservation and Scientific Research Proceedings of a Symposium Organized by the J. Paul Getty Museum and the Getty Conservation Institute, November 1991. Marina del Rey, CA: Getty Conservation Institute, 85-118.
- Chatzidimitriou A. (2005). Paintings of Workshops and the Trades from the Archaic and Classical Periods. Archaeological Deltio, No. 92. Athens: Ministry of Culture, Greece. [Χατζηδημητρίου Α. (2005). Παραστάσεις Εργαστηρίων Και Εμπορίου Εικονογραφία Των Αρχαϊκών Και Κλασσικών Χρόνων. Δημοσιεύματα Του Αρχαιολογικού Δελτίου, Αρ. 92. Αθήνα: Ταμείο Αρχαιολογικών Πόρων και Απαλλοτριώσεων; Υπουργείο Πολιτισμού.]

- Chen J. and Lai Y. (2009). Towards Elastic Anisotropy and Strain-Induced Void Formation in Cu–Sn Crystalline Phases. *Microelectronics Reliability* 49 (3), 264-268.
- Chin G.Y. (1985). Textured Structures. In ASM (ed.), Metallography and Microstructures, Metals Handbook, Volume 9, 9th Edition. Ohio: American Society for Metals, 700-705.
- Chippindale C. (1994). Editorial. *Antiquity* 68 (258), 5-6.
- Christodoulou C. and Hirst D. (1985). The Chemistry of Chromite from Two Mafic--Ultramafic Complexes in Northern Greece. *Chemical Geology* 49 (4), 415-428.
- Chrysostomou A. and Chrysostomou P. (2000). The Cemeteries at Archontiko near Yiannitsa., Archaeological Works in Macedonia and Thrace 2000, 14. Thessaloniki: Ministry of Culture Greece; Aristotle University of Thessaloniki, 473-489. [Χρυσοστόμου Α. and Χρυσοστόμου Π. (2002). Τα Νεκροταφεία Του Αρχοντικού Γιαννιτσών. Το Αρχαιολογικό Έργο Στη Μακεδονία Και Θράκη 2000, 14. Θεσσαλονίκη: Υπουργείο πολιτισμού, Ταμείο Αρχαιολογικών Πόρων, Πανεπιστήμιο Θεσσαλονίκης, 473-489.]
- Chrysostomou A. and Chrysostomou P. (2001). Excavation at the Western Cemetery at Archontiko Pella's During 2001. Archaeological Works in Macedonia and Thrace 15. Thessaloniki: Ministry of Culture Greece; Aristotle University of Thessaloniki, 477-488. [Χρυσοστόμου Α. and Χρυσοστόμου Π. (2001). Ανασκαφή Στη Δυτική Νεκρόπολη Του Αρχοντικού Πέλλας Κατά Το 2001. Το Αρχαιολογικό Έργο Στη Μακεδονία Και Θράκη, 15. Θεσσαλονίκη: Υπουργείο πολιτισμού, Ταμείο Αρχαιολογικών Πόρων, Αριστοτέλειο Πανεπιστήμιο Θεσσαλονίκης, 477-488.]
- Chrysostomou A. and Chrysostomou P. (2002). Excavation of the Western Cemetery of Archontiko Pella's During 2002 Archaeological Works in Macedonia and Thrace 16. Thessaloniki: Ministry of Culture Greece; Aristotle University of Thessaloniki, 465-478. [Χρυσοστόμου Α. and Χρυσοστόμου Π. (2002). Ανασκαφή Στη Δυτική Νεκρόπολη Του Αρχοντικού Πέλλας Κατά Το 2002. Το Αρχαιολογικό Έργο Στη Μακεδονία Και Θράκη, 16. Θεσσαλονίκη: Υπουργείο πολιτισμού, Ταμείο Αρχαιολογικών Πόρων; Αριστοτέλειο Πανεπιστήμιο Θεσσαλονίκης, 465-478.]
- Chrysostomou A. and Chrysostomou P. (2003). West Cemetery of Archontiko at Pella. Group of Burials of Aristocratic Family from the Archaic Period. Archaeological Works in Macedonia and Thrace, 17. Thessaloniki: Ministry of Culture Greece; Aristotle University of Thessaloniki, 505-516. [Χρυσοστόμου Α. and Χρυσοστόμου Π. (2003). Δυτική Νεκρόπολη Του Αρχοντικού Πέλλας- Συστάδα Τάφων Αριστοκρατικής Οικογένειας Των Αρχαϊκών Χρόνων. Το Αρχαιολογικό Έργο Στη Μακεδονία Και Θράκη, 17. Θεσσαλονίκη: Υπουργείο πολιτισμού, Ταμείο Αρχαιολογικών Πόρων, Αριστοτέλειο Πανεπιστήμιο Θεσσαλονίκης, 505-516.]
- Chunchun X. and Julin W. (2003). Investigation of the Chemical and Electrochemical Behaviour of Mass Transfer at an Archaeological Bronze/Soil Interface. *Anti-Corrosion Methods and Materials* 50 (5), 326-333.
- Clarke M. and Britton S. (1963). Passivity of Electrodeposited Tin-Nickel Alloy and Other Intermetallic Tin Compounds. *Corrosion Science* 3 (4), 207-216.
- Clegg W., Blake A.J., Gould R.O. and Main P. (2001). Crystal Structure Analysis: Principles and Practice. International Union of Crystallography Texts on Crystallography, 6. Oxford ; New York: Oxford University Press.
- Colacicchi-Alessandri O. and Ferretti M. (2002). Indagini Su Manufatti Di Bronzo Del V S.A.C. Provenienti Dalla Necropoli Di Vaglio, in Italia Meridionale. In Giunilia-Mair A. (ed.), I Bronzi Antichi: Produzione E Tecnologia, Atti Del Xv Congresso Internazionale Sui

- Bronzi Antichi, Organizzato Dall' Università Di Udine, Sede Di Gorizia Grado-Aquileia, 22-26 Maggio 2001. Monographies Instrumentum 21. Montagnac: monique mergoil, 137-142.
- COST (2006). COST Action MP0602 Memorandum of Understanding: Advanced Solder Materials for High-Temperature Application- Their Nature, Design, Process and Control in a Multiscale Domain. Brussels: COST Office.
- COST (2008). Action MP0602: Advanced Solder Materials for High Temperature Application (Hisold). Monitoring Progress Report from 16/5/2007 to 31/12/2007 COST Action MP0602. Brussels: COST Office.
- Cottis R.A. (2010). Introduction to the Modelling of Corrosion. Chapter 2.37. In Cottis R.A., Graham J.M., Lindsay R., Lyon S.B., Richardson J.A., Scantlebury J.D. and Scott F.H. (eds), Shreir's Corrosion 4th edn., Vol. 2. Amsterdam: Elsevier, 1581-1584.
- Craddock P.T. (1976). The Composition of the Copper Alloys Used by the Greek, Etruscan and Roman Civilizations: 1. The Greeks before the Archaic Period. *Journal of Archaeological Science* 3, 93-113.
- Craddock P.T. (1977). The Composition of the Copper Alloys Used by the Greek, Etruscan and Roman Civilizations: 2. The Archaic, Classical and Hellenistic Greeks. *Journal of Archaeological Science* 4, 103-123.
- Craddock P.T. and Lang J. (1983). Spinning, Turning, Polishing. *Journal of Historical Metallurgy Society* 17 (2), 79-81.
- Craddock P.T. (1988). Copper Alloys of the Hellenistic and Roman World, New Analyses and Old Authors. In Jones J.E. (ed.), Aspects of Ancient Mining and Metallurgy: Acta of a British School at Athens Centenary Conference, University College of North Wales, Bangor, 1986. Bangor, 55-65.
- Craddock P.T. and Giunlia-Mair A. (1993). Beauty Is Skin Deep: Evidence for the Original Appearance of Classical Statuary. In Craddock P.T. and La Niece S. (eds), Metal Plating and Patination : Cultural, Technical and Historical Developments. Oxford ; Boston: Butterworth-Heinemann, 30-38.
- Craddock P.T. (1999). Paradigms of Metallurgical Innovation in Prehistoric Europe. In Hauptmann A. (ed.), The Beginnings of Metallurgy : Proceedings of the International Conference "The Beginnings of Metallurgy", Bochum 1995 Der Anschnitt. Beiheft 9. Bochum: Deutsches Bergbau-Museum, 175-192.
- Craddock P.T. (2009). Scientific Investigation of Copies, Fakes and Forgeries. Oxford: Butterworth-Heinemann (Elsevier).
- CRYSTMET, (2010). Metals Structure Database. The National Research Council of Canada; TOOTH Information Systems
- Cudennec Y. and Lecerf A. (2003). The Transformation of Cu(OH)₂ into CuO, Revisited. *Solid State Sciences* 5 (11-12), 1471-1474.
- Cuthbertson J.W. (1960). Bronzes. In Hedges E.S. and Cuthbertson J.W. (eds), Tin and Its Alloys. London: Edward Arnold, 369-412.
- Daintith J. (ed.) (2009), Scattering of Electromagnetic Radiation, A Dictionary of Physics, Oxford University Press, Oxford Reference Online [Online Text] (13 November 2009)
- David W.I.F., Shankland K., McCusker L.B. and Baerlocher C. (2002a). Introduction. Chapter 1. In David W.I.F., Shankland K., McCusker L.B. and Baerlocher C. (eds), Structure Determination from Powder Diffraction Data., International Union of Crystallography Texts on Crystallography 13. Oxford: Oxford Science Publications, 1-12.

- David W.I.F., Shankland K., McCusker L.B. and Baerlocher C. (eds.), (2002b). Structure Determination from Powder Diffraction Data. International Union of Crystallography Texts on Crystallography, Oxford: Oxford Science Publications.
- Davies P.J. (1882), 'Practical Notes on Plumbing. Tinning Iron Pipes, Copper or Brass-Work, Bits, etc', *Scientific American Supplement*, 311, 4960. <http://www.gutenberg.org/1/8/3/4/18345/>, accessed Jun 12 2007.
- Davis J.R. (ed.), (2001). Copper and Copper Alloys. ASM Handbook, Vol. 9, Metals Park, Ohio: American Society for Metals.
- De Graef M. and Michael M.E. (2007). Structure of Materials. An Introduction to Crystallography, Diffraction, and Symmetry. Cambridge: Cambridge University Press.
- De Ryck I., Adriaens A., Pantos E. and Adams F. (2003). A Comparison of Microbeam Techniques for the Analysis of Corroded Ancient Bronze Objects. *Analyst* 128 (8), 1104.
- Dezco T. (1998). Oriental Influence in the Aegean and Eastern Mediterranean Helmet Traditions in the 9th-7th Centuries B.C.: The Patterns of Orientalization. BAR International Series, 691. Oxford: Archaeopress.
- Dintsis P. (1986). Hellenistische Helme. 2 vols., *Archaeologica*, 43. Roma: G. Bretschneider.
- DKL Metals Ltd (2006). Nealetin Pure Tin Solder Paint: Technical Data Sheet. Linlithgow, W. Lothian.
- Dorigo A., Fiaud C., Labbé J.P. and Robbiola L. (1998). Characterisation of the Corrosion Structures of Roman Copper Alloys by SEM and Edsx: Improvement of Means of Measurements on Archaeological Copper Alloys for Characterisation and Conservation. In Mourey W. and Robbiola L. (eds), Metal 98, Proceedings of the international conference on metals conservation, Draguignan-Figanières, France, 27-29 May 1998. London: James & James, 145-151.
- Economou-Eliopoulos M. and Vacondios I. (1995). Geochemistry of Chromitites and Host Rocks from the Pindos Ophiolite Complex, Northwestern Greece. *Chemical Geology* 122 (1-4), 99-108.
- Edward J., Fossey J.M. and Yaffe L. (1984). Analysis by Neutron Activation of Human Bone from the Hellenistic Cemetery at Asine, Greece. *Journal of Field Archaeology* 11 (1), 37-46.
- Elenco Electronics (2002). Solder Practice Kit, Model Ak-100: Lesson Manual.
- Engelberg D.L. (2010). Intergranular Corrosion. Chapter 2.06. In Cottis R.A., Graham J.M., Lindsay R., Lyon S.B., Richardson J.A., Scantlebury J.D. and Scott F.H. (eds), Shreir's Corrosion 4th edn., Vol. 2. Amsterdam: Elsevier, 810-827.
- Fairhurst C., Marek M., Butts M. and Okabe T. (1978). New Information on High Copper Amalgam Corrosion. *Journal of Dental Research* 57 (5), 725-729.
- Frankel G.S. and Cottis R.A. (2010). Principles of Corrosion in Liquids. Chapter 2.01. In Cottis R.A., Graham J.M., Lindsay R., Lyon S.B., Richardson J.A., Scantlebury J.D. and Scott F.H. (eds), Shreir's Corrosion 4th edn., Vol. 2. Amsterdam: Elsevier, 725-731.
- Frielinghaus H. (2007). Die Helme Von Delphi. *BCH* 131 (1), 139-185.
- Fujiwara K., Ohtani M., Isu T., Nango S., Kawanaka R. and Shimizu K. (1980). Interfacial Reaction in Bimetallic Sn/Cu Thin Films. *Thin Solid Films* 70 (1), 153-161.
- Fuller J.S. (1894). Art of Coppersmithing. A Practical Treatise on Working Sheet Copper into All Forms. Original edition published by D. Williams, NY. Reprint (1993) edn. Mendham, New Jersey: The Astragal Press.

- Gagliano R. and Fine M. (2001). Growth of H Phase Scallops and Whiskers in Liquid Tin-Solid Copper Reaction Couples. *JOM Journal of the Minerals, Metals and Materials Society* 53 (6), 33-38.
- Gale W.F. and Totemeier T.C. (2004). Equilibrium Diagrams. Smithells Metals Reference Book, 8th Edition. Knovel (Release Jul 11, 2006): Elsevier, 11.11-11-533.
- Giacovazzo C. (2002). The Diffraction of X-Rays by Crystals. Chapter 3. In Giacovazzo C., Monaco H.L., Artioli G., Viterbo D., Ferraris G., Gilli G., Zanotti G. and Catti M. (eds), Fundamentals of Crystallography 2nd edn., International Union of Crystallography texts on crystallography 7. Oxford: Oxford University Press, 153-226.
- Giacovazzo C., Monaco H.L., Artioli G., Viterbo D., Ferraris G., Gilli G., Zanotti G. and Catti M. (2002). Fundamentals of Crystallography. 2nd edn., International Union of Crystallography Texts on Crystallography, 7. Oxford: Oxford University Press.
- Gillis C. (2001). Tin-Covered Pottery and Chemical Analyses: A Summary. In Bassiakos Y., Aloupi E. and Facorellis Y. (eds), Archaeometry Issues in Greek Prehistory and Antiquity. Athens: Hellenic Society of Archaeometry, 451-458
- Giuliani A., Fiori F., Gysens J., Manescu A. and Rustichelli F. (2008). Analysis of Neutron Diffraction Profiles in Bronze Archaeological Statuettes Produced by Solid Lost Wax Casting. *Journal of Physics: Condensed Matter* 20 (10), 104251.
- Goldstein J. (2003). Scanning Electron Microscopy and X-Ray Microanalysis. 3rd edn. New York: Springer.
- Goodhew P.J., Beanland R. and Humphreys F.J. (2001). Electron Microscopy and Analysis. 3rd edn. London: Taylor & Francis.
- Greenewalt C.H. and Heywood A.M. (1992). A Helmet of the Sixth Century BC from Sardis. *Bulletin of the American Schools of Oriental Research*, 1-31 (Abstract).
- Fit2D. by Hammersley A., Free scientific software for conversion of diffraction image data to diffractograms. Download from http://www.esrf.eu/computing/scientific/FIT2D/aftp_fit2d.html
- Hammond C. (2001). The Basics of Crystallography and Diffraction. 2nd edn., International Union of Crystallography Texts on Crystallography, 5. Oxford ; New York: Oxford University Press.
- Han Rubin, Ma Zhaozeng, Wang Zengjun and Ko T. (1983). Studies in the Black Passive Oxide Film on Bronze Arrows Unearthed with the Terra-Cotta Warriors Near the Qin Tomb (210bc) at Lintong, Xian. *Studies in the History of Natural Sciences* 2 (4), 295-302.
- Hannon A. (2004). Neutron Diffraction. *ISIS The Neutron Training Course*, 31-70.
- Hayashi A., Kao C. and Chang Y. (1997). Reactions of Solid Copper with Pure Liquid Tin and Liquid Tin Saturated with Copper. *Scripta Materialia* 37 (4), 393-398.
- Hayes S., Chawla N. and Frear D. (2009). Interfacial Fracture Toughness of Pb-Free Solders. *Microelectronics Reliability* 49 (3), 269-287.
- Haynes D.E.L. (1992). The Technique of Greek Bronze Statuary. Mainz: Von Zabern.
- Hedges E.S. (1960). The Chemical Behaviour of Tin. In Hedges E.S. and Cuthbertson J.W. (eds), Tin and Its Alloys. London: Edward Arnold, 78-98.
- Hedges E.S. (1964). The Tin Research Institute. Tin Research Institute Publication, no 346. Greenford, Middx: Tin Research Institute.

- Hencken H.O.N. (1971). The Earliest European Helmets : Bronze Age and Early Iron Age. Bulletin, no 28. Cambridge, Mass: American School of Prehistoric Research, Peabody Museum of Archaeology and Ethnology, Harvard University.
- Henderson J. and Manti P. (2008). Access for Analysis. In Saunders D., Townsend J.H. and Woodcock S. (eds), Conservation and Access, International Institute for Conservation Congress, London, 15-19 September. London: IIC, 115-119.
- Higginson R.L. and Sellars C.M. (2003). Worked Examples in Quantitative Metallography. London: Maney Publishing for the Institute of Materials, Minerals and Mining.
- Hill R.J. and Madsen I.C. (2002). Sample Preparation, Instrument Selection and Data Collection Chapter 6. In David W.I.F., Shankland K., McCusker L.B. and Baerlocher C. (eds), Structure Determination from Powder Diffraction Data., International Union of Crystallography Texts on Crystallography 13. Oxford: Oxford Science Publications, 98-117.
- Hockey M., Johnston A., La Niece S., Middleton A. and Swaddling J. (1992). An Illyrian Helmet in the British Museum. *The Annual of the British School at Athens* 87, 281-291.
- Hoffmann H. (1972). Early Cretan Armorers. Mainz: Verlag Philipp von Zabern.
- Homer, Iliad. Translated by Fitzgerald R.(1998) Oxford: Oxford University Press.
- Hosford W.F., Jonas J.J. and Leslie W.C. (1985). Plastic Deformation Structures. In ASM (ed.), Metallography and Microstructures., Metals Handbook, Volume 9, 9th Edition. Ohio: American Society for Metals, 684-691.
- Hu H. (1985). Recovery, Recrystallisation and Grain-Growth Structures. In ASM (ed.), Metallography and Microstructures, Metals Handbook, Volume 9, 9th Edition. Ohio: American Society for Metals, 692-699.
- Hughes R. and Rowe M. (1982). The Colouring, Bronzing and Patination of Metals : A Manual for Fine Metalworkers, Sculptors and Designers. London: Thames and Hudson.
- Hughes R. (1993). Artificial Patination. In Craddock P.T. and La Niece S. (eds), Metal Plating and Patination : Cultural, Technical and Historical Developments. Oxford ; Boston: Butterworth-Heinemann, 1-18.
- Ibberson R.M. and David W.I.F. (2002). Neutron Powder Diffraction. Chapter 5. In David W.I.F., Shankland K., McCusker L.B. and Baerlocher C. (eds), Structure Determination from Powder Diffraction Data., International Union of Crystallography Texts on Crystallography 13. Oxford: Oxford Science Publications, 88-97.
- ICSD, (2010). Inorganic Crystal Structure Database FIZ Karlsruhe 2007, Accessed via <http://cds.dl.ac.uk/> the STFC Chemical Database Service (CDS) <http://icsd.ill.eu/icsd/index.html>
- Ipser H. (2007). European Cost Action 531: Basic Research on Lead-Free Soldering. *Journal of Mining and Metallurgy B: Metallurgy* 43 (2), 109-112.
- ITRI (1983). Guide to Tinplate. International Tin Research Institute Publication, No 622. Greenford: International Tin Research Institute.
- IUCr (2006). 'Online Dictionary of Crystallography', Commission for Crystallographic Nomenclature, The International Union of Crystallography, http://reference.iucr.org/dictionary/Main_Page.
- Jackson A.H. (1992). Arms and Armour at the Panhellenic Sanctuary of Poseidon at Isthmia. In Coulson W. and Kyrieleis H. (eds), Proceedings of an International Symposium on the Olympic Games, 1988. Athens: Deutsches Archäologisches Institut Athen, 141-144.

- Jackson A.H. (2004). An Early Corinthian Helmet in the Manchester Museum. *The Annual of the British School at Athens* 99, 273-282.
- Jarva E. (1995). Archaologia on Archaic Greek Body Armour. Studia Archaeologica Septentrionalia 3. Rovaniemi, Finland: Societas Historica Finlandiae Septentrionalis.
- John V.B. (1972). Introduction to Engineering Materials. London: The Macmillan press
- Joubert F. (1923). The Collection of Arms and Armour Formed by Lord Howard De Walden. London.
- Kaltsas N. (2004). Olympia. 4th edn. Athens: Ministry of Culture and the Archaeological Receipts Fund.
- Kang J., Gagliano R., Ghosh G. and Fine M. (2002). Isothermal Solidification of Cu/Sn Diffusion Couples to Form Thin-Solder Joints. *Journal of Electronic Materials* 31 (11), 1238-1243.
- Kao C. (1997). Microstructures Developed in Solid-Liquid Reactions: Using Cu-Sn Reaction, Ni-Bi Reaction, and Cu-in Reaction as Examples. *Materials science & engineering. A, Structural materials: properties, microstructure and processing* 238 (1), 196-201.
- Karavoltzos S., Sakellari A., Mihopoulos N., Dassenakis M. and Scoullou M.J. (2008). Evaluation of the Quality of Drinking Water in Regions of Greece. *Desalination* 224 (1-3), 317-329.
- Kealey D. and Haines P.J. (2002). Analytical Chemistry. Instant Notes Chemistry Series. Oxford: BIOS Scientific Publishers.
- Kim K., Kim J. and Han S. (2008). The Effect of Postbake Treatment on Whisker Growth under High Temperature and Humidity Conditions on Tin-Plated Cu Substrates. *Materials Letters* 62 (12-13), 1867-1870.
- Kinnes L.A., Craddock P.T., Needham S. and Lang J. (1979). Tin Plating in the Early Bronze Age: The Barton Stacey Axe. *Antiquity* LIII (208), 141-143
- Kinnes L.A. and Needham S. (1981). Tinned Axes Again. *Antiquity* LV (214), 133-134.
- Kockelmann W., Pantos E. and Kirfel A. (2000). Neutron and Synchrotron Radiation Studies of Archaeological Objects. In Creagh D.C. and Bradley D.A. (eds), Radiation in Art and Archaeometry. Amsterdam, Oxford: Elsevier Science, 347-380.
- Kockelmann W., Kirfel A. and Hahnel E. (2001). Non-Destructive Phase Analysis of Archaeological Ceramics Using Tof Neutron Diffraction. *Journal of Archaeological Science* 28 (2), 213-222.
- Kockelmann W., Kirfel A., Jansen E., Linke R., Schreiner M., Traum R. and Denk R. (2003a). Neutron Diffraction for Non-Destructive Texture Analysis of Minted and Cast "Taler" Coins. In., Numismatics & Technology: questions and answers, 2003a, 25/26 April. Kunsthistorisches Museum Wien, Austria. 113-123.
- Kockelmann W., Kirfel A., Linke R., Schreiner M., Traum R., Pantos E., Garner R. and Prag A.J.N.W. (2003b). Genuine or Fake? Neutron Diffraction for Non-Destructive Testing of Museum Objects., ISIS Annual Report, Science Highlights CCLRC
- Kockelmann W., Kirfel A., Siano S. and Frost C. (2004a). Illuminating the Past: The Neutron as a Tool in Archaeology. *Physics Education* 39 (2), 155-165.
- Kockelmann W., Siano S. and Schreiner M.R. (2004b). Time-of-Flight Neutron Diffraction (Tof-Nd) for Characterising Archaeological Artefacts. In Siano S. (ed.), Studio E Conservazione Di Manufatti Archaeologici. Firenze: Nardini, 431-451.

- Krauskopf K. and Bird D. (1995). Introduction to Geochemistry. 3rd edn., Earth Science and Geology Series. New York: McGraw-Hill International Editions.
- Kunze E. (1958). Helme. Bericht Über Die Ausgrabungen in Olympia, VI, Winter 1953/1954 und 1954/1955. Berlin: Deutsches Archäologisches Institut, Verlag Walter de Gruyter & Co, 118-151.
- Kunze E. (1961). Korinthische Helme. Bericht Über Die Ausgrabungen in Olympia, VII, Frühjahre 1956 bis 1958. Berlin: Deutsches Archäologisches Institut, Verlag Walter de Gruyter & Co, 56-129.
- Kunze E. (1967). Helme. Bericht Über Die Ausgrabungen in Olympia, VIII, Herbst 1958 bis Sommer 1962. Berlin: Deutsches Archäologisches Institut, Verlag Walter de Gruyter & Co, 111-183.
- Kunze E. (1994). Chalkidische Helme IV-VII Mit Nachtägen Zu I Und II. Bericht Über Die Ausgrabungen in Olympia, IX, Herbst 1962 bis Frühjahr 1966. Berlin, New York: Deutsches Archäologisches Institut, Verlag Walter de Gruyter & Co, 27-100.
- Kunze J., Maurice V., Klein L.H., Strehblow H.H. and Marcus P. (2004). In Situ STM Study of the Duplex Passive Films Formed on Cu (111) and Cu (001) in 0.1 M NaOH. *Corrosion Science* 46 (1), 245-264.
- La Niece S. (1993). Silvering. In Craddock P.T. and La Niece S. (eds), Metal Plating and Patination : Cultural, Technical and Historical Developments. Oxford ; Boston: Butterworth-Heinemann, 201-210.
- Lai Y., Tong H. and Tu K. (2009). Recent Research Advances in Pb-Free Solders. *Microelectronics Reliability* 49 (3), 221-222.
- Lang J. (1997). Metals. In Lang J. and Middleton A. (eds), Radiography of Cultural Material. Oxford ; Boston, Mass: Butterworth-Heinemann, 33-59.
- Laskin A. and Cowin J.P. (2001). Automated Single-Particle SEM/EDX Analysis of Submicrometer Particles Down to 0.1 Mm. *Analytical Chemistry* 73 (5), 1023-1029.
- Laskin A., Cowin J.P. and Iedema M.J. (2006). Analysis of Individual Environmental Particles Using Modern Methods of Electron Microscopy and X-Ray Microanalysis. *Journal of Electron Spectroscopy and Related Phenomena* 150, 260-274.
- Laurila T., Vuorinen V. and Kivilahti J. (2005). Interfacial Reactions between Lead-Free Solders and Common Base Materials. *Materials Science and Engineering: R: Reports* 49 (1-2), 1-60.
- Laurila T., Hurtig J., Vuorinen V. and Kivilahti J. (2009). Effect of Ag, Fe, Au and Ni on the Growth Kinetics of Sn–Cu Intermetallic Compound Layers. *Microelectronics Reliability* 49 (3), 242-247.
- Lee H. and Chen M. (2002). Influence of Intermetallic Compounds on the Adhesive Strength of Solder Joints. *Materials Science & Engineering A* 333 (1-2), 24-34.
- Lee Y.G. and Duh J.G. (1999). Phase Analysis in the Solder Joint of Sn-Cu Solder/Imcs/Cu Substrate. *Materials Characterization* 42 (2-3), 143-160.
- Lin L.F., Chao C.Y. and Macdonald D. (1981). A Point Defect Model for Anodic Passive Films. II. Chemical Breakdown and Pit Initiation. *Journal of Electrochemical Society* 128 (6), 1194-1198.
- Liu P. and Shang J. (2005). Segregant-Induced Cavitation of Sn/Cu Reactive Interface. *Scripta Materialia* 53 (6), 631-634.

- Louer D. (2002). Laboratory X-Ray Powder Diffraction. Chapter 3. In David W.I.F., Shankland K., McCusker L.B. and Baerlocher C. (eds), Structure Determination from Powder Diffraction Data., International Union of Crystallography Texts on Crystallography 13. Oxford: Oxford Science Publications, 29-48.
- Macdonald D.D. and Urquidi-Macdonald M. (1990). Theory of Steady-State Passive Films. *Journal of Electrochemical Society* 137 (8), 2395-2402.
- Macdonald D.D. and Engelhardt G.M. (2010). Predictive Modelling of Corrosion. Chapter 2.39. In Cottis R.A., Graham J.M., Lindsay R., Lyon S.B., Richardson J.A., Scantlebury J.D. and Scott F.H. (eds), Shreir's Corrosion 4th edn., Vol. 2. Amsterdam: Elsevier, 1630-1679.
- Manti P. and Watkinson D. (2007). Examination of Greek Bronze Helmets: Sampling and Project Design. In Degrygn C., Van Langh R., Joosten I. and Ankersmit B. (eds), Metal 07, Proceedings of the ICOM-CC Metal Working Group International Triennial Meeting, Amsterdam, 17-21 September. Rijksmuseum, Amsterdam: Rijksmuseum, ICOM-CC, 78-82.
- Manti P. and Watkinson D. (2008). From Homer to Hoplite: Scientific Investigations of Greek Copper Alloy Helmets. Chapter 12. In Paipetis S.A. (ed.), Science and Technology in Homeric Epics, History of Mechanism and Machine Science, 6: Springer Science, 167-179.
- Markov I. (1996). Method for Evaluation of the Ehrlich-Schwoebel Barrier to Intelayer Transport in Metal Homoepitaxy. *Physical Review B* 54 (24), 17930-17937.
- Mattsson E. (1996). Basic Corrosion Technology for Scientists and Engineers. 2nd edn. London: Institute of Materials.
- McCrone W.C., Delly J.G. and McCrone L.B. (1978). Polarized Light Microscopy. Michigan: Ann Arbor Science.
- McCusker L.B. and Baerlocher C. (2002). Chemical Information and Intuition in Solving Crystal Structures Chapter 17. In David W.I.F., Shankland K., McCusker L.B. and Baerlocher C. (eds), Structure Determination from Powder Diffraction Data., International Union of Crystallography Texts on Crystallography 13. Oxford: Oxford Science Publications, 307-323.
- McNamara M. (2000). Technical Studies of Four Ancient Greek Helmets at Harvard University's Arts Museum. Paper delivered at *The 26th Annual Conference of the Association of North American Graduate Programs in Conservation*, S. Dillon Ripley Center, The Smithsonian Institution, 27-29 April 2000.
- Meeks N.D. (1986). Tin-Rich Surfaces on Bronze - Some Experimental and Archaeological Considerations. *Archaeometry* 28 (2), 133-162.
- Meeks N.D. (1987). Artefacts, Surfaces and the SEM. Recent Advances in the Conservation and Analysis of Artefacts, Jubilee Conservation Conference. University of London, Institute of Archaeology, 409-410.
- Meeks N.D. (1988). Backscattered Electron Imaging of Archaeological Material. In Olsen S.L. (ed.), Scanning Electron Microscopy in Archaeology, British Archaeological Reports Series, 452. Oxford, 23-44.
- Meeks N.D. (1993a). Patination Phenomena on Roman and Chinese High-Tin Bronze Mirrors and Other Artefacts. In Craddock P.T. and La Niece S. (eds), Metal Plating and Patination : Cultural, Technical and Historical Developments. Oxford ; Boston: Butterworth-Heinemann, 63-84.
- Meeks N.D. (1993b). Surface Characterization of Tinned Bronze, High-Tin Bronze, Tinned Iron and Arsenical Bronze. In Craddock P.T. and La Niece S. (eds), Metal Plating and Patination : Cultural, Technical and Historical Developments. Oxford ; Boston: Butterworth-Heinemann, 247-275.

- Merkel T.H., Groß H.J., Werner W., Dahlke T., Reicherter S., Beuchle G. and Eberle S.H. (2002). Copper Corrosion by-Product Release in Long-Term Stagnation Experiments. *Water Research* 36 (6), 1547-1555.
- Misailidou-Despotidou V. (2003). Copper Alloy Jewelry from the Archaic Period Cemeteries of Aghia Paraskevi and Nea Philadelphia, Macedonia, Greece. [Μισαηλίδου-Δεσποτίδου, Βάσω. Χάλκινα Κοσμήματα Αρχαϊκών Χρόνων Από Τη Μακεδονία: Έρευνα Στα Χάλκινα Κοσμήματα Των Νεκροταφείων Της Αγίας Παρασκευής Και Της Νέας Φιλαδέλφειας.] PhD thesis. Thessaloniki: Aristotle University of Thessaloniki, Department of History and Archaeology, School of Philosophy.
- Monaco H.L. and Artioli G. (2002). Experimental Methods in X-Ray and Neutron Crystallography. Chapter 5. In Giacobozzo C., Monaco H.L., Artioli G., Viterbo D., Ferraris G., Gilli G., Zanotti G. and Catti M. (eds), Fundamentals of Crystallography 2nd edn., International Union of Crystallography Texts on Crystallography 7. Oxford: Oxford University Press, 295-412.
- Moore E. and Fairbridge R. (eds.), (1997). Encyclopedia of European and Asian Regional Geology. Encyclopedia of Earth Sciences Series, London: Chapman & Hall.
- Mortimer C. and Stoney M. (1997). A Methodology for Punchmark Analyses Using Electron Microscopy. In Sinclair A., Slater E. and Gowlett J. (eds), Archaeological Sciences 1995 : Proceedings of a Conference on the Application of Scientific Techniques to the Study of Archaeology ; Liverpool, July 1995, Oxbow Monograph 64. Oxford: Oxbow Books, 119-122.
- Moustaka A. (2000). Peloponnisos and Macedonia. Observations on the So Called Illyrian Type Helmets. . Μύρτος: Studies in Memory of Ioulia Vokotopoulou. . Thessaloniki, 393-410. [Μουστάκα Α. (2000). Πελοπόννησος Και Μακεδονία. Παρατηρήσεις Στα Λεγόμενα Κράνη Ιλλυρικού Τύπου. Μύρτος: Μελέτες Στην Μνήμη Της Ιουλίας Βοκοτοπούλου. Θεσσαλονίκη, 393-410.].
- Muhly J.D. (1985). Sources of Tin and the Beginnings of Bronze Metallurgy. *American Journal of Archaeology* 89, 275-291.
- Muhly J.D. (1995). Lead Isotope Analysis and the Archaeologist. *Journal of Mediterranean Archaeology* 8 (1), 54-58.
- Nakajima H. (1997). The Discovery and Acceptance of the Kirkendall Effect: The Result of a Short Research Career. *JOM Journal of the Minerals, Metals and Materials Society* 49 (6), 15-19.
- NASA 'HEASARC Tools', <http://heasarc.gsfc.nasa.gov/cgi-bin/Tools/energyconv/energyConv.pl> (April, 2010).
- NIST 'X-Ray Attenuation and Absorption Data', The National Institute of Standards and Technology (NIST), Physics Laboratory <http://www.nist.gov/physlab/data/index.cfm> (April, 2010).
- Northover P. (1991). Analysis and Metallography of Greek Bronze Helmets (Gr2a.1893 and Gr2b.1893) at the Fitzwilliam Museum, Cambridge. Internal analyses report, Oxford: Oxford University, 5/3/1991.
- Oddy W.A. (1980). Gilding and Tinning in Anglo-Saxon England. In Oddy W.A. (ed.), Aspects of Early Metallurgy British Museum Occasional Papers, 17. London: Research Laboratory, The British Museum, 129-134.
- Oddy W.A. and Meeks N.D. (1982). Unusual Phenomena in the Corrosion of Ancient Bronzes. In Brommelle N.S. and Thomson G. (eds), Science and Technology in the Service of Conservation, Preprints of the contributions to the Washington Congress, 3-9 September

1982. London: International Institute for Conservation of Historic and Artistic Works, 119-124.
- Oddy W.A. and Bimson M. (1985). Tinned Bronze in Antiquity. In Miles G. and Pollard S. (eds), Lead and Tin: Studies in Conservation and Technology UKIC Occasional Papers, 3. London: The United Kingdom Institute for Conservation, 33-39.
- OIA (1997). Quantitative Analysis Topics Using ISIS Semquant in the Scanning Electron Microscope. Oxford: Oxford Instruments Plc.
- OIA (2005). ISIS Training Course Notes. Oxford: Oxford Instruments Analytical Ltd.
- Organ R. (1962). Are Analyses of Uncorroded Ancient Alloys Representative? *Studies in Conservation* 7, 48-55.
- Organ R. (1963). Aspects of Bronze Patina and Its Treatment. *Studies in Conservation* 8, 1-9.
- Palit A. and Pehkonen S. (2000). Copper Corrosion in Distribution Systems: Evaluation of a Homogeneous Cu₂O Film and a Natural Corrosion Scale as Corrosion Inhibitors. *Corrosion Science* 42 (10), 1801-1822.
- Panagiotis, *Personal Communication on 'Traditional Tinning, Materials and Methods in Practice'*. Thessaloniki: 2007.
- Pantos E., Tang C.C., Maclean E.J., Roberts M.A., Murphy B.M., Collins S.P., Cheung K.C., Strange R.W., Murphy L.M., Papiz M.Z., Girdwood S.E., Rizkallah P.J., Clarke D.T., Clark G.F., Tobin M.J., Colston S.L., Jupe A.C., Zhilin M.G., Prag K. and Prag A.J.N.W. (2002). Applications of Synchrotron Radiation to Archaeological Ceramics. In Kilikoglou V., Hein A. and Maniatis Y. (eds), Modern Trends in Scientific Studies on Ancient Ceramics, BAR International Series 1011, The 5th European Meeting on Ancient Ceramics, Athens 1999, 377-384.
- Pantos E., Kockelmann W., Chapon L., Lutterotti L., Bennet S., Tobin M., Mosselmans J., Pradell T., Salvado N., Butí S., Garner R. and Prag A. (2005). Neutron and X-Ray Characterisation of the Metallurgical Properties of a 7th Century BC Corinthian-Type Bronze Helmet. *Nuclear Instruments and Methods in Physics Research B: Beam Interactions with Materials and Atoms* 239, 16-26.
- Payer J., Ball G., Rickett B. and Kim H. (1995). Role of Transport Properties in Corrosion Product Growth. *Materials science & engineering. A, Structural materials: properties, microstructure and processing* 198 (1-2), 91-102.
- PDF02, (2005). Powder Diffraction Files Database 02, 2005 Release. The International Centre for Diffraction Data (ICDS)
- Peng W., Monlevade E. and Marques M. (2007). Effect of Thermal Aging on the Interfacial Structure of Snagcu Solder Joints on Cu. *Microelectronics Reliability* 47 (12), 2161-2168.
- Penhallurick R.D. (1986). Tin in Antiquity : Its Mining and Trade Throughout the Ancient World with Particular Reference to Cornwall. London: Institute of Metals.
- Pernicka E., Begemann F., Schmitt-Strecker S. and Grimanis A.P. (1990). On the Composition and Provenance of Metal Artefacts from Poliochni on Lemnos. *Oxford Journal of Archaeology* 9 (3), 263-298.
- Pernicka E. (1999). Trace Element Fingerprinting of Ancient Copper: A Guide to Technology or Provenance? In Young S.M.M., Pollard A.M., Budd P. and Ixer R.A. (eds), Metals in Antiquity, BAR International Series 792. Oxford: Archaeopress, 163-171.
- Petzow G. and Elssner G. (1985). Etching. In ASM (ed.), Metallography and Microstructures, Metals Handbook, Volume 9, 9th Edition. Ohio: American Society for Metals, 57-70.

- Petzow G. (1999). Metallographic Etching : Techniques for Metallography, Ceramography, Plastography. 2nd edn. Materials Park, Ohio: ASM International.
- Pflug H. (1988a). Griechische Helme Geometrischer Zeit. In Pflug H. (ed.), Antike Helme, Monographien Des Römisch-Germanischen Zentralmuseums Band 14. Mainz: Römisch-Germanischen Zentralmuseums 11-26.
- Pflug H. (1988b). Illyrische Helme. In Pflug H. (ed.), Antike Helme, Monographien Des Römisch-Germanischen Zentralmuseums Band 14. Mainz: Römisch-Germanischen Zentralmuseums 42-64.
- Pflug H. (1988c). Korinthische Helme. In Pflug H. (ed.), Antike Helme, Monographien Des Römisch-Germanischen Zentralmuseums Band 14. Mainz: Römisch-Germanischen Zentralmuseums 65-106.
- Pflug H. (1988d). Chalkidische Helme. In Pflug H. (ed.), Antike Helme, Monographien Des Römisch-Germanischen Zentralmuseums Band 14. Mainz: Römisch-Germanischen Zentralmuseums 137-150.
- Piccardo P., Mille B. and Robbiola L. (2007). Tin and Copper Oxides in Corroded Archaeological Bronzes. Chapter 14. In Dillmann P., Beranger G., Piccardo P. and Matthiesen H. (eds), Corrosion of Metallic Heritage Artefacts - Investigation, Conservation and Prediction for Long-Term Behaviour, EFC 48. Cambridge: Woodhead Publishing for the European Federation of Corrosion and The Institute of Materials, Minerals and Mining, 239-262.
- Pieraggi B. (2010). Defects and Transport in Oxides and Oxide Scales. Chapter 1.06. In Cottis R.A., Graham J.M., Lindsay R., Lyon S.B., Richardson J.A., Scantlebury J.D. and Scott F.H. (eds), Shreir's Corrosion 4th edn., Vol. 1. Amsterdam: Elsevier, 101-131.
- Politis (2005). Interview: Haviaras Lefteris the Last Tin-Smith, *Politis* (newspaper), May 24, Chios Island, Greece. [Πολίτης, 2005. Προσωπογραφία, Χαβιάρας Λευτέρης ο τελευταίος γανωματής. Εφημερίδα ΠΟΛΙΤΗΣ. Χίος, 24 Μαΐου 2005.].
- Porter D.A. and Easterling K.E. (1992). Phase Transformations in Metals and Alloys. 2nd edn. New York: CRC Press ; Taylor & Francis.
- Pourbaix M. (1977). Electrochemical Corrosion and Reduction. In Brown B.F., Burnett H.C., Chase T., Goodway M., Kruger J. and Pourbaix M. (eds), Corrosion and Metal Artifacts -- a Dialogue between Conservators and Archaeologists and, Corrosion Scientists Proceedings of a Seminar Held at the National Bureau of Standards, Gaithersburg, Maryland, March 17 -18 1976, Special Publication 479. Maryland: National Bureau of Standards, 1-16.
- Prakash K. and Sritharan T. (2001). Interface Reaction between Copper and Molten Tin–Lead Solders. *Acta Materialia* 49 (13), 2481-2489.
- Price J.W. (1983). Tin and Tin-Alloy Plating. Ayr, Scotland: Electrochemical Publications.
- Rapp G.J. (1999). Copper, Tin and Arsenic Sources in the Aegean Bronze Age. In Betahcourt P.P. and Al E. (eds), Meletemata IV: Studies in Aegean Archaeology Presented to Malchcolm H. Wrener as He Enters His 65th Year. Liège: University de Liège, 699-704.
- ImageJ. by Rasband W., National Institute of Mental Health, Bethesda, Maryland, USA (2008). Open Source Software. Download from <http://rsbweb.nih.gov/ij/>
- Reedy T.J. and Reedy C.L. (1988). Statistical Analysis in Art Conservation Research. Research in Conservation, 1. Marina del Rey, CA: The Getty Conservation Institute.
- Reyes-Gutiérrez L., Romero-Guzmán E., Cabral-Prieto A. and Rodríguez-Castillo R. (2007). Characterization of Chromium in Contaminated Soil Studied by SEM, Eds, Xrd and

- Mössbauer Spectroscopy. *Journal of Minerals & Materials Characterization & Engineering* 7 (1), 59-70.
- Ricksecker R.E. and Bower T.F. (1985). Copper and Copper Alloys. In ASM (ed.), Metallography and Microstructures, Metals Handbook, Volume 9, 9th Edition. Ohio: American Society for Metals, 399-414.
- Rinaldi R., Artioli G., Kockelmann W., Kirfel A. and Siano S. (2002). The Contribution of Neutron Scattering to Cultural Heritage Research. *Notiziario Neutroni* 7 (30), 30-38.
- Robbiola L., Fiaud C. and Pennec S. (1993). New Model of Outdoor Bronze Corrosion and Its Implications for Conservation. ICOM-CC 10th Triennial Meeting, Washington, D.C., USA, 22-27 August 1993 : preprints, Vol. 2. Paris: ICOM Committee for Conservation, 796-802.
- Robbiola L. and Hurtel L.-P. (1997). Standard Nature of the Passive Layers of Buried Archaeological Objects: The Example of Two Roman Half-Length Portraits. In Macleod I.D., Pennec S.L. and Robbiola L. (eds), Metal 95, Proceedings of the International Conference on Metals Conservation, Semur en Auxois, 25-28 Sept. 1995. London: James & James, 109-117.
- Robbiola L., Blengino J.-M. and Fiaud C. (1998a). Morphology and Mechanisms of Formation of Natural Patinas on Archaeological Cu-Sn Alloys. *Corrosion Science* 40 (12), 2083-2111.
- Robbiola L., Pereira N., Thaury K., Fiaud C. and Labbe J.-P. (1998b). Decuprification Phenomenon of Cu-Sn Alloys in Aqueous Solution in Nearly Neutral pH Conditions. In Mourey W. and Robbiola L. (eds), Metal 98 : Proceedings of the International Conference on Metals Conservation, Draguignan-Figanières, France, 27-29 May 1998. London: James & James, 136-144.
- Robbiola L., Vilbert D., Lejars T., Bourgarit D. and Mille B. (2001). Characterisation of a Buried Archaeological Bronze from the Celtic Tomb No. 1002 of La Fosse Cotheret (Roissy-En-France). Metal 2001 : Proceedings of the ICOM Committee for Conservation, Metals Working Group. London: James & James, 237-242.
- Robbiola L., Tran T., Dubot P., Majerus O. and Rahmouni K. (2008). Characterisation of Anodic Layers on Cu-10Sn Bronze (RDE) in Aerated NaCl Solution. *Corrosion Science* 50 (8), 2205-2215.
- Ryndina N. (2009). The Potential of Metallography in Investigations of Early Objects Made of Copper and Copper-Based Alloys. *Historical Metallurgy* 43 (1), 1-18.
- Sage M.M. (1996). Warfare in Ancient Greece: A Sourcebook. London and New York: Routledge.
- Samuels L.E. (1985). Mechanical Grinding, Abrasion, and Polishing. In ASM (ed.), Metallography and Microstructures, Metals Handbook, Volume 9, 9th Edition. Ohio: American Society for Metals, 33-47.
- Sands D. (1993). Introduction to Crystallography. New York: Dover Publications.
- Satovic D., Zulj L.V., Desnica V., Fazinic S. and Martinez S. (2009). Corrosion Evaluation and Surface Characterization of the Corrosion Product Layer Formed on Cu-6Sn Bronze in Aqueous Na₂SO₄ Solution. *Corrosion Science* 51, 1596-1603.
- Saunders N. and Miodownik A.P. (1990). Cu-Sn (Copper-Tin). In Massalski T.B. (ed.), Binary Alloy Phase Diagrams 2nd edn., Vol. 12. Ohio: American Society for Metals, 1481-1483.
- Schafer W., Jansen E., Skowronek R., Will G., Kockelmann W., Schmid W. and Tietze-Jaensch H. (1995). Setup and Use of the Rotax Instrument at ISIS as Angle-Dispersive

- Neutron Powder and Texture Diffractometer. *Nuclear Instruments and Methods in Physics Research Section A: Accelerators, Spectrometers, Detectors and Associated Equipment* 364, 179-185.
- Schifer W., Kockelmann W., Jansen E. and Will G. (1997). Comparative Diffraction Experiments Using Monochromatic and Pulsed White Neutrons. *Physica B: Condensed Matter* 234-236, 1090-1092.
- Scott D.A. (1985). Periodic Corrosion Phenomena in Bronze Antiquities. *Studies in Conservation* 30, 49-57.
- Scott D.A. (1988). SEM and Microprobe Analysis: Complementary Methods of Investigation. In Olsen S.L. (ed.), Scanning Electron Microscopy in Archaeology, 452, British Archaeological Reports. Oxford, 47-54.
- Scott D.A. and Podany J. (1990). Ancient Copper Alloys: Some Metallurgical and Technological Studies of Greek and Roman Bronzes. Small Bronze Sculpture from the Ancient World, Papers delivered at a Symposium organised and held at the J. Paul Getty Museum. Malibu, California: J. Paul Getty Museum, 31-60.
- Scott D.A. (1991). Metallography and Microstructure of Ancient and Historic Metals. Marina del Rey, CA: Getty Conservation Institute in association with Archetype Books.
- Scott D.A. (2002). Copper and Bronze in Art : Corrosion, Colorants, Conservation. Los Angeles: The Getty Conservation Institute.
- Scott J.F.D. and John G. (2010). Corrosion in Soils. Chapter 2.19. In Cottis R.A., Graham J.M., Lindsay R., Lyon S.B., Richardson J.A., Scantlebury J.D. and Scott F.H. (eds), Shreir's Corrosion 4th edn., Vol. 2. Amsterdam: Elsevier, 1149-1168.
- Shennan S. (1997). Quantifying Archaeology. 2nd edn. Edinburgh: Edinburgh University Press.
- Shoukang Z. and Tangkun H. (1993). Studies of Ancient Chinese Mirrors and Other Bronze Artefacts. In Craddock P.T. and La Niece S. (eds), Metal Plating and Patination : Cultural, Technical and Historical Developments. Oxford ; Boston: Butterworth-Heinemann, 50-62.
- Siano S., Kockelmann W., Bafile U., Celli M., Iozzo M., Miccio M., Moze O., Pini R., Salimbeni R. and Zoppi M. (2002). Quantitative Multiphase Analysis of Archaeological Bronzes by Neutron Diffraction. *Applied Physics A: Materials Science & Processing* 74[Suppl.], S1139– S1142.
- Siano S., Bartoli L., Zoppi M., Kockelmann W., Daymond M., Dann J.A., Garagnani M.G. and Miccio M. (2003). Microstructural Bronze Characterisation by Time of Flight Neutron Diffraction. In(ed. Associazione Italiana Di Metallurgia). Archaeometallurgy in Europe I, Vol. 2, 24-26 September 2003, Milan, Italy. Associazione Italiana di Metallurgia, 319-329.
- Siano S., Bartoli L., Kockelmann W., Zoppi M. and Miccio M. (2004a). ‘‘Neutron Metallography’’ of Archaeological Bronzes. *Physica B: Condensed Matter* 350, 123-126.
- Siano S., Miccio M., Marinis G.D., Bartoli L. and Kockelmann W. (2004b). Texture and Phase Analysis on Etruscan Metal Artefacts. *ISIS Experimental Report*.
- Siano S., Bartoli L., Santisteban J., Kockelmann W., Daymond M.R., Miccio M. and De Marinis G. (2006). Non-Destructive Investigation of Bronze Artefacts from the Marches National Museum of Archaeology Using Neutron Diffraction. *Archaeometry* 48 (1), 77-96.
- Sidot E., Souissi N., Bousselmi L., Triki E. and Robbiola L. (2006). Study of the Corrosion Behaviour of Cu–10Sn Bronze in Aerated Na₂SO₄ Aqueous Solution. *Corrosion Science* 48 (8), 2241-2257.

- Sismanidis K. (1987). The Archaic Cemetery of Aghia Paraskevi. Άμνητος. Volume to Honour the Contribution of Manolis Andronikos, Vol. B. Thessaloniki: Aristotle University of Thessaloniki, 787-803 [Σισμανίδης Κ. (1987). Το Αρχαϊκό Νεκροταφείο Της Αγίας Παρασκευής. Άμνητος. Τιμητικός Τόμος Για Τον Καθηγητή Μανόλη Ανδρόνικο, Τόμος β'. Θεσσαλονίκη: Αριστοτέλειο Πανεπιστήμιο Θεσσαλονίκης, 787-803].
- Sismanidis K. (1988). The Archaic Cemetery of Aghia Paraskevi. Macedonia from the Mycenaean Period to Alexander the Great. Thessaloniki: Archaeological Museum of Thessaloniki [Σισμανίδης Κ. (1988). Το Αρχαϊκό Νεκροταφείο Της Αγίας Παρασκευής. Η Μακεδονία Από Τα Μυκηναϊκά Χρόνια Ως Τον Μέγα Αλέξανδρο. Θεσσαλονίκη: Αρχαιολογικό Μουσείο Θεσσαλονίκης].
- Šmit Ž., Istenič J. and Knific T. (2008). Plating of Archaeological Metallic Objects—Studies by Differential PIXE. *Nuclear Instruments and Methods in Physics Research B* 266, 2329-2333.
- Smith C.S. (1972). Metallographic Examination of Some Fragments of Cretan Bronze Armor from Afrati. Early Cretan Armorers. (Appendix III). Mainz: Verlag Philipp von Zabern, 54-56.
- Snodgrass A.M. (1964). Early Greek Armour and Weapons: From the End of the Bronze Age to 600 B.C. Edinburgh: University Press.
- Snodgrass A.M. (1967). Arms and Armour of the Greeks. Aspects of Greek and Roman Life. London: Thames & Hudson.
- Snodgrass A.M. (1982). Narration and Allusion in Archaic Greek Art : A Lecture Delivered at New College Oxford, on 29th May, 1981. J.L. Myres Memorial Lecture 11th. London: Leopard's Head Press.
- Snodgrass A.M. (1998). Homer and the Artists : Text and Picture in Early Greek Art. Cambridge ; New York: Cambridge University Press.
- Sobue K., Sugahara A., Nakata T., Imai H. and Magaino S. (2003). Effect of Free Carbon Dioxide on Corrosion Behavior of Copper in Simulated Water. *Surface & Coatings Technology* 169, 662-665.
- Srivastava K., Bates R., Yankowski E., Div I. and Junction H. (1989). A Thermally Self-Cleaning Synthetic Flux System for Tinning Processes. Proceedings of the 39th Electronic Components Conference, 901-904.
- Stephens P.W., Cox D.E. and Fitch A.N. (2002). Synchrotron Radiation Powder Diffraction. Chapter 4. In David W.I.F., Shankland K., McCusker L.B. and Baerlocher C. (eds), Structure Determination from Powder Diffraction Data., International Union of Crystallography Texts on Crystallography 13. Oxford: Oxford Science Publications, 49-87.
- Stepniewska Z., Bucior K. and De Boodt M. (2001). Chromium and Its Forms in Soils in the Proximity of the Old Tannery Waste Lagoon. *International Agrophysics* 15, 121-124.
- Subramanian K. and Lee J. (2003). Physical Metallurgy in Lead-Free Electronic Solder Development. *JOM Journal of the Minerals, Metals and Materials Society* 55 (5), 26-32.
- Subramanian K. and Lee J. (2006). Effects of Internal Stresses on the Thermomechanical Behavior of Sn-Based Solder Joints. *Materials Science & Engineering A* 421 (1-2), 46-56.
- Suh J., Tu K., Lutsenko G. and Gusak A. (2008). Size Distribution and Morphology of Cu₆Sn₅ Scallops in Wetting Reaction between Molten Solder and Copper. *Acta Materialia* 56 (5), 1075-1083.

- Sunwoo A.J., Morris J.W.J. and Lucey K.J. (1991). Pre-Tinning and Flux Considerations on the Reliability of Solder Surface. The Harry Diamond Laboratories. The U.S. Army, Report DE-AC03-76F00098.
- Swaddling J. (1987). An Unusual Greek Bronze Helmet. *The Antiquaries Journal* 67 (LXVII), 348-351.
- Tatarkiewicz W. (2006). Ancient Aesthetics. ed. Harrell J., History of Aesthetics, 1: Continuum International Publishing Group.
- Taube M., Davenport A., King A. and Chase W.T. (1996). Selective Dissolution in Copper-Tin Alloys: Formation of Corrosion-Resistant Patina on Ancient Chinese Bronze Mirrors. In Materials Research Society (ed.), Spring Meeting of the Materials Research Society, 8-12 Apr 1996. San Francisco, CA: MRS
- Taube M., King A. and Chase W.T. (2008). Transformation of Ancient Chinese and Model Two-Phase Bronze Surfaces to Smooth Adherent Patinas. *Phase Transitions* 81 (2&3), 217-232.
- Theophilus, On Divers Arts. Translated by Hawthorne J.G. and Smith C.S.(1963) Chicago: The University of Chicago Press.
- Tietze-Jaensch H., Kockelmann W., Schmid W. and Will G. (1997). The ROTAX/DIFF Time-of-Flight Diffractometer at ISIS. *Physica B: Condensed Matter* 234-236, 1149-1151.
- Tu K.N. (1973). Interdiffusion and Reaction in Bimetallic Cu-Sn Thin Films. *Acta Metallurgica* 21 (4), 347-354.
- Tu K.N. and Thompson R.D. (1982). Kinetics of Interfacial Reaction in Bimetallic CuSn Thin Films. *Acta Metallurgica* 30 (5), 947-952.
- Tu K.N. (1996). Cu/Sn Interfacial Reactions: Thin-Film Case Versus Bulk Case. *Materials Chemistry & Physics* 46 (2-3), 217-223.
- Tu K.N. and Li J. (2005). Spontaneous Whisker Growth on Lead-Free Solder Finishes. *Materials Science & Engineering A* 409 (1-2), 131-139.
- Tu K.N. (2007). Solder Joint Technology. Materials, Properties, and Reliability. Springer Series in Materials Science 92. NY: Springer Science.
- Turgoose S. (1985). The Corrosion of Lead and Tin before and after Excavation. In Miles G. and Pollard S. (eds), Lead and Tin: Studies in Conservation and Technology UKIC Occasional Papers, 3. London: The United Kingdom Institute for Conservation, 15-26.
- Turgoose S. (1989). Corrosion and Structure: Modelling the Preservation Mechanisms. In Janaway R.C. and Scott B. (eds), Evidence Preserved in Corrosion Products: New Fields in Artifact Studies. Proceedings of a Joint Conference between UKIC Archaeology Section and the Council for British Archaeology Science Committee, Leeds 1983, UKIC Occasional Papers, 8. London: United Kingdom Institute for Conservation
- Tylecote R.F. (1979). The Effect of Soil Conditions on the Long-Term Corrosion of Tin-Bronze and Copper. *Journal of Archaeological Science* 6, 345-368.
- Tylecote R.F. (1985). The Apparent Tinning of Bronze Axes and Other Artefacts. *Journal of the Historical Metallurgy Society* 19 (2), 169-175.
- Tylecote R.F. (1992). A History of Metallurgy. 2nd edn. London: Institute of Materials.
- Untracht O. (1969). Metal Techniques for Craftsmen. A Basic Manual for Craftsmen on the Methods of Forming and Decorating Metals. London: Robert Hale.
- Van Wees H. (2004). Greek Warfare: Myths and Realities. London: Duckworth.

- Vander Voort G.F. (2004a). Metallography: An Introduction. In Vander Voort G.F. and American Society for Metals (eds), Metallography and Microstructures, Metals Handbook, Volume 9, 10th Edition. Ohio: ASM, 3-20.
- Vander Voort G.F. (2004b). Color Metallography. *Microscopy and Microanalysis* 10 (Supplement S02), 70-71
- Vander Voort G.F. (2004c). Introduction to Structures in Metals. In Vander Voort G.F. and American Society for Metals (eds), Metallography and Microstructures, Metals Handbook, Volume 9, 10th Edition. Ohio: ASM, 23-28.
- Vargas I.T., Alsina M.A., Pastén P.A. and Pizarro G.E. (2009). Influence of Solid Corrosion by-Products on the Consumption of Dissolved Oxygen in Copper Pipes. *Corrosion Science* 51 (5), 1030-1037.
- Vargas I.T., Pastén P.A. and Pizarro G.E. (2010). Empirical Model for Dissolved Oxygen Depletion During Corrosion of Drinking Water Copper Pipes. *Corrosion Science* 52 (7), 2250-2257.
- Varoufakis G.J. (1980). Metallurgical Investigation of the Bronze Crater of Derveni. In Oddy W.A. (ed.), Aspects of Early Metallurgy, British Museum Occasional Papers, 17. London: Research Laboratory, The British Museum, 71-86.
- Vickers M.J. (1981). Recent Acquisitions by the Ashmolean Museum. Archäologischer Anzeiger, Heft 4. Berlin: Deutsches Archäologisches Institut. Verlag Walter de Gruyter & Co, 541-561.
- Vickers M.J. (2002). Scythian and Thracian Antiquities in Oxford. Oxford: The Ashmolean Museum, Oxford University.
- Vokotopoulou I., Despoini A., Misailidou V. and Tiverios (1985). Sindos: Catalogue of the Exhibition. Thessaloniki: Archaeological Museum of Thessaloniki. [Βοκοτοπούλου I., Δεσποίνη Α., Μισσηλίδου Β. and Τιβέριος (1985). Σίνδος, Κατάλογος Της Έκθεσης. Θεσσαλονίκη: Αρχαιολογικό Μουσείο Θεσσαλονίκης.].
- Wang C., Lu B., Zuo J., Zhang S., Tan S., Suzuki M. and Chase W.T. (1995). Structural and Elemental Analysis on the Nanocrystalline SnO₂ in the Surface of Ancient Chinese Black Mirrors. *Nanostructured Materials* 5 (4), 489-496.
- Wang H., Gao F., Ma X. and Qian Y. (2006). Reactive Wetting of Solders on Cu and Cu₆Sn₅ / Cu₃Sn / Cu Substrates Using Wetting Balance. *Scripta Materialia* 55, 823–826
- Wang K.-K., Gan D., Hsieh K.-C. and Chiou S.-Y. (2009). The Microstructure of H'-Cu₆Sn₅ and Its Orientation Relationships with Cu in the Early Stage of Growth. *Thin Solid Films*, 1-34.
- Wang W., Wu D., Zhang Q., Wang L. and Tao M. (2010). pH-Dependence of Conduction Type in Cuprous Oxide Synthesized from Solution. *Journal of Applied Physics* 107 (12), 123717.
- Wang X. (2006). The Application of Neutron Diffraction to Engineering Problems. *JOM Journal of the Minerals, Metals and Materials Society* 58 (3), 52-57.
- Watson A., Kroupa A., Ipser H., Dinsdale A. and Vrestal J. (2007). Soldering On. *Materials World* (July), 32-33.
- Weeks L.R. (1999). Lead Isotope Analyses from Tell Abraq, United Arab Emirates: New Data Regarding the “Tin Problem” in Western Asia. *Antiquity* 73, 49-64.
- Weinberg K., Böhme T. and Müller W.H. (2009). Kirkendall Voids in the Intermetallic Layers of Solder Joints in MEMS. *Computational Materials Science* 45 (3), 827-831.

- Weisser T. (1975). The De-Alloying of Copper Alloys. In Leigh D. (ed.), Conservation in Archaeology and the Applied Arts. IIC Congress, Stockholm. London: International Institute for Conservation of Historic and Artistic Works, 207-214.
- Werner P.-E. (2002). Autoindexing. Chapter 7. In David W.I.F., Shankland K., McCusker L.B. and Baerlocher C. (eds), Structure Determination from Powder Diffraction Data., International Union of Crystallography Texts on Crystallography 13. Oxford: Oxford Science Publications, 118-135.
- Wessels T., Baerlocher C., McCusker L.B. and David W.I.F. (2002). Experimental Methods for Estimating the Relative Intensities of Overlapping Reflections. Chapter 9. In David W.I.F., Shankland K., McCusker L.B. and Baerlocher C. (eds), Structure Determination from Powder Diffraction Data., International Union of Crystallography Texts on Crystallography 13. Oxford: Oxford Science Publications, 162-178.
- Whitley J. (2006). Classical Art and Human Agency: A Tale of Two Objects in Fifth-Century Greece. In Stambolidis N.C. (ed.), Γενεθλιον: Αναμνηστικός Τόμος Για Την Συμπλήρωση Είκοσι Χρόνων Λειτουργίας Του Μουσείου Κυκλαδικής Τέχνης. Athens: N.P. Goulandris Museum, 227-236.
- Whitley J. (2008). Kalopodi. *The Classical Review* 58 (2), 576-579.
- Whitley J. (2011). Hybris and Nike: Victory and Commemoration in Panhellenic Sanctuaries. In Lambert S. (ed.), Sociable Man: Essays in Greek Social Behaviour in Honour of Nick Fisher. Swansea: Classical Press of Wales, 161-191.
- Wranglén G. (1972). An Introduction to Corrosion and Protection of Metals. Stockholm: Institut for Metallskydd.
- Wu C., Yu D., Law C. and Wang L. (2004). Properties of Lead-Free Solder Alloys with Rare Earth Element Additions. *Materials Science & Engineering R* 44 (1), 1-44.
- Yu D., Wu C., Law C., Wang L. and Lai J. (2005). Intermetallic Compounds Growth between Sn-3.5 Ag Lead-Free Solder and Cu Substrate by Dipping Method. *Journal of Alloys and Compounds* 392 (1-2), 192-199.
- Yu J. and Kim J. (2008). Effects of Residual S on Kirkendall Void Formation at Cu/Sn-3.5 Ag Solder Joints. *Acta Materialia* 56 (19), 5512-5521.
- Zivkovic D. (2007). Preface. *Journal of Mining and Metallurgy B: Metallurgy* 43 (2).
- Zou H., Yang H. and Zhang Z. (2008). Morphologies, Orientation Relationships and Evolution of Cu₆Sn₅ Grains Formed between Molten Sn and Cu Single Crystals. *Acta Materialia* 56, 2649-2662.
- Ομήρου Ιλιάδα, Translated by Καζαντζάκης N. and Κακρίδης Ι.Θ. Αθήνα: Βιβλιοπωλείον της Εστίας.



APPENDICES

APPENDIX 1. DETAILS OF INVESTIGATED HELMETS

Figures in this appendix have been removed
for copyright reasons

A.1.1. ILLYRIAN

ILLYRIAN EARLY PHASE (I)

Helmet Code: OL4

Olympia, B3348, DAI Excavations

Helmet description: With single ridge crest-track and straight back (no distinct neckguard). Raised ridge and row of rivet holes run around the edge of the helmet.

ILLYRIAN MIDDLE PHASE (II)

Helmet Code: AP4

Archaeological Museum Thessaloniki M016405.

Helmet description: With double-ridged crest-track and plain strip gold foil decoration on the forehead below a horizontal ridge. Relatively large headed rivets around the edge. With hole at the forehead, pair of holes at the rear above the neckguard, and at the edge of the cheekpieces. In good condition, with some losses at the neckguard. Cleaned, with adhered fragments. The gold foil seems to be adhered with adhesive in its original position, with the perpendicular gold strips missing.

Helmet Code: AP5

Archaeological Museum Thessaloniki M016423.

Helmet description: With triple-ridged crest-track and dome-headed rivets around the edge band which has raised ridge. Tool marks on the edge band. Holes at the edge of the cheekpieces, punched from the inner side. A rectangular shaped (in cross section) hook is on the forehead, and two double holes in rhomboid arrangement appear at the rear above the neckguard. The helmet has ancient restoration: metal fragments which are mechanically attached onto the helmet with flat-headed rivets (near ear-notch). In good condition, with minor losses at the back and lower part of the crown and the neckguard. Some loose fragments do not seem to be part of the same object.

Helmet Code: PE2

Archontiko, Pella, 2002, Western Cemetery, Grave 194

Helmet description: With high ridge and other smaller ridges at the crest-track; pointy gusset on the sides; row of rivets and low-raised ridge run around the edge of the helmet. Gold leaf decoration was adhered on the helmet with organic adhesive before burial. Adhesive covers holes at the edge of each cheekpiece. With fine corrosion and severe mechanically damage at back and crown.

ILLYRIAN LATE PHASE (III)

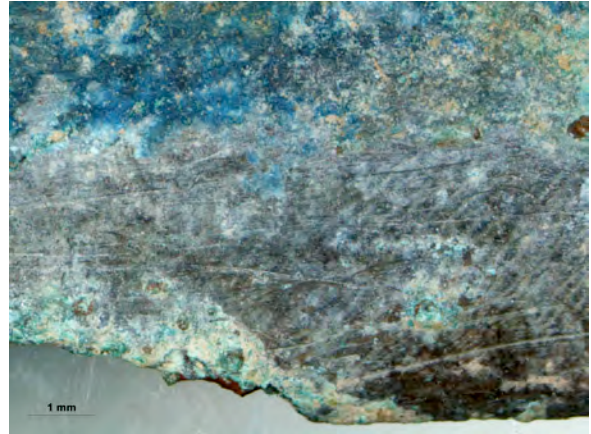
Group IIIA1 (with rivets at the rim)

Helmet Code: OL11

Olympia, B7170

Helmet description: Remains of open faced helmet, most likely of the Illyrian type. With remains of fine rivets and solid ridge running across along the remaining part of the forehead; relatively high pointy side gusset. With green patina, most likely cleaned in the past; with hard-wax reinforcement on the inner side. The crown and parts of the cheekpieces are missing.

Helmet Code: PE1



Archontiko, Pella 2001, Western Cemetery, Grave 10

Helmet description: With double-ridged crest-track; pointy gusset on the sides which reaches deep into the helmet. Row of rivets with rounded heads run along the edge; hole at the edge of each of the pointy cheekpieces, which curve slightly outwards. Very thin helmet. In good condition with some material losses, but fine patina preserved. In areas of the neckguard, the surface appears grey/silver coloured, most likely tinned.

Helmet Code: OL5

Olympia, B4821

Helmet description: With double-ridged crest-track; very pointy gusset on the sides which reaches deep into the helmet. Row of fine rivets runs along the edge; hole at the edge of each of the pointy cheekpieces, which curve slightly outwards. Very thin helmet. Rivet in the middle of the forehead. In good condition with some material losses at the back. With finely preserved localised surface, which appears highly polished and grey in colour. No evidence of conservation treatment

Helmet Code: OL9

Olympia B5115

Helmet description: With ridged crest-track; very pointy gusset on the sides which reaches deep into the helmet. Row of fine rivets runs along the edge; hole at the edge of each of the pointy cheekpieces, which curve slightly outwards. Very thin helmet. Large rivet in the middle of the forehead. In good condition with some material losses at crest-track and cheekpieces. With fine green and blue corrosion patina. No evidence of conservation treatment.

Helmet Code: PE3

Archontiko, Pella, 2001, Western Cemetery, Grave 9

Helmet description: With low double-ridge crest-track, with pointy gusset on the sides. The ridge near the row of rivets along the edge is not raised from the inside; remains of a nail in the middle of the forehead.

Helmet Code: S9

Archaeological Museum Thessaloniki M08563, Sindos Excavations

Helmet description: With ridged crest-track; very pointy gusset on the sides which reaches deep into the helmet (Λ -shape). Row of fine rivets runs along the edge; hole at the edge of each of the slightly rounded cheekpieces. Forehead is gap-filled. Severely corroded, treated helmet.

Helmet Code: FZ2

The Fitzwilliam Museum Cambridge, GR.B.5

Helmet description: With high double-ridged crest-track, which is positioned unevenly towards the forehead (right side is 5cm and left 4.3cm from the edge of the forehead). Holes at the edges of cheek-pieces. The rim around the edge carries impressions of small rivets. The rivet on the forehead is missing its head, whilst a hook is attached at the back below the crest-track. In generally good condition with some mechanical damage and losses at crest-track. Cleaned in the past, dark effect on surface, highly polished.

A.1.1.3. ILLYRIAN LATE PHASE (III)

Group IIIA2 (with punched decorative rivets at the rim)

Helmet Code: AP6

Archaeological Museum Thessaloniki M016603. Aghia Paraskevi Excavations

Helmet description: With single-ridged crest-track and punched impressions of rivets around the straight edge. The neckguard is very small and the forehead rather high. With double holes on the upper part of the forehead and double holes below the crest-track at the rear, imprint of a rectangular attachment near the holes, which is now missing. There is no hole at the edges of the cheekpieces. In good condition, with uniform fine green corrosion overlying a red corrosion layer and localised active corrosion. A fragment of the neckguard is detached and the area is gap-filled.

Helmet Code: NF5

Archaeological Museum Thessaloniki M023115. Nea Philadelphia Excavations

Helmet description: With single low-ridged crest-track and short neckguard. The ends of the cheekpieces are very pointed. Punched small circles decorate the edge around the helmet. A hole at the edge of each cheekpiece was punched from the inside. With residues of solder at the back above the neckguard, where a fitting for the attachment of the crest would have been. Treated, intensively cleaned, with black surface; some material loss and fractures at the forehead and the right cheekpiece.

A.1.1.3. ILLYRIAN LATE PHASE (III)

Group IIIA3 (with smooth rim, no rivets)

Helmet Code: OL13

Olympia, BE58

Helmet description: With single-ridge crest-track, small straight neckguard and pointy cheekpieces with holes at their corners. Pointy gusset at the side. With straight rim lacking apparent decoration apart from a slight ridge at the edge. Rivet hole in the middle of forehead. With losses at the right cheekpiece and crest-track.

Helmet Code: AP1

Archaeological Museum Thessaloniki M09119. Aghia Paraskevi Excavations

Helmet description: With low double-ridged crest-track, very pointed cheekpieces and relatively high neckguard. The edge is punched from the inner side. With nail holes at the edge of the cheekpieces. Two iron nails at the centre of the forehead, one taller than the other. With closed-hook at the rear above the neckguard. Remarkably heavy, complete, with laminating corrosion perpendicular to the edge of the helmet.

Helmet Code: S1

Archaeological Museum Thessaloniki M08561. Sindos Excavations

Helmet description: extraordinary thick helmet with thick surface deposits and mineralised organics. With high double-ridged crest-track. Gold leaf decoration is adhered around the face opening. With closed-hook at the rear above the neckguard. The helmet is intact

Helmet Code: NMW10

National Museum Wales 47.409_cat27

Helmet description: With single-ridge crest-track, small straight neckguard and pointy cheekpieces; straight edge lacking apparent decoration. Rivet hole in the middle of forehead. In good condition, minor fracture at neckguard and undisturbed corrosion on surface.

A.1.1.3. ILLYRIAN LATE PHASE (III)

Group IIB1

Helmet Code: OL78

Olympia, B4667

Helmet description: With ear openings influenced by the Chalkidian type. The cheekpieces carry repoussé decoration of a ram, hammered from the inside. With ridge around the rim and rivets holes; rivets are now missing. High double-ridged crest-track. Some material is lost, but in generally good condition, with smooth corrosion patina (green, blue). Conservation interventions on the inner side.

A.1.2. CORINTHIAN

CORINTHIAN EARLY PHASE (I)

Helmet Code: NMW6

National Museum Wales, 47.409_7.40

Description: Large helmet with straight contours and round crown. Cheekpieces and neckguard are slightly distinguished by a small step on the sides towards the neckguard; thin nose-guard. With relatively large holes around the edge. The crown is considerably thinner due to hammering. Cuttings near the ears are made from the inner side and is a deliberate damage. Mechanical damages at crown; dark green and black corrosion on the outer surface. Helmet most likely cleaned.

Helmet Code: NMW11

National Museum Wales, 47.409_cat36

Description: No visual separation between the cheekpieces and the neckguard; large eye openings and rivet holes around the edge; round shape with substantial crown, and tight face opening. Nail in the middle of the forehead. Minor mechanical damages at crown and rear; green corrosion on the outer surface.

Helmet Code: NMW5

National Museum Wales, 47.409_7.39

Description: Large helmet with rounded outline, and a slight kink at the lower part of the crown; cheekpieces are slightly separated from the neckguard by a slight step (towards the neckguard). With holes around the edge, and hammered noseguard which is now missing. The cheekpieces were bent, a sign of its deposition at a sanctuary. Mechanical damages at crown.

Helmet Code: OL21

Olympia, ab64

Description: Part of Corinthian helmet with hammered thin noseguard and small perpendicular neckguard. Part of the helmet is missing. Fine corrosion on surface, most likely cleaned mechanically.

Helmet Code: OL17

Olympia, ab34

Description: Curvy profile and round crown; distinction between the cheekpieces and neckguard (which slightly curves outwards) is made by a small pointy side gusset situated towards the neckguard. Eye-openings are roundish. With holes around the edge of the helmet, and a thin noseguard part of which is missing. Crown is very thin due to hammering. Part of left cheekpiece is missing. With fine green patina.

Helmet Code: OL31

Olympia, B2648

Description: Tall round crown, almost straight sides and small neckguard curving slightly upwards; distinction between the cheekpieces and neckguard is made by a small side curve situated slightly towards the neckguard. Eye-openings are roundish. With holes around the edge of the helmet and thin noseguard part of which is missing. Hook at the top of the crown. Part of right cheekpiece is missing. With fine dark green patina and high polish. Conservation supports at the inner side.

Helmet Code: OL41

Olympia, B10534

Description: Tall round crown, almost straight sides and small neckguard curving slightly upwards; distinction between the cheekpieces and neckguard is made by a small side gusset/step, situated slightly towards the neckguard. Eye-openings are roundish. With holes around the edge of the helmet and thin noseguard part of which is missing. A hook is on the top of the crown and two holes above the neckguard for crest support. Part of right cheekpiece is missing. With fine green patina and high polish.

Helmet Code: OL29

Olympia, B2608

Description: Relatively straight profile and round tall crown; tight face opening and large eye-openings. With small side gusset in the middle of the side separating the cheekpieces from a small neckguard. Holes around the edge of the helmet with large gaps between them. In good condition, some mechanical damage at the crown, green corrosion.

Helmet Code: NMW2

National Museum Wales, 47.409_7.26

Description: Unusually small size helmet, remarkably heavy, with cheekpieces intentionally cut. Punched decoration with double row of rivet-impressions around the edge. The neckguard is not uniformly shaped and curved outwards. Severely restored helmet with soldered neckguard and broken edges at cheekpieces. The helmet must have been re-patinated, as signs of soldering are not obvious with visual observation.

WITH CREST-TRACK AND EMBRYONIC NOSEGUARD

Helmet Code: NMW4

National Museum Wales, 47.409_7.36

Description: Corinthian type helmet with double-ridged crest-track and embryonic nose-guard. With straight contour profile, round tall crown and no obvious visual separation between the cheekpieces and neckguard. With decorative ridge around the edge, rivet hole to support crest and cheekpieces bent in antiquity. In good condition with minor mechanical damages and green/dark green corrosion.

Helmet Code: OL69

Olympia, B10527

Description: Corinthian type helmet with low double-ridged crest-track and embryonic nose-guard. Slightly curved profile, round tall crown, very short nose-guard and a slight step (situated closer to the neck-guard) separating the cheek-pieces and neck-guard. With decorative ridge around the edge, relatively large round holes at the front centre of each cheek-piece and two holes to support crest. In good condition with some material losses and green, brown/red corrosion.

CORINTHIAN MIDDLE PHASE (II)

Helmet Code: NMW3

National Museum Wales, 47.409_7.33

Description: With curvy outline and round crown; rivet holes around the edge and small stepped gap on the sides towards the rear. With thin nose-guard part of which is missing, and half a right cheek-piece; both were originally bent. Holes separated by wide gaps run around the edge. Green corrosion and other deposits on outer surface, with some mechanical damage and material loss.

Helmet Code: NMW7

National Museum Wales, 47.409_7.41

Description: Relatively thin rounded helmet with a slight distinction between crown and neckguard. With small pointed gussets on the side; fine rivet holes around the edge and a pair of small holes on the top of the crown. Missing noseguard and rectangular nail hole in the centre of the neckguard, evidence for its deposition in a sanctuary. Black corrosion patina, helmet is restored.

Helmet Code: NMW8

National Museum Wales, 47.409_7.42

Description: Rounded in shape, with complete thick stepped noseguard; small pointy side gusset; rivet holes around the edges, which are not uniformly distributed. Some mechanical damage and distortion of left side, losses on crown and flaking corrosion.

Helmet Code: OL44

Olympia, B7073

Description: Relatively thin rounded helmet with a distinction between crown and neckguard, produced by a curve above a larger than average neckguard. With small pointed gussets on the side; holes around the edge. Missing noseguard. Dark green corrosion patina of high polish.

Helmet Code: OL46

Olympia, B1501

Description: Round crown, small pointy side gusset centred between the curvy neckguard and cheekpieces, and substantial noseguard. Fine rivet stems around the edge. Helmet complete but distorted, with green and dark green corrosion and other deposits.

Helmet Code: OL57

Olympia, B10526

Description: With round crown which has slight kink in its lower part; side gusset in the middle of the side of the helmet, curvy neckguard and substantial nose-guard. Fine rivet stems around the edge. Helmet with missing fragments, with green and dark green corrosion; treated.

Helmet Code: OL49

Olympia, B4411

Description: Outline curvy in profile forming a noticeable, small neckguard and side gussets at the middle of each side. The cheekpieces are pointy, the nose-guard thick, eye-openings are almond-shaped; a slight bulge runs around the very edge of the helmet. With green and blue corrosion and areas of gap-filling.

Helmet Code: OL75

Olympia, B5178

Description: With curvy profile defining the crown, small neckguard and side gussets in the middle of each side, between each pointy cheekpiece and the curved neckguard. Almond-shaped eye-openings and thick, narrow noseguard; a slight bulge runs around the very edge of the helmet. With dark green and black corrosion.

Helmet Code: OL50

Olympia, B4698

Description: With curvy profile, small neckguard and side gussets centred between the pointy cheekpieces and the small curved neckguard. Thick but narrow noseguard; a bulge runs around the very edge of the helmet. With green and blue corrosion and areas of gap-filling on crown which is mechanically damaged.

Helmet Code: OL53

Olympia, B6550

Description: With curvy profile and slight kink, but heavily deformed and restored. Side gussets towards the middle of each side. With green corrosion and large areas of gap-filling on crown and rear.

Helmet Code: PR1

Pitt Rivers Museum, 1884.32.16

Description: With slight kink at the base of the crown ending at a V at the forehead area. Thick solid nose-guard and bulged edges around the eye-openings; curved neck-guard; hole at the top of crown. Mechanical damage and losses, severely restored, fragments are soldered on the crown.

MYROS GROUP

Helmet Code: OL27

Olympia, B9805

Description: Part of half severely corroded helmet with decoration around the rim and small stepped gap on the side between cheekpiece and the very small neckguard. On the cheekpiece, a grey fine surface is preserved between areas of voluminous corrosion.

Helmet Code: OL65

Olympia, B6131

Description: Thick helmet with round crown and side step separating the cheekpieces from the neckguard. Decoration around the rim. Noseguard was bent upwards in antiquity. With green voluminous corrosion and areas of fine grey surface. Some areas are gap-filled.

Helmet Code: OL80

Olympia, B6960

Description: Round crown, wide eye-openings and straight cheekpieces. With side step separating the cheekpieces from the neckguard; of substantial thickness throughout; decoration around the rim. With green voluminous corrosion and areas where a fine grey surface is preserved.

Helmet Code: OL58

Olympia, B10528

Description: With round and distinct crown, curvy profile and stepped gaps on each side between cheekpiece and the small neckguard. Substantially thick nose-guard and area near the eye-openings; decoration around the edge. Deformed by mechanical damage and losses at the back of the crown; with green corrosion on the surface.

Helmet Code: NM1

National Museum Wales, 47.409_7.24

Description: With decoration around the edge; has solid, relatively thick noseguard which is perhaps cast. A short neckguard is separated from the cheekpieces with a slight step on the side, situated slightly towards the back. The crown is considerably thinner than the rest of the helmet. The cheekpieces were initially bent, evidence of its deposition at a sanctuary in antiquity. In generally good condition, with minor mechanical damage at crown. With black patina in many areas and cream coloured encrustations over green corroded areas.

Helmet Code: NM9

National Museum Wales, NMGW_877

Description: Rounded in shape, with long, thick, relatively narrow noseguard and decoration around the edges. The crown is visually separated from the neckguard due to its curvy shape; a slightly pointy gusset on the sides. The cheekpieces were originally bent. Mechanical damage and material losses at crown. Black patina and fine green corrosion layer.

CORINTHIAN WITH CREST-TRACK

Helmet Code: OL_B10518

Olympia, B10518

Description: Corinthian type helmet with crest-track and a large decorative hole centred at the front of each cheekpiece. Very solid helmet, with thick noseguard and cast decoration around the edge. In excellent condition (intact), with fine surface corrosion.

Helmet Code: OL68

Olympia, B4150

Description: Part of half helmet with crest-track and large decorative hole centred at the front of the cheekpiece. Very solid helmet, with thick noseguard and decoration around the edge. Corrosion was removed during cleaning.

CORINTHIAN LATE PHASE (III)

Helmet Code: OL63

Olympia, B5177

Description: With distinct, slightly oval shaped crown, which is plastically defined by a slight kink leading to an Λ -shaped feature on the forehead, where there is an engraved lotus flower decoration. Mechanical damage and distorted shape. With long narrow noseguard, and decoration around the helmet. Losses and mechanical damage concentrate at the crown and rear where the metal is thinner; with fine green corrosion.

Helmet Code: OL74

Olympia, B5176

Description: With distinct, slightly oval shaped crown, visually separated from the rest of the helmet by a slight kink leading to an Λ -shaped feature on the forehead. With very pointy cheekpieces, almond-shaped eye-openings and small face opening; long, thick, narrow noseguard with bulge at the very edge which continues around the helmet. With small pointy gusset centred between each cheekpiece and the neckguard. In good condition, some losses and mechanical damage at the crown and rear where the metal is thinner; with fine blue and green corrosion.

Helmet Code: OL71

Olympia, B5070

Description: With distinct, egg-shaped crown, visually separated from the rest of the helmet by a kink leading to an Λ -shaped feature on the forehead, above which a decorative bird is engraved. With very pointy cheekpieces, almond-shaped eye-openings; long, and narrow noseguard with small bulge at the very edge which continues around the helmet. With small pointy gusset centred between each cheekpiece and the neckguard and engraved floral decoration just above them. In good condition, some losses and mechanical damage at the back where the metal is thinner; with fine dark green and green corrosion.

Helmet Code: OL73

Olympia, B5167

Description: With distinct, egg-shaped crown, visually separated from the rest of the helmet by a kink leading to an Λ -shaped feature on the forehead. With very pointy cheekpieces, almond-shaped eye-openings; long, thick, narrow noseguard with bulge at the very edge which continues around the helmet. With small pointy gusset in the centre of each side. In good condition, some losses and mechanical damages at the back where the metal is thinner; with fine dark green and green corrosion.

Helmet Code: OL70**Olympia, B4799**

Description: With relatively short crown, visually separated from the rest of the helmet by a kink leading to an V-shaped feature on the forehead, below which there are raised decorative spirals and impressions of eyebrows. With small neckguard, very straight cheekpieces and small face opening; the noseguard is missing. A very small pointy gusset is at the centre of each side between cheekpiece and neckguard. In good condition, some losses and mechanical damage at the neckguard and the crown where the metal is thinner; with fine blue and green corrosion.

A.1.3. ATTIC**Helmet Code: PE4****Archontiko, Pella, 2002, Western Cemetery, Grave 189**

Description: Attic helmet with round crown, generally curvy contours and neckguard. With wide gusset at the sides between cheekpiece and neckguard. With small bulge at the edge of the forehead. In good condition, with fine green corrosion.

A.1.4. CHALKIDIAN

Helmet Code: OL79

Olympia, B5239

Description: Chalkidian type helmet (most likely Type III) with impressions of ears where ear-openings are normally found and small noseguard. Each cheekpiece is hammered from the inside and shaped into a ram's head, with its mouth forming the end of the cheekpiece. The crown is visually separated with a defined kink/step from the rest of the helmet and has a small perpendicular neckguard. With physical damage at the crown neckguard and cheekpieces (part of left cheekpiece missing), where the metal is the thinnest. With dark green, green and blue corrosion.

Helmet Code: OL66

Olympia, B7080

Description: Chalkidian type helmet (Type V) with cheekpieces (now missing) hinged to the helmet. With large ear-openings and small noseguard typical of this type. The crown is visually separated from the rest of the helmet with a kink/step leading to an Λ -shaped feature on the forehead. Severely damaged at the crown where the metal is thin (part of it is missing); with dark green, green and blue corrosion.

A.1.5. ETRUSCAN

Helmet Code: PR4

Pitt Rivers Museum, Oxford, 1884.32.15

Description: Etruscan helmet of typical shape. In excellent condition apart from minor material loss at one side. The helmet was treated and areas were most likely over-painted or patinated in modern times.

APPENDIX 2. A NOTE ON RESULTS OF MODEL TINNING

THE PRESENCE OF KIRKENDALL VOIDS IN ANNEALED TOKENS

Wipe-tinned copper samples S11, S13, S15 in this experiment showed the formation of voids situated at the η -Cu₆Sn₅/Sn interface and in the δ for sample S19. These so-called Kirkendall voids (or porosity) are associated with atomic vacancy diffusion phenomena at diffusion couples where the diffusion rates of the two species are very different (Nakajima, 1997), like in the case of Cu and Sn. During vacancy atomic diffusion processes, the jumping of atoms into vacant sites in the lattice is expressed by a net flux of atoms in one direction which causes an equal net flux of vacancies in the opposite direction (Porter and Easterling, 1992: 83). When the diffusion rates of the migrating species are substantially different, as is the case with Cu and Sn, one side of the diffusion couple loses mass (volume reduction) because atoms diffuse out faster than they are replaced by atoms diffusing in the opposite direction; the other side gains in mass (Abbaschian *et al.*, 2010: 355; 356). Because not all vacancies are extinguished during this process, some coalesce together at dislocations of the crystal lattice and form voids (Porter and Easterling, 1992: 83)89). This phenomenon was first observed by Kirkendall and is named after him.

The formation, size and location of Kirkendall voids depends on applied temperatures (Laurila *et al.*, 2005), length of application (Peng *et al.*, 2007) and the presence of additional elements and impurities in the alloy (Wu *et al.*, 2004; Liu and Shang, 2005; Laurila *et al.*, 2009). In any given diffusion couple, as a rule of thumb, atoms with the lower melting point diffuse faster and are said to have a higher diffusion coefficient (D). The exact value of D varies with the composition of the alloy in addition to being temperature-dependant (Porter and Easterling, 1992: 83)86; 89). Diffusion coefficients of Cu and Sn are different at different

temperatures and in different phases; therefore, the formation and nature of Kirkendall voids is expected to be different within different experimental systems.

In the Cu-Sn diffusion system, published diffusion coefficients vary and details of diffusion in this system are yet to be understood. Voids are reported to be mainly formed in the IMC layers or at the Cu/IMC interface (Subramanian and Lee, 2003). They are reported at the Cu/ ϵ interface or in the ϵ -Cu₃Sn matrix for aging below reflow temperatures (150°C) (Peng *et al.*, 2007) although they are also observed at the η -Cu₆Sn₅/Sn interface (Subramanian and Lee, 2003). Their number generally increases with temperature (Peng *et al.*, 2007), whilst at later stages of annealing, the number of smaller voids decreases and the bigger voids are reported to grow at the expense of the smaller ones (Weinberg *et al.*, 2009). Vacancy diffusion generates stresses at the diffusion interface (Tu and Li, 2005) and Kirkendall porosity becomes detrimental to the mechanical properties of IMC layers causing reliability problems in solders used in the electronics industry (Lee and Chen, 2002; Subramanian and Lee, 2006; Yu and Kim, 2008; Weinberg *et al.*, 2009).

In this experiment, in contrast to annealed tinned copper substrates, where the presence of Kirkendall voids was extensive (S11, S13, S15, S19), annealing of the tinned bronze tokens only resulted in producing a reduced number of small Kirkendall voids at the ϵ -Cu₃Sn/ η -Cu₆Sn₅ interface of B7. This again can be attributed to the slower diffusion rate of Cu from the bronze, which allows more Cu to be available for the formation of ϵ -Cu₃Sn at the diffusion interface and limits extensive formation of Kirkendall voids at the diffusion zone. Similarly to the reliability problems that Kirkendall voids introduce to solders in electronics industry, the potential presence of extensive voids in tinning coatings on archaeological bronzes may have influenced survival of archaeological tinning layers. The extreme presence of voids may have introduced stresses between IMC layers in antiquity, and this may have led to the mechanical detachment of outer layers due to crude surface polishing or other treatments. Alternatively, it may also have affected corrosion processes of these layers during the burial.

THE PRESENCE OF AN UNUSUAL PHASE IN ANNEALED WIPE-TINNED COPPER TOKENS

An unusual phase not previously reported in the literature is observed on sample S13: a number of small 'islands' of a different phase that has an average atomic number closer to copper (based on BSE colour density) is present in the tin matrix near the top part of the η -

Cu₆Sn₅ phase (S13). Spot EDX analysis shows that this is a low-tin bronze. Similar low-tin bronze ‘islands’ are also present in areas at the bottom of the long crystals seen in S15 near the voids at the η -Cu₆Sn₅ /Sn interface (S15). Although this could be an artefact of preferred crystal orientation, which could be visible as a difference in backscattering in the BSE images, an alternative hypothesis is proposed below.

This feature may be a result of localised fluctuations in diffusion within the melt during growth of IMC phases. S11 and S15 exhibit long thin angular crystals of η -Cu₆Sn₅ in the Sn matrix. Such rod- or whisker-shaped η -Cu₆Sn₅ in the tin matrix is reported to form by reaction of Sn with Cu that becomes available at the top of the η -Cu₆Sn₅ scallops. It is suggested that η -Cu₆Sn₅ are formed because the phase is forced to elongate into whisker shapes due to a gradual reduction in the available copper in the melt (Gagliano and Fine 2001, fig.2; Laurila *et al.* 2005 fig.4). However, in this experiment whiskers are observed in samples with the thickest coating layers (S11, 85-95 μ m; S15, 230-240 μ m; Table 4.1) making this a very unlikely explanation. Suh *et al.* (2008) suggest that copper atoms at the bottom of the η -Cu₆Sn₅ scallops can be distributed only between the nearest scallops inevitably contributing in the growth of the thickness of η -Cu₆Sn₅ scallops. Atoms located in the upper part of the scallops can find their way to any scallop because they have enough time to migrate within the solder before attaching to some other scallops (Suh *et al.*, 2008). It is further likely that during this process a small amount of excess copper over the equilibrium solubility is present in the liquid tin beyond the growing η -Cu₆Sn₅ scallops (Gagliano and Fine, 2001). The unusual phase present in samples S13 and S15 can support this theory where a small amount of excess copper over its equilibrium solubility is found in the tin, forming a metastable phase on its way to be attached to other scallops or contribute to the formation of η -Cu₆Sn₅ whiskers in the tin matrix. However, no visual evidence demonstrating this hypothesis has been published so far.

Both Gagliano and Fine (2001) and Suh *et al.* (2008) refer to excess Cu and migration of Cu atoms in the Cu(solid)/Sn(liquid) system on a theoretical basis, and do not report a copper-rich phase in their cooled experimental samples. This may suggest that this copper-rich phase is only present in the melt and that it is metastable during cooling to room temperature. In this experiment, small copper-rich ‘islands’ are observed predominantly in S13 and to a smaller extent in S15, which were annealed for 5 minutes only. These islands could be evidence of a metastable phase formed in the tin melt due to diffusion mechanisms first proposed by Gagliano and Fine (2001). This would be possible if cooling of the annealed tinned samples was too fast for the phase to transform to another stable phase.

This is an important finding, which requires further systematic investigation that is beyond the remit of this study, for two main reasons: (a) it could provide material evidence to support previously reported hypotheses on the diffusion of Cu atoms in the melt and the formation of tin whiskers, and (b) existence of a metastable phase in the cooled samples suggests that cooling of the samples was too fast and far from equilibrium conditions. Even if this unusual low-tin phase could exhibit different kinetical behaviour to η -Cu₆Sn₅, the latter point would indicate that kinetical constraints restrict the transformation of high temperature phases, namely η -Cu₆Sn₅ to η' -Cu₆Sn₅, to occur in common laboratory Cu-Sn diffusion experiments. This supports Laurila's *et al.* (2005) thesis and argues for the presence of the high temperature η -Cu₆Sn₅ rather than the low temperature η' -Cu₆Sn₅ in the experimental samples. Further experimental work and replication of the results is required in order to provide further insights on the presence of such a metastable phase.